Physics of Atomic Nuclei, Vol. 66, No. 4, 2003, pp. 599–611. Translated from Yadernaya Fizika, Vol. 66, No. 4, 2003, pp. 627–639.

NUCLEI
Experiment

Structure of the ^{90,94}Zr Nuclei: Global Analysis of Data on the Elastic and Inelastic Scattering of Alpha Particles and on the Total Cross Sections for the Reactions Induced by Their Interaction with These Nuclei

A. D. Duysebaev[1)], K. A. Kuterbekov[1)], I. N. Kuchtina[*], B. M. Sadykov[1)], L. I. Slusarenko[2)], V. V. Tokarevsky[3)], and S. A. Fayans[†]

Joint Institute for Nuclear Research, Dubna, Moscow oblast, 141980 Russia

Received November 21, 2001; in final form, May 7, 2002

Abstract—A global analysis of experimental data on the elastic and inelastic scattering of alpha particles by ^{90,94}Zr nuclei and on the total cross sections for their interaction with these nuclei is performed. The deformation lengths and the neutron-to-proton multipole-matrix-element ratios for the 2_1^+ and 3_1^- states of the ^{90,92,94,96}Zr nuclei are obtained for various projectile species, and a comparative analysis of these quantities is performed. With the aim of revealing the origin of the phase shifts found in the present study, experimental data on the inelastic scattering of 35.4-, 40.0-, 50.1-, and 65.0-MeV alpha particles on ^{90,94}Zr nuclei are analyzed on the basis of a unified approach. © *2003 MAIK "Nauka/Interperiodica".*

1. INTRODUCTION

The scattering of high-energy electrons on nuclei furnishes detailed information about the distribution of the protonic component in nuclei [1], while the scattering of alpha particles, which strongly interact with nuclei, makes it possible to study the distribution of nuclear matter in nuclei. A comparison of data from such experiments permits exploring distinctions between the neutron and the proton distributions in nuclei and their structure.

Experimental data on the quasielastic scattering of composite particles are the main source of information about the distribution of matter in nuclides and about the properties of nucleus–nucleus interaction.

The parameters of the optical potential that is employed to simulate alpha-particle interaction with medium-mass nuclei at low and intermediate energies are usually determined from an analysis of the angular distributions of elastic-scattering differential cross sections that is performed within the optical model, but the results obtained in this way suffer from ambiguities, so that reliable estimates are required in these realms. A global analysis of the angular distributions of differential cross sections for elastic scattering and total reaction cross sections makes it possible to impose constraints on the ambiguities in the optical-potential parameters, since data on differential and total cross sections are basic nuclear quantities derived within the optical model. There presently exist only a few studies where the angular distributions of differential cross sections for scattering and total reaction cross sections are simultaneously analyzed within the same model. The choice of optimum optical-potential parameters would make it possible to extract, at the next stage, reliable information about the structure of excited states of the nucleus being studied.

In the present article, we report the results obtained by measuring the angular distributions of 40.0- and 50.1-MeV alpha particles that undergo elastic or inelastic scattering on ^{90,94}Zr nuclei. The measurements were performed at the U-150M Kazakh isochronous cyclotron. We also quote new data from the U-240 Kiev isochronous cyclotron on the total cross sections for the reactions on the ^{90}Zr isotope that are induced by alpha particles of energy 96(1) MeV and by ^{3}He ions of energy 95(1) MeV. Within a unified approach, we analyze experimental data on the quasielastic scattering of 35.4-, 40.0-, 50.1-, and 65.0-MeV alpha particles (see [2, 3], [4], [5], and [6], respectively) on the even

[†]Deceased.
[1)]Institute of Nuclear Physics, National Nuclear Center of the Republic of Kazakhstan, Almaty, 480082 Republic of Kazakhstan.
[2)]Institute for Nuclear Research, National Academy of Sciences of Ukraine, pr. Nauki 47, Kiev, Ukraine.
[3)]Tekhnotsentr State Specialized Enterprise, Kiev, 03680 Ukraine.
[*]e-mail: innak@jinr.ru

Table 1. Total cross sections (in millibarn units) for the interaction of alpha particles and ^{3}He ions with a ^{90}Zr nucleus

Projectile type	E_α, MeV	σ_R	$\sigma_{\rm el}$	σ_{a_q}	σ_l
α	96	1833 ± 90	40 ± 20	130 ± 70	1923 ± 120
^{3}He	95	1895 ± 85	45 ± 10	280 ± 70	2130 ± 110

isotopes of Zr, as well as data on the total cross sections for the reactions between alpha particles of these energies and the isotopes in question. The data are analyzed on the basis of the deformed-optical-potential model by using the coupled-channel and distorted-wave methods and on the basis of the semimicroscopic folding model. A comparative analysis is performed for the deformation-length parameters δ_2^N and δ_3^N characterizing low-lying states of the nuclei being investigated and for the neutron-to-proton multipole-matrix-element ratios M_n/M_p as obtained in this and other studies, the analysis being based on different methods for different projectile particles. In the angular distributions of 40.0- and 50.1-MeV alpha particles undergoing inelastic scattering, the phase shifts are investigated for the 2_1^+ and 3_1^- states of the ^{90,94}Zr nuclei.

2. EXPERIMENTAL METHODS AND EXPERIMENTAL CROSS SECTION

At the isochronous cyclotron installed at the Institute of Nuclear Physics of the National Nuclear Center of the Republic of Kazakhstan (Almaty), the angular distributions of the differential cross sections for the elastic and inelastic scattering of 40.0- and 50.1-MeV alpha particles on ^{90,94}Zr nuclei were measured in the angular range 12°–75° (in the laboratory frame) with a step varying between 0.3° and 1°. The total energy resolution of the measuring apparatus was 0.8% of the projectile energy. Reaction products were recorded and identified by means of a system that relied on the ΔE–E procedure and which employed CAMAC and PC/AT equipment [7].

The total angular resolution of the α spectrometer was measured by the method proposed in [8], the result being 0.3°. It was shown that the systematic angular uncertainty $\delta\theta$ caused by the noncollinearity of the chamber axis and the projectile-beam axis was 0.5°, on average, and that it is necessary to measure it in each series of experiments.

For targets, we employed zirconium foils enriched in the ^{90}Zr (to 95%) or in the ^{94}Zr (to 91.2%) isotope, their thickness being 2.13(8) or 2.60(8) mg/cm^2, respectively.

The errors in the absolute cross-section values were between 3 and 8% for the elastic channel and between 7 and 10% for the inelastic channel.

For the elastic scattering of 40.0- and 50.1-MeV alpha particles on ^{90,94}Zr nuclei and for the inelastic scattering of such projectiles on the target nuclei in question that is accompanied by the excitation of the 2_1^+ and 3_1^- collective states of ^{90}Zr at 2186 and 2748 keV and the excitation of the 2_1^+ and 3_1^- collective states of ^{94}Zr at 920 and 2120 keV, the resulting angular distributions of the differential cross sections are displayed in Figs. 1 and 2 for, respectively, the first and the second energy value.

The experiment devoted to determining the total reaction cross sections was performed at the U-240 Kiev isochronous cyclotron at an alpha-particle energy of 96(1) MeV and at a ^{3}He energy of 95(1) MeV. The total cross sections for the reactions induced by alpha particles and ^{3}He ions were determined by the charge-integration method [9]. The layout of our experimental facility and the procedure used to obtain total reaction cross sections were described elsewhere [10].

The ^{90}Zr target that was used in the experiments aimed at measuring the total reaction cross sections and which was manufactured by the method of pressing was 75 ± 3.60 mg/cm^2 thick and was enriched to 96.8%. The target was characterized by a high mechanical strength, but it was not free from drawback. The porosity of the target was 26.5%, while its inhomogeneity at the place hit by the beam ranged between 5 to 7%.

Originally, experiments devoted to determining the total cross sections for the reactions occurring on a ^{90}Zr nucleus were performed at an alpha-particle energy of about 100 MeV [11]. Later on, the experiment was repeated at an energy of 96.0 MeV. The discrepancy between the results obtained in [11] and those that are presented here is due not only to the energy dependence but also to introducing improvements in the experimental procedure and to more correctly taking into account corrections.

The experimentally determined attenuation of the beam in the target, q/Q, is related to the total reaction cross section (σ_R) by the equation

$$\sigma_R = \frac{1}{nx}\left(\frac{q_m}{Q}\frac{q_{\rm bg}}{Q}\right) - 2\pi\int\limits_{\theta_2}^{\pi-\theta_1}\sigma_{\rm el}(\theta)\sin\theta d\theta \quad (1)$$

$$+ 2\pi\left(\int\limits_0^{\theta_1} + \int\limits_{\pi-\theta_1}^{\pi}\right)K\sigma_{a_q}(\theta)\sin\theta d\theta,$$

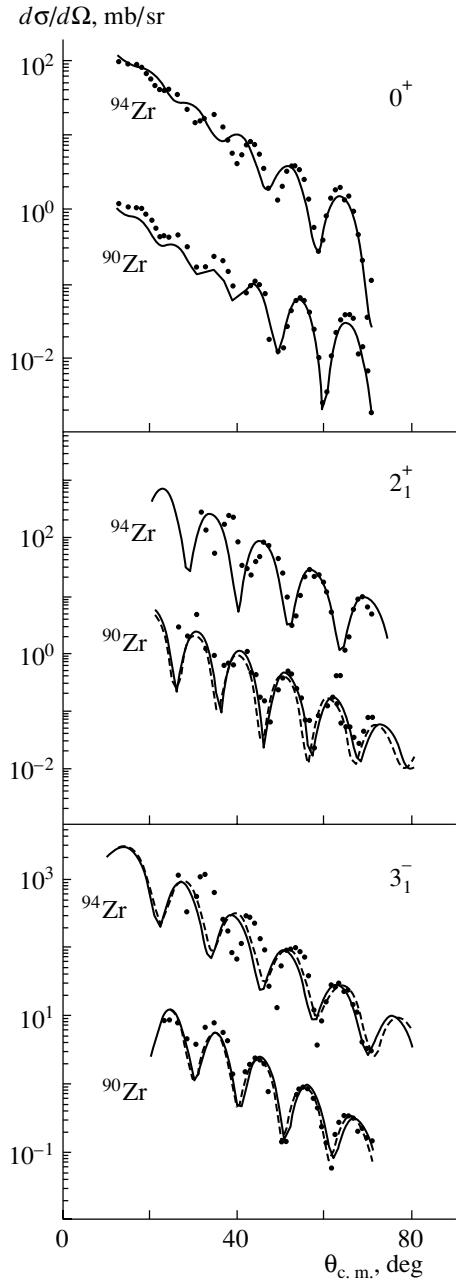

Fig. 1. Angular distributions for the elastic and inelastic scattering of alpha particles on ^{90,94}Zr nuclei at $E_\alpha =$ 40.0 MeV: (points) experimental data, (solid curves) results of a macroscopic analysis within the distorted-wave method (the values used for the relevant parameters are quoted in Table 5), and (dashed curves) results of the calculations with $r_v = 1.486$ fm for ^{90}Zr and with $r_v =$ 1.079 fm for ^{94}Zr (for ^{94}Zr, the theoretical angular distributions and experimental data were magnified in the figure by a factor of 10^2).

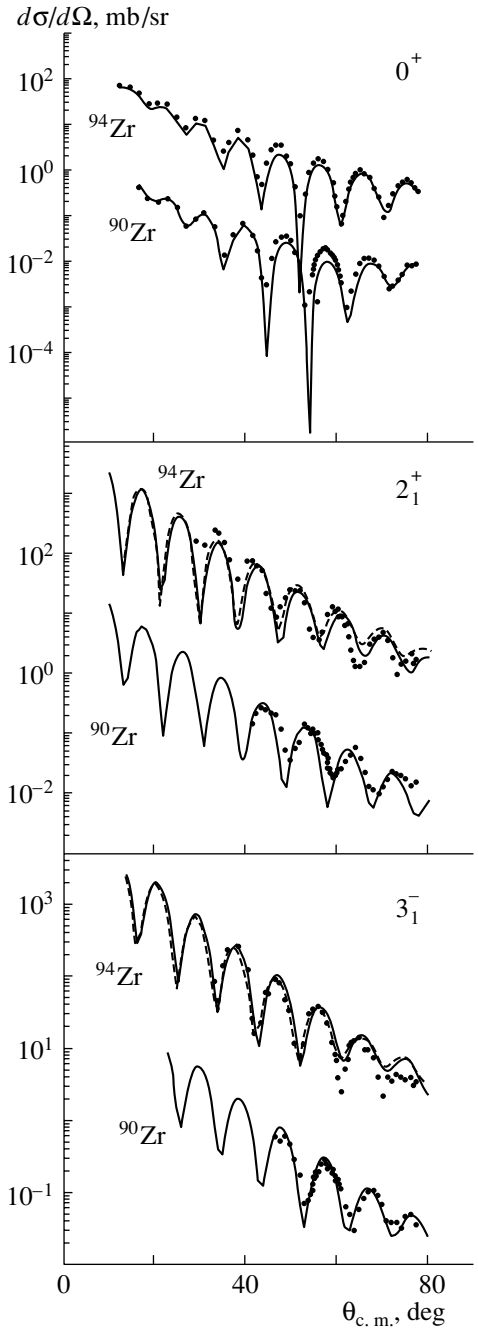

Fig. 2. As in Fig. 1, but at $E_\alpha = 50.1$ MeV.

where q_m is the total charge, which is proportional to the total number of nuclear collisions between projectile particles and target nuclei over the exposure time; $q_{\rm bg}$ is the background charge; Q is the total charge of projectile particles over the exposure time; x is the target thickness; n is the number of nuclei per unit volume of target substance; $\sigma_{\rm el}(\theta)$ is the differential cross section for elastic scattering at an angle θ; $\sigma_{a_q}(\theta)$ is the quantity that is obtained by integrating, with respect to energy, the differential cross section for the yield of charged particles of charge Z at an angle θ; K is the ratio of the charge of the product nucleus not detected by the counters used to the projectile-particle charge; θ_1 is the entrance aperture

Table 2. Total cross sections for the interaction of an alpha particle with a ^{90}Zr nucleus [13] at various energy values

E_α, MeV	σ_R, mb
40.0	1744, 1702
50.1	1856
79.5	1964
99.5	1966
104.0 [14]	2032
118.0	1982, 1979
141.7	1875
166.0	1946

of the scattering chamber ($\theta_1 = 6°$); and θ_2 is the exit aperture ($\theta_2 = 15°$).

The resulting experimental data on the total cross sections for the reactions occurring on a ^{90}Zr nucleus are presented in Table 1.

The "raw" values determined experimentally for the total reaction cross sections, σ_R, are given in the third column of the table, while the corrections for elastic scattering (recorded in the scattering chamber), $\sigma_{\rm el}$, and those for inelastic processes (not detected in the scattering chamber), σ_{a_q}, are quoted in the fourth and the fifth column, respectively. In the last column, we present values of the total reaction cross sections σ_l with allowance for all corrections. Previously, the analogous total reaction cross sections were measured for Zr targets of natural isotopic composition (51.46% ^{90}Zr, 17.40% ^{94}Zr, 17.11% ^{92}Zr, 11.23% ^{91}Zr, 2.8% ^{96}Zr) at an alpha-particle energy of 40.0 MeV [12]; for ^{3}He, there are presently no similar data.

3. THEORETICAL CALCULATIONS

3.1. Macroscopic Optical Model

In order to analyze experimental data on elastic scattering, we employed a deformed optical-model potential in the standard Woods–Saxon form

$$U_{\rm opt}(r) = -V_R f_R(r) - iW_v f_I(r) \qquad (2)$$
$$+ 4ia_I W_s (d/dr) f_I(r) + 2(\pi/mc)^2 (1/r)(d/dr)$$
$$\times V_{LS} f_{LS}(r)(\mathbf{L}\cdot\mathbf{S}) + V_{\rm Coul}(r),$$

$$R_i = r_i A^{1/3}, \quad f_i = (1 + \exp((r - R_i)/a_i))^{-1},$$
$$i = R, I, LS,$$

where the first term stands for the central part of the real potential; the second and the third term represent the potentials of, respectively, volume and surface absorption, and the next term is the potential of spin–orbit interaction. The last term in (2) is taken in the form of the Coulomb interaction of two charged spheres of radius $R_{\rm Coul} = r_{\rm Coul} A^{1/3}$, where $r_{\rm Coul} = 1.25$ fm.

Table 3. Total cross sections for the interaction of a ^{3}He ion with ^{90,92}Zr nuclei at various energy values

E_α, MeV	σ_R, mb	
	^{90}Zr	^{92}Zr
90 [15]	2072, 2180	2049
119 [16]	2002	
130 [17]	2083, 2093	
217 [18]	1850	

On the basis of the potential $U_{\rm opt}(r)$, one can determine the total reaction cross section by using S-matrix elements; that is,

$$\sigma_R = (\pi/k^2) \sum (2l+1)(1 - |S_l|^2), \qquad (3)$$

where summation is performed over all reaction channels.

Expression (2) involves a great number (from 9 to 12) of parameters; therefore, calculations of σ_R on the basis of the macroscopic optical model may possess a predictive power only if the optical-potential parameters are determined from the analysis of the corresponding angular distributions for elastic scattering. As was indicated in the Introduction, only a few measurements have been performed so far in which both the total reaction cross sections and the differential cross sections for elastic scattering were determined for the particles considered here.

The total reaction cross sections were calculated on the basis of the optical model with the optical-potential parameters determined from an analysis of data on elastic scattering at various energies.

At an energy of about 100 MeV, the geometric limit of the effective cross section seems to be achieved for the α + ^{90}Zr system. The distinction between the values calculated for σ_R on the basis of the optical model and their counterparts evaluated in the microscopic approximation proposed in [13] is within the experimental errors. The results obtained in [13] by calculating the total cross sections for (α, ^{90}Zr) reactions are quoted in Table 2. The calculations were performed with an optical potential where the form factors for the real and the imaginary part were chosen in the Woods–Saxon form (the notation employed for this potential is ОП–WS + WS). The potential

parameters were taken from an analysis of data on elastic scattering, so that no fit of the parameters was performed.

The results of the calculations of the total cross sections for the relevant (^{3}He, ^{90,92}Zr) reactions are given in Table 3, the relative errors in these calculations being 3–5%. For the energy values of 90, 119, and 130 MeV, the calculation was performed with an optical potential according to the OP–WS + W_D scheme (where W_D is the form factor for the imaginary part in the form of the derivative of the Woods–Saxon form factor), while, for the energy value of 217 MeV, use was made of the OP–WS + WS scheme.

3.2. Semimicroscopic Optical Model

In the approach used here, an optical potential $U(R)$ is constructed within the folding model on the basis of the total M3Y effective interaction and nucleon densities calculated by the method of the density-matrix functional [19]. In the first order in the effective forces, the potential simulating the interaction of two colliding nuclei can be represented as the sum

$$U(\mathbf{R}) = U^D(\mathbf{R}) + U^E(\mathbf{R}), \qquad (4)$$

where

$$U^D(\mathbf{R}) = \int\int \rho^{(1)}(\mathbf{r}_1)V^D(\mathbf{s})\rho^{(2)}(\mathbf{r}_2)d\mathbf{r}_1 d\mathbf{r}_2 \qquad (5)$$

is the direct potential in the form of double folding [20]. In expression (5), $V^D(\mathbf{s})$ is the direct component of the effective interaction ($\mathbf{s} = \mathbf{r}_2 - \mathbf{r}_1 + \mathbf{R}$), while $\rho^{(i)}(\mathbf{r}_i)$ stands for the densities of colliding nuclei ($i = 1, 2$). A similar scheme for computing the exchange potential $U^E(R)$ was formulated in [21]. The main contribution to it comes from one-nucleon-exchange effects, which are described within the density-matrix formalism [22]; that is,

$$U^E(\mathbf{R}) = \int\int \rho^{(1)}(\mathbf{r}_1, \mathbf{r}_1 + \mathbf{s})V_E(\mathbf{s})\rho^{(2)}(\mathbf{r}_2, \mathbf{r}_2 - \mathbf{s}) \times \exp(i\mathbf{k}(\mathbf{R})\cdot\mathbf{s}/\eta)d\mathbf{r}_1 d\mathbf{r}_2, \qquad (6)$$

where $V_E(\mathbf{s})$ is the exchange component of effective nucleon–nucleon forces; $\rho^{(i)}(\mathbf{r}, \mathbf{r}')$ ($i = 1, 2$) are the density matrices for colliding nuclei having the mass numbers of A_1 and A_2; $\mathbf{s} = \mathbf{r}_2 - \mathbf{r}_1 + \mathbf{R}$; and $\mathbf{k}(\mathbf{R})$ is the local momentum of relative motion of the nuclei, this momentum being given by the relation

$$k^2(\mathbf{R}) = (2m\eta/\hbar^2)[E - U(\mathbf{R}) - V_{\text{Coul}}(\mathbf{R})]. \qquad (7)$$

Here, $\eta = A_1A_2/(A_1 + A_2)$, E is the c.m. collision energy, and $V_{\text{Coul}}(\mathbf{R})$ is a Coulomb potential. Thus, the total potential becomes energy-dependent as the result of taking into account one-nucleon-exchange effects. The effective nucleon–nucleon forces, together with the proton and neutron densities in colliding nuclei, appear to be input data for calculating the potentials in question.

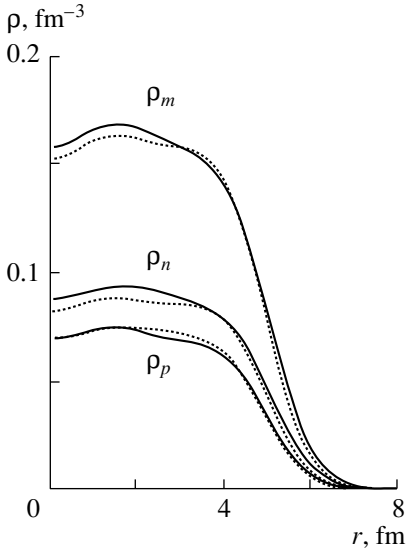

Fig. 3. Distributions of the neutron, the proton, and the nuclear-matter density in the (dotted curves) ^{90}Zr and (solid curves) ^{94}Zr nuclei.

In addition to a real part, the total optical potential must involve an imaginary part, which is responsible for the absorption of the incident particle in inelastic channels. In the case being considered, the absorption potential $W(R)$ was taken to be dependent on the calculated real part in the form [23]

$$W(R) = i[N_wU(R) - \alpha_wRdU(R)/dR], \qquad (8)$$

where $U(R)$ is the doubly folded potential (4), while N_w and α_w are parameters that characterize, respectively, the volume and the surface component of the absorption potential. A surface term that mimics the contribution of the dynamical polarization potential [24] was included in the real part of the potential.

Table 4. Root-mean-square radii (in femtometers) of the distributions of the neutron, proton, and nuclear-matter density (also given here are the values of $\Delta r_{np} = \langle r_n^2\rangle^{1/2} - \langle r_p^2\rangle^{1/2}$)

Nucleus	$\langle r_n^2\rangle^{1/2}$	$\langle r_p^2\rangle^{1/2}$	$\langle r_m^2\rangle^{1/2}$	Δr_{np}
^{4}He	1.57	1.57	1.57	0.00
^{90}Zr	4.26	4.19	4.23	0.07
^{94}Zr	4.37	4.24	4.31	0.13

Table 5. Parameters of a macroscopic optical potential

Nucleus	V, MeV	r_v, fm	a_v,fm	W, MeV	r_w, fm	a_w, fm
			$E_\alpha = 40.0$ MeV			
^{90}Zr	173.5	1.472	0.489	23.04	1.625	0.251
^{94}Zr	148.5	1.102	0.712	26.51	1.264	0.623
			$E_\alpha = 50.1$ MeV			
^{90}Zr	145.7	1.245	0.762	14.62	1.570	0.578
^{94}Zr	136.6	1.245	0.796	17.61	1.570	0.617

The total optical potential has the form

$$U_{\rm tot}(R) = U(R) - \alpha_v R dU(R)/dR + i[N_w U(R) - \alpha_w R dU(R)/dR], \quad (9)$$

where α_v, N_w, and α_w are adjustable parameters.

In order to calculate the cross sections for inelastic scattering, the inelastic-transition form factor was taken in the form $\alpha_L(dU_{\rm tot}(R)/dR)$ [25].

For alpha particles, the nucleon densities were computed in the Gaussian representation with the root-mean-square radius of 1.57 fm [26], while, for target nuclei, the corresponding densities were determined by applying the density-matrix formalism [25]. Figure 3 displays the graphs representing the distributions of the neutron, proton, and nuclear-matter densities in the ^{90,94}Zr target nuclei. The corresponding root-mean-square radii are given in Table 4. From the data in this table, it can be seen that the difference Δr_{np} of the root-mean-square radii of the neutron and the proton component in the ^{94}Zr nucleus exceeds its counterpart in the ^{90}Zr nucleus by a factor of 1.86.

Table 6. Values of the semimicroscopic-potential parameters and of relevant deformations

E_α, MeV	α_v	N_w	α_w	δ_L^N, fm	
				2_1^+	3_1^-
		^{90}Zr target nucleus			
35.4	−0.040	0.10	0.020	0.404	0.699
40.0	−0.020	0.13	0.020	0.484	0.939
50.1	−0.010	0.20	0.010	0.395	0.699
		^{94}Zr target nucleus			
35.4	−0.021	0.10	0.010	0.636	0.938
40.0	−0.020	0.13	0.020	0.754	1.056
50.1	−0.020	0.13	0.025	0.575	0.848
65.0	−0.020	0.13	0.045	0.575	1.056

Note: Here, α_v is a parameter that that characterizes the dynamical polarization potential; N_w and α_w are parameters that characterize, respectively, the volume and surface components of the absorption potential; and δ_L^N is the deformation length.

4. GLOBAL ANALYSIS OF EXPERIMENTAL DATA AND STRUCTURE OF EVEN–EVEN ZIRCONIUM ISOTOPES

Both in the calculations based on the macroscopic model and in the calculations based on the semimicroscopic model, the accuracy was chosen with allowance for the experimental uncertainties, and the relative theoretical error did not exceed 5%.

First, the experimental data were analyzed within the model of a deformed optical potential by using the SPI–GENOA code (F.G. Perey, NBI version, 1976) and within the distorted-wave method. For the input values of the optical-potential parameters, we used recommendations given in [27] for alpha-particle scattering. The global dependences obtained in [27] for the optical-potential parameters from data on the scattering of alpha particles whose energy does not

Table 7. Total cross sections for alpha-particle scattering on Zr isotopes

E_α, MeV	σ_R, mb		
	^{90}Zr target nucleus		^{94}Zr target nucleus
	1	2	3
35.4	1693		1684
40.0	1721	1744, 1771 ± 63 [12]	1801
50.1	1765	1856	1923
65.0			2084

Note: The total cross sections obtained in the calculations with a semimicroscopic potential are given in the first and third columns, while the total cross sections from Table 2 and from [12] are given in the second column.

exceed 80 MeV on light and medium-mass nuclei by using Woods–Saxon form factors were extrapolated in the present study to the region of energies being investigated. The Coulomb radius was taken to be fixed at $r_{\mathrm{Coul}} = 1.25$ fm. The optimum values of the remaining adjustable parameters are given in Table 5.

A subsequent analysis of the angular distributions of differential cross sections for inelastic scattering was performed on the basis of the distorted-wave method with the collective-model form factor according to the DWUCK4 [P.D. Kunz, computer program DWUCK4 (unpublished)]. The results obtained by fitting theoretical curves to experimental data are shown in Figs. 1 and 2. Both in our study and in [2, 3, 6], the experimental data are presented with errors not exceeding 10% (on the scale of the displayed figures, they do not go beyond the dimensions of the symbols representing experimental data).

Further, we have performed a semimicroscopic analysis of experimental data on elastic and inelastic alpha-particle scattering on ^{90,94}Zr nuclei at energies of 35.4, 40.0, 50.1, and 65.0 MeV [2–6]. The optimum values (see Table 6) of the parameters involved in this semimicroscopic analysis were obtained from a global analysis of the cross sections for elastic and inelastic scattering (accompanied by the excitation of 2_1^+ and 3_1^- levels in the latter case) and of the total reaction cross sections. Table 6 also gives the corresponding values of the deformation lengths (δ_L^N). In calculating the cross sections, we took into account errors in the experimental data. A fit of the calculated cross sections to experimental data is of a rather qualitative character, since it seemed important, above all, to reveal a trend in the variation of the parameters characterizing reaction channels other than those of elastic and inelastic scattering versus the projectile energy.

Figures 4–7 present the results obtained by fitting the calculated differential cross sections to their experimental counterparts. The theoretical results are found to agree satisfactorily with the experimental data for elastic and inelastic channels (the states excited in the latter case are those of spin–parity 2_1^+ and 3_1^-), the fitted values of the parameters N_w, α_v, and α_w changing only slightly in the energy range 35.4–65.0 MeV being considered. It is worth noting that variations in the parameter values do not affect the cross sections for elastic scattering at angles not exceeding 30°. This may suggest that, at small angles, only elastic scattering occurs in this energy range. The theoretical total cross sections σ_R calculated in the present study on the basis of the semimicroscopic approach and the total cross sections from Table 2 that allow for the energy dependence are given in Table 7; also quoted there are the cross sections from [12]. The agreement between the cross-section values within the errors confirms once again that the theoretical cross sections computed within the semimicroscopic approach that was outlined above are quite reliable.

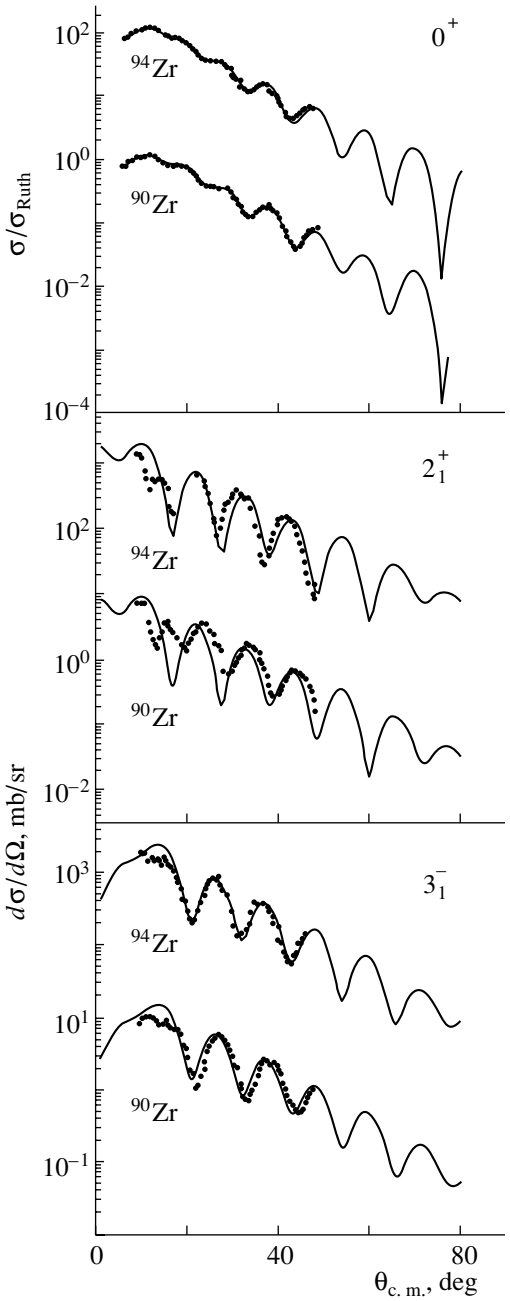

Fig. 4. Angular distributions for the elastic and inelastic scattering of alpha particles on ^{90,94}Zr at $E_\alpha = 35.4$ MeV [2, 3]: (points) experimental data and (solid curves) results of a semimicroscopic analysis (for ^{94}Zr, the theoretical results for the angular distributions and the experimental data were magnified by a factor of 10^2).

Table 8 presents the values of the deformation lengths δ_2^N and δ_3^N for low-lying states of the nu-

Table 8. Comparison of data on $B(EL)\uparrow$, δ_L^N, M_n/M_p, and N/Z for even isotopes of Zr

$B(EL)\uparrow$, e^2 b^L	δ_L^N, fm	Particle; E_α, MeV	Method of calculations	M_n/M_p	References
		2_1^+ state			
		^{90}Zr nucleus, $N/Z = 1.25$, $E^* = 2.186$ MeV			
0.063 ± 0.005	0.404 ± 0.020	α; 35.4	CC, SMA	0.85 ± 0.12	Present study
0.063 ± 0.005	0.484	α; 40	CC, SMA	1.22 ± 0.11	Present study
0.063 ± 0.005	0.395	α; 50	CC, SMA	0.81 ± 0.13	Present study
0.063 ± 0.005	0.400 ± 0.020	α; 35.4	CC, DOMP	0.84 ± 0.12	[3]
0.063 ± 0.005	0.440 ± 0.022	α; 35.4	CC, FM	1.04 ± 0.13	[3]
0.063 ± 0.005	0.396	^{6}Li; 70	CC, FM	0.82 ± 0.12	[3]
0.062 ± 0.006	0.408 ± 0.016	α; 35.4	DWBA, CC	1.22 ± 0.12	[2]
0.063 ± 0.005	0.389	t; 20	DWBA	0.78 ± 0.11	[28]
0.063 ± 0.005	0.376	p; 18.8	DWBA	0.72 ± 0.10	[28]
0.063 ± 0.005	0.370	^{3}He; 43.7	DWBA	0.70 ± 0.10	[29]
	0.44 ± 0.03	n; 8–24	CC	0.85 ± 0.06	[30]
		^{92}Zr nucleus, $N/Z = 1.30$, $E^* = 0.934$ MeV			
0.075 ± 0.010	0.673 ± 0.034	α; 35.4	CC, DOMP	1.93 ± 0.24	[3]
0.080 ± 0.010	0.758 ± 0.038	α; 35.4	CC, FM	2.22 ± 0.26	[3]
0.083 ± 0.006	0.557	^{6}Li; 70	CC, FM	1.38 ± 0.19	[3]
0.069 ± 0.006	0.731 ± 0.016	α; 35.4	DWBA, CC	2.91 ± 0.19	[2]
0.075 ± 0.010	0.616	t; 20	DWBA	1.65 ± 0.24	[31]
	0.66 ± 0.03	n; 8–24	CC	1.05 ± 0.07	[30]
		^{94}Zr nucleus, $N/Z = 1.35$, $E^* = 0.918$ MeV			
0.058 ± 0.010	0.636 ± 0.032	α; 35.4	CC, SMA	2.18 ± 0.21	Present study
0.058 ± 0.010	0.754	α; 40	CC, SMA	2.77 ± 0.28	Present study
0.058 ± 0.010	0.575	α; 50	CC, SMA	1.87 ± 0.19	Present study
0.058 ± 0.010	0.575	α; 65	CC, SMA	1.87 ± 0.19	Present study
0.058 ± 0.010	0.632 ± 0.032	α; 35.4	CC, FM	2.21 ± 0.32	[3]
0.050 ± 0.005	0.633 ± 0.016	α; 35.4	DWBA, CC	3.02 ± 0.22	[2]
0.058 ± 0.010	0.451	t; 20	DWBA	1.45 ± 0.19	[31]
0.058 ± 0.010	0.860	p; 18.8	DWBA	3.30 ± 0.46	[28]
0.058 ± 0.010	0.557	^{3}He; 43.7	DWBA	1.78 ± 0.27	[29]
	0.65 ± 0.05	n; 8–24	CC	1.50 ± 0.22	[30]
		^{96}Zr nucleus, $N/Z = 1.40$, $E^* = 1.751$ MeV			
0.025 ± 0.005	0.589 ± 0.030	α; 35.4	CC, DOMP	3.70 ± 0.53	[3]
0.022 ± 0.005	0.621 ± 0.031	α; 35.4	CC, FM	4.34 ± 0.67	[3]
0.055 ± 0.022	0.466	^{6}Li; 70	CC, FM	1.44 ± 0.22	[3]
0.027 ± 0.006	0.639 ± 0.003	α; 35.4	DWBA, CC	4.69 ± 0.64	[2]
0.027 ± 0.006	0.341	t; 20	DWBA	1.55 ± 0.23	[31]

Table 8. (Contd.)

$B(EL)\uparrow$, $e^2\,\mathrm{b}^L$	δ_L^N, fm	Particle; E_α, MeV	Method of calculations	M_n/M_p	References
3_1^- state					
^{90}Zr state, $N/Z = 1.25$, $E^* = 2.748$ MeV					
0.051 ± 0.092	0.699 ± 0.038	α; 35.4	CC, SMA	0.63 ± 0.06	Present study
0.051 ± 0.092	0.939	α; 40	CC, SMA	1.19 ± 0.11	Present study
0.051 ± 0.092	0.699	α; 50	CC, SMA	0.63 ± 0.11	Present study
0.051 ± 0.091	0.750 ± 0.038	α; 35.4	CC, DOMP	0.75 ± 0.09	[3]
0.051 ± 0.091	0.947 ± 0.047	α; 35.4	CC, FM	1.31 ± 0.11	[3]
0.071	0.686	^{6}Li; 70	CC, FM	0.35 ± 0.05	[3]
0.066 ± 0.007	0.806 ± 0.007	α; 35.4	DWBA, CC	1.80 ± 0.31	[2]
0.051 ± 0.092	0.667	t; 20	DWBA	0.55 ± 0.08	[31]
	0.86 ± 0.05	n; 8–24	CC	0.92 ± 0.13	[30]
^{92}Zr nucleus, $N/Z = 1.30$, $E^* = 2.340$ MeV					
0.047 ± 0.087	0.831 ± 0.042	α; 35.4	CC, DOMP	1.07 ± 0.10	[3]
0.047 ± 0.087	1.024 ± 0.051	α; 35.4	CC, FM	1.68 ± 0.13	[3]
0.067	0.742	^{6}Li; 70	CC, FM	0.54 ± 0.08	[3]
0.056 ± 0.008	0.894 ± 0.005	α; 35.4	DWBA, CC	2.17 ± 0.45	[2]
0.056 ± 0.008	0.784	t; 20	DWBA	0.78 ± 0.12	[31]
	0.88 ± 0.04	n; 8–24	CC	1.20 ± 0.13	[30]
^{94}Zr nucleus, $N/Z = 1.35$, $E^* = 2.057$ MeV					
0.067 ± 0.012	0.938 ± 0.047	α; 35.4	CC, SMA	0.99 ± 0.10	Present study
0.067 ± 0.012	1.056	α; 40	CC, SMA	1.24 ± 0.12	Present study
0.067 ± 0.012	0.848	α; 50	CC SMA	1.01 ± 0.12	Present study
0.067 ± 0.012	1.056	α; 65	CC, SMA	1.24 ± 0.12	Present study
0.067 ± 0.107	0.932 ± 0.047	α; 35.4	CC, DOMP	1.11 ± 0.11	[3]
0.067 ± 0.107	1.124 ± 0.056	α; 35.4	CC, FM	1.68 ± 0.13	[3]
0.079 ± 0.012	1.020 ± 0.006	α; 35.4	DWBA, CC	2.36 ± 0.51	[2]
0.067 ± 0.012	0.846	t; 20	DWBA	2.23 ± 0.33	[31]
	0.94 ± 0.05	n; 8–24	CC	1.59 ± 0.20	[30]
^{96}Zr nucleus, $N/Z = 1.40$, $E^* = 1.897$ MeV					
0.080 ± 0.160	1.111 ± 0.056	α; 35.4	CC, DOMP	1.22 ± 0.11	[3]
0.060 ± 0.180	1.330 ± 0.067	α; 35.4	CC, FM	1.82 ± 0.12	[3]
0.104 ± 0.011	1.228 ± 0.011	α; 35.4	DWBA, CC	2.67 ± 0.47	[2]
0.104 ± 0.011	0.908	t; 20	DWBA	0.58 ± 0.09	[31]

Note: The following notation is used for the methods of the calculations: (CC, SMA) approach combining the coupled-channel method with a semimicroscopic analysis; (CC, DOMP) macroscopic coupled-channel method used together with a deformed optical-model potential; (CC, FM) coupled-channel method combined with the folding model; (DWBA) distorted-wave method implemented within the Born approximation; and (CC) coupled-channel method.

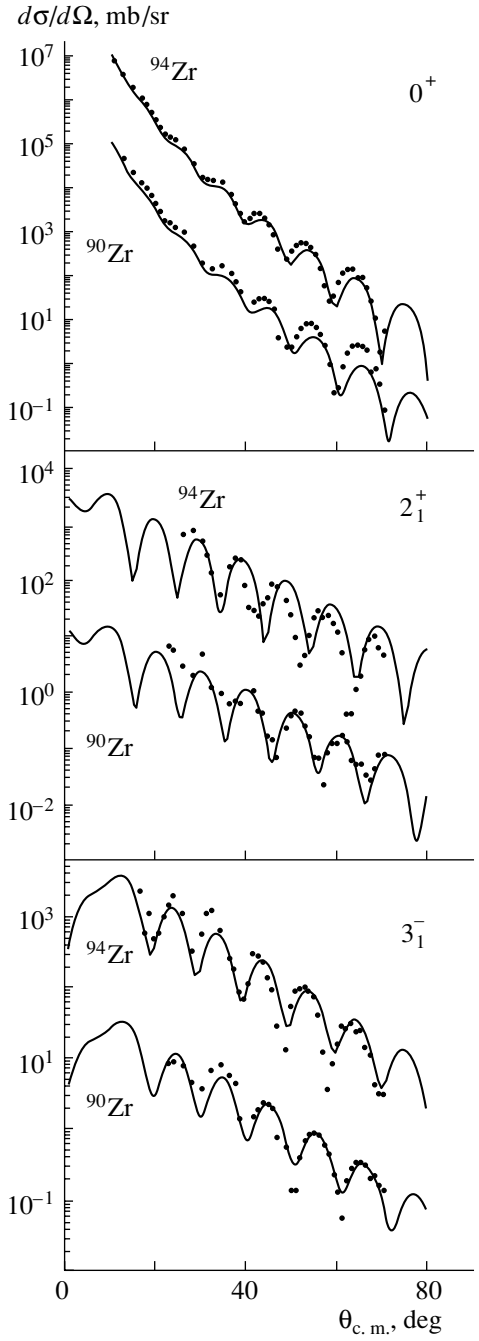

Fig. 5. As in Fig. 4, but for $E_\alpha = 40.0$ MeV [4].

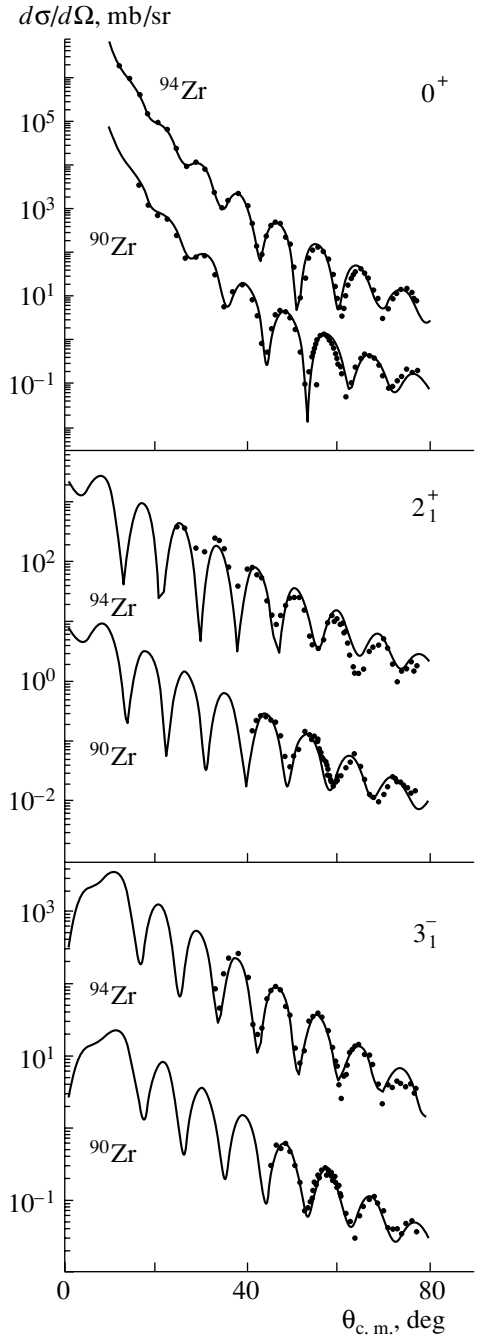

Fig. 6. As in Fig. 4, but for $E_\alpha = 50.1$ MeV [5].

clei being investigated and the values of the proton-to-neutron multipole-matrix-element ratios M_n/M_p. These values were obtained from the present analysis and analyses performed in other studies by using various methods. Also given in this table is information for different projectile species (α, ^{3}He, p, n, t, ^{6}Li), which exhibit different degrees of sensitivity to the neutronic and protonic components of the deformation lengths and of the ratios M_n/M_p. For the 2^+_1 and 3^-_1 states of the ^{90,94}Zr nuclei, both models, the macroscopic and the microscopic one, yield values of $B(EL)$ that are in good agreement with data obtained from measurements of Coulomb excitation [32] and data obtained according to the procedure for determining the lifetimes of nuclear states (levels) [33]. The values of M_n/M_p for the 2^+_1 states of ^{92,94,96}Zr are 1.1 to 3.4 times greater than the corresponding ratios N/Z, while that for the 2^+_1 state of ^{90}Zr is, on the

contrary, 0.60 to 0.98 of the corresponding value of N/Z. For the 3_1^- state of the ^{90}Zr nucleus, the ratio M_n/M_p is less than the corresponding ratio N/Z by a factor ranging between 0.28 and 0.96.

For the 3_1^- states of the ^{90,92,94,96}Zr nucleus, values were obtained in [2] for M_n/M_p that exceed the corresponding ratios N/Z by a factor of 1.4 to 1.9; in other studies (see the data in Table 8, including our results), M_n/M_p is less than N/Z by a factor ranging between 0.4 to 0.9.

By inspecting the data in Table 8, one can see that the values obtained within our semimicroscopic approach for the deformation lengths δ_2^N and δ_3^N in ^{90,94}Zr are nearly identical to or are 5 to 10% greater than the corresponding values that are extracted from experimental data (for other projectile species) by using a deformed optical-model potential within the coupled-channel or the distorted-wave method.

For the 2_1^+ and 3_1^- states of the ^{90,92,94,96}Zr nuclei, Horen *et al.* [34] present values that they found for relevant M_n/M_p by means of a microscopic description (in terms of the theory of finite Fermi systems) of experimental data from [3]. Those authors showed that, in the 2_1^+ and 3_1^- states of the ^{92,94,96}Zr nuclei, the neutronic component is more deformed than the protonic one, the ratios M_n/M_p being greater than the corresponding N/Z; in the 2_1^+ states of the ^{90}Zr nucleus, the protonic component is more deformed than the neutronic one ($M_n/M_p = 0.874$), while, in its 3_1^- state, the situation is reversed ($M_n/M_p = 1.047$).

5. PHASE SHIFTS IN THE ANGULAR DISTRIBUTIONS FOR DIFFRACTIVE ALPHA-PARTICLE SCATTERING ON Zr ISOTOPES

The experimental phase shifts between the oscillations of the angular distributions of the differential cross sections for the inelastic scattering of 50-MeV alpha particles on ^{90,94}Zr nuclei were investigated in [27]. The analyses reported in [3, 35] gave new impetus to studying phase shifts. In analyzing data from [2], Satchler [35] found phase shifts of about 1° between the calculated and measured cross sections for the 2_1^+ states of the ^{92,96}Zr nuclei, the former being obtained on the basis of a deformed optical-model potential and the folding model.

For the 2_1^+ and 3_1^- states of the ^{90,94}Zr nuclei, the phase shifts in the angular distributions for inelastic alpha-particle scattering at energies of 40.0 and 50.1 MeV were studied in [27, 36]. The data were analyzed within the model of a deformed optical potential by using the distorted-wave method (DWUCK4 code) and the coupled-channel method [ECIS-88 code: J. Raynal, ECIS-88 (unpublished)]. For ^{94}Zr, the calculations that include 2_1^+ and 3_1^- states yield phase-shift values of 0.5°. At 40.0 MeV, a good description of the angular distributions of differential cross sections for the inelastic channels involving the excitation of the 2_1^+ and 3_1^- states in ^{90}Zr and ^{94}Zr (with a "compensation" of the phase shift) was obtained in the present study by increasing the radius

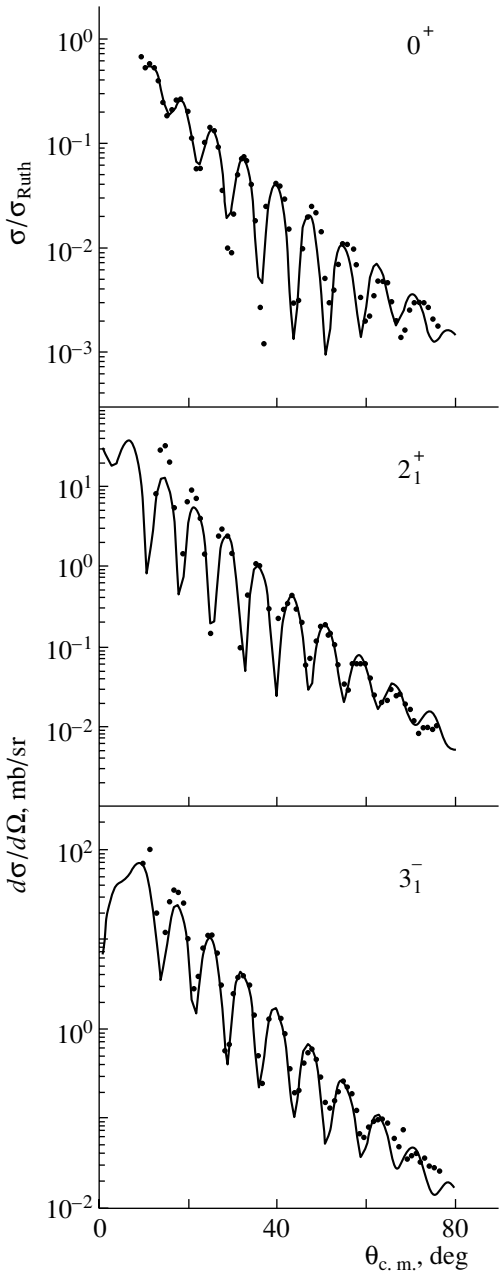

Fig. 7. Angular distributions for the elastic and inelastic scattering of alpha particles on ^{94}Zr nuclei at $E_\alpha = 65.0$ MeV [6]: (points) experimental data and (solid curves) results of a semimicroscopic analysis.

r_v of the real part, respectively, from 1.472 to 1.486 fm and from 1.102 to 1.079 fm (dashed curves in Fig. 1), which is about 1 to 2%. It should be emphasized that, in our measurements, the angular distributions of the differential cross sections were determined at favorable angular parameters (small step in the angle, high angular resolution, presence of a "physical" zero, reproducibility). At angles exceeding 40°, the effect of Coulomb interference on the presence of phase shifts is insignificant at the energy values of 40.0 and 50.1 MeV.

With the aim of revealing the origin of the phase shifts observed between the oscillations of the angular distributions of the differential cross sections for inelastic alpha-particle scattering and the origin of their energy and mass dependences, we have also performed a semimicroscopic analysis (see Figs. 4–7) at the energy values of 35.4, 40.0, 50.1, and 65.0 MeV for scattering on ^{90,94}Zr nuclei. The occurrence of this effect and its weak energy dependence have been confirmed. With increasing mass number of the nucleus, the phase shift in question becomes more pronounced.

To explain the observed effect in an alternative way, one can also assume, following [3], that the potential parameters take different values in the input and in the output channel. This assumption is valid if the density distribution in excited states differs from its counterpart in the ground state. According to the calculations performed in [3] with identical density distributions for the ground and excited states of the ^{90,92,94,96}Zr nuclei, whose diffuseness parameters were taken to be different (the phase shifts for the 2_1^+ and 3_1^- states being concurrently matched), the diffuseness parameter undergoes changes ranging between -10% for the 2_1^+ state of ^{90}Zr and $+18\%$ for the 2_1^+ state of ^{96}Zr.

6. CONCLUSION

For the first time, results have been presented that were obtained by measuring the angular distributions of the differential cross sections for the elastic and inelastic scattering of 40.0-MeV alpha particles on nuclei of the ^{90,94}Zr isotopes. The measurements were performed by using the U-150M isochronous cyclotron installed at the National Nuclear Center of the Republic of Kazakhstan (Almaty). Also, new experimental data have been reported that were obtained at the U-240 Kiev isochronous cyclotron on the total cross sections for reactions induced in the ^{90}Zr isotope by alpha particles accelerated to an energy of 96(1) MeV and by ^{3}He ions accelerated to an energy of 95(1) MeV. A global analysis (employing the optical model, the distorted-wave method, and the semimicroscopic model) of data on the angular distributions of the differential cross sections for alpha-particle scattering on even zirconium isotopes at energies of 35.4 MeV [2, 3], 40.0 MeV [4], 50.1 MeV [5], and 65.0 MeV [6] and of the total cross sections for reactions induced by such collisions has been performed.

We have carried out a comparative analysis of data obtained, by using various methods and various projectile species, for the deformation lengths δ_2^N and δ_3^N of low-lying states of the ^{90,92,94,96}Zr nuclei and for the neutron-to-proton multipole-matrix-element ratios M_n/M_p.

In analyzing the experimental angular distributions of the differential cross sections for the inelastic scattering of 40.0- and 50.1-MeV alpha particles, it has been revealed that, for the channels involving the excitation of the 2_1^+ and 3_1^- states of the ^{90,94}Zr nuclei, there is a phase shift between the experimental and calculated oscillations. It has been shown that this effect may be explained in terms of a change of 2% in the radius of the real part of the optical potential. These results supplement the data obtained in [3] by studying the phase shifts in question at the alpha-particle energy of 35.4 MeV.

ACKNOWLEDGMENTS

We are grateful to V. Z. Goldberg for stimulating discussions.

This work was supported in part by the Russian Foundation for Basic Research (project no. 0001-00617).

REFERENCES

1. A. M. Bernstein, V. R. Brown, and V. A. Madsen, Phys. Lett. B **103B**, 255 (1981); J. Heisenberg, J. Dawson, T. Milliman, *et al.*, Phys. Rev. C **29**, 97 (1984).
2. A. D. Rychel *et al.*, Z. Phys. A **326**, 455 (1987).
3. B. J. Lund *et al.*, Phys. Rev. C **51**, 635 (1995).
4. K. A. Kuterbekov, B. M. Sadykov, and A. D. Duysebaev, in *Proceedings of the International Conference on Nuclear Physics "Clustering Phenomena in Nuclear Physics," St. Petersburg, Russia, 2000*, p. 329.
5. K. A. Kuterbekov and A. V. Yushkov, Izv. Akad. Nauk SSSR, Ser. Fiz. **53**, 2098 (1989); R. B. Firestone, *Table of Isotopes*, 8th ed. (Wiley, New York, 1999).
6. C. R. Bingham, M. L. Halbert, and R. H. Bassel, Phys. Rev. **148**, 1174 (1966).
7. S. Ya. Aisina, K. A. Kuterbekov, V. N. Tolstikov, *et al.*, Preprint No. 2-82, Inst. of Nuclear Physics, Academy of Sciences of Kazakstan (Alma-Ata, 1987); A. D. Duisebaev, G. N. Ivanov, and V. N. Tolstikov, *Records of the 3rd All-Union Seminar on*

Automatization of Research Activities into the Nuclear Physics and Nearby Areas, Tbilisi, 1984, p. 164.
8. K. A. Kuterbekov and A. V. Yushkov, Prib. Tekh. Éksp., No. 3, 35 (1986).
9. K. Bearpark, W. R. Gracham, and G. Jones, Nucl. Instrum. Methods **35**, 235 (1965).
10. O. F. Nemets, L. I. Slyusarenko, and V. V. Tokarevskiĭ, Fiz. Élem. Chastits At. Yadra **6**, 827 (1975) [Phys. Part. Nucl. **6**, 335 (1975)].
11. L. N. Gorovenko, V. N. Domnikov, L. V. Dubar, *et al.*, Izv. Akad. Nauk SSSR, Ser. Fiz. **52**, 919 (1988).
12. G. Igo and B. Wilkins, Phys. Rev. **131**, 1251 (1963).
13. R. M. De Vries and J. C. Peng, Phys. Rev. C **22**, 1055 (1980).
14. G. Hauser, R. Lohken, R. Rebel, *et al.*, Nucl. Phys. A **128**, 81 (1969).
15. N. Matsuoka, K. Hatanaka, M. Fujiwara, *et al.*, Nucl. Phys. A **373**, 377 (1982).
16. M. Haykutake, I. Kumade, M. Fukada, *et al.*, Nucl. Phys. A **333**, 1 (1980).
17. H. Djaloeis, J.-P. Dideler, A. Galonsky, and W. Oelert, Nucl. Phys. A **306**, 221 (1978).
18. N. Willis, I. Brissaud, and Y. Le Bornec, Nucl. Phys. A **204**, 454 (1973).
19. O. M. Knyazkov, I. N. Kuchtina, and S. A. Fayans, Fiz. Élem. Chastits At. Yadra **30**, 870 (1999) [Phys. Part. Nucl. **30**, 369 (1999)].
20. G. R. Satchler, *Direct Nuclear Reactions* (Oxford Univ., New York, 1983).
21. O. M. Knyazkov, I. N. Kuchtina, and S. A. Fayans, Fiz. Élem. Chastits At. Yadra **28**, 1061 (1997) [Phys. Part. Nucl. **28**, 418 (1997)].
22. A. K. Ghaudhuri, D. N. Basu, and B. Sinha, Nucl. Phys. A **439**, 415 (1985).
23. S. A. Fayans, O. M. Knyazkov, I. N. Kuchtina, *et al.*, Phys. Lett. B **357**, 509 (1995).
24. D. B. Bolotov, O. M. Knyazkov, I. N. Kuchtina, and S. A. Fayans, Yad. Fiz. **63**, 1631 (2000) [Phys. At. Nucl. **63**, 1546 (2000)].
25. I. Tanihata *et al.*, Phys. Lett. B **206**, 592 (1988).
26. M. Nolte, H. Machner, and J. Bojowald, Phys. Rev. C **36**, 1312 (1987).
27. K. A. Kuterbekov, S. J. Aysina, and A. V. Yushkov, in *Proceedings of the International Conference on Nuclear Physics, the 40th Meeting on Nuclear Spectroscopy and Nuclear Structure, Leningrad, USSR, 1990*, p. 266.
28. W. S. Gray, R. A. Kenefick, and J. J. Kraushaar, Phys. Rev. **142**, 735 (1966).
29. E. F. Gibson *et al.*, Phys. Rev. **155**, 1208 (1967).
30. Y. Wang and J. Rapaport, Nucl. Phys. A **517**, 301 (1990).
31. E. R. Flynn, D. D. Armstrong, and J. G. Beery, Phys. Rev. C **1**, 703 (1970).
32. S. Raman *et al.*, At. Data Nucl. Data Tables **36**, 1 (1987).
33. D. J. Horen *et al.*, Phys. Rev. C **48**, 433 (1993).
34. D. J. Horen *et al.*, Nucl. Phys. A **600**, 193 (1996).
35. G. R. Satchler, Phys. Rev. C **51**, 635 (1995).
36. K. A. Kuterbekov, in *Proceedings of the International Conference on Nuclear Physics "Clustering Phenomena in Nuclear Physics," St. Petersburg, Russia, 2000*, p. 328.

Translated by A. Isaakyan

Physics of Atomic Nuclei, Vol. 66, No. 4, 2003, pp. 612–617. Translated from Yadernaya Fizika, Vol. 66, No. 4, 2003, pp. 640–646.

NUCLEI
Experiment

Thermonuclear Fusion in the Irradiation of Large Clusters of Deuterium Iodide with a Field of a Superatomic Femtosecond Laser Pulse

V. P. Krainov[1] and M. B. Smirnov[2]

Received April 12, 2002; in final form, June 7, 2002

Abstract—A theory of thermonuclear fusion caused by the irradiation of deuterium-iodide clusters with the field of a superatomic femtosecond laser pulse is developed. It is based on considering the process in which the sequential above-barrier multiple internal ionization of atomic ions within a cluster is accompanied by external field ionization. The theory is illustrated by taking the example of a cluster that is formed by 10^6 molecules of deuterium iodide and which is irradiated with a laser pulse of duration 50 fs and intensity 2×10^{18} W/cm^2 at the peak. This case is dominated by I^{26+} atomic ions. The yield of neutrons from thermonuclear fusion in a deuteron–deuteron collision upon the passage of a laser pulse is calculated. The result is 10^5 neutrons per laser pulse. The mean kinetic energy of deuterons is estimated at 50 keV. Owing to induced inverse bremsstrahlung in scattering on multiply charged atomic ions, the electron temperature increases up to 28 keV. The role of the Mie resonance in the heating of the electron component is discussed.

1. INTRODUCTION

The interaction of superintense laser pulses with large clusters consisting of molecules differs substantially from the interaction of such pulses with individual molecules. Upon the multiple ionization of atoms forming molecules, there arises, in the cluster, a strong internal electric field, which can itself efficiently give rise to a further internal ionization of atomic ions.

The problem being considered is quite involved, since there occur simultaneously (during the passage of a laser pulse) a sizable Coulomb expansion of the ionized cluster and the heating of the electron component of the cluster to a temperature of a few tens of keV units. Moreover, there also occurs an external ionization—that is, the emission of photoelectrons produced within the cluster outside. This results in that, immediately after the passage of a laser pulse, the substance at the focus of the laser beam appears to be quite a uniform plasma consisting of free electrons and multiply charged atomic ions. However, the exchange of energy between them is negligible because the lifetime of the plasma at the laser-beam focus is very short (about 100 ps).

There is an important theoretical problem of calculating the spectral distribution of product atomic ions with respect to their charge. This problem is very involved since, as was indicated above, the stripping of atomic ions at the forward front of a laser pulse is due not only to the laser-pulse field but also to the Coulomb field of the ionized cluster. At the same time, the standard statistical approach based on the Saha distribution [1] is inapplicable since slow recombination processes do not have time to proceed within the laser-pulse duration, which is not longer than a few tens of femtoseconds.

At the leading edge of a pulse, there usually occurs a sequential above-barrier ionization of atoms [2], which is followed by the ionization of atomic ions by the laser field.

The external ionization of a cluster is predominantly a field (cold) ionization. The role of thermal ionization according to the Richardson–Dashman law is insignificant because of a large positive ionized-cluster charge, which hinders the thermal evaporation of electrons from the cluster surface.

The main problem to be solved in the present study consists in determining the charge state of atomic ions in the cluster plasma produced upon the irradiation of clusters with a field of a superatomic femtosecond laser pulse.

For a typical object, we consider clusters consisting of deuterium iodide molecules. They are formed in a process where gaseous deuterium iodide preliminarily compressed to a pressure ranging between 3 and 8 atm escapes adiabatically through a nozzle into a vacuum. The temperature in this case decreases sharply. The dimensions of the product clusters grow

[1]Moscow Institute for Physics and Technology, Dolgoprudnyi, Moscow oblast, 141980 Russia; e-mail: krainov@online.ru

[2]Institute of Molecular Physics, Russian Research Centre Kurchatov Institute, pl. Kurchatova 1, 123182 Russia.

with increasing pressure. The diameter of the clusters is measured by investigating Rayleigh scattering. We assume that the substance in a cluster is in a liquid state. By way of example, we indicate that, for DI, the density in the liquid state is 2.87 g/cm^3. Its boiling temperature is -35.4°C.

Experiments were performed with hydrogen-iodide clusters [3, 4]. For purposes of thermonuclear fusion, the group headed by Ditmire employed clusters of pure deuterium [5]. The role of iodine that we propose to add would consist in that the multiple ionization of iodine atoms may considerably enhance the Coulomb explosion of a cluster, thereby increasing the kinetic energy of product deuterons and the cross section for the thermonuclear-fusion reaction $d + d = {}^3\mathrm{He} + n$.

The radius of of a liquid cluster (it is assumed to be spherical, which is confirmed by experiments that studied the Rayleigh scattering of light on clusters) containing 10^6 molecules is 261 Å. As will be seen below, the thickness of the skin layer either exceeds this value or is on the same order of magnitude with it; therefore, it can be assumed that the electromagnetic field of a laser pulse penetrates freely through an individual cluster. It goes without saying that, since there are a great number of such clusters at the laser-beam focus, laser radiation is strongly absorbed, which is observed experimentally [6].

In the process of multiple ionization, the concentration of free electrons within a cluster plasma is rather high; therefore, laser radiation ceases to penetrate into the plasma even at the trail edge of the laser pulse (where clusters virtually disappear, so that a cluster plasma becomes uniform), since the frequency of laser radiation becomes lower than the plasma frequency $\sqrt{4\pi n_e e^2/m_e}$ (here, n_e is the concentration of free electrons in the plasma).

The above considerations illustrate a wide variety of processes occurring in the interaction of superintense ultrashort laser pulses with large molecular clusters. In order to analyze such processes, we must therefore have at our disposal models that would make it possible to assess, to a high degree of precision, the charge composition of atomic ions at the forward front of a laser pulse and farther in the cluster plasma (before the commencement of recombination processes). This issue is of practical importance for pursuing further investigations of the line-shaped electromagnetic radiation of multiply charged atomic ions in the far x-ray range [7].

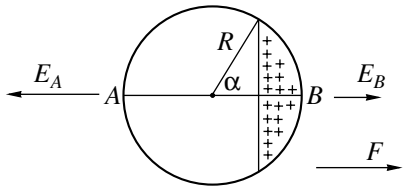

Fig. 1. Charged and neutral components of an ionized cluster subjected to the effect of a laser field.

2. MODEL OF THE ABOVE-BARRIER MULTIPLE INTERNAL AND EXTERNAL IONIZATION OF A CLUSTER

A molecular bond is broken long before the passage of the maximum of an superatomic laser pulse. Our approach to the internal multiple ionization of atoms in large clusters by a superstrong field of a laser pulse is based on the Bethe model for above-barrier ionization [8]. Since this model was repeatedly used in previous studies (see [9–11]), only a brief account of it will be given here (see also our article devoted to xenon lasers [12]).

For an atomic ion of charge Z and ionization potential E_Z to be formed in a cluster at an instant t, there must exist an electric field of strength

$$F(t) = E_Z^2/4Z. \qquad (1)$$

Hereafter, we employ the atomic system of units where the electron charge and mass and the Planck constant are set to unity, $m_e = e = \hbar = 1$.

However, the electric field in an ionized cluster does not coincide with the external field of a laser pulse. Free electrons within the cluster (there are NZ of them, where N is the number of atoms in the cluster) are displaced rather fast by the laser field against the direction of the field (see Fig. 1). After the lapse of a half-period, they are also easily displaced in the opposite direction because of the absence of inertia. In [13], it is assumed that such displacements do not disturb the spherical shape of the electron subsystem. This would be so if this structure had a large surface tension, but there are no reasons to believe that it does indeed have such a surface tension. Within the model used here, the electrons are merely displaced against the laser-field direction.

Thus, an ionized cluster consists of two regions: in the neutral part, there are electrons and atomic ions, while, in the charged part, there are only atomic ions (see Fig. 1). We assume that these two regions are separated by a planar boundary. Of course, this is an approximation, since the boundary is in fact convex toward the charged part (the degree of convexity is determined by the condition requiring that, over the entire boundary, the tangential component of the electric field be zero, which ensures the immobility of

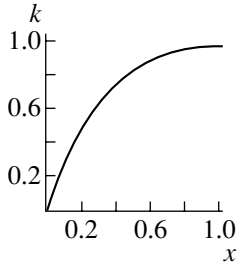

Fig. 2. Universal dependence of the fraction of electrons escaping from the cluster, $k = Q/NZ$, on the strength of the laser-pulse field, $x = FR^2/NZ$.

the electrons). However, our objective is to determine the additional electric field generated by the charged part at the cluster point that is the most remote from it (point A in Fig. 1), but this field would undergo only a slight change upon taking into account a small curvature of the boundary.

One could assume that the distribution of electrons is not that which is shown in Fig. 1 but that which extends nonuniformly over the entire volume of the cluster being considered: the number of electrons would then be enhanced (diminished) in the left-hand (right-hand) part, as occurs under the conditions of volume plasma oscillations. In this case, the cluster would have no neutral part. However, this version is less probable than that which was specified above, since plasmas always tend to be neutral. In a neutral cluster, Mie surface plasma oscillations would be generated (for a survey of the properties of Mie oscillations, the interested reader is referred to [14]).

The electric-field strength generated at the point A by the charged part of the cluster can easily be calculated as

$$E_A = \frac{NZ}{R^2}\left(1 - 3\cos^2\frac{\alpha}{2} + 2\cos^3\frac{\alpha}{2}\right), \qquad (2)$$

where R is the radius of the cluster and the angle α is shown in Fig. 1. The condition

$$F(t) = E_A \qquad (3)$$

means that the force with which the laser field pulls an electron outside is equal to the force with which this electron is attracted by the positively charged part of the ionized cluster.

The electric-field strength generated by the charged part of the cluster at the extreme right point B (Fig. 1) can also be calculated straightforwardly according to the laws of electrostatics. The result is

$$E_B = \frac{NZ}{R^2}\left(3 - 2\sin\frac{\alpha}{2}\right)\sin^2\frac{\alpha}{2}. \qquad (4)$$

This field must be added to the external field $F(t)$, since, in accordance with the well-known ignition model [15], it enhances the internal ionization of atomic ions in the cluster.

It should be borne in mind, however, that the field E_B is not operative in the neutral part of the cluster and that, even in the charged part, it contributes additively only at the maximum value of the total field—at other points of the charged part, the total field will have a different value. Of the two factors indicated immediately above, the former is of prime importance. In order to take it into account, we propose weakening the ignition field (4) by multiplying this field by the ratio of the volume V occupied by the charged part to the total cluster volume $4\pi R^3/3$. The volume occupied by the charged part is

$$V = \frac{1}{3}\pi R^3\left(2 - 3\cos\alpha + \cos^3\alpha\right), \qquad (5)$$

and the charge concentrated in this region is

$$Q = \frac{NZ}{4}\left(2 - 3\cos\alpha + \cos^3\alpha\right) \qquad (6)$$

(this is of course the charge of the ionized cluster). If the angle α is eliminated from Eqs. (2), (3), and (6), it is possible to obtain a universal relation between the external-field strength $F(t)$ (in units of NZ/R^2) and the ionized-cluster charge Q (in NZ units). This relation is illustrated in Fig. 2. It enables one to calculate the degree of external ionization of any cluster at a given strength of the electric field of the applied laser pulse.

Thus, the effective value of the strength of the ignition field, which enhances ionization, is given by

$$F_{\text{eff}} = \frac{NZ}{4R^2}\left(2 - 3\cos\alpha + \cos^3\alpha\right) \times \left(3 - 2\sin\frac{\alpha}{2}\right)\sin^2\frac{\alpha}{2}. \qquad (7)$$

Adding it to the applied field $F(t)$, we obtain the actual field that produces the internal ionization of atomic ions in an ionized cluster and which, in accordance with the Bethe condition (1), must be equated to the quantity $E_Z^2/4Z$. As a result, we obtain the equation

$$\frac{E_Z^2}{4Z} = \frac{NZ}{4R^2}\left(2 - 3\cos\alpha + \cos^3\alpha\right) \times \left(3 - 2\sin\frac{\alpha}{2}\right)\sin^2\frac{\alpha}{2} + \frac{NZ}{R^2}\left(1 - 3\cos^2\frac{\alpha}{2} + 2\cos^3\frac{\alpha}{2}\right). \qquad (8)$$

Given the ionization potential E_Z of a given atomic ion and the current value of its radius $R(t)$, which increases with time because of the Coulomb explosion of the ionized cluster, we can calculate the angle α on the basis of this equation.

Dynamics of the internal and external ionization of a cluster formed by 10^6 molecules of deuterium iodide and irradiated with a laser pulse of duration 50 ps and intensity 2×10^{18} W/cm^2 at the peak

Z	E_Z, eV	$-t$, fs	F, a.u.	Q, 10^6	R, a.u.	T_e, eV
1, $5p^5$	10.4	103	0.021	0.019	261	20
2, $1s$(D)	13.6	98	0.037	0.033	261	24
3, $5p^4$	19.1	97	0.039	0.036	261	27
4, $5p^3$	33	91	0.073	0.066	261	66
5, $5p^2$	48	87	0.110	0.100	261	212
6, $5p^1$	60	85	0.137	0.124	261	663
7, $5s^2$	90	79	0.240	0.213	263	1168
8, $5s^1$	103	77	0.269	0.246	265	1410
9, $4d^{10}$	170	68	0.564	0.498	270	6000
10, $4d^9$	200	65	0.686	0.637	273	6326
11, $4d^8$	230	63	0.807	0.745	275	6656
12, $4d^7$	260	61	0.926	0.863	278	7131
13, $4d^6$	290	59	1.046	0.991	281	7762
14, $4d^5$	320	58	1.163	1.12	283	8168
15, $4d^4$	350	56	1.284	1.25	287	9233
16, $4d^3$	390	54	1.458	1.45	291	10 508
17, $4d^2$	420	53	1.572	1.60	294	11 192
18, $4d^1$	450	52	1.690	1.75	297	12 016
19, $4p^6$	550	46	2.28	2.35	321	21 011
20, $4p^5$	580	45	2.35	2.79	326	21 400
21, $4p^4$	620	44	2.54	3.09	331	21 870
22, $4p^3$	650	43	2.63	3.29	336	22 310
23, $4p^2$	700	41	2.88	3.68	348	23 267
24, $4p^1$	740	40	3.06	4.14	354	23 800
25, $4s^2$	820	37	3.47	4.85	376	25 510
26, $4s^1$	900	33	4.00	6.01	412	27 650
27, $3d^{10}$	1400	0	8.73	13.0	1190	28 000

Upon calculating the angle α, one can find the ionized-cluster charge Q on the basis of relation (6). By using relations (2) and (3), one can further find the field strength $F(t)$. The result is

$$F(t) = \frac{NZ}{R^2}\left(1 - 3\cos^2\frac{\alpha}{2} + 2\cos^3\frac{\alpha}{2}\right). \quad (9)$$

Knowing the field strength, one can calculate the instant t at which there occurred internal ionization that produced atomic ions of charge Z. For this, we make use of the relation

$$F(t) = F_0\exp(-t^2/\tau^2), \quad (10)$$

assuming that the amplitude of the strength of the laser-pulse field, F_0, and the laser-pulse duration, τ, are known.

At the last step, one calculates the increase in the radius of the ionized cluster because of its Coulomb expansion. This calculation was performed here on the basis of Newton's second law for the motion of

an atomic ion at the cluster surface; that is,

$$\frac{d^2R}{dt^2} = \frac{Q(t)Z(t)}{MR^2(t)}, \qquad (11)$$

where M is the mass of the atomic ion being considered (iodine ion in our case). We solved this equation numerically, disregarding the fact that some deuterons escape from the cluster at a higher speed than atomic iodine ions.

3. RESULTS OF THE CALCULATION OF THE NEUTRON YIELD

For the interaction of a cluster containing 10^6 deuterium-iodide molecules with a laser pulse of duration (FWHM for the case of a Gaussian distribution) 50 fs and intensity 2×10^{18} W/cm^2 at the peak, the results of the calculations performed according to the scheme outlined above are quoted in the table. These laser-pulse parameters correspond to typical values in the experiments reported in [3–5, 16–19]. The distribution of the envelope of the laser-field strength then has the form

$$F(t) = 7.43 \exp\left(-t^2/\tau^2\right) \text{ [a.u.]}, \qquad (12)$$

where $\tau = 42.47$ fs. The internal ionization of deuterium proceeds after the single ionization of iodine atoms. There then occurs a double ionization of iodine atoms, which is followed by a higher multiplicity ionization of iodine. For high multiplicities, the ionization potentials of iodine atoms were chosen on the basis of the known values for the neighboring xenon atom [12].

From the table, it can be seen that, at first, the rate of the external ionization is much lower than the rate of internal ionization, so that the charge of the ionized cluster grows slowly at this stage. At the peak of the laser pulse, however, about half of the electrons that escaped from iodine atoms leave the cluster; therefore, the cluster eventually consists of positively charged iodine ions (whose charge multiplicity Z is predominantly 26 to 27), deuterons, and some electrons.

Because of Coulomb expansion, the cluster dimensions increase considerably even at the leading edge of the laser pulse. By way of example, we indicate that, at the instant $t = 0$, which corresponds to the peak value of the laser-pulse intensity, the diameter of the cluster is four times as large as its original value. A typical distance to the neighboring cluster is greater than the cluster diameter by a factor ranging between 10 and 20. Thus, we can see that, even within a laser pulse, clusters virtually disappear with the result that the plasma becomes nearly uniform in space. The expansion of a cluster was calculated by tracing the motion of atomic iodine ions at the cluster surface. Deuterons are lighter than iodine ions, but the deuteron charge is much less than the typical charge of atomic iodine ions; it follows that, although some deuterons escape from the cluster earlier than iodine ions, the majority of the deuterons expand together with iodine ions.

Deuterons acquire kinetic energy during the Coulomb explosion of the cluster. This occurs from the instant $t = 0$ to the instant at which the cluster radius reaches a value that is ten times as large as the original one. The maximum value of the deuteron kinetic energy is estimated as the difference of the corresponding Coulomb potential energies. The average energy was taken to be equal to half the maximum value. The calculations lead to the average kinetic energy of 50 keV.

The cross section for the deuteron-fusion reaction leading to the production of a ^{3}He nucleus and a neutron is 10^{-26} cm^2 at this energy value. In experiments of the type being considered, a typical volume of the laser focus is 10^{-5} cm^3 at a focusing-spot radius of 50 μm. Under the assumption that the concentration of deuterons in the laser plasma after the passage of a pulse is $n_d = 10^{19}$ cm^{-3}, the yield of neutrons per laser pulse is 10^5.

4. GROWTH OF THE ELECTRON TEMPERATURE IN A CLUSTER

The electron temperature T_e is also given in the table. It increases owing to induced inverse bremsstrahlung in elastic electron scattering on atomic ions in the presence of a laser field. The frequency of collisions between electrons and atomic ions is given by the formula

$$\nu_{ei} = \frac{4\sqrt{2\pi}}{3} \frac{Zn_e}{T_e^{3/2}} \ln\Lambda,$$

which is well known in plasma theory and which involves the Coulomb logarithm approximately equal to 10. In the case of single ionization, the concentration of free electrons within the cluster is equal to $n_e = 1.3 \times 10^{22}$ cm^{-3}. With increasing multiplicity of ionization, this concentration becomes higher, but its growth is moderated at a later stage because of the expansion of the cluster.

The increment of the electron energy per collision between an electron and an ion of charge multiplicity Z under the condition that the collision frequency is much lower than the frequency of the laser field is given by

$$\Delta E = F^2/2\omega^2, \qquad (13)$$

where ω is the frequency of the laser field and F is its amplitude, which is determined by the envelope of the laser pulse.

But if the collision frequency is higher than the frequency of the laser field, the increment of the electron energy per collision with an atomic ion has the different form [20]

$$\Delta E = \frac{16}{3\pi}\frac{F^2}{\nu_{ei}}. \quad (14)$$

From the calculations, it follows that relation (14) holds for $Z = 1$–6, while relation (13) is valid for $Z \geq 7$. It is these relations that were used to calculate the electron temperature (see table).

The depth at which the laser field penetrates into a cluster decreases with increasing intensity at the leading edge of the pulse. It was estimated as the thickness of the skin layer according to the formula $l = c/\omega_p$, where $\omega_p = \sqrt{4\pi n_e}$ is the plasma frequency (in atomic units). This yields $l = 270$ Å at $Z = 1$ and $l = 90$ Å at $Z = 25$. Thus, we can conclude that the field penetrates quite deeply into a cluster despite rather large dimensions of the clusters and despite a large number of free electrons within a cluster.

5. CONCLUSION

From the results of the present study, it can be concluded that, for the case of irradiation with a superatomic femtosecond laser pulse, clusters of silver iodide are a better target than clusters from pure deuterium, which were used previously in experiments. The procedure employed in the present calculations was tested earlier in [21] by applying it to clusters of hydrogen iodide.

We have also found that, within a laser pulse, clusters transform, through Coulomb explosion, into quite a uniform plasma consisting of hot electrons (their temperature ranging between 20 and 30 keV) and multiply charged iodine atoms (and deuterons as well). This plasma exists for about 100 ps. Monochromatic neutrons of energy 2.45 MeV are emitted within this period of time. Such a source of monochromatic neutrons may be used in radiation material science. In addition, the plasma in question serves as a source of hard line-shaped x-ray radiation that is generated as the result of radiative transitions in multiply charged ions. A femtosecond laser having a superatomic intensity and a contrast not lower than 10^8 necessary for eliminating the effect of a precursor pulse is a mandatory element for performing such experiments.

ACKNOWLEDGMENTS

This work was supported in part by the International Center for Science and Technology (project no. 2155), CRDF (project no. MO-011-0), and the Russian Foundation for Basic Research (project nos. 01-02-16056 and 02-02-16678).

REFERENCES

1. B. M. Smirnov, *Physics of Ionized Gases* (Wiley, New York, 2001).
2. N. B. Delone and V. P. Krainov, *Multiphoton Processes in Atoms*, 2nd ed. (Springer, Berlin, 2000).
3. J. W. G. Tisch, N. Hay, E. Springate, *et al.*, Phys. Rev. A **60**, 3076 (1999).
4. E. Springate, J. W. G. Tisch, N. Hay, *et al.*, Laser and Atom Beams **18**, 507 (2000).
5. J. Zweiback, T. E. Cowan, R. A. Smith, and T. Ditmire, Phys. Rev. Lett. **85**, 3640 (2000).
6. M. Schnürer, S. Ter-Avetisyan, H. Stiel, *et al.*, Eur. Phys. J. D **14**, 331 (2001).
7. T. Auguste, P. D'Oliveira, S. Hulin, *et al.*, Pis'ma Zh. Éksp. Teor. Fiz. **72**, 54 (2000) [JETP Lett. **72**, 38 (2000)].
8. H. A. Bethe and E. E. Salpeter, *Quantum Mechanics of One- and Two-Electron Atoms* (Rosetta, New York, 1977).
9. V. P. Krainov and M. B. Smirnov, Zh. Éksp. Teor. Fiz. **120**, 555 (2001) [JETP **93**, 485 (2001)].
10. V. P. Krainov and M. B. Smirnov, Zh. Éksp. Teor. Fiz. **119**, 719 (2001) [JETP **92**, 626 (2001)].
11. V. P. Krainov and A. S. Roshchupkin, J. Phys. B **34**, L297 (2001).
12. V. P. Krainov and M. B. Smirnov, Zh. Éksp. Teor. Fiz. **121**, 867 (2002) [JETP **94**, 745 (2002)].
13. P. B. Parks, T. E. Cowan, R. B. Stephens, and E. M. Campbell, Phys. Rev. A **63**, 063203 (2001).
14. V. P. Krainov and M. B. Smirnov, Usp. Fiz. Nauk **170**, 969 (2000) [Phys.-Usp. **43**, 901 (2000)].
15. C. Rose-Petruck, K. J. Schafer, K. R. Wilson, and C. P. J. Barty, Phys. Rev. A **55**, 1182 (1997).
16. H. Honda, E. Miura, K. Katsura, *et al.*, Phys. Rev. A **61**, 023201 (2000).
17. W. A. Schroeder, T. R. Nelson, A. B. Borisov, *et al.*, J. Phys. B **34**, 297 (2001).
18. K. Boyer, B. D. Thomson, A. McPherson, and C. K. Rhodes, J. Phys. B **27**, 4373 (1994).
19. T. Ditmire, T. Donnelly, A. M. Rubenchik, *et al.*, Phys. Rev. A **53**, 3379 (1996).
20. B. M. Smirnov, *Physics of Weakly Ionized Gas*, 3rd ed. (Nauka, Moscow, 1985; Mir, Moscow, 1981, transl. of the 1st ed.).
21. V. P. Krainov and A. S. Roshchupkin, Phys. Rev. A **64**, 063204 (2001).

Translated by A. Isaakyan

Physics of Atomic Nuclei, Vol. 66, No. 4, 2003, pp. 618–631. Translated from Yadernaya Fizika, Vol. 66, No. 4, 2003, pp. 647–660.

NUCLEI
Theory

Probabilistic Scission of a Fissile Nucleus into Fragments

G. D. Adeev and P. N. Nadtochy

Omsk State University, pr. Mira 55A, Omsk, 644077 Russia

Received November 8, 2001; in final form, August 27, 2002

Abstract—A probabilistic criterion is proposed for the scission of a fissile nucleus into fragments. The probability of the rupture of the neck between would-be fragments is estimated by considering scission as a fluctuation. The energy of the prescission configuration and the energy of the separated-fragment configuration are computed on the basis of a macroscopic model that takes into account a finite range of nuclear forces and the diffuseness of the nuclear surface. The effect of the probabilistic criterion of nuclear scission on fission-process observables, such as the moments of the mass–energy distribution of fission fragments, the mean multiplicity of prescission neutrons, and mean fission times, is demonstrated. It is shown that the Strutinsky criterion, according to which nuclear scission occurs at a finite neck radius of $0.3R_0$, is a rather good approximation to the probabilistic scission criterion in Langevin dynamical calculations employing the one-body nuclear-viscosity mechanism modified in such a way that the wall-formula contribution is reduced, the reduction factor satisfying the condition $k_s < 0.5$. © *2003 MAIK "Nauka/Interperiodica".*

1. INTRODUCTION

Any theoretical description or simulation of nuclear scission—that is, a process through which the primary compound nucleus disintegrates predominantly into two fragments—inevitably has to consider the condition under which scission occurs. By scission, one means here a transition from a continuous nuclear configuration that becomes unstable for a number of reasons to a configuration in which the nuclear system being considered consists of separated fragments. The problem of the rupture of the neck between would-be fragments has been addressed many times (see, for example [1–6]), but it has yet to be solved completely. From the outset, we note that the theory of the fission process employs most often two criteria (conditions) of scission that are obvious limiting cases with respect to each other. By way of example, we indicate that Nix and his collaborators [7–9], as well as some other authors [10, 11], formulate the scission criterion as the condition requiring the vanishing of the neck radius (the simplest condition of geometric scission), $R_N = 0$. Although this scission condition is consistent with the model representing a nucleus as a liquid drop with a sharp boundary [1, 12], it turn out to be unsatisfactory since the description of a nucleus within the liquid-drop model becomes meaningless as soon as the neck radius appears to be commensurate with the distance between nucleons [2]. Defining the scission condition on the basis of the criterion of the instability of a nucleus against variations in the thickness of its neck [2], in which case the ridge between the fission valley and the valley of separated fragments disappears, is attractive from the physical point of view. This scission condition corresponds to prescission configurations of a fissile nucleus that are characterized by a neck of finite radius, on average equal to $0.3R_0$ (R_0 is the radius of the primary spherical nucleus) [1, 2, 13–16]. We note that the presence of two valleys separated by a ridge that disappears for elongated nuclear shapes is corroborated by microscopic calculations within the Hartree–Fock method [17]. The nuclear-scission criterion based on the balance between the Coulomb repulsion of would-be fragments and the nuclear attraction between them [18] is also physically reasonable and acceptable. It was shown in [18] that, in the region of actinide nuclei, this scission criterion leads to prescission configurations that have approximately the same neck radius, $0.3R_0$. In the random-neck-rupture model proposed by Brosa and his collaborators [3], use was made of the criterion of the hydrodynamic instability of the neck against rupture. It also leads to prescission nuclear configurations with a neck radius in the range $(0.2–0.3)R_0$.

2. THEORY

In the cases of zero or a finite neck radius, the conditions under which the primary compound nucleus disintegrates into fragments determine, in the space of collective coordinates, the scission line (for two collective coordinate) or the scission surface (for three collective coordinates), which clearly delimit prescission (continuous) and already separated nuclear shapes. It is generally assumed in calculations that, as soon as the primary nucleus reaches, in the

1063-7788/03/6604-0618$24.00

process of its evolution, this line or surface, it disintegrates into fragments with a probability equal to unity.

In the present study, we are going to consider all nuclear shapes featuring a neck as prescission shapes. As soon as a neck appears in the nuclear shape, it becomes possible to single out would-be fragments by cutting the primary compound nucleus within the neck, and we assume that, in this case, the probability for this nucleus to undergo disintegration into fragments is nonzero in any of its configurations. In order to estimate this probability, we propose considering the rupture of the neck connecting would-be fragments as a fluctuation. In this case, the scission probability is given by [19]

$$W = \exp(-\Delta E/T), \qquad (1)$$

where ΔE is the change in energy due to a fluctuation and T is the temperature of the nucleus being considered. A fissile nucleus undergoes scission into fragments because of fluctuations in the region of the neck, which is in an unstable state. It is difficult to formulate the criterion of neck instability with respect to rupture. In [20], the fragmentation condition was associated with the reduction of the matter density to some critical value, while, in [3], the scission of a fissile nucleus was considered as a manifestation of hydrodynamic Rayleigh instability induced by random surface vibrations. However, the results of those and some other studies (see [1, 2]) give no way to make quantitatively precise predictions as to the critical neck radius at which rupture occurs. It seems that only the study of Davies *et al.* [18], where the critical neck radius at which the scission of a nucleus into fragments occurs was determined by equating the forces of Coulomb repulsion to nuclear-attraction force, stands out in this respect. Thus, the approach based on considering the energy dependence of the scission probability according to Eq. (1) may provide a reasonable solution to this extremely involved physical problem. We note that the application of formula (1) assumes that the initial and final states of the system undergoing fluctuations that lead to scission are not separated by an energy barrier. If there is an energy barrier between the initial and final states, the height of this barrier must be used in (1) instead of the quantity ΔE.

The ideas of the theory of fluctuations have been repeatedly and successfully used for a long time to analyze the scission of a nucleus into fragments [3] and to describe the formation of the mass and charge distributions and many other observables of the fission process [21]. By way of example, we indicate that, in the model of random neck rupture, Brosa and his collaborators [3] proposed using a Boltzmann-type formula similar to (1) in estimating the probability of neck rupture at a point other than that which corresponds to the minimum neck radius. In calculating the energy difference ΔE as an additional surface energy that arises upon such a rupture, they relied on the model of a liquid drop with a sharp nuclear edge [1, 12]. In order to calculate scission probabilities, Startsev [5] employed an approach that is similar to our approach in the present study and which is based on the liquid-drop model taking into account the diffuseness of the nuclear surface and a finite range of nuclear forces [22]. It should be emphasized, however, that, in calculating the quantity ΔE appearing in (1), he chose specific initial and final states that differ from those adopted here.

In order to describe the nuclear shape, we have used a modified version of the well-known $\{c, h, \alpha\}$ parametrization [2]. We have introduced the parameter α' related to α by the scaling transformation $\alpha' = \alpha c^3$ [14, 15].

In cylindrical coordinates, the equation of the nuclear surface has the form [2, 14, 15]

$$\rho_s^2(z) = \begin{cases} c^{-2}(c^2 - z^2)(A_s c^2 + Bz^2 + \alpha' z/c^2), & B \geq 0, \\ c^{-2}(c^2 - z^2)(A_s c^2 + \alpha' z/c^2)\exp(Bcz^2), & B < 0, \end{cases} \qquad (2)$$

where z is the coordinate along the symmetry axis and ρ_s is the value of the coordinate ρ at the nuclear surface. The quantities A_s and B are expressed in terms of the nuclear-shape parameters (c, h) as

$$B = 2h + \frac{c-1}{2}, \qquad (3)$$

$$A_s = \begin{cases} c^{-3} - B/5, & B \geq 0; \\ -\dfrac{4}{3}\dfrac{B}{\exp(Bc^3) + (1 + 1/(2Bc^3))\sqrt{-\pi Bc^3}\,\mathrm{erf}(\sqrt{-Bc^3})}, & B < 0. \end{cases}$$

In Eqs. (2) and (3), c is the elongation parameter, h is a parameter that specifies the neck thickness at a given elongation, and α' is the mass-asymmetry parameter. Shapes that are symmetric with re-

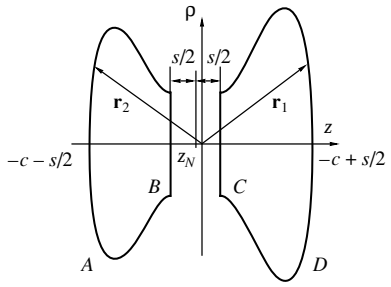

Fig. 1. Fragment-configuration shape obtained by cutting a continuous shape with a plane specified by equation $z = z_N$. The resulting fragments are separated by the distance s. The fragment surfaces specified by the function $\rho_s(z)$ are denoted by A and D, while the surfaces of the planar sections formed upon cutting the continuous shape are denoted by B and C.

spect to the $z = 0$ plane correspond to the case of $\alpha' = 0$.

The emergence of a neck in the evolving nuclear shape is associated with the instant at which the profile function $\rho_s(z)$, whose rotation about the symmetry axis determines the nuclear surface, develops three extrema, two maxima corresponding to nascent fragments and a minimum between the maxima, which specifies the minimum neck thickness. The minimum occurs at the point

$$z_N = 2\sqrt{\frac{p}{3}}\cos\left(\frac{4\pi}{3} + \frac{1}{3}\arccos\left(\frac{q\sqrt{27}}{2p^{3/2}}\right)\right) - \frac{\alpha'}{4c^2B}, \tag{4}$$

where

$$p = -\frac{c^2}{4B}\left(\frac{2}{c^3} - \frac{12}{5}B - \frac{3\alpha'^2}{4Bc^6}\right), \tag{5}$$

$$q = -\frac{\alpha'}{4B}\left(\frac{\alpha'^2}{8B^2c^6} - \frac{2}{5} - \frac{1}{2Bc^3}\right). \tag{6}$$

The condition of the existence of a neck in the nuclear shape can be written in the form

$$\frac{q^2}{4} - \frac{p^3}{27} < 0. \tag{7}$$

Before the emergence of a neck, the profile function has only one extremum, a maximum, the corresponding nuclear shapes being monoshapes. The coordinates of the extrema of the profile function and the values of $\rho_s(z)$ at these extrema vary in response to variations in the shape parameters. The equation for the scission surface can be written in the form

$$\rho_s(z_N) = R_N, \tag{8}$$

where R_N is the neck radius corresponding to the prescission shape. The condition of geometric rupture or of zero neck radius corresponds to the case of $\rho_s(z_N) = 0$. It can be rewritten in terms of the equations

$$A_s = 0, \tag{9}$$

$$A_s - \frac{\alpha'^2}{4Bc^6} = 0. \tag{10}$$

Formula (9) determines the scission line in the case of two collective coordinates, while formula (10) specifies the scission surface in the case of three collective coordinates.

2.1. Energies of Prescission Shapes of a Fissile Nucleus and Energies of the System of Fragments

In applying formula (1) to calculating the probability of the disintegration of a compound nucleus into fragments, it is necessary to perform a complete characterization of prescission nuclear shapes and of the corresponding configurations of the system of fragments. In other words, it is necessary to formulate a method for going over from a continuous prescission nuclear shape to a configuration of the system of fragments. However, no unambiguous method for describing such a transition has been developed at the present time. It was shown in [6] that the rupture of the neck occurs rather quickly, within a time of $\tau_r \simeq 10^{-23}$ s; this makes it possible to relate the parameters of a continuous configuration to the parameters of the fragment configuration by requiring that the lowest moments of the density distribution prior to and after scission be equal. This equality has the simple physical meaning of the conservation of the number of particles, of the position of the center of mass, of the dimensions of the system along the z and ρ axes, and so on. For example, Brosa and his collaborators [3] assumed that fragments have ellipsoidal shapes and used, in order obtain the shape parameters, the conditions requiring the conservation of the number of particles and of the size of the system along the z axis. In [23], the shapes of fragments were also parametrized in terms of ellipsoids, but the shape parameters of the fragments were found by using the laws of conservation of the energy and the maximum entropy of the system of fragments. Intuitively, a parametrization of the fragment shape by ellipsoids does not seem quite correct; it is more probable that, immediately after the rupture of the neck, the fragments have pearlike shapes [24, 25], which are characterized by the presence of quadrupole and octupole deformations simultaneously. However, the description of pearlike shapes requires introducing at least four fragment-shape parameters. Their determination on the basis of the maximum-entropy condition [23] or on the basis of the condition requiring the equality of the density-distribution moments before and after

scission [6] leads to rather cumbersome calculations. In our case, where all nuclear shapes featuring a neck are used as prescission nuclear shapes, these calculations become even more complicated. In the present study, we therefore parametrized the fragment shape on the basis of a continuous prescission nuclear shape that was cut by a plane orthogonal to the z axis at a minimal thickness of the neck. The resulting fragments were moved apart at a distance s (see Fig. 1). It should be noted that, in the limit $s \to 0$, this parametrization of the fragment shape ensures the equality of all density-distribution moments prior to and after the rupture of the neck. At s values that are much smaller than the dimensions of the continuous shape, lower density-distribution moments are also conserved to a high precision. On the other hand, it is obvious from the physical point of view that, immediately after scission, the fragment configurations chosen here are energetically unfavorable because of a large surface area and because of the presence of planar sections. Within a short time immediately after the rupture of the neck, the planar sections are smoothed, with the result that the shape of the fragments becomes nearly pearlike. The relationship between the fragment deformations and octupole and quadrupole deformations is studied here and will also be the subject of our future publications.

In Eq. (1), ΔE has the meaning of the difference of the potential energies of the system of two fragments separated by a distance s (see Fig. 1) and the potential energy of the prescission (continuous) nuclear shape ($s = 0$). For both prescission and separated shapes, the potential energy of a fissile nucleus was calculated here on the basis of the macroscopic nuclear model [22, 26] with allowance for a finite range of nuclear forces and the diffuse distribution of the nuclear density. Within this model, the generalized surface energy (nuclear energy) E_n is represented in the form of a double integral over the volume of the nucleus being considered; that is,

$$E_n = -\frac{c_s}{8\pi^2 r_0^2 a^3} \int\limits_V \int\limits_V \left(\frac{r}{a} - 2\right) \frac{e^{-\frac{r}{a}}}{r} d^3r_1 d^3r_2. \quad (11)$$

In order to calculate the Coulomb energy E_C with allowance for the diffuse distribution of the charge density, we use the expression

$$E_C = \frac{15E_C^0}{32\pi^2 R_0^5} \times \int\limits_V \int\limits_V \left(1 - \left(1 + \frac{r}{2a_d}\right) e^{-r/a_d}\right) \frac{d^3r_1 d^3r_2}{r}, \quad (12)$$

where $c_s = a_s(1 - kI^2)$; $I = (N - Z)/A$; $r = |\mathbf{r}_1 - \mathbf{r}_2|$; $E_C^0 = 3Z^2e^2/(5R_0)$; A is the mass number; and Z and N are the numbers of, respectively, protons and neutrons in the nucleus. The parameter values of $a = 0.68$ fm, $a_d = 0.7$ fm, $r_0 = 1.16$ fm, $a_s = 21.13$, and $k = 2.3$ were chosen in accordance with [26]. By applying Gauss' theorem two times, expressions (11) and (12) for, respectively, the nuclear and the Coulomb component of the potential energy of a continuous fissile-nucleus shape can each be reduced to a double surface integral [22, 27]. For the axially symmetric case corresponding to the profile function (recall that it specifies the nuclear surface) in the form $\rho_s(z)$, the resulting double surface integrals can be expressed in terms of the triple integral

$$E = \int\limits_{-c}^{c} \int\limits_{-c}^{c} \int\limits_{0}^{2\pi} F(r)\rho_s(z_1)\Big(\rho_s(z_1) - \rho_s(z_2)\cos\phi - \frac{\partial\rho_s(z_1)}{\partial z_1}(z_1 - z_2)\Big)\rho_s(z_2)\Big(\rho_s(z_2) - \rho_s(z_1)\cos\phi + \frac{\partial\rho_s(z_2)}{\partial z_2}(z_1 - z_2)\Big) dz_1 dz_2 d\phi, \quad (13)$$

where

$$r = (\rho_s^2(z_1) + \rho_s^2(z_2) - 2\rho_s(z_1)\rho_s(z_2)\cos\phi + (z_1 - z_2)^2)^{1/2}, \quad (14)$$

$$F(r) = \begin{cases} -\dfrac{c_s}{4\pi r_0^2 r^4}\left(2 - \left(2 + 2\dfrac{r}{a} + \left(\dfrac{r}{a}\right)^2\right)e^{-r/a}\right) & \text{for calculating } E_n, \\ \dfrac{15E_C^0}{16\pi R_0^5}\left(\dfrac{1}{a_d}\left(\dfrac{a_d}{r}\right)^4\left[2\dfrac{r}{a_d} - 5 + \left(5 + 3\dfrac{r}{a_d} + \dfrac{1}{2}\left(\dfrac{r}{a_d}\right)^2\right)e^{-r/a_d}\right] - \dfrac{1}{6r}\right) & \text{for calculating } E_C. \end{cases} \quad (15)$$

In this study, triple integrals of the form (13) were calculated according to the Gauss quadrature formulas featuring 32 nodes.

Since the shape of the fragments does not change as they are displaced apart at a distance s, the quantity ΔE can be represented as the difference $U(\mathbf{q}, s) - U(\mathbf{q}, 0)$, where $U(\mathbf{q}, s)$ is the fragment-interaction energy at the corresponding spacing between the

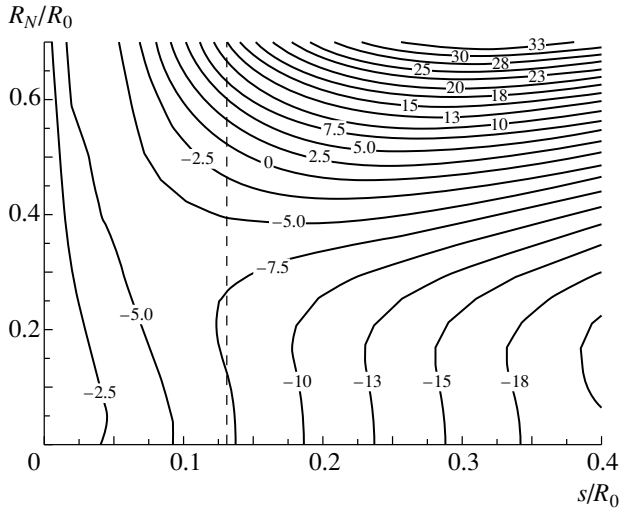

Fig. 2. Energy of fragment interaction for the ^{244}Cm nucleus as a function of the distance s between the fragments and the neck radius R_N. The numbers on isolines stand for energy values in MeV. The dashed straight line at $s = 0.13R_0$ corresponds to the case of touching fragments (see explanations in the main body of the text).

fragments; that is, $U(\mathbf{q}, s) = U_{\rm C}(\mathbf{q}, s) + U_n(\mathbf{q}, s)$, with $U_{\rm C}(\mathbf{q}, s)$ and $U_n(\mathbf{q}, s)$ being, respectively, the Coulomb repulsion energy and the nuclear-attraction energy of the fragments separated by the distance s. By going over from the potential energy to the fragment-interaction energy, we can improve the accuracy of the calculations. Moreover, the interaction energy $U(\mathbf{q}, 0)$ added to the prescission kinetic energy of fragment motion ($E_{\rm ps}$) will yield the total fragment kinetic energy (E_K) observed in experiments.

If fragments possess axial symmetry, as in the case illustrated in Fig. 1, the energies of the Coulomb and nuclear interaction can be represented as the sum

$$U(\mathbf{q}, s) = U_{\rm AD}(\mathbf{q}, s) + U_{\rm AC}(\mathbf{q}, s) + U_{\rm BD}(\mathbf{q}, s) + U_{\rm BC}(\mathbf{q}, s), \qquad (16)$$

where $U_{\rm AD}(\mathbf{q}, s)$, $U_{\rm AC}(\mathbf{q}, s)$, $U_{\rm BD}(\mathbf{q}, s)$, and $U_{\rm BC}(\mathbf{q}, s)$ have the form of various surface integrals, explicit expressions for them in the system of cylindrical coordinates being given in the Appendix.

The values of ΔE that were calculated here for the ^{244}Cm nucleus are given in Fig. 2 versus the distance s between the fragments for various values of the neck thickness. One can see from this figure that, with increasing s, ΔE becomes positive for shapes having a rather thick neck ($R_N = (0.5{-}0.7)R_0$). This means that the rupture of a thick neck is energetically unfavorable, since the arising additional sections of fairly large area make a sizable contribution to the nuclear-fragment-attraction energy, which appears to be greater than the energy of Coulomb repulsion at distances $s < (0.3{-}0.4)R_0$. Thus, the nuclear-attraction energy hinders the separation of fragments. At large distances, the energy of nuclear attraction decreases fast, so that only the energy of Coulomb repulsion is operative there. For shapes having a rather thin neck ($R_N < 0.4R_0$), the separation of a continuous shape into fragments becomes energetically favorable, since the energy of nuclear attraction appears to be small in relation to the energy of the Coulomb repulsion of fragments. In this case, the energy of nuclear attraction is unable to prevent the separation of the nucleus into fragments. The result that we obtained here for the dependence of ΔE on s and R_N is qualitatively similar to the result quoted in [5]. The quantitative distinction stems from the fact that, in [5], the quantity ΔE was calculated as the difference of the energy of the system of fragments and the energy of the continuous prescission configuration, which, in [5], differed somewhat from the configuration used here.

A specific distance s at which we calculated the scission probability by formula (1) was selected in the following way. In the statistical approximation, the energy of a nucleus was represented in the form of a functional of the nucleon density ρ_n and of its gradient [28]. The gradient term, which is responsible for the finiteness of the nuclear-force range, was taken in the form

$$E_s = \text{const} \cdot \int\limits_{\infty} (\nabla \rho_n(\mathbf{r}_1))^2 d^3 r_1. \qquad (17)$$

That integration in (17) is performed over the entire space is indicated by an infinity sign in the limit of integration. It was shown in [27] that the nuclear-density distribution can be expressed in terms of a convolution integral involving the Yukawa function over the volume of a nucleus with a sharp boundary; that is,

$$\rho_n(\mathbf{r}_1) = \frac{\rho_{n0}}{4\pi a_Y^3} \int\limits_V \frac{e^{-r/a_Y}}{r/a_Y} d^3 r_2, \qquad (18)$$

where $a_Y = 0.75$ fm is the parameter of the Yukawa function; ρ_{n0} is the value of the nucleon density at the center of the nucleus, $\rho_{n0} = A/V$; and integration is performed over entire volume V of the nucleus. The parameter value of $a_Y = 0.75$ fm was chosen from the condition requiring that the diffuseness of the nuclear surface be 2.4 fm [27].

If we choose const $= c_s a_Y/(\pi r_0^2 \rho_0^2)$ in (17) and the nuclear-density distribution in the form (18), we obtain formula (11). The integral in (17) can be calculated by the method described in [27]. Thus, formula (11) represents the surface (gradient) term in

the statistical functional of the nuclear energy for the density distribution (18). In the particular case of a semi-infinite medium ($z < 0$), the density distribution (18) takes the form

$$\rho_n(z) = \begin{cases} \dfrac{\rho_{n0}}{2}\left(2 - e^{z/a_Y}\right), & z \le 0, \\ \dfrac{\rho_{n0}}{2} e^{-z/a_Y}, & z \ge 0. \end{cases} \tag{19}$$

This interpretation (it was proposed in [5]) of the nuclear energy within the liquid-drop model taking into account a finite range of nuclear forces and the diffuse distribution of the nuclear density is of importance for the present study in what is concerned with specifying the concept of a scission nuclear configuration. On the basis of formula (18), we can consider the distribution of the nucleon density and, accordingly, introduce the concept of the contact of fragments at the instant of scission. If the nucleon-density distribution is specified in the form (18), the sharp boundary of a nucleus is an effective surface that lies within a diffuse layer, where the nuclear density is one-half as great as the density at the center of a nucleus, $\rho_n = \rho_{n0}/2$. In this case, a continuous form will correspond, at $s = 0$, to the fragments depicted in Fig. 1. As the fragments move apart at a distance $s > 0$, the density at the point z_N gradually decreases. The contact of fragments is realized when the value of the density at the point z_N is equal to $\rho_n = \rho_{n0}/2$. In the case of half-spaces of nuclear matter, it follows from formulas (19) that this value of the density will be achieved for fragments separated by the distance $s_{\text{rup}} = 2a_Y \ln 2$. The calculations performed in [5] revealed that, at a finite neck radius ($R_N \ge 0.2R_0$), the density at the midpoint between two fragments is $\rho_{n0}/2$ at approximately the same value of s. For $A > 200$ heavy nuclei, which are considered in the present study, we have $s_{\text{rup}} \simeq 0.13R_0$. It can be seen from Fig. 2 that, if we choose $s_{\text{rup}} = 0.13R_0$ for the spacing between the fragments, the initial and final states of the system are not separated by a barrier; in calculating the scission probability by formula (1), we therefore use the difference of the initial- and the final-state energies, $\Delta E = U(\mathbf{q}, s_{\text{rup}}) - U(\mathbf{q}, 0)$.

2.2. Wall-Plus-Window Formula for One-Body Dissipation and Probabilistic Scission of a Nucleus

In connection with the probabilistic scission of a fissile nucleus into fragments—and this is the subject of the present study—it is worth noting that, within macroscopic collective nuclear dynamics, a similar approach has already been developed and successfully used in calculating the friction properties of a fissile nucleus within the mechanism of one-body dissipation [29]. Upon introducing a number of simplifications concerning the mechanism of collisions between nucleons and the nuclear surface, the authors of [30] were able to obtain simple formulas for the one-body mechanism of dissipation (wall and wall-plus-window formulas). A quantum analysis of one-body dissipation revealed [31] that the magnitude of viscosity in a nucleus is only about 10% of values computed by the wall formula [32, 30] [bracketed expression on the right-hand side of formula (20) below], but that the functional dependence of viscosity on the nuclear shape is reproduced correctly by this formula. In view of this, Nix and Sierk [29, 33] proposed a modified version of one-body dissipation. In this version, referred to as the surface-plus-window one, the contribution of the wall formula to dissipation is reduced with the aid of a coefficient k_s. In the surface-plus-window mechanism of dissipation, the expression for the friction-tensor components has the form

$$\gamma_{ij}^{\text{sw}} = \frac{1}{2}\rho_m \bar{v}\left\{\frac{\partial R}{\partial q_i}\frac{\partial R}{\partial q_j} S_w + \frac{32}{9}\frac{1}{S_w}\frac{\partial V_1}{\partial q_i}\frac{\partial V_1}{\partial q_j}\right. \tag{20}$$

$$+ k_s\left[\pi \int_{z_{\min}}^{z_N} \left(\frac{\partial \rho_s^2}{\partial q_i} + \frac{\partial \rho_s^2}{\partial z}\frac{\partial D_1}{\partial q_i}\right)\left(\frac{\partial \rho_s^2}{\partial q_j} + \frac{\partial \rho_s^2}{\partial z}\frac{\partial D_1}{\partial q_j}\right)\right.$$

$$\times \left(\rho_s^2 + \left(\frac{1}{2}\frac{\partial \rho_s^2}{\partial z}\right)^2\right)^{-\frac{1}{2}} dz$$

$$+ \pi \int_{z_N}^{z_{\max}} \left(\frac{\partial \rho_s^2}{\partial q_i} + \frac{\partial \rho_s^2}{\partial z}\frac{\partial D_2}{\partial q_i}\right)\left(\frac{\partial \rho_s^2}{\partial q_j} + \frac{\partial \rho_s^2}{\partial z}\frac{\partial D_2}{\partial q_j}\right)$$

$$\left.\left.\times \left(\rho_s^2 + \left(\frac{1}{2}\frac{\partial \rho_s^2}{\partial z}\right)^2\right)^{-\frac{1}{2}} dz\right]\right\},$$

where ρ_m is the nuclear density; $\bar{v}$ is the mean velocity of intranuclear nucleons; S_w is the area of the window—that is, the neck between the two would-be fragments; R is the distance between the centers of mass of the would-be fragments; D_1 and D_2 are the positions of their centers of mass with respect to the coordinates of the center of mass of the entire system; $z_{\min}$ and $z_{\max}$ are, respectively, the left and the right boundary of the nuclear surface; z_N is the neck coordinate chosen at the minimum of the function $\rho_s^2(z)$; V_1 is the volume of one of the would-be fission fragments; and k_s is a factor that characterizes the reduction of the wall-formula contribution. The value of the reduction factor k_s was determined from an analysis of the experimental widths of giant resonances; the result was $k_s = 0.27$. From a comparison of the calculated mean values of the kinetic energies of fission fragments with experimental data,

it was found that the reduction factor k_s lies in the range $0.2 < k_s < 0.5$ [33]. The value of $k_s = 1$ corresponds to the total one-body viscosity; in this case, formula (20) is referred to as the wall-plus-window formula.

In the following, we denote by γ_{ij}^w the friction-tensor components computed by the wall formula. In the present calculations, formula (20) was supplemented with an additional term (second term in the braced expression) that takes into account dissipation associated with the change in the volumes of the would-be fragments that is caused by nucleon exchange between them [34, 35]. The inclusion of this term in dynamical calculations is necessary for performing an adequate analysis of the formation of the mass distribution.

For nuclear shapes featuring no neck, the friction tensor was calculated by the wall formula with a reduction factor k_s. For the intermediate case where a neck has already appeared, but where its radius is not very small in relation to the radius of the maximum section of the smaller fragment, the exact expression for the rate of energy dissipation within the mechanism of one-body dissipation is not known. For this reason, use in made of a rather arbitrary interpolation between the wall and surface-plus-window formulas. It has the form [36]

$$\gamma_{ij} = \begin{cases} k_s\gamma_{ij}^w & \text{for nuclear shapes featuring no neck,} \\ k_s\gamma_{ij}^w f + \gamma_{ij}^{\text{sw}}(1-f) & \text{for nuclear shapes featuring a neck,} \end{cases} \tag{21}$$

$$f = \sin^2(\pi R_N/(2R_L)),$$

where R_N is the neck radius and R_L is the maximum value of the function $\rho_s(z)$ for the smaller fragment.

In the probabilistic scission mechanism discussed here, the emergence of a neck in the nuclear shape corresponds to the appearance of the window term [first term in the braced expression on the right-hand side of (20)] in (21), the corresponding deformations being initial ones in considering probabilistic scission. At zero neck radius in (21), only the surface-plus-window formula contributes to the friction tensor, γ_{ij}^{sw}, these deformations being final ones in considering the probabilistic scission of a nucleus into fragments. The space of collective deformations between the initial and final deformations is taken into account through the corresponding factors both in the one-body mechanism of dissipation and in our mechanism of the probabilistic scission of a nucleus into fragments.

2.3. Method for Calculating Observables of the Fission Process in Probabilistic Scission

A simulation of the process through which a nucleus disintegrates into fragments was performed within the stochastic approach [37, 38] based on Langevin equations. A detailed description of the model used here is given in [14, 15]. For this reason, we describe here only the method for calculating observables in the probabilistic simulation of neck rupture.

In a difference form, the Langevin equations can be written as

$$p_i^{(n+1)} = p_i^{(n)} - \left(\frac{1}{2}p_j^{(n)}p_k^{(n)}\left(\frac{\partial\mu_{jk}(\mathbf{q})}{\partial q_i}\right)^{(n)}\right. \tag{22}$$
$$\left. + \left(\frac{\partial V(\mathbf{q})}{\partial q_i}\right)^{(n)} + \gamma_{ij}^{(n)}(\mathbf{q})\mu_{jk}^{(n)}(\mathbf{q})p_k^{(n)}\right)\tau$$
$$+ \theta_{ij}^{(n)}\xi_j^{(n)}\sqrt{\tau},$$
$$q_i^{(n+1)} = q_i^{(n)} + \frac{1}{2}\mu_{ij}^{(n)}(\mathbf{q})(p_j^{(n)} + p_j^{(n+1)})\tau,$$

where $\mathbf{q} = (c, h, \alpha')$ are collective coordinates; $\mathbf{p} = (p_c, p_h, p_{\alpha'})$ are the momenta conjugate to them; m_{ij} ($||\mu_{ij}|| = ||m_{ij}||^{-1}$) is the tensor of inertia; γ_{ij} is the friction tensor; V is the potential energy of the nucleus being considered; θ_{ij} is the amplitude of a random force; τ is a time step in integrating the Langevin equations; the superscripts (n) and $(n+1)$ label, respectively, the nth and the $(n+1)$th step in integration; and ξ_j is a random variable that possesses the following statistical properties:

$$\langle\xi_i^{(n)}\rangle = 0, \tag{23}$$
$$\langle\xi_i^{(n_1)}\xi_j^{(n_2)}\rangle = 2\delta_{ij}\delta_{n_1n_2}.$$

The angular brackets in Eq. (23) denote averaging over the statistical ensemble. Summation over dummy indices from 1 to 3 is implied in Eqs. (22) and (23). By numerically solving the set of Eqs. (22), we obtain, in the space of collective coordinates, a stochastic trajectory that reflects nuclear shapes appearing in the fission process.

In this study, we assume that a nucleus inevitably undergoes fission within the time interval between the instant at which the nuclear shape develops a neck and the instant of the geometric scission of the nucleus. The sum of the probabilities over all scission configurations that the nucleus assumes in the process of evolution is equal to unity. This is the

normalization condition for the probability of scission. In simulating the fission process, we began, for each trajectory, from a spherical shape of a nucleus, $\mathbf{q}_0 = (c = 1, h = 0, \alpha' = 0)$, and terminated the simulation when the the neck radius vanished. Upon the appearance of a neck in the nuclear shape, we determined, at each nth step of the integration of the Langevin equations, the relative probabilities of nuclear scission into fragments, W_n, by formula (1). Simultaneously, we found the masses of fragments and the kinetic energy of their relative motion by using the values of the collective coordinates and of the momenta conjugate to them. In order to obtain the two-dimensional mass–energy distribution, we added, in the corresponding mass and energy bins, the relative probabilities W_n of the realization of these values of the mass and kinetic energy of fragments. For each reaction, we simulated about 10^4 trajectories. The resulting mass–energy distribution was normalized to 200%.

For the ^{215}Fr nucleus at $T = 1.5$ MeV, the relative scission probability W as a function of c and h is displayed in Fig. 3*a* for $\alpha' = 0$. We can see from this figure that the scission probability increases with increasing h—that is, the scission probability is higher for more compact shapes than for elongated ones. This is explained by stronger Coulomb repulsion forces in the former case. Figure 3*b* shows that the scission probability begins to increase sharply only for nuclear shapes having a neck of radius smaller than $0.4R_0$. For shapes featuring a neck of greater radius, the scission probability is nearly vanishing. This is because the sign of ΔE in negative in (1) for such shapes.

In general, any observable Q (this may be the masses and kinetic energies of fragments, prescission multiplicities of light particles, fission times, and so on) can depend on collective coordinates, the momenta conjugate to them, and time. In order to find the kth moments of Q, we used the formula

$$\langle\overline{Q^k}\rangle = \sum_{i=1}^{J}\sum_{n=1}^{M_i} Q_{in}^k W_n \Bigg/ \left(J\sum_{n=1}^{M_i} W_n\right), \qquad (24)$$

where M_i is the number of steps from the instant of neck formation in the nuclear shape to the instant at which the thickness of the neck vanishes for the ith trajectory and J is the total number of trajectories. Summation over n means averaging over the scission configurations within the ith trajectory, while summation over i is averaging over trajectories. The notation Q_{in}^k means that the observable Q is taken at the nth step of the ith trajectory and is raised to a power of k. By using formula (24), we found the mean values and variances of the mass and energy distributions, the mean fission times, and the multiplicities of prescission neutrons, as well as the asymmetry and kurtosis of the mass–energy distribution, which are determined in terms of the third and the fourth moment of the distribution.

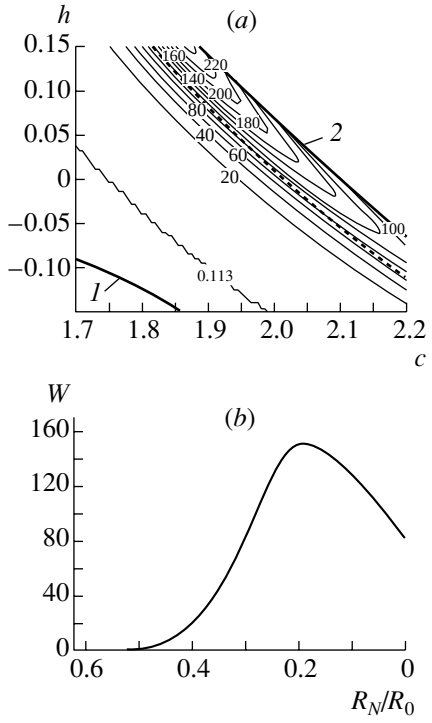

Fig. 3. Probability of nuclear scission into fragments versus the nuclear-shape parameters: (*a*) probability of nuclear scission in the ch plane at $\alpha' = 0$ [numbers on isolines represent the unnormalized probability of nuclear scission into fragments according to the calculations by formula (1)], where curves *1* and *2* correspond to the nuclear shapes developing a neck and having a neck of zero radius, respectively, while the dashed curve corresponds to nuclear shapes featuring a neck of radius $R_N = 0.3R_0$; (*b*) unnormalized nuclear-scission probability calculated by formula (1) as a function of the neck thickness for the case of $h = \alpha' = 0$.

3. RESULTS OF THE CALCULATIONS AND DISCUSSION

In order to investigate the effect of the probabilistic-scission mechanism on observables, we have performed calculations for the reactions

$^{12}\mathrm{C} + {}^{194}\mathrm{Pt} \to {}^{206}\mathrm{Po}$ ($E_{\mathrm{lab}} = 99$ MeV) [39],

$^{18}\mathrm{O} + {}^{197}\mathrm{Au} \to {}^{215}\mathrm{Fr}$ ($E_{\mathrm{lab}} = 158.8$ MeV) [40],

$^{12}\mathrm{C} + {}^{232}\mathrm{Th} \to {}^{244}\mathrm{Cm}$ ($E_{\mathrm{lab}} = 97$ MeV) [41],

$^{20}\mathrm{Ne} + {}^{240}\mathrm{Pu} \to {}^{260}\mathrm{Rf}$ ($E_{\mathrm{lab}} = 142$ MeV) [39].

Indicated above for each reaction are the references from which we borrowed experimental data. For these reactions, there exists a rather vast body of experimental data; moreover, we previously performed calculations for them by using the scission condition $R_N = 0.3R_0$ [14–16].

Table 1. Parameters of the mass and energy distributions for the reactions $^{12}C + {}^{194}Pt \to {}^{206}Po$ ($E_{lab} = 99$ MeV) [39], $^{18}O + {}^{197}Au \to {}^{215}Fr$ ($E_{lab} = 158.8$ MeV) [40], $^{12}C + {}^{232}Th \to {}^{244}Cm$ ($E_{lab} = 97$ MeV) [41], and $^{20}Ne + {}^{240}Pu \to {}^{260}Rf$ ($E_{lab} = 142$ MeV) [39] according to the calculations for two scission conditions versus the factor characterizing the reduction of the wall-formula contribution

C.N.	k_s	σ_M^2, (amu)^2	$(\sigma_M^2)_W$, (amu)^2	$\sigma_{E_K}^2$, MeV^2	$(\sigma_{E_K}^2)_W$, MeV^2	$\langle E_K\rangle$, MeV	$\langle E_K\rangle_W$, MeV
^{206}Po	0.25	280 ± 26	307 ± 29	169 ± 15	175 ± 21	154.1	148.8
	0.50	234 ± 24	261 ± 27	113 ± 11	171 ± 12	151.7	147.7
	1.00	222 ± 25	273 ± 26	102 ± 12	198 ± 19	150.5	138.0
Expt. [39]		165 ± 4		106 ± 3		146.5 ± 0.8	
^{215}Fr	0.25	328 ± 15	354 ± 33	210 ± 9	195 ± 18	159.7	156.1
	0.50	261 ± 5	295 ± 17	139 ± 2	189 ± 8	157.2	155.0
	1.00	219 ± 13	270 ± 16	109 ± 6	207 ± 12	155.1	154.2
Expt. [40]		272		190		154	
^{244}Cm	0.25	315 ± 14	345 ± 17	143 ± 6	180 ± 11	188.1	180.6
	0.50	271 ± 23	298 ± 15	110 ± 9	195 ± 12	187.8	179.3
	1.00	233 ± 35	245 ± 16	106 ± 15	206 ± 12	187.6	177.8
Expt. [41]		366		259		178	
^{260}Rf	0.25	365 ± 12	346 ± 17	202 ± 7	263 ± 12	218.3	207
	0.50	315 ± 14	327 ± 19	173 ± 7	274 ± 15	218.0	206
	1.00	254 ± 25	279 ± 23	157 ± 15	310 ± 24	217.8	205
Expt. [39]		506 ± 12		372 ± 13		195 ± 2	

Note: The following notation is used in the table: (C.N.) compound nucleus, (k_s) factor characterizing the reduction of the wall-formula contribution, (σ_M^2) variance of the mass distribution, ($\sigma_{E_K}^2$) variance of the energy distribution, and ($\langle E_K\rangle$) mean kinetic energy of fragments. The subscript W on a quantity means that it was calculated by using the probabilistic scission condition. The quantities carrying no subscript W were calculated under the scission condition $R_N = 0.3R_0$ [14–16]. Some values presented in this table differ from their counterparts in [14–16] since statistics were larger in our present calculations.

For each of the above reactions, we have calculated the two-dimensional mass–energy distribution $Y(E_K, M)$, the mean prescission-neutron multiplicity $\langle n_{pre}\rangle$, and the mean fission time $\langle t_f\rangle$. The results obtained by calculating the two-dimensional mass–energy distribution will analyzed in terms of the one-dimensional mass and energy distributions. The one-dimensional mass distribution can be derived by integrating $Y(E_K, M)$ with respect to E_K, while the one-dimensional energy distribution is obtained by integrating $Y(E_K, M)$ with respect to M.

The results of the calculations are presented in Tables 1 and 2 and in Figs. 4–6. In a probabilistic simulation of the scission of a nucleus into fragments, the set of prescission configurations becomes much wider than in the calculations where a specific value of the neck radius is chosen as a scission criterion. A transition from the scission condition $R_N = 0.3R_0$ to a probabilistic simulation of nuclear scission leads to a moderate increase (of 5 to 10%) in the variance of the mass distribution, irrespective of the mass of a fissile nucleus and k_s. We have also calculated the asymmetry γ_3 and the kurtosis γ_4 of the mass and energy distributions. These quantities characterize the deviation of the distributions under investigation from a Gaussian distribution, for which one has $\gamma_3 = \gamma_4 = 0$. The results of the calculations show that the mass distribution retains a Gaussian shape (the kurtosis and asymmetry virtually vanish). Figure 4 shows the mass distribution for the ^{244}Cm nucleus according to the calculations for the scission condition $R_N = 0.3R_0$ and according to the calculations with the probabilistic scission condition at $k_s = 0.25$.

As might have been expected on the basis of physical considerations, the change in the scission condition leads to a considerable variation in the parameters of the energy distribution. As can be seen from Fig. 5, the scission probability is maximal for nuclear shapes having a neck radius less than $0.3R_0$. For such

Table 2. Asymmetry and kurtosis of the energy distribution, mean multiplicity of prescission neutrons, and mean fission times for the reactions $^{12}C + {}^{194}Pt \to {}^{206}Po$ ($E_{lab} = 99$ MeV) [39], $^{18}O + {}^{197}Au \to {}^{215}Fr$ ($E_{lab} = 158.8$ MeV) [40], $^{12}C + {}^{232}Th \to {}^{244}Cm$ ($E_{lab} = 97$ MeV) [41], and $^{20}Ne + {}^{240}Pu \to {}^{260}Rf$ ($E_{lab} = 142$ MeV) [39] according to the calculations for two scission conditions versus the factor characterizing the reduction of the wall-formula contribution

C.N.	k_s	γ_3	$(\gamma_3)_W$	γ_4	$(\gamma_4)_W$	$\langle n_{pre}\rangle$	$\langle n_{pre}\rangle_W$	$\langle t_f\rangle, 10^{-21}$ s	$\langle t_f\rangle_W, 10^{-21}$ s
^{206}Po	0.25	−0.52	0.37	1.55	1.83	2.8	3.2	111	143
	0.50	−0.19	0.61	0.97	1.3	3.6	3.7	213	252
	1.00	−0.1	0.67	0.78	0.72	3.9	4.4	305	361
Expt. [39]						2.8			
^{215}Fr	0.25	−0.71	−0.4	1.6	1.17	3.0	3.3	33.6	42
	0.50	−0.33	0.34	0.63	0.42	4.3	4.4	82	97
	1.00	−0.15	0.2	0.35	0.15	5.2	5.2	152	179
Expt. [40]						4.1			
^{244}Cm	0.25	−0.6	0.22	1.74	1.52	2.0	2.4	24	34
	0.50	−0.11	0.15	1.59	1.34	3.2	3.5	64	82
	1.00	0.05	0.19	0.32	0.71	4.2	4.4	154	171
Expt. [41]						3.0			
^{260}Rf	0.25	−0.52	0.36	1.67	1.22	1.3	1.3	15	16
	0.50	−0.26	0.27	0.91	0.65	2.0	2.1	30	34
	1.00	−0.12	0.18	0.54	0.44	2.9	3.0	69	76
Expt. [39]						3.5			

Note: The following notation is used in the table: (C.N.) compound nucleus, (k_s) factor characterizing the reduction of the wall-formula contribution, (γ_3) asymmetry of the energy distribution, (γ_4) kurtosis of the energy distribution, ($\langle n_{pre}\rangle$) mean multiplicity of prescission neutrons, and ($\langle t_f\rangle$) mean fission time. The subscript W on a quantity means that it was calculated by using the probabilistic scission condition. The quantities carrying no subscripts W were calculated under the scission condition $R_N = 0.3R_0$ [14, 15].

prescission shapes, the kinetic energy of fragments (E_K) appears to be less than that for shapes characterized by the neck radius of $R_N = 0.3R_0$. In view of this, the values obtained for $\langle E_K\rangle$ by using the probabilistic scission condition proved to be less by 5–8 MeV, on average, than those calculated under the scission condition $R_N = 0.3R_0$, and this improves the agreement between the calculated values and experimental data on $\langle E_K\rangle$.

According to the experimental data reported in [44], where the asymmetry γ_3 and the kurtosis γ_4 of the energy distributions were investigated for compound nuclei from Os to U at various excitation energies, the energy distributions are characterized by invariability and a small magnitude of these moments: $\gamma_3 \simeq -0.1$ and $\gamma_4 \simeq 0$. Table 2 gives γ_3 and γ_4 values calculated for the two scission mechanisms at various values of k_s. It can be seen from Table 2 and from Fig. 6 that a transition from the scission condition $R_N = 0.3R_0$ to the probabilistic scission results in that the shape of the energy distributions becomes closer to a Gaussian shape.

The change in the scission condition also leads to an increase in the variance of the energy distribution. It appears, however, that the increase in the variance of the energy distribution depends on the factor k_s characterizing the reduction of the wall-formula contribution. By way of example, we indicate that, at $k_s = 1$, the values of the variance increase approximately by a factor of two for all nuclei considered in this study, while, at $k_s = 0.25$, the values of the variance remained unchanged within the statistical error. This behavior of the variance of the energy distributions versus k_s is explained by the dependence of the character of the motion of the nucleus descending from the saddle to the scission point on viscosity. In the case of low viscosity ($k_s = 0.25$), the energy of the collective motion of the nucleus is rather high, so that the set of prescission shapes appears to be quite wide even under the scission condition $R_N = 0.3R_0$, the variance of the energy distributions accordingly

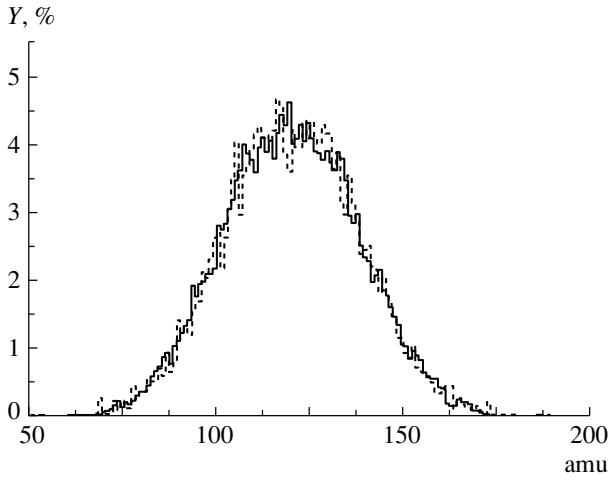

Fig. 4. Mass distributions calculated for the reaction $^{12}C + {}^{232}Th \to {}^{244}Cm$ ($E_{lab} = 97$ MeV) at $k_s = 0.25$: (solid-line histogram) results obtained by using the probabilistic condition of scission and (dashed-line histogram) results obtained with the scission condition $R_N = 0.3R_0$ [14].

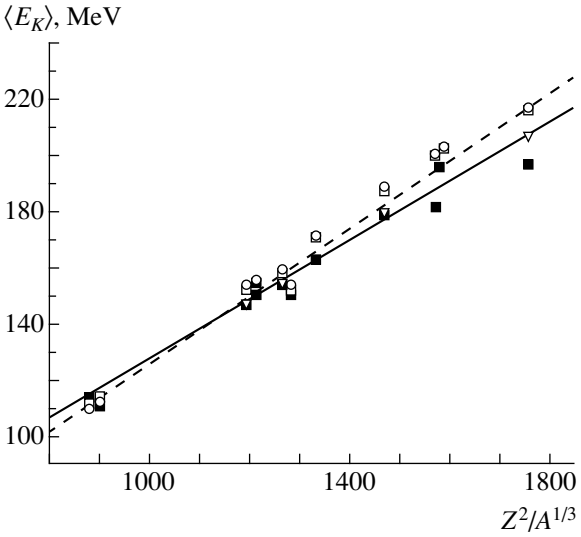

Fig. 5. Mean kinetic energy of fragments, $\langle E_K \rangle$, as a function of the parameter $Z^2/A^{1/3}$: (closed boxes) experimental data; (open boxes and circles) results of the calculations at $k_s = 0.5$ and $k_s = 0.25$, respectively, under the scission condition $R_N = 0.3R_0$ [14–16]; (open triangles) results of the calculations at $k_s = 0.5$ under probabilistic scission conditions; (solid line) systematics obtained by Rusanov and his collaborators [42] ($\langle E_K \rangle = (0.104Z^2/A^{1/3} + 24.3)$ MeV in the range $Z^2/A^{1/3} = 900$–1800); and (dashed line) systematics of Viola and his collaborators [43] ($\langle E_K \rangle = (0.1189Z^2/A^{1/3} + 7.3)$ MeV).

proving to be quite large. In this case, a transition to the probabilistic simulation of scission only leads to a change in the shape of the energy distribution—it becomes closer to a Gaussian shape—but there does not occur a considerable increase in the variance. At a high viscosity ($k_s = 1$), in which case the nuclei are superviscous, with the result that the system occurs in the regime of overdamping, the energy of collective motion is low. A major part of the excitation energy will be converted into internal energy and will be carried away by evaporating light prescission particles. Evolving in the overdamped mode, the system will slowly creep to the scission surface along the bottom of the fission valley, the nucleus slowly changing its shape. In the case of the scission condition $R_N = 0.3R_0$, this will lead to a rather meager set of prescission shapes. Upon going over to the probabilistic simulation of the scission of a nucleus into fragments, the set of prescission shapes becomes considerably richer owing to the inclusion of additional shapes that the nucleus had at the stage of descent from the instant of neck formation in the nuclear shape to the instant at which the neck thickness vanishes. In this case, not only does the shape of the energy distribution change but also its variance increases considerably.

Upon a transition from the scission condition $R_N = 0.3R_0$ to the probabilistic simulation of scission, the fission time and, hence, the multiplicity of prescission neutrons increase (see Table 2). This is because the maximum fission probability corresponds to nuclear shapes having a neck radius smaller than $0.3R_0$ (see Fig. 3).

In [5], the parameters of the mass–energy distribution of fission fragments were also computed by using the probabilistic scission condition, and the results obtained there for the mean kinetic energy of fragments and for the variances of the mass and energy distributions were found to be in good quantitative agreement with available experimental data for a large number of nuclear species. It should be noted, however, that, in [5], no account was taken of the evaporation of light prescission particles, which has a pronounced effect on the parameters of the mass–energy distribution [11], since evaporating particles carry away a significant part of the excitation energy, thereby reducing the variances of the mass and energy distributions. Also, the simulation of fission dynamics in [5] completely disregarded dissipative and fluctuation phenomena, which, in our opinion, play, a significant role in the formation of fragment distributions.

4. CONCLUSION

Our calculations have revealed that the Strutinsky criterion according to which the scission of a nucleus occurs at a finite thickness of the neck [1, 2] is a good approximation to the probabilistic scission criterion for $k_s < 0.5$. The shape of the energy distribution

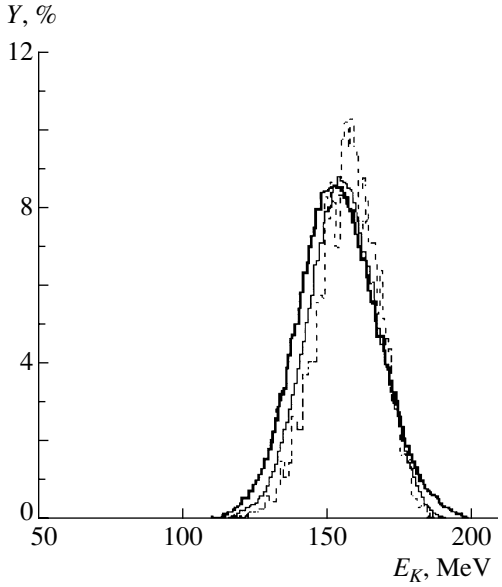

Fig. 6. Energy distributions calculated for the reaction $^{18}O + {}^{197}Au \rightarrow {}^{215}Fr$ ($E_{lab} = 158.8$ MeV) at $k_s = 0.5$: (thin-solid-line histogram) results of the calculations with the probabilistic scission condition, (dashed-line histogram) results of the calculations with the scission condition $R_N = 0.3R_0$ [15], (thick-solid-line histogram) experimental data borrowed from [40].

changes upon going over from the scission condition $R_N = 0.3R_0$ to a probabilistic simulation. It becomes closer to a Gaussian shape, and its variance increases; this is in better agreement with experimental data. In the case of a probabilistic simulation of scission, the calculated values of $\langle E_K \rangle$ also become closer to available experimental data and systematics [42, 43]. The variance of the mass distribution increases by approximately 5 to 10%, irrespective of k_s values. A transition from the scission condition $R_N = 0.3R_0$ to the probabilistic simulation also leads to an increase in the mean multiplicity of neutrons and in the fission time. As in [14], we were unable, however, to reproduce simultaneously the mean multiplicity of prescission neutrons and the variances of the mass and energy distributions for ^{260}Rf, which was the heaviest nucleus considered in the present study. Therefore, the conclusion drawn previously in [14, 15] remains in force: for reactions involving the formation of heavy nuclei (like Fm and heavier ones) and occurring with high angular-momentum transfers, in which case the fission barrier disappears, it would be incorrect to begin calculations from the statistically equilibrium ground state of a nucleus, but it is necessary to consider fission dynamics with allowance for the entrance channel of the fusion–fission reaction.

ACKNOWLEDGMENTS

We are grateful to Drs. A.Ya. Rusanov and A.V. Karpov for numerous enlightening discussions and for carefully reading the manuscript of this article and to O.V. Lakhina for performing testing calculations within two-dimensional Langevin dynamics.

APPENDIX

In order to derive expressions for the Coulomb and the nuclear energy of the interaction of the system of two fragments shown in Fig. 1, we used a method that is similar to that described in [18]. It should be emphasized that the authors of [18] calculated the forces (rather than the energies) of the Coulomb and nuclear interactions of fragments in the limit $s \to 0$. Also we calculated the energies of fragment interaction by using the sum of the Yukawa and the exponential nuclear potential [22] and not the mere Yukawa potential, as in [18]. The energies of the Coulomb and nuclear interactions determined within the liquid-drop model taking into account the diffuse boundary of the nuclear surface and a finite range of nuclear forces have the form

$$U = \int_{V_1}\int_{V_2} f(|\mathbf{r}_1 - \mathbf{r}_2|)d^3r_1 d^3r_2, \qquad \text{(A.1)}$$

where f is is a scalar function of $|\mathbf{r}_1 - \mathbf{r}_2|$, its explicit form being given by the integrands in (11) and (12) for the nuclear and the Coulomb interaction, respectively. In contrast to Eqs. (11) and (12), where integration is performed over the entire volume of a nucleus, the calculation of the interaction energies involves integration over the volumes V_1 and V_2 of the left- and the right-hand fragment, respectively.

Let us apply Gauss' theorem to the integral in (A.1). Since the surface of each fragment consists of the surface formed by the rotation of the function $\rho_s(z)$ about the z axis (surfaces A and D in Fig. 1) and the planar-cut surface formed upon the disintegration of the continuous nuclear shape into fragments (surfaces B and C in Fig. 1), the integral in (A.1) can be written in the form

$$U = \oint_{S_1}\oint_{S_2} \Big\{ (d\mathbf{S}_A \cdot \mathbf{r})\,(d\mathbf{S}_D \cdot \mathbf{r}) \qquad \text{(A.2)}$$
$$+ (d\mathbf{S}_A \cdot \mathbf{r})\,(d\mathbf{S}_C \cdot \mathbf{r}) + (d\mathbf{S}_B \cdot \mathbf{r})\,(d\mathbf{S}_D \cdot \mathbf{r})$$
$$+ (d\mathbf{S}_B \cdot \mathbf{r})\,(d\mathbf{S}_C \cdot \mathbf{r}) \Big\} F(r)$$
$$= U_{AD} + U_{AC} + U_{BD} + U_{BC},$$

where $\mathbf{r} = \mathbf{r}_2 - \mathbf{r}_1$, the surface S_1 is formed by the surfaces S_A and S_B, and the surface S_2 is formed by the surfaces S_C and S_D.

By explicitly expressing the elements $d\mathbf{S}$ and $\mathbf{r}$ in terms of cylindrical coordinates, we obtain

$$U_{AD} = 2\int\limits_{-c-s/2}^{z_N-s/2} dz_1 \int\limits_0^{2\pi} d\phi \int\limits_{z_N+s/2}^{c+s/2} dz_2 \qquad \text{(A.3)}$$

$$\times \left[\rho_s(z_1)\rho_s(z_2)\cos\phi - \rho_s^2(z_1) - \rho_s(z_1)\right.$$

$$\left.\times \frac{\partial\rho_s(z_1)}{\partial z_1}(z_2 - z_1)\right]\left[\rho_s^2(z_2) - \rho_s(z_1)\rho_s(z_2)\cos\phi\right.$$

$$\left. - \rho_s(z_2)\frac{\partial\rho_s(z_2)}{\partial z_2}(z_2 - z_1)\right]F(r),$$

$$r = (\rho_s^2(z_1) + \rho_s^2(z_2) - 2\rho_s(z_1)\rho_s(z_2)\cos\phi + (z_1 - z_2)^2)^{1/2},$$

$$U_{AC} = -2\int\limits_{-c-s/2}^{z_N+s/2} dz_1 \int\limits_0^{2\pi} d\phi \int\limits_0^{\rho_s(z_N+s/2)} \rho_2 d\rho_2 \quad \text{(A.4)}$$

$$\times (z_N + s/2 - z_1)\left[\rho_s(z_1)\rho_2\cos\phi - \rho_s^2(z_1)\right.$$

$$\left. - \rho_s(z_1)\frac{\partial\rho_s(z_1)}{\partial z_1}(z_N + s/2 - z_1)\right]F(r),$$

$$r = \left(\rho_s^2(z_1) + \rho_2^2 - 2\rho_s(z_1)\rho_2\cos(\phi) + (z_N + s/2 - z_1)^2\right)^{1/2},$$

$$U_{BD} = 2\int\limits_0^{\rho_s(z_N-s/2)} \rho_1 d\rho_1 \int\limits_0^{2\pi} d\phi \int\limits_{z_N+s/2}^{c+s/2} dz_2 \quad \text{(A.5)}$$

$$\times \left(z_2 - z_N + \frac{s}{2}\right)\left[\rho_s^2(z_2) - \rho_1\rho_s(z_2)\cos\phi\right.$$

$$\left. - \rho_s(z_2)\frac{\partial\rho_s(z_2)}{\partial z_2}\left(z_2 - z_N + \frac{s}{2}\right)\right]F(r),$$

$$r = (\rho_1^2 + \rho_s^2(z_2) - 2\rho_1\rho_s(z_2)\cos(\phi) + (z_2 - z_N + s/2)^2)^{1/2},$$

$$U_{BC} = -2s^2\int\limits_0^{\rho_s(z_N-s/2)} \rho_1 d\rho_1 \qquad \text{(A.6)}$$

$$\times \int\limits_0^{2\pi} d\phi \int\limits_0^{\rho_s(z_N+s/2)} \rho_2 d\rho_2 F(r),$$

$$r = \left(\rho_1^2 + \rho_2^2 - 2\rho_1\rho_2\cos(\phi) + s^2\right)^{1/2}.$$

Here, the function $F(r)$ for the Coulomb ($U_{\mathrm{C}}(\mathbf{q}, s)$) and the nuclear ($U_n(\mathbf{q}, s)$) interaction is given by Eqs. (15), and s is the spacing between the fragments.

REFERENCES

1. V. M. Strutinsky, N. Ya. Lyashchenko, and N. A. Popov, Nucl. Phys. **46**, 639 (1963).
2. M. Brack *et al.*, Rev. Mod. Phys. **44**, 320 (1972).
3. U. Brosa, S. Grossmann, and A. Müller, Phys. Rep. **194**, 167 (1990); U. Brosa and S. Grossmann, Z. Phys. A **310**, 177 (1983).
4. M. G. Itkis and A. Ya. Rusanov, Fiz. Élem. Chastits At. Yadra **29**, 389 (1998) [Phys. Part. Nucl. **29**, 160 (1998)].
5. A. I. Startsev, in *Proceedings of the XIII Meeting on Physics of Nuclear Fission (SSCRF–IPPE), Obninsk, 1995*, Ed. by B. D. Kuzminov, p. 94.
6. V. A. Rubchenya and S. G. Yavshits, Yad. Fiz. **40**, 649 (1984) [Sov. J. Nucl. Phys. **40**, 416 (1984)].
7. J. R. Nix and W. J. Swiatecki, Nucl. Phys. **71**, 1 (1965); J. R. Nix, Nucl. Phys. A **130**, 241 (1969).
8. K. T. R. Davies, A. J. Sierk, and J. R. Nix, Phys. Rev. C **13**, 2385 (1976).
9. J. W. Negele, S. E. Koonin, P. Möller, and J. R. Nix, Phys. Rev. C **17**, 1098 (1978); A. J. Sierk, S. E. Koonin, and J. R. Nix, Phys. Rev. C **17**, 646 (1978).
10. R. W. Hasse, Nucl. Phys. A **128**, 609 (1969); Phys. Rev. C **4**, 572 (1971).
11. G.-R. Tillack, R. Reif, A. Schülke, *et al.*, Phys. Lett. B **296**, 296 (1992); G.-R. Tillack, Phys. Lett. B **278**, 403 (1992).
12. S. Cohen, F. Plasil, and W. J. Swiatecki, Ann. Phys. (N.Y.) **82**, 557 (1974).
13. J. Bao, Y. Zhuo, and X. Wu, Z. Phys. A **352**, 321 (1995).
14. A. V. Karpov, P. N. Nadtochy, D. V. Vanin, and G. D. Adeev, Phys. Rev. C **63**, 054610 (2001).
15. P. N. Nadtochy, A. V. Karpov, and G. D. Adeev, Yad. Fiz. **65**, 832 (2002) [Phys. At. Nucl. **65**, 799 (2002)].
16. P. N. Nadtochy, G. D. Adeev, and A. V. Karpov, Phys. Rev. C **65**, 064615 (2002).
17. J. F. Berger, M. Girod, and D. Gogny, Nucl. Phys. A **428**, 23c (1984); **502**, 85c (1989).
18. K. T. R. Davies, R. A. Managan, J. R. Nix, and A. J. Sierk, Phys. Rev. C **16**, 1890 (1977).
19. L. D. Landau and E. M. Lifshitz, *Statistical Physics*, Parts 1 and 2, 3rd ed. (Pergamon Press, Oxford, 1980; Nauka, Moscow, 1976).
20. A. T. D'yachenko, V. A. Rubchenya, and V. P. Éĭsmont, Izv. Akad. Nauk SSSR, Ser. Fiz. **45**, 764 (1981).
21. S. A. Karamyan, Yu. Ts. Oganesyan, and B. I. Pustyl'nik, Yad. Fiz. **11**, 982 (1970) [Sov. J. Nucl. Phys. **11**, 546 (1970)].
22. H. J. Krappe, J. R. Nix, and A. J. Sierk, Phys. Rev. C **20**, 992 (1979).
23. G. I. Kosenko, D. V. Vanin, and G. D. Adeev, Yad. Fiz. **61**, 416 (1998) [Phys. At. Nucl. **61**, 356 (1998)].

24. P. Fong, Phys. Rev. **102**, 434 (1956).
25. R. W. Hasse and W. D. Myers, *Geometrical Relationships of Macroscopic Nuclear Physics* (Springer-Verlag, Berlin, 1988).
26. A. J. Sierk, Phys. Rev. C **33**, 2039 (1986).
27. K. T. R. Davies and J. R. Nix, Phys. Rev. C **14**, 1977 (1976).
28. H. A. Bethe, *Theory of Nuclear Matter* (Paolo Alto, California, 1971; Mir, Moscow, 1974); Ann. Rev. Nucl. Sci. **21**, 93 (1971).
29. J. R. Nix and A. J. Sierk, in *Proceedings of the International School–Seminar on Heavy Ion Physics, Dubna, USSR, 1986*, Ed. by M. I. Zarubina and E. V. Ivashkevich (JINR, Dubna, 1987), p. 453; J. R. Nix, Nucl. Phys. A **502**, 609 (1989).
30. J. Blocki *et al.*, Ann. Phys. (N.Y.) **113**, 330 (1978); J. Randrup and W. J. Swiatecki, Ann. Phys. (N.Y.) **125**, 193 (1980).
31. J. J. Griffin and M. Dworzecka, Nucl. Phys. A **455**, 61 (1986).
32. A. J. Sierk and J. R. Nix, Phys. Rev. C **21**, 982 (1980).
33. J. R. Nix and A. J. Sierk, in *Proceedings of the 6th Adriatic Conference on Nuclear Physics "Frontiers of Heavy Ion Physics," Dubrovnik, Yugoslavia, 1987*, Ed. by N. Cindro, R. Caplar, and W. Greiner (World Sci., Singapore, 1990), p. 333.
34. H. T. Feldmeier, Rep. Prog. Phys. **50**, 915 (1987).
35. J. Randrup and W. J. Swiatecki, Nucl. Phys. A **429**, 105 (1984).
36. J. Blocki, H. T. Feldmeier, and W. J. Swiatecki, Nucl. Phys. A **459**, 145 (1986).
37. H. A. Kramers, Physica **7**, 284 (1940).
38. H. J. Krappe, in *Proceedings of the International Workshop on Dynamical Aspects of Nuclear Fission, Smolenice, Slovakia, 1991*, Ed. by J. Kristiak and B. I. Pustylnik (JINR, Dubna, 1992), p. 51.
39. G. G. Chubaryan, M. G. Itkis, S. M. Luk'yanov, *et al.*, Yad. Fiz. **56** (3), 3 (1993) [Phys. At. Nucl. **56**, 286 (1993)].
40. D. J. Hinde *et al.*, Phys. Rev. C **45**, 1229 (1992).
41. M. G. Itkis, S. M. Luk'yanov, and V. N. Okolovich, Yad. Fiz. **52**, 23 (1990) [Sov. J. Nucl. Phys. **52**, 15 (1990)].
42. A. Ya. Rusanov, M. G. Itkis, and V. N. Okolovich, Yad. Fiz. **60**, 773 (1997) [Phys. At. Nucl. **60**, 683 (1997)].
43. V. E. Viola, K. Kwiatkowski, and M. Walker, Phys. Rev. C **31**, 1550 (1985).
44. S. V. Zhdanov, M. G. Itkis, S. M. Mul'gin, *et al.*, Yad. Fiz. **55**, 3169 (1992) [Sov. J. Nucl. Phys. **55**, 1766 (1992)]; **56** (2), 55 (1993) [Phys. At. Nucl. **56**, 175 (1993)].

Translated by A. Isaakyan

Physics of Atomic Nuclei, Vol. 66, No. 4, 2003, pp. 632–643. Translated from Yadernaya Fizika, Vol. 66, No. 4, 2003, pp. 661–672.

NUCLEI
Theory

Spectrum of ^{10}Be in the Approximation of the Leading Irreducible Representation of the $SU(3)$ Group

G. F. Filippov[1], K. Kato[2], S. V. Korennov[1,2], and Yu. A. Lashko[1]

Received November 1, 2001; in final form, June 14, 2002

Abstract—An algorithm for implementing the approximation of the leading irreducible representation of the $SU(3)$ group is expounded for a microscopic Hamiltonian involving the potential energy of nucleon–nucleon interaction. An effective Hamiltonian is constructed that reproduces the results of calculations with nucleon–nucleon potentials used in the theory of light nuclei. It is shown that, in many respects, the structure of the effective Hamiltonian is similar to the structure of the Hamiltonian of a triaxial rotor and that, for the wave functions in the Elliott scheme, one can go over to a space where linear combinations of Wigner D functions appear to be the transforms of these functions, but where their normalization requires dedicated calculations. © *2003 MAIK "Nauka/Interperiodica".*

1. INTRODUCTION

In order to investigate the excitation spectrum of valence nucleons in light and medium-mass nuclei, Elliott [1] proposed basis states that are associated with the (λ, μ) irreducible representations of the $SU(3)$ group and which satisfy the Pauli exclusion principle. Special attention was given to the most symmetric irreducible representations, which were referred to as leading irreducible representations. These states feature the maximum number of even nucleon pairs (having an even orbital angular momentum of the relative motion of the nucleons forming a pair, their interaction being represented by the components V_{31} and V_{13} of the central exchange nucleon–nucleon potential) and the minimum number of odd pairs (having an odd orbital angular momentum of the relative motion of the nucleons forming a pair, their interaction being represented by the components V_{33} and V_{11}). While even components correspond to a strong attraction between nucleons, odd components correspond to repulsion, which is necessary for ensuring saturation and consistency with the observation that the nuclear volume is proportional to the number of nucleons. However, the character of nucleon–nucleon forces did not play a major role in justifying the importance of the leading representation in the Elliott scheme. The key argument here hinged upon the properties of the operator of quadrupole–quadrupole interaction chosen to simulate the potential energy of nucleon systems,

$$-\eta \mathbf{Q}\mathbf{Q} = -\eta \left(\hat{G}_2 - \frac{1}{2}\hat{\mathbf{L}}^2 \right).$$

Here, $\mathbf{Q}$ is the tensor of the mass quadrupole moment, η is a positive phenomenological parameter, $\hat{G}_2$ is the second-order Casimir operator of the $SU(3)$ group, and $\hat{\mathbf{L}}^2$ is the square of the orbital angular momentum. The eigenvalue g_2 of the operator $\hat{G}_2$ is maximal for the leading representation. As a result, we can see that, first, the operator $-\eta\mathbf{Q}\mathbf{Q}$ has a minimum eigenvalue in the leading-representation states (this also follows from an analysis of the character of nucleon–nucleon interaction) and, second, the model reproduces the order of the first levels in the ground-state rotational band.

The Elliott scheme was further developed upon the appearance of the pseudo-$SU(3)$ model [2–4] and especially in connection with the trimming-mode problem [5], in which case it is necessary to employ a more complicated phenomenological Hamiltonian and to refine the wave functions both for the ground states of even–even nuclei and for states to which isovector $M1$ transitions occur [6–8]. Light neutron-rich nuclei, such as ^{9,11}Li and ^{10,11}Be, for which (in just the same way as for other light nuclei) calculations can be performed, without recourse to approaches involving a phenomenological Hamiltonian, by using various versions of a microscopic nucleon–nucleon potential, represent yet another possible domain of the application of the $SU(3)$ model. Here, it proved to be possible to solve the problem of constructing an effective Hamiltonian such that (i) it is expressed in terms of the generators of the $SU(3)$ group and (ii) its spectrum coincides with the spectrum of the

[1]Bogolyubov Institute for Theoretical Physics, National Academy of Sciences of Ukraine, Metrologicheskaya ul. 14b, Kiev, 252143 Ukraine.
[2]Hokkaido University, Sapporo 060, Japan.

1063-7788/03/6604-0632$24.00

microscopic Hamiltonian and to answer the question of which of the known $O(3)$ scalar constructions composed of the $SU(3)$ generators must be involved in this effective Hamiltonian.

The objective of this study is to show that, in many respects, the Elliott scheme is analogous to the triaxial-rotor model. In particular, its basis states allowed by the Pauli exclusion principle and the eigenfunctions of a triaxial rotor can both be represented in the form of a superposition of Wigner D functions, although their normalization is determined by the fact that the density matrix in the Elliott scheme corresponds to a mixed state rather than a pure state, which is what we have in the case of a triaxial rotor. This conclusion is also confirmed by the structure of the effective Hamiltonian in the Elliott scheme. It has the form of a linear superposition of scalar constructions that are composed of the generators of the $SU(3)$ group and reduces to the triaxial-rotor Hamiltonian and to integral powers of this Hamiltonian, the maximal power here increasing as the number of quanta in the valence shell grows.

We demonstrate our approach to implementing the approximation of the leading irreducible representation of the $SU(3)$ group by taking the example of the ^{10}Be nucleus. In just the same way as in other microscopic calculations of the spectra of light nuclei, the nucleon–nucleon interaction is simulated by the well-known Volkov ([9]) and Minnesota ([10]) central exchange potentials in order to find out whether it is possible to reproduce, with these potentials, the energies of the observed excitations in the ^{10}Be nucleus. As a rule, the Elliott scheme was employed for rather simple phenomenological effective potentials. For this reason, we present here the most important details of an algorithm for a microscopic Hamiltonian that retain significance in a general case. Further, we give explicit expressions for basic scalar constructions that are composed of the generators of the $SU(3)$ group and show that their linear superposition with arbitrary coefficients reduces to a Hamiltonian for a triaxial rotor. Finally, we determine the parameters of a phenomenological effective potential that is equivalent, in the leading-representation limit, to the microscopic potential of the nucleon–nucleon interaction.

2. ELLIOTT SCHEME AND TRIAXIAL ROTOR

In many respects, the Elliott scheme is similar to the theory of a rigid triaxial rotor [11]. This becomes obvious if we go over to a space where spherical Wigner functions are, as in the case of a rigid rotor, the transforms of the basis wave functions of the leading irreducible representation of the $SU(3)$ group. A transition to this space is accomplished by constructing, for a multinucleon system, a Slater determinant that is a wave function asymmetric under permutations of nucleons—this ensures fulfillment of the requirements of the Pauli exclusion principle—and which, simultaneously, appears to be an invariant quantity generating a complete basis of the leading irreducible representation. As a result, the procedure for calculating matrix elements is considerably simplified both for the operators $\hat{\mathbf{L}}\mathbf{Q}\hat{\mathbf{L}}$ and $\hat{\mathbf{L}}\mathbf{Q}\mathbf{Q}\hat{\mathbf{L}}$, which were introduced in [12] as combinations of the generators of the $SU(3)$ group and which have a direct algebraic interpretation, and for the operators representing the potential energies of central exchange forces and of tensor and spin–orbit nucleon–nucleon interaction and entering into the expression for the microscopic Hamiltonians.

In order to demonstrate the method for constructing the generating function in the form of a Slater determinant and a subsequent transition to the basis of the leading representation of the $SU(3)$ group in terms of linear combinations of Wigner D functions, we consider the ^{10}Be nucleus as a simple example. The problem to be solved at this stage does not reduce to determining the quantum numbers of the basis states. They are known, and we only confirm the fact that our approach reproduces them correctly. Simultaneously, we determine an explicit form of basis functions, along with their normalization, which is necessary for calculating the excitation spectrum within a microscopic theory; we also derive explicit expressions for the probabilities of electromagnetic transitions between various states.

We begin by listing orbitals that we will actually use, distinguishing neutron and proton single-particle states of the ^{10}Be nucleus. In doing this, we consider the minimal number of oscillatory quanta that is allowed by the Pauli exclusion principle.

Omitting the spin–isospin factors, we write two proton orbitals (s and p) in the form

$$\phi_{0\pi}(\mathbf{r}) = \frac{1}{\pi^{3/4}} \exp\left(-\frac{r^2}{2}\right), \qquad (1)$$

$$\phi_{1\pi}(\mathbf{r}) = \frac{\sqrt{2}(\mathbf{u}\cdot\mathbf{r})}{\pi^{3/4}} \exp\left(-\frac{r^2}{2}\right),$$

where the unit vector $\mathbf{u}$ is the first independent vector variable in the space where we will further construct Wigner functions. In each of the two states, $\phi_0(\mathbf{r})$ and $\phi_1(\mathbf{r})$, there are two protons of oppositely directed spins.

We distribute six neutrons of the ^{10}Be nucleus in pairs over three states:

$$\phi_{0\nu}(\mathbf{r}) = \frac{1}{\pi^{3/4}} \exp\left(-\frac{r^2}{2}\right), \qquad (2)$$

$$\phi_{1\nu}(\mathbf{r}) = \frac{\sqrt{2}(\mathbf{u}\cdot\mathbf{r})}{\pi^{3/4}}\exp\left(-\frac{r^2}{2}\right),$$

$$\phi_{2\nu}(\mathbf{r}) = \frac{\sqrt{2}}{\pi^{3/4}}\frac{[\mathbf{w}\times\tilde{\mathbf{u}}]\cdot\mathbf{r}}{\mathbf{u}\cdot\tilde{\mathbf{u}}}\exp\left(-\frac{r^2}{2}\right). \quad (3)$$

Here, there has appeared yet another vector variable—the unit vector $\mathbf{w}$, which is orthogonal to the vector $\mathbf{u}$. By $\tilde{\mathbf{u}}$ and $\tilde{\mathbf{w}}$, we denote the vectors of the conjugate orbitals. These two vectors are mutually orthogonal, but their orientation differs from the orientation of the vectors $\mathbf{u}$ and $\mathbf{w}$.

It can easily be shown that

$$\int \tilde{\phi}_{0\pi}(\mathbf{r})\phi_{0\pi}(\mathbf{r})d\mathbf{r} = 1,\ \int \tilde{\phi}_{1\pi}(\mathbf{r})\phi_{1\pi}(\mathbf{r})d\mathbf{r} = \mathbf{u}\cdot\tilde{\mathbf{u}},$$

$$\int \tilde{\phi}_{0\nu}(\mathbf{r})\phi_{0\nu}(\mathbf{r})d\mathbf{r} = 1,\ \int \tilde{\phi}_{1\nu}(\mathbf{r})\phi_{1\nu}(\mathbf{r})d\mathbf{r} = \mathbf{u}\cdot\tilde{\mathbf{u}},$$

$$\int \tilde{\phi}_{2\nu}(\mathbf{r})\phi_{2\nu}(\mathbf{r})d\mathbf{r} = \frac{\mathbf{w}\cdot\tilde{\mathbf{w}}}{\mathbf{u}\cdot\tilde{\mathbf{u}}}.$$

We compose first the Slater determinant Ψ for the ^{10}Be nucleus from the orbitals in (1)–(3) and the corresponding spin–isospin factors and then the second determinant $\tilde{\Psi}$ from the conjugate orbitals. The latter can be considered as that which is obtained upon rotating the coordinate frame in such a way that the vectors $\mathbf{u}$ and $\mathbf{w}$ become coincident with the vectors $\tilde{\mathbf{u}}$ and $\tilde{\mathbf{w}}$. As a matter of fact, the ensuing manipulations implement the Peierls–Yoccoz algorithm [13] for projecting the wave function onto states characterized by a specific value of the orbital angular momentum. This algorithm consists in evaluating the overlap integral—that is, the integral of the product of these determinants with respect to all single-particle vectors $\mathbf{r}_i$, $i = 1$–10—and subsequently expanding the overlap integral in spherical Wigner functions.

The overlap integral reduces to the simple expression

$$\int \tilde{\Psi}\Psi d\mathbf{r}_1 d\mathbf{r}_2\cdots d\mathbf{r}_{10} = \langle\tilde{\Psi}\Psi\rangle \quad (4)$$
$$= I(^{10}\mathrm{Be}) = (\mathbf{u}\cdot\tilde{\mathbf{u}})^2(\mathbf{w}\cdot\tilde{\mathbf{w}})^2.$$

This expression is the density matrix for a mixed state [14] of a nucleon system. Although integration in (4) is performed with respect to all single-particle variables (and this is the reason why the situation here is unusual), the subsystem of rotational degrees of freedom remains amenable to investigation owing to the generator parameters—that is, the Euler angles that determine the orientation of the vectors $\mathbf{u}$, $\mathbf{w}$, $\tilde{\mathbf{u}}$, and $\tilde{\mathbf{w}}$. Here, we denote by θ_1, θ_2, and θ_3 the angles specifying the orientation of the vectors $\mathbf{u}$ and $\mathbf{w}$ and by $\tilde{\theta}_1$, $\tilde{\theta}_2$, and $\tilde{\theta}_3$ the angles specifying the orientation of the vectors $\tilde{\mathbf{u}}$ and $\tilde{\mathbf{w}}$. The irreducible representation of the $SU(3)$ group yields a mixed state because the basis of this irreducible representation reproduces the dynamics of only rotational degrees of freedom against the background of the dynamics of all the remaining (heat-bath) degrees of freedom that is fixed for all excitations. As is well known (see, for example, [14]), the wave functions in the energy representation [15] are introduced for mixed states inclusive in order to diagonalize the relevant density matrix and to find states in which the system may occur. These states are referred to as eigenstates of the density matrix, the eigenvalues of the density matrix often being associated with the norm of the eigenfunctions. In the following, we will determine both the eigenfunctions and the eigenvalues.

The overlap integral (4) (or, more precisely, an expression of this type) is sometimes referred to as the kernel of normalization. This expression is symmetric under the interchange of the pair formed by the vectors $\mathbf{u}$ and $\tilde{\mathbf{u}}$ and the pair formed by the vectors $\mathbf{w}$ and $\tilde{\mathbf{w}}$. The spatial orientation of the vectors $\mathbf{u}$ and $\mathbf{w}$ is determined by three Euler angles. The other two vectors $\tilde{\mathbf{u}}$ and $\tilde{\mathbf{w}}$ generate yet another trio of Euler angles. Therefore, the overlap integral can be considered as the symmetric kernel of the integral equation; upon determining its eigenfunctions and eigenvalues, this kernel can be represented in the the form of a Hilbert–Schmidt expansion—this corresponds to reducing the density matrix to a diagonal form and to calculating its eigenvalues. It will become clear below that the $SU(3)$ kernel is separable; therefore, a determination of its eigenfunctions and eigenvalues reduces to some simple algebraic operations. Frequently, one includes the eigenvalues in the eigenfunctions, thereby renormalizing the latter. This is the origin of the term "normalization kernel."

Evaluation of the overlap integral (4) is an important step in the realization of the generator-coordinate method in deriving the Hill–Wheeler equation. The overlap integral specifies the space of wave functions that are easy to use in the $SU(3)$ Elliott scheme, and the Euler angles θ_1, θ_2, and θ_3 play the role of generator coordinates. It was shown in [16] that, within the $SU(3)$ scheme, the principal axes of the quadrupole-moment tensor can be associated with valence nucleons; therefore, the motion of valence nucleons can be considered as the rotation of these principal axes. As matter of fact, a transition to functions in the generator-coordinate representation is performed via an integral transformation of functions associated with the $SU(3)$ model. By way of example, we indicate that, if $\phi(\{\mathbf{r}_i\})$ is a coordinate-representation wave function in the $SU(3)$ scheme, the corresponding wave function

$\psi(\{\theta_i\})$ in the generator-coordinate representation is given by

$$\psi(\theta_1,\theta_2,\theta_3) = \int \Psi(\theta_1,\theta_2,\theta_3;\{\mathbf{r}_i\})\phi(\{\mathbf{r}_i\})d\mathbf{r}_1 d\mathbf{r}_2\cdots d\mathbf{r}_{10}.$$

The inverse transformation, if necessary, can also be performed via integration, and it returns the function to the coordinate representation. In principle, this transformation is analogous to a transition from the coordinate representation to the momentum or some other representation.

Yet another comment concerning the strategy of further manipulations is in order. In performing all the ensuing calculations and transformations, it is convenient to employ, instead of wave functions, the overlap integrals of the Slater determinants and the identity operator, the Hamiltonian, and operators corresponding to various transitions and to determine the spectrum of the nuclear system in question by diagonalizing these overlap integrals.

In the p shell, the ^{10}Be nucleus has two particles (protons) and two neutron holes, the symmetry indices λ and μ of the corresponding leading representation being $\lambda = 2$ and $\mu = 2$. This follows, for example, from relation (4), which, in view of the fact that the vectors $\mathbf{u}$, $\mathbf{w}$, $\tilde{\mathbf{u}}$, and $\tilde{\mathbf{w}}$ are of unit length, can be recast into the more convenient form

$$I(^{10}\mathrm{Be}) = (\mathbf{u}\cdot\tilde{\mathbf{u}})^2(\mathbf{w}\cdot\tilde{\mathbf{w}})^2 = d_{11}^2 d_{22}^2, \qquad (5)$$

where d_{11} and d_{22} are elements of the matrix of rotations of Cartesian vectors. As usual, all elements of this matrix depend only on three Euler angles. Of course, the relations $\mathbf{u}\cdot\tilde{\mathbf{u}} = d_{11}$ and $\mathbf{w}\cdot\tilde{\mathbf{w}} = d_{22}$ hold. The Elliott basis appears upon expanding expression (5) in Wigner D functions, where the same Euler angles appear as independent variables. From the point of view of the Peierls–Yoccoz projection method, this expansion is necessary for calculating the weights of states characterized by different values of the orbital angular momentum.

For the (λ,μ) irreducible representation, the overlap integral has the form

$$I(\lambda,\mu) = d_{11}^{\lambda} d_{22}^{\mu} \qquad (6)$$

and its analysis reduces to determining the coefficients $C^L_{K\tilde{K}}$ in the expansion of this integral in Wigner D functions. First, we write this expansion in the form

$$d_{11}^{\lambda} d_{22}^{\mu} = \sum_L \sum_{K\tilde{K}} C^L_{K\tilde{K}} D^L_{K,\tilde{K}}. \qquad (7)$$

It is obvious that $C^L_{K\tilde{K}} = C^L_{\tilde{K}K}$ and that the matrix formed by these expansion coefficients is Hermitian.

General considerations as to which of the Wigner D functions enter into the expansion in (7) can be formulated on the basis of the properties of the D_2 point group [17]. The transformations of this group consist in the reversal of the sign of one of the vectors $\mathbf{u}$ and $\mathbf{w}$ ($\tilde{\mathbf{u}}$ and $\tilde{\mathbf{w}}$) or of the vector orthogonal to the vectors $\mathbf{u}$ and $\mathbf{w}$ ($\tilde{\mathbf{u}}$ and $\tilde{\mathbf{w}}$). If the indices λ and μ are even, the expression $(\mathbf{u}\cdot\tilde{\mathbf{u}})^{\lambda}(\mathbf{w}\cdot\tilde{\mathbf{w}})^{\mu}$ is invariant under these transformations; therefore, it involves only D functions that belong to the symmetric representation of the D_2 group, that is,

$$D^0_{0,0},\ D^2_{0,0},\ D^2_{2+,0},\ D^2_{0,2+},\ D^2_{2+,2+},\ D^3_{2-,2-},$$

and so on (see [17]).

Among the totality of these functions, there are those that cannot appear in the expansion being considered, whose actual composition depends on the choice of the directions for the axes of the original and the rotated coordinate frame. The number of independent states that are involved in the overlap integral does not depend on this choice, but the structure of the states depends on it. We will clarify this statement by considering the example of the overlap integral (5). Following Elliott, we take the z ($\tilde{z}$) and x ($\tilde{x}$) axes to be aligned with the vectors $\mathbf{u}$ ($\tilde{\mathbf{u}}$) and $\mathbf{w}$ ($\tilde{\mathbf{w}}$), respectively. The expansion of the overlap integral then takes the form

$$\begin{aligned} d_{11}^2 d_{22}^2 &= \frac{2}{15}D^0_{0,0} + \frac{5}{21} \qquad (8)\\ &\times\left(\frac{1}{4}D^2_{0,0} + \frac{\sqrt{3}}{4}D^2_{0,2+} + \frac{\sqrt{3}}{4}D^2_{2+,0} + \frac{3}{4}D^2_{2+,2+}\right)\\ &+\frac{1}{3}\left(\frac{3}{4}D^2_{0,0} - \frac{\sqrt{3}}{4}D^2_{0,2+} - \frac{\sqrt{3}}{4}D^2_{2+,0} + \frac{1}{4}D^2_{2+,2+}\right)\\ &+\frac{1}{6}D^3_{2-,2-} + \frac{9}{70}\left(\frac{4}{9}D^4_{0,0} - \frac{2\sqrt{5}}{9}D^4_{0,2+}\right.\\ &\left.-\frac{2\sqrt{5}}{9}D^4_{2+,0} + \frac{5}{9}D^4_{2+,2+}\right). \end{aligned}$$

The five coefficients in front of the five terms on the right-hans side of (8) are the weight factors of the basis states, and their sum is

$$\frac{2}{15} + \frac{5}{21} + \frac{1}{3} + \frac{1}{6} + \frac{9}{70} = 1,$$

as it must be.

Thus, we have reduced the density matrix (4) to a diagonal form, actually listed the quantum numbers of the eigenfunctions of the density matrix, and determined the corresponding eigenvalues. Moreover, it follows from expansion (8) that the basis-state wave functions ψ^{α}_{Lm} (where m is the projection of the orbital angular momentum onto the external axis

and the superscript α stands for an additional quantum number that appears in the case of need) are expressed in terms of Wigner D functions. This is natural since we consider the dynamics of rotational degrees of freedom. The last statement will become obvious upon representing each of the $D^L_{K,\tilde{K}}$ functions in the form

$$D^L_{K,\tilde{K}} = \sum_m D^L_{K,m} D^L_{m,\tilde{K}}.$$

For example, we then have $\psi_0 = 1$ for the ^{10}Be ground state, whose weight is $2/15$, and $\psi_{3m} = D^3_{2-,m}$ for the $L = 3$ state, whose weight is $1/6$. For one of the $L = 2$ states (its weight is $5/21$), we obtain

$$\psi^1_{2m} = \frac{1}{2} D^2_{0,m} + \frac{\sqrt{3}}{2} D^2_{2+,m},$$

while, for the other state, which has the weight of $1/3$, the corresponding result is

$$\psi^2_{2m} = \frac{\sqrt{3}}{2} D^2_{0,m} - \frac{1}{2} D^2_{2+,m}.$$

Finally, the result for the only $L = 4$ state, whose weight is $9/70$, has the form

$$\psi_{4m} = \frac{2}{3} D^4_{0,m} - \frac{\sqrt{5}}{3} D^4_{2+,m}.$$

Thus, we have obtained the wave functions that are identical to the wave functions for the nonaxial-rotor model [11] for the case where the nonaxiality parameter is $\gamma = \pi/6$. In this way, we have established the relationship between two models based on significantly different assumptions.

Thus, the overlap integral [in general, of the form (7) for arbitrary values of the symmetry indices λ and μ and, in particular, of the form (5) for $\lambda = \mu = 2$] is simultaneously a density matrix that was computed by integrating the product of two Slater determinants with respect to all single-particle variables. In contrast to the standard density matrix (see [14]) for which integration is performed with respect to only some of the single-particle vectors, the other vectors playing the role of independent variables of the density matrix, our independent variables of the density matrix are expressed in terms of the vector parameters $\mathbf{u}$ and $\mathbf{w}$ ($\tilde{\mathbf{u}}$ and $\tilde{\mathbf{w}}$) of the Slater determinants. In other words, a determination of the density matrix is accompanied by going over from the space of single-particle variables to the space of Euler angles that appear as independent variables in the simplest realization of the basis states of the irreducible representations of the $SU(3)$ group—that is, in spherical Wigner functions.

We have obtained a density matrix that is diagonal in the representation of the above basis functions. At the same time, the weight factors for different basis functions differ from one another. This confirms once again that our matrix is associated with a mixed state of the nucleon system rather than with a pure state, for which all weight factors would be identical, with their sum being equal to unity, as in the above case.

Suppose that λ and μ are even. We can then expand the density matrix as

$$I(\lambda,\mu) = \sum_L \sum_\alpha w^\alpha_L(\lambda,\mu) \sum_m \psi^\alpha_{Lm} \tilde{\psi}^\alpha_{Lm}, \quad (9)$$

where $w^\alpha_L(\lambda,\mu)$ are weight factors that satisfy the condition

$$\sum_L \sum_\alpha w^\alpha_L(\lambda,\mu) = 1. \quad (10)$$

If $\lambda \geq \mu$ and L is even, we have

$$\psi^\alpha_{Lm} = \sum_{K=0}^{\mu} C^\alpha_{LK} D^L_{K+,m}. \quad (11)$$

But if L is odd, we have

$$\psi^\alpha_{Lm} = \sum_{K=0}^{\mu} C^\alpha_{LK} D^L_{K-,m}. \quad (12)$$

In either case, the following relation holds:

$$\sum_{K=0}^{\mu} C^\alpha_{LK} C^{\alpha'}_{LK} = \delta_{\alpha,\alpha'}. \quad (13)$$

In particular, we have

$$w_0(\lambda,\mu) = \frac{(\lambda-1)!!(\mu-1)!!(\lambda+\mu)!!}{\lambda!!\mu!!(\lambda+\mu+1)!!}, \quad (14)$$

$$w^1_2(\lambda,\mu) = w_0(\lambda,\mu) \frac{5}{2} \frac{\lambda(\lambda+2)+\mu(\mu+2)}{(\lambda+2)(\mu+2)(\lambda+\mu+3)} \times \left\{ \frac{2}{\sqrt{3}} \frac{\lambda\mu+\lambda+\mu}{\lambda-\mu} y - \sqrt{1+y^2} \right\}, \quad (15)$$

$$C^1_{20} = \sqrt{\frac{\sqrt{1+y^2}+1}{2\sqrt{1+y^2}}}, \quad C^1_{22} = \sqrt{\frac{\sqrt{1+y^2}-1}{2\sqrt{1+y^2}}}, \quad (16)$$

where

$$y = \sqrt{3} \frac{(\lambda+\mu+2)(\lambda-\mu)}{\lambda(\lambda+2)+\mu(\mu+2)};$$

$$w^2_2(\lambda,\mu) = w_0(\lambda,\mu) \frac{5}{2} \frac{\lambda(\lambda+2)+\mu(\mu+2)}{(\lambda+2)(\mu+2)(\lambda+\mu+3)} \times \left\{ \frac{2}{\sqrt{3}} \frac{\lambda\mu+\lambda+\mu}{\lambda-\mu} y + \sqrt{1+y^2} \right\}, \quad (17)$$

$$C_{20}^2 = \sqrt{\frac{\sqrt{1+y^2}-1}{2\sqrt{1+y^2}}}, \quad C_{22}^2 = -\sqrt{\frac{\sqrt{1+y^2}+1}{2\sqrt{1+y^2}}}. \tag{18}$$

The actual number of the terms in the sum in (9) (the ranges of the orbital angular momentum L and the additional quantum number α) is determined by the Elliott rules listing the basis states of an irreducible representation of the $SU(3)$ group.

The choice of axes that was proposed by Elliott simplifies the classification of the basis states. It seems, however, that the Elliott model is at odds with experimental data in what is concerned with the structure of the wave functions for the states involved: in the case of the ^{10}Be nucleus considered here, the orbital-angular-momentum projection K onto the intrinsic axis of the nucleus is not an integral of the motion for either of the two D_2-symmetric states of orbital angular momentum $L = 2$—at the same time, experimental data indicate that rotational states combine into $K = 0,\ K = 2$, etc, bands.

In order to remove this contradiction, it is sufficient to direct the z ($\tilde{z}$) axis along the vector orthogonal to the vectors $\mathbf{u}$ and $\mathbf{w}$ ($\tilde{\mathbf{u}}$ and $\tilde{\mathbf{w}}$). In this case, we obtain an expansion that has a different structure of the basis functions, but where the values of the weight factors remain unchanged; that is,

$$d_{11}^2 d_{22}^2 = \frac{2}{15}D_{0,0}^0 + \frac{5}{21}D_{0,0}^2 + \frac{1}{3}D_{2+,2+}^2 \tag{19}$$
$$+ \frac{1}{6}D_{2-,2-}^3 + \frac{9}{70}\left(\frac{35}{36}D_{4+,4+}^4 - \frac{\sqrt{35}}{36}D_{4+,0}^4 - \frac{\sqrt{35}}{36}D_{0,4+}^4 + \frac{1}{36}D_{0,0}^4\right).$$

It follows from (19) that, in contrast to the standard Elliott choice, the new choice of the rotational axis ensures the conservation of K at $L = 2$, and this leads to agreement between the Elliott scheme and the classification used in interpreting experimental data, which assumes that K is a good quantum number. As to the only $L = 4$ state, the weight of its main component, which is characterized by $K = 4$, is 35/36; there is no $K = 2$ component, and the weight of the $K = 0$ component is as small as 1/36. So a drastic change in the structure of states upon going over from $L = 2$ to $L = 4$ can be associated with the observed phenomenon of a significant change in the orbital-angular-momentum projection K for states of the lowest rotational band as soon as L reaches some critical value.

As to the most general ideas concerning the choice of axis about which rotation occurs, they can reduce to the following statements depending on the symmetry indices λ and μ of the the leading representation.

(i) For the $(\lambda, 0)$ representations, with the corresponding overlap integral being given by

$$(\mathbf{u}\cdot\tilde{\mathbf{u}})^\lambda,$$

the rotation axis must be aligned with the vector $\mathbf{u}$ ($\tilde{\mathbf{u}}$); for all allowed states, the orbital-angular-momentum projection K can then take only zero value. But if $\mu \ll \lambda$, there appear $K \neq 0$ components; however, their amplitude in the wave functions for the ground-state rotational band is small, whence it follows that, as previously, the states of the ground-state band can be interpreted as the $K = 0$ states.

(ii) For the $(0, \mu)$ representations, in which case the overlap integral is

$$(\mathbf{w}\cdot\tilde{\mathbf{w}})^\mu,$$

the rotation axis must be directed along $\mathbf{w}$ ($\tilde{\mathbf{w}}$). As before, only $K = 0$ states are possible here; if $\lambda \ll \mu$, the situation prevalent in the preceding case is reproduced.

(iii) Finally, let us consider the $\lambda = \mu$ representations, for which the rotation axis is chosen to be aligned with $\mathbf{u}\times\mathbf{w}$ ($\tilde{\mathbf{u}}\times\tilde{\mathbf{w}}$). At close values of λ and μ, there appears a small admixture of $K = 2$ components in states of the ground-state rotational band and a small admixture of $K = 0$ components in states of the $K = 2$ rotational band.

3. OVERLAP INTEGRAL INVOLVING A HAMILTONIAN

The next step in implementing the Elliott model for the ^{10}Be spectrum will be to calculate the overlap integral involving the generating Slater determinants and the Hamiltonian $\hat{H} = \hat{T} + \hat{U}$, where $\hat{T}$ is the kinetic-energy operator and $\hat{U}$ is the potential of a central exchange interaction of the Gaussian type. This integral,

$$\int \tilde{\Psi}\hat{H}\Psi d\mathbf{r}_1 d\mathbf{r}_2 \cdots d\mathbf{r}_{10} = \langle\tilde{\Psi}|\hat{H}|\Psi\rangle, \tag{20}$$

is a function of the Euler angles θ_i and $\tilde{\theta}_i$. Along with the overlap integral $\langle\tilde{\Psi}|\Psi\rangle$, which, as we already know, depends on the same angles, the overlap integral involving the Hamiltonian can be reasonably interpreted in terms of the Hill–Wheeler equation

$$\int \left\{\langle\tilde{\Psi}|\hat{H}|\Psi\rangle - E\langle\tilde{\Psi}|\Psi\rangle\right\}\psi(\theta_i)d\Omega = 0, \tag{21}$$

where $d\Omega = d\theta_1 \sin\theta_2 d\theta_2 d\theta_3$. Our next step is to prove that Eq. (21) can be solved by means of a simple procedure.

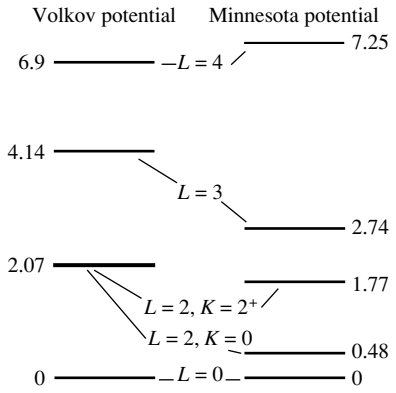

Spectrum of the ^{10}Be nucleus in the approximation of the leading representation of the $SU(3)$ group for the Volkov potential at the mixing-parameter value of $m = 0.6$ and for the Minnesota potential at the mixing-parameter value of $u = 0.98$ (the energy is given in MeV).

The explicit form of the overlap integral involving the potential-energy operator can be straightforwardly found by using the fact that the Slater determinants are constructed in terms of biorthogonal orbitals

$$\langle\Psi|\hat{U}|\Psi\rangle = A(I_1 + I_2) + CI_3 + (D - 2A)I, \quad (22)$$

where

$$I_1 = u^2\tilde{u}^2(\mathbf{w}\cdot\tilde{\mathbf{w}})^2, \quad I_2 = w^2\tilde{w}^2(\mathbf{u}\cdot\tilde{\mathbf{u}})^2,$$
$$I_3 = ([\mathbf{u}\times\tilde{\mathbf{u}}]\cdot[\mathbf{w}\times\tilde{\mathbf{w}}])(\mathbf{u}\cdot\tilde{\mathbf{u}})(\mathbf{w}\cdot\tilde{\mathbf{w}}).$$

The coefficients A, C, and D can be expressed in terms of the intensities of the even components V_{31} and V_{13} of the potential simulating the nucleon–nucleon interaction and the parameter

$$z^{-1} = 1 + \frac{2r_0^2}{b_0^2},$$

where r_0 is the oscillator length and b_0 is the radius of the Gaussian potential. The result has the form

$$A = z^{3/2}\left(\frac{1-z}{2}\right)^2 V_{13}, \quad (23)$$
$$C = z^{3/2}\left(\frac{1-z}{2}\right)^2 (V_{13} + 3V_{31}).$$

The coefficient D is not involved in the terms of the Hamiltonian that split the spectrum; therefore, the expression for this coefficient is not presented here.

In the integral in (22), we retain only those terms that are responsible for the splitting of the spectrum. All the remaining terms determine the energy from which one reckons the positions of the excited states of the nucleus; here, they are not presented below. If here we direct the z ($\tilde{z}$) axis along $\mathbf{u}\times\mathbf{w}$ ($\tilde{\mathbf{u}}\times\tilde{\mathbf{w}}$), then

$$I_1 + I_2 = \frac{2}{3}D^0_{0,0} + \frac{1}{3}D^2_{0,0} + D^2_{2+,2+},$$

$$I_3 = \frac{1}{30}D^0_{0,0} + \frac{2}{21}D^2_{0,0} - \frac{9}{70}\left(\frac{35}{36}D^4_{4+,4+} - \frac{\sqrt{35}}{36}D^4_{4+,0} - \frac{\sqrt{35}}{36}D^4_{0,4+} + \frac{1}{36}D^4_{0,0}\right).$$

It is now straightforward to find the energies of five states of the ^{10}Be nucleus. For the energy of the 0^+ state, we have

$$E_0 = 5A + \frac{1}{4}C. \quad (24)$$

In order to determine the excitation energies of the remaining four states, we will reckon their positions from the 0^+ state. We have

$$E_2^1 - E_0 = -\frac{18}{5}\left(A - \frac{C}{4}\right) - \frac{3}{4}C, \quad (25)$$

$$E_2^2 - E_0 = -2\left(A - \frac{C}{4}\right) - \frac{3}{4}C, \quad (26)$$

$$E_3 - E_0 = -5\left(A - \frac{C}{4}\right) - \frac{3}{2}C, \quad (27)$$

$$E_4 - E_0 = -5\left(A - \frac{C}{4}\right) - \frac{5}{2}C. \quad (28)$$

It is noteworthy that, for the Volkov potential, two $L = 2$ states of $K = 0$ and $K = 2$ have identical energies since $V_{31} = V_{13}$ for this potential. The ^{10}Be spectrum obtained with the Volkov potential at the mixing-parameter value of $m = 0.6$ and the oscillator length of $r_0 = 1.64$ fm is shown in the left part of the figure. This value of r_0 was obtained from a variational calculation. It minimizes the energy of the ground state and corresponds to the root-mean-square radius of 2.29 fm. The observed value of the ^{10}Be root-mean-squared radius is 2.3 ± 0.2 fm [18].

While the Volkov potential produces the observed value of the ^{10}Be radius, a variational calculation on the basis of the Minnesota potential at the mixing parameter of $u = 0.98$ (it is this value of u that appears to be optimal for nuclei from the first half of the class of p-shell nuclei) yields $r_0 = 1.43$ fm, which is a value that leads to incorrect results both for the root-mean-squared radius (it proves to be considerably underestimated) and for the order of excited states. No saturation arises either for the Minnesota or for the Volkov potential, but this is manifested earlier (for lighter nuclei) for the Minnesota potential at $u = 0.98$ than for the Volkov potential at $m = 0.6$. But if, for the

Minnesota potential, we set $r_0 = 1.64$ fm, we arrive at the spectrum shown in the right part of the figure. Here, the two 2^+ states have different energies since $V_{31} \neq V_{13}$ in this potential. However, the difference of the energies of these states is 1.29 MeV, which is nearly one-half as great as the observed value of 2.59 MeV. The difference $E_2^2 - E_2^1$ is proportional to $V_{31} - V_{13}$. In trying to reach agreement with experimental data within the approximation being considered, it is therefore necessary to increase the difference $V_{31} - V_{13}$ appropriately. The introduction of a similar correction is also motivated by the fact that the result

$$\frac{1}{2}(E_2^2 + E_2^1) - E_0 = 1.125 \text{ MeV},$$

which was obtained on the basis of the Minnesota potential, is one-fourth as great as the experimental value and is nearly one-half as great as its counterpart calculated with the Volkov potential, for which it is 2.07 MeV.

We note that both potentials were constructed long ago on the basis of experimental data for nuclei from the beginning of the p shell. It is clear that their extension to nuclei from the second half of the p shell must be accompanied by an appropriate correction of these potentials.

The Elliott scheme predicts the existence of two more excitations, those of spin–parity 3^+ and 4^+. The energy of the former is close to the sum of the energies of the 2^+ excitations. The 4^+ state is dominated by the $K = 4$ components, and this affects the probabilities of $E2$ transitions. The isoscalar electric transition from the 4^+ state to the $L = 2, K = 0$ state is forbidden, and only the transition to the $L = 2$, $K = 2$ state occurs.

It is important that, at an arbitrary choice of version for the central exchange potential for the nucleon–nucleon interaction, the matrix elements of the potential between the $L = 2, K = 0$ and $L = 2, K = 2$ states vanish.

4. EFFECTIVE HAMILTONIAN OF THE $SU(3)$ MODEL

In calculating the overlap integral (22), the result of applying the operator $\hat{H}$ to the generating Slater determinant Ψ, whose $SU(3)$ symmetry is (2, 2), was projected onto a state that has the same (2, 2) symmetry. Projecting was performed via integration. Taking the overlap integral (22), we do not therefore go beyond the basis of the (2, 2) irreducible representation. In order to understand how the Hamiltonian $\hat{H}$ acts in the space spanned by the basis states of this irreducible representation, we define a new operator $\hat{H}(\mathbf{u}, \mathbf{w})$, setting

$$\langle\Psi|\hat{H}|\Psi\rangle = \hat{H}(\mathbf{u}, \mathbf{w})\langle\Psi|\Psi\rangle. \tag{29}$$

Operators such that their application to basis states of an irreducible representation of the $SU(3)$ group does not result in going beyond the $SU(3)$ basis are known. These are generators of the $SU(3)$ group. Needless to say, we are interested only in the scalar $O(3)$ constructions formed by generators. They are also known [19, 20]. The operator $\mathbf{QQ}$, which was introduced by Elliott, and two more operators $\hat{\Omega} = \hat{\mathbf{L}}\mathbf{Q}\hat{\mathbf{L}}$ and $\hat{\Omega}_1 = \hat{\mathbf{L}}\mathbf{Q}\mathbf{Q}\hat{\mathbf{L}}$ [12] are the simplest of these. Each of the remaining operators can be represented as a polynomial of these three basic operators.

In the approximation used here, the wave functions reduce to superpositions of Wigner D functions. Therefore, it is natural that all operators in this representation can be expressed, in just the same way as in the case of a triaxial-rotor Hamiltonian, in terms of the $SU(3)$-symmetry indices λ and μ and in terms of $\hat{L}_1$, $\hat{L}_2$, and $\hat{L}_3$, which are the projections of the orbital-angular-momentum operator $\hat{\mathbf{L}}$ onto the intrinsic axes of the system. It was shown in [16] that

$$-\hat{\Omega} = a\hat{L}_1^2 + b\hat{L}_2^2 + c\hat{L}_3^2 + \hat{\Omega}_2, \tag{30}$$

$$-\hat{\Omega}_1 = a^2\hat{L}_1^2 + b^2\hat{L}_2^2 + c^2\hat{L}_3^2 - \frac{2}{3}\hat{\mathbf{L}}^2 - \hat{L}_2^2 + \frac{1}{2}(\hat{L}_1^2\hat{L}_3^2 + \hat{L}_3^2\hat{L}_1^2) + 2b\hat{\Omega}_2, \tag{31}$$

where

$$a = \frac{2\lambda + \mu + 3}{3}, \quad b = \frac{-\lambda + \mu}{3}, \quad c = \frac{-\lambda - 2\mu - 3}{3}; \tag{32}$$

$$\hat{\Omega}_2 = \frac{i}{6}\left(\hat{L}_1\hat{L}_2\hat{L}_3 + \hat{L}_2\hat{L}_3\hat{L}_1 + \hat{L}_3\hat{L}_1\hat{L}_2 + \hat{L}_2\hat{L}_1\hat{L}_3 + \hat{L}_3\hat{L}_2\hat{L}_1 + \hat{L}_1\hat{L}_3\hat{L}_2\right). \tag{33}$$

The structure of the operators $\hat{\Omega}$ and $\hat{\Omega}_1$ is similar to the structure of the triaxial-rotor Hamiltonian, the only difference being that, instead of the principal values of the inertia tensor, the principal values of the tensor of the intrinsic quadrupole moment in the case of $\hat{\Omega}$ and the squares of these principal values in the case of $\hat{\Omega}_1$ appear here for the inertia parameters (coefficients of $\hat{L}_1^2$, $\hat{L}_2^2$, and $\hat{L}_3^2$). The additional terms

$$\hat{\Omega}_2 \quad \text{and} \quad \frac{1}{2}(\hat{L}_1^2\hat{L}_3^2 + \hat{L}_3^2\hat{L}_1^2)$$

affect only the details that ensure a finite number of basis functions for each irreducible representation of the $SU(3)$ group, in contrast to an infinite number of basis functions for a triaxial rotor.

The operators $\hat{\Omega}$ and $\hat{\Omega}_1$ commute with the operator $\hat{\mathbf{L}}^2$; therefore, the orbital angular momentum L is an integral of the motion, as it must be. Moreover, these operators are invariant under the transformations of the D_2 group; hence, each of their eigenfunctions has a specific D_2 symmetry. But among the eigenfunctions of the operators $\hat{\Omega}$ and $\hat{\Omega}_1$, only those have a physical meaning whose D_2 symmetry is identical to the D_2 symmetry of the basis states involved in the overlap integral (7).

It is natural to construct the eigenfunctions $\phi_{L,m}$ of the operator $\hat{\Omega}$ (or $\hat{\Omega}_1$, or a linear combination of the operators $\hat{\Omega}$ and $\hat{\Omega}_1$ with arbitrary coefficients) in the form of a linear superposition of the renormalized functions

$$\sqrt{w_L^\alpha}\psi_{Lm}^\alpha,$$

where $\sqrt{w_L^\alpha}$ is the weighted norm—that is, in the form

$$\phi_{Lm} = \sum_\alpha B_{L,\alpha}\sqrt{w_L^\alpha}\psi_{Lm}^\alpha. \tag{34}$$

Upon renormalizing the basis functions in this way, we must also renormalize the matrix elements. As usually occurs in such a situation, the new coefficients $B_{L\alpha}$ in the expansion satisfy the set of linear algebraic equations

$$\sum_{\alpha'}(\langle L,\alpha|\hat{\Omega}|L,\alpha'\rangle - \delta_{\alpha,\alpha'})B_{L,\alpha'} = 0. \tag{35}$$

In order to calculate the matrix elements $\langle L,\alpha|\hat{\Omega}|L,\alpha'\rangle$ explicitly, we can first evaluate the overlap integral involving the generating determinants and the operator $\hat{\Omega}$ and then represent it in the form of the expansion

$$\langle\Psi|\hat{\Omega}|\Psi\rangle \tag{36}$$
$$= \sum_L\sum_{\alpha,\alpha'}\sqrt{w_L^\alpha(\lambda,\mu)w_L^{\alpha'}(\lambda,\mu)}\langle L,\alpha|\hat{\Omega}|L,\alpha'\rangle \times \sum_m \psi_{Lm}^\alpha\tilde{\psi}_{Lm}^{\alpha'}.$$

The simple explicit form (30) of $\hat{\Omega}$ makes it possible to solve this problem by using the relation

$$\hat{\Omega}\sqrt{w_L^\alpha}\psi_{Lm}^\alpha = \sum_{\alpha'}\langle L,\alpha|\hat{\Omega}|L,\alpha'\rangle\sqrt{w_L^{\alpha'}}\psi_{Lm}^\alpha. \tag{37}$$

In order to derive relation (37), it is sufficient to employ known formulas (see, for example, [14]) that specify the result of applying the operators $\hat{L}_1$, $\hat{L}_2$, and $\hat{L}_3$ to Wigner D functions. The two approaches lead to the same Hermitian matrix

$$||\langle L,\alpha|\hat{\Omega}|L,\alpha'\rangle||,$$

whose diagonalization yields the eigenvalues of the operator Ω. At each fixed value of L, the dimension of this matrix depends on the number of possible values of α.

Finally, there is yet another possibility that consists in constructing an expansion of ϕ_{Lm} directly in terms of Wigner D functions; that is,

$$\phi_{Lm} = N_L\sum_K A_{L,K}D_{K\pm,m}^L. \tag{38}$$

This is the simplest method for solving the eigenvalue problem in question, although we obtain, upon such calculations, a non-Hermitian matrix,

$$||\langle L,K\pm|\hat{\Omega}|L,K'\pm\rangle||, \tag{39}$$

since the operator $\hat{\Omega}_2$, which enters into the composition of both $\hat{\Omega}$ and $\hat{\Omega}_1$, involves an imaginary unit as a common factor and is therefore not self-conjugate. By no means does this imply that the matrix in question will have complex eigenvalues.[3)] The set of equations for the coefficients $A_{L,K}$ has the form

$$\sum_{K'}(\langle L,K\pm|\hat{\Omega}|L,K'\pm\rangle - \delta_{K,K'})A_{L,K'} = 0, \tag{40}$$

where the matrix elements $\langle L,K\pm|\hat{\Omega}|L,K'\pm\rangle$ are determined from the relation

$$\hat{\Omega}D_{K\pm,m}^L = \sum_{K'}\langle L,K\pm|\hat{\Omega}|L,K'\pm\rangle D_{K'\pm,m}^L. \tag{41}$$

The norm N_L of the eigenfunction in (38) is determined from the condition

$$N_L\sum_\alpha\frac{1}{\sqrt{w_L^\alpha}}\sum_K A_{L,K}C_{LK}^\alpha = 1. \tag{42}$$

For states that are allowed by the Pauli exclusion principle, the coefficients C_{LK}^α were defined previously [see Eqs. (11), (12)]. In order to calculate them, we must expand the overlap integral (7) in the basis states of an irreducible representation of the $SU(3)$ group. Summation over K in (42) has the meaning of projecting the eigenfunction of the operator $\hat{\Omega}$ onto states that are allowed by the Pauli exclusion principle.

Among the eigenfunctions of the operator $\hat{\Omega}$, there are, however, forbidden states. A forbidden state must

[3)] We recall that a Hermitian matrix has only real eigenvalues. If, however, a matrix is non-Hermitian, its eigenvalues are not necessarily complex-valued—they also can be real-valued.

be orthogonal to all of the allowed states. Of the eigenfunctions of the operator $\hat{\Omega}$ that were obtained by diagonalizing the matrix in (39), those are therefore forbidden for which each of the sums

$$\sum_K A_{L,K} C^{\alpha}_{LK},$$

which differ by possible values of the additional quantum number α of allowed states, vanish. Such states do not satisfy the Pauli exclusion principle and must be discarded. Forbidden states will inevitably appear as the orbital angular momentum L increases, and this must be taken into account in explicitly calculating the excitation spectrum if these calculations reduce to the diagonalization of the matrix in (39).

5. GENERAL CONSIDERATIONS ON THE EFFECTIVE HAMILTONIAN

At the first stage, at least, it is reasonable to construct the effective Hamiltonian in the form of a linear combination of the operators **QQ**, $\hat{\Omega}$, and $\hat{\Omega}_1$. It has now become clear that, as a result, we actually arrive at the triaxial-rotor Hamiltonian supplemented with a few additional terms that can play an important role in explicitly calculating the spectrum of the leading representation. Coefficients of each of the three operators can be phenomenological parameters in this approach.

There arises the question of whether such a Hamiltonian can explain the observed spectra of the first excited states of even–even nuclei. It is reasonable to assume that phenomenological parameters take identical values for a rather wide range of nuclei and that the $SU(3)$-symmetry indices change from one nucleus to another, as is prescribed by general rules.

This approach was used by Draayer and Weeks in [19, 20], but, in addition, they attempted to extend the model to states characterized by higher values of L, not restricting themselves to the first excited states. In this case, one must answer another question, that of whether the theory can be restricted to the first powers of the above three operators or whether it is necessary to include higher powers of these operators in the model Hamiltonian.

For the example of the ^{20}Ne and ^{44}Ti nuclei, it was shown in [21] that the effective Hamiltonian derived for their $(\lambda, 0)$ leading representations of the $SU(3)$ group [(8,0) for ^{20}Ne and (12,0) for ^{44}Ti] from the overlap integrals involving the generating Slater determinants and the potential energy of the central exchange nucleon–nucleon interaction of the Gaussian type features the first and the second power of the operator **QQ** in the case of ^{20}Ne and its first, second, and third powers in the case of ^{44}Ti. Simultaneously, it became clear that, as we go over to the next oscillator shells, there appear higher terms in powers of the operator **QQ**. The higher the orbital angular momentum L, the more pronounced the effect of these terms. For the $(\lambda, 0)$ representations, the operators $\hat{\Omega}$ and $\hat{\Omega}_1$ degenerate, becoming equivalent to the operator $\hat{\mathbf{L}}^2$. In order to derive terms involving high powers of $\hat{\Omega}$ and $\hat{\Omega}_1$, it is therefore necessary to invoke leading representations specified by nonvanishing values of both λ and μ and to go beyond the p shell. Of course, high powers of $\hat{\Omega}$ and $\hat{\Omega}_1$ can also be included in the Hamiltonian by applying phenomenological considerations.

6. OPERATOR OF THE MASS QUADRUPOLE MOMENT

We now explain why a, b, and c are the principal values of the quadrupole moment. The starting point in discussing the problem of the mass quadrupole operator $\hat{Q}_{\alpha\beta}$ and the explicit form of the operator representing its components in the intrinsic coordinate frame are presented in [16]. For our choice of axis, this operator can be rewritten as

$$\hat{Q}_{2m} = \frac{1}{3}(-\lambda+\mu)D^2_{m,0} + \frac{\sqrt{3}}{3}(\lambda+\mu)D^2_{m,2+} \quad (43)$$
$$- \frac{\sqrt{3}}{3}\left(D^2_{m,1+}\hat{L}_1 + iD^2_{m,1-}\hat{L}_3 + D^2_{m,2-}\hat{L}_2\right),$$

where

$$\frac{1}{3}(-\lambda+\mu) \quad \text{and} \quad \frac{\sqrt{3}}{3}(\lambda+\mu)$$

are the principal values of the traceless quadrupole-moment tensor.

From (43), it immediately follows that

$$\mathbf{QQ} = \frac{2}{3}(\lambda^2+\lambda\mu+\mu^2+3\lambda+3\mu) - \frac{1}{2}\hat{\mathbf{L}}^2. \quad (44)$$

We also note that

$$-\frac{\sqrt{3}}{3}\left(D^2_{m,1+}\hat{L}_1 + iD^2_{m,1-}\hat{L}_3 \right. \quad (45)$$
$$\left. + D^2_{m,2-}\hat{L}_2\right) D^2_{m',2+} = -\frac{\sqrt{3}}{3}\left(D^2_{m,1+}D^2_{m',1+}\right.$$
$$\left. - D^2_{m,1-}D^2_{m',1-} + 2D^2_{m,2-}D^2_{m',2-}\right).$$

Thus, we have obtained the required expression, which is invariant under the transformations of the D_2 group. This is obvious since the application of the quadrupole-moment operator to a D_2-symmetric expression must lead to a symmetric expression as well.

For the choice of axes that was proposed by Elliott, we have

$$\hat{Q}_{2m} = \frac{2}{3}\left\{\left(\bar{a} - \frac{\bar{b}+\bar{c}}{2}\right)D^2_{m,0} + \frac{\sqrt{3}}{2}\left(\bar{b}-\bar{c}\right)D^2_{m,2+}\right\} + \ldots = \frac{1}{3}(2\lambda+\mu)D^2_{m,0} + \frac{\sqrt{3}}{3}\mu D^2_{m,2+} + \ldots.$$

By definition, the following relations hold:

$$\bar{a} = \frac{1}{3}(2\lambda+\mu) = a-1, \quad \bar{b} = \frac{1}{3}(-\lambda+\mu) = b,$$
$$\bar{c} = \frac{1}{3}(-\lambda-2\mu) = c+1.$$

According to this definition, the expression for the quadrupole-moment operator for the $(\lambda,0)$ representation and the Elliott choice has the form

$$\hat{Q}_{2m} = \frac{2\lambda}{3}D^2_{m,0} + \ldots. \qquad (46)$$

In this case, an axisymmetric nucleus is prolate; therefore, the intrinsic quadrupole moment[4)] is directed along the rotation axis and is positive.

Another choice,

$$\hat{Q}_{2m} = \frac{2}{3}\left\{\left(\bar{c} - \frac{\bar{a}+\bar{b}}{2}\right)D^2_{m,0} + \frac{\sqrt{3}}{2}(\bar{a}-\bar{b})D^2_{m,2+}\right\} + \ldots = -\frac{1}{3}(2\mu+\lambda)D^2_{m,0} + \frac{\sqrt{3}}{3}\lambda D^2_{m,2+} + \ldots,$$

is convenient for the $(0,\mu)$ limiting transition, in which case

$$\hat{Q}_{2m} = -\frac{2\mu}{3}D^2_{m,0} + \ldots. \qquad (47)$$

Now, the nucleus is oblate and the intrinsic quadrupole moment directed along the rotation axis is negative.

Finally, we represent the matrix elements for the isoscalar $E2$ transition from the ground state to the ψ^α_{2m} states of the Elliott basis for arbitrary even values of the symmetry indices λ and μ. We have

$$\langle L=2,\alpha=1,m|\hat{Q}_{2m}|L=0\rangle = \sqrt{\frac{w_0}{w^1_2}}\left\{\frac{1}{3}(-\lambda+\mu)C^1_{20} + \frac{\sqrt{3}}{3}(\lambda+\mu)C^1_{22}\right\}, \qquad (48)$$

$$\langle L=2,\alpha=2,m|\hat{Q}_{2m}|L=0\rangle = \sqrt{\frac{w_0}{w^2_2}}\left\{\frac{1}{3}(-\lambda+\mu)C^2_{20} + \frac{\sqrt{3}}{3}(\lambda+\mu)C^2_{22}\right\}. \qquad (49)$$

[4)]The quadrupole moment is a traceless tensor whose two principal components are Q_{20} and Q_{22+}. In the axisymmetric case, the second component vanishes; therefore, it can be stated that the quadrupole moment is oriented along one of its three principal axes.

7. EFFECTIVE HAMILTONIAN FOR ^{10}Be

Our next task is to construct the effective Hamiltonian $\hat{H}(\mathbf{u},\mathbf{w})$ for the ^{10}Be nucleus as a linear combination of the operators $\hat{\mathbf{L}}^2$, $\hat{\Omega}$, and $\hat{\Omega}_1$. The only condition unambiguously specifying this Hamiltonian is that the spectrum of its eigenfunctions and eigenvalues must be identical to the spectrum previously constructed in the approximation of the leading irreducible representation of the $SU(3)$ group.

We set

$$\hat{H}(\mathbf{u},\mathbf{w}) = C\left(\frac{3}{2} - \frac{1}{8}\hat{\mathbf{L}}^2\right) + \left(A - \frac{C}{4}\right) \times \left(p + q\hat{\mathbf{L}}^2 + r\hat{\Omega}_1 + s\hat{\Omega}\right), \qquad (50)$$

where p, q, r, and s are coefficients that must be determined.

As was indicated above, the overlap integral involving a unity vector and the overlap integral involving the Hamiltonian are diagonal in the representation of the basis functions ψ^1_{2m} and ψ^2_{2m} for the $L=2$ states. At the same time, the eigenfunctions of the operator $\hat{\Omega}$ are mixtures of these states. It follows that $s=0$, which means that the two $L=2$ energy levels can be split only owing to the operator $\hat{\Omega}_1$. From (25) and (26), it follows that

$$E^2_2 - E^1_2 = \frac{8}{5}\left(A - \frac{C}{4}\right). \qquad (51)$$

The eigenvalues of the operator $\hat{\Omega}_1$ in the same states can easily be calculated. The result are

$$\hat{\Omega}_1\psi^1_{2m} = -44\psi^1_{2m}, \quad \hat{\Omega}_1\psi^2_{2m} = -12\psi^2_{2m}. \qquad (52)$$

Considering that

$$E_0 = 5A + \frac{1}{4}C,$$
$$E^1_2 - E_0 = -\frac{18}{5}\left(A - \frac{C}{4}\right) - \frac{3}{4}C,$$

we determine the coefficients p, q, and r and obtain, in this way, the explicit form of the effective Hamiltonian:

$$\hat{H}(\mathbf{u},\mathbf{w}) = C\left(\frac{3}{2} - \frac{1}{8}\hat{\mathbf{L}}^2\right) + \left(A - \frac{C}{4}\right) \qquad (53)$$

$$\times \left(5 - \frac{7}{30}\hat{\mathbf{L}}^2 + \frac{1}{20}\,\hat{\Omega}_1\right).$$

One can directly prove that, for the $L = 3$ and $L = 4$ states, this Hamiltonian leads to the values E_3 and E_4, respectively, identical to those found above.

In the approach based on a phenomenological effective Hamiltonian, the coefficients A and C are chosen in such a way as to reproduce the ^{10}Be spectrum observed experimentally. However, it is sufficient for this to use the known energies of the three first states, E_0, E_2^1, and E_2^2. The energies E_3 and E_4 could then be used as a test, but the values of these energies have yet to be determined.

8. CONCLUSION

Thus, a realization of the approximation of the leading irreducible representation of the $SU(3)$ group on the basis of a microscopic Hamiltonian with potentials of the nucleon–nucleon interaction that are adopted in the theory of light nuclei (specifically, the Volkov and the Minnesota potential) can be reduced to calculations involving an effective Hamiltonian, which appears to be a linear combination of the operator $\hat{\mathbf{L}}^2$ and the operators $\hat{\Omega}$ and $\hat{\Omega}_1$ introduced by Bargmann and Moshinsky or of powers of these operators. In many respects, it is similar to the Hamiltonian of a triaxial rotor. However, the inertia parameters of such a rotor are not in inverse proportion to the principal values of the tensor of inertia, but but they are proportional to the principal values of the quadrupole-moment tensor. It has been shown that, in just the same way as basis functions for a rotor, basis functions of the irreducible representation of the $SU(3)$ group are superpositions of Wigner D functions, only their norm requiring a dedicated calculation.

Problems have been indicated that arise in the case of applying the Volkov or the Minnesota potential in spectroscopic calculations for nuclei from the second half of the p shell.

General arguments concerning the form of the effective Hamiltonians for medium-mass and heavy nuclei have been adduced.

REFERENCES

1. J. P. Elliott, Proc. R. Soc. London, Ser. A **245**, 128, 562 (1958).
2. A. Arima, M. Harvey, and K. Shimizu, Phys. Lett. B **30B**, 517 (1969).
3. K. T. Hecht and A. Adler, Nucl. Phys. A **137**, 129 (1969).
4. R. D. Ratna Raji, J. P. Draayer, and K. T. Hecht, Nucl. Phys. A **202**, 433 (1973).
5. N. Lo Iudice and F. Palumbo, Phys. Rev. Lett. **41**, 1532 (1978).
6. T. Beushel, J. P. Draayer, D. Rompf, and J. G. Hirsch, Phys. Rev. C **57**, 1233 (1998).
7. J. G. Hirsch, P. O. Hess, L. Hernandez, *et al.*, Rev. Mex. Fis. Suppl. **45** (2), 86 (1999).
8. D. Rompf, T. Beushel, J. P. Draayer, *et al.*, Phys. Rev. C **57**, 1703 (1998).
9. A. B. Volkov, Nucl. Phys. **74**, 33 (1965).
10. D. R. Thompson, M. LeMere, and Y. C. Tang, Nucl. Phys. A **286**, 53 (1977).
11. A. S. Davydov and G. F. Filippov, Nucl. Phys. **8**, 237 (1958).
12. V. Bargmann and M. Moshinsky, Nucl. Phys. **18**, 4 (1960).
13. R. E. Peierls and J. Yoccoz, Proc. Phys. Soc. London **70**, 381 (1957).
14. L. D. Landau and E. M. Lifshits, *Quantum Mechanics: Non-Relativistic Theory* (Nauka, Moscow, 1989, 4th ed.; Pergamon, Oxford, 1977, transl. of the 3rd ed.).
15. E. M. Lifshits and L. P. Pitaevskiĭ, *Physical Kinetics* (Nauka, Moscow, 1979; Pergamon, Oxford, 1981).
16. G. F. Filippov and J. P. Draayer, Fiz. Élem. Chastits At. Yadra **29**, 1329 (1998) [Phys. Part. Nucl. **29**, 549 (1998)].
17. A. S. Davydov, *Quantum Mechanics*, 2nd ed. (Nauka, Moscow, 1973; Pergamon, Oxford, 1976).
18. I. Tanihata *et al.*, Phys. Lett. B **206**, 592 (1988).
19. J. P. Draayer and K. J. Weeks, Phys. Rev. Lett. **51**, 1422 (1983).
20. J. P. Draayer and K. J. Weeks, Ann. Phys. (N.Y.) **156**, 41 (1984).
21. I. P. Okhrimenko and A. I. Steshenko, Preprint No. ITF-82-96R (Bogolyubov Inst. for Theoretical Physics, Kiev, 1982).

Translated by A. Isaakyan

Physics of Atomic Nuclei, Vol. 66, No. 4, 2003, pp. 644–658. Translated from Yadernaya Fizika, Vol. 66, No. 4, 2003, pp. 673–687.

NUCLEI
Theory

Parameters of the Proton Shell Structure of the ^{40,42,44,46,48}Ca Nuclei and Their Analysis within the Dispersive Optical Model

O. V. Bespalova, I. N. Boboshin, V. V. Varlamov, B. S. Ishkhanov, E. A. Romanovsky, and T. I. Spasskaya

Institute of Nuclear Physics, Moscow State University, Vorob'evy gory, Moscow, 119899 Russia

Received December 26, 2001

Abstract—By matching data on proton-stripping and proton-pickup reactions occurring on the same nuclear species, new experimental results for single-particle energies, occupation numbers, and fragmentation widths of proton states in the vicinity of the Fermi energy are obtained for the even–even isotopes ^{40,42,44,46,48}Ca. These results, along with the experimental values determined in the relevant $(p, 2p)$ reaction for the single-particle energies of deep hole states in ^{40}Ca, are analyzed on the basis of the dispersive-optical-model version proposed in the present study. The results of this analysis are compared with the predictions of various nuclear models, including the relativistic mean-field model.

1. INTRODUCTION

A great number of experimental and theoretical studies are devoted to exploring the properties of the doubly magic nucleus ^{40}Ca. In view of the spherical symmetry of the mean nuclear field, the structure of single-particle states in ^{40}Ca is the simplest; therefore, it is extensively used as a testing ground for calculations performed within various nuclear models that have been vigorously developed in recent years, including the relativistic mean-field model (see [1] and references therein) and the dispersive optical model (see [2, 3] and references therein).

Much attention has also been given to studying the properties of another doubly magic nucleus, ^{48}Ca, and of even–even isotopes of Ca that occur between ^{40}Ca and ^{48}Ca, since, in order to test a model of nuclear structure, it is important to trace, within its framework, changes in the isotope structure with increasing number of neutrons.

Currently prevalent concepts of the single-particle facets of nuclear structure are based on information that is extracted from analyses of data on one-nucleon-transfer and one-nucleon-knockout reactions [that is, reactions of the $(e, e'p)$, $(p, 2p)$, and (p, pn) types].

According to [4], the ground-state spin–parity values for the ^{39,41,43,45}K nuclei are $3/2^+$, while that for ^{47}K is $1/2^+$. This means that the sequence of single-particle levels near the Fermi energy must be $1d_{3/2}$, $2s_{1/2}$, $1d_{5/2}$ in ^{40,42,44,46}Ca and $2s_{1/2}$, $1d_{3/2}$, $1d_{5/2}$ in ^{48}Ca. From data presented in [5–7], which were obtained from analyses of one-nucleon-transfer reactions, it follows, however, that the sequence of levels in ^{44,46}Ca is identical to that in ^{48}Ca.

Within the relativistic mean-field model, single-particle spectra were studied in [1] for a large number of spherical nuclei over a wide range of mass numbers A, including the $^{40-48}$Ca nuclei. The results obtained by comparing the computed energies of single-particle proton levels with their experimental counterparts were presented in that article for ^{40,48}Ca. According to [1], the sequence of single-particle levels in ^{44,46}Ca is identical to that in ^{48}Ca, but this is at odds with data on the spin values in the ground states of ^{43,45,47}K [4]. Thus, the problem of changes in the order of proton levels in Ca isotopes as the number of neutrons approaches $N = 28$ has not yet been adequately described.

In [2, 8, 9], the parameters of the proton shell structure of ^{40}Ca were calculated within various versions of the method relying on the dispersive optical model, and it was shown there that the results comply well with the experimental parameter values. For the ^{42,44,46,48}Ca nuclei, however, the parameters of the shell structure have not yet been calculated within the dispersive optical model.

The objective of the present study is to calculate, on the basis of the dispersive optical model, the parameters of the shell structure of the nuclei of the even–even isotopes ^{40,42,44,46,48}Ca and to compare the results with the values obtained on the basis of the relativistic mean-field model and those found from a reanalysis of experimental data that is performed by

1063-7788/03/6604-0644$24.00

the method developed in [10] for matching data on stripping and pickup reactions occurring on the same nucleus.

The need for performing such a reanalysis of experimental data on stripping and pickup reactions is motivated by a glaring discrepancy between the values obtained in different studies for the parameters of the shell structure in the ^{40,42,44,46,48}Ca nuclei by using similar procedures. It turns out frequently that, instead of clarifying the situation, experimental information deduced from analyses of new studies leads to contradictions with previously available information or introduces an additional degree of uncertainty. In [10], a method was developed that makes it possible to match experimental data on nucleon-stripping and nucleon-pickup reactions and to derive the most reliable information about the parameters of the single-particle structure of nuclei. This method was not previously applied to the ^{40,42,44,46,48}Ca isotopes.

The ensuing exposition is organized as follows. Section 2 is devoted to determining, by the method proposed in [10], the experimental values of the energies, occupation probabilities, and fragmentation widths for the proton single-particle states of the ^{40,42,44,46,48}Ca nuclei. In order to determine the parameters of a dispersive optical potential, a dispersive-optical-model version that is applicable in the case where available experimental information is insufficient for performing an analysis within the traditional dispersive optical model (for example, this is so for the ^{42,44,46,48}Ca nuclei) is developed in Section 3. In Section 4, we present the results obtained by calculating, within the proposed version of the dispersive optical model, the parameters of the single-particle levels in ^{40,42,44,46,48}Ca. The parameter values found in this way are compared with their experimental counterparts and with those computed on the basis of other models of nuclear structure. The basic conclusions of this study are formulated in the last section of the article.

2. SINGLE-PARTICLE ENERGIES AND FRAGMENTATION WIDTHS OF LEVELS IN THE ^{40,42,44,46,48}Ca NUCLEI AND THEIR OCCUPATION NUMBERS ACCORDING TO DATA ON STRIPPING AND PICKUP REACTIONS

The parameters of the proton shell structure of levels in the vicinity of the Fermi energy (E_F) were determined by the method that makes it possible to match data on stripping and pickup reactions and which relies on the sum-rule approximation. Such an analysis involves determining, for subshells characterized by the quantum numbers n, l, j, the nucleon occupation numbers (N_{nlj}) and the single-particle energies (E_{nlj}) in terms of, respectively, the ordinary and the energy-weighted sums of the spectroscopic factors (S_{nlj}). However, a direct determination of single-particle energies of levels and their occupation numbers on the basis of known formulas in terms of the sums and centroids of spectroscopic factors is hardly possible, as a rule, because of large systematic errors in spectroscopic factors and because of uncertainties in the angular-momentum transfer j.

In order to remove such uncertainties, the entire body of available experimental data was analyzed here within the method for matching data on stripping and pickup reactions [10]. Specifically, the following was done:

(i) For each nuclear species under investigation, we took simultaneously into account both data on proton-pickup reactions and data on proton-stripping reactions.

(ii) For each type of experiments, we analyzed experimental information and, from the ENSDF database [4], selected the most comprehensive and reliable data on the spectroscopic features of the levels being considered.

(iii) In order to determine the total angular-momentum transfer j, we employed all data on the spins of final-state nuclei from the ENSDF international file of estimated data [4].

(iv) The spectroscopic-factor values selected in this way were rescaled on the basis of the model-independent sum rules used.

Briefly, the most significant points of the analysis are as follows. We denote by $S^{-,+}_{nlj}(E_x)$ the values that are determined for the spectroscopic factors of the nlj states of energy E_x from the analysis of $(-)$ pickup and $(+)$ capture reactions and by $S^{-,+}_{nlj}$ the respective values of the total spectroscopic factors; that is,

$$S^-_{nlj} \equiv \sum_x S^-_{nlj}(E_x), \quad S^+_{nlj} \equiv \sum_x S^+_{nlj}(E_x). \quad (1)$$

On the basis of data on the energies E_x of these states and the corresponding spectroscopic factors $S^{-,+}_{nlj}(E_x)$, we determine the energies of the centroids for the single-particle states in final nuclei as

$$e^-_{nlj} = \frac{\sum_x E_x S^-_{nlj}(E_x)}{S^-_{nlj}}, \quad e^+_{nlj} = \frac{\sum_x E_x S^+_{nlj}(E_x)}{S^+_{nlj}}. \quad (2)$$

The energies e^-_{nlj} and e^+_{nlj} are reckoned from, respectively, the energies $B(Z)$ and $B(Z+1)$ required for nucleon separation from the nuclei of charge number Z and $Z+1$; that is,

$$E^-_{nlj}(Z) = -B(Z) - e^-_{nlj}, \quad (3)$$

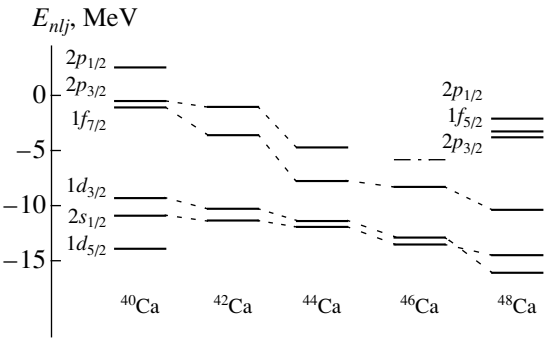

Fig. 1. Single-particle proton energies in the ^{40,42,44,46,48}Ca nuclei. The dash-dotted line represents an estimated lower bound on the energy of the $2p_{3/2}$ level in ^{46}Ca.

$$E^+_{nlj}(Z) = -B(Z+1) + e^+_{nlj}. \tag{4}$$

The method of matching consists in choosing a procedure for correcting the experimental values S^+_{nlj} and S^-_{nlj} in such a way as to ensure fulfillment of the condition

$$S^+_{nlj} + S^-_{nlj} = 2j + 1 \tag{5}$$

for subshells such that data on them that are deduced from the analysis of experimental cross sections are the most comprehensive and fulfillment of the following condition for all other subshells:

$$S^+_{nlj} + S^-_{nlj} \le 2j + 1. \tag{6}$$

It is well known that, because of residual interactions, intranuclear nucleons are redistributed among subshells. If the number of nucleons in the valence subshell (that is, in the last populated subshell) is denoted by $Z_{\rm val}$, it follows from classical shell theory that the above statement can be represented as

$$\left| \sum_{nlj} S^-_{nlj} - \sum_{nlj} S^+_{nlj} - Z_{val} \right| \to 0. \tag{7}$$

In (7), summation of S^-_{nlj} is performed over all subshells lying above the Fermi energy $E_{\rm F}$ on the energy scale and including the valence subshell, while summation of S^+_{nlj} is performed over subshells lying below the valence subshell.

For the relationships in (5)–(7) to be satisfied, we introduce normalization factors n^- and n^+ for the spectroscopic factors S^-_{nlj} and S^+_{nlj}, respectively, and sample all combinations of the products $S^-_{nlj}n^-$ and $S^+_{nlj}n^+$, the latter procedure being necessary because of the uncertainty in the total angular momentum j for some states of the final nucleus.

Condition (5) makes it possible to find the mean proton-subshell occupation number by the formula

$$N_{nlj} = \frac{\left[S^-_{nlj} + (2j + 1 - S^+_{nlj})\right]}{2(2j+1)}. \tag{8}$$

By using the spectroscopic-factor values as determined in pickup and stripping reactions, one can evaluate the single-particle energy of the state being considered by the formula

$$E_{nlj} = \frac{S^-_{nlj}E^-_{nlj} + S^+_{nlj}E^+_{nlj}}{S^-_{nlj} + S^+_{nlj}}. \tag{9}$$

With the aid of the definition of N_{nlj} in (8) and relations (3) and (4), it can straightforwardly be shown that

$$\begin{aligned} -E_{nlj} = (1 - N_{nlj}) \left[B(Z+1) - e^+_{nlj}\right] \\ + N_{nlj} \left[B(Z) + e^-_{nlj}\right]. \end{aligned} \tag{10}$$

In order to determine the energy positions of the proton subshells in the even–even isotopes of Ca and their occupation numbers, the relevant spectroscopic factors and the orbital angular momenta of transferred nucleons were borrowed from studies devoted to pickup and stripping reactions. The total angular momenta of transferred nucleons were determined on the basis of data on spin–parities for nuclei appearing in the final states of relevant reactions. However, the spin–parity values are not known for all states. Therefore, only for some of the particle or hole states could the quantum numbers l and j be established unambiguously; for others, l is determined unambiguously, but j may take the value of $l + 1/2$ or $l - 1/2$. In the present study, the problem is solved for all possible values of j. This results in the scatter of the occupation numbers and of the energies of the subshells (that is, different solutions yield different values of N_{nlj} and E_{nlj}). The entire set of solutions makes it possible to estimate, for these parameters, the boundaries of the ranges beyond which experimental data on pickup and stripping reactions cannot be matched either with each other or with sum rules. It should be noted that these uncertainties in determining the energies of the levels are due exclusively to imperfect knowledge of the spin–parities of the states being considered. In addition to those uncertainties, one must also take into account errors in determining the relative values of the spectroscopic factors of states in the studies from which the data in question were borrowed. On the basis of an analysis of the data from those studies, it was concluded that the error in question is about 10–15%.

The distribution widths were computed by the formula

$$\Gamma^{\downarrow}_{nlj} = 2.35\sqrt{M2^{+}_{nlj} + M2^{-}_{nlj}}, \qquad (11)$$

where

$$M2^{+}_{nlj} = \frac{\sum\limits_{x}(E^{+}_{x} - e^{+}_{nlj})^2 S^{+}_{nlj}(E_x)}{S^{+}_{nlj}}, \qquad (12)$$

$$M2^{-}_{nlj} = \frac{\sum\limits_{x}(E^{-}_{x} - e^{-}_{nlj})^2 S^{-}_{nlj}(E_x)}{S^{-}_{nlj}}$$

and where summation is performed over excited states characterized by the corresponding values of n, l, and j. The quantity $\Gamma^{\downarrow}_{nlj}$ characterizes the degree of fragmentation of a particle or a hole state—that is, the width of its distribution over nuclear states. It should be borne in mind that this quantity depends more sharply on the quality of experimental data than the occupation numbers and single-particle energies considered above. If the sensitivity of the experimental procedure is insufficiently high for recording small values of spectroscopic factors, the introduction of rescaling factors makes it possible to estimate, to a fairly high degree of precision, the occupation numbers and the energy centroids on the basis of data on the features of states characterized by large spectroscopic factors. The absence of states having low values of $S^{+,-}_{nlj}$ would obviously lead to an erroneous determination of the widths.

For ^{40}Ca, data on proton pickup were borrowed from the article of Doll *et al.* [11], who studied the reaction ^{40}Ca(d, ^{3}He)^{39}K, while data on stripping were taken from [12] with a correction based on the results presented by Bock *et al.* [13], who investigated the reaction ^{40}Ca(^{3}He, d)^{41}Sc. This correction was necessary for matching the data given in those studies with each other. For the ground state of the ^{41}Sc nucleus and its excited state at 1.7 MeV, the spectroscopic factors corresponding to the $1f_{7/2}$ and $2p_{3/2}$ single-particle states are, respectively, 8.96 and 3.4 in [12] and 7.36 and 3.64 in [13]. The ratio of these values is 2.6 in the former and 2.0 in the latter case. We use the arithmetic mean of these two, 2.3, and the value of 7.92 for the absolute spectroscopic factor of the ground state.

Data on the proton pickup on a ^{42}Ca nucleus were also taken from the article of Doll *et al.* [11], who studied the reaction ^{42}Ca(d, ^{3}He)^{41}K, while data on proton stripping in the reaction ^{42}Ca(^{3}He, d)^{43}Sc were borrowed from [14].

Attempts at matching data on proton stripping and pickup on a ^{44}Ca nucleus run into considerable difficulties. The results obtained by studying the stripping reaction ^{44}Ca(^{3}He, d)^{45}Sc yield the following values of S_{nlj} for the $1d_{3/2}$ state: 1.9 [15], 2.12 [16], and 0.89 [17]. An analysis has revealed that a large number of vacancies in the subshells of ^{44}Ca below the Fermi energy are not compensated by particles in subshells above the Fermi energy. In [15], it is indicated that, at such large values of the spectroscopic factors for the stripping of protons into $1d_{3/2}$ states, there arises a contradiction with data on pickup. In order to reduce this contradiction, we used here, for the spectroscopic factor S_{nlj} of the 12.4-keV state in ^{45}Sc, the value of 0.89, which is the smallest of all quoted in the literature. The spectroscopic parameters of ^{43}K were taken from [11, 18], where they were determined in the reaction ^{44}Ca(d, ^{3}He)^{43}K, and from [19], where they were determined in the reaction ^{44}Ca(^{11}B, ^{12}C)^{43}K. By sampling all possible values of the spins in the final states of ^{43}K and ^{45}Sc, we found a few solutions that match data on stripping with data on pickup and which, at the same time, yield a correct value for the total number of protons in the ^{44}Ca nucleus.

The spectroscopic factors of the ^{45}K nucleus were determined in [20] from an analysis of the pickup reaction ^{46}Ca(t, α)^{45}K, while the analogous data for ^{47}Sc were found from an analysis of the stripping reaction ^{46}Ca(^{3}He, d)^{47}Sc [16].

The spectroscopic-factor values for the ^{47}K and the ^{49}Sc nucleus were determined from the analyses of, respectively, the reaction ^{48}Ca(t, α)^{47}K in [21] and the reaction ^{48}Ca(^{3}He, d)^{49}Sc in [22, 23]. It is worth noting that alternative two-step reaction mechanisms were considered in those studies for individual states; accordingly, alternative values of the spectroscopic factors were given there. All such versions were computed individually, and the single-particle parameters obtained in this way were taken into account in the eventual results.

With allowance for all possible values of j for individual levels, the subshell occupation numbers N_{nlj}, the single-particle energies E_{nlj} of the levels, and their fragmentation widths Γ_{nlj} are given in Table 1. To provide a visual illustration, the average values (obtained on the basis of the E_{nlj} values quoted in Table 1) of the single-particle proton levels in the $^{40-48}$Ca nuclei are displayed in Fig. 1.

An analysis of the values presented in Table 1 and in Fig. 1 makes it possible to draw the following conclusions.

As can be seen from Table 1, the energy of the $1f_{7/2}$ level in ^{40}Ca lies in the range between -1.5 and -1.8 MeV. For the energy of this level, a value

Table 1. Occupation numbers N_{nlj} of single-particle orbits, energies $-E_{nlj}$ (in MeV) of single-particle proton states, and their fragmentation widths Γ_{nlj} (in MeV) for the ^{40,42,44,46,48}Ca nuclei according to data on nucleon-stripping and nucleon-pickup reactions

nlj		^{40}Ca	^{42}Ca	^{44}Ca	^{46}Ca	^{48}Ca
$1d_{5/2}$	N_{nlj}	0.96				
	$-E_{nlj}$	14.32				
	Γ_{nlj}	2.9				
$2s_{1/2}$	N_{nlj}	1.00	0.90	0.77	0.93–0.94	0.77–0.96
	$-E_{nlj}$	10.94	> 11.3	11.39	13.88–13.95	13.76–15.92
	Γ_{nlj}	0.9	2.7	1.7	3.6	5.1
$1d_{3/2}$	N_{nlj}	1.00	0.73–0.79	0.72–0.73	0.90–0.97	0.90–0.99
	$-E_{nlj}$	8.33	8.90–11.15	10.79–10.83	13.23–13.84	15.36–16.56
	Γ_{nlj}	0.0	0.8	0.8	0	6.3
$1f_{7/2}$	N_{nlj}	0.04–0.07	0.05–0.10	0.10–0.16	0.00–0.03	0.00–0.03
	$-E_{nlj}$	1.52–1.82	3.90–4.28	7.51–7.85	7.29–8.49	8.11–9.42
	Γ_{nlj}	0.6	4.7	0.0	3.1	5.1
$2p_{3/2}$	N_{nlj}	0.07–0.11	0.01–0.02	0.03–0.06	≈ 0	0.00–0.02
	$-E_{nlj}$	0.44–1.02	1.17–1.43	4.86–5.12	< 5.80	3.58–4.55
	Γ_{nlj}	4.6	5.5	3.2	4.2	7.0
$2p_{1/2}$	N_{nlj}	0.0	0.00			0.00–0.01
	$-E_{nlj}$	−(2.35–2.41)	< 0.129			1.71–3.12
	Γ_{nlj}	0.3	0.0			7.2
$1f_{5/2}$	N_{nlj}					0.00
	$-E_{nlj}$					3.68–4.67
	Γ_{nlj}					6.5

of −1.09 MeV, which is equal to the proton binding energy in ^{41}Sc, is quoted in a large number of studies; that is, it is assumed that a level characterized by the largest value of the spectroscopic factor corresponds to the ground state of ^{41}Sc.

From our analysis, it follows that the $2p_{3/2}$ level of the ^{40}Ca nucleus is bound. According to data presented in [11], six states of the ^{39}K nucleus that are characterized by the orbital-angular-momentum transfer of $l = 1$ have the total spectroscopic factor of 0.35. This means that the population of the $2p_{3/2}$ shell is quite sizable (quantitative estimates of this population are given in Table 1), which, according to (10), leads to a reduction of its energy in relation to the completely empty shell. All articles known to the present authors give energy values corresponding to a quasibound state. This is not so only in [1], where, in Fig. 15, this level is shown as a bound one ($E_{nlj} \cong -0.6$ MeV).

Figure 1 shows that, with increasing isotope mass number, the distinction between the energies of the $1d_{3/2}$ and $2s_{1/2}$ levels decreases, but the order of these levels remains unchanged. In ^{48}Ca, the order of the levels changes; here, all solutions yield a stable result: the $1d_{3/2}$ levels is below the $2s_{1/2}$ level on the energy scale. The difference of the energies of the $2s_{1/2}$ and $1d_{3/2}$ levels changes from 0.7 to 2.5 MeV as one goes over from one solution to another.

Our data comply with data on the ground-state spins of the $^{39-47}$K nuclei (the spin–parity of the ^{47}K ground state is $1/2^+$; for all other isotopes being studied, the ground-state spin–parity is $3/2^+$ [4]). It should be noted that this unambiguous result was obtained by the method for matching data on

nucleon-stripping and nucleon-pickup reactions. In the studies that were reported in [5–7] and which were performed earlier, information that is at odds with the results obtained in [4] was deduced either from an analysis of data on stripping reactions or from an analysis of data on pickup reactions.

As can be seen from Fig. 1, the positions of the subshells on the energy scale become lower with increasing number of neutrons in a nucleus; however, this monotonic general lowering of the subshell positions has some special features. First of all, we note that the decrease in the energy of the $1f_{7/2}$ subshell is faster than the decrease in the energies of the other subshells. In the ^{40}Ca nucleus, the $1f_{7/2}$ subshell appears to be nearly coincident with the higher lying $2p_{3/2}$ subshell. As the number of neutrons in a nucleus increases, the spacing between the $1f_{7/2}$ and the $2p_{3/2}$ level also increases; as a result, the arrangement of the shells in the ^{44}Ca nucleus proves to be such that the $1f_{7/2}$ level occurs approximately in the middle of a large energy gap between the $1d_{3/2}$ and the $2p_{3/2}$ level. This pattern remains valid for the heavier isotopes as well. Thus, Fig. 1 demonstrates the formation of the $N = 28$ shell and the way in which 28 becomes a magic number.

In connection with subshell populations (occupation numbers)—see Table 1—the following comments are in order. To some extent, configuration splitting is inherent in all isotopes of Ca; in ^{48}Ca, this phenomenon is the least pronounced. The case of ^{44}Ca stands out in this respect. From the data in Table 1, it follows that the best value of the total number of nucleons according to the criterion in (7) corresponds to the maximum populations of the $1f_{7/2}$ and $2p_{3/2}$ states. In the $1d_{3/2}$ and $2s_{1/2}$ subshells, there are 1.5 to 2 vacancies in this case; accordingly, 1.5 to 2 protons occur above the Fermi energy in the $1f_{7/2}$ and $2p_{3/2}$ subshells (a nonintegral number of nucleons reflects the probability of finding the system in the corresponding state).

In the present study, we were unable to determine the energy of the $1d_{5/2}$ state in ^{48}Ca by using the method for matching data on stripping and pickup reactions. In Section 4, two values, $E_{nlj} = -21.5$ MeV [7] and $E_{nlj} = -20.5$ MeV [24], are therefore used for this level in deriving the required estimates.

In Section 4, the above special features in the single-particle properties of proton states in the vicinity of the Fermi energy in the $^{40-48}$Ca nuclei are analyzed in terms of the dispersive optical model.

3. DETERMINATION OF THE PARAMETERS OF A DISPERSIVE OPTICAL POTENTIAL FOR THE $p + {}^{40,42,44,46,48}$Ca SYSTEMS

The method used within the dispersive optical model to calculate the energies of single-particle states in spherical nuclei is described in detail elsewhere [2, 3]. Below, we therefore only present the formulas required for the calculations and discuss methods for determining the parameters of the dispersive optical potential employed.

In order to calculate the positions (energies) of levels corresponding to single-particle states, we solve the Schrödinger equation for bound states; that is,

$$\left[\frac{-\nabla^2}{2m} + V(r, E_{nlj})\right]\Phi_{nlj}(\mathbf{r}) = E_{nlj}\Phi_{nlj}(\mathbf{r}), \quad (13)$$

where m is the reduced nucleon mass; E_{nlj} are single-particle energies; $\Phi_{nlj}(\mathbf{r})$ are single-particle wave functions; and $V(r, E_{nlj})$ is the real part of the dispersive optical potential,

$$V(r, E_{nlj}) = V_{\rm HF}(r, E_{nlj}) + \Delta V_s(r, E_{nlj}) + \Delta V_d(r, E_{nlj}) - V_{\rm C}(r) + U_{\rm so}(r, E_{nlj}). \quad (14)$$

Here, $V_{\rm HF}(r, E_{nlj})$ is the Hartree–Fock component of the dispersive optical potential, $\Delta V_i(r, E_{nlj})$ stands for $(i = s)$ the volume and $(i = d)$ the surface component of the dispersive optical potential, $V_{\rm C}(r)$ is the Coulomb potential, and $U_{\rm so}(r, E_{nlj})$ is the spin–orbit potential.

In terms of the Woods–Saxon parametrization, the dispersive optical potential can be written as

$$-U(r, E) = V_{\rm HF}(E)f(r, r_{\rm HF}, a_{\rm HF}) + \Delta V_s(E)f(r, r_s, a_s) - 4a_d\Delta V_d(E)\frac{d}{dr}f(r, r_d, a_d) + iW_s(E)f(r, r_s, a_s) - i4a_dW_d(E)\frac{d}{dr}f(r, r_d, a_d) + 2V_{\rm so}(E)\frac{1}{r}\frac{d}{dr}f(r, r_{\rm so}, a_{\rm so})\mathbf{l}\cdot\mathbf{s} - V_{\rm C}(r), \quad (15)$$

where $f(r, r_i, a_i) = 1/(1 + \exp\left[(r - r_iA^{1/3})/a_i\right])$ is the Woods–Saxon function $(i = s,\ d,\ \text{so})$, the Coulomb potential $V_{\rm C}(r)$ is taken in the form of the potential of a uniformly charged sphere of radius $R_{\rm C} = r_{\rm C}A^{1/3}$, and the components $\Delta V_i(r, E)$ are calculated with the aid of the dispersion relation

$$\Delta V_{s(d)}(r, E) = \frac{(E_{\rm F} - E)}{\pi} \times {\rm P}\int\limits_{-\infty}^{\infty}\frac{W_{s(d)}(r, E')}{(E' - E_{\rm F})(E - E')}dE' \quad (16)$$

[the symbol P here means that the principal-value prescription is applied to the integral in (16)]. The

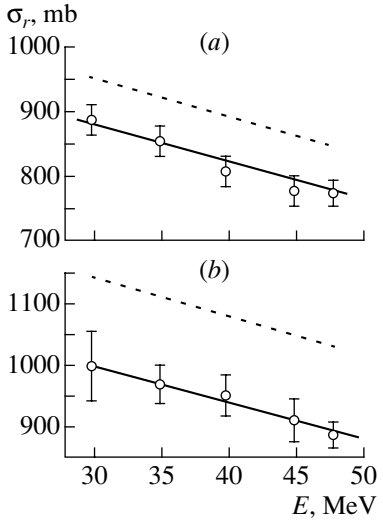

Fig. 2. Total reaction cross sections $\sigma_r(E_k)$ for (*a*) the $p + {}^{40}$Ca and (*b*) the $p + {}^{48}$Ca system. In Fig. 2*a*, open circles represent experimental data from [27], while the solid and the dashed line correspond to the calculations with, respectively, the CH89* [26] ($a_d^* = a_s^* = 0.60$ fm) and the CH89 [25] ($a_d = a_s = 0.69$ fm) parameters. The notation in Fig. 2*b* is similar to that in Fig. 2*a*, the only exception being that the solid line in the latter case was computed with the parameter values of $a_d^* = a_s^* = 0.54$ fm.

analogous dispersion relations are valid for the volume integrals of the potentials ($\Delta J_{s(d)}(E)$, $J_{s(d)}(E)$).

In order to determine the dependences $W_{s(d)}(r, E)$, we evaluated, within the traditional optical model, the volume integrals of the imaginary potential, $J_{s(d)}(E_k)$, for various specific values of the energy E_k, whereupon we approximated $J_{s(d)}(E_k)$ by a continuous function chosen in such a way that the integral in (16) could be calculated analytically (for details, the interested reader is referred to [2]).

In the present study, the volume integrals $J_I(E_k) = J_s(E_k) + J_d(E_k)$, $J_s(E_k)$, and $J_d(E_k)$ were approximated by using the Jeukenne–Mahaux expressions (see the corresponding reference in [2]); that is,

$$J_i^{\mathrm{JM}}(E) = \alpha_i \frac{(E - E_{\mathrm{F}})^4}{(E - E_{\mathrm{F}})^4 + \beta_i^4}, \quad \text{where } i = I, s, \tag{17}$$

$$J_d^{\mathrm{JM}}(E) = J_I^{\mathrm{JM}}(E) - J_s^{\mathrm{JM}}(E). \tag{18}$$

In the studies developing methods of a dispersive optical-model analysis, it was shown that all parameters of the dispersive optical potential that are used in calculating the features of single-particle states can be determined from experimental scattering cross sections [9]. However, experimental information about the cross sections and polarizations for protons scattered by nuclei is still incomplete. By way of example, we indicate that, for the $p + {}^{40}$Ca system, experimentalists performed a large number of measurements that yielded data on $\sigma^{\mathrm{expt}}(\theta)$ and $P^{\mathrm{expt}}(\theta)$ over the range from 20 to 80 MeV, but that, for the $p + {}^{42-48}$Ca systems, there are data only for a few values of E_k. The values calculated for $J_V(E_k)$, $J_s(E_k)$, and $J_d(E_k)$ by using the individual parameters of the traditional optical potential have a wide scatter, and this adversely affects the accuracy of determining the parameters of the dispersive optical potential. All these circumstances constrain the potential of the dispersive optical model as means for analyzing the single-particle structure of nuclei.

Usually, the energy dependence of the imaginary part of the dispersive optical potential is determined on the basis of the parameters of the traditional optical potential that are chosen individually for a given system, while the real part is specified on the basis of a fit to available experimental data on scattering. In the present article, we propose a dispersive-optical-model version that is based on the CH89 systematics [25] of the average parameters of the traditional optical potential for nucleons. On average, the scattering cross sections and polarizations calculated as functions of angles with the CH89 parameters comply well with experimental data over rather wide ranges of energy ($20 \le E \le 65$ MeV) and mass numbers ($40 \le A \le 208$). The use of the parameter values from the CH89 systematics makes it possible to describe the positions of the maxima and minima in the differential cross sections for elastic scattering. However, it is necessary to vary the parameters $a_d = a_s$ in order to obtain the best agreement between the computed elastic-scattering cross sections at the maxima and minima and their experimental counterparts. In [26], it is shown that this is achieved with such values of $a_d^* = a_s^*$ at which the cross section σ_r^{TOM} computed within the traditional optical model (TOM) complies with the experimental cross sections σ_r^{expt} determined to a precision of about 3%. (For the sake of brevity, the parameters of the CH89 systematics where, instead of the average value of $a_d = 0.69$ fm, use is made of $a_d^* = a_s^*$ values chosen individually for each system are denoted in [26] by CH89*.)

For ^{40,42,44,48}Ca, the values measured for the total reaction cross sections σ_r to a precision of about 3% over the energy range from approximately 30 to 50 MeV are quoted in [27]. By way of example, the experimental total proton cross sections $\sigma_r^{\mathrm{expt}}(E_k)$ for the $p + {}^{40,48}$Ca systems from [27] are displayed

in Fig. 2 along with the computed dependences $\sigma_r^{\mathrm{CH89}}(E)$ ($a_d = a_s = 0.69$ fm) and $\sigma_r^{\mathrm{CH89^*}}(E)$ ($a_d^* = a_s^* = 0.60$ fm for ^{40}Ca and $a_d^* = a_s^* = 0.54$ fm for ^{48}Ca). For ^{46}Ca, there is no experimental information about $\sigma_r(E_k)$. In order to determine $a_d^* = a_s^*$ for ^{46}Ca, use was therefore made of $\sigma_r(E_k)$ values interpolated according to data from [27] on the $p + {}^{40,42,44,48}$Ca systems.

The possibility of determining, for each system individually, the values of $a_d^* = a_s^*$ from a comparison of $\sigma_r^{\mathrm{CH89^*}}$ with σ_r^{expt} is of importance for the following reasons. First, these quantities can be estimated via extrapolations and interpolations on the basis of data on $\sigma_r^{\mathrm{expt}}(E_k)$ accumulated to date for various nuclei. Second, such measurements are among the most easily implementable in experiments with radioactive nuclear beams, as was indicated in a large number of studies.

We have calculated the angular dependences of the ratios of the differential cross sections for elastic proton scattering on Ca targets to the corresponding Rutherford cross sections ($\sigma/\sigma_{\mathrm{R}}$) by using the CH89* parameters. By way of example, the results of these calculations at $E = 45.5$ MeV for ^{40}Ca and at 45.0 MeV for ^{42,44,48}Ca are contrasted in Fig. 3 against the corresponding experimental values. A comparison of these theoretical and experimental results gives grounds to conclude that the use of the parameters $a_d^* = a_s^*$ from the CH89* systematics leads to a good description of experimental differential cross sections for elastic scattering. A similar conclusion follows from a comparison at other energy values in the range $20 \le E_k \le 65$ MeV.

In the proposed version of the dispersive optical model, the model scattering cross sections computed with the CH89* parameters are used for a further analysis instead of their experimental cross-section values. This significantly simplifies the procedure for determining the average values of the dispersive-optical-potential parameters without impairing their accuracy.

As follows from (17), the parameter α_I corresponds to the value of $J_I(E)$ for $E \to \infty$. In order to determine α_I, it is sufficient to find the average value of $J_I(E_k)$ for $E_k \approx 40$–60 MeV. In the studies relying on the dispersive optical model, the authors present tables containing the traditional-optical-potential parameters determined individually for each nucleus and, on the basis of these data, calculate the values of $J_I(E_k)$, which are then used to find $J_I(E)$.

In [3], a method was proposed according to which the parameter α_I is defined as that which corresponds to the $J_I^{\mathrm{CH89^*}}$ value averaged over the energy range 40–60 MeV. The parameters α_I evaluated in this way

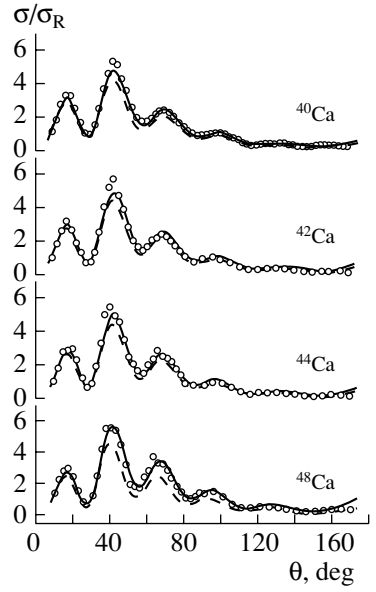

Fig. 3. Angular dependences of the ratio of the differential cross sections for elastic proton scattering on ^{40,42,44,48}Ca nuclei to the corresponding Rutherford cross sections ($\sigma/\sigma_{\mathrm{R}}$): (open circles) experimental data, (dashed curves) results of the calculation with the CH89 parameters [25] ($a_d = a_s = 0.69$ fm), and (solid curves) results of the calculation with the CH89* parameters [26] ($a_d^* = a_s^* = 0.60$ fm at $E = 45.5$ MeV for ^{40}Ca; $a_d^* = a_s^* = 0.605$, 0.61, and 0.54 fm at $E = 45.0$ MeV for ^{42}Ca, ^{44} Ca, and ^{48}Ca, respectively).

for $^{40-48}$Ca are quoted in Table 2. Also given in this table are the parameters $a_s^* = a_d^*$ and the CH89 parameters $r_s = r_d$, r_V, r_{so}, and r_{C}. We have performed all the ensuing calculations with the parameters $r_s = r_d$ fixed according to the CH89 systematics and with the individual values of the parameters $a_s^* = a_d^*$ from Table 2.

In CH89, the imaginary potential changes smoothly with energy. Concurrently, there occurs a continuous transition from a surface absorption at low energies to a volume absorption at high energies. It should be noted that attempts at directly calculating the imaginary potential were made in a number of studies, but these calculations were rather complicated and cumbersome and were often based on restrictive assumptions. The introduction of a complex-valued renormalization in the folding-potential model is one of the means for calculating the imaginary potential (see, for example, [28]).

We determined the parameter β_s by imposing the condition requiring that the dependences $J_s^{\mathrm{JM}}(E)$ and $J_s^{\mathrm{CH89^*}}(E)$ intersect at half the maximum value of the latter. For $^{40-48}$Ca, the parameter β_s found in this way ranges between 60 and 70 MeV (see Table 2). The calculations reveal that the calculated values of

the fragmentation widths Γ_{nlj} of deep hole states depend on the choice of values for the parameter β_s. Therefore, the β_s values estimated in the way outlined above were then corrected on the basis of data on $\Gamma_{nlj}^{\text{expt}}$.

The parameter β_I characterizes the energy dependence $J_I(E)$ in the energy region around the barrier and in the vicinity of E_F. Within traditional versions of the dispersive optical model, this parameter is determined on the basis of data on $J_I(E_k) \cong J_d(E_k)$ that are extracted from an analysis of cross sections and polarizations within the traditional optical model in the energy region around the barrier. In Ca isotopes, large uncertainties in determining the parameter β_I arise because of the excitation of isobar-analog resonances in this energy region. In the present study, the values of the parameter β_I were selected on the basis of a comparison of the calculated and experimental energies of levels in the vicinity of E_F. For the $^{40-48}$Ca isotopes, the values of β_I proved to lie between 8 and 12.5 MeV. Problems associated with the choice of this parameter will be discussed below.

The energy E_F can be determined as

$$E_\text{F} = \frac{E_{nlj}^+ + E_{nlj}^-}{2}, \qquad (19)$$

where E_{nlj}^+ is the energy of the most strongly bound particle level ($1f_{7/2}$ for $^{40-48}$Ca), while E_{nlj}^- is the energy of the least bound level ($1d_{3/2}$ for $^{40-46}$Ca and $2s_{1/2}$ for ^{48}Ca). By analyzing solutions for ^{40,42,44,46,48}Ca (see Table 1), we obtained the following ranges for $-E_\text{F}^{\text{expt}}$: 4.9–5.1 MeV for ^{40}Ca, 6.4–7.7 MeV for ^{42}Ca, 9.1–9.3 MeV for ^{44}Ca, 10.3–11.1 MeV for ^{46}Ca, and 10.9–12.7 MeV for ^{48}Ca. If, in (19), the energies of the levels are replaced by the sign-reversed proton binding energies in the Z and $Z+1$ nuclei (see [4]), the mass-number dependence of the Fermi energy (-4.7 MeV for ^{40}Ca, -7.6 MeV for ^{42}Ca, -9.5 MeV for ^{44}Ca, -11.1 MeV for ^{46}Ca, and -12.7 MeV for ^{48}Ca) will be close to a linear dependence. We have estimated the mass-number dependence of the Fermi energy (19) for Ca isotopes, assuming that it has a linear form. The result is

$$E_\text{F}^{\text{est}} = -\left[5.2 + 0.89\,(A-40)\right] \ \text{MeV}. \qquad (20)$$

The estimated values E_F^{est} (see Table 2) are close to those that were calculated by using the proton binding energies in the Z and $Z+1$ nuclei.

Problems associated with determining the parameters r_HF and a_HF were discussed in a large number of studies devoted to applications of the dispersive optical model. In [9], Mahaux and Sartor proposed equating the parameter a_HF to the energy-averaged diffuseness parameter of the real potential in the traditional optical model, a_V. In that study, the average value a_V was found to be 0.70 fm. We set $a_\text{HF} = a_V^{\text{CH89}} = 0.69$ fm for all Ca isotopes.

Dispersive-optical-model versions where the energy independence of the parameter r_HF was postulated and where various means for determining the optimum values of this parameter were considered were substantiated in [2]. The range $1.18 \le r_\text{HF} \le 1.24$ fm of its possible values at $a_\text{HF} = 0.70$ fm was established in [9] for the $p + {}^{40}$Ca system, and it was shown there that the optimum value is $r_\text{HF} = 1.20 \pm 0.02$ fm.

If the parameters r_HF and a_HF are fixed, then, for $E < 0$, the values $V_\text{HF}(E_{nlj}^{\text{expt}})$ are found by solving Eq. (13). For the energy range $E > 0$, the values of $V_\text{HF}(E_k)$ were determined in the present study by using the expressions

$$V_\text{HF}(E_k) = J_\text{HF}(E_k)/g(r_\text{HF}, a_\text{HF}), \qquad (21)$$

where

$$J_\text{HF}(E_k) = J_V^{\text{CH89}}(E_k) - \Delta J_V(E_k), \qquad (22)$$

$$g(r_\text{HF}, a_\text{HF}) = \int f(r, r_\text{HF}, a_\text{HF})\, d\mathbf{r}. \qquad (23)$$

The resulting values of $V_\text{HF}(E_{nlj})$ and $V_\text{HF}(E_k)$ for $E < 0$ and $E > 0$, respectively, were used to determine the parameters of two dependences proposed for describing $V_\text{HF}(E)$ (see [2, 3]). These are

(i) the exponential dependence

$$V_\text{HF}(E) = V_\text{HF}(E_\text{F}) \exp\left(\frac{-\gamma(E-E_\text{F})}{V_\text{HF}(E_\text{F})}\right), \qquad (24)$$

where γ is a parameter, and

(ii) the dependence that combines an exponential and a linear function in the form

$$V_\text{HF}(E) = V_\text{HF}^1(E_\text{F}) + V_\text{HF}^2(E_\text{F}) \exp\left[\frac{-\lambda(E-E_\text{F})}{V_\text{HF}^2(E_\text{F})}\right] \qquad (25)$$

$$\text{for } E > E_\text{F},$$

$$V_\text{HF}(E) = V_\text{HF}(E_\text{F}) - \lambda(E-E_\text{F}) \ \text{ for } E < E_\text{F}, \qquad (26)$$

where λ is a parameter and

$$V_\text{HF}(E_\text{F}) = V_\text{HF}^1(E_\text{F}) + V_\text{HF}^2(E_\text{F}). \qquad (27)$$

In (24)–(27), the values of $V_\text{HF}(E_\text{F})$ were determined by the formula

$$V_\text{HF}(E_\text{F}) = \frac{V_\text{HF}(E_{nlj}^+) + V_\text{HF}(E_{nlj}^-)}{2}. \qquad (28)$$

Table 2. Parameters of the dispersive optical potential for the $p + {}^{40,42,44,46,48}$Ca systems (r_d, r_s, a_d^*, a_s^*, r_V, r_C, and $r_{\rm HF}$ are given in femtometers; α_I is given in MeV fm^3 units; and $E_{\rm F}^{\rm est}$ and β_s are given in MeV)

Isotope	$r_d = r_s$	$a_d^* = a_s^*$	α_I	r_V	$r_{\rm so}$	$r_{\rm C}$	β_s	$-E_{\rm F}^{\rm est}$	$r_{\rm HF}$
^{40}Ca	1.207	0.600	103.49	1.184	0.989	1.272	57.0	5.2	1.207
^{42}Ca	1.209	0.605	109.00	1.185	0.995	1.271	61.0	7.0	1.218
^{44}Ca	1.211	0.610	113.90	1.186	1.000	1.271	63.7	8.8	1.221
^{46}Ca	1.213	0.615	118.27	1.187	1.005	1.270	66.7	10.7	1.227
^{48}Ca	1.214	0.540	109.32	1.187	1.010	1.270	73.0	12.5	1.227

We note that the values of $V_{\rm HF}(E_{\rm F})$ depend on the choice of values for the parameters $r_{\rm HF}$, $a_{\rm HF}$, and $V_{\rm so}$ at fixed values of $r_{\rm so}$ and $a_{\rm so}$, but that they feature no significant dependence on α_I, β_s, and β_I.

If the parameter γ is determined on the basis of scattering data, an error of about 3% in γ leads to an error of about 5% in computing, according to (13), the energy $E_{1s1/2}$ of the deepest level (for the $1s_{1/2}$ state, we have $(E - E_{\rm F})/V_{\rm HF}(E_{\rm F}) \cong 1$). Since the experimental value of the energy $E_{1s1/2}$ for ^{40}Ca is known to a fairly high precision (according to data reported in [29], $E_{1s1/2} = -53.6 \pm 0.7$ MeV), which is sufficient for our purposes, we can specify conditions under which the error in calculating $E_{1s1/2}$ by using the parameter γ found from data for $E > 0$ will be minimal. With this aim in view, we compared the values of the parameter γ that were found in calculating the values of $V_{\rm HF}(E_{\rm F})$ (28) and $V_{\rm HF}(E_{1s1/2})$ and in calculating $V_{\rm HF}(E_k = 30, 40, 50,$ and 60 MeV) (21)–(23) for three values of the parameter $r_{\rm HF}$ (1.184, 1.207, and 1.24 fm). All of the parameters of the dispersive optical potential, with the exception of β_I, were fixed at the values quoted above. The parameters γ determined on the basis of data for $E < 0$ are virtually independent of β_I, while those that rely on data for $E > 0$ do depend on this parameter. By way of example, we indicate that, for the $p + {}^{40}$Ca system, the values of the parameter γ at $\beta_I \cong 8$–9 MeV prove to be consistent for all three values of $r_{\rm HF}$. It follows that, in order to predict the positions of the levels on the energy scale, including the $1s_{1/2}$ level, which is the deepest one, it is of paramount importance to determine the parameter γ to the highest possible degree of precision. If this parameter is found on the basis of data for $E > 0$, it is necessary to evaluate the parameter β_I with minimum possible errors.

In [2, 3], it was shown that, in calculating the energies $E_{nlj}^{\rm DOM}$ (the abbreviation DOM in the superscript stands for the dispersive optical model) for $E < E_{\rm F}$, the closest agreement with $E_{nlj}^{\rm expt}$ is achieved with the linear dependence $V_{\rm HF}(E)$ in the form (26); for $E > E_{\rm F}$, the best results are obtained with the exponential form (25). The parameter λ can then be determined by using the expression

$$\lambda = \frac{V_{\rm HF}(E_{1s1/2}) - V_{\rm HF}(E_{\rm F})}{E_{1s1/2} - E_{\rm F}}. \qquad (29)$$

In just the same way as the parameter γ, the parameter λ varies with $r_{\rm HF}$, all of the remaining parameters of the dispersive optical potential being fixed. We have found that, for the $p + {}^{40}$Ca system, the quantities λ and $r_{\rm HF}$ are related by the equation

$$\lambda = Cr_{\rm HF} - 0.507, \qquad (30)$$

where $C = 0.893$ fm^{-1} and $r_{\rm HF}$ is measured in femtometers.

In order to investigate the dependence of the E_{nlj} values calculated according to (13) on the choice of the parameter $r_{\rm HF}$ (at fixed values of all of the remaining parameters of the dispersive optical potential), we have calculated the energies of single-particle levels in ^{40}Ca for two values of $r_{\rm HF}$: $r_{\rm HF} = 1.184$ fm ($\lambda = 0.55$) and $r_{\rm HF} = 1.24$ fm ($\lambda = 0.60$). The results of these calculations are quoted in Table 3 (columns 2 and 3, respectively). The same table also presents the experimental energies of single-particle levels (column 15) for the $1s_{1/2}$, $1p_{3/2}$, and $1p_{1/2}$ states—these are data from [29]; for the remaining states, the corresponding data are given in Table 1. From a comparison of the calculated and measured energies of the levels, one can conclude that the scatter of the calculated values of E_{nlj} is insignificant, whence it follows that the optimum value of the parameter $r_{\rm HF}$ can hardly be determined from a comparison of the calculated and measured energies of the levels.

In order to determine $r_{\rm HF}$ from scattering data, we went over, according to [9], from the real part of the dispersive optical potential—this real part consists of three terms involving different form factors—to a real part featuring one term whose form factor $f(r, r_V, a_V)$ has the Woods–Saxon form. We set

$a_V \equiv a_{\rm HF}$ and found the parameters r_V and V from the condition requiring that the volume integral of the real potential and its value at $r = 0$ be fixed, the parameter r_V appearing to be energy-dependent in this case.

We have calculated the dependences $r_V = r_V(E)$ for three fixed values of $r_{\rm HF}$ in the range 1.18–1.24 fm. It turned out that the r_V values computed for $10 \leq E \leq 60$ MeV were in the best agreement with data available from the literature {in performing this comparison, we selected, from the tables given in [28], only those values of the optical-potential parameters that were obtained by independently varying all of the parameters and which were such that the $\sigma_r^{\rm OM}$ values calculated with them (on the basis of the optical model) were consistent with $\sigma_r^{\rm expt}$ [27]} at $r_{\rm HF} = 1.20 \pm 0.02$ fm.

We have determined $r_{\rm HF}$ for a few values of E_k ($20 \leq E \leq 60$ MeV) by comparing scattering cross sections calculated on the basis of the dispersive optical model with model-dependent cross sections. It turned out that $r_{\rm HF} = 1.207$ fm for the $p + {}^{40}$Ca system at $E_k = 30$ MeV. At $E_k = 30$ MeV, the values of the parameters $r_{\rm HF}$ for the $p + {}^{42,44,46,48}$Ca systems were found in a similar way. All of the resulting values are quoted in Table 2.

We assumed that the dependence that is specified by Eq. (30) and which was found on the basis of data for the $p + {}^{40}$Ca system can be used to determine the parameters λ for the ${}^{42-48}$Ca isotopes. According to (30), λ changes within the range 0.57–0.59 in response to a variation of $r_{\rm HF}$ from 1.207 to 1.227 fm. In all of the subsequent calculations, the parameter λ was therefore set to

$$\lambda = 0.58 \pm 0.01, \qquad (31)$$

the remaining parameters, with the exception of the parameters β_I and $V_{\rm so}$, being fixed at the values quoted in Table 2.

4. COMPARISON OF THE CALCULATED AND EXPERIMENTAL PARAMETERS OF SINGLE-PARTICLE LEVELS IN ^{40,42,44,46,48}Ca

For each nuclear species studied here, the energy positions of single-particle bound states in the mean-field potential were calculated in the following way. The Schrödinger Eq. (13) was solved numerically with the potential $V(r, E_i)$ (15) by using the parameter values quoted in Table 2 and some energy value E_i that plays the role of an estimate of E_{nlj}. In choosing E_i, we tried to reduce, as the number i of iterations was increased, the distinction between the calculated eigenvalue $E_{nlj}(E_i)$ and E_i, $\Delta_{nlj}^{(i)} = |E_{nlj}^{(i)}(E_i) - E_i|$. In the present study—in just the same way as in [3, 30]—E_i was treated as the eigenvalue E_{nlj} if $\Delta_{nlj}^{(i)} \leq 10$ keV.

The energies of single-particle proton levels in ^{40}Ca according to the calculations at various values of the parameter β_I for $V_{\rm so} = 5.9$ MeV fm^2 are given in Table 3 (columns 4–7). From a comparison of E_{nlj} (columns 4–7) with $E_{nlj}^{\rm expt}$ (column 15), it follows that, at $\beta_I = 17$ MeV, the energies E_{nlj} of the $1p$ and $1d$ levels differ from their experimental counterparts $E_{nlj}^{\rm expt}$. At $\beta_I = 12.5$ MeV, the best agreement between $E_{nlj}^{\rm DOM}$ and $E_{nlj}^{\rm expt}$ is attained for all levels, with the exception of $2p_{3/2}$.

According to the data in Table 1, the $2p_{3/2}$ state in ^{40}Ca is bound. From Table 3, it can be seen that the energy values calculated in the present study for the $2p_{3/2}$ level correspond to quasibound states if $\beta_I > 9$ MeV. This table also shows that, for β_I values chosen in the range between 8 and 9 MeV, there is good agreement between $E_{nlj}^{\rm DOM}$ and $E_{nlj}^{\rm expt}$ for all levels in the vicinity of the Fermi energy $E_{\rm F}$ if one takes into account a 10% error (in addition to the error because of the uncertainty in the spin value) in determining $E_{nlj}^{\rm expt}$. We also note that, for $8 \leq \beta_I \leq 12.5$ MeV, the computed energy of the $1f_{7/2}$ level is about -2 MeV. This energy value complies with that which was calculated on the basis of the nonrelativistic mean-field model [31] (see Table 3, column 14).

Table 3 also presents the results obtained by calculating the energies of the levels in the dispersive optical potential [8, 9] (columns 8, 9). The values computed in [8, 9] for the energies of the $1s_{1/2}$ levels are below the experimental values by 3 to 4 MeV. From Table 3, it is also obvious that, for the energies of the $1s_{1/2}$, $1p_{3/2}$, and $1p_{1/2}$ levels, the calculations performed in [1, 32–34] on the basis of the relativistic mean-field model with various parameter sets (the results are given in columns 10–13) usually exceed their experimental counterparts.

The energies found for the levels in ^{42,44,46,48}Ca from to our present calculations based on the dispersive optical model, the calculations of Koura and Yamada [31] within the nonrelativistic mean-field model, the calculations relying on its relativistic generalization [1, 32, 33] are given in Table 4, along with the experimental data from Table 1 and from [7, 24, 29]. Comparing the values of $E_{nlj}^{\rm DOM}$ (Table 4) with $E_{nlj}^{\rm expt}$ (Table 1) for ^{42,46}Ca, one can conclude that good agreement is obtained at $V_{\rm so} = 5.9$ MeV fm^2, which is identical to the choice of this parameter for ^{40}Ca.

Table 3. Energies $-E_{nlj}$ (in MeV) of single-particle proton states in ^{40}Ca

1	2	3	4	5	6	7	8	9	10	11	12	13	14	15
nlj	DOM	DOM	DOM	DOM	DOM	DOM	DOM [8]	DOM [9]	RMFM [1]	RMFM [32]	RMFM [33]	RMFM [34]	NRMFM [31]	Experiment [7,24,29]
$2p_{1/2}$	−1.75	−1.83	−2.18	−1.71	−1.30	−1.24	−2.02	−2.47						−(2.35–2.41)
$2p_{3/2}$	−0.50	−0.64	−0.94	−0.45	−0.03	0.04	−0.92	−1.34	−1.7		−(1.1–1.5)		0.73–(−1.15)	0.44–1.02
$1f_{7/2}$	1.86	2.06	1.66	2.02	2.38	2.38	1.15	0.94	1.7		1.5–2.1		1.71–2.13	1.52–1.82
$1d_{3/2}$	8.63	8.40	8.88	8.41	8.24	7.95	8.88	8.91	9.08	10.0–15.3	7.7–8.5	8.87–9.5	8.13–8.60	8.33
$2s_{1/2}$	10.34	10.01	10.68	10.03	9.72	9.38	10.67	10.41	10.02	10.8–15.5	9.8–10.9	8.83–9.43	8.59–9.09	10.94
$1d_{5/2}$	14.30	14.15	15.11	14.30	13.67	13.50	14.95	14.73	16.65	14.1–21.5	14.4–15.0	15.18–15.9		14.32
$1p_{1/2}$	29.28	28.83	28.50	29.19	29.75	29.87	31.62	30.4	28.25	26.5–35.0		25.9–26.35		29.1–30.5
$1p_{3/2}$	34.52	34.70	34.09	34.75	35.07	35.16	36.52	35.0	32.99	25.8–38.6		29.44–30.66		34.4–35.0
$1s_{1/2}$	53.60	53.60	53.60	53.60	53.60	53.60	57.38	58.2	49.94	43.5–55.7		43.5–45.43		52.9–54.3

Note: Here and in Table 4, the the abbreviations DOM, RMFM, and NRMFM stand for, respectively, the dispersive optical model, the relativistic optical model, and the nonrelativistic optical model. The energies $E_{nlj,}$ were calculated in the present study with the parameters of the dispersive optical potential that were set to the following values: (column 2) $r_{\rm HF} = 1.184$ fm and $\beta_I = 12.5$ MeV, (column 3) $r_{\rm HF} = 1.24$ fm and $\beta_I = 12.5$ MeV, (column 4) $r_{\rm HF} = 1.207$ fm and $\beta_I = 17.0$ MeV, (column 5) $r_{\rm HF} = 1.207$ fm and $\beta_I = 12.5$ MeV, (column 6) $r_{\rm HF} = 1.207$ fm and $\beta_I = 9.0$ MeV, and (column 7) $r_{\rm HF} = 1.207$ fm and $\beta_I = 8.0$ MeV; $V_{\rm so} = 5.9$ MeV fm^2, $\lambda = 0.574$.

Table 4. Energies $-E_{nlj}$ (in MeV) of single-particle proton states in ^{42,44,46,48}Ca

1	2	3	4	5	6	7	8	9	10	11	12	13	14
	^{42}Ca		^{44}Ca		^{46}Ca		^{48}Ca						
nlj	DOM	RMFM [1]	DOM	RMFM [1]	DOM	RMFM [1]	DOM	DOM	RMFM [1]	RMFM [32]	RMFM [33]	NRMFM [31]	Experiment [7, 24, 29]
$2p_{1/2}$	−0.07		1.37		2.87		3.65	4.16			1.3–2.4		1.7–3.1
$2p_{3/2}$	1.29		3.38		4.41		4.75	4.95			3.0–3.6	5.84–6.06	3.6–4.5
$1f_{7/2}$	4.11		7.23		7.82		8.11	7.92			9.3–10.4	10.47–10.91	8.1–9.4
$1d_{3/2}$	9.88	11.28	11.26	13.49	13.55	15.64	16.62	17.75	17.97	15.9–21.7	16.0–17.0	15.63–16.54	15.4–16.6
$2s_{1/2}$	11.15	11.63	13.30	13.23	14.47	14.74	16.55	16.95	16.20	17.2–24.4	15.3–16.4	15.61–15.75	13.8–15.9
$1d_{5/2}$	15.16	18.71	18.57	20.31	18.61	22.83	20.54	20.56	25.07	21.3–29.9	22.5		20.5–21.5
$1p_{1/2}$	31.39	30.37	32.70	32.51	34.89	33.61	37.99	39.53	36.97	32.9–43.7			28–42
$1p_{3/2}$	36.60	34.84	39.42	36.77	39.77	38.64	41.51	42.04	40.75	34.5–46.7			28–42
$1s_{1/2}$	54.29	51.28	56.08	52.67	56.52	54.06	59.85	60.76	55.66	47.8–62.2			46–64

Note: The energies E_{nlj} were calculated in the present study with the parameters of the dispersive optical potential were set to the following values: (columns 2, 6) $\beta_I = 9$ MeV and $V_{\rm so} = 5.9$ MeV fm^2, (column 4) $\beta_I = 9$ MeV and $V_{\rm so} = 7.9$ MeV fm^2, (column 8) $\beta_I = 12.5$ MeV and $V_{\rm so} = 4.2$ MeV fm^2, and (column 9) $\beta_I = 12.5$ MeV and $v_{\rm so} = 3.0$ MeV fm^2.

Table 5. Energies Δ (in MeV) of spin–orbit splitting for the $1p$ and $1d$ states in ^{40}Ca and in ^{48}Ca

Nucleus	Shells	Δ^{expt}	Δ^{DOM}	Δ^{RMFM}						
				[1]	[32]	[33]	[34]	[35]	[36]	[37]
^{40}Ca	$1p$	4.9 ± 1.0	5.3–5.6	4.7	2.0-3.8		3.5–4.4			4.1–5.1
	$1d$	6.0	5.7	7.6	3.3–6.2	6.6 ± 0.7	5.7–6.9	6.0–7.7	8.01	6.6–6.9
^{48}Ca	$1p$		2.5–3.5	3.8	1.6–3.0					3.2–3.8
	$1d$	5.0 ± 1.1	2.8–3.9	7.1	4.1–5.5	5.5–6.5		1.3–7.4	4.06	6.1–6.6

Table 6. Occupation numbers N_{nlj} for single-particle proton orbits in ^{40,42,44,46,48}Ca

nlj	^{40}Ca			^{42}Ca			^{44}Ca			^{46}Ca			^{48}Ca		
	N_{nlj}^{expt}	N_{nlj}^{DOM}	N_{nlj}	N_{nlj}^{expt}	N_{nlj}^{DOM}	N_{nlj}	N_{nlj}^{expt}	N_{nlj}^{DOM}	N_{nlj}	N_{nlj}^{expt}	N_{nlj}^{DOM}	N_{nlj}	N_{nlj}^{expt}	N_{nlj}^{DOM}	N_{nlj}
$2s_{1/2}$	1.00	0.84	0.565	0.90	0.83	0.480	0.77	0.85	0.486	0.94	0.84	0.462	0.86	0.84	0.450
$1d_{3/2}$	1.00	0.81	0.565	0.76	0.80	0.592	0.72	0.83	0.625	0.93	0.82	0.636	0.94	0.84	0.631
$1f_{7/2}$	0.05	0.18	0.424	0.07	0.19	0.479	0.13	0.16	0.486	0.01	0.17	0.462	0.01	0.16	0.449

Note: The N_{nlj}^{expt} values were determined by means of averaging over the data in Table 1; the N_{nlj}^{DOM} values were obtained as the result of our present calculations; and the N_{nlj} values were borrowed from the data reported in [38].

At the same time, we were able to reach satisfactory agreement between E_{nlj}^{DOM} and E_{nlj}^{expt} only under the assumption that $V_{\text{so}} = 7.9$ MeV fm^2 for ^{44}Ca and $V_{\text{so}} = 3.0$–4.2 MeV fm for ^{48}Ca.

From a comparison of E_{nlj}^{DOM} and E_{nlj}^{RMFM} for $^{40-48}$Ca (Tables 3, 4) with E_{nlj}^{expt} (Table 1), one can conclude that, within the dispersive optical model, variations of E_{nlj} in response to an increase in the isotope mass number can be described by using, for the parameters of the dispersive optical potential, their average values, which, with the exception of the parameter $V_{\text{so}}(A)$, change smoothly with A. For the order of the levels being considered, the predictions based on the calculated energies E_{nlj}^{RMFM} are in poorer agreement with experimental results.

It is well known that, within the relativistic mean-field model, the spin–orbit potential can be calculated correctly in a form that involves no free parameters. In this connection, it is of interest to compare the energies of spin–orbit splitting, $\Delta_{nl} = \Delta_{nlj=l-1/2} - \Delta_{nlj=l+1/2}$, that were calculated on the basis of the dispersive optical model and on the basis of the relativistic mean-field model with experimental data. In Table 5, the values of Δ_{nl} are given for the $1p$ and $1d$ states in ^{40,48}Ca. The values calculated for Δ_{1p} in ^{40}Ca within the two models in question comply well with $\Delta_{1p}^{\text{expt}}$; for ^{48}Ca, it turns out that $\Delta_{1p}^{\text{DOM}} \cong \Delta_{1p}^{\text{RMFM}}$. We note that Δ_{1p}^{DOM} for ^{48}Ca is approximately one-half as great as Δ_{1p}^{DOM} for ^{40}Ca. The calculated values of $\Delta_{1p}^{\text{RMFM}}$ for ^{48}Ca have a wide scatter, but they exhibit a trend toward a reduction of these values for ^{48}Ca in relation to those for ^{40}Ca.

For ^{40}Ca, the computed value Δ_{1d}^{DOM} is in accord with $\Delta_{1d}^{\text{RMFM}}$ and $\Delta_{1d}^{\text{expt}}$. If, for ^{48}Ca, use is made of the value of -20.5 MeV for $E_{1d5/2}$ [24], then $\Delta_{1d}^{\text{expt}} = 4.5 \pm 0.6$ MeV, this result being compatible with the values obtained on the basis of the dispersive optical model (2.8–3.9 MeV) and with those calculated within the relativistic mean-field model [36]. The energies $\Delta_{1d}^{\text{RMFM}}$ from [1] and from [33, 37] are approximately twice as great as Δ_{1d}^{DOM}. The most comprehensive analysis of problems concerning the distinctions between $\Delta_{1d}^{\text{RMFM}}$ for ^{40}Ca and its counterpart for ^{48}Ca was given in [36], where it was shown that Δ_{1d} for ^{40}Ca is greater than that for ^{48}Ca by a factor of about 2. This result complies with the results of our calculations on the basis of the dispersive optical model. Taking into account data on the energies Δ_{1p} and Δ_{1d} for ^{40}Ca and ^{48}Ca, one can therefore conclude that the change in the order of the levels in ^{48}Ca in relation to that in $^{40-46}$Ca is due to a change in the strength of the spin–orbit potential.

For a single-particle state, the occupation number N_{nlj} as derived within the dispersive optical model

is determined by the formulas quoted in [2, 3]. The occupation numbers N_{nlj} calculated in the present study for single-particle proton states in ^{40}Ca are in good agreement with the results of the calculations performed on the basis of the dispersive optical model in [8, 9]. In those studies, the results obtained on this basis for N_{nlj} in ^{40}Ca were also compared with the corresponding results of different theoretical calculations.

For single-particle proton orbits in the $^{40-48}$Ca nuclei, the mass dependences of the occupation numbers were calculated in [38] on the basis of a phenomenological model that allows for short-range correlations. According to [38], the behavior of N_{nlj} for the $1s_{1/2}$ states undergoes sharp changes with increasing A (see Fig. 6 in [38]). The occupation numbers N_{nlj} calculated in the present study for the $1s_{1/2}$ states are somewhat less than unity and change smoothly with increasing isotope mass number. It is difficult to verify the reliability of the predictions made in [38] since the experimental values of N_{nlj} for deep proton-hole states are available only for ^{40}Ca. In [38], sharp mass-number dependences of N_{nlj} are predicted for the $2s_{1/2}$, $1d_{3/2}$, and $1f_{7/2}$ states as well. The experimental values of N_{nlj} for these states were obtained in the present study by the method for matching data on stripping and pickup reactions. In this connection, it is of interest to compare the N_{nlj} values as computed on the basis of the dispersive optical model and as obtained in [38] with experimental data. Such a comparison is illustrated in Table 6, whence it can be seen that the N_{nlj} values computed in the present study on the basis of the dispersive optical model comply with experimental data within errors of about 10% (on average) and change only slightly with increasing A for the states being considered. For the $2s_{1/2}$ and $1d_{3/2}$ states, the values of N_{nlj} that were obtained in [38] fall significantly short of the experimental values evaluated within the dispersive optical model and change irregularly with increasing mass number A; at the same time, the N_{nlj} values given in [38] for the $1f_{7/2}$ state are significantly greater N_{nlj}^{DOM} and N_{nlj}^{expt}.

5. CONCLUSIONS

(i) In the present study, the method proposed in [10] for performing a global analysis of data on stripping and pickup reactions has been used to determine refined data on the energies of single-particle proton states in the ^{40,42,44,46,48}Ca nuclei and on their occupation numbers. Regularities in the diagrams of single-particles levels in the even–even isotopes ^{40,42,44,46,48}Ca have been investigated on the basis of these refined data.

(ii) The refined experimental data have been compared with the results our calculations performed within the dispersive optical model. In order to determine the dispersive optical potential for protons in the ^{40,42,44,46,48}Ca nuclei, a dispersive-optical-model version has been developed that is based on an analysis of model-dependent cross sections for elastic proton scattering by nuclei of these isotopes and the use of some parameters of the dispersive optical potential for the ^{40}Ca nucleus, for which available experimental information is the most comprehensive. It has been shown that, for the energies of single-particle proton states in ^{40,42,44,46,48}Ca, the results of the calculations relying on the dispersive optical model are in good agreement with experimental data.

(iii) The energies calculated here for single-particle proton states in ^{40,42,44,46,48}Ca on the basis of the dispersive optical model and their experimental counterparts have been compared with the predictions of the relativistic mean-field model. As a rule, the energies calculated within the relativistic mean-field model are less in magnitude for deep levels than the experimental energies and than those that were computed with the dispersive optical potential constructed in the present study and are somewhat exaggerated for hole states in the vicinity of the Fermi energy. The best agreement with experimental data was attained within the relativistic-mean-field-model version realized in [33].

(iv) It has been shown that occupation numbers calculated in the present study for the $2s_{1/2}$, $1d_{3/2}$, and $1f_{7/2}$ states in ^{40,42,44,46,48}Ca on the basis of the dispersive optical model are in good agreement with the refined experimental data.

(v) On the basis of an analysis performed for the first time ever to test the consistency of the features of proton states in ^{40,42,44,46,48}Ca with the refined experimental data, one can conclude that calculations based on the dispersive optical model provide correct predictions for variations in the properties of single-particle proton states with increasing number of intranuclear neutrons.

ACKNOWLEDGMENTS

We are grateful to Prof. S. Typel for placing at our disposal the results obtained by numerically calculating, on the basis of the relativistic mean-field model, the positions of single-particle levels in nuclei on the energy scale [1].

REFERENCES

1. S. Typel and H. H. Wolter, Nucl. Phys. A **656**, 331 (1999).
2. G. Mahaux and R. Sartor, Adv. Nucl. Phys. **20**, 1 (1991).
3. E. A. Romanovsky, O. V. Bespalova, S. A. Goncharov, *et al.*, Yad. Fiz. **63**, 468 (2000) [Phys. At. Nucl. **63**, 399 (2000)].
4. T. W. Burrows, Nucl. Instrum. Methods Phys. Res. A **286**, 595 (1990).
5. D. J. Millener and P. E. Hodgson, Nucl. Phys. A **209**, 59 (1973).
6. F. Malaguti and P. E. Hodgson, Nucl. Phys. A **257**, 37 (1976).
7. L. Ray and P. E. Hodgson, Phys. Rev. C **20**, 2403 (1979).
8. W. Tornow, Z. P. Chen, and J. P. Delaroche, Phys. Rev. C **42**, 693 (1990).
9. G. Mahaux and R. Sartor, Nucl. Phys. A **528**, 253 (1991).
10. I. N. Boboshin *et al.*, Nucl. Phys. A **496**, 93 (1989).
11. P. Doll *et al.*, Nucl. Phys. A **263**, 210 (1976).
12. D. H. Youngblood *et al.*, Phys. Rev. C **2**, 477 (1970).
13. R. Bock, H. H. Duhm, and R. Stock, Phys. Lett. **18**, 61 (1965).
14. J. Bommer *et al.*, Nucl. Phys. A **160**, 577 (1971).
15. A. von der Decken *et al.*, Phys. Lett. B **41B**, 477 (1972).
16. J. J. Schwartz and W. P. Alford, Phys. Rev. **149**, 820 (1966).
17. U. Lynen *et al.*, in *Proceedings of the Conference "Direct Reactions with ^{3}He," Tokyo, 1968,* Ed. by K. Matsuda and H. Kamitsubo.
18. D. Dehnhard and M. E. Gade, Nucl. Phys. A **230**, 393 (1974).
19. D. Dehnhard, in *Proceedings of the Conference on Medium-Light Nuclei, Florence, 1978*, p. 505.
20. R. Santo *et al.*, Nucl. Phys. A **118**, 409 (1968).
21. C. A. Ogilvie *et al.*, Nucl. Phys. A **465**, 445 (1987).
22. S. Fortier, E. Hourani, and J. M. Maison, Nucl. Phys. A **346**, 285 (1980).
23. S. Fortier *et al.*, Nucl. Phys. A **346**, 303 (1980).
24. A. M. Oros, PhD Thesis (University of Köln, 1996).
25. R. L. Varner *et al.*, Phys. Rep. **201**, 57 (1991).
26. E. A. Romanovsky, O. V. Bespalova, I. N. Kuchtina, *et al.*, Yad. Fiz. **61**, 37 (1998) [Phys. At. Nucl. **61**, 32 (1998)].
27. R. F. Carlson, At. Data Nucl. Data Tables **68**, 93 (1996).
28. D. V. Bolotov, O. M. Knyazkov, I. N. Kuchtina, and S. A. Fayans, Yad. Fiz. **63**, 1631 (2000) [Phys. At. Nucl. **63**, 1546 (2000)].
29. S. S. Volkov *et al.*, Yad. Fiz. **52**, 1339 (1990) [Sov. J. Nucl. Phys. **52**, 848 (1990)].
30. Y. Wang *et al.*, Phys. Rev. C **47**, 2677 (1993).
31. H. Koura and M. Yamada, Nucl. Phys. A **671**, 96 (2000).
32. C. Fuchs, H. Lenske, and H. H. Wolter, Phys. Rev. C **52**, 3043 (1995).
33. K. Rutz *et al.*, Nucl. Phys. A **634**, 67 (1998).
34. M. Rashdam, Phys. Rev. C **63**, 044303 (2001).
35. Hua-Lin Shi and Bao-Qiu Chen, Phys. Rev. C **52**, 144 (1995).
36. M. Lopez-Quelle *et al.*, Phys. Rev. C **61**, 064321 (2000).
37. Z. Ren and H. Toki, Prog. Theor. Phys. **104**, 595 (2000).
38. G. A. Lalazissis and S. E. Massen, Phys. Rev. C **53**, 1599 (1996).

Translated by A. Isaakyan

Physics of Atomic Nuclei, Vol. 66, No. 4, 2003, pp. 659–664. Translated from Yadernaya Fizika, Vol. 66, No. 4, 2003, pp. 688–693.

NUCLEI
Theory

Effect of Nuclear-Surface Diffuseness on the Energy and Width of the Giant Dipole Resonance

B. S. Ishkhanov and V. N. Orlin

Institute of Nuclear Physics, Moscow State University, Vorob'evy gory, Moscow, 119899 Russia

Received September 28, 2001; in final form, December 17, 2001

Abstract—The effect of nuclear-surface diffuseness on the energy and width of the giant dipole resonance is studied, and approximating formulas are obtained for these quantities. These formulas make it possible to describe experimental data in the mass range $16 < A < 240$. © *2003 MAIK "Nauka/Interperiodica".*

1. INTRODUCTION

By a giant dipole resonance (GDR), one means one or two to three collective states of a nucleus (in the presence of a static deformation) in the continuous spectrum that have a width of a few MeV. These states are excited by an electric dipole field $rY_{1\mu}(\mathbf{n})$ and are known to saturate the sum rule for $E1$ transitions almost completely. In light nuclei ($A < 40$) featuring unfilled shells, the pattern of a nuclear response to the electric dipole field $rY_{1\mu}(\mathbf{n})$ becomes more complicated. There arise an intermediate GDR structure that is associated with single shell effects and, additionally, a configuration splitting of GDR, the latter being due to the fact that the energy of single-particle $E1$ transitions from an inner filled shell to the outer, partially filled, shell is much greater than the energy of single-particle transitions from the outer shell to free unfilled levels (see the review articles quoted in [1–3] and the original study reported in [4]). Even for light nuclei, one can nevertheless state that there occurs the collectivization of the GDR because, under the effect of residual forces, which lead to coherent effects, the centroid of $E1$ transitions shifts by about 5 MeV toward higher energies.

The collective nature of the giant resonance assumes the presence of specific general regularities for its global characteristics such as the energy and width. At the same time, the existing collective and statistical models of the nucleus provide a satisfactory description of these regularities only for heavy nuclei ($A \gtrsim 100$). For light and medium-mass nuclei, the theory yields incorrect results. To some extent, this can be attributed to the influence of single-particle shell effects, which manifest themselves most strongly precisely in light nuclei, and to the fact that, in vibrational spherical nuclei ($40 < A < 80$), the GDR broadens and develops a more complex structure owing to the interaction of dipole and low-energy quadrupole nuclear vibrations. This is, however, not the whole story in all probability, since the theory disagrees with experimental data not only for nuclei with unfilled shells but also for spherical magic nuclei and for rigid deformed nuclei, in which single-particle effects and surface vibration have but a slight influence on the structure and width of the GDR.

It is peculiar to the situation in question that the deviation of experimental data from theoretical predictions (for example, for the GDR energy) becomes more pronounced with decreasing nuclear mass number. This gives grounds to assume that the disregard of the nuclear-surface-layer effect in the existing collective and statistical models is one of the main reasons behind the disagreement between the theory and experimental data (the contribution of this effect to the whole nuclear size increases from 30 to 100% with decreasing nuclear mass number A).

2. SELECTION OF THE EXPERIMENTAL DATA

In order to simplify the analysis of experimental data and to avoid the need for taking into account effects due to the energy scatter of doorway $1p1h$ states and to quadrupole vibrations of the nuclear surface, we will consider the GDR only for (spherical) magic and severely deformed nuclei in the mass range $16 \leq A < 240$. This selection of nuclei makes it possible to find the required characteristics of dipole resonances—namely the energy (E), the width (Γ), and the amplitude (Σ)—by approximating the total photoabsorption cross section

$$\sigma_{\text{abs}}(\gamma) = \sigma(\gamma, sn) + \sigma(\gamma, p) + \sigma(\gamma, 2p) + \ldots$$

by one or two Lorentzian lines [for heavy nuclei, this cross section is approximately equal to the total photoneutron cross section $\sigma(\gamma, sn) = \sigma(\gamma, n) + \sigma(\gamma, np) + \sigma(\gamma, 2n) + \cdots + \sigma(\gamma, \text{fis})$].

1063-7788/03/6604-0659$24.00

Parameters of the approximating Lorentzian lines and dipole-resonance widths estimated by means of the semiempirical formula (19)

Nucleus	E_1, MeV	Γ_1, MeV	Σ_1, mb	E_2, MeV	Γ_2, MeV	Σ_2, mb	E, MeV	ΔE, MeV	References
^{16}O	23.7	6.3 (5.92)	26.9	–	–	–	23.7	17.0–29.5	[5]
^{24}Mg	19.46	3.89 (4.65)	24.2	24.35	7.32 (7.29)	25.7	22.72	15.0–30.0	[6]
^{40}Ca	20.1	5.46 (5.85)	87.1	–	–	–	20.1	10.0–32.0	[5]
^{90}Zr	16.74	4.16 (4.96)	211	–	–	–	16.74	14.0–19.0	[7]
^{124}Sn	15.35	4.72 (4.44)	278	–	–	–	15.35	10.0–22.0	[8]
^{142}Nd	14.95	4.48 (4.32)	359	–	–	–	14.95	10.0–20.0	[9]
^{150}Nd	12.25	3.00 (2.93)	167	15.96	5.55 (4.97)	229	14.91	10.0–20.0	[9]
^{154}Sm	12.19	3.04 (2.91)	189	15.72	5.62 (4.84)	207	14.55	9.0–20.0	[10]
^{156}Gd	12.39	2.65 (3.01)	224	15.69	4.88 (4.83)	233	14.56	9.0–20.0	[10]
^{165}Ho	12.37	2.56 (3.03)	217	15.48	4.22 (4.75)	229	14.34	9.0–20.0	[10]
^{168}Er	11.88	2.86 (2.80)	221	15.32	4.51 (4.66)	280	14.17	9.0–20.0	[10]
^{178}Hf	11.99	2.81 (2.88)	289	15.12	4.75 (4.58)	342	14.07	9.0–20.0	[10]
^{184}W	11.84	2.57 (2.82)	310	14.74	4.57 (4.38)	326	13.73	9.0–18.0	[10]
^{208}Pb	13.45	3.77 (3.71)	652	–	–	–	13.45	7.5–27.5	[5]
^{238}U	10.92	2.60 (2.49)	291	13.98	4.72 (4.09)	383	12.96	9.0–16.5	[11]

The parameters E_i, Γ_i, and Σ_i found in this way for one ($i = 1$) or two ($i = 1, 2$) dipole resonances are quoted in the table (columns from the second to the seventh one). In addition, the width values calculated by means of formula (19) (see below) are given parenthetically in the third and the sixth column. In the eighth column, we present the experimental value determined for the GDR energy by using Eq. (13) given below. The energy interval of the approximation and the source of experimental information are given in the ninth and the tenth column, respectively.

3. GDR ENERGY

The collective models assuming a sharp nuclear boundary predict that the giant-resonance energy E varies with the mass number A in proportion to $A^{-1/3}$ or in proportion to $A^{-1/6}$. The $A^{-1/3}$ behavior implies [12, 13] that dipole vibrations are coupled vibrations of the independent compressible liquids of protons and neutrons within a nucleus bounded by a rigid surface, these vibrations being maintained by forces that are proportional to the deviation of the density difference $\rho_p - \rho_n$ from its equilibrium value. The $A^{-1/6}$ dependence is based on the assumption [12] that the force restoring charge balance is proportional to the nuclear-surface area, which can change during vibrations.

Of these two models, only the hydrodynamic model [12, 13] is widely used, because it provides a proper description of the strength and the energy position of the GDR for heavy nuclei ($A \gtrsim 100$). However, the dependence $E \propto A^{-1/3}$ leads to wrong predictions for light nuclei. In this region of nuclei, the energy E is therefore often approximated by a linear combination of $A^{-1/3}$ and $A^{-1/6}$ terms; that is,

$$E \approx 31.2A^{-1/3} + 20.6A^{-1/6}\ \text{MeV}, \qquad (1)$$

where the numerical coefficients are determined from a fit to experimental data [14]. Although this approximation improves the agreement between theoretical predictions and experimental data (predominantly, owing to an increase in the number of adjustable parameters), it does not contribute to advances in the theory.

In this respect, analysis of the effect of nuclear-surface diffuseness on the features of the GDR looks more promising. According to the hydrodynamic model, the energy of dipole vibrations of a homogeneous spherical nucleus with a sharp boundary is inversely proportional to its radius $R \propto A^{1/3}$; that is,

$$E \approx 2.08\hbar \left(\frac{2C_{\text{sym}}}{M}\right)^{1/2} R^{-1}, \qquad (2)$$

where C_{sym} is a coefficient that characterizes the symmetry energy of a nucleus, $E_{\text{sym}} = C_{\text{sym}}(A - 2Z)^2A^{-1}$, and M is the nucleon mass (in what follows, we will use the value of $C_{\text{sym}} = 23.7$ MeV [15], which follows from the semiempirical Weizsäcker mass formula).

In fact, the nuclear surface is not sharp, however: the nuclear density $\rho = \rho_p + \rho_n$ falls off gradually from 90 to 10% of its maximal value within the surface layer, whose width varies insignificantly from one nucleus to another. As follows from data on electron scattering the distribution of nuclear matter for all nuclei, including extremely light ones, can be well approximated by the formula

$$\rho(r) = \rho_0 f(r), \tag{3}$$

where

$$f(r) = \left[1 + \exp\left(\frac{r - R_0}{a}\right)\right]^{-1} \tag{4}$$

is the radial Fermi form factor, $R_0 \approx 1.07A^{1/3}$ fm is the distance from the center of the nucleus to points where the nuclear density ρ decreases by a factor of 2, and $a \approx 0.55$ fm is the parameter of nuclear-surface diffuseness.

The constant ρ_0 characterizing the density at the center of the nucleus can be found from the normalization condition

$$4\pi\rho_0 \int_0^\infty f(r) r^2 dr = A. \tag{5}$$

With allowance for the smallness of the parameter a/R_0, this approximately yields

$$\rho_0 \cong \frac{3A}{4\pi R_0^3 \left[1 + \pi^2 (a/R_0)^2\right]}. \tag{6}$$

(The relative error in this result is very small: $\delta\rho_0 < 6(a/R_0)^3 \times \exp\{-R_0/a\}$.)

For actual nuclei having a diffuse surface, the parameter R in Eq. (2) must be treated as the radius of the equivalent homogeneous sphere with the same dispersion of matter; that is,

$$R = \left[\frac{5}{3}\langle r^2\rangle\right]^{1/2}, \tag{7}$$

where $\sqrt{\langle r^2\rangle}$ is the root-mean-square radius of the nucleon distribution in the nucleus.

It is generally assumed that the radius R is equal to $1.2A^{1/3}$ fm. For this case, the giant-resonance energy E is given by the expression

$$E \approx 77A^{-1/3}\ \text{MeV}, \tag{8}$$

which describes satisfactorily the behavior of the energy E for heavy nuclei, but which gives strongly exaggerated values for light nuclei (see Fig. 1).

It can be seen from (2) and (7) that, in order to take into account the effect of surface diffuseness on the giant-resonance energy, it is necessary to calculate the mean square $\langle r^2\rangle$ of the distance of nucleons from the center of the nucleus for distribution (3). Neglecting small terms (less than $0.002\langle r^2\rangle$ for $A \geq 10$ nuclei), we obtain

$$\langle r^2\rangle = \frac{4\pi\rho_0}{A}\int_0^\infty r^2 f(r) r^2 dr \cong \frac{3}{5}R_0^2\theta^2(a/R_0), \tag{9}$$

where the function $\theta(x)$ is given by

$$\theta(x) = \left[\frac{1 + \frac{10}{3}\pi^2x^2 + \frac{7}{3}\pi^4x^4}{1 + \pi^2x^2}\right]^{1/2}. \tag{10}$$

As a result, we find that the radius of the equivalent homogeneous sphere is

$$R = R_0\theta(a/R_0) \tag{11}$$

and that the giant-resonance energy (in MeV) is

$$E \approx 86A^{-1/3}\theta^{-1}(a/R_0). \tag{12}$$

[The parameters R_0 and a appearing in these formulas were specified above—see Eq. (4).]

In Fig. 1, experimental data on the giant-resonance energies for selected nuclei,

$$E = \begin{cases} E_1 & \text{for spherical nuclei} \\ \dfrac{E_1\Sigma_1\Gamma_1 + E_2\Sigma_2\Gamma_2}{\Sigma_1\Gamma_1 + \Sigma_2\Gamma_2} & \text{for deformed nuclei,} \end{cases} \tag{13}$$

are contrasted against the results of the calculations by formulas (1), (8), and (12) (see Section 2).

From the data in this figure, one can see that, upon taking into account the effect of nuclear-surface diffuseness on dipole vibrations of the proton–neutron liquid, a satisfactory description of the giant-resonance energy can be obtained not only for heavy but also for light nuclei. It is worth noting that, in contrast to what was done for Eq. (1), no special adjustment of the parameters to experimental data was performed in Eq. (12).

4. DIPOLE-RESONANCE WIDTH

Collective models describe the energy position and the strength of a dipole resonance, but they are unable to describe its width. This quantity can be found only

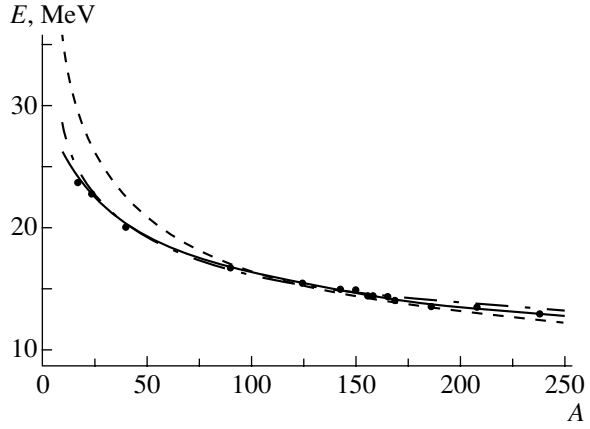

Fig. 1. GDR energy as a function of the mass number A. The points represent experimental data (see the eighth column in the table). The solid, dashed, and dash-dotted curves correspond to the calculations by formulas (12), (8), and (1), respectively.

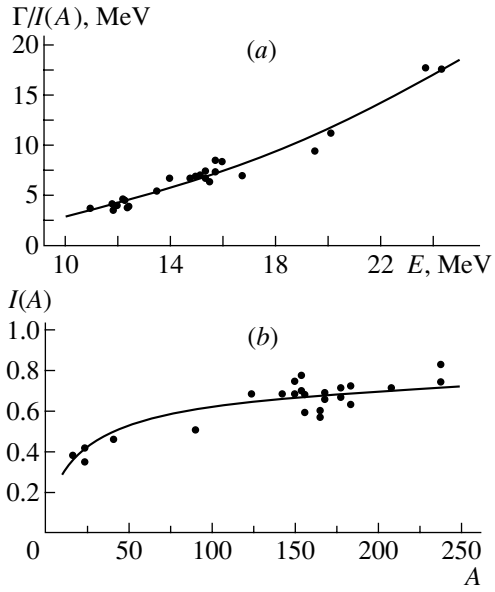

Fig. 2. Systematics of dipole-resonance widths: (a) energy dependence [the experimental widths divided by the theoretical factor $I(A)$ (closed circles) are contrasted against the function $gE^2 \approx 0.0293E^2$ (curve)] and (b) dependence on the mass number A [the experimental widths divided by the function gE^2 (closed circles) are contrasted against the theoretical function $I(A)$ (curve)]. The experimental data for the widths were taken from the third and sixth columns of the table.

via microscopic calculations. The problem of microscopically describing the damping of dipole vibrations because of their interaction with other degrees of freedom of nuclei was first considered in [16, 17] and was then examined in greater detail in [18–20] by using the random-phase approximation. However, detailed microscopic calculations of giant resonances are rather cumbersome [21–24]. In practice, one often therefore applies semimicroscopic approaches where the fragmentation of a collective giant resonance into more complex nucleon configurations is performed in a phenomenological way by using adjustable parameters (see, for example, [25–27]).

An approximate estimate of the dipole-resonance width (Γ) can be obtained as follows. Let us assume that a collective dipole state $|\Psi_{\text{dip}}\rangle$ falls, as usually occurs, within that region of the energy spectrum where the density of various excited nuclear configurations $|\Psi_i\rangle$ is high and that the interaction of these configurations with the dipole state has approximately the same strength over the energy range $\Delta E \gtrsim \Gamma$. The GDR strength function then has the form of a Lorentz line whose width is [28]

$$\Gamma = 2\pi\overline{\langle\Psi_i|V|\Psi_{\text{dip}}\rangle^2}\omega_i(E), \qquad (14)$$

where $\overline{\langle\Psi_i|V|\Psi_{\text{dip}}\rangle^2}$ is the mean square of dipole-state interaction with the configurations $|\Psi_i\rangle$, while $\omega_i(E)$ is the density of these configurations at the dipole-resonance energy E.

The collective dipole state $|\Psi_{\text{dip}}\rangle$ can be treated as a coherent mixture of nuclear excitations formed by one particle and one hole ($1p1h$) [29]. The most probable process of energy transfer from dipole vibrations to other degrees of freedom proceeds as follows: an excited dipole particle or hole collides with a nucleon occupying a level below the Fermi surface, producing one more additional particle–hole pair. The dissipation of the energy of a collective dipole state into noncollective $2p2h$ configurations interacting with it leads to the emergence of the so-called spreading width of the resonance ($\Gamma^{\downarrow}$).

The width $\Gamma^{\downarrow}$ plays a vital role in the statistical models of nuclear reaction [30–32], because this quantity determines the rate of thermalization of the primary-nuclear-excitation energy through its redistribution over an ever greater number of nucleons. An analysis of data on nucleon–nucleus reactions within statistical models (see, for example, [33, 34]) reveals that, at moderate excitation energies of a compound system ($E \lesssim 30$ MeV), the probability that one more particle–hole pair is produced, $\lambda^{\downarrow}$, can be approximated by the expression

$$\lambda^{\downarrow} = \frac{\Gamma^{\downarrow}}{\hbar} \approx \text{const} \cdot E^2. \qquad (15)$$

As can be seen from (15), the estimate of $\lambda^{\downarrow}$ (and, hence, of $\Gamma^{\downarrow}$) does not depend on the mass number A. This can be explained by the fact that the probability that an excited particle or hole undergoes a collision with an unexcited nucleon is proportional

to the nuclear-matter density ρ, which is known to have approximately the same value for all nuclei. The appearance of the factor E^2 in (15) is associated with the assumption that the density of final states [these are $2p2h$ states in (14)] populated in the production of a particle–hole pair can be described in terms of the equidistant model of single-particle levels [35].

As was indicated above, the dipole-resonance width Γ has the width $\Gamma^{\downarrow}$ as a dominant component. It is therefore not surprising that a few attempts were made to describe available data on the GDR widths by using expressions of the form

$$\Gamma \approx gE^{\delta}, \tag{16}$$

where g and δ are adjustable parameters (see, for example, [36, 37]).

However, these attempts were futile. It turned out that such a description of the GDR width is appropriate only for relatively narrow intervals of the mass number A. The application of this equation beyond such an interval (for example, the use of g and δ parameters determined from data on deformed rare-earth nuclei in the region of light and moderately heavy nuclei) leads to serious deviations from experimental data, Eq. (16) fitted to heavy nuclei yielding greatly exaggerated values of the widths Γ for light nuclei.

It is straightforward to understand this trend because, with decreasing mass number A, the number of nucleons occurring in the dilute surface region of a nucleus increases, which leads to a decrease in the average nuclear density and, hence, in the probability of excitation-energy transfer from one nucleon to another. In order to evaluate this effect, we assume that the distribution of particles and holes is similar to the distribution of nuclear matter [see Eq. (3)]. We then obtain

$$\lambda^{\downarrow} \propto \langle \rho \rangle \approx 4\pi \int_0^{\infty} \rho(r) \frac{\rho(r)}{A} r^2 dr \cong 0.1949 I(A), \tag{17}$$

where

$$I(A) = \frac{1}{1+\pi^2\left(\frac{a}{R_0}\right)^2}\left[1 - 3\frac{a}{R_0}\frac{1+\frac{\pi^2}{3}\left(\frac{a}{R_0}\right)^2}{1+\pi^2\left(\frac{a}{R_0}\right)^2}\right] \tag{18}$$

is the required mass form factor featuring the parameters a and R_0 defined in (4). [In order to derive Eq. (17), we have used formulas (3)–(6) and the identity $f^2(r) = f(r) + af'(r)$ for the Fermi form factor.]

It follows from (15) and (17) that the dipole-resonance width can be approximated by the expression

$$\Gamma \approx gI(A)E^2. \tag{19}$$

For the constant g, a fit of this expression to the experimental values of the dipole-resonances widths Γ (see table) yields $g = 0.0293$ MeV^{-1}. The theoretical results for Γ that were calculated by formula (19) with this value of g are quoted parenthetically in the third and sixth columns of the table, along with experimental estimates of the widths.

From a comparison of the experimental and theoretical data, one can deduce that Eq. (19) adequately describes both the energy and the mass dependence of the dipole-resonance width. This can also be seen from Fig. 2, where the theoretical functions gE^2 and $I(A)$ are contrasted against the quantities $\Gamma_{\text{expt}}/I(A)$ and $\Gamma_{\text{expt}}/(gE^2)$ evaluated on the basis of experimental data.

5. CONCLUSION

Let us briefly summarize the basic results of our analysis:

(i) The inclusion of the nuclear-surface-diffuseness effect on dipole charge vibrations makes it possible to obtain a reasonable description of experimental GDR energies within the hydrodynamic model both for heavy and for light nuclei.

(ii) The basic features of the spreading GDR width can be described within statistical models of nuclear reactions upon considering that the probability of the production of a new particle–hole pair decreases in the surface region of a nucleus.

REFERENCES

1. *Electric and Magnetic Resonances in Nuclei* (World Sci., Singapore, 1991).
2. B. S. Ishkhanov, N. P. Yudin, and R. A. Eramzhyan, Fiz. Élem. Chastits At. Yadra **31**, 313 (2000) [Phys. Part. Nucl. **31**, 149 (2000)].
3. B. S. Ishkhanov, I. M. Kapitonov, V. G. Neudachin, *et al.*, Fiz. Élem. Chastits At. Yadra **31**, 1343 (2000) [Phys. Part. Nucl. **31**, 674 (2000)].
4. R. A. Eramzhyan, B. S. Ishkhanov, I. M. Kapitonov, *et al.*, Phys. Rep. **136**, 230 (1986).
5. J. Ahrens, Nucl. Phys. A **446**, 229 (1985).
6. B. S. Dolbilkin, V. I. Korin, L. E. Lazareva, *et al.*, Nucl. Phys. **72**, 137 (1965).
7. A. H. Leprêtre, H. Beil, R. Bergère, *et al.*, Nucl. Phys. A **175**, 609 (1971).
8. A. H. Leprêtre, H. Beil, R. Bergère, *et al.*, Nucl. Phys. A **219**, 39 (1974).
9. P. Carlos, H. Beil, R. Bergère, *et al.*, Nucl. Phys. A **172**, 437 (1971).

10. G. M. Gurevich, L. E. Lazareva, V. M. Mazur, *et al.*, Nucl. Phys. A **351**, 257 (1981).
11. A. Veyssière, H. Beil, R. Bergère, *et al.*, Nucl. Phys. A **199**, 45 (1973).
12. M. Goldhaber and E. Teller, Phys. Rev. **74**, 1046 (1948).
13. H. Steinwedel and J. H. D. Jensen, Z. Naturforschteil A **5**, 413 (1950).
14. B. L. Berman and S. C. Fultz, Rev. Mod. Phys. **47**, 713 (1975).
15. S. Moshkovsky, in *Structure of Atomic Nuclei* (West Berlin, 1957; Inostr. Lit., Moscow, 1959), p. 471.
16. M. Danos and W. Greiner, Phys. Rev. **138**, B876 (1965).
17. F. A. Zhivopistsev, V. M. Moskovkin, and N. P. Yudin, Izv. Akad. Nauk SSSR, Ser. Fiz. **30**, 306 (1966).
18. V. V. Voronov and V. G. Solov'ev, Fiz. Élem. Chastits At. Yadra **14**, 1380 (1983) [Phys. Part. Nucl. **14**, 583, (1983)].
19. J. Speth and J. Wambach, Int. Rev. Nucl. Phys. **7**, 1 (1991).
20. S. Kamerdzhiev, J. Speth, G. Tertychny, *et al.*, Nucl. Phys. A **555**, 90 (1993).
21. J. Birkolz, Nucl. Phys. A **189**, 385 (1972).
22. E. N. Golovach, B. S. Ishkhanov, and V. N. Orlin, Nucl. Phys. A **653**, 45 (1999).
23. E. N. Golovach, B. S. Ishkhanov, and V. N. Orlin, Yad. Fiz. **63**, 444 (2000) [Phys. At. Nucl. **63**, 377 (2000)].
24. S. Kamerdzhiev, G. Tertychny, V. Tselyaev, *et al.*, Phys. Lett. B **267**, 12 (1991).
25. G. A. Chekomazov and M. H. Urin, Phys. Lett. B **354**, 7 (1995).
26. E. A. Moukhai, V. A. Rodin, and M. H. Urin, Phys. Lett. B **447**, 8 (1999).
27. M. L. Gorelik, S. Shlomo, and M. H. Urin, Phys. Rev. C **62**, 044301 (2000).
28. A. Bohr and B. R. Mottelson, *Nuclear Structure,* Vol. 2: *Nuclear Deformations* (Benjamin, New York, 1974; Mir, Moscow, 1977).
29. G. E. Brown and M. Bolterserly, Phys. Rev. Lett. **3**, 472 (1959); V. V. Balashov, *Abstracts of Papers, LI Conference on Nuclear Spectroscopy and Nuclear Structure, Sarov, Russia, 2001*, p. 8.
30. J. J. Griffin, Phys. Rev. Lett. **17**, 478 (1966).
31. M. Blann, Phys. Rev. Lett. **27**, 337 (1971).
32. H. Feshbach, A. Kerman, and S. Koonin, Ann. Phys. (N.Y.) **125**, 429 (1980).
33. K. Seidel, D. Seeliger, R. Reif, *et al.*, Fiz. Élem. Chastits At. Yadra **7**, 499 (1976) [Phys. Part. Nucl. **7**, 192 (1976)].
34. M. G. Braga-Marcazzan *et al.*, Phys. Rev. C **6**, 1398 (1972).
35. F. C. Williams, Nucl. Phys. A **166**, 231 (1971).
36. M. G. Huber, M. Danos, H. J. Weber, *et al.*, Phys. Rev. **155**, 1073 (1967).
37. P. Carlos, R. Bergère, A. Veyssière, *et al.*, in *Proceedings of the International Conference on Photonuclear Reactions and Applications, Pacific Grove, California, 1973*, Ed. by B. L. Berman (Lawrence Livermore Laboratory, Livermore), p. 1053.

Translated by S. Slabospitsky

Physics of Atomic Nuclei, Vol. 66, No. 4, 2003, pp. 665–672. From Yadernaya Fizika, Vol. 66, No. 4, 2003, pp. 694–701.

NUCLEI
Theory

Tunneling between Asymmetric Potential Wells and Mixing of Normal and Superdeformed Nuclear Bands*

A. Ya. Dzyublik**

Institute for Nuclear Research, National Academy of Sciences of Ukraine, Kiev, Ukraine

Received January 4, 2002; in final form, April 18, 2002

Abstract—The equation for the nuclear deformational motion in an asymmetric potential with two minima is solved quasi-classically in analogy with the familiar symmetric case. Taking into account the tunneling, we obtained formulas for the energies and wave functions similar to those which were previously derived for two-band mixing. This enabled us to interpret the mixing of close-lying levels of normal and superdeformed rotational bands in ^{133}Nd as a manifestation of tunneling. In addition, mixing of superdeformed levels with normal configurations is analyzed in the framework of the theory of overlapping resonant levels. © *2003 MAIK "Nauka/Interperiodica".*

1. INTRODUCTION

Calculations by Strutinsky [1] have revealed that the nuclear potential energy as a function of the deformation parameter β represents a two-well shape. The first minimum of this potential corresponds to normal (N) deformation of the nucleus with equilibrium value $\beta_N^{(0)} \sim 0.2$–0.3, and the second one, to a superdeformed (SD) shape with large $\beta_S^{(0)}$ ($\beta_S^{(0)} \approx 0.6$ for the isotope ^{152}Dy [2]). In the ground state of the nucleus, the SD minimum of its potential $V_0(\beta)$ lies much higher than the N one. At great spins I, the SD minimum becomes lower than N, since the effective potential energy of the nucleus $V_I(\beta)$ contains the centrifugal barrier. Specifically, for axially symmetric nuclei, the Bohr–Mottelson equation leads to

$$V_I(\beta) = V_0(\beta) + \frac{\hbar^2 I(I+1)}{6B\beta^2}, \qquad (1)$$

where B is the mass parameter [3, 4]. The cranked-shell model corrections provide, certainly, a more complicated dependence of $V(\beta)$ on I.

The problem of tunneling through two-humped potential barriers was discussed first in connection with fissioning isomers (see the review [5]). Later, a similar task arose in studies of interband electromagnetic transitions linking SD and N rotational bands [6–15].

The main feature of most γ spectra of superdeformed nuclei is that the intensity of their lines, weakly depending on the value of spin, abruptly falls at some $I \approx I_{1/2}$ [10]. This fact has been explained by a statistical model [6–8]. Its main idea is that, at spin $I_{1/2}$, the level $|s\rangle$, which consists mainly of the SD component, lies much higher than the yrast line. Therefore, it is surrounded by a lot of excited configurations $|\alpha\rangle$, which are located inside the N well. The wave function $|s\rangle$, having a tail in the N well, mixes with $|\alpha\rangle$ by a residual interaction $\hat{V}'$. These configurations are linked with lower states by strong $E1$ transitions. As a result, the fraction of nuclei escaping from the SD band into the normal well at spin $I_{1/2}$ becomes $F_N \sim 0.5$. This leads to weakening of $E2$ transitions inside the SD band and their subsequent quenching.

One can estimate the matrix elements $\langle\alpha|\hat{V}'|s\rangle$ knowing the magnitude of the tail of the function $|s\rangle$, i.e., the amplitude of the N wave function, which is admixed to the SD state. In other words, we need the solution of the Schrödinger equation with potential V, having two minima. There is such a quasi-classical (WKB) solution for the case where V consists of two symmetric potential wells separated by the barrier [16] (more rigorous calculations for N symmetric wells (one-dimensional crystal) are given in [17]). This solution describes quite different objects, such as the molecule NH_3 [18] and nuclei having stable octupole deformations [19].

An attempt to find the energies E_I and wave functions ψ_I in the case of an asymmetric potential was undertaken by Lynn [5, 20]. He split the effective potential with two minima into two parts:

$$V_I(\beta) = V_I^{(1)}(\beta) + V_I^{(2)}(\beta). \qquad (2)$$

*This article was submitted by the author in English.

**e-mail: dzyublik@kinr.kiev.ua

1063-7788/03/6604-0665$24.00

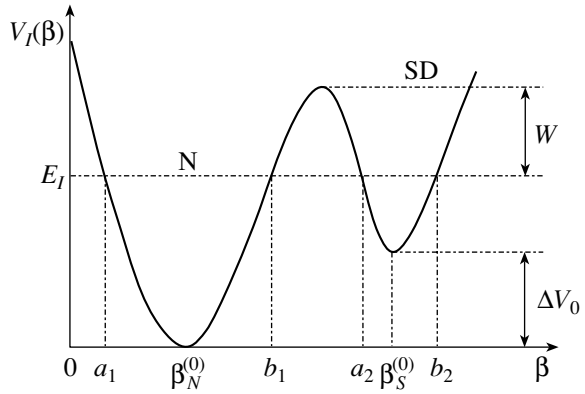

The nuclear potential energy with two minima at low spins as a function of the deformation parameter β.

The first potential $V_I^{(1)}(\beta) = V_I(\beta)$ within the first (normal) well as $-\infty < \beta \leq \beta_B^{(0)}$, while $V_I^{(1)}(\beta) = V_I(\beta_B^{(0)})$ otherwise. Here, $\beta_B^{(0)}$ indicates the position of the barrier top. The second potential $V_I^{(2)}(\beta) = V_I(\beta)$ when $\beta_B^{(0)} < \beta < \infty$, while $V_I^{(2)}(\beta) = V_I(\beta_B^{(0)})$ otherwise. The wave function was approximated by a superposition

$$\psi = c_1\psi^{(1)} + c_2\psi^{(2)}, \tag{3}$$

where the functions $\psi^{(n)}$ were solutions of the Schrödinger equations

$$\left(\hat{T} + V_I^{(n)}(\beta)\right)\psi^{(n)}(\beta) = \varepsilon_n\psi^{(n)}(\beta) \tag{4}$$

with the kinetic energy operator $\hat{T}$. Substituting (3) into the Schrödinger equation $(\hat{T} + V_I(\beta))\psi = E_I\psi$ and transforming it to a system of two algebraic equations, Lynn found cumbersome formulas for the coefficients c_n and nuclear energies E_I. Unfortunately, they do not agree with familiar expressions for energies in the symmetric case [16, 17]. One possible reason for this discrepancy is that Lynn took $\langle\psi^{(1)}|\psi^{(2)}\rangle = 0$ along with $\langle\psi^{(1)}|V_I^{(n)}|\psi^{(2)}\rangle \neq 0$, i.e., overlapping of the functions $\psi^{(1)}$ and $\psi^{(2)}$ was neglected in one place and taken into account in another. Note that, in the symmetric case, strict quasiclassical calculations [17] do not deal at all with oscillator overlapping functions.

The WKB calculations were also performed for the two-humped barriers [21]. Unfortunately, they did not take into consideration the barrier confining $V_I(\beta)$ on the left-hand side.

In previous papers [5–11, 15], it was assumed that the tunneling through the barrier leads to the exponential decay of the SD state into N one, and the following quasi-classical formula has been used for the tunneling width:

$$\Gamma_{\text{tunn}} = \hbar w, \quad w = (\omega_S/2\pi)T, \tag{5}$$

where ω_S is the circular frequency of oscillations in the SD well and T stands for the transmission coefficient of the wave through a barrier separating the SD and N regions, which equals

$$T \approx \exp(-2A), \tag{6}$$

with A determined by the integral

$$A = \frac{1}{\hbar}\int_{b_1}^{a_2} d\beta|p(\beta)| \tag{7}$$

over the region between turning points, in which $E_I = V_I(\beta)$ (see figure). Here,

$$p(\beta) = \sqrt{2B(E_I - V_I(\beta))}. \tag{8}$$

Let us recall that formulas (6) and (7) were derived for the one-dimensional case, when at the infinity there is a plane wave e^{ikx} incident on the barrier. The corresponding WKB calculations (see, e.g., [16, 17, 22]) give us the transmitted wave Ce^{ikx} and, respectively, the transmission coefficient $T = |C|^2$. These results of scattering theory cannot be applied directly to bound states localized in the potential well. Therefore, in (5), the probability of transition per unit time w is determined by the product of T and the so-called knocking rate $\omega_S/2\pi$. The only motivation for the latter factor is that the classical particle, vibrating with frequency $\omega_S/2\pi$, knocks the barrier $\omega_S/2\pi$ times per second [23].

On the other hand, in the case of a symmetric potential with two minima, the tunneling (see, e.g., [18]) gives rise to coherent Rabi oscillations between wells if at the initial moment the wave function is concentrated in one of the wells. In other words, there is no exponential tunneling decay in the symmetric case. It would be strange to think that such an incoherent process appears due to an asymmetry of the potential.

In standard textbooks (see, e.g., [16, 22]), the tunneling of the particle through a barrier means its penetration into the classically inaccessible region due to its wave properties. Just such tunneling leads to (6) for T. Nevertheless, in [5–15], the transitions from superdeformed state $|s\rangle$ to configurations $|\alpha\rangle$ in normally deformed nuclei were also called tunneling, although they are caused by a residual interaction $\hat{V}'$. Moreover, it was accepted in [5–11, 15] that $\Gamma_{\text{tunn}} = \Gamma$, where Γ is the spreading width of the $|s\rangle$ state, given by

$$\Gamma = 2\pi|\langle\alpha|\hat{V}'|s\rangle|^2/D_N, \tag{9}$$

and D_N is the average spacing of levels $|\alpha\rangle$.

All these inconsistencies forced us to perform straightforward quasi-classical calculations for bound states in an asymmetric potential with two minima.

The most elaborate theory for mixing of the superdeformed level with a single configuration was built by Stafford and Barrett [14], who took into account simultaneously both their mixing and interaction with the electromagnetic field. Here, we shall extend such an approach to the case of N configurations. Special attention will be paid to mixing of levels $|s\rangle$ with quasi-continuum spectra of configurations.

2. WKB SOLUTION

The Bohr–Mottelson equation after separation of rotation reduces to an equation for the deformational motion [3, 4]

$$\left\{-\frac{\hbar^2}{2B}\frac{\partial^2}{\partial\beta^2}+V_I(\beta)\right\}\varphi_I(\beta)=E_I\varphi_I(\beta). \quad (10)$$

More refined theory [9] deals with the deformational motion in multidimensional configurational space, which is reduced, nevertheless, to one-dimensional motion with some mass M. The WKB solution of (10) in the region $\beta < a_1$, which attenuates for $\beta \to -\infty$, is

$$\varphi_I(\beta)=\frac{c_N}{\sqrt{|p|}}\exp\left(-\frac{1}{\hbar}\int\limits_{\beta}^{a_1}|p|d\beta\right). \quad (11)$$

According to standard rules [16, 17, 22], it is matched with the function

$$\varphi_I(\beta)=\frac{2c_N}{\sqrt{p}}\cos\left(\frac{1}{\hbar}\int\limits_{a_1}^{\beta}pd\beta-\frac{\pi}{4}\right) \quad (12)$$

in the region $a_1 < \beta < b_1$.

Let us introduce the notation

$$\phi_1=\frac{1}{\hbar}\int\limits_{a_1}^{b_1}pd\beta,\quad \phi_2=\frac{1}{\hbar}\int\limits_{a_2}^{b_2}pd\beta. \quad (13)$$

Approximating the potential between turning points in N and SD wells ($a_{1(2)} < \beta < b_{1(2)}$) by parabolas

$$V_I(\beta)\approx B\omega^2_{N(S)}(\beta-\beta^{(0)}_{N(S)})^2/2, \quad (14)$$

one has

$$\phi_1=\frac{\pi E_I}{\hbar\omega_N},\quad \phi_2=\frac{\pi(E_I-\Delta V_0)}{\hbar\omega_S}, \quad (15)$$

where

$$\Delta V_0=V_I(\beta^{(0)}_S)-V_I(\beta^{(0)}_N). \quad (16)$$

Then, function (12) may be rewritten as

$$\varphi_I(\beta)=\frac{2c_N}{\sqrt{p}}\left\{\sin\phi_1\cos\left(\frac{1}{\hbar}\int\limits_{\beta}^{b_1}pd\beta-\frac{\pi}{4}\right)-\cos\phi_1\sin\left(\frac{1}{\hbar}\int\limits_{\beta}^{b_1}pd\beta-\frac{\pi}{4}\right)\right\}. \quad (17)$$

Under the barrier, $b_1 < \beta < a_2$, the cosine is connected with an exponentially attenuating wave and the sine with a growing one [22], so that

$$\varphi_I(\beta)=\frac{c_N}{\sqrt{|p|}}\left\{\sin\phi_1\exp\left(-\frac{1}{\hbar}\int\limits_{b_1}^{\beta}|p|d\beta\right)+2\cos\phi_1\exp\left(\frac{1}{\hbar}\int\limits_{b_1}^{\beta}|p|d\beta\right)\right\}. \quad (18)$$

In order to use the matching rules near the turning point b_2, we transform (18) to

$$\varphi_I(\beta)=\frac{c_N}{\sqrt{|p|}}\left\{\sin\phi_1e^{-A}\exp\left(\frac{1}{\hbar}\int\limits_{\beta}^{a_2}|p|d\beta\right)+2\cos\phi_1e^{A}\exp\left(-\frac{1}{\hbar}\int\limits_{\beta}^{a_2}|p|d\beta\right)\right\}, \quad (19)$$

where A is defined by (7) and (8). Approximating the barrier by the inverse parabola with frequency ω_B, one has the well-known expression

$$A=\pi W_I/\hbar\omega_B, \quad (20)$$

where

$$W_I=V_I(\beta^{(0)}_B)-E_I \quad (21)$$

determines the distance from the level to the top of the barrier.

In the SD well, at $a_2 < \beta < b_2$, the wave function takes the form

$$\varphi_I(\beta)=\frac{c_N}{\sqrt{p}}\left\{-\sin\phi_1e^{-A}\sin\left(\frac{1}{\hbar}\int\limits_{a_2}^{\beta}pd\beta-\frac{\pi}{4}\right)+4\cos\phi_1e^{A}\cos\left(\frac{1}{\hbar}\int\limits_{a_2}^{\beta}pd\beta-\frac{\pi}{4}\right)\right\}. \quad (22)$$

It may be rewritten as

$$\varphi_I(\beta) = \frac{2c_N}{\sqrt{p}} \left\{ C_1 \cos\left(\frac{1}{\hbar} \int_\beta^{b_2} p d\beta - \frac{\pi}{4} \right) + C_2 \sin\left(\frac{1}{\hbar} \int_\beta^{b_2} p d\beta - \frac{\pi}{4} \right) \right\}, \quad (23)$$

where the coefficients are

$$C_1 = (\sin\phi_1 \cos\phi_2 e^{-A} + 4\cos\phi_1 \sin\phi_2 e^{A})/2, \quad (24)$$

$$C_2 = (\sin\phi_1 \sin\phi_2 e^{-A} - 4\cos\phi_1 \cos\phi_2 e^{A})/2.$$

The first term in (23) generates under the barrier the exponentially attenuating function, while the second generates the growing one. Since the square-integrable function $\varphi \to 0$ as $\beta \to \infty$, we must introduce the constraint $C_2 = 0$, which is equivalent to

$$4\cot\phi_1 \cot\phi_2 = \exp(-2A). \quad (25)$$

As a consequence, the wave function (23) becomes

$$\varphi_I(\beta) = \frac{2c_S}{\sqrt{p}} \cos\left(\frac{1}{\hbar} \int_\beta^{b_2} p d\beta - \frac{\pi}{4} \right), \quad (26)$$

where

$$c_S/c_N = (\sin\phi_1/2\cos\phi_2) e^{-A}. \quad (27)$$

Under the barrier, $\beta > b_2$, the wave function will be

$$\varphi_I(\beta) = \frac{c_S}{|p|} \exp\left(-\int_{b_2}^{\beta} |p| d\beta \right). \quad (28)$$

3. ENERGIES AND WAVE FUNCTIONS

Usually, the barrier has small transparency, $\exp(-2A) \ll 1$. Then, constraint (25) is fulfilled if

$$\phi_1 \approx (n_1 + 1/2)\pi \quad (29)$$

or/and

$$\phi_2 \approx (n_2 + 1/2)\pi, \quad (30)$$

where $n_i = 0, 1, 2, \ldots$

Exact equalities (29) and (30) are the familiar Bohr–Sommerfeld conditions for binding the particle in one of the potential wells in the absence of tunneling ($A = \infty$). Combining them with definitions (15), we obtain the energy levels of the harmonic oscillators in N and SD wells:

$$\epsilon_1 = \hbar\omega_N(n_1 + 1/2), \quad \epsilon_2 = \Delta V_0 + \hbar\omega_S(n_2 + 1/2). \quad (31)$$

Let both approximate conditions (29) and (30) be fulfilled simultaneously; i.e., the level with n_1 phonons in the N well resonates with the n_2 level in the SD well. Such resonance occurs if the angles

$$\alpha_{N(S)} = \frac{\pi(\epsilon_1 - \epsilon_2)}{\hbar\omega_{N(S)}} \quad (32)$$

are small, i.e., $|\alpha_{N(S)}| \ll 1$. It enables us to replace $\cot\phi_i$ in (25) by $-\Delta\phi_i = -(\phi_i - (n_i + 1/2)\pi)$.

Then, using the notation

$$n = \{n_1, n_2\}, \quad \omega_0^2 = \omega_N \omega_S, \quad v = (\hbar\omega_0/2\pi)\exp(-A), \quad (33)$$

we arrive at the quadratic equation

$$E^2 - (\epsilon_1 + \epsilon_2)E + \epsilon_1\epsilon_2 - v^2 = 0, \quad (34)$$

giving us the energies

$$E_{I,n}^{(\pm)} = \bar{\epsilon} \pm (1/2)\sqrt{(\Delta\epsilon)^2 + 4v^2}, \quad (35)$$

where

$$\Delta\epsilon = \epsilon_1 - \epsilon_2, \quad \bar{\epsilon} = (\epsilon_1 + \epsilon_2)/2. \quad (36)$$

The tunneling leads to repulsion of unperturbed levels:

$$\Delta E_{I,n} = E_{I,n}^{(+)} - E_{I,n}^{(-)} = \sqrt{(\Delta\epsilon)^2 + 4v^2}. \quad (37)$$

In the symmetric case, when $\Delta\epsilon = 0$, it reduces to the well-known splitting $\Delta E_{I,n} = 2v$ [16, 17].

Let us introduce the functions $|N\rangle$ and $|S\rangle$:

$$c_N|N\rangle = \begin{cases} \varphi_{In}(\beta), & 0 < \beta \le \beta_B^{(0)}, \\ 0, & \beta > \beta_B^{(0)}, \end{cases} \quad (38)$$

and

$$c_S|S\rangle = \begin{cases} 0, & 0 < \beta < \beta_B^{(0)}, \\ \varphi_{In}(\beta), & \beta \ge \beta_B^{(0)}. \end{cases} \quad (39)$$

Then, the wave function is rewritten as

$$\varphi_{In}(\beta) = c_N|N\rangle + c_S|S\rangle. \quad (40)$$

The components $c_N|N\rangle$ and $c_S|S\rangle$ inside the corresponding wells are determined by (12) and (26), respectively. In the resonance case, they are approximated by the oscillator functions

$$|N\rangle \approx \psi_{n_1}(\xi_1), \quad |S\rangle \approx \psi_{n_2}(\xi_2), \quad (41)$$

which depend on the dimensionless coordinates

$$\xi_{1(2)} = \left(\hbar/B\omega_{N(S)}\right)^{-1/2} (\beta - \beta_{N(S)}^{(0)}). \quad (42)$$

From definitions (38) and (39), it follows that the oscillator functions should be cut off at the point $\beta_B^{(0)}$. This means that their overlapping is absent. As

$\pi|\Delta\epsilon| \ll \hbar\omega_0$, the ratio of the amplitudes (27) reduces to

$$(c_N/c_S)_\pm = f(E^{(\pm)}_{I,n} - \epsilon_2)/v, \qquad (43)$$
$$f = (-1)^{n_1+n_2+1}(\omega_N/\omega_S)^{1/2}.$$

In the symmetric case, when $\Delta V_0 = 0$ and $\omega_N = \omega_S$, from (35) and (43), one gets the familiar result

$$\varphi^{(\pm)}_n \approx (1/\sqrt{2})(\psi_n(\xi_1) \mp \psi_n(\xi_2)). \qquad (44)$$

Thus, the lower level of the doublet $E^{(-)}$ is described by the symmetric function $\varphi^{(-)}$ and the higher level $E^{(+)}$ by the antisymmetric one $\varphi^{(+)}$ (see also [16]).

Far from the resonance, only one of the conditions (29) and (30) can be realized. Then, the nucleus is located mainly in one of the wells N or SD, and the corresponding wave functions can be specified by the indices n or s. Their amplitudes are

$$c^{(s)}_S \approx 1, \quad c^{(s)}_N \approx (-1)^{n_1+n_2}\frac{1}{2\sin\alpha_N}e^{-A} \ll 1 \qquad (45)$$

for the s state, and

$$c^{(n)}_N \approx 1, \quad c^{(n)}_S \approx (-1)^{n_1+n_2+1}\frac{1}{2\sin\alpha_S}e^{-A} \ll 1 \qquad (46)$$

for the n state. The corresponding energies are

$$E^{(s)} \equiv E^{(-)} = \epsilon_2 - \frac{\hbar\omega_S}{4\pi}e^{-2A}\cot\alpha_N, \qquad (47)$$
$$E^{(n)} \equiv E^{(+)} = \epsilon_1 + \frac{\hbar\omega_N}{4\pi}e^{-2A}\cot\alpha_S.$$

In the transition region

$$2v \ll |\Delta\epsilon| \ll \hbar\omega_{N(S)}/\pi, \qquad (48)$$

the solutions (35) and (47) coincide:

$$E^{(+)} \approx \epsilon_1 + v^2/\Delta\epsilon, \quad E^{(-)} \approx \epsilon_2 - v^2/\Delta\epsilon. \qquad (49)$$

In this case, the amplitudes become

$$c^{(s)}_S \approx 1, \quad c^{(s)}_N \approx (-1)^{n_1+n_2}\sqrt{\frac{\omega_N}{\omega_S}}\frac{v}{\Delta\epsilon} \qquad (50)$$

and

$$c^{(n)}_N \approx 1, \quad c^{(n)}_S \approx (-1)^{n_1+n_2+1}\sqrt{\frac{\omega_S}{\omega_N}}\frac{v}{\Delta\epsilon}. \qquad (51)$$

4. BAND MIXING CAUSED BY TUNNELING

The nuclear wave function in the adiabatic approximation reads

$$\psi = \Phi(\beta;\xi)\varphi_{In}(\beta)|IM\rangle, \qquad (52)$$

where the function $\Phi(\beta;\xi)$ describes internal motion of the nucleons, whose position is determined by the coordinates ξ, and $|IM\rangle$ denotes the rotational function, which is represented by a superposition of the D functions, depending on the Euler angles [2, 3]. The internal function $\Phi(\beta;\xi)$ depends on the deformational variable β as on the parameter. It is therefore not surprising that normal and superdeformed rotational bands, observed by Bazzacco [11] in ^{133}Nd, are built on different orbitals. The SD and other bands have close-lying levels for spins $I = 17/2^+$ and $29/2^+$. The experimental differences of their energies are $\Delta E_{17/2} = 64$ keV and $\Delta E_{29/2} = 39$ keV. Bazzacco explained strong interband transitions and repulsion of nearby levels, which arise at these spins, using the band-mixing model of Bengtsson and Frauendorf [24], who interpreted mixing of two rotational bands with the aid of a standard solution of the Schrödinger equation for two close-lying (degenerate) levels, coupled by the interaction v (see, e.g., [16]). Employing the equation derived by Bengtsson and Frauendorf [24], Bazzacco extracted the interaction matrix elements $v = 22$ keV at $I = 17/2^+$ and $v = 11$ keV at $I = 29/2^+$. Note, however, that this equation coincides formally with our Eq. (35), in which v means a strength of tunneling through the barrier separating N and SD wells, and has nothing to do with any residual interaction. As to the ratio of the amplitudes c_N/c_S, provided by the tunneling, it differs from the corresponding ratio of standard two-level theory [16] by an extra factor f.

It seems to be more natural to explain the observed phenomena by the tunneling between N and SD shapes rather than by the mixing caused by constant interaction. Then, for the tunneling strength v, one must use (20) and (33). Adopting Bazzacco's estimations for v and setting $\omega_0 = \omega_B = 0.6$ MeV, we found the distances W_I from the zero-phonon levels with spin I to the top of the barrier: $W_{17/2} = 0.28$ MeV and $W_{29/2} = 0.41$ MeV. This correlates with the general tendency of the barrier height to increase with spin growth [10]. Such values of W_I are so small that no superdeformed bands built on β phonons can be excited in this nucleus.

5. MIXING OF SD STATES WITH CONFIGURATIONS

In the nuclei around ^{152}Dy and ^{192}Hg, another (statistical) mechanism accounts for the interband transitions. For these nuclei, the admixture of the N state to SD one is too small, $c^2_S \approx 1$ and $c^2_N \approx (fv/\Delta\epsilon)^2 \ll 1$. But at low spins, these levels mix with neighboring configurations $|\alpha\rangle$ [5–15]. Since the configuration α overlaps only with the N component of the function $|s\rangle$, then

$$\langle\alpha|\hat{V}'|s\rangle = c_N\langle\alpha|\hat{V}'|N\rangle. \qquad (53)$$

This matrix element enters the spreading width (9). Thus, the tunneling (in the traditional sense [16, 22]) manifests itself in the spreading width Γ only by means of the factor $(fv/\Delta\epsilon)^2$. This tunneling ensures mixing of the N and SD functions into the $|s\rangle$ state, whereas the spreading width Γ determines the rate for further decay of $|s\rangle$ into normal configurations $|\alpha\rangle$. Thus, the equality $\Gamma_{\rm tunn} = \Gamma$, adopted in [5–11, 15], makes no sense.

Below, we shall consider the mixing of the states $|s\rangle$ and $|\alpha\rangle$, taking into account simultaneously mixing and interaction with the field. Such an approach of overlapping (close-lying) resonances was used previously in [25–27] for other purposes. We shall write the Hamiltonian of the system (nucleus + electromagnetic field) as

$$\hat{H} = \hat{H}_0 + \hat{V}, \quad \hat{H}_0 = \hat{H}_n + \hat{H}_{rad}, \quad \hat{V} = \hat{V}_r + \hat{V}', \tag{54}$$

where $\hat{H}_n$ and $\hat{H}_{rad}$ denote the Hamiltonians of the nucleus and electromagnetic field, respectively, and $\hat{V}$ is the perturbation operator, which includes the interaction $\hat{V}_r$ of the nucleus with the field and the residual interaction $\hat{V}'$ of nucleons.

The states of the system with near energies are described by the functions $|a\rangle$ that are the products of the nuclear wave functions $|s\rangle$ or $|\alpha\rangle$ to the vacuum function $|0\rangle$ of the electromagnetic field. The functions of the final states $|b\rangle$ are products of the functions for the nucleus in a lower SD state and the field with one $E2$ γ quantum or the nucleus in the N state and the field with an $E1$ or $E2$ photon. The functions $|a\rangle$ and $|b\rangle$ are the eigenfunctions of unperturbed Hamiltonian $\hat{H}_0$ with corresponding eigenvalues E_a and E_b.

Let, at the initial moment $t = 0$, the system be described by the wave function $\Psi_a(0) = |s\rangle|0\rangle$. At any subsequent moment $t \geq 0$, it will be [27]

$$\Psi(t) = -\frac{1}{2\pi i}\int\limits_{-\infty}^{\infty} d\varepsilon e^{-i\varepsilon t/\hbar}\hat{G}^+(\varepsilon)\Psi_a(0), \tag{55}$$

where the Green's operator is related to the complete Hamiltonian by

$$\hat{G}^+(\varepsilon) = \hat{G}(\varepsilon + i\eta) = (\varepsilon + i\eta - \hat{H})^{-1} \tag{56}$$

with $\eta \to +0$.

The probability of finding the system at moment t in one of the states $|b\rangle$ or $|a\rangle$ is given by [28]

$$P_{b(a')}(t) = |\mathcal{G}_{b(a')}(t)|^2, \tag{57}$$

where the probability amplitude is

$$\mathcal{G}_{b(a')}(t) = -\frac{1}{2\pi i}\int\limits_{-\infty}^{\infty} d\varepsilon e^{-i\varepsilon t/\hbar}\langle b(a')|\hat{G}^+(\varepsilon)|a\rangle. \tag{58}$$

The Green's matrix G_{ba} is related to $G_{a'a}$ by

$$G_{ba}(\varepsilon) = (\varepsilon - E_b)^{-1}\sum_{a'} V_{ba'}G_{a'a}(\varepsilon). \tag{59}$$

The general system of algebraic equations for the matrix $G^+_{aa'}$ is [27]

$$\sum_{a''}\left\{(\varepsilon + i\eta - E_a)\delta aa'' - R^+_{aa''}(\varepsilon)\right\}G^+_{a''a'}(\varepsilon) = \delta_{aa'}, \tag{60}$$

where the R matrix reads

$$R^+_{aa'}(\varepsilon) \approx V_{aa'} + \sum_{b\neq a}\frac{V_{ab}V_{ba'}}{\varepsilon + i\eta - E_b}. \tag{61}$$

We denote the radiative widths of the states $|S\rangle$ and $|s\rangle$ by Γ_S and Γ_s, respectively. Moreover, we take into account that $\Gamma_s \approx \Gamma_S$ since $c_N \approx 0$. In addition, we assume that the radiative widths of all configurations are equal to Γ_N and that the matrix elements for the residual interaction do not depend on the number α. Then,

$$R^+_{ss} = -i\Gamma_S/2, \quad R^+_{\alpha\alpha} = -i\Gamma_N/2, \tag{62}$$
$$R^+_{s\alpha} = \langle s|\hat{V}'|\alpha\rangle \equiv v'.$$

Here, $|s\rangle \equiv |a\rangle$, $|\alpha\rangle \equiv |a' \neq a\rangle$. Substituting (62) into (60), one has the equations

$$(\varepsilon - E_s + i\Gamma_S/2)\,G^+_{ss}(\varepsilon) - v'\sum_{\alpha=1}^{N} G^+_{\alpha s}(\varepsilon) = 1, \tag{63}$$
$$-v'G^+_{ss}(\varepsilon) + (\varepsilon - E_\alpha + i\Gamma_N/2)\,G^+_{\alpha s}(\varepsilon) = 0.$$

Their solution is

$$G^+_{\alpha s}(\varepsilon) = \frac{v'}{\varepsilon - E_\alpha + i\Gamma_N/2}G^+_{ss}(\varepsilon), \tag{64}$$
$$G^+_{ss}(\varepsilon) = \left\{\varepsilon - E_s + i\frac{\Gamma_S}{2} - \sum_{\alpha=1}^{N}\frac{v'^2}{\varepsilon - E_\alpha + i\Gamma_N/2}\right\}^{-1}.$$

Let, at $t \to \infty$, the final state $|b\rangle$ describe the nucleus in the SD state and γ quantum with energy E. Summing the corresponding probabilities $P_b(\infty)$ over all possible states of emitted photons, one gets the probability of finding the nucleus in the SD pocket:

$$F_S = (\Gamma_S/2\pi)\int\limits_{-\infty}^{\infty} dE|G^+_{ss}(E)|^2. \tag{65}$$

Respectively, the probability that the nucleus attributes normal shape after decay is $F_N = 1 - F_S$.

Following [29], we shall assume that the levels $|\alpha\rangle$ form an infinite equidistant spectrum with energies $E_\alpha = E_0 + \alpha D_N$, where $\alpha = 0, \pm 1, \pm 2, \ldots$. Then, at small D_N, we can pass in (64) from summation to integration:

$$\sum_{\alpha=-\infty}^{\infty} \frac{D_N}{\varepsilon - E_\alpha + i\Gamma_N/2} \tag{66}$$
$$\to -\int_{-\infty}^{\infty} d\varepsilon' \frac{1}{\varepsilon' - \varepsilon - i\Gamma_N/2} = \pi i.$$

As a result, the matrix element G^+_{ss} takes the form

$$G^+_{ss}(\varepsilon) = \frac{1}{\varepsilon - E_s + i(\Gamma_S + \Gamma)/2} \tag{67}$$

with spreading width Γ given by (9). Only in such a situation is the probability of finding the nucleus in the initial state governed by the exponential law of decay $P_s(t) = \exp(-(\Gamma_S + \Gamma)t/\hbar)$.

Inserting (67) into (65), for the quasi-continuum spectrum of configurations, one has

$$F_S = \Gamma_S/(\Gamma_S + \Gamma). \tag{68}$$

In the two-level case, we get the results of [14].

6. CONCLUSION

Thus, we obtained a quasi-classical solution to describe nuclear deformational motion in the potential with two minima, which is similar to the solution for a symmetric potential [16, 17]. It is interesting that expression (35) for the energies $E^{(\pm)}$ coincides with the well-known formula for two levels coupled by any interaction [16, 24]. It enabled us to associate Bazzacco's observations [11] with tunneling through a low barrier, separating normal and superdeformed shapes. In the symmetric case, Rabi transitions between wells occur if we get at the initial moment a coherent sum of states $|+\rangle$ and $|-\rangle$, i.e., at $t = 0$, the wave function is $\psi = (1/\sqrt{2})(\psi^{(+)} + \psi^{(-)})$. However, separation of the vibrational nuclear levels in different potential wells $|\Delta\epsilon| \sim 100$ keV, whereas the radiative widths $\Gamma_{N(S)} \sim 1$ meV. As a result, the levels $\varphi^{(+)}_I$ and $\varphi^{(-)}_I$ can be populated only independently of each other by the decay $I + 2 \to I$. In reality, due to the same inequality $\Gamma_{N(S)} \ll |\Delta\epsilon|$, only one state $|s\rangle$ with a predominant contribution of the SD component ($c_S \approx 1$, $|c_N| \ll 1$) is populated. Moreover, for the nucleus, described by $\varphi^{(s)}_I$, the tunneling does not alter the amplitudes c_N and c_S. In other words, traditional tunneling [16, 22] does not lead to decay of the SD state into the N state; i.e., expression (5) for the tunneling width cannot be applied here. Something like this expression might be useful for treatment of the tunneling through the exterior barrier.

On the other hand, mixing of the state $|s\rangle$ with normally deformed configurations $|\alpha\rangle$ ensures such transitions between wells. For two levels, when the state $|s\rangle$ mixes only with a single configuration, our general formulas (64) and (65) lead to the results of [14]. In this case, during decay of the nucleus, there are oscillating transitions between two potential wells. On the other hand, in the case of a quasi-continuum spectrum of configurations, the decay of the $|s\rangle$ state proceeds exponentially. Then, the nucleus has two competing channels of decay—radiative and spreading, characterized by the widths Γ_S and Γ, respectively. The total width of the level $|s\rangle$ will be $\Gamma_S + \Gamma$, and the probability of decay in one of these channels is determined by the ratio of the corresponding partial width to the total width [see (68)]. If the spacing of levels greatly exceeds their radiative widths, one can diagonalize the Green's matrix $G^+_{aa'}$ by diagonalizing the Hamiltonian matrix $H_{aa'}$. Doing so, we come to the same general result for F_N as in [7, 8]. Nevertheless, in the case of a quasi-continuum spectrum of configurations, which corresponds to the strong-coupling limit of Vigezzi *et al.* [8], our result $F_N = \Gamma/(\Gamma + \Gamma_S)$ deviates from the corresponding Eq. (17) of [8]. The latter contains a redundant dependence of F_N on D_N and Γ_N, which leads to such unreasonable consequences as negative F_N at small Γ_N or $F_N \approx 1$ as $D_N \approx 0$ for finite Γ.

The quasi-classical solution obtained for asymmetric potential wells, separated by the barrier, can also be used for other applications such as tunneling of hydrogen atoms between nonequivalent sites in a crystal.

ACKNOWLEDGMENTS

I thank V.P. Aleshin and T.L. Khoo for helpful discussions.

REFERENCES

1. V. M. Strutinsky, Nucl. Phys. A **95**, 420 (1967).
2. W. Nazarewicz, R. Wyss, and A. Johnson, Nucl. Phys. A **503**, 285 (1989).
3. A. Bohr and B. Mottelson, *Nuclear Structure* (Benjamin, New York, 1974), Vol. 2.
4. A. S. Davydov, *Excited States of Nuclei* (Atomizdat, Moscow, 1967).
5. S. Bjørnholm and J. E. Lynn, Rev. Mod. Phys. **52**, 725 (1980).
6. K. Schiffer, B. Herskind, and J. Gascon, Z. Phys. A **332**, 17 (1989).

7. E. Vigezzi, R. A. Broglia, and T. Døssing, Phys. Lett. B **249**, 163 (1990).
8. E. Vigezzi, R. A. Broglia, and T. Døssing, Nucl. Phys. A **520**, 179c (1990).
9. Y. R. Shimizu, E. Vigezzi, T. Døssing, and R. A. Broglia, Nucl. Phys. A **557**, 99c (1993).
10. T. L. Khoo, T. Lauritsen, I. Ahmad, *et al.*, Nucl. Phys. A **557**, 83c (1993).
11. D. Bazzacco, Nucl. Phys. A **583**, 191 (1995).
12. H. A. Weidenmüller, P. von Brentano, and B. R. Barrett, Phys. Rev. Lett. **81**, 3603 (1998).
13. S. Åberg, Phys. Rev. Lett. **82**, 299 (1999).
14. C. A. Stafford and B. R. Barrett, Phys. Rev. C **60**, 051305 (1999).
15. Y. R. Shimizu, M. Matsuo, and K. Yoshida, Nucl. Phys. A **682**, 464c (2001).
16. L. D. Landau and E. M. Lifshitz, *Quantum Mechanics* (Nauka, Moscow, 1974).
17. J. Heading, *An Introduction to Phase-Integral Methods* (Wiley, New York, 1962).
18. R. P. Feynman, R. B. Leighton, and M. Sands, *The Feynman Lectures in Physics* (Addison-Wesley, Reading, 1965), Vol. 3.
19. V. Yu. Denisov and A. Ya. Dzyublik, Nucl. Phys. A **589**, 17 (1995).
20. J. E. Lynn, Harwell Report AERE-R (1968), p. 5891.
21. E. V. Gai, A. V. Ignatyuk, N. S. Rabotnov, and G. N. Smirenkin, in *Physics and Chemistry of Fission* (IAEA, Vienna, 1967), p. 337.
22. D. Bohm, *Quantum Theory* (Prentice-Hall, New York, 1952).
23. J. Blatt and V. Weisskopf, *Theoretical Nuclear Physics* (New York, 1952; Inostrannaya Literatura, Moscow, 1954).
24. R. Bengtsson and S. Frauendorf, Nucl. Phys. A **314**, 27 (1979).
25. I. Yu. Kobzarev, N. N. Nikolaev, and L. B. Okun, Yad. Fiz. **10**, 864 (1969) [Sov. J. Nucl. Phys. **10**, 499 (1969)].
26. A. Ya. Dzyublik, Phys. Status Solidi B **104**, 81 (1981).
27. A. Ya. Dzyublik, Teor. Mat. Fiz. **87**, 86 (1991).
28. M. L. Goldberger and K. M. Watson, *Collision Theory* (Wiley, New York, 1964).
29. A. Bohr and B. Mottelson, *Nuclear Structure* (Benjamin, New York, 1969), Vol. 1.

Physics of Atomic Nuclei, Vol. 66, No. 4, 2003, pp. 673–678. Translated from Yadernaya Fizika, Vol. 66, No. 4, 2003, pp. 702–707.

NUCLEI
Theory

Elastic Scattering of Light Alpha-Cluster Nuclei by ^{12}C Nuclei

Yu. A. Berezhnoy and V. P. Mikhailyuk[1)]

Kharkov State University, pl. Svobody 4, Kharkov, 61077 Ukraine

Received November 2, 2001; in final form, August 2, 2002

Abstract—The differential cross sections for the elastic scattering of ^{12}C and ^{16}O nuclei by ^{12}C nuclei are calculated on the basis of the theory of multiple diffractive scattering and the dispersive alpha-cluster model. The calculations were performed by using either an effective or a free $\alpha\alpha$ amplitude. It is shown that the results obtained in these two cases are noticeably different. © *2003 MAIK "Nauka/Interperiodica".*

In many cases, investigation of the interaction of light nuclei makes it possible to obtain important information about the structure and properties of colliding nuclei. At rather high energies ($E \geq 100$ MeV per nucleon), in which case the time of projectile interaction with a nucleus is short in relation to the time of intranuclear motion, investigation of the features of the elastic scattering of such nuclei also enables us to get an idea of the strength and the character of interaction between the structural components of colliding nuclei in nuclear matter.

Light nuclei often exhibit a cluster structure. The presence of this mode in the wave function for light nuclei manifests itself both in calculating structural features of nuclei and in calculating observables for scattering and reactions. In many cases, an α particle, which possesses high stability and symmetry, appears as a cluster.

A model where it is assumed that the positions of alpha particles in a nucleus are fixed and where no antisymmetrization of the wave function is performed [1] is the simplest version of the alpha-particle model. This model makes it possible to explain qualitatively the behavior of elastic form factors for some light nuclei and other features of the elastic scattering of high-energy particles by light nuclei (see, for example, [2]).

In the more realistic alpha-particle model proposed in [3], one takes into account the possibility of nucleon exchange between the alpha particles involved and performs antisymmetrization of the nuclear wave functions in all filled nucleon states. The form factors for elastic electron scattering that were calculated within this model proved to be sensitive not only to the positions of the alpha particles but also to the alpha-cluster structure, which differs considerably from the structure of a free alpha particle.

A dispersive alpha-cluster model for ^{12}C, ^{16}O, and ^{20}Ne was proposed in [4–6]. It was assumed in [4, 5] that the carbon and the oxygen nucleus consist of, respectively, three and four alpha-particle clusters occurring at the vertices of an equilateral triangle in the former case and at the vertices of a tetrahedron in the latter case. These alpha-particle clusters can be displaced in a specific way from their most probable equilibrium positions. In [6], the ^{20}Ne nucleus was considered as that which consists of a deformed core (^{16}O nucleus) and an additional alpha-particle cluster. In [7], it was shown that this alpha-particle cluster occurs most probably within the core.

On the basis of this model and the theory of multiple diffractive scattering, the observables of elastic and inelastic proton scattering on these nuclei were computed in [5–7]. The results of those calculations revealed that, since the time of projectile interaction with a target nucleus is much shorter than the characteristic time of intranuclear motion, nucleon exchange between the alpha-particle clusters involved and antisymmetrization of the nuclear wave function have but a small effect on the cross section. In other words, the target nucleus cannot feel nucleon exchange between alpha-particle clusters within the time of its interaction with the projectile, since this exchange occurs rather rarely and slowly; moreover, the projectile energy significantly exceeds the Fermi energy, whence it follows that the correlations of intranuclear nucleons that are caused by the Pauli exclusion principle cannot be operative in the case of elastic scattering. Even at high energies of scattered particles, however, we cannot disregard vibrations of alpha-particle clusters about their most probable positions since these vibrations lead to an increase

[1)]Institute for Nuclear Research, National Academy of Sciences of Ukraine, pr. Nauki 47, Kiev, Ukraine.

1063-7788/03/6604-0673$24.00

in the effective dimensions of alpha-particle clusters.

We note that, for elastic p^{12}C and p^{16}O scattering, the free $p\alpha$ amplitude was used in the calculations. In other words, the parameters of the $p\alpha$ amplitude were determined from a comparison of the calculated and measured observables for p^4He scattering. The calculated and measured observables were matched with available experimental data.

In [8, 9], the approach proposed in [4, 5] was developed for the case of the elastic scattering of composite particles (deuterons, alpha particles) by ^{12}C and ^{16}O nuclei. In the calculations, use was made of effective $d\alpha$ and $\alpha\alpha$ amplitudes whose parameters were determined from a comparison of the calculated and measured differential cross sections for elastic d^{12}C and α^{12}C scattering. The differential cross sections for d^{16}O and α^{16}O scattering were calculated without adjustable parameters. The results of those calculations were consistent with available experimental data on particle scattering both by ^{12}C and by ^{16}O nuclei. In [8], the differential cross sections for elastic d^{12}C scattering were also calculated by using the free amplitudes for the elastic scattering of projectile-deuteron nucleons by the ^{4}He nuclei. The differential cross sections calculated in this way were at odds with experimental data.

It should be noted that, according to [10, 11], the observables of the elastic scattering of light nuclei by nuclei at energies of $E \sim 100$ MeV per nucleon cannot be satisfactorily described on the basis of the theory of multiple diffractive scattering with elementary free nucleon–nucleon amplitudes, which are commonly used in this case. In other words, the properties of composite nuclei undergo changes in the scattering process, so that the free amplitudes must be replaced by effective ones.

An approach to investigating the elastic scattering of deuterons and of ^{6}He and ^{6}Li nuclei by ^{12}C nuclei at intermediate energies was proposed in [12]. The calculations there were performed on the basis of the theory of multiple diffractive scattering and the dispersive alpha-cluster model under the assumption that the projectile particle has a two-cluster (for deuterons and ^{6}Li nuclei) or a three-cluster (for ^{6}He nuclei) structure. The differential cross sections calculated for elastic ^{6}He^{12}C and ^{6}Li^{12}C scattering within this approximation differed from each other considerably; at the same time, the resulting differential cross section for d^{12}C scattering was in agreement with experimental data.

At present, there are no experimental data on elastic ^{6}He^{12}C and ^{6}Li^{12}C scattering at intermediate energies. In view of this, it is of interest to employ here the approach proposed in [12] for describing experimentally measured properties of the elastic scattering of light nuclei by ^{12}C nuclei. In this study, the elastic scattering of ^{12}C and ^{16}O nuclei by carbon nuclei is considered within the dispersive alpha-cluster model.

According to the theory of multiple diffractive scattering, the amplitude for the elastic scattering of a three-cluster system by a nucleus can be represented in the form

$$F(\mathbf{q}) = 3F_1(\mathbf{q}) + 3F_2(\mathbf{q}) - F_3(\mathbf{q}), \quad (1)$$

$$F_1(\mathbf{q}) = \frac{k}{k_\alpha} f(\mathbf{q}) S_1(\mathbf{q}), \quad (2)$$

$$F_2(\mathbf{q}) = \frac{ik}{2\pi k_\alpha^2} \int d^2q' f(\mathbf{q}') f(\mathbf{q}-\mathbf{q}') S_2(\mathbf{q},\mathbf{q}'), \quad (3)$$

$$F_3(\mathbf{q}) = \frac{k}{(2\pi)^2 k_\alpha^3} \int d^2q' d^2q'' f(\mathbf{q}-\mathbf{q}'-\mathbf{q}'') \times f(\mathbf{q}') f(\mathbf{q}'') S_3(\mathbf{q},\mathbf{q}',\mathbf{q}''), \quad (4)$$

where $F_1(\mathbf{q})$, $F_2(\mathbf{q})$, and $F_3(\mathbf{q})$ are the amplitudes for, respectively, the single, the double, and the triple scattering of alpha-particle clusters of the projectile by the target nucleus; $f(\mathbf{q}) = f_{\mathrm{C,O}}(\mathbf{q})$ stands for the amplitudes characterizing the elastic scattering of alpha-particle clusters of the projectile on the alpha-particle clusters of the target nucleus; $\mathbf{q}$ is the momentum transfer from an alpha-particle cluster of the projectile; $\mathbf{k}$ is the projectile wave vector; and $\mathbf{k}_\alpha$ is the wave vector of an alpha-particle cluster of the projectile.

In these formulas, the structure form factors $S_1(\mathbf{q})$, $S_2(\mathbf{q},\mathbf{q}')$, and $S_3(\mathbf{q},\mathbf{q}',\mathbf{q}'')$ are given by

$$S_1(\mathbf{q}) = \int d^3\gamma_1 d^3\gamma_2 \rho(\boldsymbol{\gamma}_1,\boldsymbol{\gamma}_2) e^{-(2i/3)\mathbf{q}\cdot\mathbf{w}}, \quad (5)$$

$$S_2(\mathbf{q},\mathbf{q}') = \int d^3\gamma_1 d^3\gamma_2 \rho(\boldsymbol{\gamma}_1,\boldsymbol{\gamma}_2) e^{(i/3)\mathbf{q}\cdot\mathbf{w} - i\mathbf{q}_1\cdot\mathbf{s}}, \quad (6)$$

$$S_3(\mathbf{q},\mathbf{q}',\mathbf{q}'') = \int d^3\gamma_1 d^3\gamma_2 \rho(\boldsymbol{\gamma}_1,\boldsymbol{\gamma}_2) e^{-i\mathbf{q}_2\cdot\mathbf{w} - i\mathbf{q}_3\cdot\mathbf{s}}, \quad (7)$$

where $\rho(\boldsymbol{\gamma}_1,\boldsymbol{\gamma}_2)$ is the projectile density; $\boldsymbol{\gamma}_1$ and $\boldsymbol{\gamma}_2$ are the Jacobi coordinates of the alpha-particle clusters of the projectile; $\mathbf{s}$ and $\mathbf{w}$ are the projections of, respectively, the vector $\boldsymbol{\gamma}_1$ and the vector $\boldsymbol{\gamma}_2$ onto the plane orthogonal to the incident-beam axis; and $\mathbf{q}_1 = \mathbf{q}/2 - \mathbf{q}'$, $\mathbf{q}_2 = 2\mathbf{q}/3 - \mathbf{q}' - \mathbf{q}''$, and $\mathbf{q}_3 = \mathbf{q}' - \mathbf{q}''$. Considering that, in the approach used here, the amplitudes for the scattering of ^{16}O nuclei by ^{12}C nuclei coincide with those for the scattering of ^{12}C nuclei by ^{16}O nuclei, the projectile density $\rho(\boldsymbol{\gamma}_1,\boldsymbol{\gamma}_2)$ in

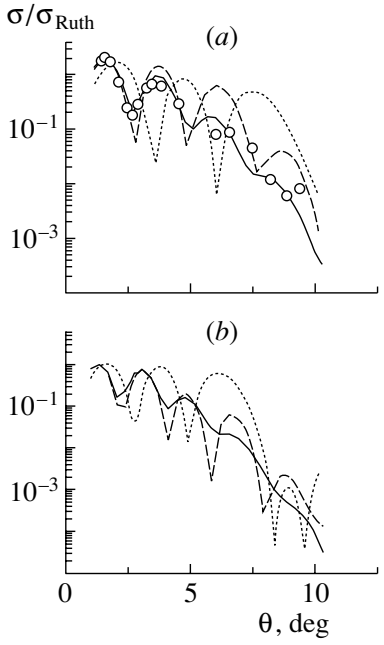

Fig. 1. Ratios $\sigma/\sigma_{\mathrm{Ruth}}$ of the differential cross sections for the elastic scattering of the (a) ^{12}C and (b) ^{16}O nuclei by ^{12}C nuclei at energies of 2400 and 3200 MeV, respectively, to the corresponding Rutherford cross sections. Experimental data borrowed from [13] were used for elastic ^{12}C^{12}C scattering. The notation for the curves is explained in the main body of the text.

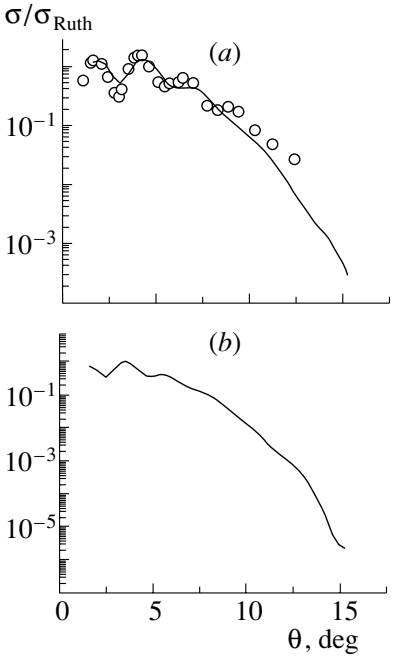

Fig. 2. As in Fig. 1, but at the energies of 1449 and 1932 MeV.

Eqs. (5)–(7) is equivalent to the ^{12}C density specified below.

The amplitudes $f_{\mathrm{C}}(\mathbf{q})$ and $f_{\mathrm{O}}(\mathbf{q})$ for the elastic α^{12}C and α^{16}O scattering have the form

$$f_{\mathrm{C}}(\mathbf{q}) = \frac{ik_\alpha}{2\pi}\int d^2b d^3\xi d^3\eta e^{i\mathbf{q}\cdot\mathbf{b}}\rho_\Delta^{(\mathrm{C})}(\boldsymbol{\xi},\boldsymbol{\eta})\Omega(\mathbf{b},\{\mathbf{s}_j\}), \tag{8}$$

$$f_{\mathrm{O}}(\mathbf{q}) = \frac{ik_\alpha}{2\pi}\int d^2b d^3\xi d^3\eta d^3\zeta e^{i\mathbf{q}\cdot\mathbf{b}} \times \rho_\Delta^{(\mathrm{O})}(\boldsymbol{\xi},\boldsymbol{\eta},\boldsymbol{\zeta})\Omega(\mathbf{b},\{\mathbf{s}_j\}), \tag{9}$$

$$\Omega(\mathbf{b},\{\mathbf{s}_j\}) = 1 - \prod_{j=1}^{N}\left[1 - \frac{1}{2\pi ik_\alpha}\int d^2q e^{-i\mathbf{q}\cdot(\mathbf{b}-\mathbf{s}_j)}\tilde{f}_{\alpha\alpha}(\mathbf{q})\right], \tag{10}$$

where $\mathbf{b}$ is the impact parameter; $\mathbf{s}_j$ are the coordinates of the alpha-particle clusters of the target nucleus; $\tilde{f}_{\alpha\alpha}(\mathbf{q})$ is the amplitude of elastic $\alpha\alpha$ scattering; and $N = 3$ and 4 for ^{12}C and ^{16}O nuclei, respectively.

The amplitude $\tilde{f}_{\alpha\alpha}(\mathbf{q})$ was chosen in the form

$$\tilde{f}_{\alpha\alpha}(\mathbf{q}) = k_\alpha\sum_{i=1}^{3} G_{ci}\exp(-\beta_{ci}q^2). \tag{11}$$

The parameters G_{c1} and β_{c1} are adjustable, while the remaining parameters in (11) are expressed in terms of G_{c1} and β_{c1} as

$$G_{c2} = \frac{3iG_{c1}^2}{32\beta_{c1}}, \quad \beta_{c2} = \frac{1}{2}\beta_{c1}; \tag{12}$$

Table 1. Parameters of the effective $\alpha\alpha$ amplitude

Energy, MeV	β_1, fm^2	G_1, fm^2
800	$0.984 + i0.375$	$-0.536 + i2.455$
483	$1.134 + i0.993$	$-0.876 + i3.273$
339	$0.865 + i0.992$	$-0.909 + i3.342$

Table 2. Parameters of the free $\alpha\alpha$ amplitude

Energy, MeV	β_1, fm^2	G_1, fm^2
620	$0.700 + i0.123$	$-0.018 + i3.314$
850	$0.247 + i0.118$	$-0.443 + i1.336$

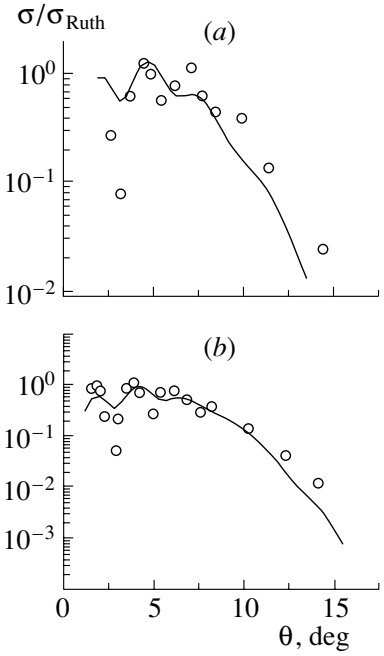

Fig. 3. As in Fig. 1, but at the energies of 1016 and 1503 MeV. The displayed experimental data were borrowed from [14, 15].

$$G_{c3} = -\frac{G_{c1}^3}{192\beta_{c1}^2}, \quad \beta_{c3} = \frac{1}{3}\beta_{c1}. \tag{13}$$

According to the dispersive alpha-cluster model, the multiparticle densities of the ^{12}C and ^{16}O nuclei are given by

$$\rho_\Delta^{(\mathrm{C})}(\boldsymbol{\xi},\boldsymbol{\eta}) = \int d^3\xi' d^3\eta' \rho_0^{(\mathrm{C})}(\boldsymbol{\xi}',\boldsymbol{\eta}') \times \Phi_\Delta^{(\mathrm{C})}(\boldsymbol{\xi}-\boldsymbol{\xi}',\boldsymbol{\eta}-\boldsymbol{\eta}'), \tag{14}$$

$$\rho_0^{(\mathrm{C})}(\boldsymbol{\xi},\boldsymbol{\eta}) = \frac{1}{4\sqrt{3}\pi^2 d^2}\delta(\xi-d) \times \delta\left(\eta - \frac{\sqrt{3}}{2}d\right)\delta(\boldsymbol{\xi}\cdot\boldsymbol{\eta}), \tag{15}$$

$$\Phi_\Delta^{(\mathrm{C})}(\boldsymbol{\xi},\boldsymbol{\eta}) = \frac{1}{(\sqrt{3}\pi\Delta^2)^3}\exp\left(-\frac{\xi^2+\frac{4}{3}\eta^2}{2\Delta^2}\right), \tag{16}$$

$$\rho_\Delta^{(\mathrm{O})}(\boldsymbol{\xi},\boldsymbol{\eta},\boldsymbol{\zeta}) = \int d^3\xi' d^3\eta' d^3\zeta' \rho_0^{(\mathrm{O})}(\boldsymbol{\xi}',\boldsymbol{\eta}',\boldsymbol{\zeta}') \times \Phi_\Delta^{(\mathrm{O})}(\boldsymbol{\xi}-\boldsymbol{\xi}',\boldsymbol{\eta}-\boldsymbol{\eta}',\boldsymbol{\zeta}-\boldsymbol{\zeta}'), \tag{17}$$

$$\rho_0^{(\mathrm{O})}(\boldsymbol{\xi},\boldsymbol{\eta},\boldsymbol{\zeta}) = \frac{1}{(4\pi)^2}\delta(\xi-d)\delta\left(\eta-\frac{\sqrt{3}}{2}d\right) \times \delta\left(\zeta-\sqrt{\frac{2}{3}}d\right)\delta(\boldsymbol{\xi}\cdot\boldsymbol{\eta})\delta(\boldsymbol{\xi}\cdot\boldsymbol{\zeta})\delta(\boldsymbol{\eta}\cdot\boldsymbol{\zeta}), \tag{18}$$

$$\Phi_\Delta^{(\mathrm{O})}(\boldsymbol{\xi},\boldsymbol{\eta},\boldsymbol{\zeta}) = \frac{1}{8(\pi\Delta^2)^9} \times \exp\left(-\frac{\xi^2+\frac{4}{3}\eta^2+\frac{3}{2}\zeta^2}{2\Delta^2}\right), \tag{19}$$

where $\boldsymbol{\xi}$, $\boldsymbol{\eta}$, and $\boldsymbol{\zeta}$ are the Jacobi coordinates of the alpha-particle clusters forming the ^{12}C and ^{16}O nuclei. The parameters d and Δ characterize the distance between the alpha-particle clusters and the magnitude of their deviation from their most probable equilibrium positions at the vertices of an equilateral triangle and of a tetrahedron in the former and the latter, respectively. The values obtained for the parameters d and Δ in [4, 5] make it possible to describe the measured form factors for the ^{12}C and ^{16}O nuclei within the momentum-transfer region $q \le 3$ fm^{-1}.

On the basis of the proposed approach, we have calculated the differential-cross-section ratios $\sigma/\sigma_{\mathrm{Ruth}}$ (where σ_{Ruth} is the corresponding Rutherford cross section—that is, the differential cross section for Coulomb scattering) for the elastic scattering of ^{12}C and ^{16}O nuclei by ^{12}C nuclei. The results of these calculations are displayed in Figs. 1–3.

Figures 1*a* and 2*a* show the calculated (solid curves) and measured (see [13]) differential cross sections for elastic ^{12}C^{12}C scattering at the energies of 2400 and 1449 MeV, respectively. In the calculations, we have used the effective $\alpha\alpha$ amplitude $\tilde{f}_{\alpha\alpha}(\mathbf{q})$ (11) in the form of the sum of two Gaussian functions ($G_{c3} = 0$). The parameters of the effective $\alpha\alpha$ amplitude at the relevant energy values of 800 and 483 MeV are quoted in Table 1.

Similar agreement between the calculated and the measured observables for ^{12}C^{12}C scattering at 2400 MeV was obtained in [16], where the differential cross section for elastic carbon-nucleus scattering at this energy value was calculated on the basis of the optical limit of the theory of multiple diffractive scattering and the effective amplitude for the scattering of projectile nucleons on the target nucleus. The density of the ^{12}C nucleus was approximated by the sum of Gaussian functions. However, the use of the optical limit of the theory of multiple diffractive scattering is hardly justifiable in this case; therefore, the resulting effective nucleon–nucleus amplitude may be insufficiently realistic.

The dashed and the dotted curve in Fig. 1*a* represent the results of the calculations performed with the free $\alpha\alpha$ amplitudes at the energies of 620 and 850 MeV, respectively. In the calculations, we have used the amplitude $\tilde{f}_{\alpha\alpha}(\mathbf{q})$ in the form of the sum of three Gaussian functions [see Eq. (11)], since the differential cross sections for elastic $\alpha\alpha$ scattering at

the energies of 620 and 850 MeV were experimentally measured [17, 18] in the region of rather high momentum transfers (the corresponding angular region is $\theta \geq 50^\circ$), where the use of the model being considered is not well justified and where the amplitude $\tilde{f}_{\alpha\alpha}(\mathbf{q})$ parametrized as the sum of two Gaussian functions does not lead to an adequate description of available experimental data. The parameters of the free $\alpha\alpha$ amplitude are given in Table 2.

From Fig. 1*a*, it can be seen that the differential cross sections for elastic $^{12}C^{12}C$ scattering at an energy of 2400 MeV that were calculated by using the effective and free $\alpha\alpha$ amplitude $\tilde{f}_{\alpha\alpha}(\mathbf{q})$ differ considerably. In the case of elastic alpha-particle scattering by ^{12}C nuclei at an energy of 1.37 GeV [9], where the parameters of the free $\alpha\alpha$ amplitude were determined quite reliably, the calculated differential cross sections exhibit similar behavior. Therefore, it seems that the ambiguity in choosing the parameters of the free $\alpha\alpha$ amplitude at the energies of 620 and 850 MeV is not expected to have a pronounced effect on the behavior of the differential cross sections computed in the present study.

It should be noted that we have also calculated the differential cross section for elastic $^{12}C^{12}C$ scattering at the energy of 2400 MeV by using the effective $\alpha\alpha$ amplitude $\tilde{f}_{\alpha\alpha}(\mathbf{q})$ parametrized as the sum of three Gaussian functions [see Eq. (11)]. The result is virtually coincident with that displayed in Fig. 1*a* (solid curve).

Figures 1*b* and 2*b* display the results obtained by calculating the differential cross sections for the elastic scattering of ^{16}O nuclei by ^{12}C nuclei. The notation for the curves here is identical to that in Figs. 1*a* and 2*a*.

Figure 3 shows the calculated and measured (see [14, 15]) differential cross sections for elastic $^{12}C^{12}C$ and $^{16}O^{12}C$ scattering at energies of 1016 and 1503 MeV, respectively. The differential cross section for elastic $^{12}C^{12}C$ scattering (Fig. 3*a*) was calculated with the effective $\alpha\alpha$ amplitude, whose parameters were determined from a fit to available experimental data (Table 1, the energy value of 339 MeV). The resulting set of parameters of the effective $\alpha\alpha$ amplitude was then used to describe the differential cross section for elastic $^{16}O^{12}C$ scattering (Fig. 3*b*)—that is, this differential cross section was calculated without adjustable parameters.

The existing distinctions between the calculated and measured observables at scattering angles around $\theta \approx 3^\circ$ can be explained by the disregard of the interference between the nuclear and Coulomb interactions, which, at the projectile energies being considered, governs the behavior of the differential cross sections in the region of the first diffraction minimum.

Figures 1–3 show that, in the scattering-angle region $\theta \geq 8^\circ$, there are distinctions between the calculated and measured observables. In all probability, the reason behind this behavior of the differential cross sections is that the dispersive alpha-cluster model used here makes it possible to describe the measured form factors for the ^{12}C nucleus only within the momentum-transfer region $q \leq 3$ fm^{-1}—that is, the use of this model at higher momentum-transfer values is not quite legitimate.

We note that an attempt at employing the parameters of the projectile density as adjustable parameters did not lead to noticeable variations in the behavior of the calculated differential cross sections since, in this model, the deformation of projectiles is automatically taken into account in the effective $\alpha\alpha$ amplitude.

Our calculations have revealed that the model proposed in [12] for studying the elastic scattering of loosely bound particles (deuterons, ^6He nuclei) by ^{12}C nuclei also makes it possible to obtain satisfactory agreement between the calculated and measured observables for the elastic scattering of strongly bound light alpha-cluster nuclei (^{12}C, ^{16}O) by carbon nuclei. The agreement between the calculated and measured differential cross sections for elastic $^{12}C^{12}C$ scattering is improved with increasing projectile energy, since the conditions of applicability of the theory of multiple diffractive scattering are better satisfied at higher energies. Unfortunately, there are presently no data on $^{16}O^{12}C$ scattering at these energies. The results of the calculations performed in this and in earlier studies show that the agreement between the observables calculated within the model proposed [12] and the measured observables is attained with realistic densities of alpha-cluster nuclei and realistic effective elementary amplitudes, whereby one takes automatically into account variations in the properties of projectiles due to their polarizability. Therefore, experimental investigations into the elastic scattering of light alpha-cluster nuclei by similar nuclei at higher energies would make it possible to obtain more comprehensive information both about the structure of colliding nuclei and about the strength and the character of interaction between the structural components of these nuclei within nuclear matter.

REFERENCES

1. E. V. Inopin and B. I. Tishchenko, Zh. Éksp. Teor. Fiz. **38**, 1160 (1960) [Sov. Phys. JETP **11**, 840 (1960)].
2. I. Ahmad, Phys. Lett. B **36B**, 301 (1971).
3. D. M. Brink, H. Friedrich, A. Weiguny, and C. W. Wong, Phys. Lett. B **33B**, 143 (1970).

4. Yu. A. Berezhnoy, V. V. Pilipenko, and G. A. Khomenko, J. Phys. G **10**, 63 (1984).
5. Yu. A. Berezhnoy, V. P. Mikhailyuk, and V. V. Pilipenko, J. Phys. G **18**, 85 (1992).
6. Yu. A. Berezhnoy and V. P. Mikhaĭlyuk, Yad. Fiz. **63**, 783 (2000) [Phys. At. Nucl. **63**, 715 (2000)].
7. Yu. A. Berezhnoĭ and V. P. Mikhaĭlyuk, Izv. Akad. Nauk, Ser. Fiz. **65**, 721 (2001).
8. V. P. Mikhailyuk, Mod. Phys. Lett. A **10**, 2915 (1995).
9. Yu. A. Berezhnoy and V. P. Mikhailyuk, Z. Phys. A **355**, 1 (1996).
10. M. E. Brandan, H. Chehime, and K. W. McVoy, Phys. Rev. C **55**, 1353 (1997).
11. M. E. Brandan and K. W. McVoy, Phys. Rev. C **55**, 1362 (1997).
12. V. P. Mikhailyuk, Eur. Phys. J. A **9**, 473 (2000).
13. M. C. Mermaz, B. Bonin, M. Buenerd, and J. Y. Hostachy, Phys. Rev. C **34**, 1988 (1986).
14. M. Buenerd *et al.*, Nucl. Phys. A **424**, 313 (1984).
15. P. Roussel *et al.*, Phys. Rev. Lett. **54**, 1779 (1985).
16. B. Abu-Ibrahim and Y. Suzuki, Phys. Rev. C **62**, 034608 (2000).
17. K. A. G. Rao *et al.*, Phys. Rev. C **62**, 014607 (2000).
18. J. C. Fong *et al.*, Nucl. Phys. A **265**, 365 (1976).

Translated by A. Isaakyan

Physics of Atomic Nuclei, Vol. 66, No. 4, 2003, pp. 679–683. Translated from Yadernaya Fizika, Vol. 66, No. 4, 2003, pp. 708–712.

NUCLEI
Theory

T-Odd Angular Asymmetry in Nuclear Reactions Involving Sequential Particle Emission

A. L. Barabanov[1)], V. E. Bunakov[2)], I. S. Guseva[2)], and G. A. Petrov[2)]

Received April 19, 2002

Abstract—A triple T-odd angular correlation is considered in the kinematically similar reactions $^{10}\mathrm{B}(n,\alpha\gamma)$ and $^{233}\mathrm{U}(n,\alpha f)$ induced by cold polarized neutrons. It is shown that, in the former reaction, this correlation is suppressed by the double parity-conservation selection rule due to the two-step character of the process; however, T invariance does not impose any specific constraints on this correlation. The mechanism through which the T-odd correlation found in ternary-fission reactions is formed seems to be closely related to a nearly simultaneous disintegration of the nucleus involved into two fission fragments and an alpha particle. © *2003 MAIK "Nauka/Interperiodica".*

1. INTRODUCTION

The results obtained by measuring the T-odd correlation $\boldsymbol{\sigma}_n \cdot [\mathbf{p}_\alpha \times \mathbf{p}_\gamma])$ in the two-step reaction $^{10}\mathrm{B}(n,\alpha\gamma)$ induced by cold polarized neutrons were reported in [1]. Here, $\boldsymbol{\sigma}_n$ is neutron spin, while $\mathbf{p}_\alpha$ and $\mathbf{p}_\gamma$ are, respectively, the alpha-particle and the photon momentum. The asymmetry of photons emitted along and against the direction of the vector $\boldsymbol{\sigma}_n \times \mathbf{p}_\alpha$ proved to be $D_\gamma = -(0.09 \pm 1.9) \times 10^{-4}$ (that is, the effect was compatible with zero). Those measurements were motivated by a nonzero T-odd correlation $\boldsymbol{\sigma}_n \cdot [\mathbf{p}_\alpha \times \mathbf{p}_f]$ that was revealed recently in the ternary-fission reaction $^{233}\mathrm{U}(n,\alpha f)$ also induced by cold polarized neutrons (see [2]). Here, the vector $\mathbf{p}_f$ is the momentum of the lightest fragment. The corresponding asymmetry coefficient measured in [2] is $D_f = (2.35 \pm 0.05) \times 10^{-3}$.

Previously, it was repeatedly indicated (see, for example, [3, 4]) that, in contrast to the case of parity, it is only in elastic-scattering processes that a nonzero T-odd correlation is directly related to T violation. In inelastic processes (including, among others, alpha and gamma decays and fission), this relationship can be established only if the process is treated in the first Born approximation, and it is valid apart from Born terms of higher orders. Corrections induced by those terms (effects of initial- and final-states interaction) can conceal, to a considerable extent, the aforementioned relationship even in electromagnetic processes (see, for example, [3]). Fission and alpha-decay processes featuring strong interaction can hardly be described in the Born approximation. Hence, the experimental result from [2] is more probably associated with special features of the respective reaction mechanism rather than with T violation.

At the same time, the reactions $^{10}\mathrm{B}(n,\alpha\gamma)$ and $^{233}\mathrm{U}(n,\alpha f)$ appear to be kinematically similar. This brings about the question of whether the absence of the triple T-odd correlation in the former reaction is merely accidental. If this is not so, then it is desirable to reveal, in the reaction mechanisms, distinctions that cause the absence of the triple T-odd correlation in the reaction $^{10}\mathrm{B}(n,\alpha\gamma)$.

In seeking solutions to these problems, we have analyzed the reaction $^{10}\mathrm{B}(n,\alpha\gamma)$ induced by cold polarized neutrons. This reaction proceeds in two steps that are well separated in time. The first step of the reaction $^{10}\mathrm{B}(n,\alpha)$ results in the formation of a few broad ($\Gamma > 100$ keV) overlapping resonances of the compound nucleus $^{11}\mathrm{B}$, which undergo alpha decay, producing the daughter nucleus $^{7}\mathrm{Li}$ in an excited $1/2^-$ state. The neutron polarization is partly transferred to the daughter nucleus. At the second step, its duration being 10^{-14} s, the polarized $^{7}\mathrm{Li}$ nucleus decays to the ground $(3/2^-)$ state by emitting a photon.

2. ANGULAR CORRELATIONS IN $(n,\alpha\gamma)$ REACTIONS

Before pursuing our analysis further, we briefly recall basic elements of the spin-tensor technique within the theory of nucleus orientation. The spin state of a spin-I nucleus is determined by the amplitudes $a_M(I)$ corresponding to the spin projections M onto

[1)]Russian Research Centre Kurchatov Institute, pl. Kurchatova 1, Moscow, 123182 Russia;
e-mail: barab@pretty.mbslab.kiae.ru

[2)]Petersburg Nuclear Physics Institute, Russian Academy of Sciences, Gatchina, 188350 Russia.

1063-7788/03/6604-0679$24.00

the z axis. The spin state of an ensemble of nuclei is determined by the density matrix

$$\rho_{MM'}(I) = \langle a_M(I) a^*_{M'}(I) \rangle \tag{1}$$

or by a set of the orientation spin-tensors

$$\tau_{Qq}(I) = \sum_{MM'} C^{IM'}_{IMQq} \rho_{MM'}(I). \tag{2}$$

If an ensemble of nuclei is oriented along a unit vector $\mathbf{n}_I$, then

$$\tau_{Qq}(I) = \left(\frac{4\pi}{2Q+1}\right)^{1/2} Y_{Qq}(\mathbf{n}_I) \tau'_{Q0}(I), \tag{3}$$

where $\tau'_{Q0}(I)$ are spin-tensors in the reference frame where the z' axis is directed along the orientation axis. The ensemble is refered to as a polarized one if its spin-tensor $\tau'_{10}(I)$ differs from zero. This spin-tensor is related to the polarization $p(I) = \langle M \rangle / I$ by the equation

$$\tau'_{10}(I) = \sqrt{\frac{I}{I+1}}\, p(I). \tag{4}$$

The $Q = 2$ spin-tensors control the alignment of the ensemble. By specifying all spin-tensors $\tau'_{Q0}(I)$ up to the highest rank of $Q = 2I$, one presets the occupation numbers w_M for all the spin substates M.

We now consider the first step of the reaction $^{10}\mathrm{B}(n, \alpha\gamma)$. A ^{10}Be target nucleus of spin $I = 3$ absorbs a cold polarized neutron of spin $s = 1/2$ producing an alpha particle of spin zero and an excited daughter nucleus $^7\mathrm{Li}^*$ of spin $I' = 1/2$. The dynamics of this reaction is completely determined by its S matrix—that is, by the amplitudes $S_J(lj \to L_\alpha)$ describing the transition from the initial to the final state. Here, l and j are the orbital angular and the total angular momentum of the neutron ($\mathbf{j} = \mathbf{l} + \mathbf{s}$), J is the compound-nucleus spin ($\mathbf{J} = \mathbf{j} + \mathbf{I}$), and L_α is angular momentum of the alpha particle in the output channel ($\mathbf{L}_\alpha + \mathbf{I}' = \mathbf{J}$). The spin-tensors of the ensemble of spin-I' nuclei in the output channel are given by

$$\begin{aligned}
\tau_{Qq}(I') = \sum_{Aa} \sum_{JJ'} \sum_{lj\, l'j'} \xi_{Aa}(l'j'J', ljJ) \\
\times \sum_{L_\alpha L'_\alpha} S^*_{J'}(l'j' \to L'_\alpha) S_J(lj \to L_\alpha) \\
\times \sum_{Hh} \left(\frac{(2H+1)(2A+1)}{4\pi}\right)^{1/2} C^{Aa}_{HhQq} \\
\times Y^*_{Hh}(\mathbf{n}_\alpha) \left((2J+1)(2I'+1)(2L_\alpha+1)\right)^{1/2} \\
\times C^{L'_\alpha 0}_{L_\alpha 0 H 0} \begin{Bmatrix} J' & L'_\alpha & I' \\ J & L_\alpha & I' \\ A & H & Q \end{Bmatrix},
\end{aligned} \tag{5}$$

where

$$\begin{aligned}
\xi_{Aa}(l'j'J', ljJ) = g_{J'} \left(\frac{2J+1}{2J'+1}\right)^{1/2} \\
\times \left((2j'+1)(2l+1)(2s+1)\right)^{1/2} \\
\times \sum_{K\Lambda} \left(\frac{(2K+1)(2\Lambda+1)}{2A+1}\right)^{1/2} \tau'_{K0}(s)\, C^{l'0}_{l0\Lambda 0} \\
\times U(Ij'JA, J'j) \begin{Bmatrix} j' & l' & s \\ j & l & s \\ A & \Lambda & K \end{Bmatrix} \\
\times 4\pi \sum_{\lambda\kappa} C^{Aa}_{\Lambda\lambda K\kappa} Y_{\Lambda\lambda}(\mathbf{n}_k) Y_{K\kappa}(\mathbf{n}_s).
\end{aligned} \tag{6}$$

Here, $U(abcd, ef) = \sqrt{(2e+1)(2f+1)} \times W(abcd, ef)$ is a normalized Racah function. The incident-neutron-polarization direction is determined by the unit vector $\mathbf{n}_s$, and the spin-tensor $\tau'_{10}(s) = p(s)/\sqrt{3}$ is proportional to the polarization value. The unit vectors $\mathbf{n}_k$ and $\mathbf{n}_\alpha$ are directed along the momenta of neutron and the alpha particle, respectively. The polarization of spin-I' nuclei is specified by the set of spin-tensors $\tau_{1q}(I')$, which can always be recast into the form (3)—that is, expressed in terms of the polarization $p(I')$ by means of Eq. (4). The quantity $g_J = (2J+1)/\left((2I+1)(2s+1)\right)$ is the ordinary spin factor.

We now consider the second step of the reaction $^{10}\mathrm{B}(n, \alpha\gamma)$—that is, the gamma decay of the polarized daughter nucleus, $^7\mathrm{Li}^*(1/2^-) \to {}^7\mathrm{Li}(3/2^-) + \gamma$.

In our particular case, the angular distribution of photons is described by the expression (see, for example, [5])

$$\begin{aligned}
\frac{dw_\gamma}{d\Omega} \sim \tau_{00}(I') \sum_{L=1,2} \left(|\mathcal{A}(ML)|^2 + |\mathcal{A}(EL)|^2\right) \\
+ 6 \left(\frac{4\pi}{3}\right)^{1/2} \sum_q \tau_{1q}(I') Y^*_{1q}(\mathbf{n}_\gamma) \\
\times \left(C^{21}_{1110} U\left(\frac{3}{2}\frac{1}{2} 21, 1\frac{1}{2}\right) \mathrm{Re}(\mathcal{A}(M1)\mathcal{A}^*(M2) \right. \\
\left. + \mathcal{A}(E1)\mathcal{A}^*(E2)\right)
\end{aligned} \tag{7}$$

$$+\sum_{L=1,2} C^{L1}_{L110} U\left(\frac{3}{2}\frac{1}{2}L1, L\frac{1}{2}\right)\mathrm{Re}(\mathcal{A}(ML)\mathcal{A}^*(EL))\Bigg),$$

where $\mathcal{A}(ML)$ [$\mathcal{A}(EL)$] is the amplitude of the magnetic (electric) transition of multipole order L and $\mathbf{n}_\gamma$ is the unit vector directed along the photon momentum. The first term on the right-hand side in (7) determines the total probability of the gamma transition. If parity is conserved, then only $M1$ and $E2$ amplitudes contribute to the total probability. In the case of parity violation, there arise small $E1$ and $M2$ amplitudes. The experimentally measured asymmetry is described by the second term on the right-hand side of (7). It can be seen that this asymmetry is not zero only if parity is violated in the ^{7}Li nucleus, in which case the $E1$ and $M2$ transitions admix to $M1$ and $E2$ ones. However, the magnitude of the parity-violation effects in the ^{7}Li nucleus hardly exceeds a level of 10^{-8}–10^{-7}.

It should be noted that, in the particular case of $I' = 1/2$, there exist only spin-tensors of rank $Q = 0$ and of rank $Q = 1$ (polarization), which give rise to two terms in (7). At higher values of the spin I', the situation is more complicated, because spin-tensors of higher ranks (up to $Q = 2I'$) appear in (7). However, all terms involving odd Q values will include the products of radiation amplitudes corresponding to the emission of opposite-parity photons, just as in our case of $Q = 1$. Therefore, their contribution to the measured asymmetry will be controlled by the degree of parity violation. Terms involving even values of Q are not constrained by parity selection rules, and the correlation of the vectors $\mathbf{n}_s$, $\mathbf{n}_k$, $\mathbf{n}_\alpha$ and $\mathbf{n}_\gamma$ that is associated with them will generally be nonzero. However, each of those terms will include [see Eqs. (3), (7)] spherical harmonics $Y_{Qq}(\mathbf{n}_\gamma)$ featuring even values of Q. These functions are invariant under the inversion of the vector $\mathbf{n}_\gamma$; therefore, they do not contribute to the measured asymmetry under consideration. Hence, the only distinction between the case of $I' = 1/2$ and the cases of higher values of I' is the isotropy of gamma radiation (if parity is conserved).

3. ASYMMETRY OF PARTICLE EMISSION IN TWO-STEP REACTIONS

Thus, we can conclude that, in a two-step reaction, the T-odd asymmetry under consideration can differ from zero only owing to effects of parity violation. This conclusion can easily be generalized to the case of any sequential process $A + B \to C + D \to C + (E + F)$. Let us demonstrate this explicitly. Following [1, 2], we take the y axis to be aligned with the relative momentum of colliding particles A and B. Suppose that relative motion of particles C and D proceeds along the z axis and that particles E and F move along or against the x axis. Particles E and F originate from the decay of particle D. We now consider the rest frame of particle D, where the probabilities of the emission of particles F with oppositely directed momenta $\mathbf{p}_F$ and $-\mathbf{p}_F$ can be different only in the case where the isotropy of space is violated—that is, in the case where there exists a specific direction. However, the D-particle spin $\mathbf{I}'$ is the only vector specifying such a direction. Therefore, the asymmetry of F emission in the D rest frame can arise only owing to the P-odd correlation $\mathbf{p}_F \cdot \mathbf{I}_D$.

In the laboratory frame, there is also the D-momentum vector. However, this vector leads only to a trivial shift of the momentum $\mathbf{p}_F$ along the direction of motion of particle D. Under the conditions of the experiments reported in [1, 2], particles F and D move along the x and z axes, respectively, which are perpendicular to each other. Therefore, the asymmetry of F emission along and against the x axis cannot depend on the D-momentum direction. It follows that, for the emergence of measurable asymmetry, it is necessary that

(i) Particle D in the reaction $A + B \to C + D$ be polarized, which generates a specific direction for the spin $\mathbf{I}' = \mathbf{I}_D$;

(ii) parity in the decay $D \to E + F$ be violated, which leads to a nonzero correlation $\mathbf{p}_F\mathbf{I}_D$.

One can easily prove that it is precisely these conditions that ensure a nonzero value of the last term on the right-hand side of (7).

4. TRIPLE T-ODD CORRELATION IN $(n, \alpha\gamma)$ REACTION

In the angular distribution of gamma rays emitted in the process $^7\mathrm{Li}^*(1/2^-) \to {}^7\mathrm{Li}(3/2^-)$ at the second stage of the reaction $^{10}\mathrm{B}(n, \alpha\gamma)$, the term that is proportional to the T-odd correlation $\mathbf{n}_s \cdot [\mathbf{n}_\alpha \times \mathbf{n}_\gamma]$ is of particular interest. The angular distribution of gamma rays is given by (7), information here about the first step of the reaction being completely absorbed in the spin-tensors $\tau_{1q}(I')$.

We substitute these spin-tensors, determined by Eqs. (5) and (6), into (7). Since the T-odd triple correlation in question does not involve the vector $\mathbf{n}_k$, we retain only the $\Lambda = 0$ terms in (6). It can easily be seen that, in this case, $l = l'$ in (5) and (6); that is, there is no interference in the initial orbital angular momenta of the neutron. Taking into account only s waves for cold incident neutrons, we reduce the factor appearing in (7) to the form

$$\sum_q \tau_{1q}(I') Y^*_{1q}(\mathbf{n}_\gamma) \qquad (8)$$

$$= \frac{9\sqrt{2}}{(4\pi)^{3/2}}\tau'_{10}(s)\,(\mathbf{n}_s\cdot[\mathbf{n}_\alpha\times\mathbf{n}_\gamma])$$
$$\times\sum_{JJ'}g_{J'}\left(\frac{2J+1}{2J'+1}\right)^{1/2}U\left(I\frac{1}{2}J1,J'\frac{1}{2}\right)$$
$$\times\sum_{L'_\alpha>L_\alpha}\left((2J+1)(2I'+1)(2L_\alpha+1)\right)^{1/2}$$
$$\times C^{L'_\alpha 0}_{L_\alpha 010}\begin{Bmatrix}J' & L'_\alpha & I'\\ J & L_\alpha & I'\\ 1 & 1 & 1\end{Bmatrix}$$
$$\times\,\mathrm{Im}\left(S^*_{J'}\left(0\frac{1}{2}\to L'_\alpha\right)S_J\left(0\frac{1}{2}\to L_\alpha\right)\right)+\ldots.$$

The ellipsis on the right-hand side indicates that we have taken into account only one term that is proportional to the triple T-odd correlation in question.

Our result is of interest in two respects.

First, we have shown that, for the correlation in question to emerge, the output orbital angular momenta of emitted alpha particles of opposite parities ($L'_\alpha = L_\alpha \pm 1$) must interfere at the first step of the reaction. Since parity is fixed in the input neutron channel (s and p waves do not interfere), the triple T-odd correlation can emerge in the reaction $^{10}\mathrm{B}(n,\alpha\gamma)$ only if parity is violated both at the second step (which is what has been shown earlier) and at the first step of the reaction. It is obvious that this is because of a P-even character of the correlation in question. Hence, the same is true for any two-step process $A+B\to C+D\to C+(E+F)$. Clearly, the above finding leads to the conclusion that the scale of the expected asymmetry of photon emission is constrained to be 10^{-16}–10^{-14}.

Second, expression (8) is of interest because it illustrates directly the statement formulated in the Introduction that there is no connection between the T-odd correlation in an inelastic process and T violation. We see that T invariance imposes no constraints on the T-odd correlation in the reaction $^{10}\mathrm{B}(n,\alpha\gamma)$.

5. CONCLUSION

For the example of the reaction $^{10}\mathrm{B}(n,\alpha\gamma)$, we have shown that, in a two-step process where two sequential stages are well separated in time, a triple T-odd correlation of the type that was studied experimentally in [1, 2] is suppressed by the double parity-induced selection rule. At the same time, T invariance imposes no specific constraints on this correlation.

In a general two-step process of the $A+B\to C+D\to C+(E+F)$ type, the separation of stages in time means that the decay $D\to E+F$ proceeds when particle C has travelled so far that its nuclear and electromagnetic fields do not affect the motion of particles E and F. In the $(n,\alpha\gamma)$ reaction considered here, the lifetime of the decaying ^{7}Li nucleus is about 10^{-14} s, owing to which the alpha particle moves away to a distance of about 10^3 units of the atomic radius. Thus, two steps of this reaction are well separated.

We can now return to a comparison of the reactions $^{10}\mathrm{B}(n,\alpha\gamma)$ and $^{233}\mathrm{U}(n,\alpha f)$. The main distiction between them is that ternary fission is not a two-step process. The alpha particle is emitted either by a strongly deformed nucleus at the final stage of the fission process from the neck connecting prefragments or directly upon the rupture of the neck. Even if the alpha particle is emitted in the process of the "double rupture of the neck" by one of the prefragments, the distance between the prefragments does not exceed a few femtometers. It follows that, even at the stage where short-range strong and weak interactions no longer act between the prefragments, the Coulomb forces at the instant of alpha-particle emission remain so strong that all parts of the system are still involved in energy-, momentum-, and angular-momentum-exchange processes. Thus, fission and alpha-particle emission cannot be treated as sequential stages well separated in time. It is precisely this feature of ternary fission that seems responsible for so large a value of asymmetry measured in the ternary-fission process (about 10^{-3}) that it cannot be associated with parity-violation effects not exceeding a level of 10^{-4} [6–8] in the case of ternary fission involving alpha-particle emission.

The problem of the mechanism behind the emergence of a triple T-odd correlation in ternary fission is beyond the scope of this study. The analysis presented here is of value for two reasons: (i) By considering the example of the inelastic process $^{10}\mathrm{B}(n,\alpha\gamma)$, which is kinematically similar to the ternary-fission $^{233}\mathrm{U}(n,\alpha f)$ reaction, we have directly demonstrated that T invariance does not forbid the T-odd angular correlations. This is an additional argument in favor of the conjecture that the T-odd asymmetry measured in [2] is not due to T violation. (ii) In the view of our present analysis, the very fact of the emergence of asymmetry in ternary fission suggests quite independently that this reaction is the simultaneous three-body decay of the primary nucleus into two fragments and an alpha particle rather than a sequential process. The hypotheses put forth in [9, 10] to explain the results reported in [2] were based on precisely this pattern of ternary process.

ACKNOWLEDGMENTS

The work was supported in part by INTAS (project no. 99-0229) and by the Russian Foundation for Basic Research (project nos. 99-02-17275, 00-15-96590).

REFERENCES

1. A. M. Gagarski, G. V. Val'ski, G. A. Petrov, *et al.*, Pis'ma Zh. Éksp. Teor. Fiz. **72**, 416 (2000) [JETP Lett. **72**, 286 (2000)].
2. P. Jesinger, A. Kotzle, *et al.*, Nucl. Instrum. Methods Phys. Res. A **440**, 618 (2000).
3. R. Blin-Stoyle, *Fundamental Interactions and Nuclei* (North-Holland, Amsterdam, 1973).
4. V. E. Bunakov and L. B. Pikelner, Prog. Part. Nucl. Phys. **39**, 337 (1997).
5. A. Z. Dolginov, in *Gamma Rays*, Ed. by L. A. Sliv (Izd. Akad. Nauk SSSR, Leningrad, 1961), Chap. 6.
6. G. Petrov, G. Val'ski, *et al.*, Nucl. Phys. A **502**, 297 (1989).
7. A. Belozerov, G. Danilyan, *et al.*, Pis'ma Zh. Éksp. Teor. Fiz. **54**, 136 (1991) [JETP Lett. **54**, 132 (1991)].
8. F. Goennenwein *et al.*, Nucl. Phys. A **567**, 303 (1994).
9. V. E. Bunakov, Yad. Fiz. **65**, 648 (2002) [Phys. At. Nucl. **65**, 616 (2002)]; V. E. Bunakov and F. Goennenwein, Yad. Fiz. **65**, 2096 (2002) [Phys. At. Nucl. **65**, 2036 (2002)].
10. A. L. Barabanov, in *Proceedings of the 9th International Seminar on Interaction of Neutrons with Nuclei* (JINR, Dubna, 2001), E3-2001-192, p. 93.

Translated by O. Chernavskaya

Physics of Atomic Nuclei, Vol. 66, No. 4, 2003, pp. 684–689. Translated from Yadernaya Fizika, Vol. 66, No. 4, 2003, pp. 713–718.

NUCLEI
Theory

Coulomb Breakup of Light Nuclei in the Field of a Heavy Ion at Relativistic Collision Energies

B. F. Irgaziev*, Sh. Kalandarov, and A. M. Mukhamedzhanov[1)]**

Uzbekistan National University, Tashkent, 700174 Uzbekistan

Received May 6, 2002

Abstract—A simple method for calculating the amplitude and the cross section for the Coulomb breakup of a light nucleus into two fragments in the field of a heavy ion at relativistic collision energies is proposed on the basis of time-dependent perturbation theory. It is shown that the resulting amplitude for the process in question has a correct nonrelativistic limit. The contribution of the longitudinal component of the Coulomb field of a heavy ion tends to zero in the ultrarelativistic limit. A specific implementation of the method is demonstrated by taking the example of the Coulomb breakup reaction ^{208}Pb(^{8}B, ^{7}Bep)^{208}Pb at various collision energies. The results are found to be in agreement with experimental data. © *2003 MAIK "Nauka/Interperiodica".*

1. INTRODUCTION

Processes involving the excitation of nuclei by the Coulomb field of a heavy ion have attracted the attention of researches for many years [1–3]. In connection with the advent of accelerators of relativistic nuclei, there have appeared new possibilities for studying various nuclear reactions, including the Coulomb breakup reactions, which are investigated with the aim of extracting the astrophysical S factor. The point is that it is next to impossible to extract the astrophysical-factor value in the zero-energy region from data on radiative-capture reactions since the cross section for this process decreases exponentially with decreasing energy of the relative motion of colliding nuclei. In order to determine the astrophysical-factor value at zero energy, one therefore has to extrapolate the cross section from energies of about 100 to 200 keV, but this can lead to errors in determining the astrophysical-factor value at zero energy. In view of this, it is always useful to have an independent source of information about astrophysical S factors. A method that relies on studying Coulomb breakup reactions can be used as such a source. At low collision energies, there arises, however, the problem of taking into account three-body Coulomb effects in the final state (so-called postacceleration-effect problem) [4, 5]. It was shown in [4, 5] that the contribution of such three-body effects becomes less pronounced with increasing collision energy. Indeed, this is clear from the physical point of view: at high collision energies, breakup fragments quickly leave the region where the ion field is operative, having no time to be accelerated. It follows that the best way to extract the astrophysical factor in the zero-energy region is to perform such experiments at relativistic energies of a nucleus–ion collision.

The theory of Coulomb breakup at relativistic velocities of a collision was developed by Winther and Alder [6] and was briefly surveyed, for example, in the review article of Bertulani and Baur [2]. From this theory, it is not obvious, however, that, at velocities close in magnitude to the speed of light, the contribution of the longitudinal component of the Coulomb field tends to zero. In fact, this must be so because, at ultrarelativistic velocities of a charge, the properties of its field become close to the properties of the field generated by photons. Moreover, it is difficult, on the basis of the results presented in [6], to accomplish the limiting transition to the case of nonrelativistic collision energies in order to obtain the known formulas for Coulomb excitation in the nonrelativistic case. The authors of many studies devoted to Coulomb breakup apply nonrelativistic theory even at high collision energies, disregarding relativistic corrections, which can nevertheless make a sizable contribution to the breakup amplitude.

It is well known that, at charge velocities close in magnitude to the speed of light, the electromagnetic field of the charge being considered suffers a Lorentz contraction in the the direction of charge motion, and the potential of an ultrarelativistic ion can be represented (see [7]) as the product of the delta function $\delta(x - ct)$ (the coordinate x is chosen along

[1)]Cyclotron Institute, Texas A&M University, TX 77843, USA.

*e-mail: qcd@uzsci.net

**e-mail: akram@cyclotronmail.tamu.edu

the direction of charge motion) and a solution to the two-dimensional Laplace's equation in the plane orthogonal to the charge velocity. By using this potential, Baltz [7] obtained an exact solution to the Dirac equation and employed it to calculate the ionization of the hydrogen atom and the production of an electron–positron pair in the field of an ultrarelativistic ion [8].

In this study, Coulomb breakup in the field of a heavy ion is examined on the basis of time-dependent perturbation theory. A specific implementation of the method is demonstrated by taking the example of the Coulomb breakup reaction $^{208}\mathrm{Pb}(^{8}\mathrm{B}, ^{7}\mathrm{Be}\,p)^{208}\mathrm{Pb}$ at various collision energies. All calculations are performed in the system of units where $\hbar = c = 1$.

2. EXCITATION AMPLITUDE AND CROSS SECTION FOR COULOMB BREAKUP

It is well known that, in the semiclassical theory of the dissociation of nucleus a into fragments b and c by the Coulomb field of ion A, the triple-differential cross section is given by

$$\frac{d^3\sigma}{dE_{bc}d\Omega_{bc}d\Omega_a} = \frac{d\sigma_R}{d\Omega_a}\frac{1}{2J_i+1}\sum_{m_i,m_j}|a_{fi}|^2\frac{\mu_{bc}k_{bc}}{(2\pi)^3}, \tag{1}$$

where E_{bc} (k_{bc}) is the energy (momentum) of the relative motion of the fragments b and c of nucleus a after breakup, $d\sigma_\mathrm{R}/d\Omega_a$ is the Rutherford cross section for the scattering of nucleus a in the field of ion A, μ_{bc} is the reduced mass of particles b and c, J_i is the initial-state spin of nucleus a, and a_{fi} is the amplitude for the dissociation of the nucleus from the initial state $|i\rangle$ to the final state $|f\rangle$. As usual, summation over the projections m_j of the final-state total angular momentum of the nucleus and averaging over the projections m_i of its initial-state total angular momentum are performed in (1). In time-dependent perturbation theory, the total excitation amplitude is given by the expression

$$a_{fi} = \delta_{fi} + a_{fi}^{(1)} + a_{fi}^{(2)} + \ldots. \tag{2}$$

We restrict our consideration to the first order of perturbation theory—this corresponds to the one-photon approximation—since we consider excitations at low energies of the relative motion of particles b and c. Taking into account the smallness of the momentum transfer, we assume that the c.m. velocity of nucleus a remains unchanged in the breakup process. This makes it possible to go over to the coordinate frame comoving with nucleus a, where ion A will move at a high velocity along a straight-line trajectory. In this reference frame, the breakup fragments will have nonrelativistic velocities. For the wave functions describing the relative motion in the initial and the final state, we can therefore take solutions to the Schrödinger equation.

In the first order of perturbation theory, the amplitude for the dissociation of the nucleus from the state at energy E_i to the state at energy E_f can be represented as

$$a_{fi}^{(1)} = \frac{1}{i}\langle f|\int_{-\infty}^{+\infty}V(t)e^{i\omega t}dt|i\rangle, \tag{3}$$

where $\omega = E_f - E_i$ and the interaction potential is given by

$$V(t) = \int d^3r\left[\rho(\mathbf{r})\varphi(\mathbf{r},t) - \mathbf{j}(\mathbf{r})\cdot\mathbf{A}(\mathbf{r},t)\right]. \tag{4}$$

Here,

$$\rho(\mathbf{r}) = \sum_i Z_i e\delta(\mathbf{r}-\mathbf{r}_i) \tag{5}$$

is the charge-density operator;

$$\mathbf{j}(\mathbf{r}) = \frac{1}{2}\sum_i\frac{Z_i e}{m_i}\left[\delta(\mathbf{r}-\mathbf{r}_i)\mathbf{p}_i + \mathbf{p}_i\delta(\mathbf{r}-\mathbf{r}_i)\right] + \sum_i \mathrm{rot}\left[\boldsymbol{\mu}_i\delta(\mathbf{r}-\mathbf{r}_i)\right] \tag{6}$$

is the particle-current-density operator; $Z_i e$, m_i, and $\mathbf{r}_i$ are, respectively, the charge, the mass and the radius vector of particle i; and $\mathbf{p}_i$ and $\boldsymbol{\mu}_i$ are its momentum and magnetic-moment operators, respectively. The scalar potential $\varphi(\mathbf{r},t)$ and the potential vector $\mathbf{A}(\mathbf{r},t)$ of the field generated by a fast ion at the point specified by the radius vector $\mathbf{r}$ have the form of the Liénard–Wiechert potentials

$$\varphi(\mathbf{r},t) = \frac{Z_A e}{\sqrt{[(\boldsymbol{\rho}-\mathbf{b})/\gamma]^2 + (x-vt)^2}}, \tag{7}$$

$$\mathbf{A}(\mathbf{r},t) = \mathbf{v}\varphi(\mathbf{r},t), \tag{8}$$

where Z_A is the charge of the ion, $\mathbf{b}$ is the impact parameter, $\boldsymbol{\rho}$ is the transverse component of the radius vector $\mathbf{r}$ with respect to the direction of ion motion, x is the projection of the radius vector $\mathbf{r}$ onto the direction of ion motion, $\mathbf{v}$ is the velocity of ion A, and $\gamma = 1/\sqrt{1-v^2}$. It is well known that the potentials are determined apart from a gauge transformation. Following [7], we chose the gauge function in the form

$$\chi(\mathbf{r},t) = \frac{Z_A e}{v}\ln\left[\gamma(x-vt) + \sqrt{b^2+\gamma^2(x-vt)^2}\right]. \tag{9}$$

This function preserves the chosen gauge apart from $O(1/\gamma^2)$ terms; for $v \to 1$, the gauge transformation

with this function does not change the gauge conditions for the potentials (7) and (8). By using this gauge function, we find the new potentials

$$\varphi'(\mathbf{r},t)\varphi(\mathbf{r},t) - \frac{\partial\chi}{\partial t} \tag{10}$$
$$= \frac{Z_A e}{\sqrt{[(\boldsymbol{\rho}-\mathbf{b})/\gamma]^2 + (x-vt)^2}} - \frac{Z_A e}{\sqrt{\mathbf{b}^2/\gamma^2 + (x-vt)^2}},$$

$$\mathbf{A}'(\mathbf{r},t)\mathbf{v}\varphi'(\mathbf{r},t). \tag{11}$$

It can easily be shown that, for $v \to 1$ and a finite value of the impact parameter b, the potential (10) takes the form

$$\varphi'(\mathbf{r},t) = -Z_A e\delta(x-t)\ln\frac{(\boldsymbol{\rho}-\mathbf{b})^2}{b^2}, \tag{12}$$

whence we can see that the field of an ultrarelativistic ion becomes similar to a superposition of the fields generated by photons of different frequencies, the amplitudes here being, however, dependent on the point of the field. With the potential (12), we will now calculate the amplitude for the excitation of a nucleus. Since Coulomb breakup occurs at small scattering angles—that is, at impact-parameter values exceeding the dimensions of colliding particles—we have $\rho \ll b$. On the other hand, the choice of this condition is justified by the fact the wave function for the bound state of nucleus a decreases exponentially with increasing distance, so that the significant region of ρ can be bounded by a dimension of $1/\sqrt{2\mu_{bc}\varepsilon}$, where ε is the binding energy. Taking all the aforesaid into account, we expand the function $\ln(\boldsymbol{\rho}-\mathbf{b})^2/b^2$ in powers of the ratio $(\mathbf{b}\cdot\boldsymbol{\rho})/b^2$. Retaining only the first term, we then have

$$\varphi'(\mathbf{r},t) = \frac{2Z_A e(\mathbf{b}\cdot\boldsymbol{\rho})}{b^2}\delta(x-t) + O\left(\frac{1}{b^2}\right). \tag{13}$$

If, for $\delta(x-t)$, use is made of the integral representation

$$\delta(x-t) = \frac{1}{2\pi}\left[\int_0^\infty e^{i\xi(x-t)}d\xi + \int_0^\infty e^{-i\xi(x-t)}d\xi\right], \tag{14}$$

the amplitude in (3) can be reduced to the form

$$a_{fi}^{(1)} = \frac{2Z_A e}{i} \tag{15}$$
$$\times\langle f|\int d^3r e^{i\omega x}\left[\rho(\mathbf{r}) - \mathbf{n}\cdot\mathbf{j}(\mathbf{r})\right]\frac{(\mathbf{b}\cdot\boldsymbol{\rho})}{b^2}|i\rangle,$$

where $\mathbf{n}$ is a unit vector parallel to the ion-velocity vector. Since the condition $\omega r \ll 1$ holds at energies of the relative motion of breakup fragments that is of interest for our analysis, we can approximately set

$$e^{i\omega x} \approx 1 + i\omega x. \tag{16}$$

If we are interested only in electric transitions, the current can be taken in the form

$$\mathbf{j}(\mathbf{r}) = \frac{1}{2}\sum_i Z_i e\delta(\mathbf{r}-\mathbf{r}_i)[H,\mathbf{r}_i] \tag{17}$$
$$+\frac{1}{2}\sum_i Z_i e[H,\mathbf{r}_i]\delta(\mathbf{r}-\mathbf{r}_i),$$

where H is the Hamiltonian of nucleus a. As a result, we obtain the following expression for the amplitude $a_{fi}^{(1)}$:

$$a_{fi}^{(1)} = \frac{2Z_A e}{i}\langle f|\sum_i Z_i\frac{(\mathbf{b}\cdot\boldsymbol{\rho}_i)}{b^2}|i\rangle. \tag{18}$$

Let us now consider the case of $v \ll 1$. Winther and Alder [6] first performed a Fourier transformation of the field and then constructed a multipole expansion. In contrast to that, we first expand the potential (7) in powers of $\dfrac{2(\mathbf{b}\cdot\boldsymbol{\rho}) - \rho^2}{\gamma^2[b^2/\gamma^2 + (x-vt)^2]}$ and retain only the first two terms of the expansion.[2)] This yields

$$\varphi(\mathbf{r},t) = \frac{Z_A e}{[b^2/\gamma^2 + (x-vt)^2]^{1/2}} \tag{19}$$
$$+\frac{Z_A e(\mathbf{b}\cdot\boldsymbol{\rho})}{\gamma^2\left[b^2/\gamma^2 + (x-vt)^2\right]^{3/2}} + O\left(\frac{1}{b^3}\right).$$

Substituting, into Eq. (3), the potentials $\varphi(\mathbf{r},t)$ and $\mathbf{A}(\mathbf{r},t)$ defined according to (19) and performing integration with respect to time, we obtain

$$a_{fi}^{(1)} = \frac{2Z_A e}{iv}\langle f|\int d^3r e^{\frac{i\omega x}{v}}\left[\rho(\mathbf{r}) - \mathbf{v}\cdot\mathbf{j}(\mathbf{r})\right] \tag{20}$$
$$\times\left[\frac{\omega}{\gamma v}(\hat{\mathbf{b}}\cdot\boldsymbol{\rho})K_1\left(\frac{\omega b}{\gamma v}\right) + K_0\left(\frac{\omega b}{\gamma v}\right)\right]|i\rangle,$$

where $\hat{\mathbf{b}} = \frac{\mathbf{b}}{b}$ and $K_0(x)$ and $K_1(x)$ are the Macdonald functions of the zeroth and the first order, respectively. If we do not go beyond, as before, the approximations specified by Eqs. (16) and (17) and retain, in (20), only terms of order ωr, we obtain

$$a_{fi}^{(1)} = \frac{2Z_A e^2\omega}{iv^2}\langle f|\left[\frac{1}{\gamma}K_1\left(\frac{\omega b}{\gamma v}\right)\sum_i Z_i(\hat{\mathbf{b}}\cdot\boldsymbol{\rho}_i)\right. \tag{21}$$

[2)] Since we consider only an electric dipole transition, we discard terms involving ρ^2.

$$+ i(1-v)K_0\left(\frac{\omega b}{\gamma v}\right)\sum_i Z_i x_i\Bigg]|i\rangle,$$

where the first and the second term represent the contributions of, respectively, the transverse and the longitudinal component of the ion field. It can easily be seen that, for $v \to 1$, the contribution of the longitudinal component tends fast to zero. Taking into account the properties of the Macdonald functions $K_i(x)$ in the limit $x \to 0$, we can easily find that, in the limit $v \to 1$, the amplitude in question reduces to the form (18) and that, at low velocities ($v \ll 1$), we have

$$a_{fi}^{(1)} = \frac{2Z_A e^2\omega}{iv^2}\langle f|\Bigg[K_1\left(\frac{\omega b}{v}\right)\sum_i Z_i(\hat{\mathbf{b}}\cdot\boldsymbol{\rho}_i) + iK_0\left(\frac{\omega b}{v}\right)\sum_i Z_i x_i\Bigg]|i\rangle. \quad (22)$$

This is the well-known expression for the transition amplitude at large impact-parameter values for nonrelativistic collision velocities [9].

For the wave functions describing the initial and final states, we take two-body wave functions, disregarding, in the final state, the nuclear interaction of the breakup fragments since the energy of their relative motion is small. In experimentally studying the Coulomb breakup of a nucleus, the double-differential cross section $d^2\sigma/dE_{bc}/d\Omega_a$ is the quantity that is measured most often. It can be obtained from (1) by performing integration with respect to all directions of the relative momentum $\mathbf{k}_{bc}$. In this case, a transition to the relative coordinates of particles b and c yields the double-differential cross section in the form

$$\frac{d^2\sigma}{dE_{bc}d\Omega_a} = \frac{1}{3}\left[\frac{8\pi Z_A Z_{\text{eff}}e^2\omega}{\gamma v^2 k_{bc}}\right]^2\frac{d\sigma_{\text{R}}}{d\Omega_a} \times \sum_{l_f}(\langle l_f|r|l_i\rangle C_{l_i010}^{l_f0})^2\left[K_1^2\left(\frac{\omega b}{\gamma v}\right) + (1-v)^2\gamma^2 K_0^2\left(\frac{\omega b}{\gamma v}\right)\right]\frac{\mu_{bc}k_{bc}}{(2\pi)^3}, \quad (23)$$

where

$$\langle l_f|r|l_i\rangle = \int_0^\infty dr\varphi_{l_i j_i}(r) r F_{l_f}(k_{bc}r); \quad (24)$$

$Z_{\text{eff}} = \mu_{bc}(Z_b/m_b - Z_c/m_c)$; $C_{l_i010}^{l_f0}$ is a Clebsch–Gordan coefficient; $\varphi_{l_i j_i}(r)$ is the radial wave function for nucleus a; l_i and j_i are, respectively, the orbital angular and the total momentum of nucleus c moving in the field of nucleus b; and $F_l(x)$ is the regular Coulomb function.

For the relativistic and nonrelativistic cases, the Rutherford cross sections for the Coulomb scattering at small scattering angles are given by the same expression

$$\frac{d\sigma_{\text{R}}}{d\Omega_a} = 4\left(\frac{\eta_a}{k_a}\right)^2\frac{1}{\theta^4}, \quad (25)$$

where $\eta_a = \dfrac{Z_A Z_a e^2}{v}$ is the Coulomb parameter, k_a is the momentum of nucleus a with respect to ion A, and θ is the scattering angle.

Upon integrating the cross section (23) with respect to angles within the limits that are determined by a specific experiment, we obtain the cross section as a function of the relative energy of diverging fragments. The result is

$$\frac{d\sigma}{dE_{bc}} = \frac{\pi}{3}\left[\frac{8\pi Z_A Z_{\text{eff}}e^2\omega}{\gamma v^2 k_{bc}}\right]^2\sum_{l_f}(\langle l_f|r|l_i\rangle C_{l_i010}^{l_f0})^2 \times \left[F_1(b_1,b_2) - (1-v)^2\gamma^2 F_0(b_1,b_2)\right]\frac{\mu_{bc}k_{bc}}{(2\pi)^3}, \quad (26)$$

where

$$F_0(b_1,b_2) = b_1^2\left[K_1^2\left(\frac{\omega b_1}{\gamma v}\right) - K_0^2\left(\frac{\omega b_1}{\gamma v}\right)\right] - b_2^2\left[K_1^2\left(\frac{\omega b_2}{\gamma v}\right) - K_0^2\left(\frac{\omega b_2}{\gamma v}\right)\right], \quad (27)$$

$$F_1(b_1,b_2) = b_1^2\left[K_0\left(\frac{\omega b_1}{\gamma v}\right)K_2\left(\frac{\omega b_1}{\gamma v}\right) - K_1^2\left(\frac{\omega b_1}{\gamma v}\right)\right] - b_2^2\left[K_0\left(\frac{\omega b_2}{\gamma v}\right)K_2\left(\frac{\omega b_2}{\gamma v}\right) - K_1^2\left(\frac{\omega b_2}{\gamma v}\right)\right]. \quad (28)$$

The limiting values of the impact parameter can be expressed in terms of the relevant angles, b_1 (b_2) corresponding to the maximum (minimum) value of the scattering angle θ. For $b \to \infty$, which corresponds to $\theta \to 0$, the contributions of the second terms in (27) and (28) tend to zero, and this is the adiabatic limit. We note that the minimum value of the impact parameter cannot be less than the radius of colliding nuclei—otherwise, it is necessary to take into account nuclear interaction in addition to Coulomb interaction.

3. BREAKUP OF A ^{8}B NUCLEUS ON A ^{208}Pb ION

The radiative-capture reaction $^7\text{Be}(p,\gamma)^8\text{B}$ has a direct bearing on the solar-neutrino problem. Therefore, a determination of the astrophysical S factor is

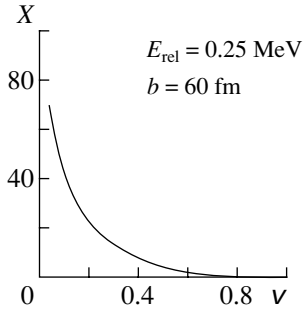

Fig. 1. Fraction (in percent) of the contribution of the longitudinal component of the field of a ^{208}Pb ion to the cross section for the Coulomb breakup reaction $^{208}\mathrm{Pb}(^{8}\mathrm{B}, ^{7}\mathrm{Be}\,p)^{208}\mathrm{Pb}$ as a function of the collision velocity.

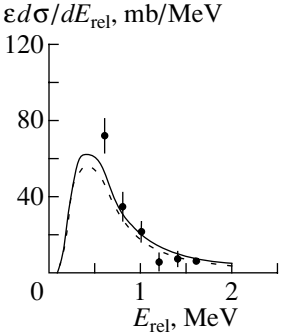

Fig. 2. Cross section for the Coulomb breakup reaction $^{8}\mathrm{B} + {}^{208}\mathrm{Pb} \to {}^{7}\mathrm{Be} + p + {}^{208}\mathrm{Pb}$ as a function of the relative energy of the fragments at the collision energy 46.5 MeV per nucleon (ε is the efficiency of an experiment): (solid curve) results of the relativistic calculations and (dashed curve) results of the nonrelativistic calculations. The displayed experimental data were borrowed from [10].

a problem of paramount importance. Investigation of the Coulomb breakup reaction $^{208}\mathrm{Pb}(^{8}\mathrm{B}, ^{7}\mathrm{Be}\,p)^{208}\mathrm{Pb}$ provides one way to find it. Experiments studying the Coulomb breakup of ^{8}B nuclei on ^{208}Pb were performed at the collision energies of $E(^{8}\mathrm{B}) = 46.5$, 51.9, and 254 MeV per nucleon (see [10], [11], and [12], respectively). As was indicated in the Introduction, the higher the collision energy, the more reliable the extracted values of the astrophysical factor.

The ^{8}B nucleus has one loosely bound state of binding energy $\varepsilon = -137$ MeV and a few resonances. Of these, one occurs in the vicinity of the breakup threshold, having an energy of $\varepsilon = 0.63$ MeV and a width of $\Gamma = 37$ keV [13]. Investigations of proton scattering on a ^{7}Be nucleus revealed that the phase shifts for potential scattering are virtually equal to zero up to an energy of 2 MeV. In calculating the cross section for the Coulomb breakup at low energies of the relative motion of the proton and ^{7}Be nucleus involved, Coulomb functions were therefore used for final-state wave functions. In the theoretical studies reported in [14, 15], it was shown that electric quadrupole transitions make a much smaller contribution to the breakup cross section than the relevant electric dipole transition. The experimental measurements performed in [11, 16] yielded a nearly zero value for the contribution of quadrupole transitions to the cross section for the ^{8}B breakup at energies of the relative motion of the proton and the ^{7}Be nucleus that are less than 1.75 MeV. For this reason, we took into account only the electric dipole transition.

For the nuclear potential simulating the p^{7}Be interaction, we took the Woods–Saxon potential supplemented with a spin–orbit component; that is,

$$V(r) = \left[V_0 - V_{ls}(\mathbf{L}\cdot\mathbf{S})\frac{1}{m_\pi^2 r}\frac{d}{dr}\right] \qquad (29)$$

$$\times \left[1 + \exp\left(\frac{r-R}{a}\right)\right]^{-1},$$

where m_π is the pion mass. The parameters were determined in such a way as to reproduce the energy of the ^{8}B ground state and the resonance at $\varepsilon = 0.63$ MeV; this yielded the following values: $V_0 = -45.693$ MeV, $V_{ls} = -3.202$ MeV, $R = 2.391$ fm, and $a = 0.65$ fm. A similar potential, but with different parameter values, was used in [14]. The radial wave function found for the bound state by solving the Schrödinger equation for the relative motion of the proton and the ^{7}Be nucleus asymptotically goes over to the Whittaker function at a distance of $r = 4$ fm. Since ^{8}B is a loosely bound nucleus, the evaluation of the overlap integral (24) amounted to performing integration up to 300 fm in order to achieve convergence. We also note that, since the ^{8}B nucleus is loosely bound, the main contribution to the overlap integral comes from the asymptotic part of the radial wave function for the bound state of the nucleus.

The cross sections were calculated both for relativistic and for nonrelativistic kinematics. Figure 1 gives the ratio

$$X = (1-v)^2\gamma^2\frac{K_0^2\left(\dfrac{\omega b}{\gamma v}\right)}{K_1^2\left(\dfrac{\omega b}{\gamma v}\right)}, \qquad (30)$$

which specifies the fraction of the contribution of the longitudinal component of the field of a ^{208}Pb ion to the cross section as a function of the collision velocity. One can see from Fig. 1 that this fraction decreases fast with increasing collision velocity, becoming less

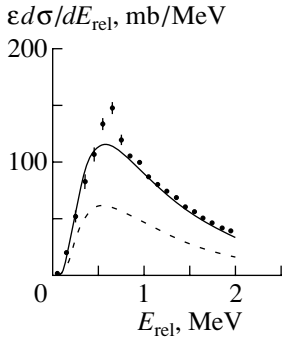

Fig. 3. As in Fig. 2, but at the collision energy of 254 MeV per nucleon. The displayed experimental data were borrowed from [12].

than 20% at collision velocities equal to and above 25% of the speed of light.

In [10], the astrophysical-factor value at zero energy was extracted from the cross section $d\sigma/dE_{\rm rel}$ that was obtained by integrating the double differential cross section with respect to the angle over the interval 2°–6°. We have also integrated the double differential cross section $d^2\sigma/dE_{\rm rel}d\Omega_8$ ($E_{\rm rel} = E_{^7{\rm Be}\,p}$, $d\Omega_8 = d\Omega_{^8{\rm B}}$) over the same interval. The result is presented in Fig. 2. From this figure, we can see that our results describe fairly well experimental data everywhere, with the exception of the energy region around 0.6 MeV, where there is a resonance; therefore, it is necessary to take additionally into account there the relevant magnetic dipole transition. One can also see from Fig. 2 that the calculations on the basis of relativistic kinematics give cross-section values that exceed their counterparts obtained by using nonrelativistic kinematics. It should be noted that a moderate change in the lower limit of integration with respect to the scattering angle leads to a significant change in the impact parameter, and this enables us to reproduce the experimental value of the cross section even within nonrelativistic kinematics. At high collision energies, however, no agreement with experimental data can be achieved by using nonrelativistic kinematics. This is confirmed by the results of our calculations performed at the collision energy of $E = 254$ MeV per nucleon. Figure 3 demonstrates that the electric dipole transition makes it possible to reproduce, to a very high degree of precision, the energy dependence of the cross section for the Coulomb breakup of a ^{8}B nucleus everywhere, as before, with the exception of the resonance region. The nonrelativistic calculations underestimate the cross section in question considerably, the distinction between the results obtained on the basis of relativistic and nonrelativistic kinematics becoming more pronounced with increasing collision energy.

Summarizing the results of the present study, we can draw the following conclusions:

(i) At high energies of a collision between a light nucleus and a heavy ion, one can use semiclassical theory.

(ii) Calculations within relativistic kinematics are not more involved than calculations within the nonrelativistic approximation.

(iii) Allowances for a quadrupole and for a magnetic dipole transition do not present serious difficulties, and we will take such transitions into account in the future.

ACKNOWLEDGMENTS

B.F. Irgaziev is grateful to V.I. Matveev for discussions that concerned the applicability of an exact solution of the Dirac equation to problems associated with ionization and the production of an electron–positron pair in the field of an ultrarelativistic ion and which stimulated this study.

REFERENCES

1. J. M. Eisenberg and W. Greiner, *Excitation Mechanisms of the Nucleus* (North-Holland, Amsterdam, 1970; Atomizdat, Moscow, 1973).
2. C. A. Bertulani and G. Baur, Phys. Rep. **163**, 299 (1988).
3. T. Tokimoto *et al.*, Phys. Rev. C **63**, 035801 (2001).
4. S. Typel and G. Baur, Phys. Rev. C **50**, 2104 (1994).
5. E. O. Alt, B. F. Irgaziev, A. T. Muminov, and A. M. Mukhamedzhanov, Yad. Fiz. **58**, 1967 (1995) [Phys. At. Nucl. **58**, 1860 (1995)].
6. A. Winther and K. Adler, Nucl. Phys. A **319**, 518 (1979).
7. A. J. Baltz, Phys. Rev. A **52**, 4970 (1995).
8. A. J. Baltz, Phys. Rev. Lett. **78**, 1231 (1997).
9. B. M. Smirnov, *Physics of Weakly Ionized Gases* (Nauka, Moscow, 1978; Mir, Moscow, 1978).
10. T. Motobayashi *et al.*, Phys. Rev. Lett. **73**, 2680 (1994).
11. T. Kikuchi *et al.*, Eur. Phys. J. A **3**, 213 (1998).
12. N. Iwasa *et al.*, Phys. Rev. Lett. **83**, 2910 (1999).
13. F. Ajzenberg-Selove, Nucl. Phys. A **490**, 1 (1988).
14. C. A. Bertulani, Z. Phys. A **356**, 293 (1996).
15. C. A. Bertulani and G. Moshe, Nucl. Phys. A **636**, 227 (1998).
16. T. Kikuchi *et al.*, Phys. Lett. B **391**, 261 (1997).

Translated by A. Isaakyan

Physics of Atomic Nuclei, Vol. 66, No. 4, 2003, pp. 690–699. Translated from Yadernaya Fizika, Vol. 66, No. 4, 2003, pp. 719–728.

ELEMENTARY PARTICLES AND FIELDS
Experiment

Measurement of the Differential Cross Section and of the Tensor and Vector Analyzing Powers for the Fragmentation of 4.5-GeV/c Deuterons on Beryllium in the Reaction Involving Proton Emission at an Angle of 80 mrad

L. S. Azhgirey*, V. V. Arkhipov, S. V. Afanasiev, V. K. Bondarev, V. N. Zhmyrov, L. S. Zolin, V. I. Ivanov, A. Yu. Isupov, A. A. Kartamyshev, V. A. Kashirin, V. I. Kolesnikov, V. A. Kuznetsov, V. P. Ladygin, N. B. Ladygina, A. G. Litvinenko, S. G. Reznikov, P. A. Rukoyatkin, A. Yu. Semenov, I. A. Semenova, G. D. Stoletov, G. Filipov[1)], A. N. Khrenov, and N. P. Yudin[2)]

Joint Institute for Nuclear Research, Dubna, Moscow oblast, 141980 Russia

Received January 24, 2002; in final form, April 29, 2002

Abstract—The invariant differential cross section, the tensor analyzing power A_{yy}, and the vector analyzing power A_y for the reaction $^9\mathrm{Be}(d,p)X$ are measured at an initial deuteron momentum of 4.5 GeV/c and a proton detection angle of about 80 mrad. The data obtained for the differential cross section are consistent with the results of measurements at 3.5 and 5.78 GeV/c and a proton emission angle of 2.5°. The values found for the tensor analyzing power A_{yy} are compared with similar data obtained previously for the deuteron-fragmentation process occurring on a carbon target at various values of the initial deuteron momentum and leading to proton emission at zero angle. The data on the differential cross section for the reaction $^9\mathrm{Be}(d,p)X$ can be satisfactorily described within the relativistic impulse approximation by using standard deuteron wave functions; however, the approach based on this conceptual framework proves to be inadequate in dealing with data on the tensor analyzing power. These results indicate that it is necessary either to change the method for describing the relativistic deuteron or to take into account additional mechanisms. © *2003 MAIK "Nauka/Interperiodica"*.

1. INTRODUCTION

In recent years, $A(d,p)X$ reactions at relativistic deuteron energies have been considered as an important source of information about the structure of the deuteron at short internucleon distances. Although the deuteron is strictly speaking described by a large number of form factors even in the impulse approximation (pole diagram in the t channel), the first experiments were able to impose stringent constraints on the search for ways to describe the structure of the deuteron. It turned out that, at rather high momenta of internal motion, invariant differential cross sections for inclusive $A(d,p)X$ reactions correlate well with the deuteron wave function, where the momentum k used as a kinematical variable of light-front dynamics [1] appears as an argument. This initiated a series of studies devoted to exploring experimentally the fragmentation of relativistic deuterons and to interpreting data obtained in this way within light-front dynamics.

Until recently, measurements of the invariant differential cross sections for the process where deuteron fragmentation on nuclei leads to the emission of a proton detected at zero angle with respect to the momentum of the deuteron incident on the target were the main source of information about $A(d,p)X$ reactions [2–5]. As a further development of such studies, the differential cross sections for deuteron fragmentation on nuclei were measured for the case where the emitted proton had high transverse momenta [6]. It turned out that data obtained in such experiments are satisfactorily described on the basis of the relativistic hard-scattering model [7, 8] employing the deuteron wave function for the Paris po-

[1)]Institute for Nuclear Research and Nuclear Energy, Blvd. Tsarigradsko chaussee 72, BG-1784 Sofia, Bulgaria, and Joint Institute for Nuclear Research, Dubna, Moscow oblast, 141980 Russia.

[2)]Moscow State University, Vorob'evy gory, Moscow, 119899 Russia, and Joint Institute for Nuclear Research, Dubna, Moscow oblast, 141980 Russia.

*e-mail: azhgirey@cv.jinr.ru

tential [9], provided that the momentum k, a kinematical variable for light-front dynamics (see above), is taken for an argument. Within this model, the main contribution to the yield of protons at nonzero angles with respect to the incident-deuteron momentum comes from direct deuteron fragmentation and from the scattering of a deuteron nucleon on a target nucleon, the contribution of the rescattering and virtual-pion-production mechanisms being insignificant. We note from the outset that the inclusive features of deuteron-fragmentation reactions depend only slightly on the target-nucleus species, especially at high momenta of secondary protons, and are similar to corresponding data on deuteron–proton interactions [6].

Measurement of the spin properties of $A(d,p)X$ reactions was an important advancement. Cross sections and momentum spectra are determined by the squares of partial-wave amplitudes, while spin observables are controlled by the interference between different amplitudes and are similar to optical interference effects. It is therefore clear that an interpretation of such experiments will specify a new and much more detailed level of our understanding of reaction dynamics and of the structure of the deuteron.

Experimental data on the tensor analyzing power T_{20} for deuteron fragmentation occurring on nuclei and involving proton emission at zero angle [4, 10–12] have so far been obtained up to a value of $k \sim 1$ GeV/c. These data demonstrate that there is virtually no dependence on the initial deuteron energy or on the mass number of the target nucleus, as this must be in the relativistic impulse approximation. In contrast to what occurs in the impulse approximation, however, the quantity T_{20} does not reach a value of $-\sqrt{2}$ at $k \sim 300$ MeV/c, retaining a negative value of about -0.3 at high internal momentum of the proton [11, 12]. The inclusion of mechanisms beyond the impulse approximation that are associated with the relativistic character of additional components in the deuteron wave function [13–15] does not lead to a substantial improvement in the description of experimental data. Only in [16] could reasonable agreement with experimental data be attained within the relativistic impulse approximation by taking into account multiple scattering and the contribution of six-quark configurations in the deuteron.

In [17], it was indicated that, in the case where protons originating from relativistic-deuteron-fragmentation reactions are recorded at nonzero angles, spin observables may prove to be more sensitive, owing to sizable transverse momenta of emitted protons, to the short-distance structure of the deuteron than the results of measurements at zero angle, and this was the motivation for measuring the differential cross section, along with the tensor analyzing power A_{yy} and the vector analyzing power A_y, for $^{12}\mathrm{C}(d,p)X$ reactions at a primary deuteron energy of 9 GeV/c that result in proton emission at an angle of 85 mrad [18, 19]. The conditions of those measurements corresponded to the region where the contribution of the direct-fragmentation process was much greater than the contribution of the hard-scattering process [8], so that the data obtained there were related most directly to the structure of the deuteron.

It turned out that, although the differential cross section can be satisfactorily described on the basis of the relativistic hard-collision model [8] employing standard deuteron wave functions from [9, 20], the behavior of the tensor analyzing power A_{yy}, which remains positive up to the highest momentum of recorded protons, is at odds with the predictions of this model [17]. The sign of A_{yy} appeared to be identical to its sign in the data obtained at zero angle [11, 12], the absolute values being approximately one-half as great as those in the zero-emission-angle case. (We recall that, at zero angle, the relation $A_{yy} = -T_{20}/\sqrt{2}$ holds.)

The observed transverse-momentum dependence of A_{yy} indicates that the usual impulse approximation is insufficient for describing the structure of the deuteron at high values of internal momenta. It is necessary either to consider new physical mechanisms of the reaction or to change the method for describing the relativistic deuteron in a radical way.

That a comparison of experimental results obtained for deuteron fragmentation in the cases where secondary protons were emitted at angles of 0° [11, 12] and 85 mrad [18, 19] furnished evidence for the dependence of the parameter A_{yy} in this process on their transverse momenta was a motivation for performing experiments aimed at obtaining data for transverse-momentum values not considered previously.

In this article, we describe the results of new measurements of the invariant differential cross section, the vector analyzing power A_y, and the tensor analyzing power A_{yy} for the fragmentation of 4.5-GeV/c deuterons on a beryllium target via the inclusive reaction $^{9}\mathrm{Be}(d,p)X$ leading to the emission of secondary protons at an angle of about 80 mrad in the laboratory frame, the range of proton transverse momenta under study extending from 220 to 300 MeV/c.

2. DESCRIPTION OF THE EXPERIMENT

The present experiment, performed with the aid of the SFERA facility [18, 19, 21], employed a polarized deuteron beam extracted from the synchrophasotron installed at the Joint Institute for Nuclear Research (JINR, Dubna). For the details of the experimental

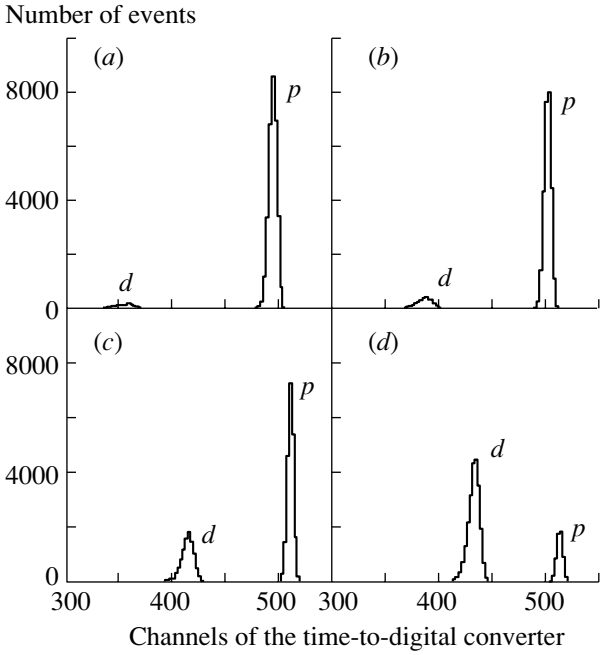

Fig. 1. Time-of-flight spectra obtained at various current settings in the magnetic elements of the experimental equipment. The momenta of the secondaries are (*a*) 2.75, (*b*) 3.0, (*c*) 3.3, and (*d*) 3.6 GeV/*c*.

procedure and for the results of measurements of the tensor analyzing power A_{yy} for inelastic deuteron scattering on beryllium at an angle of about 80 mrad, the interested reader is referred to [21]. Here, we will only give a brief account of the main features of our experimental procedure.

Polarized deuterons were produced by the POLARIS ion source [22]. The sign of beam polarization was changed in a regular way from one accelerator pulse to another in the following order: 0, −, +; here, 0 means the absence of polarization, while + and − correspond to the sign of p_{zz}, the quantization axis being orthogonal to a plane that contains the trajectory of the beam in the accelerator. The tensor polarization of the beam was measured at regular time intervals during the experiment by recording protons of momentum $p_p \sim (2/3)p_d$ that were emitted at zero angle in the reaction $A(d,p)X$ [23]. The tensor-polarization values averaged over the entire run of the experiment were $p_{zz}^{+} = 0.798 \pm 0.002(\text{stat.}) \pm 0.040(\text{syst.})$ and $p_{zz}^{-} = -0.803 \pm 0.002(\text{stat.}) \pm 0.040(\text{syst.})$ for, respectively, the + and the − spin state of the beam.

The vector polarization of the beam was monitored throughout the experiment by measuring the asymmetry of elastic proton–proton scattering in a thin polyethylene target placed in the beam upstream of the beryllium target at a distance of about 20 m from it [24]. The vector polarization was evaluated on the basis of the results obtained by measuring the asymmetry in the scattering of 4.5-GeV/c protons at an angle of 8°. The effective analyzing power $A(CH_2)$ of the polarimeter was taken to be 0.146 ± 0.007 [25]. The values of the vector polarization of the beam were $p_z^{+} = 0.231 \pm 0.014(\text{stat.}) \pm 0.012(\text{syst.})$ and $p_z^{-} = 0.242 \pm 0.014(\text{stat.}) \pm 0.012(\text{syst.})$.

A tensorially polarized deuteron beam of momentum 4.5 GeV/c, duration 0.5 s, and intensity 5×10^8 particles per accelerator spill was incident on a 20-cm-thick beryllium target. The intensity of the beam was monitored by an ionization chamber positioned upstream of the target. In each accelerator spill, the positions of the beam and its profiles in specific sections of the ion guide were checked by the profilemeters of the slow-extraction system. The dimensions of the beam at the target location were $\sigma_x \sim 0.4$ cm and $\sigma_y \sim 0.9$ cm in the horizontal and the vertical direction, respectively.

Experimental data were obtained at five values of the secondary-particle momentum in the range between 2.5 and 3.6 GeV/c. Secondaries emitted from the target at an angle of about 80 mrad were transported to the recording equipment by means of magnetic elements.

The recorded particles were identified via an offline analysis on the basis of information from two independent measurements of the time of flight over the base of length about 34 m. The resolution in the time of flight was better than 0.2 ns (1σ). The background from inelastically scattered deuterons was negligible at 2.5 GeV/c, but it increased with increasing momentum of secondaries. The time-of-flight spectra obtained at 2.75, 3.0, 3.3, and 3.6 GeV/c are displayed in Fig. 1. These spectra demonstrate a good separation of secondary protons and deuterons. In data processing, only those events were selected for which at least two of the measured time-of-flight spectra were correlated. This made it possible to eliminate the background from deuterons completely.

In order to determine the invariant differential cross section for proton emission at an angle of 80 mrad in the reaction $^9\text{Be}(d,p)X$ induced by 4.5-GeV/c deuterons, a special measurement was performed in our experiment in order to determine the yield of 6-GeV/c protons at zero angle from the fragmentation of 9-GeV/c deuterons on a carbon target. For the reaction $^9\text{Be}(d,p)X$, the calibration constant C_{cal} was found from a comparison of the result of that measurement with data on the absolute values of the differential cross section for the reaction

Invariant differential cross section $\sigma_{\text{inv}} = Ed^2\sigma/(p^2dpd\Omega)$, tensor analyzing power A_{yy}, and vector analyzing power A_y for the reaction $^9\text{Be}(d,p)X$ at a primary deuteron momentum of 4.465 GeV/c and a proton emission angle of 80 mrad

p, GeV/c	Δp (FWHM), GeV/c	x	p_T, GeV/c	$(\sigma \pm d\sigma)_{\text{inv}}$, GeV mb (GeV/$c$)$^{-3}$ sr^{-1}	$A_{yy} \pm dA_{yy}$	$A_y \pm dA_y$
2.523	0.130	0.558	0.222	93.1 ± 2.6	0.069 ± 0.076	0.166 ± 0.086
2.775	0.135	0.611	0.239	14.7 ± 0.5	0.326 ± 0.093	0.232 ± 0.105
3.015	0.149	0.661	0.258	5.34 ± 0.13	0.379 ± 0.063	0.099 ± 0.070
3.312	0.168	0.723	0.283	2.80 ± 0.07	0.427 ± 0.059	0.083 ± 0.067
3.596	0.172	0.783	0.300	0.719 ± 0.021	0.389 ± 0.076	0.135 ± 0.085

Note: Here, p is the proton momentum in the laboratory frame, Δp is the full width at half maximum (FWHM) of the momentum distribution of recorded protons, x is the deuteron-longitudinal-momentum fraction carried away by the proton in the infinite-momentum frame [1], and p_T is the transverse momentum of the proton. The values of p, Δp, x, and p_T were obtained by means of a Monte Carlo simulation. The quoted errors are purely statistical.

$^{12}\text{C}(d,p)X$ induced by 9.1-GeV/c deuterons that involves the emission of protons at zero angle [2, 5]:

$$E\frac{d^2\sigma}{p^2dpd\Omega} = C_{\text{cal}}\bar{E}\frac{n^0}{\bar{p}^2\Delta p\Delta\Omega}\frac{1}{\rho L N_{\text{A}}}. \qquad (1)$$

Here, $Ed^2\sigma/(p^2dpd\Omega)$ is the invariant differential cross section obtained in [2, 5]; n^0 is a value that is obtained, upon performing a normalization to the number of monitor counts and introducing a correction for the dead-time effect [26], for the number of protons recorded in the calibration experiment; $\Delta p\Delta\Omega$ is the acceptance of the facility used; $\bar{p}$ and $\bar{E} = \sqrt{\bar{p}^2 + m_p^2}$ are the mean values of the proton momentum and energy, respectively; ρ and L are the target density and thickness, respectively; and N_{A} is Avogadro's number. The thickness of the carbon target in the calibration experiment was 27.2 g/cm^2.

The angular and momentum acceptances of the facility were determined on the basis of a Monte Carlo simulation with allowance for the parameters of the incident deuteron beam; nuclear interactions and multiple scattering in the target, air, windows, and the detectors used; the energy losses of primary and secondary deuterons; and so on. As a result, the polar-angle and momentum acceptances proved to be (FWHM) ± 8 mrad and $\Delta p/p \sim \pm 2\%$, respectively.

It should be noted that the data in [2] and [5] on the differential cross section for the reaction $^{12}\text{C}(d,p)X$ at a proton momentum of about 6 GeV/c differ by approximately 30%. This distinction is due to the methodological reasons explained in [27]. In order to determine the calibration constant C_{cal}, we used data from [5]. The reference invariant differential cross section was set to 38.2 ± 0.8 GeV mb (GeV/c)$^{-3}$ sr^{-1}, with the result for C_{cal} being 14.0 ± 1.7.

For a beryllium target of thickness 20 cm, the invariant differential cross section for the reaction $^9\text{Be}(d,p)X$ was evaluated on the basis of relation (1) with the aid of the value found for C_{cal} and other input data, including the results of the Monte Carlo simulation of the acceptance. Target-free measurements were performed for secondaries of momentum 4.0 GeV/c. The ratio of the deuteron yield in the target-free measurements to that in the measurement with a beryllium target was less than 1%.

The tensor analyzing power A_{yy} and the vector analyzing power A_y were computed on the basis of the numbers n^+, n^-, and n^0 of deuterons recorded for the different polarization states of the beam, these numbers being rescaled to the same beam intensity and corrected for the dead-time effect [26], by using the expressions

$$A_{yy} = 2\frac{p_z^-(n^+/n^0 - 1) - p_z^+(n^-/n^0 - 1)}{p_z^- p_{zz}^+ - p_z^+ p_{zz}^-}, \qquad (2)$$

$$A_y = -\frac{2}{3}\frac{p_{zz}^-(n^+/n^0 - 1) - p_{zz}^+(n^-/n^0 - 1)}{p_z^- p_{zz}^+ - p_z^+ p_{zz}^-}.$$

These expressions take into account the different values of polarization for different spin states of the beam and become much simpler in form at $p_z^+ = p_z^-$ and $p_{zz}^+ = p_{zz}^-$.

Our present data on the invariant differential cross section, the tensor analyzing power A_{yy}, and the vector analyzing power A_y for inelastic deuteron scattering on beryllium are compiled in the table. The

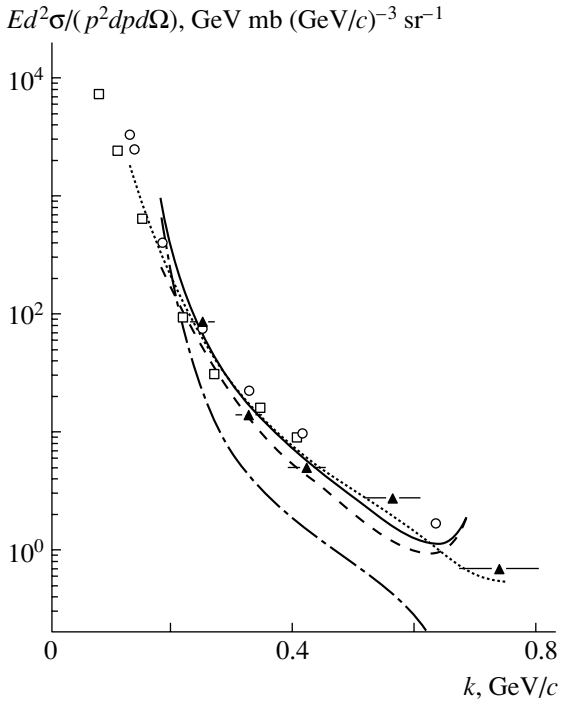

Fig. 2. Invariant differential cross section for the reaction $^9\mathrm{Be}(d,p)X$ as a function of the internal nucleon momentum k in the deuteron (experimental points and theoretical curves): (closed triangles) data of the present experiment at the initial deuteron momentum of 4.5 GeV/c and a proton emission angle of 80 mrad, [open boxes (circles)] data from [28] at a primary momentum of 3.5 (5.78) GeV/c and a proton emission angle of 2.5°, (solid curve) results of the calculation within the hard-collision model [8] with the deuteron wave function for the Paris potential [9], (dash-dotted curve) contribution of hard scattering, (dashed curve) contribution of direct fragmentation, and (dotted curve) results of the calculation at an initial deuteron momentum of 5.78 GeV/c and a proton emission angle of 2.5°.

quoted errors are purely statistical. The systematic errors amount to 20, 5, and 8% for the differential cross section, A_{yy}, and A_y, respectively.

The values presented in the table for the secondary-deuteron momentum p, the momentum acceptance Δp, the transverse momentum p_T, and the deuteron-longitudinal-momentum fraction x carried away by the recorded proton in the infinite-momentum frame were obtained via a Monte Carlo simulation. We note that, because of taking into account effects associated with nuclear and multiple scattering, the p_T values quoted in the table differ from those that would emerge from a calculation by the formula $p_T = p\sin\theta$ ($\theta = 80$ mrad). With allowance for energy losses in the target, the mean value of the primary momentum of the deuteron that would hit the midpoint of the target was 4.465 GeV/c.

3. RESULTS

The resulting values of the invariant differential cross section for proton emission in the reaction $^9\mathrm{Be}(d,p)X$ at an angle of 80 mrad are displayed in Fig. 2 (closed triangles), along with analogous data obtained at 3.5 and 5.78 GeV/c for a proton emission angle of 2.5° [28] (open boxes and circles, respectively). These results are plotted versus the intrinsic deuteron-nucleon momentum k defined within light-front dynamics as [1]

$$k^2 = \frac{m_p^2 + p_T^2}{4x(1-x)} - m_p^2, \qquad (3)$$

where m_p and p_T are respectively, the mass and the transverse momentum of the recorded proton. The variable x is the deuteron-longitudinal-momentum fraction carried away by the proton in the infinite-momentum frame; that is,

$$x = \frac{E_p + p_L}{E_d + P_d}, \qquad (4)$$

where E_p and p_L are, respectively, the energy and the momentum of the recorded proton, while E_d and P_d are those of the incident deuteron.

The invariant differential cross section for proton emission in the reaction $^9\mathrm{Be}(d,p)X$ was calculated on the basis of the hard-collision model [8] with the deuteron wave function for the Paris potential [9]. In Fig. 2, the dash-dotted, the dashed, and the solid curve represent, respectively, the contribution of hard scattering, the contribution of direct fragmentation, and the total contribution of the two mechanisms. The computed values were normalized to the experimental results [since the calculations were performed for the reaction $^1\mathrm{H}(d,p)X$], the normalization factor being 2.22. The dotted curve shows the results of the calculation for the initial deuteron momentum of 5.78 GeV/c. From Fig. 2, it can be seen that (i) all three sets of experimental data are in reasonable agreement with one another and with the results of the calculations; (ii) as one approaches the kinematical boundary of the spectrum for 4.5 GeV/c, the calculated curves show an increase in the cross section, this being due to final-state interaction; and (iii) under the chosen kinematical conditions, the contribution of direct fragmentation exceeds ever more greatly the contribution of hard scattering as one approaches the upper boundary of the spectrum, the distinction between the two contributions in question at the boundary of the spectrum being as large as one order of magnitude.

In Fig. 3, values obtained in the present experiment for the tensor analyzing power A_{yy} (closed symbols) are displayed versus the recorded-proton momentum. Also shown in this figure are the results of

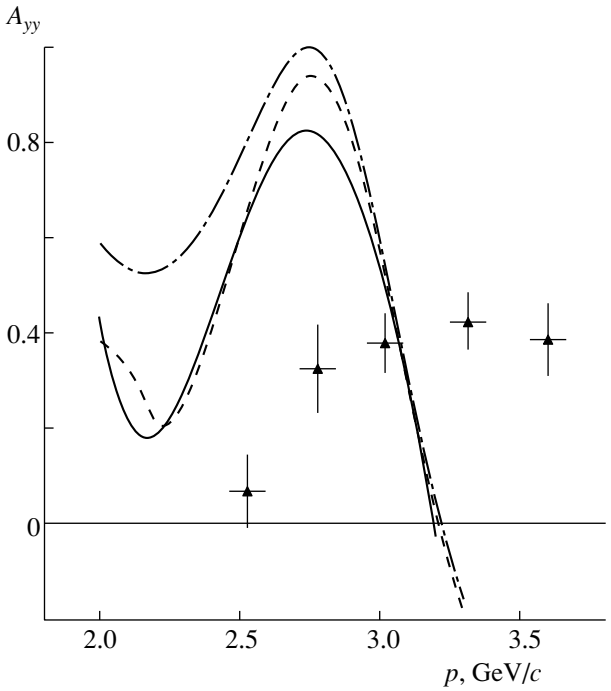

Fig. 3. Tensor analyzing power A_{yy} for the reaction $^9\mathrm{Be}(d,p)X$ at 4.5 GeV/c and a proton emission angle of 80 mrad as a function of the recorded-proton momentum p. Our experimental data are shown by closed triangles. The dash-dotted and the dashed curve represent the results of the calculations for, respectively, the contribution of direct fragmentation alone and the total contribution of direct fragmentation and hard scattering. The solid curve corresponds to the results obtained for the total contribution of the two mechanisms with allowance for the momentum resolution of the experimental facility used.

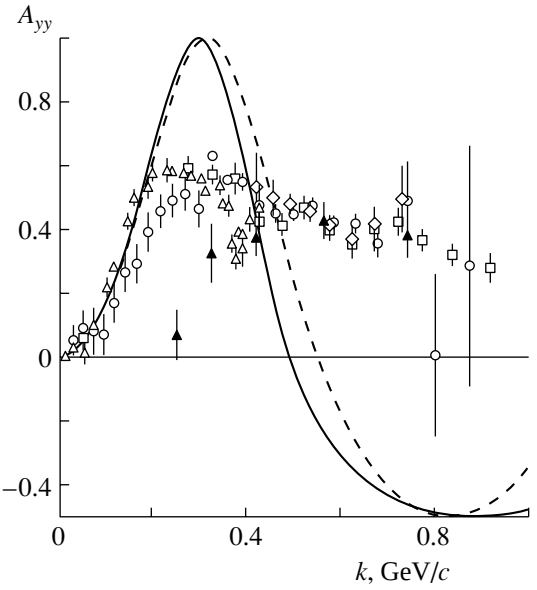

Fig. 4. Tensor analyzing power A_{yy} for deuteron fragmentation as a function of the internal nucleon momentum k (closed triangles) according to our present data obtained for the reaction $^9\mathrm{Be}(d,p)X$ and according to measurements performed for deuteron fragmentation on carbon nuclei for zero proton emission angle at (open triangles) 2.5 GeV/c in [4]; (open circles and boxes) 9 GeV/c in [10] and [11], respectively; and (open diamonds) 4.5 and 5.5 GeV/c in [12]. The solid and the dashed curve represent the results of the calculations where the fragmentation of 9-GeV/c deuterons that is accompanied by proton emission at zero angle is treated in the relativistic impulse approximation with the deuteron wave functions for, respectively, the Paris ([9]) and the Bonn ([20]) potential.

the calculations (curves) based on the hard-collision model [17] that employ the deuteron wave function for the Paris potential [9]. The dash-dotted and the dashed curve represent, respectively, the contribution of hard fragmentation alone and the total contribution of direct fragmentation and hard scattering, while the solid curve corresponds to the total contribution of the two mechanisms in question that was computed with allowance for the momentum resolution of the experimental facility used. It can be seen that the computed values of A_{yy} at the maximum become smaller upon consistently taking into account the contribution of hard scattering and the contribution of the experimental resolution, that the growth of the proton momentum results in that the discrepancy between the theoretical and experimental data becomes more pronounced and that the direct-deuteron-fragmentation process plays an ever increasing role in the formation of the momentum dependence of A_{yy}.

In Fig. 4, the results obtained in the present experiment by measuring the tensor analyzing power A_{yy} (closed symbols) are plotted versus k (closed symbols). Also shown in this figure are data on A_{yy} that were obtained in [4, 10–12] with a carbon target at various values of the primary deuteron momentum between 2.5 and 9 GeV/c for the case where secondary protons are emitted at zero angle (open symbols). In the same figure, the results of the calculations in the relativistic impulse approximation for the direct fragmentation of 9-GeV/c deuterons that is accompanied by proton emission at zero angle are represented by the solid and the dashed curve corresponding to the use of the deuteron wave functions for, respectively, the Paris ([9]) and the Bonn B ([20]) potential in these calculations. For all of the data sets, the values of A_{yy} remain positive over the entire proton-momentum range investigated here; at the same time, the relativistic impulse approximation implemented with standard deuteron wave functions predicts a change in the sign of A_{yy} in the region of k values greater than $\sim$550 MeV/c. It can be seen that, over the region of the momentum k where its values are determined primarily by the longitudinal momenta

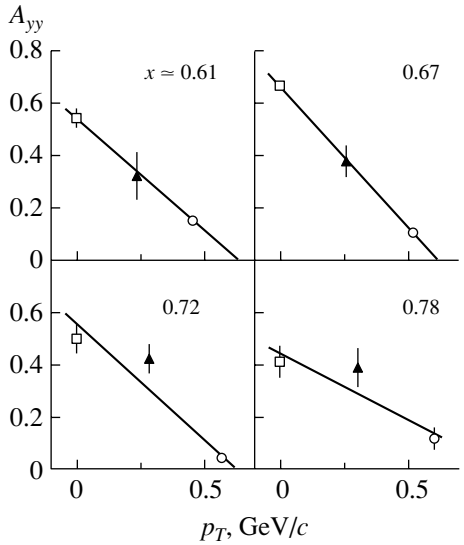

Fig. 5. Tensor analyzing power A_{yy} for deuteron fragmentation on nuclei as a function of the transverse momentum p_T of emitted protons at longitudinal-momentum-fraction (x) values close to 0.61, 0.67, 0.72, and 0.78. Closed triangles represent data of the present experiment. Other data displayed in this figure were obtained in experiments with a carbon target at 9 GeV/c for proton emission angles of (open circles) 85 mrad [18, 19] and (open boxes) 0° [12]. The solid straight lines represent the dependences $A_{yy}(p_T)$ calculated in the linear approximation on the basis of the experimental points.

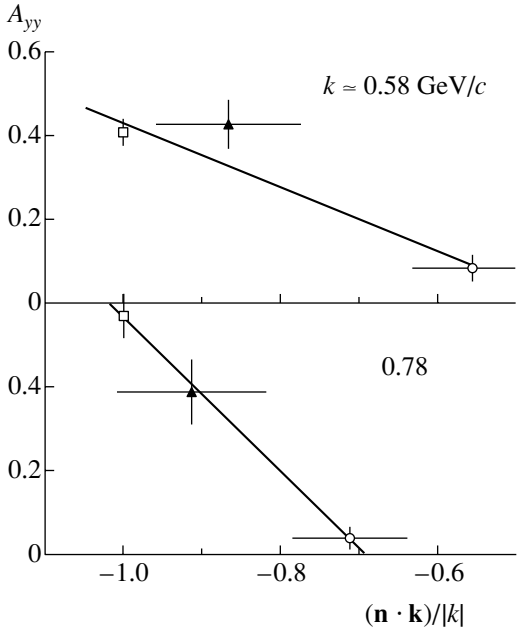

Fig. 6. Tensor analyzing power A_{yy} for deuteron fragmentation on nuclei as a function of the parameter $(\mathbf{n} \cdot \mathbf{k})/|k|$ at k values of about 0.58 and 0.78 GeV/c. Closed triangles represent data of the present experiment. Other data displayed in this figure were obtained in experiments with a carbon target at 9 GeV/c for proton emission angles of (open circles) 85 mrad [18, 19] and (open boxes) 0° [12]. The solid straight lines represent the dependences $A_{yy}((\mathbf{n} \cdot \mathbf{k})/|k|)$ calculated in the linear approximation on the basis of the experimental points.

of secondary protons, the data obtained in the present experiment for the tensor analyzing power are in good agreement with data from [4, 10–12] for zero proton emission angle.

The new data on the tensor analyzing power for the inclusive fragmentation of relativistic deuterons confirm the conclusion drawn previously in [18, 19] that A_{yy} is approximately independent of the deuteron energy; therefore, the internal momentum k proves to be an approximate scaling variable at low p_T. However, a comparison of these data with the results of other measurements performed at various values of p_T and x makes it possible to reveal new interesting regularities.

For four values of the longitudinal-momentum fraction x that occur in the vicinities of 0.61, 0.67, 0.72, and 0.78, Fig. 5 displays the data on the tensor analyzing power A_{yy} versus p_T. In this figure, closed triangles, open circles, and open boxes represent, respectively, the data of the present experiment, data obtained with a carbon target at a primary deuteron momentum of 9 GeV/c and a proton detection angle of 85 mrad [18, 19], and the results of measurements (for carbon as well) reported in [12] for a primary deuteron momentum of 9 GeV/c and zero proton emission angle. The straight solid lines correspond to the dependences $A_{yy}(p_T)$ calculated in the linear approximation on the basis of the experimental points.

It can be seen that the values of the tensor analyzing power A_{yy} that correspond to different values of the longitudinal-momentum fraction x depend greatly on the proton transverse momentum p_T. The quantity A_{yy} has a large positive value at low p_T, but it decreases with increasing transverse momentum, irrespective of x values. At the current accuracy of the measurements, the dependences $A_{yy}(p_T)$ are well approximated by straight lines, but this does not comply with the results obtained in the relativistic impulse approximation [17] with standard deuteron wave functions. It should be noted, however, that, in calculating A_{yy} in [17], some simplifications were made (in particular, the spin-dependent component of the amplitude for nucleon–nucleon scattering was disregarded), which will be removed upon taking into account new experimental data.

In the present study, we only discuss modifications on the impulse approximation without going beyond it. Such modifications can be performed along various lines. One of these consists in considering that the deuteron vertex is specified by eight form

factors, and each of them can affect, to some degree, the features of the reaction being studied. Another line of development takes the origin in the studies reported in [7, 8], and its conceptual framework is the following. The usual impulse approximation employs a deuteron wave function that is represented as a superposition of S and D waves, the dependence on the transverse momentum being determined there by a spherical function describing S and D waves. Within the concept proposed by Blankenbecler *et al.* [7], the description of the deuteron within light-front dynamics is constructed in terms of the structure function

$$G(x,k_T) = \frac{N_0}{2(2\pi)^3} \times \frac{[x(1-x)]^g}{[M^2(x)+k_T^2]^2[1+k_T^2/(\delta^2+M^2(x))]^{(g-1)}}, \quad (5)$$

where

$$M^2(x) = (1-x)\tilde{m}_p^2 + xm_p^2 - x(1-x)m_d^2,$$

with $\tilde{m}_p$, m_n, and m_d being the masses of, respectively, the proton, the neutron, and the deuteron (one of the nucleons is off the mass shell). In particular, a functions of the form in (5) was used to describe the spectrum of protons emitted at an angle of 139 mrad in the interactions of 9-GeV/c deuterons with hydrogen nuclei [29]. A satisfactory description of those data was achieved at the parameter values of $g = 3$, $\delta = 0.6\,(\mathrm{GeV}/c)^2$, and $N_0 = 331.5\,(\mathrm{GeV}/c)^2$. The dependences of the structure function on the longitudinal-momentum fraction x and on the transverse momentum k_T may differ significantly from those in the usual impulse approximation. This new mode of describing the structure of a fast deuteron may set in quite early, even at momentum values slightly in excess of 1 GeV/c per nucleon.

A further development and specification of this concept was due to Karmanov *et al.* [30]. In the approach of these authors, the structure of the deuteron is described in terms of six functions that are dependent on two variables, the momentum k defined within light-front dynamics via Eq. (3) and the quantity $(\mathbf{n}\cdot\mathbf{k})$, the latter being given by

$$(\mathbf{n}\cdot\mathbf{k}) = \sqrt{\frac{m_p^2+p_T^2}{x(1-x)}}\left(\frac{1}{2}-x\right). \quad (6)$$

The vector $\mathbf{n}$ is a unit normal to the light-front surface. The variables x and k_T are unambiguously expressed in terms of k and $(\mathbf{n}\cdot\mathbf{k})$.

It is interesting to trace the dependence of our data on the variable $(\mathbf{n}\cdot\mathbf{k})$. The dependence of the tensor analyzing power A_{yy} on this variable at k values of about 0.58 and 0.78 GeV/c is shown in Fig. 6, where closed triangles represent the data of our experiment, while open circles and boxes stand for data obtained at a primary deuteron momentum of 9 GeV/c for proton emission angles of, respectively, 85 mrad [18, 19] and zero [12]. The solid straight lines correspond to the dependences $A_{yy}((\mathbf{n}\cdot\mathbf{k})/|k|)$ calculated in the linear approximation on the basis of experimental points.

Although the available data are incomplete, it can be seen that, in the values of the tensor analyzing power, there is a trend toward an increase with increasing $(\mathbf{n}\cdot\mathbf{k})/|k|$. In the relativistic impulse approximation implemented with standard deuteron wave functions, there is no dependence of the parameter A_{yy} on the variable $(\mathbf{n}\cdot\mathbf{k})/|k|$. However, such a dependence may appear upon going over to the description of the structure of the deuteron on the basis of concepts similar to those that were developed in [7] or in [30].

The values that were obtained in our experiment for the vector analyzing power A_y fall within the range 0.1–0.15. Being quite modest, they are nevertheless nonvanishing. In view of this, a modification of the impulse-approximation version used here may also consist in taking into account the spin dependence of the amplitude for nucleon–nucleon interaction.

4. CONCLUSIONS

The results of the present study can be summarized as follows:

(i) The invariant differential cross section, the tensor analyzing power A_{yy}, and the vector analyzing power A_y for the reaction $^9\mathrm{Be}(d,p)X$ have been measured at a primary nucleon momentum of 4.5 GeV/c and a proton emission angle of 80 mrad. The measurements cover the range of proton transverse momenta p_T that extends from 220 to 300 MeV/c.

(ii) The measured values of the invariant differential cross section are in reasonably good agreement with data obtained previously at 3.5 and 5.78 GeV/c for a proton emission angle of 2.5° [28], provided that these values are plotted versus the internal nucleon momentum k defined in light-front dynamics. Calculations on the basis of the hard-scattering model with the deuteron wave function for the Paris potential [9] reproduce our experimental data satisfactorily.

(iii) The tensor analyzing power A_{yy} remains positive at all values of the momentum of recorded protons, but this is at odds with the results of the calculations relying on the hard-scattering model and employing standard deuteron wave functions [9, 20]. In the region of k greater than 400 MeV/c, the data on the parameter A_{yy} from the present experiment are in qualitative agreement with similar data obtained in

[4, 10–12] for the case where the emitted protons are recorded at zero angle. Thus, it can be concluded that, in the region where k is determined primarily by the longitudinal momentum of the recorded proton, the parameter A_{yy} depends only slightly on the primary deuteron momentum and on the proton emission angle.

(iv) Data on the tensor analyzing power A_{yy} from the present experiment, along with data obtained at a primary deuteron momentum of 9 GeV/c for zero proton emission angle [10–12, 18] and a proton emission angle of 85 mrad [19], that are plotted versus the proton transverse momentum p_T at fixed values of the variable x (the deuteron-longitudinal-momentum fraction carried away by the proton in the infinite-momentum frame) exhibit a pronounced dependence on p_T. This observation seems to suggest that, at relativistic energies, the deuteron structure function is characterized by a rather sharp dependence on k_T.

(v) That the present experiment has yielded a nonzero tensor analyzing power for the reaction $^9\mathrm{Be}(d,p)X$ is indicative of a significant contribution to the reaction mechanism from the spin-dependent amplitude of nucleon–nucleon interaction.

Thus, the results obtained in this study indicate that there are presently no adequate ideas of what occurs in the deuteron at short distances. In view of the great importance of this issue, it would be highly desirable (in what is concerned with experimental investigations) to perform more detailed measurements of the angular dependence of the tensor analyzing power for $A(d,p)X$ reactions, on one hand, and (in what is concerned with theoretical studies) to examine more closely a transition from a nonrelativistic to a relativistic description—in particular, various dependences of the deuteron wave function on k_L and k_T—and to take into account the contributions of other reaction mechanisms, on the other hand.

ACKNOWLEDGMENTS

We are indebted to A.I. Malakhov, director of the Laboratory of High Energies at JINR, and to V.N. Penev, deputy director of this laboratory, for permanent support of this investigation. We are also grateful to the personnel of the synchrophasotron and the personnel of the POLARIS source for ensuring appropriate experimental conditions. The assistance of L.V. Budkin, V.P. Ershov, V.V. Fimushkin, A.S. Nikiforov, Yu.K. Pilipenko, V.G. Perevozchikov, E.V. Ryzhov, A.I. Shirokov, and O.A. Titov in performing the experiment is gratefully acknowledged. Special thanks are also due to V.A. Karmanov and J. Carbonell, as well as to V.I. Komarov, for stimulating discussions.

This work was supported in part by the Russian Foundation for Basic Research (project nos. 00-02-17691 and 01-02-17299).

REFERENCES

1. P. A. M. Dirac, Rev. Mod. Phys. **21**, 392 (1949); S. Weinberg, Phys. Rev. **150**, 1313 (1966); L. L. Frankfurt and M. I. Strikman, Phys. Rep. **76**, 215 (1981).
2. V. G. Ableev *et al.*, Pis'ma Zh. Éksp. Teor. Fiz. **37**, 196 (1983) [JETP Lett. **37**, 233 (1983)]; V. G. Ableev *et al.*, Nucl. Phys. A **393**, 491 (1983); **411**, 541 (1983).
3. L. Anderson *et al.*, Phys. Rev. C **28**, 1224 (1983).
4. C. F. Perdrisat *et al.*, Phys. Rev. Lett. **59**, 2840 (1987); V. Punjabi *et al.*, Phys. Rev. C **39**, 608 (1989).
5. V. G. Ableev *et al.*, Kratk. Soobshch. OIYaI, No. 1[52]-92, 10 (1992).
6. L. S. Azhgireĭ *et al.*, Yad. Fiz. **46**, 1134 (1987) [Sov. J. Nucl. Phys. **46**, 661 (1987)]; **53**, 1591 (1991) [Sov. J. Nucl. Phys. **53**, 977 (1991)]; L. S. Azhgirey *et al.*, Nucl. Phys. A **528**, 621 (1991).
7. I. A. Schmidt and R. Blankenbecler, Phys. Rev. D **15**, 3321 (1977); Ch.-Y. Wong and R. Blankenbecler, Phys. Rev. C **22**, 2433 (1980); M. Chemtob *et al.*, Nucl. Phys. A **314**, 387 (1979).
8. L. S. Azhgireĭ *et al.*, Yad. Fiz. **48**, 87 (1988) [Sov. J. Nucl. Phys. **48**, 55 (1988)].
9. M. Lacombe, B. Loiseau, R. Vinh Mau, *et al.*, Phys. Rev. C **21**, 861 (1980); Phys. Lett. B **101B**, 139 (1981).
10. V. G. Ableev *et al.*, Pis'ma Zh. Éksp. Teor. Fiz. **47**, 558 (1988) [JETP Lett. **47**, 649 (1988)]; Kratk. Soobshch. OIYaI, No. 4[43]-90, 5 (1990).
11. T. Aono *et al.*, Phys. Rev. Lett. **74**, 4997 (1995).
12. L. S. Azhgirey *et al.*, Phys. Lett. B **387**, 37 (1996).
13. W. W. Buck and F. Gross, Phys. Rev. D **20**, 2361 (1979).
14. M. A. Braun and M. Tokarev, Part. Nucl. **22**, 1237 (1991).
15. L. Kaptari *et al.*, Phys. Lett. B **351**, 400 (1995).
16. A. P. Kobushkin, Phys. Lett. B **421**, 53 (1998).
17. L. S. Azhgirey and N. P. Yudin, Yad. Fiz. **57**, 160 (1994) [Phys. At. Nucl. **57**, 151 (1994)].
18. S. V. Afanasiev *et al.*, Phys. Lett. B **434**, 21 (1998).
19. L. S. Azhgirey, V. V. Arkhipov, S. V. Afanasiev, *et al.*, Yad. Fiz. **62**, 1796 (1999) [Phys. At. Nucl. **62**, 1673 (1999)].
20. R. Machleidt, K. Holinde, and Ch. Elster, Phys. Rep. **149**, 1 (1987).
21. V. P. Ladygin *et al.*, Eur. Phys. J. A **8**, 409 (2000).
22. N. G. Anishchenko *et al.*, in *Proceedings of the 5th International Symposium on High Energy Spin Physics, Brookhaven, 1982*; AIP Conf. Proc. **95**, 445 (1983).
23. L. S. Zolin *et al.*, Kratk. Soobshch. OIYaI, No. 2[88]-98, 27 (1998).
24. L. S. Azhgirey *et al.*, Prib. Tekh. Éksp., No. 1, 51 (1997).

25. L. S. Azhgirey *et al.*, Kratk. Soobshch. OIYaI, No. 3[95]-99, 20 (1999).
26. V. P. Ladygin, Nucl. Instrum. Methods Phys. Res. A **437**, 98 (1999).
27. L. S. Azhgirey, M. A. Ignatenko, and N. P. Yudin, Z. Phys. A **343**, 35 (1992).
28. J. Papp, Ph. D. Thesis, University of California (Berkeley, 1975) (unpublished).
29. L. S. Azhgirey, S. V. Razin, and N. P. Yudin, Yad. Fiz. **46**, 1657 (1987) [Sov. J. Nucl. Phys. **46**, 988 (1987)].
30. V. A. Karmanov and A. V. Smirnov, Nucl. Phys. A **575**, 520 (1994); J. Carbonell and V. A. Karmanov, Nucl. Phys. A **581**, 625 (1994).

Translated by A. Isaakyan

Physics of Atomic Nuclei, Vol. 66, No. 4, 2003, pp. 700–706. Translated from Yadernaya Fizika, Vol. 66, No. 4, 2003, pp. 729–735.

ELEMENTARY PARTICLES AND FIELDS
Experiment

Observation of a New Resonance at 2000 MeV in the K_SK_S System

V. V. Vladimirsky, V. K. Grigor'ev*, I. A. Erofeev, O. N. Erofeeva, A. F. Karelin, Yu. V. Katinov, V. I. Lisin, V. N. Luzin, V. N. Nozdrachev, V. V. Sokolovsky, E. A. Fadeeva, and Yu. P. Shkurenko

Institute of Theoretical and Experimental Physics, Bol'shaya Cheremushkinskaya ul. 25, Moscow, 117259 Russia

Received July 30, 2002

Abstract—This article continues a series of publications devoted to previously unknown narrow resonances in the K_SK_S system that are observed in experimental data coming from the 6-m spectrometer of the Institute of Theoretical and Experimental Physics (ITEP, Moscow). The experimental data on the production of K_S pairs were obtained in π^-p interactions at 40 GeV by using a neutral trigger. In the K_SK_S system, a maximum of width not exceeding 15 MeV is observed at a mass of about 2000 MeV, the statistical significance of this maximum being not less than five standard deviations. With a high degree of reliability, the spin–parity of this structure is $J^P = 4^+$. The observed phenomenon may be interpreted as a resonance whose parameters are equal to the above values. © *2003 MAIK "Nauka/Interperiodica".*

The last two decades of the past century saw considerable advances in the field of hadrons, which are particles that are involved in strong interactions. Of particular interest are so-called exotic mesons—that is, particles whose structure can be inconsistent with the concept of their $q\bar{q}$ content or whose properties differ from those of ordinary mesons. Such particles are referred to as exotic states of the first kind if they are characterized by manifestly exotic values of quantum numbers such as charge Q, strangeness S, and isospin I or exotic states of the second kind if they are characterized by exotic combinations of quantum numbers such as spin S, parity P, and charge parity C. Exotic states of the third kind include mesons whose quantum numbers are consistent with the concept of their $q\bar{q}$ content, but whose properties differ from those of ordinary mesons—for example, those that feature nonstandard branching fractions of decay channels, anomalously small widths, or unusual production mechanisms (see [1, 2] for details).

The present article is devoted to a feature that is observed in the mass spectrum of the K_SK_S system revealed in the region around 2000 MeV. A small width of this resonance feature (not greater than 15 MeV) is a usual property suggesting its affinity with exotic states of the third kind. For usual resonances in this mass region, the expected width is not less than 100 MeV [3].

The experimental data subjected to the present analysis had been accumulated over the period between 1985 and 1990 by using the 6-m spectrometer developed at the Institute of Theoretical and Experimental Physics (ITEP, Moscow) and installed in a 40-GeV π^--meson beam from the U-70 accelerator at the Institute for High Energy Physics (IHEP, Protvino). A liquid-hydrogen target was used in the exposures that provided the data analyzed in this study. The system of two K_S mesons that was recorded under the experimental conditions of the 6-m spectrometer is produced in the following two reactions:

$$\pi^-p \to K_SK_Sn, \quad (1)$$

$$\pi^-p \to K_SK_S + (n + m\pi^0, p + \pi^-, \ldots). \quad (2)$$

Some of the narrow resonances revealed in this system (those at masses of 1450 and 1768 MeV [4, 5]) are produced only in reaction (1), while others (those at masses of 1245, 1520, 1545, and 1786 MeV [5–8]) are produced both in reaction (1) and in reaction (2). The resonance feature studied in this article is observed only in reaction (1).

A detailed description of the 6-m spectrometer is presented in [9, 10]. The spectrometer records, with a high efficiency, K_S mesons going in the forward direction and decaying into two charged π mesons. The large magnetic-field volume filled with track detectors permits a high-precision measurement of the effective mass of the K_SK_S system (within a few MeV). Reaction (1) is separated with a trigger facility based on veto counters surrounding the liquid-hydrogen target. The counters form a double protective layer

*e-mail: grigorvk@vitep1.itep.ru

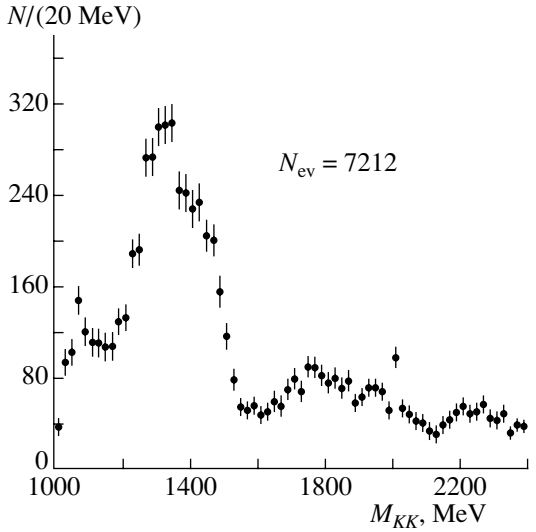

Fig. 1. Effective-mass spectrum of two K_S mesons. Events were selected according to the quality criterion (see main body of the text) and according to the missing mass squared ($0.3 < MM^2 < 1.5$ GeV^2). The latter cut ensures a separation of the reaction involving the production of two K_S mesons accompanied by a neutron.

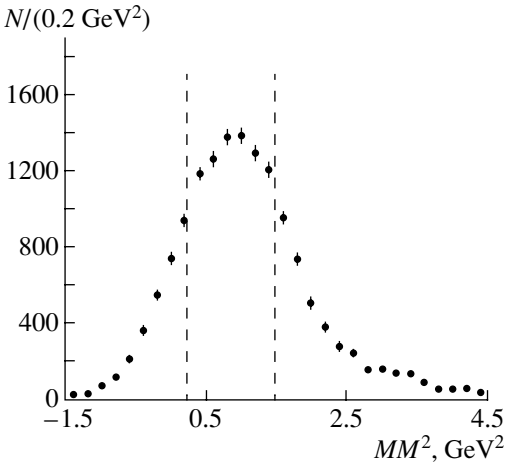

Fig. 2. Distribution of events with respect to the missing mass squared. The boundaries of the cuts imposed to isolate events that are used to construct the distributions are indicated by the dashed lines.

around the target. To suppress events where photons are emitted from the target together with charged particles, lead converters of thickness about two radiation lengths each are arranged between the counters. Because of imperfect trigger operation, some fraction of events of reaction (2) are recorded by the setup.

Product K_S mesons are identified by their decays into a $\pi^+\pi^-$ pair. The recording efficiency is about 40% for the K_SK_S system in the mass region around 2000 MeV and depends on the K_S-meson momenta. The efficiency is determined by the arrangement of the veto counters, which reject, at the trigger level, events where one K_S meson or both of them decay inside the volume surrounded by these counters. The contribution of these events can easily be taken into account. It is more difficult to take into account the efficiency of recording K_S mesons of momenta below 7 GeV in the tracking detector. In this case, the efficiency is calculated by the Monte Carlo method, the accuracy of these calculations being not higher than 20%. However, the fraction of these events is not very large.

The accuracy in measuring the direction of the π-meson momenta is about 0.2 mrad in the spectrometer. The resolution is not less than 10 MeV (FWHM) for the effective mass of the $\pi^+\pi^-$ pair from K_S-meson decay. We note that the estimate of the uncertainty in the effective mass of the K_SK_S system on the basis of the observed K_S-meson width agrees well with the widths of the narrow features revealed earlier at the 6-m spectrometer (see, for example, [5–7]).

In analyzing the K_SK_S system, we used the following kinematical variables: the effective mass M_{KK} of the pair of K_S mesons; the missing mass squared MM^2 defined as the squared mass of particles that are produced together with the K_SK_S system and which are not recorded in the spectrometer; the 4-momentum transfer from the beam to the system being studied, $-t$; the cosine of the Gottfried–Jackson angle, $\cos\theta_{GJ}$; and the Treiman–Yang angle, ϕ_{TY}. The angles are calculated in the rest frame of the pair of K_S mesons, the beam-axis direction in this system being taken for the polar axis. The plane from which the Treiman–Yang angle is reckoned is spanned by the momenta of the beam and of the target proton in this reference frame.

In order to refine particle parameters that affected physically significant quantities (the effective mass and the Gottfried–Jackson and Treiman–Yang angles), the fitting procedure was applied individually to each of the two vees. The following requirements were imposed: the effective mass of the two pions forming a vee had to be equal to the tabular K_S-meson mass, and their tracks had to intersect (at a single point). The implementation of the fitting procedure resulted in determining χ^2_v and the kinematical parameters of a vee. This procedure was considered in detail, for example, in [8]; here, we note only that it improves significantly the accuracy in calculating physical parameter.

Figure 1 shows the mass spectrum of the system of two K_S mesons from their production threshold to 2400 MeV with a bin width being 20 MeV. The feature considered in this article manifests itself as a

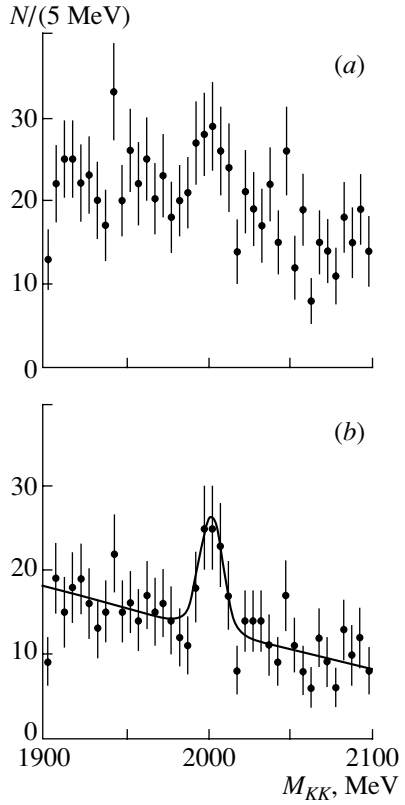

Fig. 3. Distributions with respect to the effective mass of two K_S mesons (a) for events not subjected to a selection according to the quality criterion and (b) events selected according to this criterion. The curve represents an MLM fit where the resonance and the background are approximated by a Breit–Wigner function and a linear function, respectively.

maximum in the vicinity of 2000 MeV. The signal-to-background ratio ($S:B$) is 0.83 ($S = 45$, $B = 53$), and the parameters characterizing the statistical significance are the following: $S/\sqrt{B} > 6$ and $S/\sqrt{B+S} \sim 4.5$. The events for which the effective-mass spectrum is shown in Fig. 1 were selected according to the criterion requiring that the missing mass squared lie in the range $0.3 < MM^2 < 1.5$ GeV^2 (the other cuts will be described below). The cut on MM^2 was used to suppress the contribution of reaction (2); as a result, the number of events was reduced by 51%. Figure 2 shows the distribution events with respect to this variable.

Events recorded by the spectrometer have different uncertainties in the measured kinematical variables. The lower the uncertainties, the higher the quality of an event and the higher the resolving power of the analysis of the K_SK_S system. The level of the uncertainties in the measured parameters of the events can be identified with the concept of event quality. In our analysis of the events, their quality will be taken into account by applying a set of cuts.

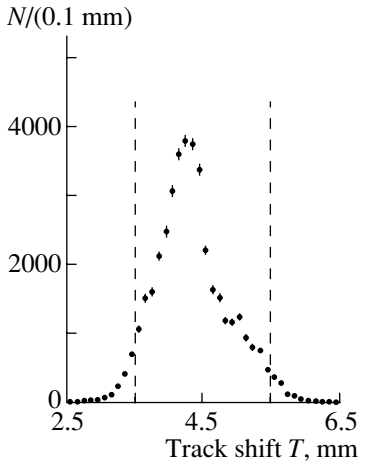

Fig. 4. Distribution of events with respect to track shifts in the spark chambers. The dashed lines show the boundaries of the cuts.

In studying the feature corresponding to the mass of 2000 MeV (as well as other narrow resonances observed with the 6-m spectrometer of ITEP), event selections according to the quality criterion are of great importance. Figure 3 shows the section of the spectrum between 1900 and 2100 MeV for (a) events not subjected to a selection according to the quality criterion and (b) events selected according to this criterion. The use of this selection improves the statistical significance of the observed phenomenon from 4.8 to 6 standard deviations.

The quality selection of events involves the following procedures. Sampling according to the time of matching the track-detection instant with the trigger signal is of greatest importance for isolating the feature in question. The spark chambers of the spectrometer recorded tracks formed between -2.5 and $+0.7$ μs. Ions produced by a charged particle passing through the spark-chamber gas are due to the action of crossed electric and magnetic fields. This displacement is directly measured in the experiment. The directions of the electric fields in even chambers are opposite to those in odd ones; therefore, ions drift in different directions. It is the distance between the tracks from the same charged particle in even and odd chambers that is a measure of the time that elapsed since the instant of particle passage to the instant of feeding of a high-voltage pulse causing breakdown in the spark chamber. Below, this distance will be referred to as a track shift or the age of a track (T). Figure 4 shows the distribution with respect to this parameter. Upon applying a cut whose boundaries are indicated by the dashed lines in the figure, about 20% events are rejected, the S/B ratio increasing

concurrently by about 30%. The application of this cut made it possible not only to eliminate events that were erroneously taken for those associated with a K_SK_S pair but also to remove events measured with a large uncertainty for one reason or another (for instance, because of an overlap of a track and the beam area).

The remaining cuts—each of them separately—improve the S/B ratio to a considerably smaller extent. The cut on the D distance between the trajectories of the K_S mesons at the point of their closest approach is the most significant. Under the condition $D < 8$ mm, the S/B ratio increases by 5%, 2% of events being rejected in this case. The cuts on the effective mass of particles forming a vee result in a similar improvement of the S/B value. In this case, we select events for which the deviation of the effective mass of a vee from the tabular value of the K_S-meson mass is not greater than 40 MeV. Cuts on the number of points on each track (not less than 6) and on the χ^2_v values for a fit in testing pion-track intersection at a single point and for a fit to the tabular value of the K_S-meson mass are also applied. The concerted effect of all cuts, except for the age selection, results in an increase of about 15% in the S/B ratio, the loss of events being about 14% in this case.

That any of the cuts that favor separation of events recorded with smaller uncertainties leads to an increase in the S/B ratio indicates that the feature being studied is indeed an actually existing object rather than a result of a random coincidence of several factors (statistical fluctuation, a spectrometer-operation property, etc.). It is appropriate to note at this point that the correlation between the cuts is insignificant. The pair of T and D is an exception: their correlation is close to the maximum. The application of all of the cuts reduces the number of events by 25%, but the S/B ratio increases by a factor of 1.5.

The fitting of vees also improves the S/B ratio. Figure 5 illustrates the influence of fitting on the effective-mass spectrum of the K_SK_S system. Figure 5*a* displays the spectrum obtained on the basis of unfitted data. The distinction between the distribution in Fig. 5*b* and that in Fig. 5*a* is that, in constructing the former, the vee masses were set to the tabular mass of the K_S meson. In plotting the spectrum in Fig. 5*c*, we used the momenta obtained by fitting the vees to the tabular value of the kaon mass and by requiring that the tracks of a vee intersect at one point. It can be seen that the S/B ratio increases by about 15% upon the application of the above procedures.

In order to determine the parameters of the observed resonance feature and its statistical significance, the experimental data were fitted by the maximum-likelihood method (MLM). The main advantage of this method over histogramming is that the mass and angles are not averaged over the bin width in the fitting procedure, so that the result does not depend on the choice of the reference point and the number of bins into which the mass range under study is divided. Describing the experimental data, we used the probability-density function $F(P;\Omega)$, where P is the set of the parameters specified below, the effective mass of two K_S mesons, the cosine of the Gottfried–Jackson angle θ, and the Treiman–Yang angle ϕ being elements of the phase space Ω.

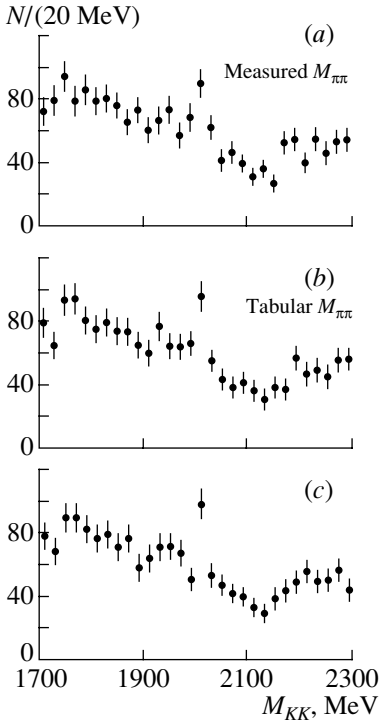

Fig. 5. Distribution of events with respect to the effective mass of the K_SK_S system: (*a*) no fitting procedure is applied, and the effective mass of two π mesons is calculated from the experimental data; (*b*) no fitting procedure is applied and the effective mass of two π mesons taken to be equal to the K_S-meson mass; and (*c*) fitted data.

Fitting was performed for events falling within the range 1850–2150 MeV of K_SK_S masses. There were 828 events in this range. A first-degree polynomial proved to be sufficient for describing the mass dependence of the background. The resonance was approximated by a relativistic Breit–Wigner function. The angular dependences are linear combinations of squared amplitudes of the S, D_0, D_+, D_{++}, G_0, and G_+ waves. For these, we have

$$S^2 = 1/4\pi, \tag{3}$$

$$D_0^2 = 5(3\cos^2\theta - 1)^2/16\pi, \tag{4}$$

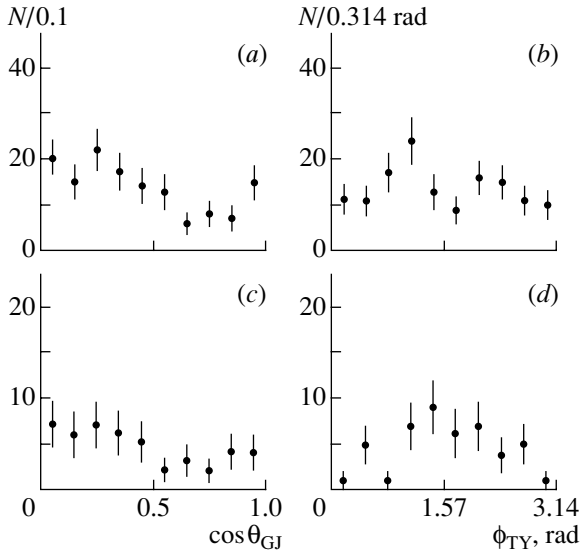

Fig. 6. Distributions of events with respect to $\cos\theta_{\mathrm{GJ}}$ and ϕ_{TY} (*a, b*) for events populating mass ranges adjacent to the resonance region ($1950 < M_{KK} < 1985$ MeV, $2015 < M_{KK} < 2050$ MeV) and (*c, d*) for events falling within the resonance region ($1993 < M_{KK} < 2007$ MeV).

$$D_+^2 = 15(\sin 2\theta \sin\phi)^2/4\pi, \quad (5)$$

$$D_{++}^2 = 15(\sin^2\theta \sin 2\phi)^2/4\pi, \quad (6)$$

$$G_0^2 = 9(35\cos^4\theta - 30\cos^2\theta + 3)^2/256\pi, \quad (7)$$

$$G_+^2 = 45(\sin\theta\cos\theta(7\cos^2\theta - 3)\sin\phi)^2/32\pi. \quad (8)$$

The angular distributions of the background and the resonance are described by different sets of waves.

Thus, the coefficients in the polynomial describing the mass dependence of the background (two parameters); the amplitude, the mass M, and the width Γ appearing in the Breit–Wigner function (three parameters); and, additionally, the coefficients of the squared amplitudes of the angular distributions are the parameters P to be determined. The number of these parameters depended on the result of fitting—the amplitudes of the angular distributions were discarded if their contributions did not affect χ^2.

In order to obtain the most probable values of the parameters, we minimized the functional

$$\int_\Omega \epsilon(\Omega)F(P;\Omega)d\Omega - \ln L, \quad (9)$$

where $\epsilon(\Omega)$ is the event-detection recording and $L = \prod_{i=1}^N F(P;\Omega_i)$, N being the number of events. To compare the probabilities of experimental-data description with different parameter sets, we calculated χ^2 by the formula (see [3], p. 197)

$$\chi^2 = -2\ln L + \text{const}. \quad (10)$$

The constant was chosen in such a way that χ^2 obtained via minimization without allowing for the Breit–Wigner function was equal to 100. The results of various versions of fitting are given in the table, where the number of events in each of the waves of the background and the resonance is displayed, along with the central values of the resonance mass and width. The last column shows the χ^2 values, with the number of degrees of freedom $N_{\mathrm{d.}f}$ being subtracted.

The result of fitting without allowing for the Breit–Wigner function and without discarding events falling within the resonance region is presented in the first line. The table gives angular-distribution moments that yield appreciable values of the amplitudes. Figure 6 shows the angular distributions themselves. The character of the dependence on the Treiman–Yang angle in the mass ranges adjacent to the resonance region indicates the presence of interference terms. However, an attempt at incorporating these terms into the description of the background angular distributions was not successful, since the number of adjustable parameters increased abruptly in this description owing to the introduction of phases. Moreover, it proved to be necessary to introduce an individual mass dependence for each of the waves if interference was taken into account. All that led to instability of the resulting solutions, and we had to restrict ourselves to a minimum set of waves. This did not affect the basic conclusions of this study, because the resonance parameters are virtually independent of the method describing the background.

It also follows from Fig. 6 that the angular distributions of events falling within the resonance region differ noticeably from the distributions of background events. This concerns primarily the distribution with respect to the azimuthal angle. A maximum in the vicinity of $\pi/2$ suggests the presence of $m = 1$ waves. Fitting confirmed this qualitative conclusion. But first of all, we tried to describe the resonance with the same set of waves and the same relations between them as those that were observed for the background. The result of this fitting is quoted in the table (line 2). As follows from the last column of the table, the decrease in χ^2 with respect to the value obtained in fitting without a resonance is about 19 units, which corresponds to four standard deviations.

At the same time, a description in terms of the G_+ wave alone yields a χ^2 value less by 29 units (line 4). This corresponds to more than five standard deviations, and the probability of this description is approximately 10 times as great as that of the description that uses the set of background waves. In

Table

	Background waves, N_{ev}				Resonance waves, N_{ev}						Resonance mass and width, MeV		χ^2
	S	D_0	D_{++}	G_0	S	D_0	D_+	D_{++}	G_0	G_+	M	Γ	
1	1235	425	346	70	–	–	–	–	–	–	–	–	100
2	1085	435	346	53	88	32	–	27	4	–	1999	16	81.2
3	1171	394	335	106	–	–	78	–	–	–	1995	12	79.2
4	1122	304	356	171	–	–	–	–	–	122	1998	14	70.9
5	1045	404	378	128	–	–	24	–	–	103	1999	12	71.3
6	1079	390	381	71	–	–	–	–	44	109	1999	13	70.3

carefully studying the mass spectrum of the K_SK_S system within the range 1900–2100 MeV outside the resonance region (mass ranges 1900–1980 MeV and 2020–2100 MeV), we revealed no trace of the G_+ wave. Among other waves, only the D_+ wave had a satisfactory value of χ^2 (line 3). The result of fitting in terms of the sum of G_+ and D_+ waves is quoted in line 5. It is evident that the contribution of the D_+ wave is five times less than the contribution of the G_+ wave, χ^2 taking the same value as in the case of description with the G_+ wave alone. We tried to reveal the possible presence of any other components of the G wave. The results of fitting in terms of the G_0 and G_+ waves are given in line 6. It can be seen that the contribution of G_0 can formally be disregarded (χ^2 changed by 0.6). However, the G_0 wave appears in the description of the background, whence it follows that, in principle, the actual contribution of this wave can be concealed because of the interference between the background and the resonance. From the other G wave components, the G_{++} wave was sought, but no trace of it was observed. The distribution with respect to Treiman–Yang angle has a sinusoidal character. Hence, it can be concluded that the exchanged particle in the reaction of resonance production has a natural spin–parity relation; in particular, this can be a ρ^+ meson. This fact is confirmed by the momentum-transfer distributions that are presented in Fig. 7 for events from the left- and right-hand regions adjacent to the resonance region (Fig. 7*a*) and from the resonance region (Fig. 7*b*). It is noteworthy that resonance events are concentrated in the region between 0 and 0.5 GeV^2 and that they do not feature a peak that occurs in the vicinity of zero and which is typical of π-meson exchange, but that there is such a peak in the distribution of background events.

In order to determine the statistical uncertainties in the resonance mass and width, we analyzed χ^2 as a function of these quantities. At a 65% confidence level, the uncertainty in the mass and the width proved to be ± 2.5 MeV and ± 5 MeV, respectively. The systematic uncertainty in the mass was not more than ± 5 MeV. As was mentioned above, the instrumental mass resolution was about 10 MeV for the K_SK_S system in the region around 2000 MeV. Therefore, the value of Γ in the Breit–Wigner function does not exceed 15 MeV according to our estimate.

It follows from the table that the statistical significance at which a resonance with these parameters was observed is not less than five standard deviations. The conclusion that the feature in question is not a statistical fluctuation is also corroborated by its observation in all three runs of data accumulation. The

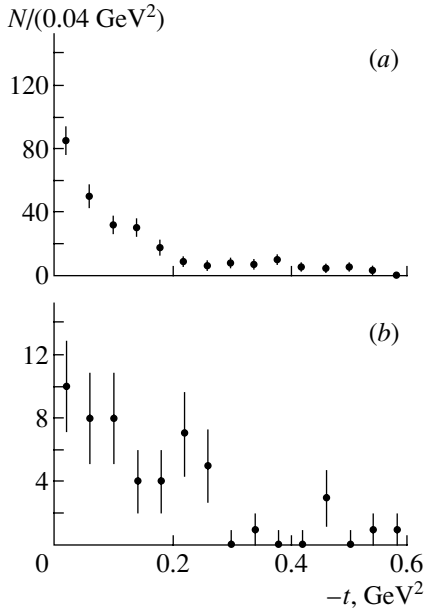

Fig. 7. Momentum-transfer distribution (*a*) of events from the effective-mass regions of the K_SK_S system that are adjacent to the resonance band from the left and from the right ($1950 < M_{KK} < 1985$ MeV, $2015 < M_{KK} < 2050$ MeV) and (*b*) of events from the resonance band ($1990 < M_{KK} < 2010$ MeV).

production of this resonance was also studied in various sectors of the azimuthal angle in the laboratory frame, the axis being aligned with the beam direction. The distinction between the number of events in the resonance region appeared to be compatible with expected statistical fluctuations. The $X(2000)$ structure has a specific spin–parity of $J^P = 4^+$, and this is yet another argument in favor of the fact that we are dealing here with an actually existing phenomenon.

As a test, the data were fitted with additional cuts on the coordinates of event production and without cuts on the quality of events. The events were also fitted without taking into account the detection efficiency. All these test fits support the results quoted above for the resonance mass, width, and quantum numbers.

The product of the cross section for $X(2000)$ formation and the relevant branching ratio, $\sigma\mathrm{Br}(K_SK_S)$, is estimated at about 6 nb.

Let us summarize the results of this study. At the significance of not less than five standard deviations, we have obtained an indication of the existence of a resonance feature having a mass of 1998 ± 3 MeV and a width not greater than 15 MeV. The spin–parity of the resonance is $J^P = 4^+$; the angular-momentum projection onto the quantization axis is $|m| = 1$, but we were unable to rule out an admixture of the projection $m = 0$. We note that the resonance feature in question cannot be described by using the same set of waves as those providing a good fit in adjacent regions of the mass spectrum.

ACKNOWLEDGMENTS

We are grateful to the staff of the IHEP U-70 accelerator and the ITEP 6-m spectrometer, who ensured the accumulation of the experimental data used in this article.

This work was supported by the Russian Foundation for Basic Research (project nos. 02-02-16623, 00-15-96545).

REFERENCES

1. L. G. Landsberg, Yad. Fiz. **57**, 47 (1994) [Phys. At. Nucl. **57**, 42 (1994)].
2. L. G. Landsberg, Usp. Fiz. Nauk **164**, 1129 (1994) [Phys.-Usp. **37**, 1043 (1994)].
3. Particle Data Group, Eur. Phys. J. (2000).
4. V. V. Vladimirsky, V. K. Grigor'ev, O. N. Erofeeva, *et al.*, Yad. Fiz. **64**, 1979 (2001) [Phys. At. Nucl. **64**, 1895 (2001)].
5. V. K. Grygor'ev, O. N. Baloshin, B. P. Barkov, *et al.*, Yad. Fiz. **62**, 513 (1999) [Phys. At. Nucl. **62**, 470 (1999)].
6. V. K. Grygor'ev, O. N. Baloshin, B. P. Barkov, *et al.*, Yad. Fiz. **59**, 2187 (1996) [Phys. At. Nucl. **59**, 2105 (1996)].
7. B. P. Barkov, V. V. Vladimirskiĭ, V. K. Grigor'ev, *et al.*, Pis'ma Zh. Éksp. Teor. Fiz. **70**, 242 (1999) [JETP Lett. **70**, 248 (1999)].
8. V. V. Vladimirskiĭ, V. K. Grigor'ev, O. N. Erofeeva, *et al.*, Pis'ma Zh. Éksp. Teor. Fiz. **72**, 698 (2000) [JETP Lett. **72**, 486 (2000)].
9. B. V. Bolonkin, O. N. Baloshin, A. M. Blagorodov, *et al.*, Preprint No. 86 (Institute of Theoretical and Experimental Physics, Moscow, 1973).
10. B. V. Bolonkin, V. V. Vladimirsky, A. P. Grishin, *et al.*, Preprint No. 154 (Institute of Theoretical and Experimental Physics, Moscow, 1981).

Translated by E. Kozlovskii

Physics of Atomic Nuclei, Vol. 66, No. 4, 2003, pp. 707–711. Translated from Yadernaya Fizika, Vol. 66, No. 4, 2003, pp. 736–740.

ELEMENTARY PARTICLES AND FIELDS
Experiment

Inelastic Scattering of Tritium-Source Antineutrinos on Electrons of Germanium Atoms

V. I. Kopeikin, L. A. Mikaelyan, and V. V. Sinev*

Russian Research Centre Kurchatov Institute, pl. Akademika Kurchatova 1, Moscow, 123182 Russia

Received May 7, 2002

Abstract—Processes of the inelastic magnetic and weak scattering of tritium-beta-source antineutrinos on the bound electrons of a germanium atom are considered. The results obtained by calculating the spectra and cross sections are presented for the energy-transfer range between 10 eV and 18 keV. © *2003 MAIK "Nauka/Interperiodica".*

1. INTRODUCTION

This study was performed in connection with the experiment planned by researchers from three institutions (Institute of Theoretical and Experimental Physics, Joint Institute for Nuclear Research, and the All-Russia Research Institute for Experimental Physics) to seek the magnetic moment of the electron neutrino [1]. This experiment is presumed to study the spectra of energy deposited in a detector material upon the inelastic scattering of tritium-source antineutrinos on atomic electrons. The sensitivity to the magnitude of the neutrino magnetic moment is assumed to be $\mu \sim 3 \times 10^{-12}\mu_B$ (μ_B is the Bohr magneton), which is nearly two orders of magnitude better than the upper limit, $\mu \leq 2 \times 10^{-10}\mu_B$, set in experiments performed at the Savannah River nuclear reactors, the Rovensk nuclear power plant, and Krasnoyarsk neutrino laboratory [2].

The discovery of the neutrino magnetic moment would suggest the existence of phenomena beyond the fundamentals of electroweak-interaction theory and would have far-reaching consequences for particles physics and astrophysics. (For a discussion on the issues concerning the motivation of searches for the neutrino magnetic moment in laboratory experiments and the status and prospects of investigations along these lines, see, for example, the original study of Neganov *et al.* [1], the review articles quoted in [3], and references therein.)

The magnetic moment can be sought by analyzing the measured spectrum of events of $\bar{\nu}_e e$ scattering. In the case of scattering on a free electron, the cross section for weak $\bar{\nu}_e e$ scattering tends to a finite limit, while the cross section for magnetic scattering grows indefinitely. Therefore, the experimental sensitivity to the magnitude of the neutrino magnetic moment increases with decreasing energy of measured events. As the energy of an event decreases, however, the effects of electron binding in target atoms begin to affect relevant cross sections and their energy dependence.

A feature peculiar to the experiment proposed in [1] is that, in the majority of cases, the energy q deposited in the target upon the scattering of tritium neutrinos $\bar{\nu}_e$ is below 1 keV. The experiment will employ germanium and silicon detectors that, owing to the internal-signal-amplification mechanism, will make it possible to perform measurements in the region of energies as low as those indicated immediately above.

In this study, we consider the inelastic scattering of tritium-source antineutrinos on germanium-atom electrons. The ensuing exposition is organized as follows. First, we recall the expression for the cross sections for elastic $\bar{\nu}_e e$ scattering, whereupon we briefly dwell on features of inelastic scattering and on the procedure for calculating relevant cross sections. Further, we display the results obtained by calculating the spectra of inelastic scattering on electrons of germanium-atom subshells and, finally, present the total spectra and integrated cross sections in a form that is suitable for a direct comparison with experimental data.

2. ELASTIC AND INELASTIC SCATTERING OF ANTINEUTRINOS ON AN ELECTRON

1. The differential cross section for the magnetic scattering of a neutrino on a free electron at rest is proportional to the squared magnetic moment μ^2 [4]; that is,

$$(d\sigma^M/dq)_{\text{free}} = \pi r_0^2(\mu/\mu_B)^2(1/q - 1/E), \qquad (1)$$

*e-mail: e-mail:sinev@polyr.kiae.sv

1063-7788/03/6604-0707$24.00

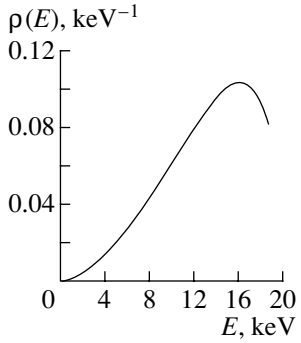

Fig. 1. Spectrum $\rho(E)$ of tritium-source antineutrinos.

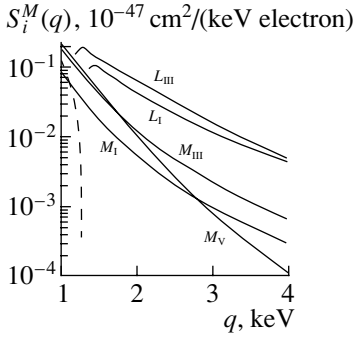

Fig. 2. Spectra S_i^M(q) of the inelastic magnetic ($\mu = 5 \times 10^{-12}\mu_B$) scattering of antineutrinos on electrons of the L_I, L_{III}, M_I, M_{III}, M_V germanium-atom shells in the energy-transfer range $q = 1$–4 keV. The dashed curve corresponds to scattering on a free electron.

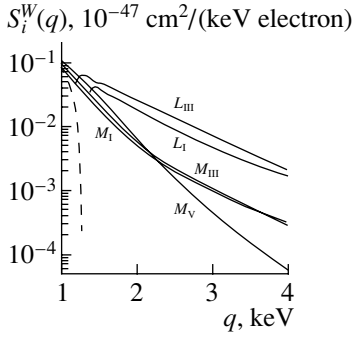

Fig. 3. As in Fig. 2, but for the inelastic weak scattering of $\bar{\nu}_e$.

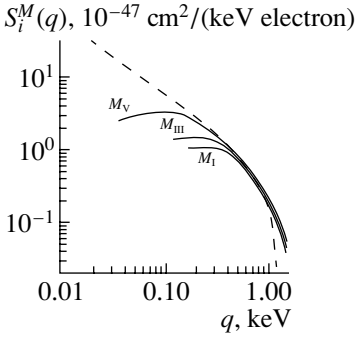

Fig. 4. Spectra $S_i^M(q)$ of the inelastic magnetic ($\mu = 5 \times 10^{-12}\mu_B$) scattering of antineutrinos on electrons of the L_I, L_{III}, M_I, M_{III}, M_V germanium-atom shells in the energy-transfer range $q = 0.01$–1.5 keV. The dashed curve corresponds to scattering on a free electron.

where $\pi r_0^2 = 2.495 \times 10^{-25}$ cm^2; E is the incident-neutrino energy; and q is the energy transfer, which coincides, in this case, with the recoil-electron kinetic energy.

The differential cross section for the electroweak scattering of an antineutrino on a free electron at rest has the form (see, for example, [5])

$$(d\sigma^W/dq)_{\text{free}} = G_F^2(m/2\pi)[4x^4 + (1+2x^2)^2(1-q/E)^2 - 2x^2(1+2x^2)mq/E^2], \quad (2)$$

where m is the electron mass; $G_F^2(m/2\pi) = 4.31 \times 10^{-48}$ cm^2/keV; and $x^2 = \sin^2\theta_W = 0.232$, θ_W being the Weinberg angle.

For a given value of primary neutrino energy E, the energy transfer to the electron involved is restricted by the kinematical condition

$$q \le q_{\max} = 2E^2/(2E+m). \quad (3)$$

In the region $q > q_{\max}$, free-scattering cross sections are zero. In the case of tritium-source antineutrinos $\bar{\nu}_e$ whose endpoint energy is 18.6 keV, $q_{\max} = 1.26$ keV.

With decreasing energy, the cross section for free magnetic scattering increases in proportion to $1/q$, while the cross section (2) tends to a finite limit of 1.016×10^{-47} cm^2/keV. At the magnetic-moment value of $\mu = 3 \times 10^{-12}\mu_B$, the spectra of weak and magnetic antineutrino ($\overline{\nu}_e$) scattering intersect at an energy transfer of $q \approx 0.3$ keV.

2. In calculating the differential cross sections $d\sigma_i^M/dq$ and $d\sigma_i^W/dq$ for inelastic scattering on the electrons of the ith shell, we use the approach developed in [6]. In the initial state, there are a germanium atom ($Z = 32$) and incident antineutrinos of energy E; in the final state, there are a knock-on electron, an outgoing neutrino, and a vacancy in one of the atomic shells. The wave functions for the target atom and the electron binding energies are calculated in the self-consistent relativistic Hartree–Fock–Dirac model. The wave functions for the knock-on electron can be found by numerically integrating the Dirac equation in the same self-consistent potential. The energy-transfer spectra $S_i^M(q)$ and $S_i^W(q)$ are obtained as convolutions of the differential cross sections $d\sigma_i^M/dq$

Table 1. Calculated electron binding energies ε_i (in keV) in germanium atomic shells (n_i is the number of electrons in a shell)

	K $(1s_{1/2})$	$L_{\rm I}$ $(2s_{1/2})$	$L_{\rm II}$ $(2p_{1/2})$	$L_{\rm III}$ $(2p_{3/2})$	$M_{\rm I}$ $(3s_{1/2})$	$M_{\rm II}$ $(3p_{1/2})$	$M_{\rm III}$ $(3p_{3/2})$	$M_{\rm IV}$ $(3d_{3/2})$	$M_{\rm V}$ $(3d_{5/2})$	$N_{\rm I}$ $(4s_{1/2})$	$N_{\rm II}$ $(4p_{1/2})$
n_i	2	2	2	4	2	2	4	4	6	2	2
ε_i	10.9	1.37	1.22	1.19	0.17	0.12	0.115	0.031	0.030	(0.013)	(0.005)

and $d\sigma_i^W/dq$ with the spectrum $\rho(E)$ of the tritium-source antineutrinos (Fig. 1) that was calculated by using the Coulomb function [7]. The resulting spectra $S^{M,W}(q)$ for scattering on a germanium atom can be derived by taking a sum over the shells of the spectra $S_i^{M,W}$ with allowance for the number n_i of electrons in each shell:

$$S^{M,W}(q) = \sum (n_i/Z) S_i^{M,W}(q). \qquad (4)$$

All the spectra $S_i^{M,W}$ and the resulting spectra $S^{M,W}$(q) are normalized to one electron and are calculated in units of 10^{-47} cm^2/(keV electron). In all the calculations of cross sections and magnetic-scattering spectra, the neutrino magnetic moment is taken to be $5 \times 10^{-12}\mu_{\rm B}$.

The energy transfer q to the atom involved in an inelastic-scattering event is the sum of the kinetic energy T of the knock-on electron and the electron binding energy ε_i in the ith atomic shell:

$$q = T + \varepsilon_i. \qquad (5)$$

The radiation generated upon the filling of the vacancy and the knock-on electron are absorbed in a detector material. As a result, the value determined experimentally for the energy of an event coincides with the energy transfer q in this collision event.

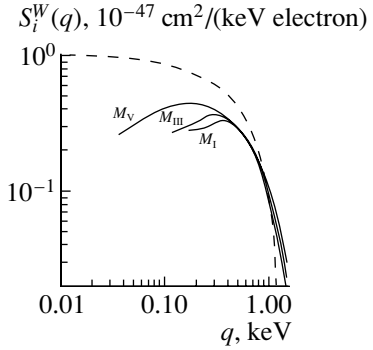

Fig. 5. As in Fig. 4, but for the inelastic weak scattering of $\bar{\nu}_e$.

The cross sections for weak and magnetic inelastic scattering on an electron of the ith shell vanish for $q \le \varepsilon_i$. (We disregard transitions of the knock-on electron to discrete excited optical levels of the target atom.) In contrast to what is known for free scattering, these cross sections do not vanish at $q = q_{\max}$ [see (3)]; in the "forbidden" region $q > q_{\max}$, the inelastic-scattering cross sections decrease and vanish only at the q value equal to the incident-antineutrino energy E.

The calculated electron binding energies in the shells of a free germanium atom (Table 1) agree with experimental data to within 5%. This is not true only for four valence electrons, but their binding energy is so low that, in calculating cross sections and spectra, we use, for them, the formulas for scattering on free electrons.

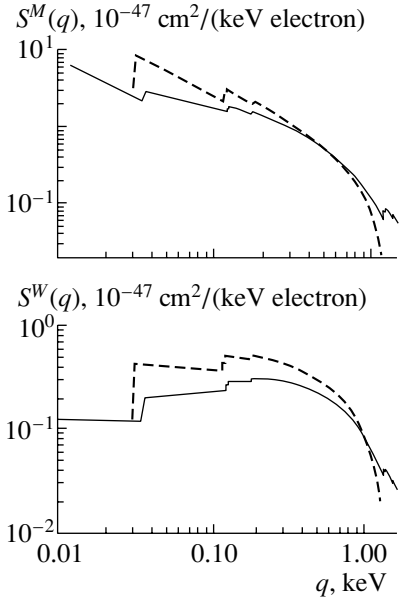

Fig. 6. Spectra of the inelastic magnetic and weak antineutrino scattering [$S^M(q)$ ($\mu = 5 \times 10^{-12}\mu_{\rm B}$) and $S^W(q)$, respectively] on germanium-atom electrons in the energy-transfer range of $q = 0.01$–1.5 keV. The dashed curves correspond to the step-function approximation.

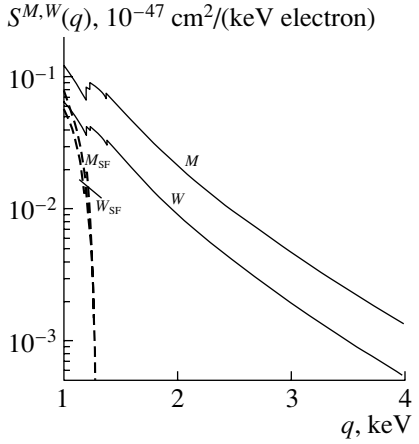

Fig. 7. As in Fig. 6, but in the energy-transfer range $q = 1$–4 keV.

3. DISCUSSION OF THE RESULTS FOR SPECTRA AND CROSS SECTIONS

The scattering-event spectra $S_i^{M,W}(q)$ depends substantially on the binding energy ε_i in a shell, their shapes being different in the regions $q > q_{\max}$ and $q < q_{\max}$, where $q_{\max} = 1.26$ keV is the kinematical limit given by (3).

Table 2. Integrated cross sections $I^M(q)$ and $I^W(q)$ (in units of 10^{-47} cm^2/electron) for the inelastic magnetic ($\mu = 5 \times 10^{-12}\mu_B$) and weak scattering of tritium neutrinos on germanium-atom electrons ($\nu_e e$) in the energy range 0.01–q keV

q, keV	$I^M(q)$	$I^W(q)$
0.02	0.0540	0.0012
0.03	0.0855	0.0025
0.05	0.1372	0.0061
0.10	0.2386	0.0173
0.20	0.4046	0.0455
0.35	0.5733	0.0892
0.50	0.6771	0.1254
0.75	0.7225	0.1671
1.00	0.8184	0.1907
1.26	0.8420	0.2031
2.03	0.8771	0.2186
3.00	0.8870	0.2228
5.00	0.8903	0.2241
10.94	0.8908	0.2243
18.60	0.8909	0.2243

Figures 2 and 3 display the results obtained by calculating the spectra of inelastic scattering on electrons of the L and M germanium shells in the energy-transfer range $q = 1$–4 keV, whose larger part lies in the region $q > q_{\max}$, which is forbidden for free scattering. With the exception of a small local enhancement near the threshold for the scattering of antineutrinos $\overline{\nu}_e$ on electrons of the L shells, we observe a decrease in spectra with increasing energy q. A general trend is that the lower the electron binding energy in a shell, the steeper this decrease.

In the energy region $q < q_{\max}$ (Figs. 4, 5), L-shell electrons make virtually no contribution. This region is dominated by the scattering on electrons of M atomic shells and on valence electrons. The spectra of magnetic scattering on M shells in the immediate vicinity of the threshold lie much lower than the spectrum of scattering on a free electron. With increasing energy, the distinction between these spectra decreases fast; in a certain energy interval, they virtually coincide, while, for $q > 0.8$ keV, the inelastic-scattering spectra lie above the free-scattering spectrum. A similar behavior is also observed for weak scattering, but the spectra of elastic and inelastic scattering approach each other more slowly in this case.

The spectra $S^M(q)$ and $S^W(q)$ of magnetic and weak inelastic scattering that include the contributions from all germanium atomic shells are represented by the solid curves in Figs. 6 and 7. They can be used to perform a comparison with experimental data. The numbers of scattering events occurring within a given energy interval are determined by the integrals $I^M(q)$ and $I^W(q)$ of the spectra $S^M(q)$ and $S^W(q)$. Figure 8 and Table 2 display the integrals from the lower detection threshold of 0.01 keV to a variable upper boundary q.

From the data given in Figs. 7 and 8 and in Table 2, it can be seen that, for the chosen value of the neutrino magnetic moment, the magnetic scattering is more intense than weak scattering over the entire energy region. It should be noted that nearly 80% of all magnetic-scattering events fall within the energy-transfer range from 0.05 to 1.26 keV; the energy region of $q > q_{\max}$ involves only about 6% of such scattering events; and their fraction in the interval from 0.01 to 0.05 keV amounts to about 15%.

It is interesting to compare the "exact" spectra $S^{M,W}(q)$ and integrated cross sections $I^{M,W}(q)$ with the values obtained in the step-function approximation. In this approximation, it is assumed that the spectrum of inelastic scattering on an electron of the ith shell is coincident with the spectrum of scattering on a free electron for energies of $q > \varepsilon_i$ and that it vanishes for $q < \varepsilon_i$. In this approximation, the "exact"

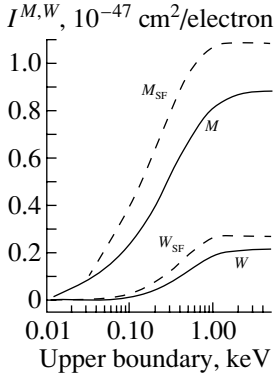

Fig. 8. Integrated cross sections $I^{M,W}(q)$ for magnetic ($\mu = 5 \times 10^{-12}\mu_B$) and weak scattering of antineutrinos on germanium-atom electrons versus the upper boundary of the energy transfer q. The dashed curves correspond to the step-function approximation.

expression (4) for the resulting inelastic-scattering spectra reduces to the form

$$S_{SF}^{M,W}(q) = S_{free}^{M,W}(q)\sum(n_i/Z)\theta(q-\varepsilon_i), \qquad (6)$$

where summation is performed over all atomic shells and $\theta(q-\varepsilon_i)$ is the Heaviside step function equal to unity for $q > \varepsilon_i$ and to zero for $q < \varepsilon_i$. It was shown in [8] that, in the case where antineutrinos generated by a reactor and by a ^{90}Sr–^{90}Y source are scattered on electrons of iodine and germanium atoms, the approximate spectra (6) agree with the spectra in (4) to within 2% for the energy transfer q ranging from 1–1.5 to 200–300 keV.

From the data shown in Fig. 6, it can be seen that the approximation specified by Eq. (6) is inadequate for both magnetic and weak scattering in the case of a soft spectrum of tritium antineutrinos. The integrated cross sections found in the step-function approximation exceed the corresponding "exact" values by about 25% (Fig. 8).

ACKNOWLEDGMENTS

We would like to emphasize the leading role of S.A. Fayans, who prematurely passed away in 2001, in developing and applying the procedure used in this study. We are grateful to L.N. Bogdanova and A.S. Starostin for stimulating discussions.

This work was supported by the Russian Foundation for Basic Research; by the program Leading Scientific Schools (grant no. 00-15-96708); and, in part, by the Department of Atomic Science and Technology of the Ministry for Atomic Industry of the Russian Federation (contract no. 6.25.19.19.02.969).

REFERENCES

1. B. S. Neganov *et al.*, Yad. Fiz. **64**, 2033 (2001) [Phys. At. Nucl. **64**, 1948 (2001)].
2. F. Reines, H. Gurr, and H. Sobel, Phys. Rev. Lett. **37**, 315 (1976); G. S. Vidyakin, V. N. Vyrodov, I. I. Gurevich, *et al.*, Pis'ma Zh. Éksp. Teor. Fiz. **55**, 212 (1992) [JETP Lett. **55**, 206 (1992)]; A. V. Derbin *et al.*, Pis'ma Zh. Éksp. Teor. Fiz. **57**, 755 (1993) [JETP Lett. **57**, 768 (1993)].
3. A. V. Derbin, Yad. Fiz. **57**, 236 (1994) [Phys. At. Nucl. **57**, 222 (1994)]; L. A. Mikaelyan, Yad. Fiz. **65**, 1206 (2002) [Phys. At. Nucl. **65**, 1173 (2002)].
4. H. Bethe, Proc. Cambridge Philos. Soc. **35**, 108 (1935); G. V. Domogatskiĭ and D. K. Nadezhin, Yad. Fiz. **12**, 1233 (1970) [Sov. J. Nucl. Phys. **12**, 678 (1971)].
5. M. B. Voloshin, M. I. Vysotskiĭ, and L. B. Okun', Zh. Éksp. Teor. Fiz. **91**, 754 (1986) [Sov. Phys. JETP **64**, 446 (1986)].
6. S. A. Fayans, V. Yu. Dobretsov, and A. B. Dobrotsvetov, Phys. Lett. B **291**, 1 (1992); V. Yu. Dobretsov, A. B. Dobrotsvetov, and S. A. Fayans, Yad. Fiz. **55**, 2126 (1992) [Sov. J. Nucl. Phys. **55**, 1180 (1992)].
7. B. S. Dzhelepov *et al.*, *Beta Processes* (Nauka, Leningrad, 1972).
8. S. A. Fayans, L. A. Mikaelyan, and V. V. Sinev, Yad. Fiz. **64**, 1551 (2001) [Phys. At. Nucl. **64**, 1475 (2001)]; V. I. Kopeikin *et al.*, Yad. Fiz. **60**, 2032 (1997) [Phys. At. Nucl. **60**, 1859 (1997)].

Translated by V. Bukhanov

Physics of Atomic Nuclei, Vol. 66, No. 4, 2003, pp. 712–723. From Yadernaya Fizika, Vol. 66, No. 4, 2003, pp. 741–753.

ELEMENTARY PARTICLES AND FIELDS
Experiment

Search for Solar *pp* Neutrinos with an Upgrade of CTF Detector*

O. Ju. Smirnov, O. A. Zaimidoroga, and A. V. Derbin[1)]**

Joint Institute for Nuclear Research, Dubna, Moscow oblast, 141980 Russia

Received October 3, 2001; in final form, January 30, 2002

Abstract—The possibility of using ultrapure liquid organic scintillator as a low-energy solar neutrino detector is discussed. The detector with an active volume of 10 t and 4π coverage will count 1.8 *pp* neutrinos and 5.4 ^{7}Be neutrinos per day with an energy threshold of 170 keV for the recoil electrons. The evaluation of the detector sensitivity and backgrounds is based on the results obtained by the Borexino collaboration with the Counting Test Facility (CTF). The detector can be build at the LNGS underground laboratory as an upgrade of the CTF detector using already developed technologies. © *2003 MAIK "Nauka/Interperiodica"*.

1. INTRODUCTION

Present information on the solar neutrino spectrum is based on the very tail of the total neutrino flux (about 0.2%). Meanwhile, the spectrometry of the solar neutrino spectrum is the main source of information on new neutrino physics. The *pp*-neutrino measurement is a critical test of stellar evolution theory and of neutrino oscillation solutions. A discussion of the physics potential of the solar *pp*-neutrino flux can be found in [1, 2]. The low-energy part of the spectrum (and, in particular, the *pp*-neutrino flux) has not been measured directly until now. A number of projects aiming to build *pp*-neutrino spectrometers are at the initial stages of development. The principal characteristics of the existing proposals are shown in Table 1. The existing radiochemical experiments sensitive to solar *pp* neutrinos (SAGE [12] and GALLEX [13]) are not cited in the table.

2. BOREXINO AND ITS COUNTING TEST FACILITY

Borexino, a real-time detector for low-energy neutrino spectroscopy, is near completion in the underground laboratory at Gran Sasso (see [14] and references therein). The main goal of the detector is the direct measurement of the flux of solar ^{7}Be neutrinos of all flavors via neutrino–electron scattering in an ultrapure liquid scintillator. Borexino will also address several other frontier questions in particle physics, astrophysics, and geophysics.

The Counting Test Facility (CTF) was constructed and installed in Hall C of the Gran Sasso Laboratory. The main goal of the CTF was a demonstration of the possibility of liquid scintillator purification on the scale of several tons. Although the CTF is a large-scale detector (4 t of liquid scintillator), its size is nonetheless modest in comparison to Borexino (300 t). A mass in the 4-t range was set by the need to make the prevailing scintillator radioimpurities measurable via delayed coincidence of tagged events,[2)] while a water shield thickness of approximately 4.5 m was needed in order to suppress the external radiation. The primary goal of the CTF was to develop a solution directly applicable to operational issues for Borexino; in the future there will also be the long-range goal of performing quality control during Borexino operations. Detailed reports on the CTF have been published [15–17]. As a simplified scaled version of the Borexino detector, a volume of liquid scintillator is contained in a 2-m-diameter transparent inner nylon vessel mounted at the center of an open structure that supports 100 phototubes (PMT) [18] which detect the scintillation signals. The whole system is placed within a cylindrical tank (11 m in diameter and 10 m in height) that contains 1000 t of ultrapure water, which provides shielding against neutrons originating from the rock and against external γ rays from PMTs and other construction materials. The scintillator used for the major part of tests in the CTF was a binary mixture consisting of pseudocumene[3)] (PC) as a solvent and 1.5 g/l of PPO (2,5-diphenyloxazole) as a fluor. The upgrade of the CTF-I detector (CTF-II) was

*This article was submitted by the authors in English.

[1)]Petersburg Nuclear Physics Institute, Russian Academy of Sciences, Gatchina, 188350 Russia.

**e-mail: osmirnov@jinr.ru

[2)]Key components in the decay chains of U–Th and in the β decay of ^{85}Kr are emitted as time-correlated coincidence pairs which can be tagged with high specificity.

[3)]1,2,4-trimethylbenzene C_9H_{12}.

1063-7788/03/6604-0712$24.00

Table 1. Key characteristics of the solar-neutrino projects sensitive to the *pp* neutrino

Project (reference)	Method	Threshold, keV	Resolution	Mass, t	Reaction	*pp* events/d
LENS [3]	^{176}Yb, LS	301(ν)	7% (1 MeV)	20 (8% nat ^{176}Yb)	$^{176}\mathrm{Yb} + \nu_e \rightarrow {}^{176}\mathrm{Lu} + e^-$	0.5
INDIUM [4]	^{115}In, LS	118(ν)	5–10% (1 MeV)	4	$^{115}\mathrm{In} + \nu_e \rightarrow {}^{115}\mathrm{Sn}^*(613) + e^-$	1.0
GENIUS [5]	^{76}Ge, Scattering	11(e^-) 59(ν)	0.3% (300 keV)	1 10	$\nu + e^- \rightarrow \nu + e^-$	1.8 18
HERON [6]	Superfluid ^{4}He, rotons/phonons + UV	50(e^-) 141(ν)	8.3% (364 keV)	10	$\nu + e^- \rightarrow \nu + e^-$	14
XMASS [7]	Xe, LS	50(e^-) 141(ν)	17.5% (100 keV)	10	$\nu + e^- \rightarrow \nu + e^-$	14
HELLAZ [8]	He (5 atm), TPC	100(e^-) 217(ν)	6% (800 keV)	2000 m^3	$\nu + e^- \rightarrow \nu + e^-$	7
MOON [9]	Drift chambers	168(ν)	12.4% FWHH (1 MeV)	3.3	$\nu_e + {}^{100}\mathrm{Mo} \rightarrow {}^{100}\mathrm{Tc} + e^-$	1.1
MUNU [10]	TPC, CF_4, direction	100(e^-) 217(ν)	16% FWHH (1 MeV)	0.74 (200 m^3)	$\nu + e^- \rightarrow \nu + e^-$	0.5
NEON [11]	He, Ne, scintillator	20(e^-) 82(ν)	16% FWHH (100 keV)	10	$\nu + e^- \rightarrow \nu + e^-$	18
Present work	LS	170(e^-) 310(ν)	10.5% (200 keV)	10	$\nu + e^- \rightarrow \nu + e^-$	1.8

operating with an alternate liquid-scintillator (LS) solvent, phenylxylylethane (PXE, $C_{16}H_{18}$).[4)] The scintillator is carefully purified to ensure that the ^{238}U and ^{232}Th in it are less than some units of 10^{-16} g/g. The PMTs are 8-in. Electron Tubes Limited (ETL) model 9351 tubes made of low-radioactivity glass and characterized by high quantum efficiency (26% at 420 nm), limited transit time spread (1 ns), and good pulse-height resolution for single photoelectron pulses (peak/valley = 2.5). The number of photoelectrons recorded by one PMT for a 1-MeV energy deposit at the detector's center is about 3.5 for both scintillators.

[4)] With *p*-diphenylbenzene (para-terphenyl) as a primary wavelength shifter at a concentration of 3 g/l along with a secondary wavelength shifter 1,4-bis (2-methylstyrol) benzene (bis-MSB) at 50 mg/l.

3. UPGRADE OF THE CTF DETECTOR

The geometry of the proposed upgrade is presented in Fig. 1 in comparison with Borexino and CTF. The inner vessel is a transparent spherical nylon bag with a radius of 240 cm, containing 50 t of ultrapure pseudocumene with 1.5 g/g of PPO. The active shielding is provided by 100 cm of the outer layer of scintillator. The 800 PMTs are mounted on the open structure at a distance of 440 cm from the detector's center (distance is counted from the PMT photocathode). The comparison of the geometrical parameters of Borexino, CTF, and its upgrade is presented in Table 2.

The choice of the geometry is motivated by the following reasons:

The detector should fit in the existing CTF external tank, which is 10 m high and 11 m in diameter.

The light registration system should provide the maximum possible geometric coverage with a minimum number of PMTs required.

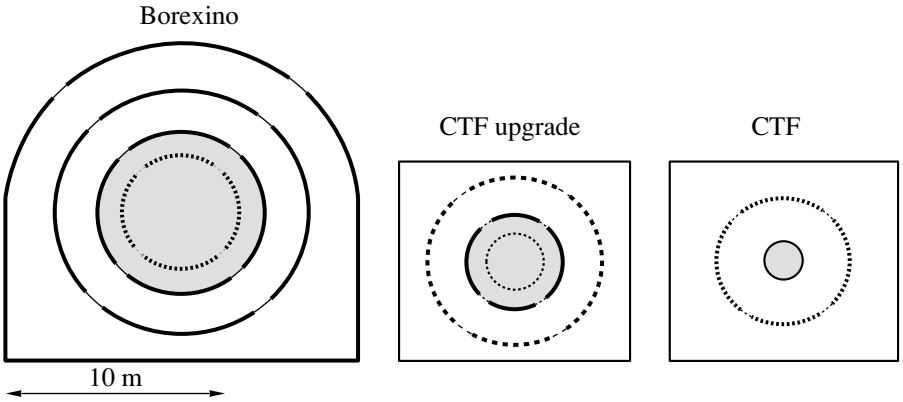

Fig. 1. Comparison of the geometry of the Borexino, CTF, and proposed upgrade of the CTF detector. The inner vessel with scintillator is shown with a gray color. The dashed circumference inside the inner vessel defines the fiducial volume; the outer layer protects the fiducial volume from the external gammas. PMTs are uniformly distributed by the surface shown with a solid line on the Borexino drawing and with a dashed line on the other two.

The active shielding of the fiducial volume is provided by at least 100 cm of PC.

The passive shielding from the gammas originated from PMT impurities is provided by 200 cm of ultrapure water.

The fiducial volume of the detector should be on the order of 10 t.

The inner-vessel size should be as small as possible in order to avoid the loss of light in the scintillator and to provide better detector uniformity.

To lower the detector's threshold ($<$35 keV) in order to acquire the ^{14}C-spectrum shape without deformations caused by the threshold effects.

The Borexino-sized detector is an unfavorable solution because of the huge number of PMTs necessary to provide 4π coverage. The big inner-vessel volume in turn decreases the amount of light escaping from the interior part of the detector. The spatial reconstruction of the lower energy events is complicated because of the multiple absorption and reemission of light on the way to the PMT with a characteristic length of 1 m [17].

The beta decays of ^{14}C in the liquid organic scintillator set a lower threshold on the detector sensitivity. The content of the ^{14}C in pseudocumene used in the CTF detector was at the level of 2×10^{-18} g/g with respect to the ^{12}C content. Although the end point of the ^{14}C β decay is only 156 keV, the energy resolution of the CTF (and Borexino) is not good enough at this energy to set the threshold lower than 250 keV. We suggest using additional PMTs supplied with hexagonal light concentrators in order to provide 4π coverage, in comparison to 21% for CTF and 30% for Borexino. Additional energy resolution improvement (about 15%) in the low-energy region can be achieved by using an energy reconstruction technique discussed in [19].

We considered the contamination of the pseudocumene with the radionuclides of the U–Th chain and with ^{40}K on the level envisaged for the Borexino scintillator. These levels were achieved on the CTF. In such a way, we expect about 2 events/d due to the internal background in 10 t of scintillator. Due to the better energy resolution, there is a possibility of recognizing the signals of the unidentified alpha particles in the region between 350 and 500 keV that give about 30% of the total background in the Borexino "neutrino window" (250–700 keV). The better energy and spatial resolutions will permit us to improve the α/β discrimination capability of the CTF upgrade in comparison to CTF. The decrease in the threshold energy will also allow us to improve the delayed coincidence (DC) discrimination of the events from the radioactive chains.

The outer layer of active volume (100 cm) is used as an active shield against the gammas (mainly from the ^{40}K contained in the PMT glass bulbs). Additional passive shielding with 200 cm of ultrapure water is considered in the present design.

The detector should be supplied with an external muon veto system. The muon veto system consisting of about 50 additional PMTs can be mounted on the top and on the bottom of the cylindrical external tank. The muon recognition efficiency should be at the level of 99.99% in order to guarantee a missed muon count of $<$0.1 per day.

4. DETECTOR'S ENERGY RESOLUTION

A detailed analysis of the energy resolution of the large-volume liquid-scintillator detector can be found in [19, 20]. We give here a brief overview of the main

Table 2. Comparison of the main features of the CTF, Borexino, and proposed upgrade of the CTF detector

Parameter	CTF	Borexino	CTF upgrade
Geometric coverage, %	21	30	$\cong 100$
Light yield, p.e./MeV	360	400	1800
Light yield per PMT for the event at the detector's center μ_0, p.e./PMT/1 MeV	3.6	0.25	2.25
Energy resolution at 200 keV, keV ($\sim 1/\sqrt{\text{Light yield}}$)	27	26	10.5
Threshold, keV	250	250	170
Muon veto PMTs	16	200	50
Number of PMTs	100	2200	800
Total natural K content in the PMTs, g	8	176	64
Distance between the PMTs and detector's center, cm	330	675	440
Spatial resolution at 200 keV, cm ($\sim\langle 1/\sqrt{N_{\text{hit}}}\rangle \cong 1/\sqrt{N_{\text{PM}}(1-e^{-0.2\mu_0})}$)	20	45	8

results because of their importance for further discussion. Taking into account the dependence of the recorded charge on energy, one can write for the CTF charge resolution:[5)]

$$\frac{\sigma_Q}{Q} = \sqrt{\frac{1+\overline{v_1}}{AEf(k_B,E)v_f} + v(p)}. \qquad (1)$$

Here, $\overline{v_1} = (1/N_{\text{PM}})\sum_{i=1}^{N_{\text{PM}}} s_i v_{1i}$ is the relative variance of the PMT single-photoelectron-charge spectrum (v_{1i}) averaged over all CTF PMTs (N_{PM}), taking into account the ith PMT relative sensitivity s_i; A is the scintillator light yield measured in photoelectrons (p.e.) per MeV; $f(k_B,E)$ is a function taking into account suppression of the light yield at low energies, so-called ionization quenching; this function has been studied in [21]; $v(p)$ is a parameter that takes into account the variance of the signal for the source uniformly distributed over the detector's volume. Because of the detector's spherical symmetry, one can describe the dependence of the recorded charge on the distance from the event to the detector's center $\mathbf{r}$ with a function $Q(r)$ of a single parameter $\mathbf{r}$, $Q(r) = Q_0 f_R(r)$, where Q_0 is the charge collected for an event of the same energy occurring at the detector's center. The $v(p)$ parameter is the relative variance of the $f_R(r)$ function over the detector volume:

$$v(p) \equiv \frac{\langle f_R^2(r)\rangle_V}{\langle f_R(r)\rangle_V^2} - 1; \qquad (2)$$

v_f is the volume factor, coming from the averaging of the signals over the CTF volume, $v_f \equiv \langle Q(r)\rangle_V / Q_0$.

For the details of the meaning of the parameters, see [19, 20]. For the signal calculation, we used the following parameters: $A = 1800$ p.e./MeV, $v_1 = 0$, $v_f = 1$, $v(p) = 2.3\times 10^{-3}$, $k_B = 0.0167$.

The signal $S(Q)$ recorded by the detector is the convolution of the "pure" signal spectrum $S_0(Q)$ with the detector's resolution:

$$S(Q) = N_0 \int S_0(E(Q'))\frac{dE}{dQ}\text{Res}(Q,Q')dQ', \qquad (3)$$

where

$$Res(Q,Q') = \frac{1}{\sqrt{2\pi}\sigma_Q}\exp\left[-\frac{1}{2}\left(\frac{Q-Q'}{\sigma_Q}\right)^2\right]$$

is the detector response function and σ_Q is defined by (1).

5. DETECTOR'S SPATIAL RESOLUTION

The spatial resolution of the detector is proportional to the mean of the inverse number of PMTs hit in the event:

$$\sigma_{x,y,z} = \sigma_0 \left\langle \frac{1}{\sqrt{N_{\text{hit}}}} \right\rangle \qquad (4)$$

[5)] This is the case when no energy reconstruction is performed and the energy is defined by dividing the total recorded charge by the p.e. yield A: $E = Q/A$.

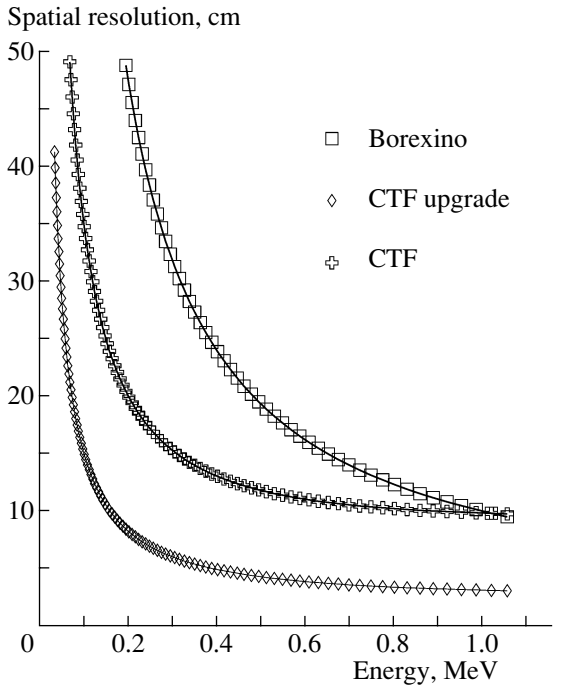

Fig. 2. Spatial resolution of three detectors as a function of event energy.

$$\cong \frac{\sigma_0}{\sqrt{N_{\mathrm{PM}}(1-\exp(-\mu_0 E F(T_{\mathrm{cut}},\mu)))}},$$

where μ_0 is the mean p.e. number recorded for an event of 1 MeV at the detector's center, N_{PM} is the number of PMTs of the detector, $F(T,\mu) = \int_{T_{\min}}^{T} \rho(t,\mu)dt$ is the part of the p.d.f. of the first p.e. recorded, that has been taken into account in the reconstruction algorithm.

The results of the estimation of the spatial resolution for three-detector geometries (CTF, Borexino, and CTF upgrade) are shown in Fig. 2. The σ_0 value for the CTF detector is $\sigma_0(1\,\mathrm{MeV}) = 10$ cm (measured value, [15]); for the Borexino, we used the results of MC simulations giving $\sigma_0(1\,\mathrm{MeV}) = 10$ cm ([14]); and $\sigma_0 = 3.5$ cm for the CTF upgrade was obtained by scaling the CTF result by the factor $\sqrt{N_{\mathrm{PM}}(\mathrm{Upgrade})/N_{\mathrm{PM}}(\mathrm{CTF})} = \sqrt{8}$.

6. BACKGROUNDS

The sensitivity of the detector depends on the presence of the background in the 170–250 keV energy window. As in Borexino and CTF (see [14, 15]), the main sources of background are:

internal background, including ^{14}C beta-decay counts in the neutrino window;

background from the radon dissolved in the buffer;

external gamma background;

cosmic ray background.

In the following subsections, we give an estimate of the background contribution from each source.

6.1. Internal Background from the Metallic Ions

The contamination of the scintillator with natural radioactive isotopes gives a total rate of 2400 event/yr with the following assumptions:

secular equilibrium of the radioactive elements in the decay chains;

the ^{238}U, ^{232}Th, and K_{nat} (natural potassium) content in the scintillator equal to 10^{-16} g/g;

90% capability to reject alphas (α/β-discrimination technique based on the different shape of the detector response to α and β);

95% rejection efficiency of the delayed coincidence method based on the tagging of the ^{214}Bi–^{214}Po decay chain;

95% efficiency of the statistical subtraction method based on deducing the isotopes in the chain preceding the Bi–Po coincidence.

A more complete discussion of the background reduction techniques can be found in [22]. The detector's excellent resolution can improve the efficiency of all the techniques.

Only 140 events of the total amount fall into the 170–250 keV energy window.

6.2. ^{14}C Background

6.2.1. ^{14}C spectrum. The major part of the CTF background in the energy region up to 200 keV is induced by β activity of ^{14}C. The β decay of ^{14}C is an allowed ground-state-to-ground-state ($0^+ \to 1^+$) Gamow–Teller transition with an endpoint energy of $E_0 = 156$ keV and half-life of 5730 yr. The β-energy spectrum with a massless neutrino can be written in the form [23]

$$dN(E) \sim F(Z,E)C(E)pE(Q-E)^2 dE, \quad (5)$$

where E and P are the total electron energy and momentum, $F(E,Z)$ is the Fermi function with correction of screening by atomic electrons, and $C(E)$ contains departures from the allowed shape.

For $F(E,Z)$, we used the function from [24] that agrees with the tabulated values of the relativistic calculation [25]. A screening correction has been made using Rose's method [26] with screening potential $V_0 = 495$ eV. The ^{14}C spectrum shape factor can be parametrized as $C(E) = 1 + \alpha E$. In our calculation, we used the value $\alpha = -0.72$ [27].

The total amount in the 170–250 keV energy window with the energy resolution corresponding to 1800 p.e./MeV is 3485 event/yr if the ^{14}C-content is 2×10^{-18} g/g. This is the content achieved with the CTF-I setup [27]. The yearly ^{14}C event counts for a 10-t fiducial volume of the proposed detector are tabulated in Table 3. The counts from other background sources are presented in the same table.

6.2.2. ^{14}C spectrum and the detector's threshold. In order to separate events from the background on the ^{14}C spectrum tail, it is necessary to acquire the part of the spectrum under the physical threshold of the detector (170 keV). We propose to use the following technique for the detector triggering. First, the lower level trigger is produced as a coincidence of the signals from 20 PMTs in the 50-ns gate. This will give a random coincidence rate at the level of $<10^{-10}$ event/yr if all the PMTs have a dark rate less than 5 kHz. The high-level trigger is produced if the total collected charge is greater than the preset threshold $Q_{\rm th}$. The choice of this threshold will be defined by the resolution of the detector. Let us estimate the last quantity. The mean number of channels fired for the event with an energy E at the detector's center is

$$\langle N \rangle = N_{\rm PM}(1 - e^{-\mu_0}), \qquad (6)$$

where μ_0 is the mean number of photoelectrons registered by one PMT in an event of energy E and $N_{\rm PM} = 800$ is the number of the PMTs in the detector. The solution to (6) for $\langle N \rangle = 20$ will yield $\mu_0 \simeq 0.025$, i.e., a total collected charge of 20 p.e. This value is the detector threshold in the sense that only 50% of the events with an energy corresponding to this charge are recorded. Of course, this causes a significant spectrum deformation near the threshold. In order to avoid these deformations, one should set the threshold at a level that will cut the events with energies not providing 100% detection, i.e., $Q_{\rm th} + 3\sigma_{Q_{\rm th}} = 20 + 3\sqrt{20} = 33.4$ p.e. This charge corresponds to approximately 35 keV if the ionization quenching at this energy is 50%. Although the calculation was performed for an event at the detector's center and the real situation is complicated by the electronics threshold, it gives a value very close to the one obtained with Monte Carlo simulation.

6.2.3. ^{14}C pileup events. A potential danger are the ^{14}C pileup events, i.e., events occurring sequentially within a coincidence window. Such an event can in principle influence the ^{14}C spectrum tail, as one can see in Fig. 3. The fraction of ^{14}C pileup events with energies above 170 keV is about 5%. The total amount of pileup events depends on the ^{14}C relative abundance and on the coincidence window:

$$N_{\rm p.u.} = \tau_{\rm gate} \times f_{^{14}{\rm C}}^2 \times T, \qquad (7)$$

Table 3. ^{14}C event counts and other internal background sources' events in the 10-t fiducial volume of the proposed upgrade of the CTF detector (for 1 yr of data taking). (The expected effect for the *pp*, ^{7}Be, and total neutrino count in the SSM is presented for comparison.)

E, keV	^{14}C	Int. bkg.	$\sqrt{\text{bkg}}$	*pp*	^{7}Be	Total ν's
148.4	73 291.8	6.8	270.7	74.6	13.7	93.3
151.6	49 755.8	6.7	223.1	71.7	13.7	90.4
154.8	32 443.6	6.7	180.1	68.9	13.7	87.5
158.1	20 254.8	6.6	142.3	66.0	13.7	84.6
161.3	12 070.3	6.5	109.9	63.2	13.6	81.8
164.5	6846.4	6.4	82.8	60.4	13.6	78.9
167.7	3686.5	6.4	60.8	57.6	13.6	76.1
170.9	1879.8	6.3	43.4	54.7	13.6	73.2
174.1	905.8	6.2	30.2	52.0	13.6	70.4
177.3	411.6	6.2	20.4	49.2	13.6	67.6
180.6	176.1	6.1	13.5	46.4	13.5	64.8
183.8	70.8	6.0	8.8	43.7	13.5	62.1
187.0	26.7	6.0	5.7	41.1	13.5	59.4
190.2	9.4	5.9	3.9	38.5	13.5	56.8
193.4	3.1	5.9	3.0	35.9	13.5	54.2
196.6	1.0	5.8	2.6	33.4	13.5	51.7
199.8	0.3	5.7	2.5	31.0	13.5	49.2
203.0	0.1	5.7	2.4	28.7	13.4	46.9
206.2	0.0	5.6	2.4	26.4	13.4	44.5
209.4	0.0	5.6	2.4	24.2	13.4	42.2
212.7	0.0	5.5	2.3	22.0	13.4	40.0
215.9	0.0	5.5	2.3	19.9	13.4	37.7
219.1	0.0	5.4	2.3	17.8	13.4	35.6
222.3	0.0	5.3	2.3	15.8	13.4	33.4
225.5	0.0	5.3	2.3	13.9	13.3	31.3
228.7	0.0	5.2	2.3	12.1	13.3	29.3
231.9	0.0	5.2	2.3	10.4	13.3	27.5
235.1	0.0	5.1	2.3	8.8	13.3	25.7
238.3	0.0	5.1	2.3	7.3	13.3	24.1
241.5	0.0	5.0	2.2	5.9	13.3	22.6
244.7	0.0	5.0	2.2	4.7	13.3	21.4
247.9	0.0	4.9	2.2	3.6	13.3	20.3

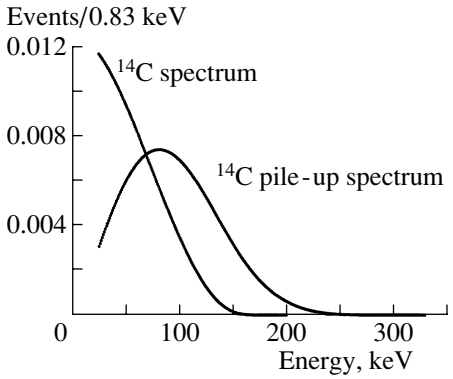

Fig. 3. Spectrum of pileup events in comparison to the ^{14}C spectrum.

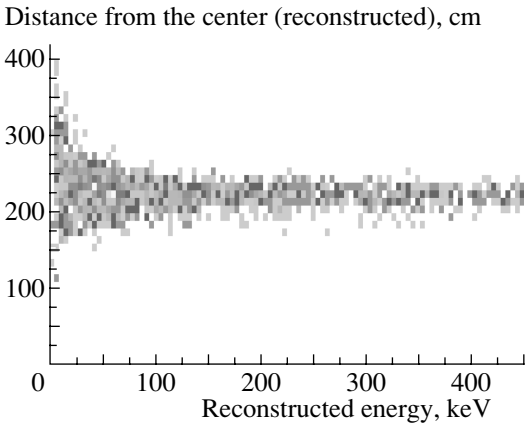

Fig. 4. External gamma background simulation in the energy window up to 450 keV (1 d). One can see that an $R < 150$ cm spatial cut will eliminate all the events in the *pp*-neutrino window (170–250 keV).

where T is the total time of data taking, $\tau_{\text{gate}} = 60$ ns is the coincidence gate width, and f_{14_C} is the frequency of ^{14}C events. For a ^{14}C abundance of 2×10^{-18} g/g, the mean rate of events caused by ^{14}C β decay is 2.2 Hz. With these values the number of pileup events is 2.5/d, and the number of events with energy greater than 170 keV is only about 0.13/d.

The excellent spatial resolution of the detector provides a further possibility of suppressing the number of these events by a factor of at least $\left(\frac{4}{3}\pi(3\sigma_R)^3/V_{\text{FV}}\right)^2 = (3\sigma_R/R_{\text{FV}})^6 \simeq 10^{-5}$, where σ_R is the spatial resolution at 170 keV and $R_{\text{FV}} = 140$ cm is the radius of the fiducial volume. Thus, one can conclude that pileup events do not influence the shape of the ^{14}C spectrum within the considered energy interval.

Table 4. The sensitivity of the detector to the SSM *pp* neutrinos as a function of the content of ^{14}C in the scintillator (energy in keV)

^{14}C, g/g	2×10^{-18}	10^{-19}	10^{-20}	10^{-21}
Threshold ($\sqrt{\text{bkg}} = \text{eff}$)	174 (40)	145	0	0
Threshold ($2\sqrt{\text{bkg}} = \text{eff}$)	182	156	125	0
Energy interval	170–250	160–250	150–250	150–250
^{14}C events	3485	1304	643	64
Int. bkg (Borexino)	140	159	180	180
pp	647	829	1035	1035
Total ν	1092	1329	1591	1591
Fitted region	40–330	40–330	40–330	40–330
Uncertainty (1σ C.L.), fit	0.056	0.05	0.04	0.034

6.3. Background from the Radon in the Water Buffer

This background is expected to be efficiently rejected by the radial cut. The special nylon shroud tested with the CTF-II setup should prevent the diffusion of the external radon into the scintillator volume, reducing the background observed in the CTF by a factor of 10 to 1000.

The raw count observed in CTF-I was 0.3 event/(kg keV yr) in the 250–800 keV energy window; in CTF-II, it was about 0.1 event/(kg keV yr). But in the latter case, this background was dominated by the ^{40}K contained in the strings supporting the inner vessel [28].

6.4. External-Gamma Background

The background count, caused mainly by the radioactive contamination of the PMT glass with ^{40}K and the elements of the U–Th chain, has been evaluated with an EGS4 code. We include in the MC simulation the ionization quenching effect [21] and the limited spatial reconstruction ability at lower energies. The assumed content of ^{238}U, ^{232}Th, and K_{nat} in the PMTs is 112.4 μg/PMT, 47.3 μg/PMT, and 62.3 mg/PMT, respectively, which corresponds to the measured radioactive contamination of the phototubes produced with high-purity glass. We add 30% to these values to account for the radioactive contamination of the concentrator and PMT divider, sealing, and support structure.

The results of the simulation are presented in Fig. 4. One can see that an R < 150 cm spatial cut

Table 5. The *pp*-neutrino count rate (counts/yr) in different solar-neutrino-oscillation scenarios for an energy window of 170–250 keV

	SSM	SMA	LMA	LOW	LOW (day)	LOW (night)
pp	647	434	424	414	342	488
Total ν	1092	535	676	673	570	776
^{14}C (2×10^{-18} g/g)				3485		
Int. bkg (Borexino)				140		
Uncertainty (1σ C.L.), fit in 40–330 keV region	0.056	0.077	0.074	0.07	0.085	0.068
Int. bkg ($10 \times$ Borexino)				1400		
Uncertainty (1σ C.L.), fit in 40–330 keV region	0.09	0.13	0.13	0.13	0.15	0.11

Table 6. The discrimination between different neutrino-oscillation scenarios

	SSM			SMA			LMA			LOW		
	N_ϕ	σ	χ^2	N_ϕ	σ	χ^2	N_ϕ	σ	χ^2	N_ϕ	σ	χ^2
SSM	1.02	0.06	72.8	0.53	0.04	85.3	0.66	0.08	72.9	0.64	0.05	72.4
SMA	1.96	0.08	115.1	1.01	0.08	71.0	1.05	0.13	76.3	1.10	0.08	85.2
LMA	1.62	0.09	74.7	0.85	0.07	81.4	1.03	0.13	73.3	1.00	0.08	72.9
LOW	1.64	0.09	74.0	0.85	0.07	82.4	1.05	0.13	73.2	1.02	0.08	72.7

will eliminate all the events in the neutrino window (170–250 keV).

In order to reduce the background from the penetrating gammas, we suggest reducing the amount of construction materials contributing to the background. A significant amount of the material in Borexino is contained in the mu-metal shield of the PMTs, which provides the screening of the PMTs against the terrestrial magnetic field. An alternative solution based on the orientation of PMTs has been studied in [29]. The effect of PMT orientation is comparable to the one achieved with PMT screening with a metal having a high magnetic permeability. Use of this technique could eliminate about 1 kg of material for each PMT in proximity to the inner vessel.

Another possibility of reducing the gamma background is assuming the use of a different topology of the events produced by electrons and gammas. The excellent spatial resolution of the CTF upgrade will permit distinguishing pointlike energy deposits for electrons from the distributed gamma events (β/γ discrimination). The study of the possibility of such discrimination for the Borexino detector is now in progress.

6.5. Cosmic-Ray-Induced Background

The cosmic-ray-induced background can be subdivided into three categories:

(i) muons crossing the water buffer of the detector, producing the Cherenkov light;

(ii) neutrons produced by muon interactions and sequentially stopped in the water or scintillator and emitting 2.2-MeV annihilation gamma;

(iii) secondary radioactive nuclei produced in the muon interactions inside the detector.

Most of the background counts associated with muons can be effectively removed by the muon identifying system (muon veto). One can use the time and spatial structure of the muon-induced events in order to recognize them. The muon identification procedure was able to recognize 95% of the muon-induced events in the CTF-I detector [15]. We also assume the use of a set of PMTs situated on the top and bottom of the cylindrical external tank that will increase the muon identification to a value approaching 100%.

Some of the radioactive products of the muon interactions with the scintillator have a significant lifetime, which makes impossible the use of a muon tag. These isotopes are ^{11}Be (β^-, 11.5 MeV, 13.8 s), ^{10}C (β^+, 1.9 MeV + γ, 0.72 MeV, 19.3 s), ^{11}C (β^+,

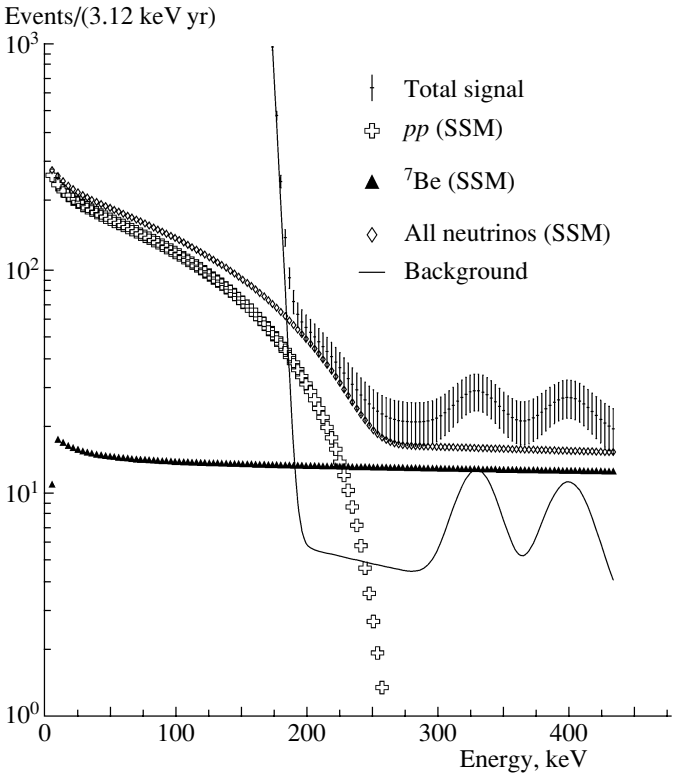

Fig. 5. Signal and background shape for the SSM neutrino fluxes. ^{14}C content is 2×10^{-18} g/g. Other background components are considered to be the same as the Borexino background. Detector mass is 10 t. The resolution is calculated under the assumption of 100% geometric coverage using CTF-I light output (i.e., 1800 p.e./MeV) and is assumed to be $1/\sqrt{N_{\text{p.e.}}}$. The signals shown correspond to 1 yr of data taking.

0.99 MeV, 20.38 min), and ^{7}Be (γ, 0.478 MeV, 53.3 d). The considered neutrino window is too narrow to pick up a significant amount of events from these isotopes. The precise evaluations are now in progress for the Borexino detector [30], but this background will certainly be negligible in comparison to the other sources considered.

6.6. ^{14}C Content: Is It Critical?

It is commonly assumed that the ^{14}C content sets the limit on sensitivity in the low-energy region in the liquid organic scintillator. A ratio as low as 2×10^{-18} g/g was achieved with the CTF detector. There are indications that content of ^{14}C can be even smaller, on the order of 10^{-21} g/g [31].[6)] In this case, the ^{14}C contribution in the background can be reduced by a factor of 2000. It is interesting to study the sensitivity of the detector to *pp* neutrinos as a function of the content of ^{14}C in the scintillator. The results of the study are summarized in Table 4. One can see that the detector sensitivity varies rather slowly with a decrease in the ^{14}C content in the scintillator. There are several reasons for this behavior. First of all, the rate of *pp* neutrinos is quite low, and with minimal background contribution, the statistical fluctuations of the *pp* rate are the major source of the uncertainty. Another source of uncertainty is the irreducible internal background, which becomes comparable to the contribution of ^{14}C events at a lower ^{14}C content. The last reason is the lower threshold of the detector of about 25 keV, which cannot be decreased without picking up random electronic noise. In order to avoid the influence of the threshold effect on the signal shape, it is necessary to set the software threshold even higher, about 40 keV. Another reason to set a higher software threshold is the presence of low-energy external gammas, which can be reconstructed inside the fiducial volume due to the poor spatial resolution at low energies.

We can conclude that lower ^{14}C would be desirable but is not critical for the detector sensitivity to *pp* neutrinos.

[6)] A new petrogeological model allows such a low value; contamination with modern ^{14}C in this case has to be excluded during petroleum refinement [31]. The existing CTF setup is a suitable device for the search for an organic LS with minimal ^{14}C contamination.

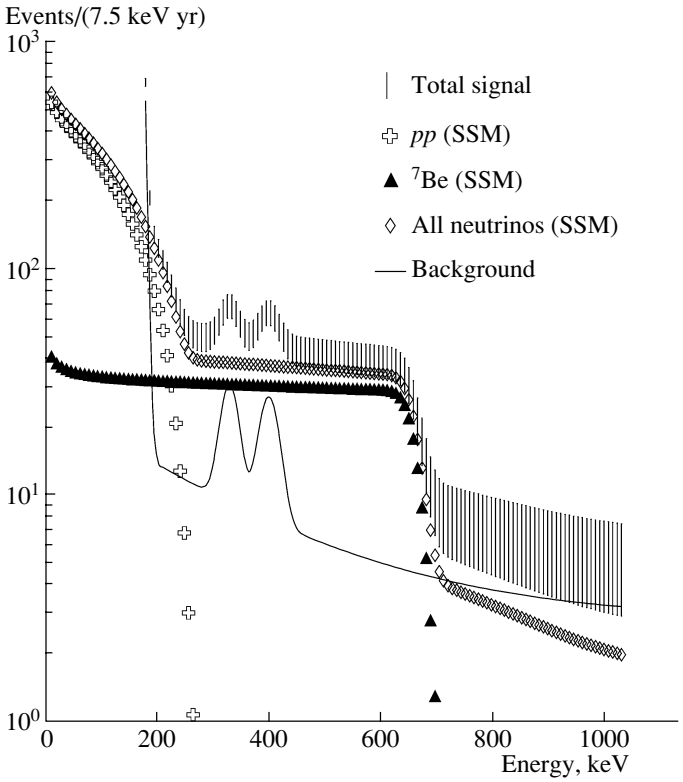

Fig. 6. CTF upgrade. Signal and background shape for the SSM neutrino fluxes. ^{14}C content is 2×10^{-18} g/g. Other background components are considered to be the same as the Borexino background. Detector mass is 10 t. The resolution is calculated under the assumption of 100% geometric coverage using CTF-I light output (i.e., 1800 p.e./MeV) and is assumed to be $1/\sqrt{N_{\text{p.e}}}$. The signals shown correspond to 1 yr of data taking.

7. NEUTRINO SIGNALS

In the calculations, we used SSM fluxes given by the standard solar model [32], neutrino energy spectra from [33–35], and survival probabilities for the different solar neutrino scenarios from [36]. Signal shapes were convolved with the detector response function using (3).

7.1. Sensitivity to pp Neutrinos

The *pp*-neutrino counts in different solar neutrino oscillation scenarios are listed in Table 5. The sensitivity was estimated with the MC method. First, the total signal was calculated with allowance for the detector's resolution. At the next step, a normally distributed random signal was generated at each bin.

A fitting function consists of the function describing the internal background (without ^{14}C), the spectrum of the ^{14}C decay, and the neutrino signal:

$$f(q) = N_{\text{bkg}}\text{bkg}(q) + N_{^{14}C}C(q) + N_\nu\phi_\nu(q). \quad (8)$$

The shape of the internal background bkg(q) was fixed, but its normalization (N_{bkg}) was free. Another free parameter is normalization of the ^{14}C spectrum, $N_{^{14}\text{C}}$.

The rates listed in Table 5 are calculated in the energy window of 170–250 keV taking into account the detector's resolution. The neutral current channel for the neutrinos of nonelectron flavors is taken into account in the calculations. Other neutrino sources also have nonnegligible contributions to the total signal in this energy window. The main source besides *pp* is ^{7}Be neutrinos with a flat spectrum (see Fig. 5).

The uncertainties of the total-neutrino-flux measurement are given in Table 5 for the case of the internal background at the level envisaged for the Borexino and for a background 10 times larger. For convenience, the uncertainties are measured in units of the corresponding model flux. The possible systematic errors due to the unknown shape of the background are not included in the estimation. We assume that MC simulation can reproduce the form of the background and that only the total normalization of this shape is unknown. This assumption is reasonable because of the quite narrow signal window, where the background is dominated by the slowly varying continuous spectrum of the soft part of the gamma spectra of radioactive impurities.

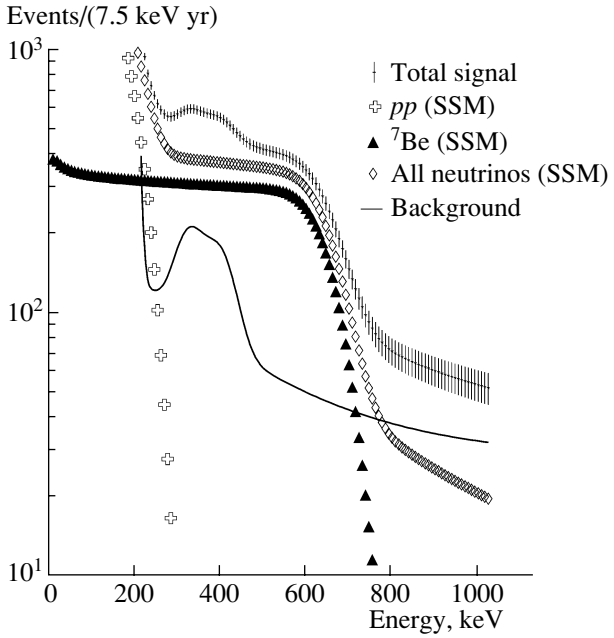

Fig. 7. Borexino. Signal and background shape for the SSM neutrino fluxes. ^{14}C content is 2×10^{-18}g/g. Detector mass is 100 t. The resolution is calculated using 400 p.e./MeV light output and is assumed to be $1/\sqrt{N_{\text{p.e.}}}$. The signals shown correspond to 1 yr of data taking.

7.2. Discrimination Ability in Respect to the Various Solar Neutrino Scenarios

In order to investigate the sensitivity of the setup to the different neutrino oscillation scenarios [36], we performed a fit of the MC-simulated data with the neutrino fluxes in all scenarios. The results are summarized in Table 6. The columns represent the model used for the MC simulation, while in the rows the results of the fit applied using different scenarios are presented. For each fit, we give the total normalization of the flux N_ϕ (in units of the corresponding scenario flux), the flux uncertainty at 1σ C.L. (measured in units of the model used for the fitted flux), and the χ^2 value (80 d.o.f.)

One can see that the small mixing angle (SMA) solution is well discriminated from the others both by the count and by the shape. The low-mixing-angle (LMA) solution and the low-mass/low-probability (LOW) solution are indistinguishable, but the LOW solution has a significant day/night variation.

7.3. Sensitivity to ^{7}Be Neutrinos

The detector will count 1840 ^{7}Be SSM neutrinos per year in the 200–700 keV energy window with the internal background of 736 events. For comparison, the Borexino detector will count 16 152 events in the 250–750 keV energy window with the background of 6468 events. We do not present here the evaluation of the sensitivity of the detector to ^{7}Be neutrinos. It is clear that the lower mass (factor of 10) in comparison to the Borexino detector will limit the sensitivity. Some gain in the sensitivity can be achieved owing to the better energy resolution of the detector (factor of 2.1). The sensitivity relative to Borexino for equal time of data taking and equal specific background can be estimated as $\sqrt{(M_{\text{Det}}/M_{\text{Borex}})(\sigma_{\text{Borex}}/\sigma_{\text{Det}})} \simeq 0.45$. In Figs. 6 and 7, the signal shape for both detectors is presented.

8. IMPROVEMENT OF THE DETECTOR PERFORMANCE

The performance of the detector can be improved by using any of the following ideas:

(i) Use of specially designed photomultipliers, providing better quantum efficiency.

The basic idea is the "recycling" of the incoming photons. Various optical arrangements have been used to improve light absorption by letting incoming light interact with the photocathode material more than once (see, i.e., [37]). This idea is revived in recent works [38, 39], where the authors reported a significant increase in the quantum efficiency, up to a factor of 2.

(ii) Use of beta/gamma discrimination techniques.

The usage of the different topology of the point-like beta events and the spatially distributed gamma events can provide the opportunity to discriminate between beta- and gamma-induced signals with high efficiency. This method exploits the superior resolution of the detector.

(iii) Choice of organic scintillator with lower content of ^{14}C.

There are indications that the content of ^{14}C can be much smaller than that measured with the CTF-I detector, namely, on the order of 10^{-21} g/g [31]. In this case, the ^{14}C contribution in the background can be significantly reduced, which will lead to improvement of the detector's characteristics.

9. CONCLUSIONS

The following upgrade of the CTF detector is considered:

geometric coverage of 100%, providing a light yield of 1800 p.e./1 MeV;

inner vessel radius of 240 cm (50 t of PC);

active shielding of the active volume with 1 m of pseudocumene;

distance of 4.3 m from the photocathode of the PMTs to the center of the detectors.

The project can compete with other existing proposals (see Table 1). At the same time, the proposed detector, being based on technologies already developed for the Borexino project, is more realistic.

Further improvement of the detector performance can be achieved using the techniques mentioned in Section 8.

ACKNOWLEDGMENTS

This work would have been impossible without the support from the INFN sez. di Milano. We would like to thank Prof. G. Bellini and Dr. G. Ranucci, who organized the stay for two of us at the LNGS laboratory during the summer of 2001, as well as the LNGS personal for their friendliness.

We would like to thank all the colleagues from the Borexino collaboration for the pleasure of working together. Special thanks are given to R. Ford for the careful reading of the manuscript.

REFERENCES

1. E. Calabresu, G. Fiorentini, and M. Lissia, astro-ph/9602045.
2. J. N. Bahcall, in *Proceedings of the International Workshop on Low Energy Solar Neutrinos, Tokyo, Japan, 2000*.
3. R. S. Raghavan, in *Abstracts of Papers of LENS Meeting at LNGS (Laboratori Nazionali del Gran Sasso), Assergi, Italy, 1998*; M. Fujiwara *et al.*, nucl-ex/0006006.
4. R. S. Raghavan, Bell Lab. Tech. Memo., 10009622-010606-19TM.
5. H. V. Klapdor-Kleingrothaus, Nucl. Phys. B (Proc. Suppl.) **100**, 350 (2001).
6. The HERON Project, in *Proceedings of the International Workshop "Neurtino Telescopes," Venice, 1999*, Vol. 1, p. 139.
7. Y. Suzuki (for the XMASS Collab.), in *Proceedings of the International Workshop on Low Energy Solar Neutrinos, Tokyo, Japan, 2000*, Ed. by Y. Suzuki (World Sc., Singapore, 2001); Y. Suzuki (for the Xenon Collab.), hep-ph/0008296.
8. A. Sarrat (on behalf of the HELLAZ Collab.), Nucl. Phys. B (Proc. Suppl.) **95**, 177 (2001).
9. H. Ejiri, in *Proceedings of the International Workshop on Low Energy Solar Neutrinos, Tokyo, 2000,* Ed. by Y. Suzuki (World Sci., Singapore, 2001).
10. C. Broggini, in *Proceedings of the International Workshop on Low Energy Solar Neutrinos, Tokyo, 2000,* Ed. by Y. Suzuki (World Sci., Singapore, 2001).
11. D. N. McKinsey and J. M. Doyle, astro-ph/9907314.
12. J. N. Abdurashitov *et al.*, Phys. Rev. C **60**, 055801 (1999).
13. W. Hampel *et al.*, Phys. Lett. B **447**, 127 (1999).
14. G. Alimonti *et al.*, Astropart. Phys. **16**, 205 (2002).
15. G. Alimonti *et al.*, Nucl. Instrum. Methods Phys. Res. A **406**, 411 (1998).
16. G. Alimonti *et al.*, Astropart. Phys. **8**, 141 (1998).
17. G. Alimonti *et al.*, Nucl. Instrum. Methods Phys. Res. A **440**, 360 (1998).
18. G. Ranucci *et al.*, Nucl. Instrum. Methods Phys. Res. A **333**, 553 (1993).
19. O. Smirnov, Borexino Intern. Note 02/27/07 (2002).
20. O. Smirnov, to be published in Prib. Tekh. Éksp. (2003) [Instr. Exp. Techn. (2003)].
21. S. Bonetti, O. Donghi, C. Salvo, and G. Testera, Borexino Intern. Rep. 98/10/15 (1998).
22. C. Arpesella *et al.*, *Borexino at Gran Sasso, Proposal for a Real Time Detector for Low-Energy Solar Neutrino,* Ed. by G. Bellini *et al.* (Dept. of Physics of the University of Milano, 1991), Vol. 1.
23. M. Morita, *Beta Decay and Muon Capture* (Benjamin, Reading, 1973), p. 33.
24. J. J. Simpson and A. Hime, Phys. Rev. D **39**, 1825 (1989).
25. H. Behrens and J. Janecke, *Numerical Tables for Beta Decay and Electron Capture* (Springer-Verlag, Berlin, 1969).
26. M. E. Rose, Phys. Rev. **49**, 727 (1936).
27. G. Alimonti *et al.*, Phys. Lett. B **422**, 349 (1998).
28. L. Cadonati, Borexino Intern. Report 00/08/27 (2000).
29. A. Ianni, G. Korga, G. Ranucci, *et al.*, Preprint No. INFN/TC-00/05 (Laboratori Nazionali del Gran Sasso, 2000).
30. T. Hagner, F. von Hentig, B. Heisinger, *et al.*, Astropart. Phys. **14**, 33 (2000).
31. E. Resconi, PhD Thesis (Universita' degli Studi di Genova, 2001); S. Schoenert, personal communication.
32. J. N. Bahcall, H. Pinsonneault, and S. Basu, astro-ph/0010346.
33. J. N. Bahcall and R. K. Ulrich, Rev. Mod. Phys. **60**, 297 (1988).
34. J. N. Bahcall, E. Lisi, D. E. Alburger, *et al.*, Phys. Rev. C **54**, 411 (1996).
35. J. N. Bahcall, Phys. Rev. C **56**, 3391 (1997).
36. J. N. Bahcall, P. I. Krastev, and A. Ju. Smirnov, Phys. Rev. D **58**, 096016 (1998).
37. W. D. Gunter, Jr., G. R. Grant, and S. A. Shaw, Appl. Opt. **9** (2), 251 (1970).
38. S. Harmer, S. Hallensleben, and P. D. Townsend, Nucl. Instrum. Methods Phys. Res. B **166–167**, 798 (2000).
39. S. Hallensleben, S. Harmer, and P. D. Townsend, Opt. Commun. **180**, 89 (2000).

Physics of Atomic Nuclei, Vol. 66, No. 4, 2003, pp. 724–736. From Yadernaya Fizika, Vol. 66, No. 4, 2003, pp. 754–767.

ELEMENTARY PARTICLES AND FIELDS
Theory

Renormalization Group Summation, Spectrality Constraints, and Coupling Constant Analyticity for Phenomenological Applications of Two-Point Correlators in QCD*

A. A. Pivovarov**

Institute for Nuclear Research, Russian Academy of Sciences, pr. Shestidesyatiletiya Oktyabrya 7a, Moscow, 117312 Russia

Received July 7, 2001; in final form, June 11, 2002

Abstract—The analytic structure in the strong coupling constant that emerges for some observables in QCD after duality averaging of renormalization-group-improved amplitudes is discussed, and the validity of the infrared renormalon hypothesis for the determination of this structure is critically reexamined. A consistent description of peculiar features of perturbation theory series related to hypothetical infrared renormalons and corresponding power corrections is considered. It is shown that perturbation theory series for the spectral moments of two-point correlators of hadronic currents in QCD can explicitly be summed in all orders using the definition of the moments that avoids integration through the infrared region in momentum space. Such a definition of the moments relies on the analytic properties of two-point correlators in the momentum variable that allows for shifting the integration contour into the complex plane of the momentum. For definiteness, an explicit case of gluonic current correlators is discussed in detail.

1. INTRODUCTION

General properties of quantum field theory impose strong constraints on model building for elementary particle phenomenology. Symmetry properties of interactions lie in the foundation of the Standard Model [1], causality leads to restrictions on the analytic structure of scattering amplitudes as functions of energy, and the freedom of redefinition of ultraviolet subtraction procedures in renormalizable theories leads to the renormalization group invariance which is a basic property of theoretical quantities corresponding to physical observables [2]. While such general properties are supposed to be valid in a full theory, there is little known about the very existence of realistic nontrivial quantum field models—only some simplified examples (mainly in two-dimensional space-time) have explicitly been constructed (e.g., [3]). The realistic four-dimensional models suitable for particle phenomenology are mainly analyzed within perturbation theory in the coupling constant and only the first few terms of perturbative expansions for physical observables are usually available. Some general results on the asymptotic behavior of high orders of perturbation theory have been obtained in simple models by using the steepest descent method for computing the functional integral determining the generating functional of Green's functions. In some models of quantum field theory, where the explicit solutions of the relevant classical equations of motion were found, the particular results on the asymptotic behavior of the coefficients of perturbation theory series are also known [4]. For example, the solutions of the classical field equations are known in the important case of non-Abelian gauge theories [5] that provides the appropriate saddle-point configurations for the steepest-descent method of evaluating the functional integrals [6] and allows for deeper understanding of the ground state structure in these models [7]. Besides the steepest-descent methods for evaluating the functional integrals, the all-order perturbation theory results are also discussed using a particular way of resumming some special subsets of perturbation theory diagrams [8, 9]. The contributions related to the renormalization group running of the coupling constant and/or masses under the integration sign are generally referred to as renormalon contributions [10].

At present, the problem of evaluating the high-order perturbation theory contributions to physical observables becomes a practical issue for high-precision tests of the Standard Model and search for new physics as the accuracy of experimental data continues to improve [11]. It is most important in perturbative QCD because the strong coupling

*This article was submitted by the author in English.

**e-mail: aapiv@ms2.inr.ac.ru

constant α_s is numerically large at low energies. Since the perturbation theory expansion in α_s is believed to be only asymptotic in general, a resummation of all-order terms gives a possible way to improve the accuracy of theoretical predictions. An example of the infinite resummation of perturbation theory diagrams is an exact account of the Coulomb interaction in the processes of heavy quark production near the threshold [12] that allows for a significant improvement in the high-precision description of the top–antitop production [13]. Note that this resummation is reliable because it does not really include the strong coupling regime of QCD. For light quarks and massless gluons with a genuine strong interaction in the infrared domain, there is no successful recipe of resumming the subsets of perturbation theory diagrams that could lead to the description of observables in terms of physical hadrons [10]. To deal with the regime of strong coupling in the low-energy hadron phenomenology, one exploits an idea of averaging over some energy interval. It is assumed that the theoretical predictions for averaged quantities obtained with the use of perturbation theory in the strong coupling constant in terms of quark–gluon degrees of freedom can reliably be confronted with experimental data measured in terms of the observed hadrons. This assumption is known as the duality concept (see, e.g., [14]). While the duality assumption is a real basis for using perturbation theory in the low-energy hadron phenomenology, it is, however, difficult to control the accuracy of this assumption quantitatively in concrete applications. The most advanced quantitative study of the validity of the duality concept has been done for the observables related to the two-point correlators of hadronic currents because of their simple analytic properties in the momentum. The accuracy of the perturbation theory series for the two-point correlators can be improved substantially by the renormalization group resummation that is an efficient tool of calculating various asymptotics of the Green's functions. The appearance of the renormalization group invariance is a consequence of the freedom of performing ultraviolet subtractions and fixing the normalization of the theory that leads to a possibility of redefinition of the coupling constant as an expansion parameter of perturbation theory. Technically, a simple way to implement the renormalization group improvement of perturbation theory series is to use a running coupling constant normalized in the vicinity of a physical scale of the process of interest. Such a choice of normalization for the coupling constant allows one to resum large logarithms related to the difference of scales in all orders of perturbation theory. Because of the final average of the strong interaction amplitudes over the energy interval, as the duality concept requires for comparison with the experimental data, one can choose whether the renormalization group improvement should be done before or after averaging. In general, these two operations—duality averaging and renormalization group improvement—do not commute. Performing the renormalization group improvement of theoretical amplitudes computed in the perturbation theory framework before the final averaging allows one to resum a lot of regular corrections relevant to the running of the coupling constant and/or masses only; one can interpret this procedure as a determination of a proper scale for the averaged observables. The technique of renormalization group improvement for the moments of two-point correlators before the final averaging necessary for physical observables is known as the contour-improved perturbation theory [15] and is especially important at low energies where the QCD coupling constant α_s is large and higher order perturbation theory terms can be numerically important: they can change the results of finite-order perturbation theory by an amount comparable with the present experimental precision. The precision of present experimental data on τ-lepton decays, for instance, suffices for distinguishing the results obtained in the contour-improved and finite-order perturbation theory frameworks [16].

Accounting for the running of the coupling constant in perturbation theory by using the renormalization group improvement under the integration sign is close in spirit to the formulation of a calculational scheme for the Green's functions within Schwinger–Dyson equations (a skeleton expansion). Within the Schwinger–Dyson formulation of perturbation theory, one can use either finite-order perturbation theory or renormalization-group-improved theory for the irreducible vertices that constitute the building blocks of the integral equations. The Schwinger–Dyson technique has extensively been used for investigating the behavior of the fermion propagator beyond the QCD perturbation theory approximation in relation to the problem of mass generation in massless theories and spontaneous symmetry breaking [17]. It is known that the reiteration of the running coupling constant into loops can be infrared dangerous (just to see how it happens, one can think of perturbation theory expansions in terms of a bare coupling constant in dimensional regularization and compare the results of such reiteration with the situation in superrenormalizable theories where the coupling constant is dimensional). The reason for the singularities is that the renormalization group summation in QCD is applicable to Green's functions at large values of momenta, while the asymptotic behavior is determined by performing an analytic

continuation of the functions obtained after the renormalization group improvement. Therefore, analytic properties of amplitudes in the whole complex plane of momenta in finite-order perturbation theory can differ from those after the renormalization group improvement. This difference in analytic properties can lead to some singularities (usually referred to as infrared renormalons in QCD) when the perturbative renormalization group running is extrapolated to the region where perturbation theory is not valid [18, 19]. For asymptotically free QCD in the leading order of the running, the structure of singularities related to the infrared renormalon dominance hypothesis in connection with power corrections in massless theories was discussed in [20].

In the present paper, the resummation of the effects of running is discussed by way of the example of the moments of two-point correlators of hadronic currents. The two-point correlators are the simplest Green's functions with well-established analytic properties in momenta. Two-point correlators are important for phenomenology; they are relevant for describing the processes of e^+e^- annihilation into hadrons and/or τ-lepton hadron decays [21]. Note that the correlators of gauge-invariant currents built from gluonic operators describe a spectrum of glueballs, the experimental observation of which would give strong additional support for QCD as a theory of hadrons. Gluonic current correlators are an actual choice for the analysis in the present paper.

2. BASIC ANALYTIC PROPERTIES OF TWO-POINT CORRELATORS AND DEFINITION OF THE SPECTRAL MOMENTS

In this section, general definitions and notation are given. The correlator of a hadronic current $j(x)$ has the form

$$i\int\langle Tj(x)j^\dagger(0)\rangle e^{iqx}dx=\Pi(q^2), \qquad (1)$$

where $\Pi(q^2)$ is an invariant function. Analytic properties of the function $\Pi(q^2)$ in the variable q^2 are fixed by a dispersion relation (Källen–Lehmann, or spectral, representation)

$$\Pi(q^2)=\int\frac{\rho(s)ds}{s-q^2}+\text{ subtractions}, \qquad (2)$$

where the spectral density $\rho(s)$ is determined by a sum over the states of the theory (e.g., see [22]) and ultraviolet subtractions are a polynomial in q^2. The spectrum of the correlator in Eq. (1), or the support of the function $\rho(s)$ from Eq. (2), is determined by the singularities of the function $\Pi(q^2)$ in the complex q^2 plane. The spectral density $\rho(s)$ is then given by the discontinuity of the function $\Pi(q^2)$ across the spectrum

$$\rho(s)=\frac{1}{2\pi i}(\Pi(s+i0)-\Pi(s-i0)), \qquad (3)$$
$$s\in[\text{spectrum}].$$

In QCD with massless quarks and gluons, a general assumption about the spectrum (spectrality condition) is $s\geq 0$ or $[\text{spectrum}]=[0,\infty]$. This assumption is based on the Fock representation for the states in terms of massless quarks and gluons (see, e.g., [22]). Note that this is an assumption, and, in fact, analytic properties of $\Pi(q^2)$ and, therefore, the support of the spectral density $\rho(s)$ depend on the interaction. The dependence of the spectrum on interaction can readily be seen in the example of heavy charged particles with Coulomb interaction. For a pair of heavy particles with masses m_1 and m_2, one would expect the spectrum start at the threshold $s_{\text{thr}}=(m_1+m_2)^2$, which is the case of a perturbation theory consideration in the Fock space. However, if Coulomb interaction is present, it is true only for the repulsive interaction, while attractive interaction leads to the appearance of Coulombic poles below the threshold. In QCD, the shape of the spectrum near the heavy quark threshold also depends on the definition of the masses used for describing heavy quarks and on other details of the interaction (e.g., the theoretical spectrum can be different at different orders of perturbation theory [23]). Such a situation is well known also from the analysis of simplified models [24]. Thus, the theoretical spectrum of a hadronic correlator is a dynamical quantity, while the constraints on the support of the spectral density stemming from the kinematical considerations based on the values of masses of the asymptotic states in perturbation theory are not always valid in the full theory.

In asymptotically free QCD, the function $\Pi(q^2)$ is reliably computable theoretically within perturbation theory in the Euclidean domain or in the complex q^2 plane sufficiently far from the positive semiaxis $q^2>0$, what allows one, in principle, to find theoretical predictions for the physical observables. Still, to extract a theoretical prediction for the spectral density $\rho(s)$ from the function $\Pi(q^2)$ is not straightforward. The point is that $\Pi(q^2)$ is only known as a perturbation theory expansion in the coupling constant at large Euclidean q^2, while $\rho(s)$ is given by a discontinuity across singularities of $\Pi(q^2)$ in the complex q^2 plane. However, the perturbation theory calculation of the function $\Pi(q^2)$ is not justified near its singularities. Therefore, the analytic continuation in the complex

q^2 plane to the vicinity of the positive semiaxis and into the infrared region is necessary. The analytic continuation is an incorrectly set operation; i.e., small errors of the initial function $\Pi(q^2)$ at Euclidean points can produce large errors in $\rho(s)$. This instability is especially important for a theoretical evaluation of $\rho(s)$ at low energies. The problem of performing an analytic continuation can also be reformulated in the language of integral equations since the dispersion relation in Eq. (2) gives the correlation function $\Pi(q^2)$ as an integral transformation of the spectral density $\rho(s)$. Relation (2) is a Fredholm integral equation of the first kind which is known to lead to an incorrectly set problem. Thus, the errors of $\rho(s)$ [as a solution to Eq. (2)] are not continuously related to the errors of $\Pi(q^2)$ [as initial data of Eq. (2)] and can be large even if errors of $\Pi(q^2)$ in the Euclidean domain are sufficiently small. The general procedure of constructing the approximate solutions to incorrectly set problems was suggested by Tikhonov and is known as regularization. Averaging the spectral density over a finite energy interval (sum rules) can be considered as a particular realization of Tikhonov's regularization procedure. One wants to theoretically study the function $\rho(s)$ at low energy because its experimental counterpart—the hadronic spectral density $\rho^{\mathrm{had}}(s)$—can directly be measured at low energy with high precision. Thus, while a pointwise description of the spectral density $\rho(s)$ at low energy is beyond the reach of perturbation theory, the appropriate quantities for the theoretical analysis in perturbative QCD are the spectral moments or integrals of $\rho(s)$ with a set of weight functions. This is a manifestation of the fact that the theoretical spectral density behaves, in general, more like a distribution rather than a continuous function of energy.

The moments of the spectral density $\rho(s)$ over a finite energy interval are defined by the relation

$$M_n = (n+1)\int^{s_0} \rho(s)\frac{s^n ds}{(s_0)^{n+1}}. \qquad (4)$$

The factor $(n+1)$ in the definition of the moments is chosen to have all contributions of the leading order of perturbation theory uniformly normalized to unity. Equivalently, one can say that all measures defined on the interval $[0, s_0]$

$$(n+1)\frac{s^n}{s_0^{n+1}}ds = d\left(\frac{s}{s_0}\right)^{n+1} \qquad (5)$$

are normalized to unity. Note that the accuracy of the perturbation theory evaluation of a given moment depends on a particular weight function.

With the dispersion relation given in Eq. (2), one can rewrite the moments in Eq. (4) as some integrals along a contour in the complex q^2 plane [25]. For practical calculations of the moments, a convenient contour is a circle with the radius s_0, although the results are independent of the shape of the contour when it is deformed in the analyticity domain of the correlator. The contour representation of the moments reads

$$M_n = (n+1)\frac{(-1)^n}{2\pi i}\oint\limits_{|z|=s_0} \Pi(z)(z/s_0)^n dz/s_0 \qquad (6)$$

$$= (n+1)\frac{(-1)^n}{2\pi i}\oint\limits_{|z|=1} \Pi(s_0 z)z^n dz$$

$$= (n+1)\frac{(-1)^n}{2\pi}\int\limits_{-\pi}^{\pi} \Pi(s_0 e^{i\varphi})e^{i(n+1)\varphi}d\varphi.$$

Note that the moments on the circle as given in Eq. (6) are just Fourier coefficients of correlation functions, which allows one to use a well-developed mathematical technique of Fourier analysis to study them.

Theoretical calculations of the moments are usually performed within the operator product expansion (OPE) for the correlation function $\Pi(q^2)$ [26–28]. The OPE expression for the correlator contains a perturbation theory part and power corrections. The perturbation theory part can further be improved by using the renormalization group summation. In this paper, we consider only the perturbation theory part of the theoretical correlator $\Pi(q^2)$. If the renormalization-group-improved $\Pi(q^2)$ is used under the integration sign for the moments, it implies a resummation of the effects of running [15]. This technique was used for τ-decay analysis [15, 29]. Power corrections within OPE—nonperturbative terms—appear by prescribing the nonvanishing vacuum expectation values to the local operators of higher dimensionality [27, 28]. The contributions of these terms to the moments can be found with the Cauchy theorem (e.g., see [30]). At present, the qualitative change in the phenomenology of sum rules is that the high-order perturbation theory terms for hadronic correlators are known in various hadronic channels and the numerical value of the strong coupling constant is larger than that of the original papers; therefore, the perturbation theory corrections are important numerically. It was already noted that, in some channels, the perturbation theory corrections can numerically dominate over the power corrections, which makes the study of perturbation theory corrections necessary for the present phenomenology [31].

3. PROPERTIES OF THE CORRELATOR OF GLUONIC CURRENTS

As a concrete example, we take a correlator of the gluonic current $G^2 = G^a_{\mu\nu}G^a_{\mu\nu}$, where $G^a_{\mu\nu}$ is a strength tensor of the gluon field. To the leading order of perturbation theory, the renormalization-group-invariant expression for the current can be chosen in the form

$$j_G = \alpha_s G^2, \tag{7}$$

where α_s is the strong coupling constant of QCD. This current is related to the trace of the QCD energy–momentum tensor θ^μ_μ in the approximation of massless quarks and can serve as an interpolating operator for glueballs. The full renormalization-group-invariant expression for θ^μ_μ in QCD with massless quarks is $(\beta(\alpha_s)/2\alpha_s)G^2$, where $\beta(\alpha_s)$ is the QCD β function; this is not important for us in the following. The correlator of the currents j_G reads

$$\frac{\pi^2}{2} i \int \langle T j_G(x) j^\dagger_G(0)\rangle e^{iqx} dx = q^4 \Pi_G(q^2). \tag{8}$$

Note that a kinematical factor q^4 is removed from the definition of the function $\Pi_G(q^2)$, which is justified within perturbation theory. The Adler function

$$D_G(Q^2) = -Q^2 \frac{d}{dQ^2}\Pi_G(Q^2), \quad Q^2 = -q^2, \tag{9}$$

has a simple form in the leading order of perturbation theory:

$$D_G(Q^2) = \alpha_s(Q^2)^2(1 + O(\alpha_s)). \tag{10}$$

This form of the correlator (the factor $\alpha_s(Q^2)^2$ for the Adler function) is the real reason for the choice of the gluonic channel, since it makes further considerations technically simpler. A theoretical prediction for the function $D_G(Q^2)$ has been calculated up to the third order of perturbation theory [32, 33]. Our main aim is to take into account the effects of running of the coupling for evaluating the moments of the spectral density; therefore, the introduction of an effective charge is convenient [34]. Indeed, high-order corrections can be accounted for by introducing the effective charge $\alpha_G(Q^2)$ in all orders of perturbation theory by the relation [32]

$$D_G(Q^2) = -Q^2 \frac{d}{dQ^2}\Pi_G(Q^2) \equiv \alpha_G(Q^2)^2. \tag{11}$$

The effective strong coupling constant $\alpha_G(Q^2)$ obeys the renormalization group equation

$$Q^2 \frac{d}{dQ^2}\frac{\alpha_G(Q^2)}{\pi} = \beta\left(\frac{\alpha_G(Q^2)}{\pi}\right) \tag{12}$$

with

$$\beta(a) = -a^2\left(\beta_0 + \beta_1 a + \beta_2^G a^2 + \beta_3^G a^3\right) + O(a^6). \tag{13}$$

The first two coefficients of the β function are scheme-independent, the higher order coefficients β_2^G and β_3^G depending on the effective charge definition in Eq. (11). The normalization is chosen such that, in QCD with n_f light quark flavors, one has

$$\beta_0 = \frac{1}{4}\left(11 - \frac{2}{3}n_f\right). \tag{14}$$

It suffices to use only the leading-order running of the coupling constant since it contains all essential features of the whole phenomenon that we want to discuss. Effects due to higher order corrections of the β function are small and do not change the basic picture, slightly affecting the values of the moments numerically [35]. Thus, we consider the leading-order renormalization group equation for the effective charge

$$Q^2 \frac{d}{dQ^2}\frac{\alpha_G(Q^2)}{\pi} = -\beta_0\left(\frac{\alpha_G(Q^2)}{\pi}\right)^2. \tag{15}$$

The renormalization-group-resummed correlation function reads

$$\Pi_G(Q^2) = \frac{\pi}{\beta_0}\alpha_G(Q^2) + \text{ subtractions}, \tag{16}$$

where

$$\alpha_G(Q^2) = \frac{\alpha_0}{1 + (\beta_0\alpha_0/\pi)\ln(Q^2/s_0)} \tag{17}$$

with $\alpha_0 = \alpha_G(s_0)$. Note that, for the process of e^+e^- annihilation into hadrons, the corresponding renormalization-group-resummed correlation function reads

$$\Pi_{e^+e^-}(Q^2) = \ln\left(\mu^2 Q^2\right) + \frac{1}{\beta_0}\ln\left(\frac{\alpha_{e^+e^-}(Q^2)}{\pi}\right) + \text{ subtractions} \tag{18}$$

with the first term being a parton contribution independent of α_s. Setting $Q^2 = s_0 e^{i\varphi}$ on the contour, one obtains an explicit expression for the correlator as a function of the angle φ:

$$\Pi_G(s_0 e^{i\varphi}) = \frac{\pi}{\beta_0}\frac{\alpha_0}{1 + i\beta_0\alpha_0\varphi/\pi} + \text{subtractions}. \tag{19}$$

With an explicit expression for the function $\Pi_G(z)$ from Eqs. (16) and (19), the analysis of the moments M_n is straightforward. The explicit expression for the

moments written through the contour representation reads

$$M_n = (n+1)\frac{(-1)^n}{2\pi}\int\limits_{-\pi}^{\pi}\frac{\pi}{\beta_0} \times \frac{\alpha_0}{1+i\beta_0\alpha_0\varphi/\pi}e^{i(n+1)\varphi}d\varphi. \quad (20)$$

Equation (20) is a basic relation for further study. Note that the form of the representation in Eq. (20) is rather general and gives a basis for other applications: higher powers of the running coupling α_s can easily be generated.

4. COUPLING CONSTANT ANALYTICITY FOR THE MOMENTS

Let us discuss the above expressions for the moments in some detail, especially in relation to their analyticity structure as functions of the coupling constant α_0. The main feature of the contour representation for the moments is that all formulas contain explicit concise functions of the coupling constant α_0. This is similar to the situation in finite-order perturbation theory where all expressions are simple polynomials in the coupling constant α_0. After formulating the particular way of resummation for the spectral moments, i.e., by defining them on the contour, there is no ambiguity in these quantities (they are not given by series in α_s as in the approaches based on infrared renormalon hypothesis but by close formulas). Therefore, in contrast to the renormalon approach where the expressions for the moments are not well defined from the outset and require additional assumptions to be made for obtaining meaningful mathematical representations, the moments defined on the contour are explicit functions of α_0 that can be studied rigorously. One should, however, remember that a particular definition of the moments on the contour has been used.

Expanding Eq. (20) in α_0, one reproduces all results of finite-order perturbation theory (e.g., see [36]). Indeed, expanding the function $\Pi_G(Q^2)$ from Eq. (16), one finds

$$\Pi_G(Q^2) = \frac{\pi}{\beta_0}\alpha_0\left\{1+\beta_0\frac{\alpha_0}{\pi}\ln\left(\frac{s_0}{Q^2}\right) + \beta_0^2\left(\frac{\alpha_0}{\pi}\right)^2\ln^2\left(\frac{s_0}{Q^2}\right)+O(\alpha_0^3)\right\} + \text{ subtractions.} \quad (21)$$

The first term (Q^2-independent) can be added to subtractions. Then, finally, one has

$$\Pi_G(Q^2) = \alpha_0^2\ln\left(\frac{s_0}{Q^2}\right) + \beta_0\frac{\alpha_0^3}{\pi}\ln^2\left(\frac{s_0}{Q^2}\right)+O(\alpha_0^4) + \text{ subtractions.} \quad (22)$$

While the expansion of the integrand in Eq. (20) in α_0 with further integration gives nothing new in comparison with the finite-order perturbation theory analysis, new features appear if one retains a resummed expression under the integration sign. The integration of renormalization-group-improved quantities over the finite energy interval is the starting point of the renormalon approach and the grounds for the conclusions about the analyticity structure of the amplitudes in the coupling constant.

The moments in Eq. (20) are expandable in a convergent series in α_0 for $\beta_0\alpha_0 < 1$. The existence of a finite radius of convergence in the complex α_0 plane within the contour technique of resummation for the moments is a general feature that persists for the running with the high-order perturbative β function. However, in QCD, the convergence radius in α_0 decreases when higher orders of the β function are included [35]. Thus, the explicit result, Eq. (20), allows for an analytic continuation in the complex α_0 plane leading to the functions $M_n(\alpha_0)$ that are analytic in α_0 at the origin, i.e., near the point $\alpha_0 = 0$. This sounds a bit unusual as one implicitly assumes that perturbation theory objects should have an essential singularity in α_0 at the origin, usually a cut along the negative semiaxis (see, e.g., [37]). Note that the moments of the heavy quark production with the infinite resummation of the Coulomb interaction effects are also given by convergent series in α_s (the explicit result in the leading order of perturbation theory is presented in [38]). The exact expression given in Eq. (20) without expansion in α_0 provides one with an analytic continuation beyond the convergence radius even when α_0 lies outside the convergence circle.

Looking at Eqs. (2), (3), (16), (17), and (19), one notices that the analytic properties in the variable q^2 declared for a general function $\Pi(q^2)$ built from the massless fields in Eqs. (2) and (3) differ from that of the explicit result given in Eqs. (16), (17), and (19): the explicit renormalization-group-improved expression $\Pi_G(q^2)$ has a pole in the Euclidean region of q^2 that is supposed to be the analyticity region from the general assumptions about the spectrum. This is an important feature to note: a concrete approximation $\Pi_G(q^2)$ in Eq. (16) has different analytic properties in the whole complex q^2 plane than is declared by the general requirements of quantum field theory, i.e., by the axiom of spectrality in this particular case. Contrary to the resummed expression given in Eq. (16), at any finite order of perturbation theory, one has only powers of logarithms given in Eq. (21) that have the correct analytic properties in

the variable q^2—a cut along the positive semiaxis—that comply with the spectrality axiom. It is just a consistency feature—the finite-order perturbation theory is an explicit example of the model of quantum field theory where all general requirements are valid. Thus, the renormalization group resummation for the hadronic correlator in asymptotically free QCD can change its analytic structure in the infrared region as compared to the finite-order perturbation theory approximation. In the leading order of the running in QCD a (Landau) pole is usually generated. This pole is included in the definition of the moments in Eqs. (6) and (20) because one encircles the origin with a large contour. There is no other possibility of working consistently in perturbation theory because the infrared region is completely nonperturbative and one is not allowed to move the integration contour to that region. The requirement of integrating only along the positive axis is an external constraint on the theory rather than its attribute. It cannot be realized in perturbation theory—the integration contour should go sufficiently far from the infrared region, which is a requirement of the applicability of perturbation theory approximations. Note that, if s_0 is not large enough so that the circular contour can include all infrared singularities, the contour should be deformed to do so. To give the results for the moments that are justified in perturbation theory (at least formally), the integration contour should be chosen such that no singularity incompatible with the general requirements lies outside it in the complex q^2 plane.

The analytic structure in the coupling constant α_0 of the moments defined on the contour is different from the analytic structure of the moments obtained in the renormalon approach because the integration region is different. Within the renormalon approach, the moments (and other quantities in general) are defined through the integration along the cut including the infrared region, which makes them nonanalytic in the coupling constant since the perturbation theory expressions for the amplitudes are not valid in this region. The moments on the contour are given by the integration through the region where perturbation theory is valid; therefore, they are analytic in the coupling constant for sufficiently small values of α_0. This constitutes the main difference between the definitions on the contour and within the renormalon hypothesis: the former is perturbative and reliably computable in perturbation theory with strict control over the accuracy, while the latter is nonperturbative and requires some additional assumptions for quantitative phenomenological applications.

After the moments are properly defined (written as Eq. (20), for instance), the practical calculation of explicit functions $M_n(\alpha_0)$ can be done in different ways. Technically, one can shrink the integration contour back to singularities of $\Pi_G(q^2)$, which is a uniquely defined mathematical operation for the explicit function $\Pi_G(q^2)$ in the complex q^2 plane. Then, one discovers a pole which is a purely computational fact without any meaning for the structure of the perturbation theory at high orders. The perturbation theory moments are constructed at high energies and cannot decipher the point-by-point structure of the spectrum in the infrared region (or singularities of $\Pi_G(q^2)$ at small q^2)—they just give a contribution from this region as it is seen from large energies (on the contour). If a high-order β function is used for the renormalization group improvement of the correlator, then the structure of singularities in the infrared region can drastically change [39]. However, this has little effect on the moments—they develop some small perturbation theory corrections independent of a particular structure of the correlation function in the infrared region obtained as a perturbation theory approximation. Of course, the parameter s_0 should be sufficiently large so that the perturbation theory expansion in the coupling α_0 would be justified. A discussion of the pointwise behavior of $\Pi(q^2)$ in the infrared region is beyond the scope of perturbation theory. Note that the possibility of restoring moments as exact functions of the coupling from their (asymptotic) perturbation theory series depends on the behavior of $\Pi(q^2)$ in the infrared region.

5. RENORMALON-BASED MOMENTS AND THE EXPLICIT FORM OF THE RESIDUAL TERM OF THE PERTURBATION THEORY SERIES

In this section, I discuss some other representations that can be obtained from Eq. (20). In particular, the relation of the moments obtained within the renormalon hypothesis to the moments on the contour is clarified. The nonanalytic terms in the coupling constant that constitute the main qualitative feature of the renormalon techniques are shown to originate from the form of the residual term of the perturbative series for the moments defined on the contour. The explicit expressions for the residual term in different representations with and without nonanalytic terms are given. Let me first consider the leading order moment $M_0(\alpha_0)$ that reads

$$M_0 = \frac{1}{2\pi}\int\limits_{-\pi}^{\pi}\frac{\pi}{\beta_0}\frac{\alpha_0}{1+i\beta_0\alpha_0\varphi/\pi}e^{i\varphi}d\varphi \qquad (23)$$

$$= \frac{\alpha_0}{2\beta_0}\int\limits_{-\pi}^{\pi}\frac{e^{i\varphi}d\varphi}{1+i\beta_0\alpha_0\varphi/\pi}.$$

With expression (23) given, one can easily study its general structure, which is rather simple. In particular, one can work out different computation techniques for it based on asymptotic expansions. In this way, one can also see the connection of renormalon-based moments with the moments on the contour. In applications, the moments on the contour are usually computed numerically [15, 29, 35]. For a general analysis and clarification of the relation to other techniques and definitions of the moments, one can also consider the analytical evaluation of the moments in various limits. Integrals of the type (23) are related to the well-known exponential integral function [40]. Formally, one can use a convergent series in α_0 for evaluating the moments, but if a numerical value of α_0 is larger than the convergence radius, then the expansion in α_0 is of no use and an analytic continuation of the function given by the series in α_0 beyond the convergence radius is necessary. The convergence radius of the function $M_0(\alpha_0)$ in the complex α_0 plane for the leading-order β function is given by $|\alpha_0| < 1/\beta_0$. For a full perturbative β function up to the fourth order in the $\overline{MS}$ scheme, it is smaller [35]. In a realistic case of τ decays, for instance, $s_0 = M_\tau^2 = (1.777\ \mathrm{GeV})^2$ and $\beta_0 = 9/4$, which leads to

$$\alpha_0 \equiv \alpha_0(s_0 = M_\tau^2 = (1.777\ \mathrm{GeV})^2) < \frac{4}{9} = 0.44\ldots; \tag{24}$$

i.e., the experimental value of the coupling $\alpha_0 \approx 0.3$ [41] lies rather close to the boundary of the convergence circle. Taking the scale s_0 for the moments smaller than the squared τ-lepton mass M_τ^2, one can get the value of α_0 lying outside the convergence circle. The convergent power series may not be the best way of computing the moments for such numerical values of the coupling constant. The more efficient approximation can be obtained by constructing an asymptotic expansion for the zero moment. Integrating by parts, one finds

$$M_0 = \frac{\alpha_0^2}{1+\beta_0^2\alpha_0^2} + \frac{\alpha_0^2}{2\pi}\int\limits_{-\pi}^{\pi} \frac{e^{i\varphi}d\varphi}{(1+i\beta_0\alpha_0\varphi/\pi)^2}. \tag{25}$$

Here, the first term gives a perturbation theory expression for the spectral density at s_0 with all corrections due to analytic continuation resummed (so-called π^2 corrections) [42]. This contribution can be obtained from the leading-order running by retaining the highest power of π at every order of perturbation theory. It also corresponds to the calculation of the moments on the cut through the boundary value of the perturbation theory spectrum [36]. Further integration by parts gives

$$M_0 = \frac{\alpha_0^2}{1+\beta_0^2\alpha_0^2} + \frac{\alpha_0^2}{\pi}\sum_{j=2}^{n}(j-1)!\left(\frac{\beta_0\alpha_0}{\pi}\right)^{j-2} \tag{26}$$
$$\times\,\frac{\sin\{j\arctan(\beta_0\alpha_0)\}}{(1+\beta_0^2\alpha_0^2)^{j/2}} + n!\frac{\alpha_0^2}{2\pi}\left(\frac{\beta_0\alpha_0}{\pi}\right)^{n-1}$$
$$\times\int\limits_{-\pi}^{\pi}\frac{e^{i\varphi}d\varphi}{(1+i\beta_0\alpha_0\varphi/\pi)^{n+1}}.$$

This result can be obtained using the recurrence relation

$$\frac{1}{2}\int\limits_{-\pi}^{\pi}\frac{e^{i\varphi}d\varphi}{(1+i\beta_0\alpha_0\varphi/\pi)^k} = \frac{\sin(k\chi)}{r^k} \tag{27}$$
$$+\,k\left(\frac{\beta_0\alpha_0}{\pi}\right)\frac{1}{2}\int\limits_{-\pi}^{\pi}\frac{e^{i\varphi}d\varphi}{(1+i\beta_0\alpha_0\varphi/\pi)^{k+1}}$$

with quantities r and χ defined by

$$1+i\beta_0\alpha_0 = re^{i\chi}, \qquad r = \sqrt{1+\beta_0^2\alpha_0^2}, \tag{28}$$
$$\chi = \arctan(\beta_0\alpha_0).$$

Retaining only leading powers of α_0 at every order of expansion (26), one recovers an asymptotic series that appears within the renormalon technique and has intensively been discussed in the literature. Indeed, taking only the leading asymptotics of every term in Eq. (26), one finds

$$M_0^{\text{leading asym}} = \alpha_0^2\left(1+2\beta_0\frac{\alpha_0}{\pi}+\ldots\right. \tag{29}$$
$$\left.+(n+1)!\beta_0^n\left(\frac{\alpha_0}{\pi}\right)^n\right)+O(\alpha_0^{n+3}).$$

The main point of interest in the series (29) is that it shows a nonalternating factorial growth of the coefficients that leads to a Borel nonsummable asymptotic series [43]. The reason for such a behavior is that approximation (29) for expansion (26) is not accurate. This means that the renormalon approximation does not take into account some important high-order terms and that the renormalon hypothesis is not correct in identifying the dominant terms of the perturbation theory expansion for the moments on the contour. Note that Borel summation (with some recipe for treating nonsummable singularities) of the leading asymptotics (29) cannot restore exact function (23) from some general principles.

While representation (26) with the leading asymptotics only leads to series (29) that fails to detect the correct analytic structure of the moment in the coupling constant, it still can be useful in some practical

applications, as it gives a way to compute result (23) numerically. Equation (26) represents an asymptotic expansion of the function $M_0(\alpha_0)$ that is analytic at the origin, $\alpha_0 = 0$. It is known that an asymptotic expansion of a function can be more efficient for its numerical evaluation than a convergent series even inside the convergence circle; it also gives an efficient way for the calculation outside the convergence circle (not too far though). One can see that result (26) is an efficient asymptotic expansion which can give better accuracy than a direct power series expansion in α_0 for some α_0 and n. This observation is in fact grounds for using the renormalon hypothesis. Indeed, when the analytic structure of the function is known, or a concise expression for the function is given as in Eq. (23), the asymptotic expansions that converge fast for the first few terms are more useful for practical calculations than formal convergent series that require many terms for achieving a reasonable numerical accuracy [44]. Still, for estimating the accuracy of the asymptotic series, one has to deal with the residual term, which is represented in our particular case by the integral in Eq. (26). In calculations with the moments on the contour, the residual term is explicitly given and can easily be estimated. However, in some practical phenomenological applications, the residual term can remain unknown. In fact, the renormalon hypothesis suggests a guess about the form of such term based on expansion (29). Because of Borel nonsummability of expansion (29), the renormalon approach claims the existence of a term that is nonanalytic in the coupling constant. For the moments on the contour, this assumption is not valid. However, such a term can be generated in some approximation for the series from Eq. (26). Indeed, by extension of the integration range in the variable φ from $-\infty$ to $+\infty$, the integral over φ can be readily computed:

$$n!\left(\frac{\beta_0\alpha_0}{\pi}\right)^{n-1}\int\limits_{-\infty}^{\infty}\frac{e^{i\varphi}d\varphi}{(1+i\beta_0\alpha_0\varphi/\pi)^{n+1}} = 2\pi\left(\frac{\pi}{\beta_0\alpha_0}\right)^2 e^{-\frac{\pi}{\beta_0\alpha_0}}. \quad (30)$$

Using the decomposition

$$\int\limits_{-\pi}^{\pi} d\varphi = \int\limits_{-\infty}^{\infty} d\varphi - \left(\int\limits_{-\infty}^{-\pi} d\varphi + \int\limits_{\pi}^{\infty} d\varphi\right), \quad (31)$$

one can write

$$n!\left(\frac{\beta_0\alpha_0}{\pi}\right)^{n-1}\int\limits_{-\pi}^{\pi}\frac{e^{i\varphi}d\varphi}{(1+i\beta_0\alpha_0\varphi/\pi)^{n+1}} = 2\pi\left(\frac{\pi}{\beta_0\alpha_0}\right)^2 e^{-\frac{\pi}{\beta_0\alpha_0}} - n!\left(\frac{\beta_0\alpha_0}{\pi}\right)^{n-1} \times\left(\int\limits_{-\infty}^{-\pi} + \int\limits_{\pi}^{\infty}\right)\frac{e^{i\varphi}d\varphi}{(1+i\beta_0\alpha_0\varphi/\pi)^{n+1}} \quad (32)$$

for any n. Therefore, the residual term in Eq. (26) is transformed into a sum of an explicit nonperturbative term proportional to $e^{-\pi/\beta_0\alpha_0}$ and a term that can be smaller than the original residual term for some values of α_0 and n. One has

$$M_0 = \left(\frac{\pi}{\beta_0}\right)^2 e^{-\frac{\pi}{\beta_0\alpha_0}} + \frac{\alpha_0^2}{1+\beta_0^2\alpha_0^2} + \frac{\alpha_0^2}{\pi}\sum_{j=2}^{n}(j-1)!\left(\frac{\beta_0\alpha_0}{\pi}\right)^{j-2} \times\frac{\sin\{j\arctan(\beta_0\alpha_0)\}}{(1+\beta_0^2\alpha_0^2)^{j/2}} - n!\frac{\alpha_0^2}{2\pi}\left(\frac{\beta_0\alpha_0}{\pi}\right)^{n-1} \times\left(\int\limits_{-\infty}^{-\pi} + \int\limits_{\pi}^{\infty}\right)\frac{e^{i\varphi}d\varphi}{(1+i\beta_0\alpha_0\varphi/\pi)^{n+1}}. \quad (33)$$

The explicit nonperturbative term $e^{-\pi/\beta_0\alpha_0}$ that is claimed in the renormalon approach has appeared in the asymptotic expansion of moment (23) written in the form of Eq. (33). This term can be rewritten as a power correction. Introducing the QCD scale for the effective charge in the gluonic channel in the form

$$\Lambda_G^2 = s_0\exp\left(-\frac{\pi}{\beta_0\alpha_0}\right), \quad (34)$$

one finds the relation between the nonanalytic term in the asymptotic expansion and the power correction

$$\left(\frac{\pi}{\beta_0}\right)^2 e^{-\frac{\pi}{\beta_0\alpha_0}} = \left(\frac{\pi}{\beta_0}\right)^2\left(\frac{\Lambda_G^2}{s_0}\right). \quad (35)$$

The difference between the expansions in Eq. (26) and Eq. (33) is not very noticeable. In fact, these two expansions are almost identical up to the residual terms. What happened is the change in the residual term. Therefore, the choice of the representation for moment (23) [Eq. (26) or Eq. (33)], i.e., with or without the explicit nonperturbative term $e^{-\pi/\beta_0\alpha_0}$, is a question of the choice of a particular form of the residual term. It can happen that, after the residual term is dropped (which is a common practice in asymptotic series calculations), the representation in the form of Eq. (33) is more accurate numerically than that in the form of Eq. (26) for some particular values of α_0 and n. It is just the claim of the renormalon technique about the necessity of adding the nonanalytic terms that represent power corrections to the perturbation theory expressions. However, a quantitative conclusion about the accuracy of the asymptotic series representation for a function can only be drawn if one

has a concise expression for the function as Eq. (23) in our case when the explicit form of the residual term is also known (see also [45], where a simplified model in quantum mechanics was considered). Any conclusions based on the terms of the series itself (for instance, based on representation (29), which is the basis for the infrared renormalon technique) can be inaccurate numerically; they can also be unjustified in a general sense of analytic behavior, as one can see from Eq. (32).

The above results are valid for any moment M_l. Namely, the recurrence relation can be generalized to read

$$(l+1)\frac{1}{2}\int\limits_{-\pi}^{\pi}\frac{e^{i(l+1)\varphi}d\varphi}{(1+i\beta_0\alpha_0\varphi/\pi)^k} \tag{36}$$
$$=\frac{\sin\{k(l+1)\chi\}}{r^k}+k\left(\frac{\beta_0\alpha_0}{\pi}\right)$$
$$\times\frac{1}{2}\int\limits_{-\pi}^{\pi}\frac{e^{i(l+1)\varphi}d\varphi}{(1+i\beta_0\alpha_0\varphi/\pi)^{k+1}}.$$

The representation with integration by parts analogous to the one given in Eq. (26) shows an improvement in the convergence for large l moments equivalent to the replacement $\alpha_0 \to \alpha_0/l$. This agrees with conclusions drawn from the analysis of finite-order perturbation theory [36]. In general, one can also modify the residual term for any moment M_n. In the literature, there are also some moments defined on the finite energy interval with different weight functions [46]; our conclusion can be generalized to those moments as well.

Now, we discuss the spectrum of the explicit resummed function $\Pi_G(q^2)$ in order to see how its analytic properties in the momentum q^2 are transformed into the analyticity of the moments in the coupling constant α_0. The structure of the spectrum in the infrared domain is most interesting for clarification of such a relation. Note that the infrared part of the spectrum is obtained by the analytic continuation from the Euclidean region where $\Pi_G(q^2)$ is calculated as a perturbation theory expansion to a region where perturbation theory is not valid, which means that the structure of the spectrum has no general physical meaning at small s pointwise. The spectrum of the explicit function $\Pi_G(q^2)$ given in Eq. (16) is a well-defined quantity in a pure mathematical sense. It is straightforward to calculate it. Using the expression for the leading-order coupling constant in the form

$$\alpha_G(Q^2)=\frac{\alpha_0}{1+(\beta_0\alpha_0/\pi)\ln(Q^2/s_0)} \tag{37}$$
$$=\frac{\pi}{\beta_0\ln(Q^2/\Lambda_G^2)},$$

where

$$\Lambda_G^2=s_0\exp\left(-\frac{\pi}{\beta_0\alpha_0}\right), \tag{38}$$

one finds

$$\Pi_G(Q^2)=\frac{\pi}{\beta_0}\alpha_G(Q^2)+\text{ subtractions} \tag{39}$$
$$=\frac{\pi^2}{\beta_0^2\ln(Q^2/\Lambda_G^2)}+\text{ subtractions}.$$

Therefore, the spectrum (a discontinuity across singularities) reads

$$\rho_G(s)=\frac{1}{2\pi i}(\Pi_G(s+i0)-\Pi_G(s-i0)) \tag{40}$$
$$=\frac{\pi^2}{\beta_0^2}\left(\Lambda_G^2\delta(\Lambda_G^2+s)+\theta(s)\frac{1}{\pi^2+\ln^2(s/\Lambda_G^2)}\right),$$

where $\delta(s)$ is a Dirac δ distribution and $\theta(s)$ is a step distribution. Explicit functions given in Eqs. (39) and (40) satisfy the integral Eq. (2). Note that the explicit spectrum in Eq. (40) contains a contribution $\delta(\Lambda_G^2+s)$ corresponding to a pole $1/(q^2+\Lambda_G^2)$ of the function $\Pi_G(q^2)$ in the region $q^2<0$, which is supposed to be the analyticity domain of the two-point correlators from general requirements (spectrality condition). The position of the pole Λ_G^2 is specific for a given channel if an effective charge is used. The expression for the theoretical spectrum given in Eq. (40) can be used in a mathematical sense for calculating integrals (moments) in Eq. (20) [an analogous approach may be used for the general case in Eq. (4)], but a physical interpretation of the spectrum at small s is rather meaningless because perturbation theory is not applicable at small momenta.

The part of the spectrum on the positive real axis is a discontinuity of the function $\Pi_G(q^2)$ across the cut [42]. It can conveniently be written in the form

$$\rho_G^{\text{cont}}(s)=\frac{\pi^2}{\beta_0^2}\frac{1}{\pi^2+\ln^2(s/\Lambda^2)}=\frac{\alpha(s)^2}{1+\beta_0^2\alpha(s)^2} \tag{41}$$

with a function

$$\alpha(s)=\frac{\pi}{\beta_0\ln(s/\Lambda_G^2)}. \tag{42}$$

Note that the function $\alpha(s)$ has a pole on the physical cut at $s=\Lambda_G^2$. It is this pole that leads to problems of Borel nonsummability in the resummation of the effects of running directly on the cut, when one integrates through the infrared region within the renormalon approach for taking into account high-order contributions of perturbation theory [cf. Eq. (29)]. However, the pole of the auxiliary function $\alpha(s)$ from Eq. (42) has no physical meaning within perturbation theory. For instance, spectral density (41) is a smooth

function at this point. While the spectral density explicitly given in Eq. (40) allows one to compute the moments by direct integration in a pure mathematical sense, it is not productive to ask whether this spectrum is physical or not because there is no possibility of answering this question within perturbation theory. The interpretations of this spectrum at low energies in the form of specific recipes of resummation for Borel nonsummable series as in Eq. (29) are additional assumptions beyond perturbation theory.

The continuous part of the spectral density in Eq. (41) can uniquely be obtained from the finite-order perturbation theory expansion by summing it in all orders. However, the pole remains hidden and cannot be restored from the summation on the cut if only the discontinuity across the cut along the positive semiaxis is considered. Note that this is also the situation in heavy quark physics—no Coulombic poles can be restored from the summation on the cut (see discussion in [47] in relation to the precision determination of heavy quark masses).

6. DISCUSSION

It is worth stressing again that the moments in Eq. (20) are analytic functions of the coupling constant α_0 at the origin. It means that the nonanalytic piece in Eq. (32) cancels the corresponding part in the residual term. Depending on the particular form of the residual term, the formal analytic structure of the expansion for the moments in the coupling constant α_0 drastically changes. This demonstrates the danger of making general conclusions about the infrared power corrections emerging from the extrapolation of the running to the infrared region based on the renormalon hypothesis. Because the infrared region is not the perturbation theory domain, the formal perturbative expansions originating from the integration over the infrared region can be strongly modified by making small changes in perturbation theory quantities like effective β functions [39]. In practice, or from a phenomenological point of view, the use of the power corrections stemming from the infrared modification of perturbation theory is difficult to appreciate if the high-order terms in the perturbative α_0 expansion are taken into account. For such observables as the moments of the spectral density, one cannot distinguish numerically the high-order perturbation theory corrections from the power corrections (nonperturbative part of the expansion): the power corrections are numerically hidden by the high-order perturbation theory corrections.

Thus, for the observables related to the two-point correlators, the problem of resumming the running effects in perturbation theory is solved by contour integration. We stress that the pole (or any singularity that may occur upon the formal analytic continuation of the perturbation theory expressions into the infrared region) is inside the integration circle (cf. the discussion in [48]). One is not allowed to use integration contours that go close to the origin because this region is completely nonperturbative and should be avoided: perturbation theory cannot decipher the structure of amplitudes in this region pointwise; only contributions to the integrals are perturbative and can be computed. This situation is to some extent analogous to the situation with Coulombic poles, especially for not very heavy quarks. For perturbation theory applications, any type of infrared singularities should be avoided by moving the integration contour far from the origin and keeping the infrared nonperturbative region inside, thereby including also the contribution of this region to the integral. The possibility of accurately applying perturbation theory for averaged quantities is a specific feature of the observables related to two-point correlators with simple analytic properties in the momentum variable. In the cases when the physical observables are obtained by the averaging of more complicated Green's functions where the analytic structure is not transparent, the effects of running are accounted for by considering a model field theory with a one-loop gluon propagator reiterated in all orders of perturbation theory (renormalon technique). To respect gauge invariance of QCD in such a model, the technique of naive non-Abelianization is used [49]. Note that, in pure gluodynamics, which is a proper theoretical model for studying glueballs, this trick is not straightforward. If analytic properties of the amplitude are unknown, one has no clear way to avoid going through infrared singularities of the running coupling constant and one is trying to perform the integration across the infrared region directly (as in the phenomenological applications based on infrared renormalons [50]). In this case, the infrared structure of the running is important for the analysis; however, it is completely nonperturbative. Therefore, the obtained qualitative results depend crucially on the additional assumptions about the infrared behavior of the running coupling constant.

For the sake of completeness, I give an expression for the resummed function $\Pi_G(q^2)$ in the second order of the β function. Taking the approximation for the β function in the form

$$\beta(a) \equiv \beta_2(a) = -a^2\,(\beta_0 + \beta_1 a)\,, \qquad (43)$$

one finds the expression for the resummed function $\Pi_G(q^2)$:

$$\Pi_G(Q^2) = \frac{\pi^2}{\beta_1}\ln\left(\beta_0 + \beta_1\frac{\alpha_G^{(2)}(Q^2)}{\pi}\right) \qquad (44)$$
$$+ \text{ subtractions},$$

where the function $\alpha_G^{(2)}(Q^2)$ is a solution to the renormalization group equation with the second-order β function

$$Q^2\frac{d}{dQ^2}\left(\frac{\alpha_G^{(2)}(Q^2)}{\pi}\right) \tag{45}$$
$$= -\beta_0\left(\frac{\alpha_G^{(2)}(Q^2)}{\pi}\right)^2 - \beta_1\left(\frac{\alpha_G^{(2)}(Q^2)}{\pi}\right)^3.$$

The generalization of the analysis to this case is straightforward.

7. CONCLUSION

To conclude, it has been shown that, for the observables related to the two-point current correlators, the summation of the effects of running can consistently be done in perturbation theory. In more complicated cases without a simple analytic structure of the respective Green's functions, the interpretation of the running in the infrared region is not unique and lies outside the scope of perturbation theory. The asymptotic structure of the perturbation theory series in the coupling constant α_0 depends on the actual treatment of the observables (there is no true asymptotic structure unless explicit assumptions are formulated). The perturbation theory series can be analytic in the expansion parameter α_0 at the origin for some definitions of the observables, as is the case for the widely used approximation with resummation on the contour. The possible power corrections stemming from such a resummation procedure have a rather computational origin and simply reflect a particular way of approximating the relevant integrals; no general conclusions on the analytic structure of the correlators in the exact theory can be drawn. Theoretically, there is no invariant meaning in splitting the results into the nonperturbative infrared power corrections and perturbation theory part (as opposed to OPE, where the power corrections are related to high-dimensional operators and determined by the projections onto other perturbation theory states than vacuum). Phenomenologically, the high-order perturbation theory terms (with high powers of inverse logarithms) can numerically mimic the renormalon-type power corrections well. In this situation, the way to go beyond the perturbation theory framework for improving the accuracy of theoretical formulas would be just a convention to use for the observables an effective scheme where all perturbative corrections are explicitly resummed into the redefinition of the coupling constant.

ACKNOWLEDGMENTS

Valuable discussions with N.V. Krasnikov and D.V. Shirkov are gratefully acknowledged. This work is supported in part by the Russian Foundation for Basic Research, project nos. 99-01-00091 and 01-02-16171.

REFERENCES

1. S. L. Glashow, Nucl. Phys. **22**, 579 (1961); S. Weinberg, Phys. Rev. Lett. **19**, 1264 (1967); A. Salam, in *Elementary Particle Theory*, Ed. by N. Svartholm (Almquist and Wiksel, 1968).
2. N. N. Bogoliubov and D. V. Shirkov, *Quantum Fields* (Benjamin, New York, 1983).
3. J. Schwinger, Phys. Rev. **82**, 664 (1951); B. Simon, *The $P(\phi)$ in Two-Dimension Euclidean (Quantum) Field Theory* (Princeton Univ., Princeton, 1974); G. 't Hooft, Nucl. Phys. B **75**, 461 (1974); A. A. Pivovarov and V. F. Tokarev, Yad. Fiz. **41**, 524 (1985) [Sov. J. Nucl. Phys. **41**, 334 (1985)]; A. A. Pivovarov, A. N. Tavkhelidze, and V. F. Tokarev, Theor. Math. Phys. **60**, 765 (1985); Phys. Lett. B **132B**, 402 (1983); I. Bigi, M. Shifman, N. Uraltsev, and A. Vainshtein, Phys. Rev. D **59**, 054011 (1999).
4. L. N. Lipatov, Zh. Éksp. Teor. Fiz. **72**, 411 (1977) [Sov. Phys. JETP **45**, 216 (1977)].
5. A. A. Belavin, A. M. Polyakov, A. S. Shvarts, and Yu. S. Tyupkin, Phys. Lett. B **59B**, 85 (1975).
6. G.'t Hooft, Phys. Rev. D **14**, 3432 (1976); Phys. Rev. D **18**, 2199 (Erratum) (1978).
7. C. G. Callan, R. F. Dashen, and D. J. Gross, Phys. Lett. B **63B**, 334 (1976).
8. G. 't Hooft, Nucl. Phys. B **72**, 461 (1974).
9. R. Coquereaux, Phys. Rev. D **23**, 2276 (1981).
10. G. 't Hooft, *Lectures Given at the International School of Subnuclear Physics, Erice, Sicily, Jul. 23–Aug. 10, 1977*.
11. Particle Data Group (D. E. Groom *et al.*), Eur. Phys. J. C **15**, 1 (2000).
12. V. S. Fadin and V. A. Khoze, Yad. Fiz. **48**, 487 (1988) [Sov. J. Nucl. Phys. **48**, 309 (1988)].
13. A. H. Hoang *et al.*, Eur. Phys. J. C **13**, 1 (2000); A. A. Penin and A. A. Pivovarov, Phys. At. Nucl. **64**, 275 (2001).
14. E. D. Bloom and F. J. Gilman, Phys. Rev. Lett. **25**, 1140 (1970); A. De Rujula, H. Georgi, and H. D. Politzer, Phys. Lett. B **64B**, 428 (1976); B. Chibisov, R. D. Dikeman, M. Shifman, and N. Uraltsev, Int. J. Mod. Phys. A **12**, 2075 (1997).
15. A. A. Pivovarov, Sov. J. Nucl. Phys. **54**, 676 (1991); Z. Phys. C **53**, 461 (1992); Nuovo Cimento A **105**, 813 (1992).
16. ALEPH Collab. (R. Barate *et al.*), Z. Phys. C **76**, 15 (1997); Eur. Phys. J. C **11**, 599 (1999).
17. H. Pagels and S. Stokar, Phys. Rev. D **20**, 2947 (1979); N. V. Krasnikov and A. A. Pivovarov, Sov. Phys. J. **25**, 55 (1982); P. I. Fomin *et al.*, Riv. Nuovo Cimento **6**, 1 (1983); V. P. Gusynin, A. H. Hams, and M. Reenders, Phys. Rev. D **53**, 2227 (1996).

18. A. H. Mueller, Nucl. Phys. B **250**, 327 (1985).
19. A. N. Vasiliev, *Quantum Field Theory Renormalization Group in the Theory of Critical Behavior and Stochastic Dynamics* (Sankt-Petersburg, 1998).
20. V. I. Zakharov, Nucl. Phys. B **385**, 452 (1992).
21. A. Pich, Nucl. Phys. B (Proc. Suppl.) **98**, 385 (2001); K. G. Chetyrkin, J. H. Kühn, and A. A. Pivovarov, Nucl. Phys. B **533**, 473 (1998).
22. C. Itzykson and J. B. Zuber, *Quantum Field Theory* (McGraw-Hill, New York, 1980).
23. S. Groote and A. A. Pivovarov, Report No. MZ-TH/01-06; hep-ph/0103047; Eur. Phys. J. C **21**, 133 (2001).
24. N. I. Ussukina and A. I. Davydychev, Phys. Lett. B **305**, 136 (1993); D. Broadhurst, Phys. Lett. B **307**, 132 (1993); A. A. Penin and A. A. Pivovarov, Phys. Lett. B **357**, 427 (1995).
25. C. Bernard, A. Duncan, J. LoSecco, and S. Weinberg, Phys. Rev. D **12**, 792 (1975); E. C. Poggio, H. R. Quinn, and S. Weinberg, Phys. Rev. D **13**, 1958 (1976); R. Shankar, Phys. Rev. D **15**, 755 (1977); K. G. Chetyrkin, N. V. Krasnikov, and A. N. Tavkhelidze, Phys. Lett. B **76B**, 83 (1978); N. V. Krasnikov and A. A. Pivovarov, Phys. Lett. B **112B**, 397 (1982); A. A. Pivovarov, Phys. At. Nucl. **62**, 1924 (1999).
26. K. G. Wilson, Phys. Rev. **179**, 1499 (1969).
27. H. D. Politzer, Nucl. Phys. B **117**, 397 (1976).
28. M. A. Shifman, A. I. Vainshtein, and V. I. Zakharov, Nucl. Phys. B **147**, 385 (1979).
29. F. Le Diberder and A. Pich, Phys. Lett. B **286**, 147 (1992).
30. N. V. Krasnikov, A. A. Pivovarov, and N. N. Tavkhelidze, JETP Lett. **36**, 333 (1982); Z. Phys. C **19**, 301 (1983).
31. A. A. Pivovarov and E. N. Popov, Phys. Lett. B **205**, 79 (1988); Sov. J. Nucl. Phys. **49**, 693 (1989); D. J. Broadhurst, A. L. Kataev, and C. J. Maxwell, Nucl. Phys. B **592**, 247 (2001).
32. A. L. Kataev, N. V. Krasnikov, and A. A. Pivovarov, Phys. Lett. B **107B**, 115 (1981); Nucl. Phys. B **198**, 508 (1982); Nucl. Phys. B **490**, 505 (Erratum) (1997).
33. T. Inami, T. Kubota, and Y. Okada, Z. Phys. C **18**, 69 (1983); K. G. Chetyrkin, B. A. Kniehl, and M. Steinhauser, Phys. Rev. Lett. **79**, 353 (1997).
34. G. Grunberg, Phys. Lett. B **95B**, 70 (1980); Phys. Lett. B **110B**, 501 (Erratum) (1982); N. V. Krasnikov, Nucl. Phys. B **192**, 497 (1981); A. Dhar and V. Gupta, Phys. Rev. D **29**, 2822 (1984).
35. S. Groote, J. G. Körner, and A. A. Pivovarov, Phys. Lett. B **407**, 66 (1997); Mod. Phys. Lett. A **13**, 637 (1998).
36. J. G. Körner, F. Krajewski, and A. A. Pivovarov, Eur. Phys. J. C **12**, 461 (2000); Eur. Phys. J. C **14**, 123 (2000).
37. N. N. Khuri, Phys. Rev. D **16**, 1754 (1977).
38. A. A. Penin and A. A. Pivovarov, Nucl. Phys. B **549**, 217 (1999).
39. N. V. Krasnikov and A. A. Pivovarov, Yad. Fiz. **64**, 1576 (2001) [Phys. At. Nucl. **64**, 1500 (2001)]; Mod. Phys. Lett. A **11**, 835 (1996).
40. I. S. Gradshteyn and I. M. Ryzhik, *Table of Integrals, Series, and Products* (Acad. Press, New York, 1980).
41. J. G. Körner, F. Krajewski, and A. A. Pivovarov, Phys. Rev. D **63**, 036001 (2001).
42. N. V. Krasnikov and A. A. Pivovarov, Phys. Lett. B **116B**, 168 (1982); A. V. Radyushkin, JINR-E2-82-159-mc (microfiche) (Dubna, 1982); JINR Rapid Commun. No. 4[78]-96, 96 (1996); A. Bottino and C. W. Kim, Lett. Nuovo Cimento **30**, 353 (1981); M. R. Pennington and G. G. Ross, Phys. Lett. B **102B**, 167 (1981); D. V. Shirkov and I. L. Solovtsov, Phys. Rev. Lett. **79**, 1209 (1997); A. P. Bakulev, A. V. Radyushkin, and N. G. Stefanis, Phys. Rev. D **62**, 113001 (2000).
43. B. Lautrup, Phys. Lett. B **69B**, 109 (1977); G. Parisi, Phys. Rep. **49**, 215 (1979).
44. G. H. Hardy, *Divergent Series* (Oxford, London, 1956).
45. A. A. Penin and A. A. Pivovarov, Phys. Lett. B **401**, 294 (1997).
46. K. Maltman, Nucl. Phys. A **663**, 977 (2000); Phys. Lett. B **462**, 195 (1999); Phys. Lett. B **440**, 367 (1998).
47. J. H. Kühn, A. A. Penin, and A. A. Pivovarov, Nucl. Phys. B **534**, 356 (1998).
48. A. A. Pivovarov, Nucl. Phys. B (Proc. Suppl.) **64**, 339 (1998).
49. D. J. Broadhurst and A. G. Grozin, Phys. Rev. D **52**, 4082 (1995); M. Beneke and V. Braun, Phys. Lett. B **348**, 513 (1995); C. N. Lovett-Turner and C. J. Maxwell, Nucl. Phys. B **452**, 188 (1995).
50. M. Beneke, Phys. Rep. **317**, 1 (1999).

Physics of Atomic Nuclei, Vol. 66, No. 4, 2003, pp. 737–740. From Yadernaya Fizika, Vol. 66, No. 4, 2003, pp. 768–771.

ELEMENTARY PARTICLES AND FIELDS
Theory

Electromagnetic Transition Form Factors of $\Lambda \to ne^+e^-$ Weak Dilepton Decay*

B. V. Martemyanov

Institute of Theoretical and Experimental Physics,
Bol'shaya Cheremushkinskaya ul. 25, Moscow, 117259 Russia

Received May 22, 2002

Abstract—Weak radiative decay $\Lambda \to ne^+e^-$ depends in general on four independent electromagnetic transition form factors. These form factors can be fixed in an extended model of dominance of vector mesons, where the asymptotic behavior of form factors is in agreement with quark counting rules. The dependence of the branching ratio of the $\Lambda \to ne^+e^-$ decay on the relative weight of four electromagnetic form factors is investigated. © *2003 MAIK "Nauka/Interperiodica".*

1. INTRODUCTION

For a long time, weak radiative decays of hyperons have been under both experimental and theoretical investigations. A detailed overview on both experimental and theoretical aspects of weak radiative decays of hyperons is given in [1–3]. None of the theoretical models could explain the experimental widths of these decays, especially in the case of neutral hyperon weak radiative decays. In this respect, the case of $\Lambda \to n\gamma$ decay is the most dramatic one, where the theoretical underestimation of the width goes up to a factor of 250 [4]. In such a situation, any additional information on $\Lambda \to n\gamma^*$ radiative transition (on electromagnetic form factors, for example) is of prime importance.

The future HADES experiment at GSI [5] will study the dilepton spectra in the energy range appropriate for the $\Lambda \to ne^+e^-$ reaction.

The amplitude of the $\Lambda \to ne^+e^-$ transition can be parametrized in terms of the magnetic, electric, and two Coulomb transition form factors. The standard vector meson dominance (VMD) model with the ground-state vector mesons predicts monopole form factors with $1/q^2$ asymptotic behavior at $q^2 \to \infty$. Such asymptotic behavior is in disagreement with quark counting rules that require $1/q^6$ asymptotic behavior [6]. Therefore, radially excited vector mesons should be added to the VMD model in order to provide the required asymptotic behavior [7].

We use the extended VMD model [8] for the description of the form factors that are finally used for the calculation of the dilepton decay $\Lambda \to ne^+e^-$.

*This article was submitted by the author in English.

2. THE $\Lambda \to n\gamma^*$ HELICITY AMPLITUDES

The electromagnetic transition current between the neutron and Λ hyperon has the form

$$J_\mu(p_*, \lambda_*, p, \lambda) = e\overline{u}_\Lambda(p_*, \lambda_*)(\Gamma_\mu^{(-)} + \Gamma_\mu^{(+)})u(p, \lambda), \quad (1)$$

where m_* and m are masses, p_* and p are momenta, λ_* and λ are helicities of the Λ hyperon and the neutron, $e = -\sqrt{4\pi\alpha}$ is the electron charge, and $\alpha = 1/137$. In the Λ-hyperon rest frame, $p_* = (m_*, 0, 0, 0)$ and $p = (E, 0, 0, -k)$.

The matrices $\Gamma_\mu^{(\mp)}$ stand for the parity-conserving and parity-violating parts of the current.

The photon polarization vectors have the form

$$\epsilon_\mu^{(\pm1)}(q) = \frac{1}{\sqrt{2}}(0, \mp1, -i, 0), \quad (2)$$
$$\epsilon_\mu^{(0)}(q) = \frac{1}{M}(k, 0, 0, \omega),$$

where $q = p_* - p = (\omega, 0, 0, k)$, $q^2 = M^2$. These vectors are transversal, $q_\mu\epsilon_\mu^{(\lambda)}(q) = 0$, and normalized by

$$\epsilon_\mu^{(\lambda)}(q)^*\epsilon_\mu^{(\lambda')}(q) = -\delta_{\lambda\lambda'}. \quad (3)$$

In the limit $M \to 0$, $\epsilon_\mu^{(0)}(q) = q_\mu/M + O(M)$. Due to the current conservation $q_\mu J_\mu = 0$, the longitudinal component of the vector current equals $\epsilon_\mu^{(0)}(q)J_\mu = O(M)$, so it vanishes for physical photons at $M = 0$.

The $\Lambda \to n\gamma^*$ decay has four independent helicity amplitudes. It means that there are four independent scalar functions ($F_{1,2}^{(\pm)}$) to fix the vertex [8]

$$\Gamma_\mu^{(+)} = \Gamma_\mu^{(+)1}F_1^{(+)} + \Gamma_\mu^{(+)2}F_2^{(+)}, \quad (4)$$

1063-7788/03/6604-0737$24.00

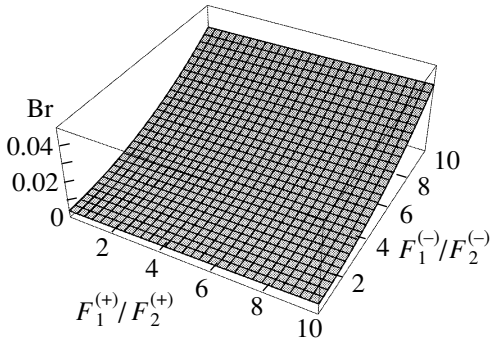

Differential branching ratio $\mathrm{Br} = \Gamma(\Lambda \to ne^+e^-)/\Gamma(\Lambda \to n\gamma)$ for various values of $F_1^{(\pm)}$ form factors.

$$\Gamma_\mu^{(-)} = \Gamma_\mu^{(-)1} F_1^{(-)} + \Gamma_\mu^{(-)2} F_2^{(-)},$$

where

$$\Gamma_\mu^{(+)1} = (q^2\gamma_\mu - \hat{q}q_\mu)\gamma_5, \tag{5}$$

$$\Gamma_\mu^{(+)2} = (P\cdot q\gamma_\mu - P_\mu q)\gamma_5, \tag{6}$$

and

$$\Gamma_\mu^{(-)1,2} = \Gamma_\mu^{(+)1,2}\gamma_5. \tag{7}$$

Here, $P = (p_* + p)/2$.

T-matrix elements ($S = 1 + iT$ with S being the S matrix),

$$\langle 1/2 J_z|T|\lambda\lambda_\gamma \mathbf{n}\rangle, \tag{8}$$

depend on the Λ-hyperon helicity J_z (because the Λ hyperon is at rest, the direction of its momentum is not defined, and J_z is the helicity of the Λ hyperon for the direction of its momentum taken along the z axis), on the neutron and photon helicities λ and λ_γ, and on the unit vector $\mathbf{n}$ in the direction of the photon momentum. The $\Lambda \to n\gamma^*$ width has the form

$$\Gamma(\Lambda \to n\gamma^*) = \frac{k}{32\pi^2 m^{*2}} \int d\Omega_{\mathbf{n}} \times \sum_{\lambda\lambda_\gamma} |\langle \lambda\lambda_\gamma \mathbf{n}|T|1/2 J_z\rangle|^2. \tag{9}$$

The angular dependence of the matrix element $\langle 1/2 J_z|T|\lambda\lambda_\gamma\mathbf{n}\rangle$ is a universal function:

$$\langle 1/2 J_z|T|\lambda\lambda_\gamma\mathbf{n}\rangle = D^{1/2}_{\lambda_* J_z}(\mathbf{n})^* \langle 1/2\lambda_*\mathbf{n}|T|\lambda\lambda_\gamma\mathbf{n}\rangle, \tag{10}$$

where $\lambda_* = -\lambda + \lambda_\gamma$ is the Λ-hyperon helicity for the direction of its momentum taken along the unit vector $\mathbf{n}$. The rotation matrices

$$D^{1/2}_{\lambda_* J_z}(\mathbf{n}) = \langle 1/2\lambda_*\mathbf{n}|1/2 J_z\rangle \tag{11}$$

are the amplitudes of probability of finding the Λ hyperon with the spin projection λ_* on the unit vector $\mathbf{n}$ in a state with the spin projection J_z on the z axis. The helicity amplitudes $\langle 1/2\lambda_*\mathbf{n}|T|\lambda\lambda_\gamma\mathbf{n}\rangle$ do not depend on the vector $\mathbf{n}$, so the symbol $\mathbf{n}$ can be suppressed. In the absence of P symmetry, there exist four helicity amplitudes, two with positive λ_* and two with negative λ_*.

The functions $D^J_{\lambda_* J_z}(\mathbf{n})$ are unitary matrices with respect to the indices λ_* and J_z. The normalization condition reads

$$\int d\Omega_{\mathbf{n}} D^J_{\lambda_* J_z}(\mathbf{n})^* D^{J'}_{\lambda'_* J'_z}(\mathbf{n}) = \frac{4\pi}{2J+1}\delta^{JJ'}\delta^{\lambda_*\lambda'_*}\delta^{J_z J'_z}. \tag{12}$$

Using the properties of $D^J_{\lambda_* J_z}(\mathbf{n})$ matrices, one obtains the $\Lambda \to N\gamma^*$ decay width in terms of four helicity amplitudes:

$$\Gamma(\Lambda \to N\gamma^*) = \frac{k}{32\pi^2 m_*^2}\frac{4\pi}{2}\sum_{\lambda\lambda_\gamma} |\langle \lambda\lambda_\gamma|T|1/2\lambda_*\rangle|^2. \tag{13}$$

Since the amplitudes $\langle \lambda\lambda_\gamma|T|1/2\lambda_*\rangle$ do not depend on the vector $\mathbf{n}$, it is convenient to choose it in the direction of the z axis. The helicity amplitudes can then be calculated in terms of the covariant form factors $F_k^{(\pm)}$ from the equations

$$\begin{aligned}
\langle 1/2\lambda_*|T|\lambda\lambda_\gamma\rangle &= \langle 1/2\lambda_*|T^{(-)}|\lambda\lambda_\gamma\rangle \\
&\quad + \langle 1/2\lambda_*|T^{(+)}|\lambda\lambda_\gamma\rangle, \\
&\quad \langle 1/2\lambda_*|T^{(-)}|\lambda\lambda_\gamma\rangle \\
&= -e\overline{u}_\Lambda(p_*,\lambda_*)\Gamma_\mu^{(-)} u(p,\lambda)\epsilon_\mu^{(\lambda_\gamma)}(q), \\
&\quad \langle 1/2\lambda_*|T^{(+)}|\lambda\lambda_\gamma\rangle \\
&= -e\overline{u}_\Lambda(p_*,\lambda_*)\Gamma_\mu^{(+)} u(p,\lambda)\epsilon_\mu^{(\lambda_\gamma)}(q),
\end{aligned} \tag{14}$$

$$\begin{aligned}
&\langle 1/2 - \lambda_*|T|-\lambda-\lambda_\gamma\rangle \\
&\quad = \langle 1/2 - \lambda_*|T^{(-)}|-\lambda-\lambda_\gamma\rangle \\
&\quad + \langle 1/2 - \lambda_*|T^{(+)}|-\lambda-\lambda_\gamma\rangle, \\
&\quad \langle 1/2 - \lambda_*|T^{(-)}|-\lambda-\lambda_\gamma\rangle \\
&\quad = -e\overline{u}_\Lambda(p_*,\lambda_*)\Gamma_\mu^{(-)} u(p,\lambda)\epsilon_\mu^{(\lambda_\gamma)}(q), \\
&\quad \langle 1/2 - \lambda_*|T^{(+)}|-\lambda-\lambda_\gamma\rangle \\
&\quad = +e\overline{u}_\Lambda(p_*,\lambda_*)\Gamma_\mu^{(+)} u(p,\lambda)\epsilon_\mu^{(\lambda_\gamma)}(q).
\end{aligned} \tag{15}$$

We use the following notation for these amplitudes:

$$\mathcal{F}^{(\pm)}_{\frac{1}{2}} = \left\langle 1/2\frac{1}{2}\left|T^{(\pm)}\right|+\frac{1}{2}1\right\rangle, \qquad \frac{M}{m_*}\mathcal{C}^{(\pm)}_{\frac{1}{2}} = \left\langle 1/2\frac{1}{2}\left|T^{(\pm)}\right|-\frac{1}{2}0\right\rangle. \tag{16}$$

The direct calculation gives the following expression for the helicity amplitudes [8]:

$$\begin{pmatrix} \mathcal{F}^{(\pm)}_{\frac{1}{2}} \\ \pm\sqrt{2}\mathcal{C}^{(\pm)}_{\frac{1}{2}} \end{pmatrix} = \frac{\lambda_0^{(\pm)}}{m_*} \times \begin{pmatrix} 2M^2 & m_+m_- \\ -2m_*m_\mp & -m_*m_\pm \end{pmatrix} \begin{pmatrix} F_1^{(\pm)} \\ F_2^{(\pm)} \end{pmatrix}. \quad (17)$$

Here, $m_\pm = m_* \pm m$. The parameters $\lambda_0^{(\pm)}$ are defined by

$$\lambda_0^{(\pm)} = e\frac{m_*}{\sqrt{2}}\sqrt{m_\pm^2 - M^2}. \quad (18)$$

The helicity amplitudes are simply connected to the electric (magnetic) and Coulomb amplitudes $G_{E/M}^{(\pm)}$ and $G_{\mathrm{C}}^{(\pm)}$ [8]:

$$\lambda_0^{(\pm)} \begin{pmatrix} \sqrt{2}G_{E/M}^{(\pm)} \\ G_{\mathrm{C}}^{(\pm)} \end{pmatrix} = \begin{pmatrix} -1 & 0 \\ 0 & 1 \end{pmatrix} \begin{pmatrix} \mathcal{F}^{(\pm)}_{\frac{1}{2}} \\ \mathcal{C}^{(\pm)}_{\frac{1}{2}} \end{pmatrix}. \quad (19)$$

Equations (17) and (19) can be combined to give the relations between the magnetic, electric, and Coulomb form factors and the form factors $F_k^{(\pm)}$. These relations have the form

$$\begin{pmatrix} G_{E/M}^{(\pm)} \\ \pm G_{\mathrm{C}}^{(\pm)} \end{pmatrix} = -\frac{1}{\sqrt{2}m_*} \times \begin{pmatrix} 2M^2 & m_+m_- \\ 2m_*m_\mp & m_*m_\pm \end{pmatrix} \begin{pmatrix} F_1^{(\pm)} \\ F_2^{(\pm)} \end{pmatrix}. \quad (20)$$

3. THE $\Lambda \to n\gamma^*$ DECAY WIDTH

The Λ-hyperon decay width can be found to be

$$\Gamma(\Lambda \to n\gamma^*) = \Gamma^{(-)}(\Lambda \to n\gamma^*) + \Gamma^{(+)}(\Lambda \to n\gamma^*), \quad (21)$$

$$\Gamma^{(\pm)}(\Lambda \to n\gamma^*) = \frac{\alpha}{8m_*}(m_\pm^2 - M^2)^{3/2} \times (m_\mp^2 - M^2)^{1/2}\left(2\left|G_{E/M}^{(\pm)}\right|^2 + \frac{M^2}{m_*^2}\left|G_{\mathrm{C}}^{(\pm)}\right|^2\right).$$

The angular asymmetry in the decay of a polarized Λ hyperon is equal to

$$\frac{d\Gamma(\Lambda \to n\gamma^*)}{d\Omega} = \frac{\Gamma(\Lambda \to n\gamma^*)}{4\pi}(1 + a \cdot n_q), \quad (22)$$

$$a = \frac{\lambda_0^{(+)}\lambda_0^{(-)}2\mathrm{Re}\left(2G_M^{(-)}G_E^{(+)} + (M^2/m_*^2)G_{\mathrm{C}}^{(-)}G_{\mathrm{C}}^{(+)}\right)}{\lambda_0^{(-)2}\left(2\left|G_M^{(-)}\right|^2 + (M^2/m_*^2)\left|G_{\mathrm{C}}^{(-)}\right|^2\right) + \lambda_0^{(+)2}\left(2\left|G_E^{(+)}\right|^2 + (M^2/m_*^2)\left|G_{\mathrm{C}}^{(+)}\right|^2\right)}\zeta,$$

where ζ is the polarization vector of the Λ hyperon.

The simplest representation for the covariant form factors consistent with quark counting rules has the form [8]

$$F_k^{(\pm)}(M^2) = \frac{F_k^{(\pm)}(0)}{\prod_{i=1}^{3}(1 - M^2/m_i^2)}, \quad (23)$$

where m_i are the masses of vector mesons (ρ, ρ', ρ'').

If the width $\Gamma(\Lambda \to n\gamma^*)$ is known, the dilepton decay rate can be represented in the form

$$d\Gamma(\Lambda \to ne^+e^-) = \Gamma(\Lambda \to n\gamma^*)M\Gamma(\gamma^* \to e^+e^-)\frac{dM^2}{\pi M^4}, \quad (24)$$

where

$$\Gamma(\gamma^* \to e^+e^-) = \frac{\alpha}{3M}(M^2 + 2m_e^2)\sqrt{1 - \frac{4m_e^2}{M^2}} \quad (25)$$

is the decay width of a virtual photon γ^* into the dilepton pair with invariant mass M, and m_e is the electron mass.

In our model, four constants $F_k^{(\pm)}(0)$ are necessary to fix the M^2 dependence of the differential decay rate $d\Gamma(\Lambda \to ne^+e^-)/dM^2$. Two of them, $F_2^{(\pm)}(0)$, enter the amplitudes of $\Lambda \to n\gamma$ decay and can be fixed by the total width of this decay and by the angular asymmetry in the decay of a polarized Λ hyperon. The other two constants, $F_1^{(\pm)}(0)$, do not enter the amplitudes for $M^2 = 0$ and are, hence, arbitrary parameters. Both the differential decay rate $d\Gamma(\Lambda \to ne^+e^-)/dM^2$ and total width $\Gamma(\Lambda \to ne^+e^-)$ are sensitive to these parameters. For example, if one takes the constant $F_2^{(+)}(0) = (m_-/m_+)F_2^{(-)}(0)$ to obtain the maximal angular asymmetry in the decay of a polarized Λ hyperon and varies the constants

$F_1^{(\pm)}(0)$ in the range

$$\frac{F_1^{(+)}(0)}{F_2^{(+)}(0)} = 0{-}10, \quad \frac{F_1^{(-)}(0)}{F_2^{(-)}(0)} = 0{-}10,$$

the differential branching ratio $\mathrm{Br} = \Gamma(\Lambda \to ne^+e^-)/\Gamma(\Lambda \to n\gamma)$ varies in the range (see figure)

$$\mathrm{Br} = \Gamma(\Lambda \to ne^+e^-)/\Gamma(\Lambda \to n\gamma) = 0.0038{-}0.039.$$

4. CONCLUSION

We conclude that weak radiative decays of hyperons and especially the decay $\Lambda \to ne^+e^-$ can be an important source for weak radiative form factors. In the situation where there is large theoretical underestimation of the amplitude of $\Lambda \to n\gamma$ decay, these form factors are of prime importance for future theoretical investigations of weak radiative decays of hyperons.

ACKNOWLEDGMENTS

I am grateful to V.T. Smolyankin, who suggested the subject of the present investigation, and to M.I. Krivoruchenko for useful discussions.

REFERENCES

1. S. Timm *et al.*, Phys. Rev. D **51**, 4638 (1995).
2. J. Lach and P. Zenczykowski, Int. J. Mod. Phys. A **10**, 3817 (1995).
3. B. Bassalleck, Nucl. Phys. A **547**, 299 (1992).
4. J. W. Bos, D. Chang, S. C. Lee, *et al.*, Phys. Rev. D **54**, 3321 (1996).
5. HADES Collab. (J. Friese *et al.*), Prog. Part. Nucl. Phys. **42**, 235 (1999).
6. A. I. Vainstein and V. I. Zakharov, Phys. Lett. B **72B**, 368 (1978).
7. A. Faessler, C. Fuchs, M. I. Krivoruchenko, and B. V. Martemyanov, nucl-th/0010056.
8. A. Faessler, C. Fuchs, M. I. Krivoruchenko, and B. V. Martemyanov, Ann. Phys. (N.Y.) **296**, 299 (2002).

Physics of Atomic Nuclei, Vol. 66, No. 4, 2003, pp. 741–754. From Yadernaya Fizika, Vol. 66, No. 4, 2003, pp. 772–785.

ELEMENTARY PARTICLES AND FIELDS
Theory

Quark–Gluonium Content of the Scalar–Isoscalar States $f_0(980)$, $f_0(1300)$, $f_0(1500)$, $f_0(1750)$, and $f_0(1420^{+150}_{-70})$ from Hadronic Decays*

V. V. Anisovich, V. A. Nikonov, and A. V. Sarantsev

Petersburg Nuclear Physics Institute, Russian Academy of Sciences, Gatchina, 188350 Russia

Received September 7, 2001; in final form, May 22, 2002

Abstract—On the basis of the decay couplings $f_0 \to \pi\pi$, $K\bar{K}$, $\eta\eta$, $\eta\eta'$ found earlier in the study of analytical ($IJ^{PC} = 00^{++}$) amplitude in the mass range 450–1900 MeV, we analyze the quark–gluonium content of the resonances $f_0(980)$, $f_0(1300)$, $f_0(1500)$, and $f_0(1750)$ and the broad state $f_0(1420^{+150}_{-70})$. The K-matrix technique used in the analysis makes it possible to evaluate the quark–gluonium content both for the states with switched-off decay channels (bare states, f_0^{bare}) and for the real resonances. We observe a significant change in the quark–gluonium composition in the evolution from bare states to real resonances, which is due to the mixing of states in the transitions $f_0(m_1) \to$ real mesons $\to f_0(m_2)$ responsible for the decay processes as well. For $f_0(980)$, the analysis confirmed the dominance of $q\bar{q}$ component, thus proving the $n\bar{n}/s\bar{s}$ composition found in the study of the radiative decays. For the mesons $f_0(1300)$, $f_0(1500)$, and $f_0(1750)$, the hadronic decays do not allow one to determine uniquely the $n\bar{n}$, $s\bar{s}$, and gluonium components, providing relative percentage only. The analysis shows that the broad state $f_0(1420^{+150}_{-70})$ can mix with the flavor singlet $q\bar{q}$ component only, which is consistent with gluonium origin of the broad resonance. © *2003 MAIK "Nauka/Interperiodica".*

1. INTRODUCTION

The present paper continues the investigation of ($IJ^{PC} = 00^{++}$) resonances started in [1, 2]: we analyze the K-matrix solution in which a scalar glueball located near 1600 MeV appears, before mixing with neighboring $q\bar{q}$ states due to decay processes.

In [1], on the basis of experimental data of the GAMS group [3], Crystal Barrel Collaboration [4], and BNL group [5], the K-matrix solution was found for the waves $00^{++}, 10^{++}$, 02^{++}, and 12^{++} covering the mass range 450–1900 MeV. Also, masses and total widths of resonances were determined for these waves. The following states were seen in the scalar–isoscalar sector:

$$00^{++}: \quad f_0(980),\ f_0(1300),\ f_0(1500),\ f_0(1420^{+150}_{-70}),\ f_0(1750). \tag{1}$$

In [6], the resonances $f_0(1300)$ and $f_0(1750)$ are referred to as $f_0(1370)$ and $f_0(1710)$. The broad state $f_0(1420^{+150}_{-70})$ is not included in the compilation [6]; the broad state is denoted in [1] as $f_0(1530^{+90}_{-250})$, which represents the mean value for three solutions found in the K-matrix analysis; here, we discuss the solution only where a primary glueball is located near 1600 MeV; in this way, we use the mass of the broad state found in this solution.

For the scalar–isovector sector, the analysis [1] points to the presence of the following resonances in the spectra:

$$10^{++}: \quad a_0(980),\ a_0(1520). \tag{2}$$

In the compilation [6], the state $a_0(1520)$ is denoted as $a_0(1450)$.

As to tensor mesons, the following states are seen:

$$12^{++}: \quad a_2(1320),\ a_2(1660), \tag{3}$$
$$02^{++}: \quad f_2(1270),\ f_2(1525).$$

Although in the analysis [1] the CERN–Münich group data [7] were not included in the fitting procedure directly, these data had been fitted in previous papers [8, 9], and it was due to special control that solutions found in [1] and [8, 9] for the $\pi\pi$ channel are in a good agreement with each other.

For the states shown in (1), (2), and (3), the K-matrix poles and K-matrix couplings to channels $\pi\pi$, $K\bar{K}$, $\eta\eta$, $\eta\eta'$, and $\pi\pi\pi\pi$ were found in [1]. The K-matrix poles are not the amplitude poles, these latter corresponding to physical resonances, but when the decays are switched off, the resonance poles turn into the K-matrix ones. In the states related to the K-matrix poles, there is no cloud of real mesons due to the decay processes, which was the reason for naming them "bare states." The K-matrix couplings for transitions bare state $\to \pi\pi$, $K\bar{K}$, $\eta\eta$, $\eta\eta'$ found

*This article was submitted by the authors in English.

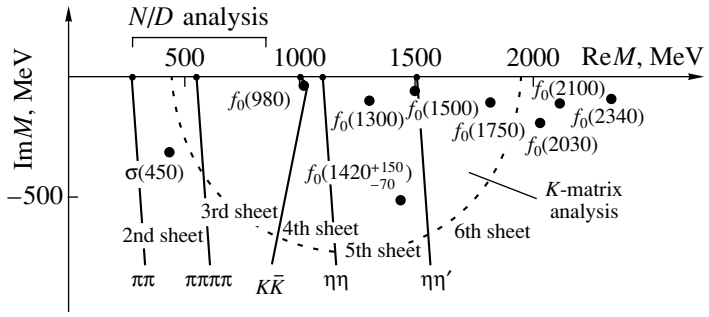

Fig. 1. Complex M plane (in MeV) for the ($IJ^{PC} = 00^{++}$) mesons. The dashed curve encircles the part of the plane where the K-matrix analysis [1] reconstructs the analytical K-matrix amplitude: the poles corresponding to the resonances $f_0(980)$, $f_0(1300)$, $f_0(1500)$, and $f_0(1750)$ and the broad state $f_0(1420^{+150}_{-70})$ are located in this area. In the low-mass region, the pole of the light σ meson is located beyond this area (shown by a point, the position of the pole, $M = (430 - i320)$ MeV, corresponds to the result of N/D analysis [13]). In the high-mass region, one has resonances $f_0(2030)$, $f_0(2100)$, and $f_0(2340)$ [15, 16]. Solid lines stand for the cuts related to the thresholds $\pi\pi$, $\pi\pi\pi\pi$, $K\bar{K}$, $\eta\eta$, and $\eta\eta'$.

in [1] confirm the $q\bar{q}$ nonet classification of bare states suggested in [10, 11].

Still, the K-matrix analysis [1] does not supply us with partial widths of the resonances directly. To determine couplings for the transitions resonance $\to$ mesons, auxiliary calculations should be performed to find the residues of the amplitude poles. Calculations of the residues were carried out in [2] for the scalar–isoscalar sector, which gives us the values of partial widths for the resonances $f_0(980)$, $f_0(1300)$, $f_0(1500)$, and $f_0(1750)$ and the broad state $f_0(1420^{+150}_{-70})$ decaying into the channels $\pi\pi$, $\pi\pi\pi\pi$, $K\bar{K}$, $\eta\eta$, and $\eta\eta'$.

In the present paper, we use the decay couplings for the reactions $f_0 \to \pi\pi$, $K\bar{K}$, $\eta\eta$, $\eta\eta'$ as a basis for the analysis of the quark–gluonium content of scalar–isoscalar resonances $f_0(980)$, $f_0(1300)$, $f_0(1500)$, $f_0(1750)$, and $f_0(1420^{+150}_{-70})$, assuming for these states a three-component structure: $n\bar{n} = (u\bar{u} + d\bar{d})/\sqrt{2}, s\bar{s}$, gluonium. We demonstrate that hadronic decays do not determine the weight of all components, but only provide the correlation between them.

The knowledge of coupling constants of bare states $f_0^{\text{bare}} \to \pi\pi$, $K\bar{K}$, $\eta\eta$, $\eta\eta'$ makes it possible to trace the evolution of the $q\bar{q}$ and gluonium components in f_0 mesons by switching on/off the decay channels, thus establishing constraints for these components in a resonance.

The paper is organized as follows. Section 2, being introductory, gives a general picture of resonances in the scalar–isoscalar sector in the mass range up to 2300 MeV and presents the $q\bar{q}$ classification of the 00^{++} states. On the basis of this classification, we analyze the K-matrix solution with a primary glueball located near 1600 MeV. Correspondingly, we explore parameters found for the broad state in this solution, $f_0(1420^{+150}_{-70})$.

In Section 3, we analyze the quark–gluonium content of the resonances $f_0(980)$, $f_0(1300)$, $f_0(1500)$, and $f_0(1750)$ and the broad state $f_0(1420^{+150}_{-70})$ based on the rules of quark combinatorics for the f_0 states [12].

In Section 4, using the K-matrix representation for the 00^{++} amplitude, we study the evolution of the quark–gluonium content of resonances $f_0(980)$, $f_0(1300)$, $f_0(1500)$, $f_0(1750)$, and $f_0(1420^{+150}_{-70})$ by gradually varying the strength of the decay channels.

Concluding, we state that our analysis based only on the study of hadronic decays is not able to fix the $q\bar{q}$/gluonium content of f_0 mesons unambiguously. For a qualitative estimate of $q\bar{q}$ and gluonium components, one needs to incorporate additional information into the analysis, such as partial widths of the f_0 mesons produced in $\gamma\gamma$ collisions, rates of radiative decays with the f_0-meson production, or the f_0 production ratios in the decays of heavy mesons.

2. RESONANCES IN SCALAR–ISOSCALAR SECTOR

The K-matrix analysis [1] performed for the scalar–isoscalar sector at 450–1900 MeV allows us to reconstruct the analytical form of the amplitude in the region shown in Fig. 1 by the dashed curve, since the threshold singularities of the 00^{++} amplitude related to the $\pi\pi$, $\pi\pi\pi\pi$, $K\bar{K}$, $\eta\eta$, and $\eta\eta'$ channels are correctly taken into account. The amplitude poles that correspond to resonances (1), broad state $f_0(1420^{+150}_{-70})$ included, are located just in the area where the analytical structure of the amplitude 00^{++} is restored.

Below the mass scale of the K-matrix analysis [1], there is a pole related to the light σ meson: in Fig. 1, its position, $M = (430 - i320)$ MeV, is shown in accordance with the results of the dispersion relation N/D analysis [13] (the mass region allowed by this analysis is also shown in Fig. 1).

The pole related to the light σ meson, with the mass $M \simeq 450$ MeV, was obtained in a number of papers (see [6] for details). In the decay $D^+ \to \pi^+\pi^+\pi^-$, the σ-meson mass was found to be $M = 480 \pm 40$ MeV [14].

Above the mass region of the K-matrix analysis, there are resonances $f_0(2030)$, $f_0(2100)$, and $f_0(2340)$ [15, 16].

2.1. Classification of Scalar Bare States

In [10, 11], in terms of bare states, the quark–gluonium classification of scalar particles has been suggested. The results of the K-matrix analysis [1] support this classification.

The bare state, being a member of a $q\bar{q}$ nonet, imposes rigid restrictions on the K-matrix parameters. The $q\bar{q}$ nonet of scalars consists of two scalar–isoscalar states $f_0^{\text{bare}}(1)$ and $f_0^{\text{bare}}(2)$, scalar–isovector meson a_0^{bare}, and scalar kaon K_0^{bare}. In the leading terms of the $1/N$ expansion [17], the decays of these four states into two pseudoscalar mesons are determined by three parameters only, which are the common coupling constant g, suppression parameter λ for strange quark production (in the limit of precise $SU(3)_{\text{flavor}}$ symmetry $\lambda = 1$), and mixing angle φ for $n\bar{n} = (u\bar{u} + d\bar{d})/\sqrt{2}$ and $s\bar{s}$ components in f_0^{bare}:

$$\psi_{\text{flavor}}(f_0^{\text{bare}}) = n\bar{n}\cos\varphi + s\bar{s}\sin\varphi. \qquad (4)$$

The mixing angle defines the scalar–isoscalar nonet partners $f_0^{\text{bare}}(1)$ and $f_0^{\text{bare}}(2)$:

$$\varphi(1) - \varphi(2) = 90^\circ. \qquad (5)$$

The restrictions imposed on coupling constants allow one to fix unambiguously the basic scalar nonet,

$$1^3P_0q\bar{q}: \quad f_0^{\text{bare}}(720 \pm 100),\ a_0^{\text{bare}}(960 \pm 30),\ K_0^{\text{bare}}(1220^{+50}_{-150}),\ f_0^{\text{bare}}(1260 \pm 30), \qquad (6)$$

as well as the mixing angle for $f_0^{\text{bare}}(720)$ and $f_0^{\text{bare}}(1260)$,

$$\varphi[f_0^{\text{bare}}(720)] = -70^{\circ\,+5^\circ}_{-10^\circ}. \qquad (7)$$

The nonet $1^3P_0q\bar{q}$ in the form of (6) was suggested in [10], where the K-matrix reanalysis of the $K\pi$ data [18] was carried out (bare states and their couplings for the 00^{++} and 10^{++} waves were found earlier in [8, 9]).

Establishing the nonet of the first radial excitations, $2^3P_0q\bar{q}$, appeared to be a more difficult problem. The K-matrix analysis [1] gives two scalar–isoscalar states in the region 1200–1650 MeV, their decay couplings satisfying the requirements imposed for a glueball; these states are as follows: $f_0^{\text{bare}}(1230^{+150}_{-30})$ and $f_0^{\text{bare}}(1600 \pm 50)$. To resolve this dilemma, one needs the systematization of $q\bar{q}$ states on the (n, M^2) plot (n being radial quantum number of the meson and M its mass): the systematization suggested in [16] definitely proves $f_0^{\text{bare}}(1600 \pm 50)$ to be a superfluous state on the $q\bar{q}$ trajectory. Correspondingly, $f_0^{\text{bare}}(1230^{+150}_{-30})$ and $f_0^{\text{bare}}(1810 \pm 30)$ should be the $q\bar{q}$ states.

Below, we present arguments based on a detailed consideration of the (n, M^2) plot, while now let us discuss the variant that satisfies the constraints given by the $q\bar{q}$ trajectories.

The nonet $2^3P_0q\bar{q}$ looks as follows:

$$2^3P_0q\bar{q}: \quad f_0^{\text{bare}}(1230^{+150}_{-30}),\ f_0^{\text{bare}}(1810 \pm 30),\ a_0^{\text{bare}}(1650 \pm 50),\ K_0^{\text{bare}}(1885^{+50}_{-100}),\ \varphi[f_0^{\text{bare}}(1230)] = 40^\circ \pm 8^\circ. \qquad (8)$$

The K-matrix analysis [1], together with previous ones [8, 9], enables one to reveal in the scalar–isoscalar sector the bare state $f_0^{\text{bare}}(1600)$, which is an extra one for the nonet classification $1^3P_0q\bar{q}$ and $2^3P_0q\bar{q}$. At the same time, the couplings of $f_0^{\text{bare}}(1600)$ to the decay channels $\pi\pi$, $K\bar{K}$, $\eta\eta$, and $\eta\eta'$ obey the requirements imposed on the glueball decay. This gives a reason to consider this state as the lightest scalar glueball,

$$0^{++} \quad \text{glueball}: \quad f_0^{\text{bare}}(1600 \pm 50). \qquad (9)$$

The lattice calculations are in reasonable agreement with such a value of the lightest glueball mass [19].

After the onset of the decay channels, the bare states are transformed into real resonances. For the scalar–isoscalar sector, we observe the following transitions by switching on the decay channels:

$$\begin{aligned} f_0^{\text{bare}}(720 \pm 100) &\to f_0(980), \\ f_0^{\text{bare}}(1230^{+150}_{-30}) &\to f_0(1300), \\ f_0^{\text{bare}}(1260 \pm 30) &\to f_0(1500), \\ f_0^{\text{bare}}(1600 \pm 50) &\to f_0(1420^{+150}_{-70}), \\ f_0^{\text{bare}}(1810 \pm 30) &\to f_0(1750). \end{aligned} \qquad (10)$$

The evolution of bare states into real resonances is illustrated by Fig. 2: the shifts of amplitude poles in the complex M plane correspond to a gradual onset of

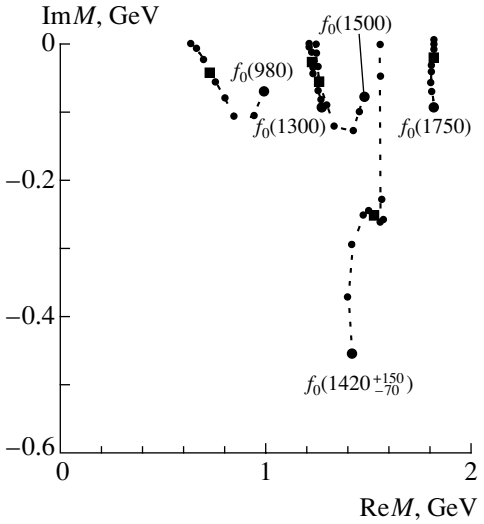

Fig. 2. Complex M plane: trajectories of the poles for $f_0(980)$, $f_0(1300)$, $f_0(1500)$, $f_0(1750)$, and $f_0(1420^{+150}_{-70})$ during gradual onset of the decay processes.

the decay channels. Technically, it is done by replacing the phase spaces ρ_a for $a = \pi\pi$, $\pi\pi\pi\pi$, $K\bar{K}$, $\eta\eta$, $\eta\eta'$ in the K-matrix amplitude as follows: $\rho_a \to \xi\rho_a$, where the parameter ξ runs in the interval $0 \le \xi \le 1$. At $\xi \to 0$, one has bare states, while the limit $\xi \to 1$ gives us the positions of real resonances.

2.2. Overlapping of f_0 Resonances in the Mass Region 1200–1700 MeV: Accumulation of Widths of the $q\bar{q}$ States by the Glueball

The occurrence of the broad resonance is not at all an accidental phenomenon. It originated due to a mixing of states in the decay processes, namely, transitions $f_0(m_1) \to$ real mesons $\to f_0(m_2)$. These transitions result in a specific phenomenon; that is, when several resonances overlap, one of them accumulates the widths of neighboring resonances and transforms into the broad state.

This phenomenon was observed in [8, 9] for scalar–isoscalar states, and the following scheme was suggested in [20, 21]: the broad state $f_0(1420^{+150}_{-70})$ is the descendant of the pure glueball, which, being in the neighborhood of $q\bar{q}$ states, accumulated their widths and transformed into the mixture of gluonium and $q\bar{q}$ states. In [21], this idea was modelled for four resonances, $f_0(1300)$, $f_0(1500)$, $f_0(1420^{+150}_{-70})$, and $f_0(1750)$, by using the language of the quark–antiquark and two-gluon states, $q\bar{q}$ and gg: the decay processes were considered to be transitions $f_0 \to q\bar{q}, gg$; correspondingly, the same processes realized the mixing of the resonances. In this model, the gluonium component was dispersed mainly over three resonances, $f_0(1300)$, $f_0(1500)$, and $f_0(1420^{+150}_{-70})$, so every state is a mixture of $q\bar{q}$ and gg components, with a roughly equal percentage of gluonium (about 30–40%).

Accumulation of widths of overlapping resonances by one of them is a well-known effect in nuclear physics [22–24]. In meson physics, this phenomenon can play a rather important role, in particular, for exotic states that are beyond the $q\bar{q}$ systematics. Indeed, being among $q\bar{q}$ resonances, the exotic state creates a group of overlapping resonances. The exotic state, which is not orthogonal to its neighbors, after accumulating the "excess" of widths, turns into the broad one. This broad resonance should be accompanied by narrow states that are the descendants of states from which the widths have been taken off. In this way, the existence of a broad resonance accompanied by narrow ones may be a signature of the exotics. This possibility, in the context of searching for exotic states, was discussed in [25, 26].

The broad state may be one of the components that form the confinement barrier: the broad states after accumulating the widths of neighboring resonances play for these latter ones the role of locking states. Evaluation of the mean radii squared of the broad state $f_0(1420^{+150}_{-70})$ and its neighboring resonances argues in favor of this idea, for the radius of $f_0(1420^{+150}_{-70})$ is significantly larger than that for $f_0(980)$ and $f_0(1300)$ [26, 27], thus making it possible for $f_0(1420^{+150}_{-70})$ to be the locking state.

2.3. Systematics of the Scalar–Isoscalar $q\bar{q}$ States on the (n, M^2) Plot

As is stressed above, the systematics of $q\bar{q}$ states on the (n, M^2) plot argues that the broad state, $f_0(1420^{+150}_{-70})$, and its predecessor, $f_0^{\text{bare}}(1600 \pm 50)$, are states beyond $q\bar{q}$ classification. Following [16], we plot in Fig. 3*a* the (n, M^2) trajectories for f_0, a_0, and K_0 states (the doubling of f_0 trajectories is due to two flavor components, $n\bar{n}$ and $s\bar{s}$). All trajectories are roughly linear, and they clearly represent the states with a dominant $q\bar{q}$ component. It is seen that one of the states, either $f_0(1420^{+150}_{-70})$ or $f_0(1500)$, is superfluous for $q\bar{q}$ systematics. Looking at the (n, M^2) trajectories for bare states (Fig. 3*b*), one can see that just $f_0^{\text{bare}}(1600)$ does not fall on any linear $q\bar{q}$ trajectory. Thus, it would be natural to conclude that $f_0^{\text{bare}}(1600)$ is an exotic state, i.e., the glueball.

Relying on the arguments given by the systematics of $q\bar{q}$ states on the (n, M^2) plot, we can state that the classification represented by (8) and (9) is a

basis for further analysis. Lattice calculations support the solution (8), (9): calculations give values for the mass of the lightest glueball in the interval of 1550–1750 MeV [19].

3. HADRONIC DECAYS, RULES OF QUARK COMBINATORICS FOR COUPLINGS, AND ESTIMATION OF THE QUARK–GLUONIUM CONTENT OF RESONANCES

In this section, on the basis of the quark combinatorics for the decay coupling constants, we analyze the quark–gluonium content of resonances $f_0(980)$, $f_0(1300)$, $f_0(1500)$, $f_0(1750)$, and $f_0(1420^{+150}_{-70})$. We would like to bring to the attention of the reader the ambiguities that are inherent in analyses studying only hadronic decays of resonances.

3.1. Quark Combinatorial Relations for the Decay Couplings

Within $1/N$ leading-order terms [17], hadronic decays of meson resonances are determined by planar diagrams. An example of the process is shown in Fig. 4*a*: the quarks flying away from the initial $q\bar{q}$ state produce in a soft way (i.e., at relatively large distances, $r \sim R_{\text{confinement}}$) a new pair of light quarks ($u\bar{u}$, $d\bar{d}$, or $s\bar{s}$) and turn into white hadrons, thus making it possible for initial quarks to leave the confinement domain. In the limit of flavor $SU(3)$ symmetry, the production of all quarks is equivalent; still, a heavier weight of strange quark results in a suppression of the production probability of an $s\bar{s}$ pair. Thus, the following ratio of production probabilities takes place:

$$u\bar{u} : d\bar{d} : s\bar{s} = 1 : 1 : \lambda, \qquad (11)$$

with λ =0.4–0.8 for meson decays [12, 28]. For similar decays, the coupling constants (see Fig. 4) differ by a coefficient that depends on the mixing angle of the $n\bar{n}$ and $s\bar{s}$ components of the initial meson and parameter λ [12]. These coefficients are shown in Table 1 for the decays $f_0 \to \pi\pi, K\bar{K}, \eta\eta, \eta\eta', \eta'\eta'$.

The planar diagram for the transition glueball → two mesons is shown in Fig. 4*b*. Below, to illustrate the estimations, we consider gluonium as a two-gluon composite system: the large value of the soft-gluon mass, $m_{\text{gluon}} \sim 700$–$1000$ MeV [29], supports the model, although, we should stress, the results have a more general meaning.

The planar diagram of Fig. 4*b* represents a two-stage transition gluonium → $q\bar{q}$ → two mesons, and the second stage is similar to the decay of a $q\bar{q}$ meson. Because of that, the relations between couplings in the transition gluonium → two pseudoscalars are

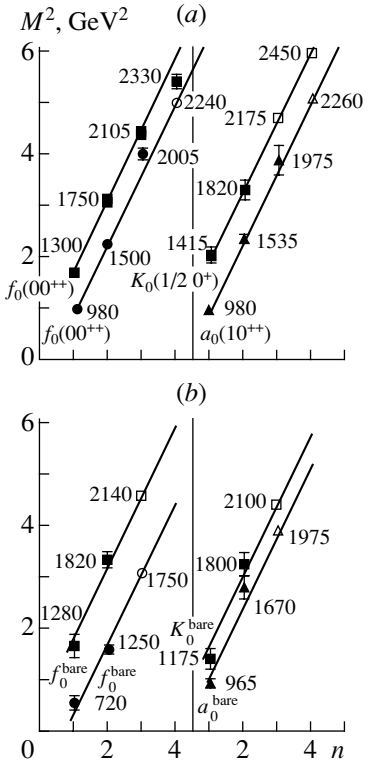

Fig. 3. Linear trajectories in the (n, M^2) plane for scalar resonances (*a*) and scalar bare states (*b*) [1]. Open points stand for predicted states.

governed by the magnitudes given in Table 1, with fixed values of mixing angle for the $n\bar{n}$ and $s\bar{s}$ components, $q\bar{q} = n\bar{n}\cos\varphi_G + s\bar{s}\sin\varphi_G$, which are formed in the process gluonium → $q\bar{q}$. The angle φ_G is determined by the parameter λ_G entering the first stage of the process gluonium → $q\bar{q}$ with relative probability $u\bar{u} : d\bar{d} : s\bar{s} = 1 : 1 : \lambda_G$. Then,

$$\cos\varphi_G = \sqrt{\frac{2}{2+\lambda_G}}. \qquad (12)$$

The relations between coupling constants for the decays gluonium → $\pi\pi$, $K\bar{K}$, $\eta\eta$, $\eta\eta'$, $\eta'\eta'$ are given in Table 1 as well. In principle, λ_G may differ from the suppression parameter inherent to transitions $q\bar{q}$ → two mesons. However, it looks reasonable to use, as the first approximation, the same value of λ for both stages of the gluonium decay, because the coefficients for the transitions $q\bar{q}$ → two mesons change rather weakly with λ belonging to the interval 0.4–0.8.

The sums of couplings squared for the decay transitions of the $q\bar{q}$ meson and gluonium are of the same order, as follows from the rules of the $1/N$ expansion [17] ($N = N_c = N_f$, where N_c and N_f are the numbers of colors and flavors). Let us denote the sum of couplings squared for transitions of Fig. 4*a* type, $q\bar{q}$ state → $\sum$mesons, as $g^2_{q\bar{q}}$ and the corresponding

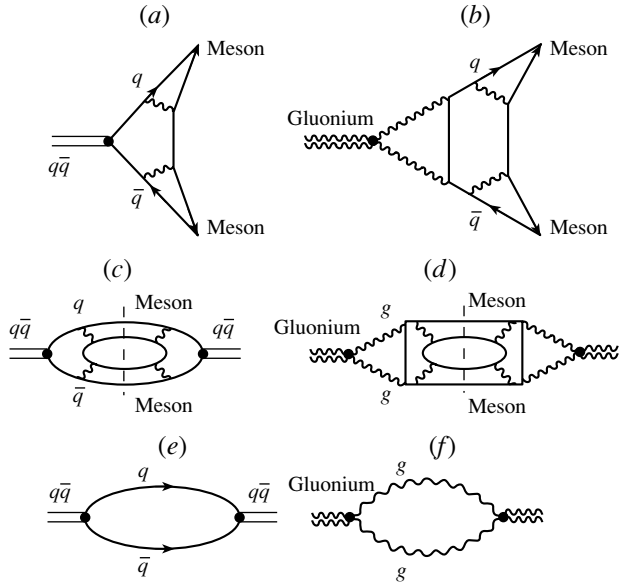

Fig. 4. (*a, b*) Diagrams responsible for the transition of the scalar–isoscalar state into two pseudoscalar mesons, $f_0 \to PP$, in the leading $1/N_c$-expansion terms. (*c, d*) Self-energy diagrams that determine $\sum g_a^2$ (for quarkonium) and $\sum G_a^2$ (for gluonium); the cutting is shown by a dashed line. (*e, f*) Self-energy diagrams that determine the order of value of couplings for the transitions quarkonium $\to q\bar{q}$ and gluonium $\to gg$.

value for the gluonium decay, gluonium $\to \sum$mesons, as g^2_{gluonium}. The values $g^2_{q\bar{q}}$ and g^2_{gluonium} can be represented as discontinuities of the self-energy diagrams of Figs. 4*c* and 4*d*, with cuttings shown by dashed lines: the cut blocks stand for the couplings shown in Figs. 4*a* and 4*b*. In terms of the $1/N$ expansion, the diagram of Fig. 4*c* (and $g^2_{q\bar{q}}$) is of the order of

$$g^2_{q\bar{q}} \sim G^2_{q\bar{q}\text{-meson}\to q\bar{q}} N_f \sim \frac{N_f}{N_c}, \qquad (13)$$

because $G^2_{q\bar{q}\text{-meson}\to q\bar{q}} \sim 1/N_c$. Likewise, for g^2_{gluonium} determined by diagrams of Fig. 4*d* type, one has

$$g^2_{\text{gluonium}} \sim G^2_{\text{gluonium}\to gg} N_f^2 \sim \frac{N_f^2}{N_c^2}. \qquad (14)$$

The coupling for the transition gluonium $\to$ two-gluon state, $G_{\text{gluonium}\to gg}$, is of the order of $G_{\text{gluonium}\to gg} \sim 1/N_c$. The estimates of couplings $G_{q\bar{q}\text{-meson}\to q\bar{q}}$ and $G_{\text{gluonium}\to gg}$ are done by using basic self-energy diagrams for composite systems, which are of the order of unity: in the cases under consideration, such are the diagrams of Figs. 4*e* and 4*f*.

The two-stage nature of the decay gluonium $\to$ two pseudoscalars is a source of ambiguities in the determination of the quark–gluon content of mesons, if we restrict ourselves to hadronic decays only. The point is that the $q\bar{q}$ meson with the quark content $n\bar{n}\cos\varphi + s\bar{s}\sin\varphi$ at $\varphi \simeq \varphi_G$ has the same ratios between coupling constants for the transitions $f_0 \to \pi\pi$, $K\bar{K}$, $\eta\eta$, $\eta\eta'$ as those for the glueball. At $0.4 \leq \lambda_G \lesssim 0.8$, we have $24^\circ \lesssim \varphi_G \lesssim 32^\circ$: it means that the analysis of hadronic decays cannot distinguish between the $q\bar{q}$ state with $\varphi \simeq \varphi_G$ and true gluonium.

3.2. Decay Couplings for the Resonances $f_0(980)$, $f_0(1300)$, $f_0(1500)$, $f_0(1750)$, and $f_0(1420^{+150}_{-70})$ into Channels $\pi\pi$, $K\bar{K}$, $\eta\eta$, $\eta\eta'$, and $\pi\pi\pi\pi$

The K-matrix fit to the data directly gives us the characteristics of the bare states only. To extract resonance parameters, one needs additional calculations to be carried out with the obtained amplitude. The couplings for resonance decay are extracted by calculating residues of the amplitude poles related to the resonances [2]. In more detail, the amplitude $A_{a\to b}$, where a and b mark the channels $\pi\pi$, $K\bar{K}$, $\eta\eta$, $\eta\eta'$, and $\pi\pi\pi\pi$, can be written near the pole as

$$A_{ab} \simeq \frac{g_a^{(n)} g_b^{(n)}}{\mu_n^2 - s} e^{i(\theta_a^{(n)} + \theta_b^{(n)})} + B_{ab}. \qquad (15)$$

The first term in (15) represents the pole singularity, and the second one, B_{ab}, is a smooth background. The pole position $s = \mu_n^2$ determines the mass of the resonance, with total width $\mu_n = M_n - i\Gamma_n/2$, and the real factors $g_a^{(n)}$ and $g_b^{(n)}$ are the decay coupling constants of the resonance to channels a and b. The couplings $g_a^{(n)}$ given in Table 2 stand for the solution with the glueball in the vicinity of 1600 MeV; also the couplings for the predecessor bare states are shown.

Table 1. Coupling constants given by quark combinatorics for the f_0 meson and glueball decaying into two pseudoscalar mesons in the leading terms of $1/N$ expansion (φ is the mixing angle for $n\bar{n}$ and $s\bar{s}$ states, $f_0 = n\bar{n}\cos\varphi + s\bar{s}\sin\varphi$, and Θ is the mixing angle for η–η' mesons: $\eta = n\bar{n}\cos\Theta - s\bar{s}\sin\Theta$ and $\eta' = n\bar{n}\sin\Theta + s\bar{s}\cos\Theta$, where $\cos\Theta \simeq 0.8$ and $\sin\Theta \simeq 0.6$)

Channel	The $q\bar{q}$-meson decay couplings in the leading terms of $1/N$ expansion	The glueball decay couplings in the leading terms of $1/N$ expansion	Identity factor in phase space
$\pi^0\pi^0$	$g\cos\varphi/\sqrt{2}$	$G/\sqrt{2+\lambda}$	1/2
$\pi^+\pi^-$	$g\cos\varphi/\sqrt{2}$	$G/\sqrt{2+\lambda}$	1
K^+K^-	$g(\sqrt{2}\sin\varphi + \sqrt{\lambda}\cos\varphi)/\sqrt{8}$	$G\sqrt{\lambda/(2+\lambda)}$	1
$K^0\bar{K}^0$	$g(\sqrt{2}\sin\varphi + \sqrt{\lambda}\cos\varphi)/\sqrt{8}$	$G\sqrt{\lambda/(2+\lambda)}$	1
$\eta\eta$	$g(\cos^2\theta\cos\varphi/\sqrt{2} + \sqrt{\lambda}\sin\varphi\sin^2\theta)$	$G(\cos^2\theta + \lambda\sin^2\theta)/\sqrt{2+\lambda}$	1/2
$\eta\eta'$	$g\sin\theta\cos\theta(\cos\varphi/\sqrt{2} - \sqrt{\lambda}\sin\varphi)$	$G\cos\theta\sin\theta(1-\lambda)/\sqrt{2+\lambda}$	1
$\eta'\eta'$	$g(\sin^2\theta\cos\varphi/\sqrt{2} + \sqrt{\lambda}\sin\varphi\cos^2\theta)$	$G(\sin^2\theta + \lambda\cos^2\theta)/\sqrt{2+\lambda}$	1/2

Table 2. Couplings squared, g_a^2 (in GeV^2 units), for bare states and their resonance descendants

State	$g^2_{\pi\pi}$	$g^2_{K\bar{K}}$	$g^2_{\eta\eta}$	$g^2_{\eta\eta'}$	$g^2_{\pi\pi\pi\pi}$	$\sum g_a^2$
$f_0^{\mathrm{bare}}(650^{+12}_{-30})$	0.167	0.528	0.06	–	0	0.755
$f_0(980)$	0.076	0.186	0.072	–	0.004	0.338
$f_0^{\mathrm{bare}}(1220^{+15}_{-30})$	0.083	0.099	0.025	–	0.517	0.724
$f_0(1300)$	0.026	0.002	0.003	–	0.132	0.163
$f_0^{\mathrm{bare}}(1265^{+15}_{-45})$	0.679	0.292	0.137	0.046	0	1.154
$f_0(1500)$	0.038	0.009	0.007	0.006	0.074	0.134
$f_0^{\mathrm{bare}}(1820 \pm 40)$	0.059	0.019	0.001	0.043	0.262	0.384
$f_0(1750)$	0.086	0.003	0.009	0.028	0.117	0.243
$f_0^{\mathrm{bare}}(1585^{+10}_{-45})$	0.106	0.062	0.028	0.009	0.924	1.129
$f_0(1420^{+150}_{-70})$	0.304	0.271	0.062	0.016	0.382	1.035

The couplings of Table 2 demonstrate a strong change of couplings during the evolution from bare states to real resonances. Note that the change occurs not only in absolute values of couplings but also in relative magnitudes. The resonances $f_0(1300)$, $f_0(1500)$, and $f_0(1750)$ demonstrate a reduction of relative weight of the coupling constant squared, $g^2_{K\bar{K}}$, while the same coupling in the broad state $f_0(1420^{+150}_{-70})$ increases.

The growth of the relative weight of $g^2_{K\bar{K}}$ in $f_0(1420^{+150}_{-70})$, that is, the glueball descendant, can be unambiguously interpreted: by accumulating the widths of neighboring resonances, this one acquires a noticeable $q\bar{q}$ component, with a large amount of $s\bar{s}$ state.

Let us look at what the quark combinatorics rules given in Table 1 tell us about the proportion of $s\bar{s}$, $n\bar{n}$, and gluonium components in the studied resonances. The coupling constants squared for $f_0 \to \pi\pi$, $K\bar{K}$, $\eta\eta$, $\eta\eta'$ can be written as follows:

$$g^2_{\pi\pi} = \frac{3}{2}\left(\frac{g}{\sqrt{2}}\cos\varphi + \frac{G}{\sqrt{2+\lambda}}\right)^2,$$

$$g^2_{K\bar{K}} = 2\left(\frac{g}{2}\left(\sin\varphi + \sqrt{\frac{\lambda}{2}}\cos\varphi\right) + G\sqrt{\frac{\lambda}{2+\lambda}}\right)^2, \tag{16}$$

$$g^2_{\eta\eta} = \frac{1}{2}\left(g\left(\frac{\cos^2\theta}{\sqrt{2}}\cos\varphi + \sqrt{\lambda}\sin\varphi\sin^2\theta\right)\right.$$

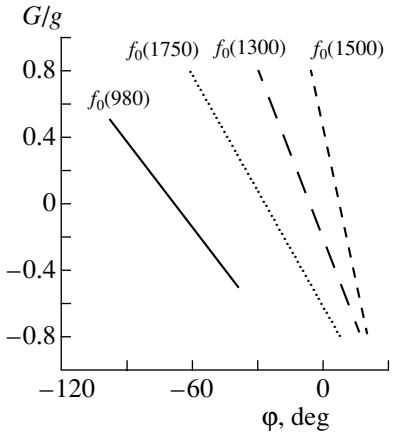

Fig. 5. $(G/g, \varphi)$ plot: the trajectories show correlations between G/g and φ for $f_0(980)$ (solid line), $f_0(1300)$ (long-dashed line), $f_0(1500)$ (dashed line), and $f_0(1750)$ (dotted line).

$$+\frac{G}{\sqrt{2+\lambda}}(\cos^2\theta+\lambda\sin^2\theta)\Bigg)^2,$$

$$g^2_{\eta\eta'}=\sin^2\theta\cos^2\theta\left(g\left(\frac{1}{\sqrt{2}}\cos\varphi-\sqrt{\lambda}\sin\varphi\right)+G\frac{1-\lambda}{\sqrt{2+\lambda}}\right)^2.$$

The term proportional to g is responsible for the transition $q\bar{q}\to$ two mesons, while the term proportional to G stands for the transition gluonium $\to$ two mesons. Correspondingly, the magnitudes g^2 and G^2 are proportional to the probabilities of finding the $q\bar{q}$ and gluonium components in the considered meson.

First of all, let us determine the mean value of the mixing angle for $n\bar{n}/s\bar{s}$ components in the intermediate state, $\langle\varphi\rangle$:

$$f_0\to\text{gluonium}+q\bar{q}\to n\bar{n}\cos\langle\varphi\rangle+s\bar{s}\sin\langle\varphi\rangle\to\text{two mesons}. \quad (17)$$

We define $\langle\varphi\rangle$ as the angle for the coupling constants squared (16) at $G=0$. Then, we have for the studied resonances

$$\begin{aligned} f_0(980):&\quad \langle\varphi\rangle\simeq-67^\circ, \quad (18)\\ f_0(1300):&\quad \langle\varphi\rangle\simeq-5^\circ,\\ f_0(1500):&\quad \langle\varphi\rangle\simeq 8^\circ,\\ f_0(1420^{+150}_{-70}):&\quad \langle\varphi\rangle\simeq 37^\circ,\\ f_0(1750):&\quad \langle\varphi\rangle\simeq-27^\circ. \end{aligned}$$

The value $\langle\varphi[f_0(1420^{+150}_{-70})]\rangle\simeq 37^\circ$ is very close to the mixing angle of the flavor singlet state, $\varphi_{\text{singlet}}=35.3^\circ$. We see that $f_0(1420^{+150}_{-70})$ is a mixture of the gluonium and $(q\bar{q})_{\text{singlet}}$.

Generally, by fitting formulas (16) to the coupling constants squared from Table 2, one can determine the mixing angle φ as a function of G/g. The curves in Fig. 5 illustrate the dynamics of φ with respect to the ratio G/g for the resonances $f_0(980)$, $f_0(1300)$, $f_0(1500)$, and $f_0(1750)$.

The magnitudes of g^2 and G^2 are proportional, correspondingly, to the probabilities for quark/gluonium components, $W_{q\bar{q}}$ and W_{gluonium}, to be in the considered resonance:

$$g^2=g^2_{q\bar{q}}W_{q\bar{q}},\quad G^2=g^2_{\text{gluonium}}W_{\text{gluonium}}. \quad (19)$$

According to the rules of $1/N$ expansion [17], the coupling constants $g^2_{q\bar{q}}$ and g^2_{gluonium} are of the same order (see Section 3.1); therefore, we take as a rough estimate

$$G^2/g^2=W_{\text{gluonium}}/W_{q\bar{q}}. \quad (20)$$

In Fig. 5, we vary G/g in the interval $-0.8\le G/g\le 0.8$; that, in accordance with (20), is related to a possible admixture of the gluonium component up to 40%: $W_{\text{gluonium}}\le 0.40$.

The $q\bar{q}$ components in the resonances $f_0(1300)$ and $f_0(1500)$ reveal a rather moderate change in φ versus the percentage of gluonium component:

$$W_{\text{gluonium}}[f_0(1300)]\le 40\%:\quad -25^\circ\le\varphi[f_0(1300)]\le 13^\circ, \quad (21)$$

and

$$W_{\text{gluonium}}[f_0(1500)]\le 40\%:\quad -3^\circ\le\varphi[f_0(1500)]\le 17^\circ. \quad (22)$$

More sensitive to the glueball admixture is the $q\bar{q}$ components in $f_0(1750)$:

$$W_{\text{gluonium}}[f_0(1750)]\le 40\%:\quad -55^\circ\le\varphi[f_0(1750)]\le -2^\circ. \quad (23)$$

The $n\bar{n}/s\bar{s}$ ratio in $f_0(980)$ is also rather sensitive to the presence of the gluonium component. However, for this case, it is hardly possible to assume the glueball admixture to be more than 20% [30]. Correspondingly, we have

$$W_{\text{gluonium}}[f_0(980)]\le 20\%:\quad -95^\circ\le\varphi[f_0(980)]\le -40^\circ. \quad (24)$$

The analysis clearly demonstrates the impossibility of fixing unambiguously the $n\bar{n}$, $s\bar{s}$, and gluonium components in the resonances $f_0(980)$, $f_0(1300)$, $f_0(1500)$, and $f_0(1750)$ by using their couplings to hadronic channels only. For better understanding of the structure of these mesons, one needs additional data.

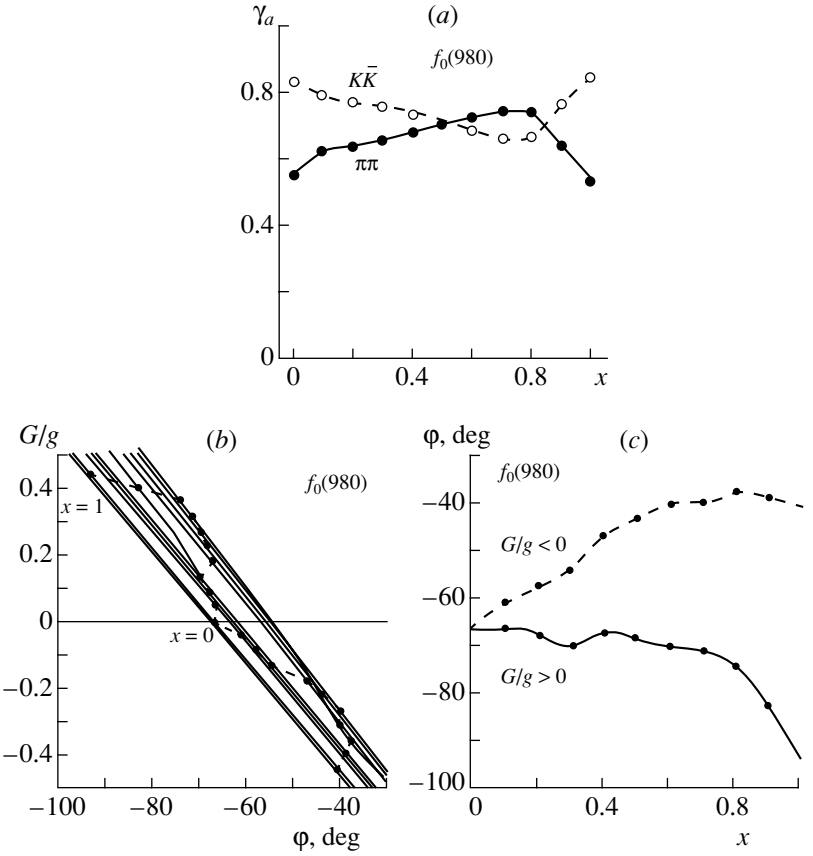

Fig. 6. The evolution of the $f_0(980)$-resonance parameters by switching on/off the decay channels ($x = 0$ corresponds to the bare state, while $x = 1$ stands for the real meson). (a) Normalized coupling constants $g_{\pi\pi}/\sqrt{g_{\pi\pi}^2 + g_{K\bar{K}}^2}$ and $g_{K\bar{K}}/\sqrt{g_{\pi\pi}^2 + g_{K\bar{K}}^2}$. ($b$) The correlation curves $(G/g, \varphi)$ at eleven fixed values of x; dashed curves stand for maximal accumulation of the gluonium component, $W_{\text{gluonium}} = 20\%$. ($c$) The evolution of φ in the $q\bar{q}$ component $q\bar{q} = n\bar{n}\cos\varphi + s\bar{s}\sin\varphi$ at maximal accumulation of the gluonium component: the solid curve stands for positive G/g and the dashed curve for negative G/g.

Still, the K-matrix analysis [1] provides us with considerable information on meson states, which makes it possible to trace the evolution of coupling constants from bare state, f_0^{bare}, to real resonances.

4. EVOLUTION OF COUPLING CONSTANTS FOR $f_0 \to \pi\pi$, $K\bar{K}$, $\eta\eta$, $\eta\eta'$ AT THE ONSET OF THE DECAY CHANNELS

In this section, based on the K-matrix-analysis results [1], we study the dynamics of parameters for the resonances $f_0(980)$, $f_0(1300)$, $f_0(1500)$, $f_0(1750)$, and $f_0(1420^{+150}_{-70})$ by gradually switching on/off the decay channels.

4.1. The Onset of Decay Channels in the K-Matrix Amplitude

When the decay channels are switched off, the coupling constants to two-meson channels are determined by the residues of the K-matrix poles, while, after switching them on, the coupling constants are determined by the residues of amplitude poles. Let us clarify this point in more detail.

The scattering amplitude of the two pseudoscalar mesons was fitted in [1] in the form

$$\hat{A} = \hat{K}\frac{I}{I - i\hat{\rho}\hat{K}}, \tag{25}$$

where $\hat{K}$ is the 5×5 matrix for five channels under investigation ($\pi\pi$, $K\bar{K}$, $\eta\eta$, $\eta\eta'$, $\pi\pi\pi\pi$). The $\hat{K}$ matrix is real and symmetrical, $K_{ab}(s) = K_{ba}(s)$; I is the unit matrix, $I = \text{diag}(1, 1, 1, 1)$; and $\hat{\rho}$ is the diagonal matrix for the phase space, $\hat{\rho} = \text{diag}(\rho_{\pi\pi}, \rho_{K\bar{K}}, \rho_{\eta\eta}, \rho_{\eta\eta'}, \rho_{\pi\pi\pi\pi})$.

The K-matrix element was represented in [1] as a sum of pole terms and smooth background $f_{ab}(s)$:

$$K_{ab}(s) = \sum_n \frac{g_a^{(n)} g_b^{(n)}}{\mu_n^2 - s} + f_{ab}(s), \tag{26}$$

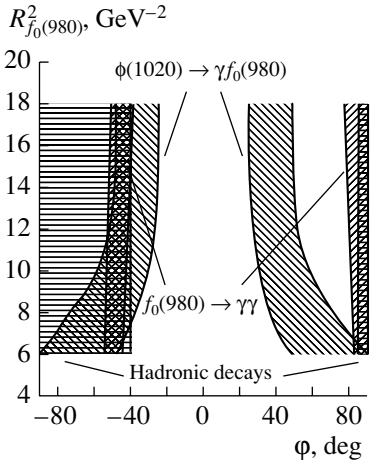

Fig. 7. The $(\varphi, R^2_{f_0(980)})$ plot: the shaded areas are the allowed ones for the reactions $\phi(1020) \to \gamma f_0(980)$, $f_0(980) \to \gamma\gamma$, and $f_0(980) \to \pi\pi, K\bar{K}$.

μ_n being the mass of bare state and $g_a^{(n)}$ being the coupling of $f_0^{\rm bare}(\mu_n)$ to the channel a.

Fitting to data performed in [1] fixes the parameters of the K-matrix amplitude (coupling constants $g_{ab}(s)$, masses of the K-matrix poles μ_n, and regular terms f_{ab}). With the completely determined parameters, we can investigate the dynamics of the onset of decaying processes.

Such an investigation of the resonance evolution was suggested in [31], where a rather simple variant was considered: in amplitude (25), the substitution $\hat{\rho} \to x\rho$ was made, with x varying in the interval $0 \le x \le 1$. The amplitude $\hat{A}(x)$ thus constructed gives us the real amplitude at $x = 1$, and at $x \to 0$, the amplitude $\hat{A}(x)$ turns into the K-matrix one, $\hat{A}(x \to 0) \to \hat{K}$, which is the amplitude for bare states. Generally, the onset of the decay channels in the K-matrix amplitude can be investigated by substituting parameters as follows:

$$g_a^{(n)} \Rightarrow \xi_n(x) g_a^{(n)}, \quad f_{ab} \Rightarrow \xi_f(x) f_{ab}. \qquad (27)$$

Here, the parametric functions $\xi_n(x)$ and $\xi_f(x)$ obey the requirements $\xi_n(0) = \xi_f(0) = 0$ and $\xi_n(1) = \xi_f(1) = 1$. A simple variant studied in [31] corresponds to $\xi_n(x) = \sqrt{x}$ and $\xi_f(x) = x$.

The parameters $\xi_n(x)$ and $\xi_f(x)$ control the dynamics of the onset of the decay channels for resonances. This dynamics may be different for different states, say, the $q\bar{q}$ state and gluonium. Below, we use $\xi_n(x) = \sqrt{x}$ for the states connected with $f_0(980)$, $f_0(1300)$, $f_0(1500)$, and $f_0(1750)$, while for the broad state the dependence $\xi_n(x) = x^{1/4}$ is taken. For the background term, we use $\xi_n(x) = x$.

4.2. Evolution of the Decay Couplings

Below, the evolution of states related to the resonances $f_0(980)$, $f_0(1300)$, $f_0(1500)$, $f_0(1750)$, and $f_0(1420^{+150}_{-70})$ will be considered one by one. The procedure is as follows: the substitution (27) is made and x takes the values $x = 0.1, 0.2, \ldots, 0.8, 0.9$. The value $x = 0$ corresponds to bare states, and the couplings and masses were found as fitting parameters in [1]; for $x = 1$, calculations were performed in [2] and the couplings are presented in Table 2. Furthermore, for different but fixed x, we find the position of poles and calculate the residues of the amplitudes thus determining $g_a^{(n)}(x)$.

4.2.1. Resonance $f_0(980)$. For $f_0(980)$, the normalized couplings $\gamma_a = g_a/\sqrt{g^2_{\pi\pi} + g^2_{K\bar{K}}}$, where $a = \pi\pi, K\bar{K}$, are shown in Fig. 6*a*. Correspondent poles at different x are placed on the trajectory $f_0^{\rm bare}(720) \to f_0(980)$ (see Fig. 2). Looking at Fig. 6*a*, one can see that, at small x, $g^2_{\pi\pi} < g^2_{K\bar{K}}$, which is natural, for the state $f_0^{\rm bare}(720)$ is close to the flavor octet. With the increase in x, the coupling constants become equal to each other, and in the interval $0.6 \le x \le 0.8$, the coupling to the pion channel is greater than to kaon channel, $g^2_{\pi\pi}(x \sim 0.7) > g^2_{K\bar{K}}(x \sim 0.7)$, thus revealing a relative reduction of the $s\bar{s}$ component. However, at $x \sim 0.8$, when the amplitude pole approaches the $K\bar{K}$ threshold (see Fig. 2), the relative weight of the $K\bar{K}$ channel is strengthened to certain extent.

For every fixed x, formula (16) has been fitted to the values of $g^2_{\pi\pi}(x)$ and $g^2_{K\bar{K}}(x)$ in order to find φ as a function of G/g: a set of curves is shown in Fig. 6*b*. At $x = 0$, the curve $\varphi(G/g)$ corresponds to the maximal possible value of the mixing angle; with the increase in x, the absolute value of mixing angle $|\varphi|$ decreases smoothly, while, at $x > 0.8$, $|\varphi|$ increases sharply. The curve for $x = 1$ is also shown in Fig. 5; it coincides with good accuracy with that at $x = 0$.

In Fig. 6*b*, there are also two curves for φ with gradual accumulation of the gluonium component, which results in $W_{\rm gluonium} = 20\%$ at $x = 1$: recall, we suggest $W_{\rm gluonium} \le 20\%$. These are dashed curves that originate from the point $G/g = 0$ at $x = 0$ (in the K-matrix analysis [1], the bare state $f_0^{\rm bare}(720)$ is the pure $q\bar{q}$) but further they drift to $G/g > 0$ and $G/g < 0$ and end at $x = 1$ with $G/g = 0.45$ and $G/g = -0.45$, respectively. These final points stand for $W_{\rm gluonium} = 20\%$. Respectively, the variations of φ are shown separately by Fig. 6*c*; the area in between the curves is just the region of reasonable values of φ with the evolution of the decay widths. The lower curve tells us that the reduction of $g^2_{K\bar{K}}$ with the

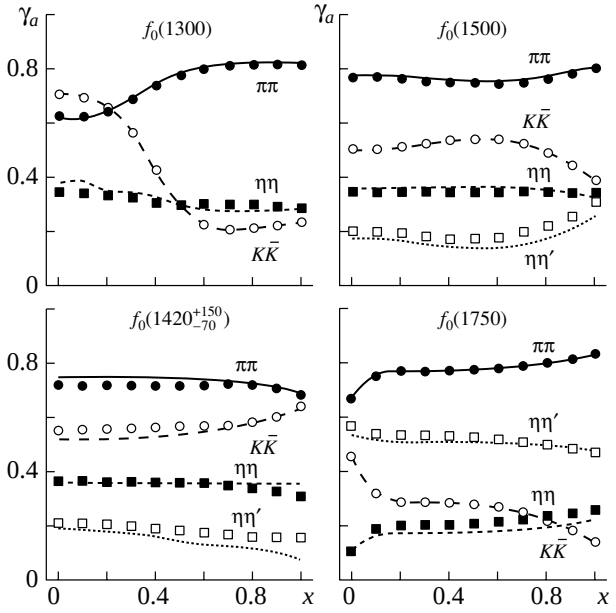

Fig. 8. Evolution of the normalized couplings $\gamma_a = g_a/\sqrt{\sum_b g_b^2}$ within onset of the decay channels for $f_0(1300)$, $f_0(1500)$, $f_0(1420^{+150}_{-70})$, and $f_0(1750)$. Points are taken from the fit in [1]. Curves illustrate the description of couplings by Eqs. (16).

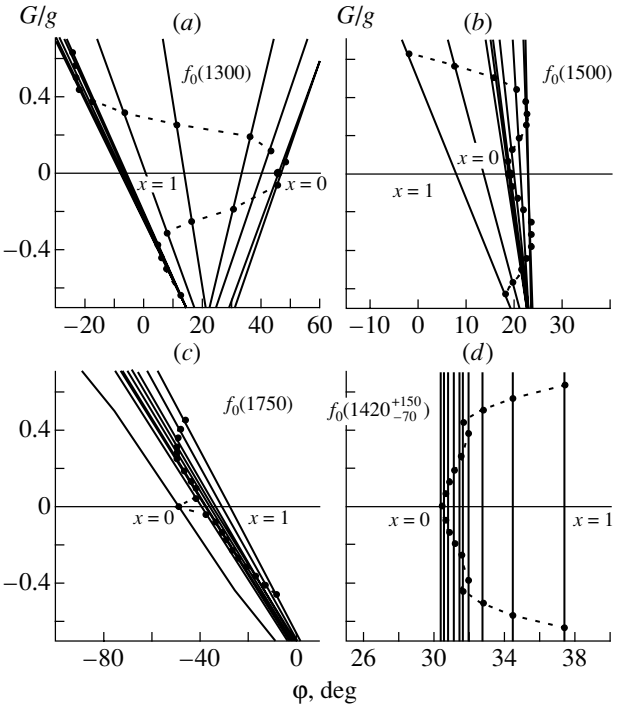

Fig. 9. Curves of correlations $(G/g, \varphi)$ for $f_0(1300)$, $f_0(1500)$, $f_0(1750)$, and $(g/G, \varphi)$ for $f_0(1420^{+150}_{-70})$ at eleven fixed values of x; dashed curves stand for maximal accumulation of the gluonium component, $W_{\text{gluonium}} = 40\%$.

increase in x to the region $x < 0.8$ is plausible due to the growth of the gluonium component leaving the ratio $n\bar{n}/s\bar{s}$ approximately constant. The upper curve related to $G/g < 0$ attests to the possible evolution when, in parallel with the increase in the gluonium component, the weight of the $s\bar{s}$ component becomes smaller. But at $x > 0.8$, both curves show a sharp increase in the $s\bar{s}$ component.

At $x = 1$, when mixing angle φ defines the quark content of $f_0(980)$ $(n\bar{n}\cos\varphi + s\bar{s}\sin\varphi)$, its value may

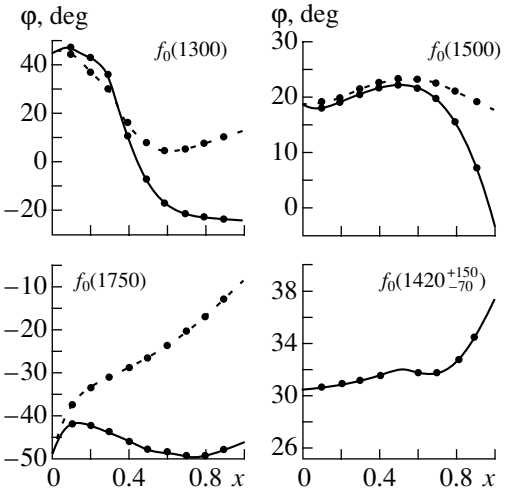

Fig. 10. The evolution of φ in the $q\bar{q}$ component $q\bar{q} = n\bar{n}\cos\varphi + s\bar{s}\sin\varphi$ at maximal accumulation of the gluonium component, $W_{\text{gluonium}} = 40\%$; solid curves stand for positive G/g and dashed curves for negative G/g. For $f_0(1420^{+150}_{-70})$, φ does not depend on the value of the adopted $q\bar{q}$ component.

vary in the intervals $-90^\circ \le \varphi \le -48^\circ$ and $85^\circ \le \varphi \le 90^\circ$ (Fig. 6*c*). It would be instructive to compare these values with mixing angles obtained for radiative decays $\phi(1020) \to \gamma f_0(980)$ and $f_0(980) \to \gamma\gamma$. The combined analysis [30] for these decays provided us with two possible solutions: $\varphi = -48^\circ \pm 6^\circ$ and $\varphi = 86^\circ \pm 3^\circ$.

The areas for $\varphi[f_0(980)]$ allowed by radiative and hadronic decays are shown in Fig. 7. One can see that the constraints for the mixing angle obtained from the study of hadronic decays of $f_0(980)$ are in nice agreement with the values obtained from the study of radiative decays [30]. However, we should stress that we cannot expect from hadronic processes more rigid limitations for the mixing angle of $f_0(980)$ than those known from radiative decays.

4.2.2. Resonances $f_0(1300)$, $f_0(1500)$, and $f_0(1750)$. For the resonances $f_0(1300)$, $f_0(1500)$, and $f_0(1750)$, the fractions of the $s\bar{s}$ component decrease, and they flow away from these resonances and enter the broad state $f_0(1420^{+150}_{-70})$. Figure 8 demonstrates normalized coupling constants squared $\gamma_a = g_a/\sqrt{\sum_b g_b^2}$ as a function of x. One can see that, for $f_0(1300)$ and $f_0(1500)$, the values $\gamma_{K\bar{K}}$ decrease, while $\gamma_{\pi\pi}$ grows. At the same time, the normalized coupling $\gamma_{K\bar{K}}$ grows for the broad state.

The description of ratios γ_a by Eq. (16) is shown in Fig. 8 for $f_0(1300)$, $f_0(1500)$, $f_0(1750)$, and $f_0(1420^{+150}_{-70})$: one can see that quark combinatorial rules reasonably describe a number of data on the decay coupling constants. But, as was stressed above, Eq. (16) does not define the content of a resonance, providing a correlation only between mixing angle φ and ratio G/g. These correlations are presented in Figs. 9*a*–9*c* for $f_0(1300)$, $f_0(1500)$, and $f_0(1750)$ at various x. Implying the predecessors of these resonances to be pure $q\bar{q}$ states, we display the correlations $(\varphi, G/g)$ at $G^2/g^2 \le 0.4$ that correspond to (21)–(23). Dashed curves in Figs. 9*a*–9*c* stand for $(\varphi, G/g)$ related to a maximal capture of the gluonium component by these resonances.

4.2.3. Broad state $f_0(1420^{+150}_{-70})$. The evolution from $f_0^{\text{bare}}(1600)$ to $f_0(1420^{+150}_{-70})$ is accompanied by the accumulation of the $q\bar{q}$ component and the growth of ratio g/G. In this way, Fig. 9*d* illustrates the correlation $(\varphi, g/G)$: for small x, when parameters of the corresponding state are close to those of $f_0^{\text{bare})}(1600)$, the ratio g/G is small. We see that, for the broad state, the mixing angle φ hardly depends on g/G at $g^2/G^2 \le 0.50$.

The value of the mixing angle at $x = 1$, $\varphi = 37^\circ$, proves that $f_0(1420^{+150}_{-70})$ can accumulate the flavor singlet component of $q\bar{q}$ only, which perfectly agrees with its gluonium origin.

Figure 10 demonstrates the change in φ with increasing x: this curve does not depend on the rate of accumulation of the $(q\bar{q})_{\text{singlet}}$ component.

5. CONCLUSION

We have performed an analysis of coupling constants for the resonances $f_0(980)$, $f_0(1300)$, $f_0(1500)$, and $f_0(1750)$ and the broad state $f_0(1420^{+150}_{-70})$ to channels $\pi\pi$, $K\bar{K}$, $\eta\eta$, and $\eta\eta'$, as well as observed the evolution of bare states into these resonances by switching on/off the decay channels [see (10) and Fig. 2]. Our analysis has been based on Solution II-2 of [1]; in this solution, the bare state $f_0^{\text{bare}}(1600 \pm 50)$ is the candidate for the glueball.

During the evolution of states, the coupling constants $f_0 \to$ hadrons change considerably not only in magnitude but also in relative weight, which is due to a strong mixing of states, because of the decay processes $f_0(m_1) \to$ real mesons $\to f_0(m_2)$. Using the language of bare states, f_0^{bare}, a rigid classification can be established for $q\bar{q}$ states; however, for real resonances, the presence of the gluonium component results in certain uncertainties.

For the resonances discussed, the results are as follows.

(i) $f_0(980)$: This resonance is dominantly the $q\bar{q}$ state; the admixture of the glueball component

is not more than 20%, $W_{\text{gluonium}} \leq 0.20$. A rather large $s\bar{s}$ component is also present. Taking account of the representation $q\bar{q} = n\bar{n}\cos\varphi + s\bar{s}\sin\varphi$, the hadronic decays give us the following constraints: $-90^\circ \leq \varphi \leq -40^\circ$ or $85^\circ \leq \varphi \leq 90^\circ$, which are in agreement with data on radiative decays $f_0(980) \to \gamma\gamma$ and $\phi(1020) \to \gamma f_0(980)$ [30] (see Fig. 7). Rather large uncertainties in the determination of the mixing angle are due to the sensitivity of coupling constants to plausible small admixtures of the gluonium component. When the gluonium component is absent, hadronic decays provide $\varphi = \langle\varphi\rangle = -67^\circ$.

(ii) $f_0(1300)$ and $f_0(1500)$: These resonances are the descendants of bare $q\bar{q}$ states $f_0^{\text{bare}}(1230^{+150}_{-30})$ and $f_0^{\text{bare}}(1260 \pm 30)$, which (both of them) are flavor singlets. The resonances $f_0(1300)$ and $f_0(1500)$ are formed due to a strong mixing with gluonium state $f_0^{\text{bare}}(1600)$ as well as with one another. The $q\bar{q}$ content, $q\bar{q} = n\bar{n}\cos\varphi + s\bar{s}\sin\varphi$, in both resonances strongly depends on the admixture of the gluonium component. At $W_{\text{gluonium}} \leq 0.40$, the mixing angles change, depending on W_{gluonium}, in the intervals $-25^\circ \leq \varphi[f_0(1300)] \leq 13^\circ$ and $-3^\circ \leq \varphi[f_0(1500)] \leq 17^\circ$.

(iii) $f_0(1750)$: This resonance is the descendant of bare state $2^3P_1 q\bar{q}$, $f_0^{\text{bare}}(1810 \pm 30)$, and this bare state has a flavor wave function close to the octet one. During evolution and mixing (presumably with the gluonium), the quark component, $q\bar{q} = n\bar{n}\cos\varphi + s\bar{s}\sin\varphi$, can change significantly: with $W_{\text{gluonium}} \leq 0.2$, we have $-45^\circ \leq \varphi[f_0(1750)] \leq -10^\circ$. Therefore, $f_0(1750)$ keeps its large $s\bar{s}$ component, and rather small coupling constant $f_0(1750) \to K\bar{K}$ should not mislead us, for the production of $K\bar{K}$ is suppressed at $\varphi \sim -30^\circ$ [see Table 1 and Eq. (16)].

(iv) $f_0(1420^{+150}_{-70})$: This broad state is the descendant of the $f_0^{\text{bare}}(1600 \pm 50)$, which we believe to be the glueball. The analysis of hadronic decays of this resonance confirms the glueball nature of this resonance: the $q\bar{q}$ component is allowed to be in the flavor singlet only, $\varphi[f_0(1420^{+150}_{-70})] \simeq 37^\circ$, although the value of the possible admixture of $(q\bar{q})_{\text{singlet}}$ cannot be fixed by hadronic decays. In this way, $f_0(1420^{+150}_{-70})$ is a mixture gluonium $+(q\bar{q})_{\text{singlet}}$; the impossibility of finding the quark–antiquark component is due to the fact that correlations between the decay coupling constants are the same for the gluonium and $q\bar{q}$ singlet.

ACKNOWLEDGMENTS

We are indebted to A.V. Anisovich, D.V. Bugg, and L.G. Dakhno for useful remarks concerning related problems.

The work is supported by the Russian Foundation for Basic Research (project no. 01-02-17861).

REFERENCES

1. V. V. Anisovich, A. A. Kondashov, Yu. D. Prokoshkin, *et al.*, Yad. Fiz. **63**, 1489 (2000) [Phys. At. Nucl. **63**, 1410 (2000)].
2. V. V. Anisovich, V. A. Nikonov, and A. V. Sarantsev, hep-ph/0102338; Yad. Fiz. **65**, 1583 (2002) [Phys. At. Nucl. **65**, 1545 (2002)].
3. D. Alde *et al.*, Z. Phys. C **66**, 375 (1995); Yu. D. Prokoshkin *et al.*, Dokl. Akad. Nauk **342**, 473 (1995) [Phys. Dokl. **40**, 266 (1995)]; A. A. Kondashov *et al.*, Preprint No. 95-137, IHEP (Protvino, 1995); F. Binon *et al.*, Nuovo Cimento A **78**, 313 (1983); **80**, 363 (1984).
4. V. V. Anisovich *et al.*, Phys. Lett. B **323**, 233 (1994); C. Amsler *et al.*, Phys. Lett. B **342**, 433 (1995); **355**, 425 (1995).
5. S. J. Lindenbaum and R. S. Longacre, Phys. Lett. B **274**, 492 (1992); A. Etkin *et al.*, Phys. Rev. D **25**, 1786 (1982).
6. Particle Data Group (D. E. Groom *et al.*), Eur. Phys. J. C **15**, 1 (2000).
7. G. Grayer *et al.*, Nucl. Phys. B **75**, 189 (1974); W. Ochs, PhD Dissertation (Münich University, 1974).
8. V. V. Anisovich and A. V. Sarantsev, Phys. Lett. B **382**, 429 (1996).
9. V. V. Anisovich, Yu. D. Prokoshkin, and A. V. Sarantsev, Phys. Lett. B **389**, 388 (1996).
10. A. V. Anisovich and A. V. Sarantsev, Phys. Lett. B **413**, 137 (1997).
11. V. V. Anisovich, Usp. Fiz. Nauk **168**, 481 (1998) [Phys. Usp. **41**, 419 (1998)].
12. C. Amsler and F. E. Close, Phys. Rev. D **53**, 295 (1996); Phys. Lett. B **353**, 385 (1995); V. V. Anisovich, Phys. Lett. B **364**, 195 (1995); Phys. Usp. **38**, 1179 (1995).
13. V. V. Anisovich and V. A. Nikonov, Eur. Phys. J. A **8**, 401 (2000).
14. E791 Collab. (E. M. Aitala *et al.*), hep-ex/0007028.
15. A. V. Anisovich, C. A. Baker, C. J. Batty, *et al.*, Phys. Lett. B **468**, 309 (1999); Nucl. Phys. A **651**, 253 (1999); D. Barberis, F. G. Binon, F. E. Close, *et al.*, Phys. Lett. B **467**, 296 (1999).
16. A. V. Anisovich, V. V. Anisovich, and A. V. Sarantsev, Phys. Rev. D **62**, 051502 (2000).
17. G.'t Hooft, Nucl. Phys. B **72**, 161 (1974); G. Veneziano, Nucl. Phys. B **117**, 519 (1976).
18. D. Aston *et al.*, Nucl. Phys. B **296**, 493 (1988).
19. G. S. Bali *et al.*, Phys. Lett. B **309**, 378 (1993); J. Sexton, A. Vaccarino, and D. Weingarten, Phys. Rev. Lett. **75**, 4563 (1995); C. J. Morningstar and M. Peardon, Phys. Rev. D **56**, 4043 (1997).
20. A. V. Anisovich, V. V. Anisovich, Yu. D. Prokoshkin, and A. V. Sarantsev, Z. Phys. A **357**, 123 (1997).
21. A. V. Anisovich, V. V. Anisovich, and A. V. Sarantsev, Phys. Lett. B **395**, 123 (1997); Z. Phys. A **359**, 173 (1997).

22. I. S. Shapiro, Nucl. Phys. A **122**, 645 (1968).
23. I. Yu. Kobzarev, N. N. Nikolaev, and L. B. Okun', Sov. J. Nucl. Phys. **10**, 499 (1970).
24. L. Stodolsky, Phys. Rev. D **1**, 2683 (1970).
25. V. V. Anisovich, D. V. Bugg, and A. V. Sarantsev, Phys. Rev. D **58**, 111503 (1998).
26. V. V. Anisovich, D. V. Bugg, and A. V. Sarantsev, Yad. Fiz. **62**, 1322 (1999) [Phys. At. Nucl. **62**, 1247 (1999)].
27. V. V. Anisovich, D. V. Bugg, and A. V. Sarantsev, Phys. Lett. B **437**, 209 (1998).
28. K. Peters and E. Klempt, Phys. Lett. B **352**, 467 (1995).
29. G. Parisi and R. Petronzio, Phys. Lett. B **94B**, 51 (1980); J. M. Cornwell and J. Papavassiliou, Phys. Rev. D **40**, 3474 (1989); V. V. Anisovich, S. M. Gerasyuta, and A. V. Sarantsev, Int. J. Mod. Phys. A **6**, 625 (1991); D. B. Leinweber *et al.*, Phys. Rev. D **58**, 031501 (1998).
30. A. V. Anisovich, V. V. Anisovich, and V. A. Nikonov, Eur. Phys. J. A **12**, 103 (2001).
31. V. V. Anisovich, A. A. Kondashov, Yu. D. Prokoshkin, *et al.*, Phys. Lett. B **355**, 363 (1995).

Physics of Atomic Nuclei, Vol. 66, No. 4, 2003, pp. 755–763. Translated from Yadernaya Fizika, Vol. 66, No. 4, 2003, pp. 786–795.

ELEMENTARY PARTICLES AND FIELDS
Theory

Heavy-Quark Production in $p\bar{p}$ Collisions and Unintegrated Gluon Distributions

N. P. Zotov*, A. V. Lipatov[1)], and V. A. Saleev[2)]

Institute of Nuclear Physics, Moscow State University, Vorob'evy gory, Moscow, 119992 Russia

Received October 30, 2001; in final form, July 5, 2002

Abstract—The inclusive production of heavy (c and b) quarks in high-energy $p\bar{p}$ collisions are considered within the semihard approach in QCD. The dependence of the cross section for heavy-quark production, $\sigma(\mathbf{p}_T > \mathbf{p}_T^{\min})$, on unintegrated gluon distributions is studied. The results of this consideration are compared with experimental data obtained by the D0 and CDF Collaborations at Tevatron.

1. INTRODUCTION

Processes leading to the production of heavy quarks (c and b) and quarkonia on protons are one of the most promising sources of information about the gluon structure function for the proton within QCD [1–4], because, at high energies, heavy quarks are predominantly produced through the subprocess of gluon–gluon fusion. Particular interest in gluon distributions is motivated by the fact that they play a key role in determining cross sections for many processes that will be investigated at next-generation colliders like LHC.

In the energy region of present-day colliders, heavy-quark production on protons proceeds through so-called semihard processes [5], which are defined as those where the characteristic scale μ of the hard subprocess of parton scattering is much less than the total c.m. energy $\sqrt{s}$ of colliding hadrons, but where it is much greater than the parameter $\Lambda_{\rm QCD}$; that is, $\Lambda_{\rm QCD} \ll \mu \ll \sqrt{s}$. As a result, the running QCD coupling constant remains small: $\alpha_{\rm QCD}(\mu^2) \ll 1$. The condition $\mu \ll \sqrt{s}$ means that cross sections for such processes are determined by the behavior of gluon structure functions for the proton in the region of $x \simeq m_Q/\sqrt{s} \ll 1$, where m_Q is the heavy-quark mass. Because of a high density of gluon distributions at such values of x, the parton-model assumption that the subprocess cross sections and hadron structure functions factorize is violated. Therefore, it is necessary to take into account the dependence of the hard-process amplitude on the gluon virtuality, transverse momentum, and longitudinal polarization. It is worth noting that the last factor makes a dominant contribution to the cross section [6–8].

The gluon distribution in the proton $xG(x,\mu^2)$ can be obtained from the Dokshitzer–Gribov–Lipatov–Altarelli–Parisi (DGLAP) evolution equation [9] in the leading-logarithm or in the doubly logarithmic approximation [that is, with allowance for $\alpha_s^n \ln^n(\mu^2/\Lambda^2_{\rm QCD})$ or $\alpha_s^n \ln^n(1/x)\ln^n(\mu^2/\Lambda^2_{\rm QCD})$ contributions, respectively]. With increasing c.m. energy of colliding particles, $\sqrt{s}$, however, terms of order $\alpha_s^n \ln^n(s/\Lambda^2_{\rm QCD}) \sim \alpha_s^n \ln^n(1/x)$, which are disregarded in the DGLAP equations, become significant. Summation of diagrams leading to terms of orders $\alpha_s^n \ln^n(\mu^2/\Lambda^2_{\rm QCD})$, $\alpha_s^n \ln^n(1/x)\ln^n(\mu^2/\Lambda^2_{\rm QCD})$, and $\alpha_s^n \ln^n(1/x)$ yields nonintegrated gluon distributions $\Phi(x,\mathbf{q}_T^2,\mu^2)$ (that is, those that depend on the transverse momentum $\mathbf{q}_T$), which satisfy the Balitsky–Fadin–Kuraev–Lipatov (BFKL) evolution equations [10] and which are related to the usual (collinear) gluon distribution $xG(x,\mu^2)$ by the equation

$$xG(x,\mu^2) = xG(x,Q_0^2) + \int\limits_{Q_0^2}^{\mu^2} \Phi(x,\mathbf{q}_T^2,\mu^2)d\mathbf{q}_T^2. \quad (1)$$

Cross sections for physical processes are determined by the convolution of unintegrated gluon distributions with the off-shell matrix element of the hard subprocess [6–8]. In addition, the polarization tensor $L^{\mu\nu}$ for virtual gluons in the matrix element for the subprocess of gluon–gluon fusion is taken, according to the prescriptions of the semihard approach [5], in

[1)]Moscow State University, Vorob'evy gory, Moscow, 119992 Russia; e-mail: artem_lipatov@mail.ru
[2)]Samara State University, ul. Akademika Pavlova 1, Samara, 443011 Russia; e-mail: saleev@ssu.samara.ru
*e-mail: zotov@theory.sinp.msu.ru

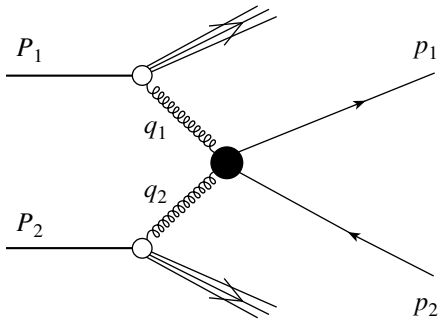

Fig. 1. Heavy quark production process $p\bar{p} \to Q\bar{Q}X$.

the form

$$L^{\mu\nu}(q) = \frac{q_T^\mu q_T^\nu}{\mathbf{q}_T^2}. \qquad (2)$$

The semihard approach was previously used to describe a number of processes [6, 11–22]—in particular, processes leading to the production and photoproduction of heavy quarks [6, 11, 14, 16, 19–21] and quarkonia [13, 15, 18, 22]. Calculations within the semihard approach result in some observable effects that could not be obtained on the basis of the standard parton model. These include a faster growth of cross sections than in the ordinary parton model [13, 15] and the broadening of p_T spectra in relation to the results produced by the parton model, the latter effect becoming more significant at higher energies [6, 11, 13–20].

Here, we employ the semihard approach in QCD to study heavy-quark production in $p\bar{p}$ interactions. Similar calculations were performed in [6, 11, 20, 21], where the authors used various nonintegrated gluon distribution functions and matrix elements for the corresponding hard scattering subprocesses (it is difficult to compare them with one another). The matrix elements used in [6] are similar to those in [7], but the expressions given in [6] contain insignificant misprints. Baranov and Smizanska [20] did not calculate matrix elements explicitly; therefore, it is hardly possible to perform a comparison with the matrix elements from [7]. Hägler *et al.* [21] did not present explicit expressions for the matrix elements either.

We are going to obtain the matrix elements for the hard process of gluon–gluon fusion independently of the previous studies and compare our results with those that are based on the use of the matrix elements from [7]. In addition, we apply here the semihard approach in QCD to study the sensitivity of the cross sections for heavy-quark production to variations in the sets of unintegrated gluon distributions and parameters of the semihard approach in order to find a "universal" gluon distribution. We pay special attention to unintegrated gluon distributions obtained by solving the BFKL evolution equations, which were used in [12, 15, 16, 19].

The preliminary results of this study were reported at the International Workshop DIS 2001 [23].

2. CROSS SECTION OF HEAVY QUARK PRODUCTION IN $p\bar{p}$ INTERACTIONS

In this section, we calculate, on the basis of the semihard approach in QCD, the total and differential cross sections for the production of heavy quarks in the process $p\bar{p} \to Q\bar{Q}X$ proceeding through the subprocess of gluon–gluon fusion (Fig. 1). In our calculations, we use expression (2) for the effective polarization tensor $L^{\mu\nu}$ of virtual gluons.

The Sudakov decomposition for the process $p\bar{p} \to Q\bar{Q}X$ (Fig. 1) assumes the form

$$p_1 = \alpha_1 P_1 + \beta_1 P_2 + p_{1T}, \qquad (3)$$
$$p_2 = \alpha_2 P_1 + \beta_2 P_2 + p_{2T},$$
$$q_1 = x_1 P_1 + q_{1T}, \qquad q_2 = x_2 P_2 + q_{2T},$$

where

$$p_1^2 = p_2^2 = m^2, \quad q_1^2 = q_{1T}^2, \quad q_2^2 = q_{2T}^2. \qquad (4)$$

Here, p_1 and p_2 stand for the 4-momenta of the heavy quarks; q_1 and q_2 are the 4-momenta of the initial virtual gluons; and p_{1T}, p_{2T}, q_{1T}, and q_{2T} are the transverse 4-momenta of the corresponding particles. In the c.m. frame of colliding particles, we have

$$P_1 = (E, 0, 0, E), \qquad P_2 = (E, 0, 0, -E), \qquad (5)$$

where

$$E = \frac{\sqrt{s}}{2}, \quad P_1^2 = P_2^2 = 0, \quad (P_1 \cdot P_2) = \frac{s}{2}. \qquad (6)$$

The Sudakov variables are given by

$$\alpha_1 = \frac{m_{1T}}{\sqrt{s}} \exp(y_1^*), \qquad \alpha_2 = \frac{m_{2T}}{\sqrt{s}} \exp(y_2^*), \qquad (7)$$
$$\beta_1 = \frac{m_{1T}}{\sqrt{s}} \exp(-y_1^*), \qquad \beta_2 = \frac{m_{2T}}{\sqrt{s}} \exp(-y_2^*),$$

where $m_{1,2T}^2 = m^2 + \mathbf{p}_{1,2T}^2$, m and $y_{1,2}^*$ standing for the heavy-quark mass and the rapidities, respectively, in the c.m. frame. The differential cross section for the process $p\bar{p} \to Q\bar{Q}X$ can be represented in the form

$$d\sigma(p\bar{p} \to Q\bar{Q}X) = \frac{dx_1}{x_1}\Phi(x_1, \mathbf{q}_{1T}^2, \mu^2)\frac{d\phi_1}{2\pi}d\mathbf{q}_{1T}^2 \qquad (8)$$
$$\times \frac{dx_2}{x_2}\Phi(x_2, \mathbf{q}_{2T}^2, \mu^2)\frac{d\phi_2}{2\pi}d\mathbf{q}_{2T}^2 d\hat{\sigma}(g^*g^* \to Q\bar{Q}),$$

where $\Phi(x_1, \mathbf{q}_{1T}^2, \mu^2)$ and $\Phi(x_2, \mathbf{q}_{2T}^2, \mu^2)$ are unintegrated gluon distributions, ϕ_1 and ϕ_2 are the azimuthal angles of the initial virtual gluons, and $d\hat{\sigma}(g^*g^* \to Q\bar{Q})$ is the differential cross section for

the hard subprocess of gluon–gluon fusion. We represent it in the form

$$d\hat{\sigma}(g^*g^* \to Q\bar{Q}) = \frac{(2\pi)^4}{2\hat{s}} \sum |M|^2_{\rm SHA}(g^*g^* \to Q\bar{Q}) \tag{9}$$
$$\times \frac{d^3p_1}{(2\pi)^3 \cdot 2p_1^0} \frac{d^3p_2}{(2\pi)^3 \cdot 2p_2^0} \delta^{(4)}(q_1 + q_2 - p_1 - p_2),$$

where $\sum |M|^2_{\rm SHA}(g^*g^* \to Q\bar{Q})$ is the matrix element calculated for the subprocess of gluon–gluon fusion, $g^*g^* \to Q\bar{Q}$, within the semihard approach in QCD. The summation sign in (9) implies averaging over the polarizations of initial-state and summation over the polarizations of final-state particles. The phase-space element can be written in the form

$$\frac{d^3p_1}{(2\pi)^3 \cdot 2p_1^0} \frac{d^3p_2}{(2\pi)^3 \cdot 2p_2^0} = \frac{d^2p_{1T}}{2(2\pi)^3} dy_1^* \frac{d^2p_{2T}}{2(2\pi)^3} dy_2^*. \tag{10}$$

We represent the four-dimensional delta function $\delta^{(4)}(q_1 + q_2 - p_1 - p_2)$ in the form

$$\delta^{(4)}(q_1 + q_2 - p_1 - p_2) = \delta(q_1^0 + q_2^0 - p_1^0 - p_2^0) \tag{11}$$
$$\times \delta(\mathbf{q}_{1T} + \mathbf{q}_{2T} - \mathbf{p}_{1T} - \mathbf{p}_{2T}) \delta(q_1^3 + q_2^3 - p_1^3 - p_2^3)$$

and, in this way, remove integration with respect to $\mathbf{p}^2_{2T}$, x_1, and x_2 in (8) and (9). With the aid of (10), we then find that the final expression for the differential cross section for the process $p\bar{p} \to Q\bar{Q}X$ within the semihard approach in QCD is

$$d\sigma(p\bar{p} \to Q\bar{Q}X) = \frac{1}{16\pi(x_1x_2s)^2} \tag{12}$$
$$\times \Phi(x_1, \mathbf{q}^2_{1T}, \mu^2) \Phi(x_2, \mathbf{q}^2_{2T}, \mu^2)$$
$$\times \sum |M|^2_{\rm SHA}(g^*g^* \to Q\bar{Q}) dy_1^* dy_2^* d\mathbf{p}^2_{1T} d\mathbf{q}^2_{1T} d\mathbf{q}^2_{2T}$$
$$\times \frac{d\phi_1}{2\pi} \frac{d\phi_2}{2\pi} \frac{d\phi_Q}{2\pi},$$

where

$$x_1 = \alpha_1 + \alpha_2, \qquad x_2 = \beta_1 + \beta_2, \tag{13}$$
$$\mathbf{q}_{1T} + \mathbf{q}_{2T} = \mathbf{p}_{1T} + \mathbf{p}_{2T},$$

and ϕ_Q is the azimuthal angle of the final heavy quark. For $\mathbf{q}^2_{1T} \to 0$ and $\mathbf{q}^2_{2T} \to 0$, averaging of (12) over the transverse directions specified by the vectors $\mathbf{q}_{1T}$ and $\mathbf{q}_{2T}$ yields the expression for the differential cross section for the process $p\bar{p} \to Q\bar{Q}X$ in the ordinary parton model; that is,

$$d\sigma(p\bar{p} \to Q\bar{Q}X) \tag{14}$$
$$= \frac{1}{16\pi(x_1x_2s)^2} x_1G(x_1, \mu^2) x_2G(x_2, \mu^2)$$
$$\times \sum |M|^2_{\rm PM}(gg \to Q\bar{Q}) dy_1^* dy_2^* d\mathbf{p}^2_{1T} \frac{d\phi_3}{2\pi},$$

where $\sum |M|^2_{\rm PM}(gg \to Q\bar{Q})$ is the matrix element calculated for the gluon–gluon fusion $gg \to Q\bar{Q}$ in the ordinary parton model. As above, the summation sign implies averaging over initial-quark polarizations and summation over final-quark polarizations. In order to perform integration with respect to $\mathbf{q}^2_{1T}$ and $\mathbf{q}^2_{2T}$ and averaging over azimuthal angles, we have used the relation

$$\int d\mathbf{q}^2_{1T} \int \frac{d\phi_1}{2\pi} \Phi(x_1, \mathbf{q}^2_{1T}, \mu^2) \int d\mathbf{q}^2_{2T} \tag{15}$$
$$\times \int \frac{d\phi_2}{2\pi} \Phi(x_2, \mathbf{q}^2_{2T}, \mu^2) \sum |M|^2_{\rm SHA}$$
$$= x_1G(x_1, \mu^2) x_2G(x_2, \mu^2) \sum |M|^2_{\rm PM},$$

where

$$\int_0^{2\pi} \frac{d\phi_{1,2}}{2\pi} \frac{q^\mu_{1,2T} q^\nu_{1,2T}}{\mathbf{q}^2_{1,2T}} = \frac{1}{2} g^{\mu\nu}. \tag{16}$$

3. UNINTEGRATED GLUON DISTRIBUTIONS

In our calculations, we use various parametrizations of unintegrated gluon distributions. In this section, we consider some special features of these parametrizations.

For the gluon distribution in the proton, the authors of [13–17] took the phenomenological ansatz proposed by Levin, Ryskin, Shuvaev, and Shabelski in [6] in the form

$$\Phi(x, \mathbf{q}^2_T) = \Phi_0 \frac{0.05}{0.05 + x} (1 - x)^3 f(x, \mathbf{q}^2_T), \tag{17}$$

where

$$f(x, \mathbf{q}^2_T) = \begin{cases} 1 \text{ for } \mathbf{q}^2_T \le q_0^2(x), \\ \left(\dfrac{q_0^2(x)}{\mathbf{q}^2_T} \right)^2 \text{ for } \mathbf{q}^2_T > q_0^2(x) \end{cases} \tag{18}$$

with $q_0^2(x) = Q_0^2 + \Lambda^2 \exp 3.56\sqrt{\ln(x_0/x)}$, the parameter values being $Q_0^2 = 2\ \text{GeV}^2$, $\Lambda = 56\ \text{MeV}$, and $x_0 = 1/3$. The normalization-factor value of $\Phi_0 = 0.97$ mb was obtained from a fit to data on b-quark production in $p\bar{p}$ interactions at the $Sp\bar{p}S$ collider energy of $\sqrt{s} = 0.63$ TeV [24]. It was indicated in [8] that this choice of Φ_0 value corresponds to a possible upper limit on the cross section for b-quark production in hadron collisions.[3)] The value of the

[3)] We note that the experimental data reported in [24] are obtained at an energy that is comparatively low for the semihard approach in QCD to be applicable.

parameter $q_0^2(x)$ can be considered as that typical scale of gluon transverse momenta in the parton cascade in a hadron which provides a natural infrared cutoff in semihard processes. The parameter $q_0^2(x)$ grows with increasing $\ln(1/x)$ and takes values in the range 2–4 GeV^2 for $x = 0.01$–0.001.

For not very small x ($0.01 < x < 0.15$), the effective gluon distribution $xG(x,\mu^2)$ obtained from (17) through integration according to expression (1) grows in proportion to $x^{-\Delta}$, where $\Delta \simeq 0.5$ corresponds to summation of the leading logarithms $\alpha_s^n \ln^n(1/x)$ in Feynman diagrams [6]. This growth persists up to the value $x = x_c$, where x_c is a solution to the equation $q_0^2(x_c) = Q^2$. In the region $x < x_c$, the parametrization specified by Eqs. (17) and (18) reproduces the gluon-density-saturation effect at $xG(x,\mu^2) \simeq \Phi_0\mu^2$. Hereafter, this parametrization will be referred to as the LRSS parametrization of unintegrated gluon distributions.

A different parametrization of unintegrated gluon distributions was proposed by Ryskin and Shabelski [12]. This parametrization, which we refer to as the RS one, corresponds to the result obtained by numerically solving the BFKL evolution equations with the Morfin–Tung structure functions [25] as initial conditions and with allowance for the shadowing corrections (saturation effects) in the low-x region. The expression for $\Phi(x,\mathbf{q}_T^2)$ has the form

$$\Phi(x,\mathbf{q}_T^2) = \frac{1}{4\sqrt{2}\pi^3}\frac{a_1}{a_2+a_3+a_4} \tag{19}$$
$$\times\left(a_2 + a_3\frac{Q_0^2}{\mathbf{q}_T^2} + a_4\left(\frac{Q_0^2}{\mathbf{q}_T^2}\right)^2 + \alpha x + \frac{\beta}{\varepsilon+\ln(1/x)}\right)$$
$$\times f(x,\mathbf{q}_T^2)\left(\frac{a_5}{a_5+x}\right)^{1/2}\left(1 - a_6 x^{a_7}\ln\left(\frac{\mathbf{q}_T^2}{a_8}\right)\right)$$
$$\times (1+a_{11}x)(1-x)^{a_9+a_{10}\ln(\mathbf{q}_T^2/a_8)},$$

where the function $f(x,\mathbf{q}_T^2)$ is determined by relation (18). All parameters (a_1–a_{11}, α, β, ε) were found in [12] by minimizing the difference of the right- and the left-hand side of the BFKL equation.

The so-called BFKL parametrization obtained by solving the BFKL equations according to the method proposed in [26] is the third parametrization used here for unintegrated gluon distributions. The method is based on directly solving the BFKL equations in the leading approximation with the collinear gluon density $xG(x,\mu^2)$ from the Glück–Reya–Vogt set [27] used as the initial condition. Technically, the unintegrated gluon distributions are calculated, in this case, as the convolution of the collinear gluon distribution $xG(x,\mu^2)$ with the universal weight factor [26]; that is,

$$\Phi(x,\mathbf{q}_T^2,\mu^2) = \int_x^1 \varphi(\eta,\mathbf{q}_T^2,\mu^2)\frac{x}{\eta}G\left(\frac{x}{\eta},\mu^2\right)d\eta, \tag{20}$$

where

$$\varphi(\eta,\mathbf{q}_T^2,Q^2) = \begin{cases} \dfrac{\bar\alpha_s}{\eta\mathbf{q}_T^2}J_0\left(2\sqrt{\bar\alpha_s\ln(1/\eta)\ln(\mu^2/\mathbf{q}_T^2)}\right) & \text{if } \mathbf{q}_T^2 \le \mu^2, \\ \dfrac{\bar\alpha_s}{\eta\mathbf{q}_T^2}I_0\left(2\sqrt{\bar\alpha_s\ln(1/\eta)\ln(\mathbf{q}_T^2/\mu^2)}\right) & \text{if } \mathbf{q}_T^2 > \mu^2, \end{cases} \tag{21}$$

with J_0 and I_0 being Bessel functions of a real and an imaginary argument, respectively. The parameter $\bar\alpha_s = 3\alpha_s/\pi$ appearing in expressions (20) and (21) is related to the Pomeron intercept Δ: specifically, we have $\Delta = 4\bar\alpha_s\ln 2 \simeq 0.53$ in the leading order of perturbation theory and $\Delta = 4\bar\alpha_s\ln 2 - N\bar\alpha_s^2$, where $N \sim 18$, in the next-to-leading order [28, 29]. However, various summation procedures proposed recently [29, 30] yield a positive value ($\Delta \sim 0.2$–0.3).

The presence of two different parameters μ^2 and $\mathbf{q}_T^2$ in expression (20) for the nonintegrated gluon distribution $\Phi(x,\mathbf{q}_T^2,\mu^2)$ is due to the following way of evolution. First, use is made of the evolution of the gluon structure function from Q_0^2 to μ^2 in the collinear approximation according to the DGLAP equations [9]; then, Eqs. (20) and (21) are employed as the result of evolution in $\mathbf{q}_T^2$, according to the BFKL equations.

The last of the parametrizations used here for the unintegrated gluon distributions is that which is obtained by differentiating the collinear gluon density $xG(x,\mu^2)$ [5, 6, 10, 31] from the standard Glück–Reya–Vogt set:

$$\Phi(x,\mathbf{q}_T^2) = \left.\frac{dxG(x,\mu^2)}{d\ln\mu^2}\right|_{\mu^2=\mathbf{q}_T^2}. \tag{22}$$

The effective gluon distribution $xG(x,\mu^2)$ is related to the nonintegrated distributions $\Phi(x,\mathbf{q}_T^2,\mu^2)$ by Eq. (1), where the contribution from the region of low $\mathbf{q}_T^2$ ($0 < \mathbf{q}_T^2 < Q_0^2$) is taken into account with the

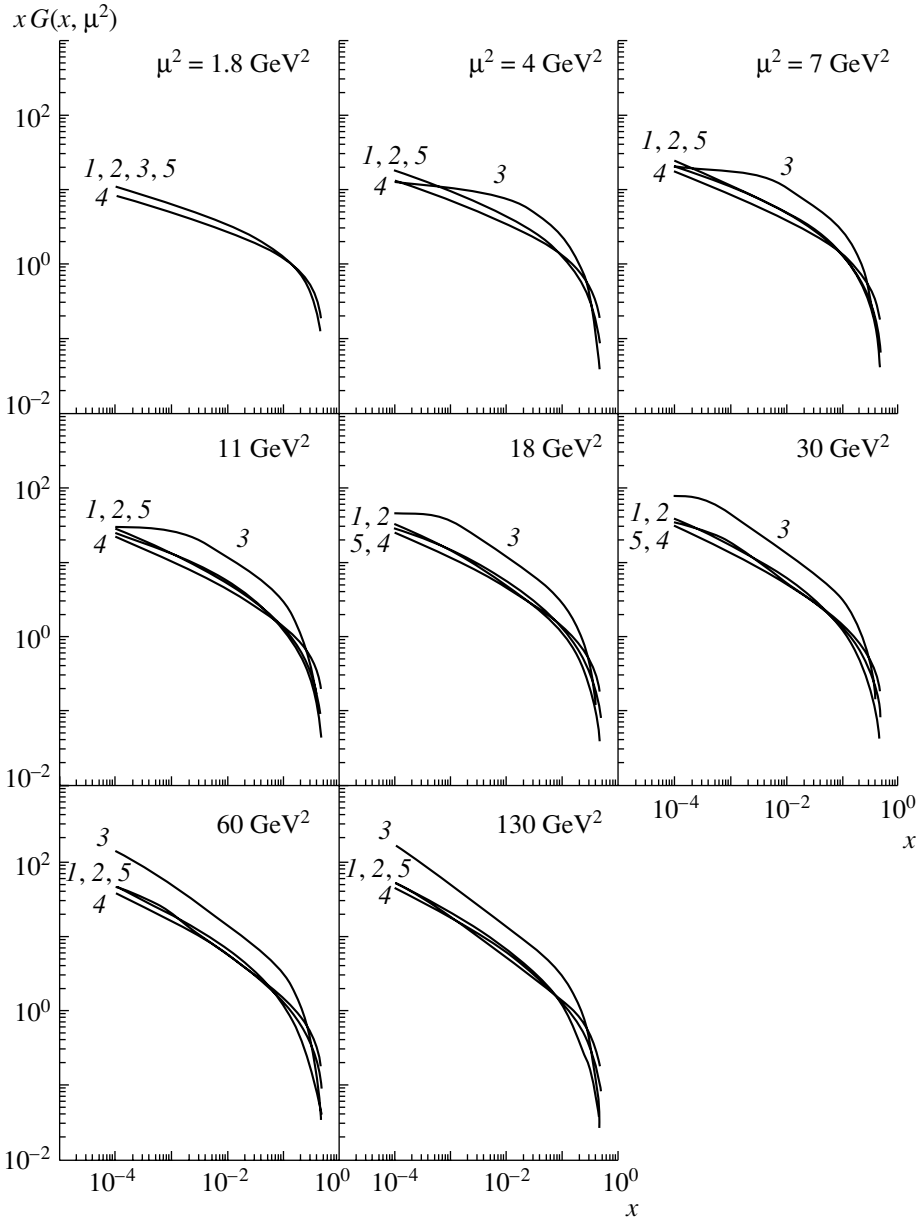

Fig. 2. Effective distributions $xG(x, \mu^2)$ versus the variable x for various values of μ^2. Curve *1* corresponds to the GRV parametrization of the collinear gluon density. Curves *2, 3, 4,* and *5* were calculated with the effective gluon distributions obtained from the nonintegrated structure functions $\Phi(x, \mathbf{q}_T^2, \mu^2)$ according to expression (1) by using the RS parametrization (at $Q_0^2 = 4\,\mathrm{GeV}^2$), the LRSS parametrization (at $Q_0^2 = 2\,\mathrm{GeV}^2$), the BFKL parametrization (at $Q_0^2 = 1\,\mathrm{GeV}^2$), and the parametrization in the form (22) (at $Q_0^2 = 1\,\mathrm{GeV}^2$), respectively.

aid of the collinear gluon density $xG(x, Q_0^2)$, where $Q_0^2 = 1{-}4\,\mathrm{GeV}^2$ for the different parametrizations.

Figure 2 displays the effective distributions $xG(x, \mu^2)$ versus the variable x for various values of μ^2. Curve *1* corresponds to the known parametrization of the collinear gluon distributions that was proposed by Glück, Reya, and Vogt (GRV parametrization). Curves *2, 3, 4,* and *5* were calculated for the effective gluon distributions obtained from the nonintegrated structure functions $\Phi(x, \mathbf{q}_T^2, \mu^2)$ according to expression (1) with the RS, LRSS, BFKL, and (22) parametrizations, respectively, for various values of the parameter Q_0^2.

The effective gluon distributions $xG(x, \mu^2)$ obtained with the LRSS parametrization of unintegrated gluon distributions are significantly different from other distributions "normalized" to GRV. The reason is that they are normalized to experimental

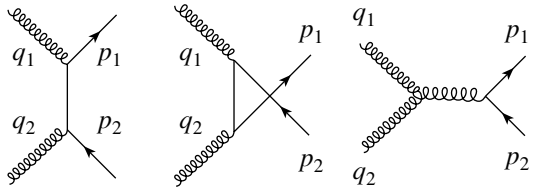

Fig. 3. Diagrams describing the subprocess $g^*g^* \to Q\bar{Q}$ in the leading order of perturbation theory.

data on $b\bar{b}$-pair production in hadron collisions at the $Sp\bar{p}S$-collider energy.

4. MATRIX ELEMENTS FOR THE SUBPROCESS OF GLUON–GLUON FUSION

In this section, we calculate the squared matrix element $\sum |M|^2_{\rm SHA}(g^*g^* \to Q\bar{Q})$ for the subprocess of gluon–gluon fusion within the theory of semihard processes and obtain an expression for $\sum |M|^2_{\rm PM}(gg \to Q\bar{Q})$ in the leading order of perturbative QCD. We will use this expression in calculations within the ordinary parton model.

As was mentioned above, expression (12) describing the differential cross section for heavy-quark production assumes the dependence of the matrix element for the subprocess of gluon–gluon fusion within the semihard approach in QCD on the virtualities $q_1^2 = -\mathbf{q}_{1T}^2 \neq 0$ and $q_2^2 = -\mathbf{q}_{2T}^2 \neq 0$ of the initial gluons. The amplitude of the subprocess $g^*g^* \to Q\bar{Q}$ in the leading order of perturbation theory is described by three diagrams in Fig. 3. The standard Feynman rules for QCD yield

$$M_A = \bar{u}(p_1)(-ig\gamma^\mu)\varepsilon_\mu(q_1)i \times \frac{\hat{p}_1 - \hat{q}_1 + m}{(p_1 - q_1)^2 - m^2}(-ig\gamma^\nu)\varepsilon_\nu(q_2)v(p_2), \quad (23)$$

$$M_B = \bar{u}(p_1)(-ig\gamma^\nu)\varepsilon_\nu(q_2)i \times \frac{\hat{p}_1 - \hat{q}_2 + m}{(p_1 - q_2)^2 - m^2}(-ig\gamma^\mu)\varepsilon_\mu(q_1)v(p_2),$$

$$M_C = \bar{u}(p_1)C^{\mu\nu\lambda}(-q_1, -q_2, q_1 + q_2) \times \frac{g^2\varepsilon_\mu(q_1)\varepsilon_\nu(q_2)}{(q_1 + q_2)^2}\gamma_\lambda v(p_2),$$

where the subscripts A, B, and C correspond to the three diagrams in Fig. 3; $\varepsilon_\mu(q_1)$ and $\varepsilon_\nu(q_2)$ are the polarization vectors of the initial gluons; and $C^{\mu\nu\lambda}(q_1, q_2, q_3)$ is the ordinary three-gluon vertex,

$$C^{\mu\nu\lambda}(q_1, q_2, q_3) = i((q_2 - q_1)^\lambda g^{\mu\nu} + (q_3 - q_2)^\mu g^{\nu\lambda} + (q_1 - q_3)^\nu g^{\lambda\mu}). \quad (24)$$

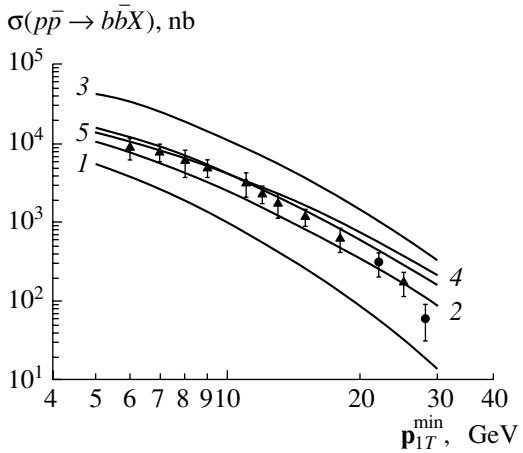

Fig. 4. Cross section for b-quark production versus $\mathbf{p}_{1T}^{\min}$ at $m_b = 4.75$ GeV, $\Lambda_{\rm QCD} = 150$ MeV, and $|y_1^*| < 1$. The notation for the curves is identical to that in Fig. 2. The displayed experimental data were obtained by the (▲) D0 and (●) CDF Collaborations.

The Mandelstam variables for the process $gg \to Q\bar{Q}$ have the form

$$\hat{s} = (q_1 + q_2)^2 = (p_1 + p_2)^2, \quad (25)$$
$$\hat{t} = (q_2 - p_2)^2 = (p_1 - q_1)^2,$$
$$\hat{u} = (q_1 - p_2)^2 = (p_1 - q_2)^2$$

and satisfy the relation

$$\hat{s} + \hat{t} + \hat{u} = 2m^2 + q_{1T}^2 + q_{2T}^2. \quad (26)$$

If we represent the expressions for M_A, M_B, and M_C in the form

$$M_{A,B,C} = \varepsilon_\mu(q_1)\varepsilon_\nu(q_2)M^{\mu\nu}_{A,B,C}, \quad (27)$$

the expression obtained for the squared matrix element upon summation over gluon polarizations and averaging over the spins of final-state particles assumes the form

$$\sum |M|^2 = C_A \sum |M|^2_A + C_B \sum |M|^2_B + C_C \sum |M|^2_C + 2C_{AB} \sum |M|^2_{AB} + 2C_{AC} \sum |M|^2_{AC} + 2C_{BC} \sum |M|^2_{BC}, \quad (28)$$

where

$$\sum |M|^2_i = \frac{1}{4}L_{\mu\alpha}(q_1)L_{\nu\beta}(q_2)M_i^{\mu\nu}M_i^{*\alpha\beta} \quad (29)$$

with $i = A, B, C, AB, AC, BC$, the color factors being $C_A = C_B = 1/12$, $C_C = 3/16$, $C_{AB} = -1/96$, and $C_{AC} = C_{BC} = 3/32$. We have already mentioned that the gluon polarization tensor $L_{\mu\nu}(q)$ is chosen in the form (2).

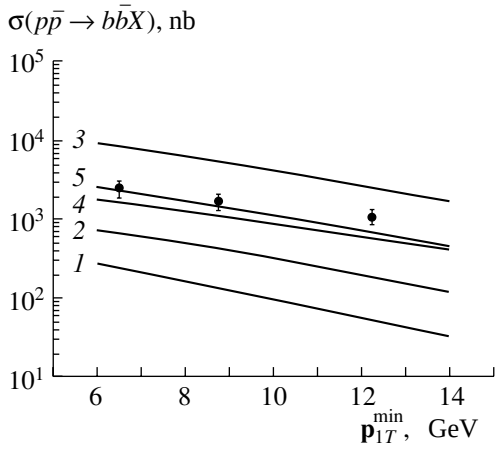

Fig. 5. Cross section for b-quark production versus $\mathbf{p}_{1T}^{\min}$ at $m_b = 4.75$ GeV, $\Lambda_{\rm QCD} = 150$ MeV, $|y_1^*| < 1$, $|y_2^*| < 1$, and $\mathbf{p}_{2T} > 6.5$ GeV. The notation for the curves is identical to that in Fig. 2. The displayed experimental data (points) were obtained by the CDF Collaboration.

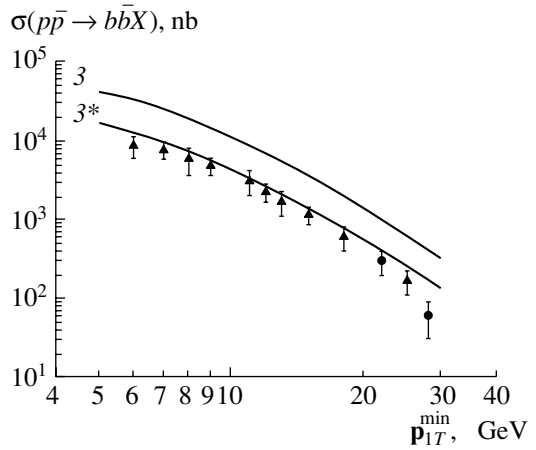

Fig. 6. Cross section for b-quark production versus $\mathbf{p}_{1T}^{\min}$ at $|y_1^*| < 1$. Curves *3* and *3** were obtained with the LRSS nonintegrated gluon distribution at $m_b = 4.75$ GeV, $\Lambda_{\rm QCD} = 150$ MeV, and $Q_0^2 = 2$ GeV^2 and $m_b = 5.0$ GeV, $\Lambda_{\rm QCD} = 100$ MeV, and $Q_0^2 = 4$ GeV^2, respectively. The displayed experimental data were obtained by the (▲) D0 and (●) CDF Collaborations.

We calculated the quantity $\sum |M|^2_{\rm SHA}(g^*g^* \to Q\bar{Q})$ analytically by using the REDUCE computer package for analytic calculations. The results are rather cumbersome, but, numerically, they agree with those presented in [7]. In calculating $\sum |M|^2_{\rm PM}(gg \to Q\bar{Q})$ within the parton model, we took the gluon polarization tensor in the axial gauge; that is,

$$L^{\mu\nu}(q_1, q_2) = -g^{\mu\nu} + \frac{q_1^\mu q_2^\nu + q_1^\nu q_2^\mu}{(q_1 \cdot q_2)} - q_2^2 \frac{q_1^\mu q_1^\nu}{(q_1 \cdot q_2)^2}. \quad (30)$$

We emphasize that the explicit expression obtained here for $\sum |M|^2_{\rm PM}(gg \to Q\bar{Q})$ coincides with the result of Babcock *et al.* [32].

5. RESULTS OF THE CALCULATIONS

In this section, we discuss the results obtained by calculating the cross section for heavy-quark production on protons at the Tevatron energies within the theory of semihard processes and compare these results with recent experimental data of the D0 and CDF Collaborations (see [33] and [34], respectively).

As was mentioned above, the total cross sections in the theory of semihard processes and in the ordinary parton model were calculated according to expressions (12) and (14), respectively. In the calculations, we set $\mu^2 = m^2 + \mathbf{p}_{1T}^2$. The limits of integration with respect to $\mathbf{p}_{1T}^2$ were chosen to be 1 GeV$^2 \le \mathbf{p}_{1T}^2 \le s/4 - m^2$. We note that the calculated cross section is virtually independent of the value of $\mathbf{p}_{1T}^{\min}$ in the range $1 \le \mathbf{p}_{1T}^{\min} \le 5$ GeV. As in [1], the region of integration with respect to $\mathbf{q}_{1T}^2$ and $\mathbf{q}_{2T}^2$ was broken down into four parts. For $\mathbf{q}_{1T}^2 \ge Q_0^2$ and $\mathbf{q}_{2T}^2 \ge Q_0^2$, we performed calculations according to (12), while, for $\mathbf{q}_{1T}^2 \le Q_0^2$ and $\mathbf{q}_{2T}^2 \le Q_0^2$, we set $\mathbf{q}_{1T}^2 = 0$ and $\mathbf{q}_{2T}^2 = 0$ in the scattering amplitude and replaced $\sum |M|^2_{\rm SHA}(g^*g^* \to Q\bar{Q})$ by $\sum |M|^2_{\rm PM}(gg \to Q\bar{Q})$. The contribution of the region where $\mathbf{q}_{1T}^2 \le Q_0^2$ and $\mathbf{q}_{2T}^2 \ge Q_0^2$ and the region where $\mathbf{q}_{1T}^2 \ge Q_0^2$ and $\mathbf{q}_{2T}^2 \le Q_0^2$ was taken into account in a similar way, one of the gluons being described by the nonintegrated distribution function $\Phi(x, \mathbf{q}_T^2, \mu^2)$ and the other being described by the collinear density $xG(x, \mu^2)$. The choice of the critical value of Q_0^2 is dictated by the requirement that the coupling constant $\alpha_s(\mathbf{q}_{1,2T}^2)$ be small in the region $\mathbf{q}_{1,2T}^2 \ge Q_0^2$. In our calculations, we used values in the range $Q_0^2 = 1$–4 GeV^2, so that $\alpha_s(\mathbf{q}_{1,2T}^2) \le 0.26$.

Figures 4–8 display the results of our calculations. Figures 4 and 5 show the cross section of b-quark production as a function of $\mathbf{p}_{1T}^{\min}$ at $m_b = 4.75$ GeV and $\Lambda_{\rm QCD} = 150$ MeV for $|y_1^*| < 1$ (Fig. 4) and for $|y_1^*| < 1$, $|y_2^*| < 1$, and $\mathbf{p}_{2T} > 6.5$ GeV (Fig. 5). Curve *1* corresponds to the calculations within the ordinary parton model that employ the gluon distribution $xG(x, Q^2)$ from the Glück–Reya–Vogt set [27], while curves *2, 3, 4,* and *5* correspond to the calculations within the theory of semihard processes using the RS nonintegrated gluon distribution ($Q_0^2 = 4$ GeV^2), the LRSS nonintegrated gluon distribution

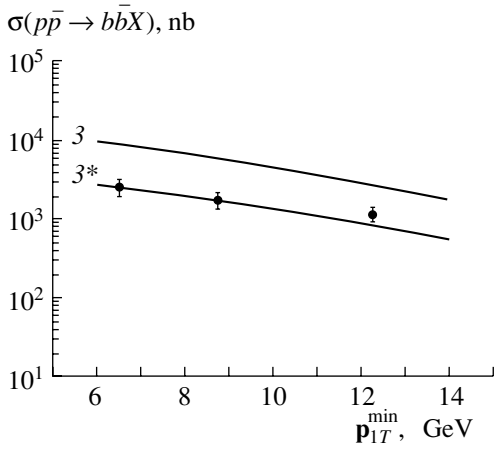

Fig. 7. Cross section for b-quark production versus $\mathbf{p}_{1T}^{\min}$ at $m_b = 4.75$ GeV, $\Lambda_{\rm QCD} = 150$ MeV, $|y_1^*| < 1$, $|y_2^*| < 1$, and $\mathbf{p}_{2T} > 6.5$ GeV. The notation for the curves is identical to that in Fig. 6. The points represent experimental data obtained by the CDF Collaboration.

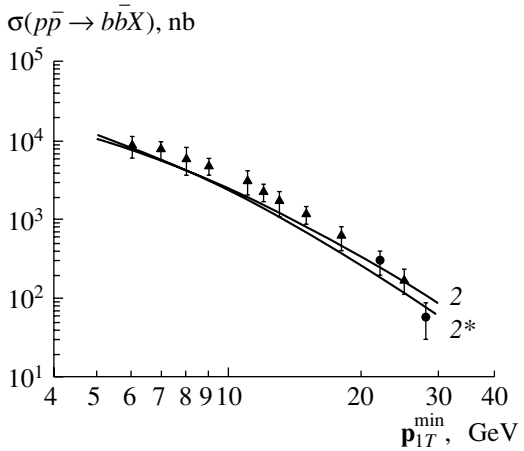

Fig. 8. Cross section for b-quark production versus $\mathbf{p}_{1T}^{\min}$ at $|y_1^*| < 1$. Curves *2* and *2** were calculated with the RS nonintegrated gluon distribution and the matrix elements for the subprocess of gluon–gluon fusion in the form (27) (*2*) and in the form taken from [7] (*2**). The displayed experimental data were obtained by the (▲) D0 and (●) CDF Collaborations.

($Q_0^2 = 2$ GeV^2), the BFKL nonintegrated gluon distribution ($Q_0^2 = 1$ GeV^2), and that in the form (22) ($Q_0^2 = 1$ GeV^2), respectively.

It is clear from Figs. 4 and 5 that the results of calculations within the parton model (curves *1*) do not agree with recent experimental data obtained by the D0 and CDF Collaborations, but that the results of the theory of semihard processes are in good agreement with the data. The use of the LRSS phenomenological gluon distribution function results in overestimating the cross section for b-quark production, but, by varying the parameters Q_0^2, m_b, and $\Lambda_{\rm QCD}$ within the limits 1 GeV$^2 \le Q_0^2 \le 4$ GeV^2, 4.5 GeV $\le m_b \le$ 5.0 GeV, and 100 MeV $\le \Lambda_{\rm QCD} \le$ 250 MeV (we used the following set of parameter values: $Q_0^2 = 4$ GeV^2, $m_b = 5.0$ GeV, and $\Lambda_{\rm QCD} =$ 100 MeV), one can reach satisfactory agreement with the data (curves *3** in Figs. 6, 7). However, ZEUS and H1 data on the photoproduction of $b\bar{b}$ quark pairs (see [35] and [36], respectively) were described only with the LRSS gluon distribution at $Q_0^2 = 2$ GeV^2 ($m_b = 4.75$ GeV and $\Lambda_{\rm QCD} = 200$ MeV) [16].

The curves in Fig. 8 were obtained with the matrix elements (27) for the subprocess of gluon–gluon fusion (curve *2*) and the matrix elements from [7] (curve *2**); here, we have used the RS nonintegrated gluon distribution. The results are in good agreement with each other.

As was noted above, the problem of seeking a "universal" nonintegrated gluon distribution is of great importance. With this aim in view, a number of processes leading to the production and photoproduction of heavy quarks and quarkonia were considered in [13–17]. In our opinion, the results obtained here and in [13–17] suggest that the RS and BFKL nonintegrated distributions, which are parametrizations of solutions to the BFKL evolution equations, may be candidates for universal gluon distributions.

6. CONCLUSION

We have considered the inclusive high-energy production of heavy (c, b) quarks within the semihard approach in QCD. We studied the dependence of the total cross sections for heavy quarks and the dependence of $\sigma(\mathbf{p}_T > \mathbf{p}_T^{\min})$ on unintegrated gluon distributions. We have paid special attention to gluon distributions derived from solutions to the BFKL evolution equations. We have shown that the theoretical results obtained with the RS gluon distribution, the BFKL gluon distribution, and that in the form (22) (at $m_b = 4.75$ GeV and $\Lambda_{\rm QCD} = 150$ MeV) and with the LRSS phenomenological distribution (at $m_b = 5.0$ GeV and $\Lambda_{\rm QCD} = 100$ MeV) are in good agreement with experimental data obtained by the D0 and CDF Collaborations.[4)]

ACKNOWLEDGMENTS

We are grateful to S.P. Baranov and H. Jung for enlightening discussions on various aspects of the semihard approach in QCD.

[4)] When this article was prepared for print, similar results obtained within the k_T-factorization approach were reported in [37, 38].

The work was supported in part by the Russian Foundation for Basic Research (project no. 02-02-17513). N. Zotov gratefully acknowledges the support of the Royal Academy of Sciences of Sweden.

REFERENCES

1. E. L. Berger and D. Jones, Phys. Rev. D **23**, 1521 (1981).
2. S. S. Gershteĭn, A. K. Likhoded, and S. R. Slabospitskiĭ, Yad. Fiz. **34**, 227 (1981) [Sov. J. Nucl. Phys. **34**, 128 (1981)].
3. R. Baier and R. Rückl, Nucl. Phys. B **218**, 289 (1983).
4. A. D. Martin, C. K. Ng, and W. J. Stirling, Phys. Lett. B **191**, 200 (1987).
5. L. Gribov, E. Levin, and M. Ryskin, Phys. Rep. **100**, 1 (1983).
6. E. M. Levin, M. G. Ryskin, Yu. M. Shabel'skiĭ, and A. G. Shuvaev, Yad. Fiz. **53**, 1059 (1991) [Sov. J. Nucl. Phys. **53**, 657 (1991)].
7. S. Catani, M. Ciafoloni, and F. Hautmann, Nucl. Phys. B **366**, 135 (1991).
8. J. C. Collins and R. K. Ellis, Nucl. Phys. B **360**, 3 (1991).
9. L. V. Gribov and L. N. Lipatov, Yad. Fiz. **15**, 781 (1972) [Sov. J. Nucl. Phys. **15**, 438 (1972)]; L. N. Lipatov, Yad. Fiz. **20**, 181 (1974) [Sov. J. Nucl. Phys. **20**, 94 (1975)]; G. Altarelli and G. Parisi, Nucl. Phys. B **126**, 298 (1977); Yu. L. Dokshitser, Zh. Éksp. Teor. Fiz. **73**, 1216 (1977) [Sov. Phys. JETP **46**, 641 (1977)].
10. É. A. Kuraev, L. N. Lipatov, and V. S. Fadin, Zh. Éksp. Teor. Fiz. **71**, 840 (1976) [Sov. Phys. JETP **44**, 443 (1976)]; **72**, 377 (1977) [**45**, 199 (1977)]; Ya. Ya. Balitskiĭ and L. N. Lipatov, Yad. Fiz. **28**, 1597 (1978) [Sov. J. Nucl. Phys. **28**, 822 (1978)].
11. M. G. Ryskin and Yu. M. Shabelski, Z. Phys. C **69**, 269 (1996).
12. M. G. Ryskin and Yu. M. Shabelski, Z. Phys. C **61**, 517 (1994); **66**, 151 (1995).
13. V. A. Saleev and N. P. Zotov, Mod. Phys. Lett. A **9**, 151 (1994).
14. V. A. Saleev and N. P. Zotov, Mod. Phys. Lett. A **11**, 25 (1996).
15. A. V. Lipatov and N. P. Zotov, Mod. Phys. Lett. A **15**, 695 (2000).
16. A. V. Lipatov, V. A. Saleev, and N. P. Zotov, Mod. Phys. Lett. A **15**, 1727 (2000).
17. A. V. Lipatov and N. P. Zotov, in *Proceedings of the 8th International Workshop on DIS and QCD DIS'2000, Liverpool, 2000*, p. 157.
18. S. P. Baranov, Phys. Lett. B **428**, 377 (1998).
19. S. P. Baranov and N. P. Zotov, Phys. Lett. B **458**, 389 (1999).
20. S. P. Baranov and M. Smizanska, Phys. Rev. D **62**, 014012 (2000).
21. P. Hägler, R. Kirschner, A. Schäfer, *et al.*, Phys. Rev. D **62**, 071502 (2000).
22. P. Hägler, R. Kirschner, A. Schäfer, *et al.*, Phys. Rev. D **63**, 077501 (2001); F. Yuan and K.-T. Chao, Phys. Rev. D **63**, 034006 (2001); hep-ph/0009224.
23. S. P. Baranov, A. V. Lipatov, and N. P. Zotov, in *Proceedings of the 9th International Workshop on DIS "DIS'2001," Bologna, 2001*; hep-ph/0106229.
24. UA-1 Collab. (C. Albajar *et al.*), Phys. Lett. B **213**, 405 (1988).
25. J. Morfin and Wu-Ki Tung, Z. Phys. C **52**, 13 (1991).
26. J. Blumlein, DESY 95-121.
27. M. Glück, E. Reya, and A. Vogt, Z. Phys. C **67**, 433 (1995).
28. V. Fadin and L. Lipatov, Phys. Lett. B **429**, 127 (1998); M. Ciafaloni and G. Camici, Phys. Lett. B **430**, 349 (1998).
29. G. Salam, J. High Energy Phys. **9807**, 019 (1998); hep-ph/9806482.
30. S. J. Brodsky, V. S. Fadin, and V. T. Kim, *et al.*, hep-ph/9901229.
31. N. Nikolaev and B. Zakharov, Phys. Lett. B **333**, 250 (1994).
32. J. Babcock, D. Sivers, and S. Wolfram, Phys. Rev. D **18**, 162 (1978).
33. D0 Collab. (S. Abachi *et al.*), Phys. Rev. Lett. **74**, 3548 (1995); Phys. Lett. B **487**, 264 (2000).
34. CDF Collab. (F. Abe *et al.*), Phys. Rev. Lett. **71**, 500 (1993); Phys. Rev. D **55**, 2546 (1997).
35. ZEUS Collab. (J. Breitweg *et al.*), Eur. Phys. J. C **18**, 625 (2001).
36. H1 Collab. (C. Adloff *et al.*), Phys. Lett. B **467**, 156 (1999).
37. Yu. Shabelsky and A. Shuvaev, hep-ph/0107106.
38. H. Jung, hep-ph/0109146; hep-ph/0110034.

Translated by M. Kobrinsky

Physics of Atomic Nuclei, Vol. 66, No. 4, 2003, pp. 764–768. From Yadernaya Fizika, Vol. 66, No. 4, 2003, pp. 796–800.

ELEMENTARY PARTICLES AND FIELDS
Theory

Novel Solutions of RG Equations for $\alpha(s)$ and $\beta(\alpha)$ in the Large-N_c Limit*

Yu. A. Simonov

Institute of Theoretical and Experimental Physics,
Bol'shaya Cheremushkinskaya ul. 25, Moscow, 117259 Russia

Received September 5, 2002

Abstract—A general solution of RG equations in the framework of background perturbation theory is written in the large-N_c limit. A simplified (model) approximation to the general solution is suggested that allows $\beta(\alpha)$ and $\alpha(s)$ to be written to any loop order. The resulting $\alpha_B(Q^2)$ coincides asymptotically at large $|Q^2|$ with standard (free) α_s, saturates at small $Q^2 \geq 0$, and has poles at timelike Q^2 in agreement with analytic properties of physical amplitudes in the large-N_c limit. © *2003 MAIK "Nauka/Interperiodica".*

1. The running α_s of standard perturbation theory (SPT) has unphysical singularities (Landau ghost pole and cuts) in the Euclidean region, which contradict analyticity of physical amplitudes and are not observed in lattice calculations of $\alpha_s(Q^2)$ [1].

As was shown in [2, 3], background perturbation theory (BPT) is free of these defects and the coupling constant α_B of BPT displays an important property of IR freezing (saturation) with $\alpha_B(Q^2=0) \approx 0.5$ [2, 3]. This behavior of α_B is well confirmed by experimental data on spin splitting of quarkonia levels [4, 5] and by lattice data [6].

Analytic properties of $\alpha_B(Q^2)$ in the Q^2 plane have not been studied heretofore and are the topic of the present paper. To this end, the large-N_c limit is exploited, which ensures that any physical amplitude has only simple poles [7]. This requires that $\alpha_B(Q^2)$ should be a meromorphic function of Q^2.

To find it explicitly, we study below the general solution of RG equations and suggest a simple model approximation to it, yielding $\beta(\alpha)$ to all orders and an explicit form of $\alpha_B(Q^2)$.

The resulting $\alpha_B(Q^2)$ can be compared with $\alpha_s(Q^2)$ of SPT and coincides with the latter asymptotically at large Q^2.

2. Separating background field B_μ in the total gluonic field $A_\mu = B_\mu + a_\mu$, and expanding in ga_μ one gets the BPT series, where coefficients depend both on the external momenta and on the combination gB_μ, which turns out to be RG invariant, if background gauge is chosen [8]. Correspondingly, $\alpha_B \equiv g^2/4\pi$ satisfies the standard RG equations, where momenta and the correlator $\mathrm{tr}\langle F_{\mu_1\nu_1}(B)F_{\mu_2\nu_2}(B)\dots F_{\mu_n\nu_n}(B)\rangle$ averaged over vacuum background enter together and will be denoted $\{\mathcal{P}_i^2\}$.

One starts with the standard definition

$$\frac{d\alpha_B(\mu)}{d\ln\mu} = \beta(\alpha_B) \tag{1}$$

and represents $\beta(\alpha_B)$ in the form

$$\beta(\alpha) = -\frac{\beta_0}{2\pi}\frac{\alpha^2}{\left[1-\dfrac{\beta_1}{2\pi\beta_0}\varphi'\left(\dfrac{1}{\alpha}\right)\right]}, \tag{2}$$

where $\varphi(z)$ is an arbitrary function with some conditions to be imposed below, and prime means derivative.

Solving (1) with the help of (2), one has

$$\alpha_B = \frac{4\pi}{\beta\left[\ln\mu^2 + \chi + \dfrac{2\beta_1}{\beta_0^2}\varphi\left(\dfrac{1}{\alpha_B}\right)\right]}. \tag{3}$$

Here, χ is an arbitrary dimensionless function of $\{\mathcal{P}_i^2\}$, while φ is partly fixed by a few coefficients of expansion of $\beta(\alpha)$,

$$\beta(\alpha) = -\frac{\beta_0}{2\pi}\alpha^2 - \frac{\beta_1}{4\pi^2}\alpha^3 - \frac{\beta_2}{64\pi^3}\alpha^4 - \frac{\beta_3}{(4\pi)^4}\alpha^5. \tag{4}$$

(Note that β_i are defined as in [9], for $n_f = 0$, $N_c = 3$, and $\overline{MS}$ scheme $\beta_0 = 11$, $\beta_1 = 51$, $\beta_2 = 2857$, $\beta_3 = 58\,486$.)

At this point, we shall use the large-N_c limit and require that $\alpha_B(Q^2)$ be a meromorphic function of Q^2. Consider, e.g., the process $e^+e^- \to$ hadrons and

*This article was submitted by the author in English.

1063-7788/03/6604-0764$24.00

the photon self-energy part $\Pi(Q^2)$, which has a pole expansion [3]

$$\Pi(Q^2,\alpha_B)=\sum_{n=0}^{\infty}\frac{C_n(\alpha_B)}{Q^2+M_n^2(\alpha_B)}+\text{subtractions}, \tag{5}$$

where pole positions $M_n^2(\alpha_B)$ and residues C_n depend on the coupling constant α_B and are different in each order α_B^n.

Expanding in α_B and doing a partial summation (equivalent to the summation of leading logarithms), one obtains a running $\alpha_B(Q^2)$ that has poles at some, generally speaking, shifted positions as compared to the poles of the lowest order—$M_n^2(0)$. The latter are proportional to n; $M_n^2(0)=m_0^2n+M_0^2$; $n=0,1,2,...$, $m_0^2=4\pi\sigma$; $C_n(0)=m_0^2$ [3]. The lowest (partonic) approximation thus reduces to

$$\Pi(Q^2,0)\sim\psi\left(\frac{Q^2+M_0^2}{m_0^2}\right),$$

where $\psi(z)=\Gamma'(z)/\Gamma(z)$.

To specify the form of the function $\varphi(1/\alpha_B)$ and $\chi(Q^2)$, we shall use two requirements:

(i) The correspondence principle with SPT, which states that, for $Q^2\gg\kappa^2$, where κ^2 is the scale of nonperturbative vacuum fields, our solution (3) should coincide with that of SPT.

(ii) $\alpha_B(Q^2)$ should be a meromorphic function of Q^2, and hence both χ and φ should be meromorphic functions of their arguments (Q^2 and $1/\alpha_B$, respectively).

The first requirement means that coefficients C_n in the sum over poles should have finite limit C_∞, i.e., one can represent this sum as the Euler function $\psi(z)$ plus a sum with fast decreasing coefficients, which we write symbolically as a finite sum. Thus, the general solution satisfying (i) and (ii) can be written as

$$\ln\mu^2+\chi=\ln\frac{m^2}{\Lambda^2}+\psi\left(\frac{Q^2+M_0^2}{m^2}\right)+\sum_{n=1}^{N_1}\frac{b_n}{Q^2+m_n^2}, \tag{6}$$

$$\varphi\left(\frac{1}{\alpha_B}\right)=\psi\left(\frac{\lambda}{\alpha_B}+\Delta\right)+P\left(\frac{1}{\alpha_B}\right), \tag{7}$$

where Λ is the SPT parameter, e.g., $\Lambda_{\rm QCD}$ in the $\overline{MS}$ scheme; Δ is some constant; and $\lambda=4\pi/\beta_0$. Here $P(x)$ is some meromorphic function. Note that our solution (6), (7) satisfies (1) and reproduces the first two coefficients in expansion (4) when all $b_n=0$ and $P\equiv0$, while our β_2 and β_3 appear to be smaller; however, the latter are scheme-dependent. It is easy to reproduce β_2 and β_3 by choosing in (7) $P\neq0$. This choice of $\varphi(1/\alpha_B)$ leads to a small numerical (around 2%) change in α_B as compared to the minimal choice [see (8) below] for all $Q^2\le0$.

3. In what follows, we confine ourselves to the minimal model of (6), (7) with all b_n and P identically zero, which yields

$$\alpha_B=\frac{4\pi}{\beta_0}\left[\ln\frac{m^2}{\Lambda^2}+\psi\left(\frac{Q^2+M_0^2}{m^2}\right)+\frac{2\beta_1}{\beta_0^2}\psi\left(\frac{\lambda}{\alpha_B}+\Delta\right)\right]^{-1}. \tag{8}$$

Equation (8) defines α_B as a meromorphic function of Q^2 in the whole Q^2 complex plane.

Moreover, Eq. (8) defines α_B to all orders in the "loop expansion" obtained by iteration of the last term in the square brackets in (8) and will be compared below to the SPT loop expansion. Consider, e.g., large Q^2, $Q^2+M_0^2/m^2\gg1$. Then, using the asymptotic expansion for $z\to\infty$

$$\psi(z)=\ln z-\frac{1}{2z}-\sum_{k=1}^{\infty}\frac{B_{2k}}{2kz^{2k}}, \tag{9}$$

where B_n are Bernoulli numbers, one obtains to the lowest order

$$\alpha_B^{(0)}=\frac{4\pi}{\beta_0\ln\left(\dfrac{Q^2+M_0^2}{\Lambda^2}\right)}, \tag{10}$$

which explicitly shows the asymptotically free (AF) behavior for large Q^2 and the absence of a Landau pole (for $M_0^2>\Lambda^2$) (see Fig. 1).

Forms (2) and (8) in general admit poles of $\alpha_B(Q^2)$ for $Q^2\ge0$ and poles of $\beta(\alpha_B)$ for $\alpha_B\ge0$, which would be unphysical. The latter poles are defined by the equation

$$1=\frac{\beta_1\lambda}{2\pi\beta_0}\psi'\left(\frac{\lambda}{\alpha}+\Delta\right)$$

and are excluded from the region $\alpha\ge0$ when $\Delta>\Delta_0=1.255$. This latter condition also excludes singularities of $\alpha_B(Q^2)$ (8) at $Q^2>0$. At the same time, $\beta(\alpha)$ has a point of condensing zeros on the negative side of $\alpha=0$, and $\beta(\alpha)$ is monotonically decreasing when $\alpha\to\infty$, as is shown in Fig. 2 and Table 1. Note that a pole of $\beta(\alpha)$ at $\alpha=\alpha^*>0$ leads to a situation when real solutions $\alpha(q)$ exist only for $\alpha\le\alpha^*$, $Q>Q^*$.

4. Although $\alpha_B(Q^2)$ does not have poles for $\Delta>\Delta_0$ in the Euclidean region, $Q^2>0$, it has an infinite number of poles for $Q^2<0$.

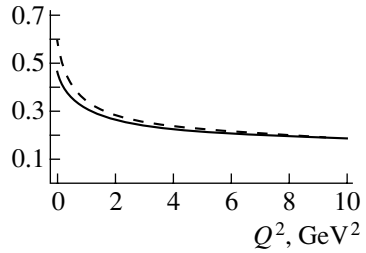

Fig. 1. Exact solution of Eq. (8) for $\alpha_B(Q^2)$ with $\Delta = 1.5$ as a function of $s \equiv Q^2$ (solid curve) and exact solution for α_B from the extended model, Eq. (3), with φ' from (21) and $\eta = 3, \Delta = 1.5$ which reproduces all known β_n coefficients (dashed curve).

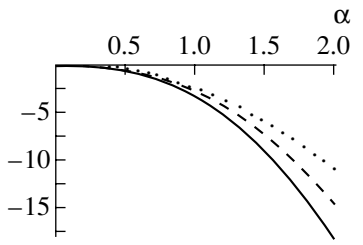

Fig. 2. $\beta_{\min}(\alpha)$ in the minimal model Eqs. (2), (7) as a function of α with $P \equiv 0$, $\Delta = 1.5$, reproducing scheme-independent coefficients β_0, β_1 (dashed curve), and $\beta_{\text{ext}}(\alpha)$ in the extended model Eqs. (2), (21) with $\eta = 3$ and $\Delta = 1.5$ (solid curve) and $\Delta = 3$ (dotted curve).

These poles are given by zeros of the denominator in (8), which can be written as

$$-Q^2 \equiv s_n = s_n^{(0)} - \delta_n, \qquad (11)$$
$$s_n^{(0)} \equiv M_n^2 = M_0^2 + nm^2,$$

and δ_n is then found from (8) to be [10]

$$\delta_n^{-1} \cong \ln(M_n^2/\Lambda^2). \qquad (12)$$

Hence, poles of α_B are shifted in comparison with poles of $\psi\left(\dfrac{Q^2+M_0^2}{m^2}\right)$, the latter describing the physical states of (double) hybrids—the background analog of gluon loops renormalizing α_s in SPT. In the vicinity of the pole, α_B has the form [10]

$$\alpha_B(s \approx s_n^{(0)} - \delta_n) = \frac{4\pi/\beta_0 - \psi'(\Delta)}{\psi'(z_n)(z - z_n)}, \qquad (13)$$
$$z = \frac{M_0^2 - s}{m^2}.$$

Hence, the perturbative series of BPT is a sum over poles of α_B and nonperturbative poles of $\Pi(Q^2, 0)$ in (5) (dual to partonic contribution), all poles being in the region $s > M_0^2 - \delta_0 > 0$, and this situation is in accord with the large-N_c analytic properties. Now, one has to show that the "physically averaged value" of $\alpha_B(s)$ corresponds to the AF behavior, as is seen, e.g., in e^+e^- annihilation. To this end, one can choose two equivalent procedures: (i) introduce the width of the pole in $\alpha_B(s)$, or (ii) equivalently consider the BPT series at the shifted value of s, $s = \bar{s}(1 + i\gamma)$ (see, e.g., [11]).

In what follows, we shall exploit the second path. Considering $\text{Im}\alpha_B$ above the real axis, at $\bar{s}(1 + i\gamma)$ with $\bar{s}$ large and γ fixed, $\gamma \ll \pi$, allows one to use asymptotic expression (10) (in one-loop order) with the result

$$\text{Im}\alpha_B(\bar{s}(1 + i\gamma)) \qquad (14)$$
$$\approx \frac{4\pi(\pi - \gamma)}{b_0\left[\ln^2\left|\dfrac{M_0^2 - \bar{s}}{\Lambda^2}\right| + (\pi - \gamma)^2\right]}.$$

Another form of discontinuity results from the expansion of the Adler function $D(Q^2) = Q^2 d\Pi(Q^2)/d\ln Q^2$, from which the hadronic ratio $R(s)$ can be obtained as [12]

$$R(s) = \frac{1}{2\pi i}\int\limits_{-s-i\varepsilon}^{-s+i\varepsilon} D(\sigma)\frac{d\sigma}{\sigma} = \frac{1}{2\pi i}\int\limits_{C(s)} D(\sigma)\frac{d\sigma}{\sigma}. \qquad (15)$$

Here, $C(s)$ is the circle of radius s around the origin, comprising all singularities of $D(\sigma)$ in the Euclidean region.

Similarly to [12], one can define the operation $\Phi\left\{\dfrac{\alpha_B}{\pi}\right\}$ transforming the known perturbative series for $R(s)$:

$$R(s) = N_c\sum_q e_q^2\left[1 + \bar{\Phi}\left\{\frac{\alpha_B}{\pi}\right\} + d_2\bar{\Phi}\left\{\left(\frac{\alpha_B}{\pi}\right)^2\right\}\right], \qquad (16)$$

where

$$\bar{\Phi}\left\{\left(\frac{\alpha_B}{\pi}\right)^k\right\} = \frac{1}{2\pi i}\int\limits_{C(s)}\left(\frac{\alpha_B(\sigma)}{\pi}\right)^k\frac{d\sigma}{\sigma}. \qquad (17)$$

We shall consider the situation where one can use logarithmic asymptotic expression (10) for α_B in the Minkowskian region. This occurs in the physical situation described above: when poles have imaginary parts (widths of resonances), or equivalently when one considers effective

$$\bar{R}(s) = \frac{1}{2i}(\Pi(s(1 + i\gamma)) - \Pi(s(1 - i\gamma)))$$

with fixed γ (so that the requirement $|\arg(z)| < \pi$ is fulfilled).

Table 1. The QCD β function $\beta(\alpha)$ for $n_f = 0, N_c = 3$ obtained numerically to all orders in α for the minimal model $\beta_{\min}(\alpha)$, Eq. (2), with $\varphi = \lambda/\alpha + \Delta$, and $\Delta = 1.5$, $\lambda = 1.14$, and for the extended model $\beta_{\rm ext}$ with φ' from (21); the last column refers to $\beta(\alpha)$ in $\overline{MS}$ as given in Eq. (4)

α	$\beta_{\min}(\alpha)$	$\beta_{\rm ext}(\alpha)$	$\beta^{(3\,\rm loop)}_{\overline{MS}}(\alpha)$
0	0	0	0
0.1	−0.0187	−0.019	−0.01895
0.2	−0.08	−0.082	−0.0833
0.5	−0.587	−0.65	−0.767
1.0	−2.85	−3.36	−6.82
1.2	−4.36	−5.23	−13.56
1.5	−7.38	−9.04	−33.35
2.0	−14.59	−18.43	−115.24

In this case, one obtains, after inserting in integral (17) the asymptotic form (10) (see [10] for details),

$$\Phi\left\{\frac{\bar\alpha_B}{\pi}\right\} \cong \frac{4}{b_0}\left\{\frac{1}{\pi}\arctan\frac{\pi}{\ln(s/\Lambda^2)} + \frac{2M_0^2}{s\ln^3(s/\Lambda^2)} + O\left(\frac{M_0^2}{s\ln^4(s/\Lambda^2)}\right)\right\}. \quad (18)$$

5. One can now compare the expansion ("loop expansion") of α_B in (8) in powers of $\alpha_B^{(0)}$ (10) with the SPT expression for α_s [9, 13]. To this end, we shall write α_B [Eq. (8)] as follows:

$$\alpha_B = \alpha_B^{(0)}\left\{1 - \frac{2\beta_1\ln L}{\beta_0^2 L} + \frac{4\beta_1^2}{\beta_0^4 L^2} \times \left[\left(\ln L - \frac{1}{2}\right)^2 + b\right]\right\}, \quad (19)$$

where $L \equiv \ln[(Q^2 + M_0^2)/\Lambda^2]$ and, for $n_f = 0$, $\Delta = 1.5$,

$$b = -\frac{\beta_0^2}{2\beta_1}\left(\Delta - \frac{1}{2}\right) - \frac{1}{4} = -1.436. \quad (20)$$

This should be compared with the $\overline{MS}$ value of SPT, $b_{\overline{MS}} = 0.26$ ($n_f = 0$).

To bring our theoretical expressions for β_2 and β_3 in agreement with the computed $\overline{MS}$ values (see [9] for the corresponding references), one should generalize the minimal model considered above by adding a term to $\varphi(1/\alpha)$:

$$\varphi'\left(\frac{1}{\alpha}\right) = \lambda\psi'\left(\frac{\lambda}{\alpha} + \Delta\right) + \frac{\tilde C\alpha^2}{1 + \alpha^2\eta^2}. \quad (21)$$

Table 2. $\alpha_B(Q^2)$ computed numerically to all orders within the minimal model, Eq. (8), with $\Lambda = 0.37$ GeV, $\Delta = 1.5$, $m = M_0 = 1$ GeV and in the extended model, Eqs. (3), (21), with $\eta = 3$, $\tilde C = 1.253$ reproducing all known coefficients $\beta_n, n = 0, \ldots, 3$, in the $\overline{MS}$ scheme for $n_f = 0$; the last two columns refer to the two-loop approximation of α_B and α_s (in SPT) with the same parameters

Q^2, (GeV^2)	$\alpha_B^{(\min)}(Q^2)$	$\alpha_B^{(\rm ext)}(Q^2)$	$\alpha_B^{(2\,\rm loop)}(Q^2)$	$\alpha_s^{(2\,\rm loop)}(Q^2)$
0	0.546	0.754	0.64	
0.5	0.394	0.462	0.359	0.73
1	0.337	0.379	0.328	0.404
1.5	0.306	0.337	0.293	0.33
2	0.286	0.311	0.27	0.293
3	0.26	0.278	0.244	0.256
5	0.232	0.245	0.217	0.229
10	0.201	0.210	0.188	0.19
40	0.159	0.163	0.15	0.149
100	0.139	0.142	0.131	0.131

Choosing $\tilde C = 1.253$ and arbitrary real η, one obtains both β_2 and β_3 in close agreement (within 1%) with $\overline{MS}$ values. In this case also, b in (20) gets a contribution from the new term and becomes $\tilde b = b + (2\pi\beta_0/\beta_1)\tilde C = 0.263$, which agrees with SPT [9]. We study numerically both the minimal model and the corrected one as explained above and present the results for $\beta(\alpha)$ in Table 1 and Fig. 2 and for $\alpha_B(Q^2)$ in Table 2 and Fig. 1.

From Table 1 and Fig. 2, it is clear that nonperturbative $\beta(\alpha)$, namely, $\beta_{\min}(\alpha)$, calculated as in (2), (7) with $P \equiv 0$, and $\beta_{\rm ext}(\alpha)$, calculated as in (2), (21), both decrease more moderately (as $(-|\text{const}|\cdot\alpha^2)$) at $\alpha > 1$ as compared to the purely perturbative three-loop expression (4). This might indicate that the series (4) is asymptotic and should be cut off after the first few terms (note that β_3 is larger than the previous three coefficients).

For $Q^2 = 100$ GeV^2 and $M_0 = 1$ GeV, the correction in $\alpha_B(Q^2)$ introduced by replacements (21) is around 2% and it decreases as Q^2 grows.

Defining $\Lambda \equiv \Lambda_B = \Lambda_{\overline{MS}}$ (since α_B and α_s practically coincide for $Q^2 > 40$ GeV^2), one can compare exact $\alpha_B(Q^2)$ obtained by solving (8) with $\alpha_s(Q^2)$ (two-loop) of SPT and observe a significant difference only at small Q^2, $Q^2 \le 10$ GeV^2.

One can see in Fig. 1 and Table 2 that the difference of $\alpha_B^{(\min)}$ and $\alpha_s^{(2\,\rm loop)}$ is 20% at 1 GeV^2 and

drops to 1.3% at 5 GeV^2, which implies that the use of $\alpha_B^{(\min)}$ instead of α_s in the Euclidean region would not produce much change in the region $Q^2 > 1$ GeV^2, while it improves the situation for $Q^2 \leq 1$ GeV^2, where $\alpha_B^{(\min)}$ saturates in agreement with experiment and lattice data (see [1–6] and [14] for the discussion of this point).

6. We have used the large-N_c limit to simplify analysis of analytic properties of background coupling constant α_B. This has also enabled us to study $\alpha_B(Q^2)$ for timelike Q^2 and to suggest a simplified model solution of exact RG equations, which yields α_B to all orders and prescribes the nonperturbative expression for $\beta(\alpha)$.

The resulting solution for α_B coincides with the standard α_s at large $|Q^2|$ and displays familiar AF properties. At the same time, $\alpha_B(Q^2)$ stays finite everywhere in the Euclidean region, demonstrating phenomenon of IR saturation. For timelike Q^2, the model $\alpha_B(Q^2)$ in the large-N_c limit acquires pole singularities, which have been treated above in the averaging procedure. It is worth noting that our minimal model correctly reproduces both scheme-independent coefficients β_0 and β_1. At the same time, scheme-dependent coefficients β_2, β_3, etc., are defined by additional pole terms with arbitrary constants in them. Several improvements are possible with the suggested model solution. First, one can consider $n_f \neq 0$, N_c finite, in which case poles would acquire width. This will not change much the averaged values of $\alpha_B(s)$ calculated above, but will enable one to make local predictions of resonance behavior. Secondly, our model is too simplified, since $\psi\left(\frac{Q^2+M_0^2}{m^2}\right)$ appearing in (8) represents only the equidistant spectrum of hybrids (equivalent of gluon loops), but this spectrum should not be equidistant for the lowest states, which yields power corrections, considered in [10].

ACKNOWLEDGMENTS

I am grateful to N.O. Agasian and A.V. Radyushkin for helpful discussions; partial financial support from the Russian Foundation for Basic Research (project nos. 00-02-17836 and 00-15-96786) and INTAS (grant nos. 00-00110 and 00-00366) is gratefully acknowledged.

REFERENCES

1. S. P. Booth *et al.*, Phys. Lett. B **294**, 385 (1992); G. S. Bali and K. Schilling, Phys. Rev. D **47**, 661 (1993); G. S. Bali, Phys. Lett. B **460**, 170 (1999).
2. Yu. A. Simonov, Yad. Fiz. **58**, 113 (1995) [Phys. At. Nucl. **58**, 107 (1995)]; JETP Lett. **57**, 525 (1993); hep-ph/9311247; Lect. Notes Phys. **479**, 139 (1996).
3. A. M. Badalian and Yu. A. Simonov, Phys. At. Nucl. **60**, 630 (1997).
4. A. M. Badalian and V. L. Morgunov, Phys. Rev. D **60**, 116008 (1999).
5. A. M. Badalian and B. L. G. Bakker, Phys. Rev. D **62**, 094031 (2000).
6. A. M. Badalian and D. S. Kuzmenko, hep-ph/0104097.
7. G. 't Hooft, Nucl. Phys. B **72**, 461 (1974); E. Witten, Nucl. Phys. B **156**, 269 (1979).
8. L. F. Abbot, Nucl. Phys. B **185**, 189 (1981).
9. Review of Particle Physics, Eur. Phys. J. C **15**, 229 (2000).
10. Yu. A. Simonov, hep-ph/0109081; Yad. Fiz. **66**, 363 (2003) [Phys. At. Nucl. **66**, 338 (2003)].
11. E. C. Poggio, H. R. Quinn, and S. Weinberg, Phys. Rev. D **13**, 1958 (1976).
12. A. Radyushkin, Preprint E-2-82-159 (Joint Institute for Nuclear Research, Dubna, 1982); hep-ph/9907228; B. Schrempp and F. Schrempp, Z. Phys. C **6**, 7 (1980); N. V. Krasnikov and A. A. Pivovarov, Phys. Lett. B **116B**, 168 (1982); D. V. Shirkov, hep-ph/0012283.
13. F. J. Yndurain, *The Theory of Quark and Gluon Interactions,* 3rd ed. (Springer-Verlag, Berlin; Heidelberg, 1999).
14. A. C. Mattingly and P. M. Stevenson, Phys. Rev. D **49**, 437 (1994); Yu. L. Dokshitzer, hep-ph/0106348; hep-ph/9812252.

Physics of Atomic Nuclei, Vol. 66, No. 4, 2003, pp. 769–779. Translated from Yadernaya Fizika, Vol. 66, No. 4, 2003, pp. 801–812.

ELEMENTARY PARTICLES AND FIELDS
Theory

Charm Contribution to the Proton Structure Function in Deep-Inelastic *ep* Scattering at the HERA Collider

A. V. Berezhnoy[1)*], V. V. Kiselev[**], and A. K. Likhoded[***]

Institute for High Energy Physics, Protvino, Moscow oblast, 142281 Russia

Received March 21, 2002

Abstract—The structure function F_2^c is evaluated within the charm-production model based on perturbative QCD. The results are compared with H1 and ZEUS data obtained at the HERA collider. It is shown that, for D^*-meson production, the spectator mechanism, which is independent of the flavors of the hadronic-remnant quarks, comes into play for $p_T > 10$ GeV and that, in calculating charm production in the kinematical domain studied at the HERA collider, it is not necessary to take into account the evolution of the c-quark distribution in the initial-state hadron. © *2003 MAIK "Nauka/Interperiodica".*

1. INTRODUCTION

It is well known that, over a wide region of kinematic variables, experimental data on deep-inelastic scattering are adequately described by using universal quark and gluon distributions satisfying equations that describe evolution with increasing photon virtuality Q^2. However, attempts at including heavy (c and b) quarks in the evolution equations for light quarks run into difficulties stemming from the need for considering the kinematical domain around $Q^2 \sim 4m_q^2$, where virtualities are quite high, and from the fact that heavy quarks cannot be treated in the massless approximation. An attempt at taking into account the heavy-quark contribution in the threshold region, where the effect of the phase-space factor is significant, and at matching this contribution with a solution to the usual Dokshitzer–Gribov–Lipatov–Altarelli–Parisi evolution equations at asymptotically high momenta of $Q^2 \gg 4m_q^2$ was made in [1, 2]. In what follows, we will restrict our consideration to c-quark production and use the notation introduced in [1], because it is convenient for matching various approximations at high Q^2 with the corresponding solutions at $Q^2 \sim 4m_c^2$.

The charm contribution to the deep-inelastic-scattering structure function is determined by the convolution of the parton distributions and the coefficient functions; that is,

$$\frac{1}{x}F_2^c(x,Q^2) = C_g(Q^2,\mu^2) \otimes f_g(\mu^2)[x] \qquad (1)$$
$$+ C_c(Q^2,\mu^2) \otimes f_c(\mu^2)[x] + C_q(Q^2,\mu^2) \otimes f_q(\mu^2)[x],$$

where f_i are the parton distributions in the proton and the symbol $\otimes$ denotes a convolution integral with respect to x:

$$a \otimes b[x] = \int_x^1 \frac{dz}{z} a(z) b\left(\frac{x}{z}\right).$$

For $\mu^2 < \mu_c^2$, the distribution function vanishes, $f_c(x,\mu^2) = 0$, so that the structure function F_2^c is determined completely by the photon–gluon fusion $\gamma^* g \to c\bar{c}$—that is, by the convolution integral $C_g(Q^2,\mu^2) \otimes f_g(\mu^2)$. The second term on the right-hand side of Eq. (1) describes the scattering of a virtual photon on a sea c quark from the initial hadron. The $\gamma^* c \to c$ contribution increases with Q^2, so that, at sufficiently high Q^2, it becomes dominant. The $\gamma^* q \to c\bar{c}q$ contribution is usually neglected because it is suppressed by an additional power of α_s, but we will show, in what follows, that this contribution can be significant at moderately high p_T and Q^2.

In addition to the problem of matching the domains $Q^2 \sim 4m_c^2$ and $Q^2 \gg 4m_c^2$, there is another important problem, that of contrasting theoretical predictions against experimental data.

The spectral function F_2^c was determined by the ZEUS and H1 Collaborations [3] from data on $D^{*\pm}$-meson production by taking into account only two decay modes, $D^* \to K2\pi$ and $D^* \to K4\pi$, the kinematical domains explored by these collaborations being specified by the following inequalities: $1 < Q^2 < 600$ GeV^2, $|\eta(D^*)| < 1.5$, $1.5 < p_T(D^*) < 15$ GeV, and $0.02 < y < 0.7$ (ZEUS) and $1 < Q^2 < 100$ GeV^2, $|\eta(D^*)| < 1.5$, $1.5 < p_T(D^*) <$

[1)]Institute of Nuclear Physics, Moscow State University, Vorob'evy gory, Moscow, 119899 Russia.
[*]e-mail: aber@ttk.ru
[**]e-mail: kiselev@mx.ihep.su
[***]e-mail: likhoded@mx.ihep.su

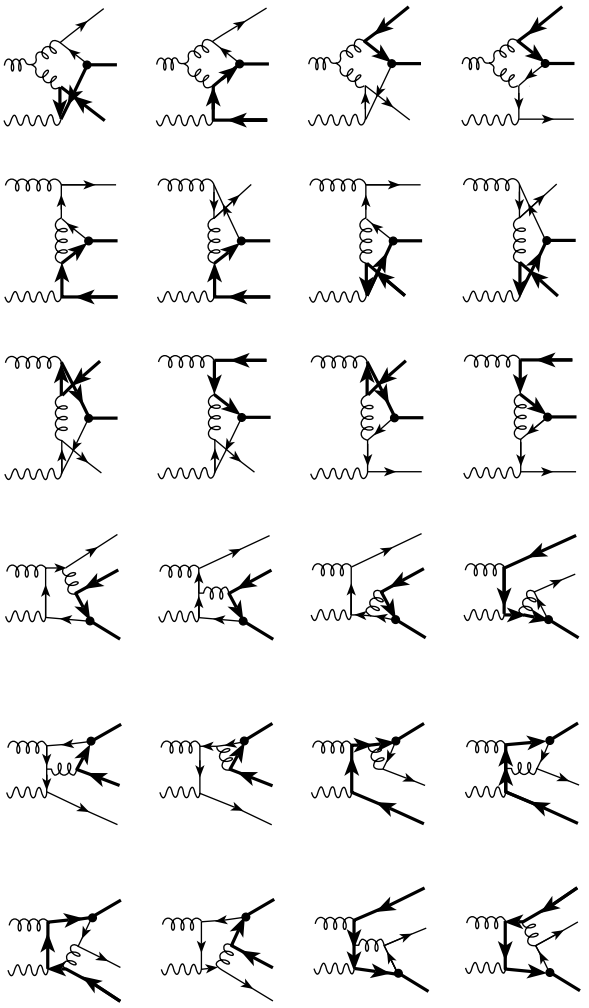

Fig. 1. Diagrams describing $c\bar{q}$ production in $\gamma^* g$ collisions in the leading order of perturbative QCD.

10 GeV, and $0.05 < y < 0.7$ (H1). Further, the cross section for charm production over the entire kinematical domain was determined from such measurements on the basis of some charm-production model.

Thus, it was the spectra of charmed hadrons detected over a kinematical domain characteristic of a specific experiment rather than spectra of c quarks that were actually measured in those experiments. Therefore, a comparison of the calculated functions $F_2^c(Q^2, x)$ with experimental data requires specifying a c-quark hadronization mechanism.

The existing procedure of hadronization is based on the application of the factorization theorem for the momentum distributions of the D^* mesons; that is,

$$\frac{d\sigma_{D^*}}{dp_T} = \frac{d\sigma_c}{dk_T} \otimes D(z), \qquad (2)$$

where $D(z)$ is the $c \to D^*$ fragmentation function and $z = p_T/k_T$. This function is usually taken in the phenomenological form proposed in [4].

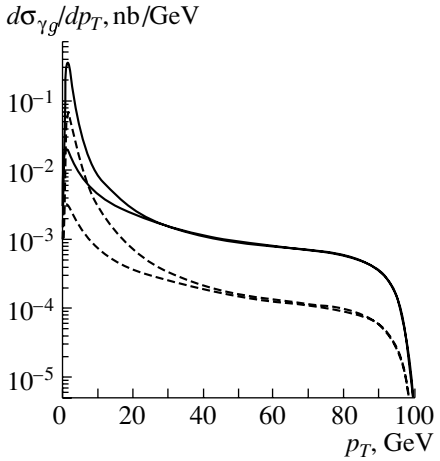

Fig. 2. Transverse-momentum distribution of the cross section for D^*-meson production in γg collisions at 200 GeV according to the calculation that takes into account all diagrams in Fig. 1 (upper curves) and according to the prediction of the fragmentation model (lower curves) for the singlet and octet contributions shown individually (solid and dashed curves, respectively).

Since the factorization theorem is no more than an approximation, formula (2) adequately describes the distributions in question only at high p_T and k_T. The application of the factorization theorem over the entire kinematical domain may lead to errors in rescaling the c-quark spectrum into the D^*-meson spectrum. This limitation of the proposed model is clearly seen in the analysis of the H1 and ZEUS data. In the pseudorapidity distributions, there is considerable excess in the proton-fragmentation region. A similar feature is observed in the distribution with respect to the variable $z_{(D^*)} = (Pp_{(D^*)})/(Pq)$, where P, $p_{(D^*)}$, and q are the 4-momenta of the proton, the D^* meson, and the virtual photon, respectively. The discrepancy between the experimental data and the predictions relying on next-to-leading-order (NLO) calculations in perturbative QCD and on formula (2) for hadronization is substantial at high $\eta_{(D^*)}$ and low $z_{(D^*)}$. To remedy this drawback, additional model assumptions are introduced in the Monte Carlo algorithms for generating events [3].

2. MODEL OF CHARM PRODUCTION

Here, we formulate a model where an attempt is made to introduce hadronization from the outset. For this purpose, we consider all $O(\alpha\alpha_s^3)$ diagrams of perturbation theory that describe the production of a $c\bar{q}$ pair having the quantum numbers of the respective charmed meson.

The complete set of such diagrams is shown in Fig. 1. According to the notation introduced in (1), we

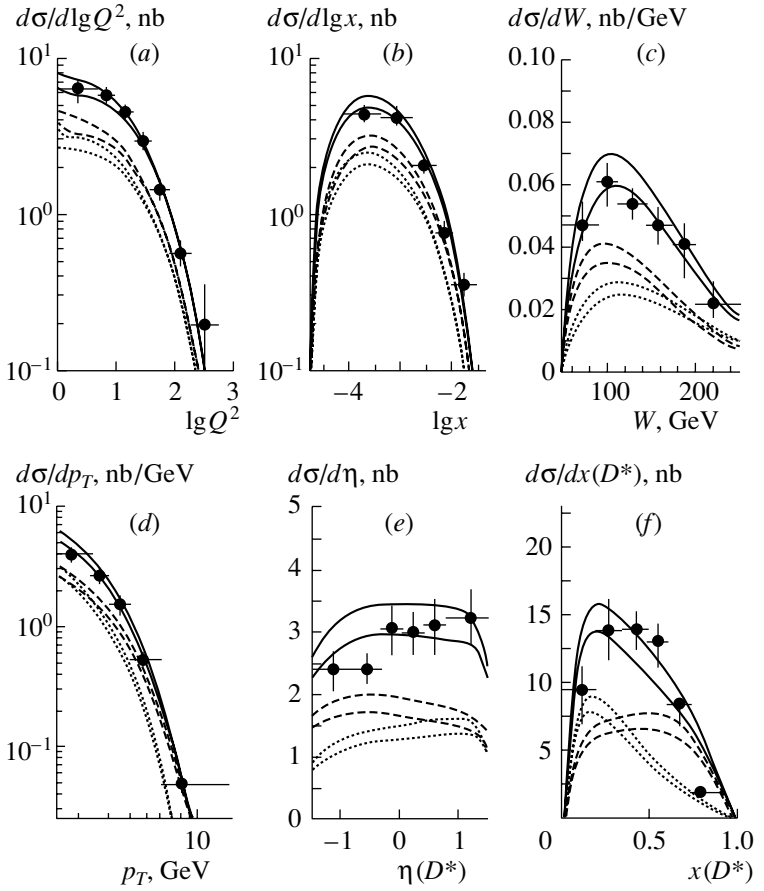

Fig. 3. Calculated differential cross sections for D^*-meson production in deep inelastic e^+p scattering with respect to (*a*) the photon virtuality (in GeV^2), (*b*) the Bjorken variable x, (*c*) the invariant mass of final-state hadrons, (*d*) the transverse momentum, (*e*) the pseudorapidity, and (*f*) the Feynman variable $x(D^*)$, along with ZEUS data. The notation for the curves is explained in the main body of the text.

restrict our consideration to the production process induced by a photon–gluon collision, $\gamma^* g \to D^* + \bar{c} + q$. That the production of a c quark is taken into account simultaneously with the production of its light partner $\bar{q}$ in the $c\bar{q}$ system requires introducing an additional nonperturbative parameter $\langle O \rangle$ that describes the fusion of the $c\bar{q}$ pair. This parameter is proportional to the D^*-meson wave function and is derived from the normalization condition involving the experimentally determined probability of $c \to D^*$ fragmentation at high transverse momenta, $W = 0.23$ [5].

The $c\bar{q}$ system can be either in a color-singlet or in a color-octet state. In our previous analysis of the charm photo- and electroproduction [6], these contributions were taken to be independent, each contribution having its own normalization factor, $\langle O_{(1)} \rangle$ or $\langle O_{(8)} \rangle$. That these factors have nearly identical values indicates that these contributions are approximately equal at low p_T, where the spectrum behaves as $1/p_T^6$, and that the color-singlet contribution is dominant in the fragmentation domain, where the spectrum decreases in proportion to $1/p_T^4$. The latter stems from the ratio of the color factors. At high p_T, both contributions go over to the fragmentation regime, behaving identically. Hadronization there is characterized by the single parameter

$$\langle O^{\mathrm{eff}} \rangle = \langle O_{(1)} \rangle + \frac{1}{8} \langle O_{(8)} \rangle.$$

It is remarkable property of the proposed model that the factorization theorem holds at high momenta; that is, formula (2) provides a good approximation for high p_T, and the hadronization process is adequately described in terms of fragmentation. With decreasing momentum, relation (2) is badly violated: there arise additional contributions depending on p_T as $1/p_T^6$, whereas this relation implies a conventional p_T dependence of the $1/p_T^4$ form.

The applicability of the factorization theorem at high p_T within our model is illustrated in Fig. 2 for the singlet and the octet contribution individually.

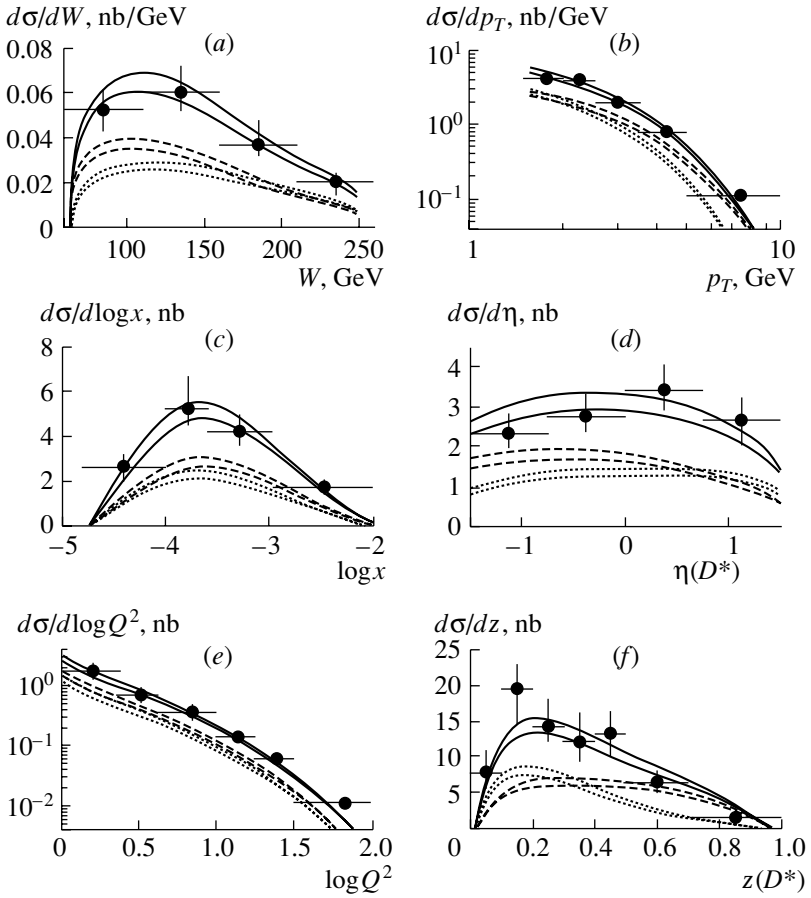

Fig. 4. Calculated differential cross sections for D^*-meson production in deep inelastic e^+p scattering with respect to (*a*) the invariant mass of final-state hadrons, (*b*) the transverse momentum, (*c*) the Bjorken variable x, (*d*) the pseudorapidity, (*e*) the photon virtuality (in GeV^2) and (*f*) the Feynman variable $z(D^*)$, along with H1 data. The notation for the curves is explained in the main body of the text.

Specifically, Fig. 2 shows the contribution of the complete set of diagrams in Fig. 1 and the contribution of fragmentation-type diagrams, which was taken in the form (2) with the fragmentation function $D(z)$ evaluated in the same approximation with the same values of the parameters $\langle O\rangle$ and m_q. The calculations were performed at the high value of $s_{\gamma g} = (p_\gamma + p_g)^2 = (200\ \mathrm{GeV})^2$, which is sufficient for the validity of the factorization condition (2).

As can be seen from Fig. 2, there exists a range of p_T values where the perturbative-recombination contribution not reducible to the form (2) is dominant. This contribution is a mere consequence of gauge invariance rather than an artifact of model assumptions. Since the p_T dependence of this contribution involves an additional factor of $1/p_T^2$, it can be neglected at high p_T, whereupon the result takes the factorized form (2).

A more detailed account of the model is given in the Appendices.

3. ELECTROPRODUCTION OF D^* MESONS

As was mentioned above, the proposed model was previously used to describe ZEUS data on charm photoproduction [7]. The fragmentation probability $W(c \to D^*)$ was determined from data on D^*-meson production in e^+e^- annihilation [5]. The parameter defining the factorization scale for the matrix elements of the quark operators $\langle O_{(1,8)}\rangle$ was set to $\mu_F = m_{D^*}$; the light-quark and the charmed-quark mass were taken to be $m_q = 0.3$ GeV and $m_c = 1.5$ GeV, respectively.

In this case, $W(c \to D^*) = 0.23$, $\langle O^{\mathrm{eff}}\rangle = 0.25\ \mathrm{GeV}^3$, and the octet-to-singlet contribution ratio is $\langle O_{(8)}\rangle/\langle O_{(1)}\rangle = 1.3$. It should be noted that the introduction of the octet contribution substantially improves the description of data, especially the description of pseudorapidity distributions, where this leads to an enhancement within the forward hemisphere (with respect to the incident proton),

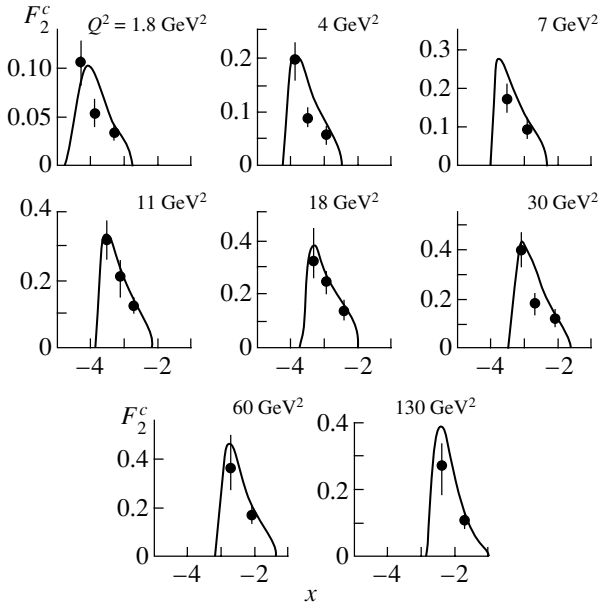

Fig. 5. ZEUS data on F_2^c, along with the predictions of the proposed model.

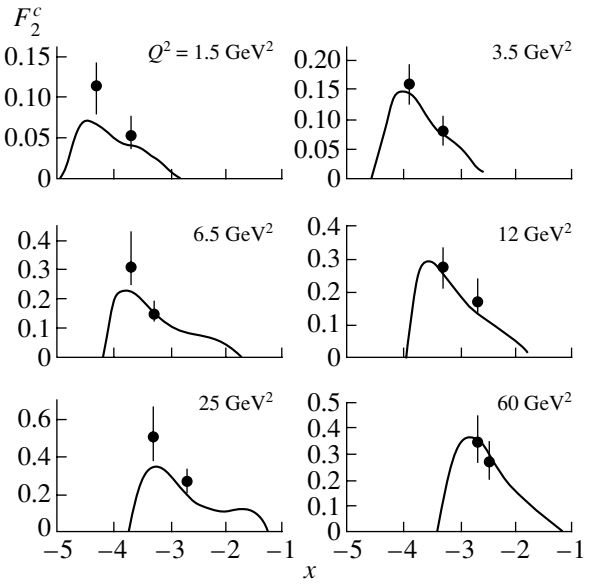

Fig. 6. H1 data on F_2^c along with the predictions of the proposed model.

whereupon a fit to data proves to be better than that which is based on NLO calculations [6].

The calculations for D^*-meson electroproduction are similar to those for photoproduction, the only difference being that the electroproduction matrix element averaged over photon and electron polarizations has the form

$$|A|^2 = \sum_{ij} \frac{k_1^i k_2^j + k_1^j k_2^i - Q^2 g^{ij}/2}{Q^4} M_i M_j^*, \qquad (3)$$

where $|A|^2$ is the square of the D^*-meson-electroproduction amplitude; M_i is the D^*-meson-photoproduction amplitude (the subscript i is the Lorentz index associated with photon polarization); k_1 and k_2 are, respectively, the initial and the final positron momentum; and $Q^2 = -(k_1 - k_2)^2$. The results of the calculations are presented in Figs. 3 and 4, where the ZEUS and H1 data, respectively, are also shown for the sake of comparison. The calculations were performed with allowance for the experimental constraints on the kinematical variables. The dashed and dotted curves represent, respectively the singlet and the octet contribution in our model, while the solid curves represent the sum of these contributions.

To fix the QCD running coupling constant in the calculations of the matrix elements, we set the renormalization scale to the value of $\mu_R = \sqrt{m_{D^*}^2 + Q^2}$ for the upper curve, to the value of $\mu_R = \sqrt{4m_{D^*}^2 + Q^2}$ for the lower curve, and to the value of $\mu_F = \sqrt{m_{D^*}^2 + Q^2}$ for the CTEQ4 parametrization of structure functions. As can be seen from the figures, the results of the calculations agree well with experimental data owing primarily to the inclusion of the octet contribution. As in the case of photoproduction, this makes it possible to improve the description of the pseudorapidity $[\eta(D^*)]$ distribution, the $z(D^*)$ distribution (measured by the H1 Collaboration), and the $x(D^*) = |\mathbf{p}^*(D^*)|/W$ distribution [measured by the ZEUS Collaboration; here, $\mathbf{p}^*(D^*)$ is the 3-momentum of the D^* meson in the reference frame comoving with the center of mass of the colliding virtual photon and proton]. Another feature peculiar to the octet contribution is that, at $\langle O_{(8)}\rangle/\langle O_{(1)}\rangle \sim 1$, it is dominated by the perturbative-recombination contribution. But in the fragmentation region, this contribution is suppressed by the color factor of

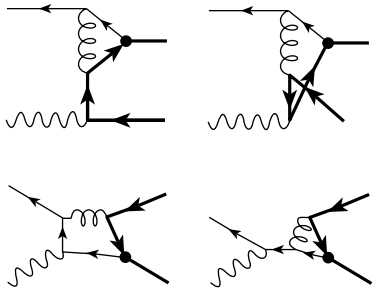

Fig. 7. Diagrams describing $c\bar{q}$ production in $\gamma^* q$ collisions in the leading order of QCD.

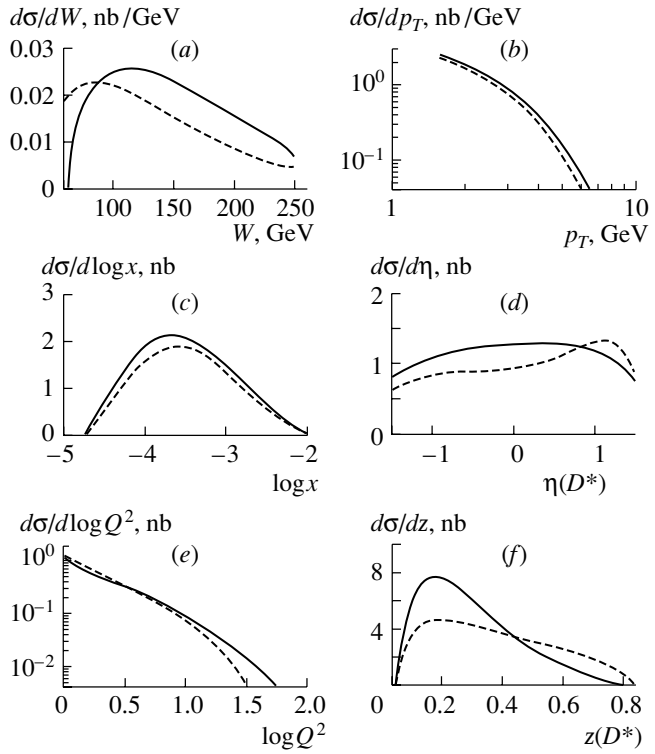

Fig. 8. Octet contribution (dashed curves) and contribution of scattering on a quark (solid curves) to D^*-meson production in deep-inelastic scattering in the H1 kinematical domain. Shown in this figure are differential distributions with respect to the same variables as in Fig. 4.

1/8, so that the color-singlet contribution becomes dominant at high transverse momenta.

Thus, we conclude that, within the proposed model, both the ZEUS data on photoproduction [7] and the H1 and ZEUS data on charm production in deep-inelastic scattering [3] can be adequately described over a wide region of kinematical variables. This provides every reason to hope that the extrapolation of experimental data to the entire region of kinematical variables is reliable. Therefore, we can compute the total rate of charm production and determine F_2^c.

4. STRUCTURE FUNCTION F_2^c

We recall that the charm contribution F_2^c to the structure function F_2 can be determined from double-differential distribution of scattered electrons for events involving charm production:

$$\frac{d^2\sigma^c(Q^2,x)}{dxdQ^2} = \frac{2\pi\alpha_s^2}{xQ^4}\left\{\left[1+(1-y)^2\right]F_2^c - y^2F_L^c(Q^2,x)\right\}. \quad (4)$$

Here, the longitudinal component F_L is neglected because of its smallness. As was indicated in the Introduction, the function F_2^c is determined from the data on D^*-meson production. In the kinematical domain not explored in current experiments, the cross section is evaluated by using an extrapolation within some model. Obviously, the cross section determined in this way is a model-dependent value. In the proposed model, one can perform such extrapolation and compare the results with what was obtained in the ZEUS and H1 experiments.

For various values of Q^2, the points in Fig. 5 represent F_2^c values obtained from experimental data and plotted versus x. These results were derived via an extrapolation of the experimental cross-section values to the entire region of kinematical variables by using the results of NLO computations and Monte Carlo codes for simulating hadronization. The curves in Fig. 5 correspond to the predictions of the proposed model, F_2^c being calculated by formula (4). The vanishing of the distributions at their ends is associated with the phase-space boundaries for the given value of the ep-interaction energy and the chosen quark masses.

The H1 data on F_2^c and the respective predictions of the model under consideration are shown in Fig. 6.

5. PERTURBATIVE RECOMBINATION

As was noted in the Introduction, the operator-product expansion (1) involves, in addition to a term

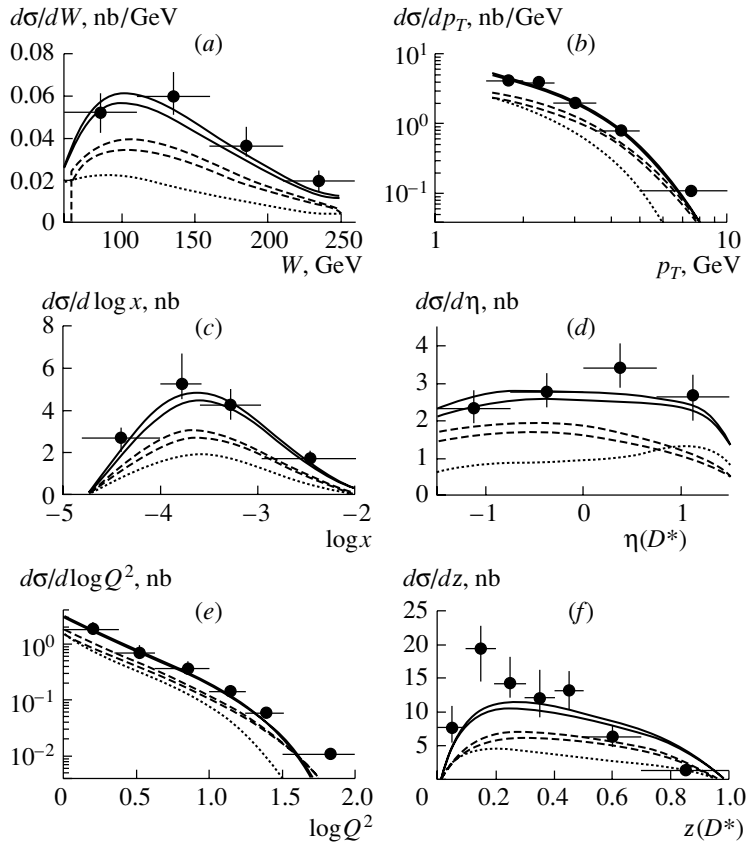

Fig. 9. H1 data, along with (solid curves) the sum of (dashed curves) the contribution from γg scattering and (dotted curves) the contribution from the scattering on a quark to the production of D^* mesons in deep-inelastic scattering. Shown in this figure are differential distributions with respect to the same variables as in Fig. 4 and for the same values of μ_R.

that corresponds to charm production in gluon–photon interaction, a term that describes charm production in photon–quark interactions. The latter is usually neglected because it is suppressed by an additional factor of α_s.

In the proposed approach, this contribution is described by the diagrams in Fig. 7.

For this set of diagrams, the cross section for the production of a color-octet state differs from the cross section for the production of a color-singlet state only by the color factor of 1/8. Therefore, we will consider only singlet production.

A recent analysis of these contributions revealed that, at high transverse momenta p_T, they are suppressed by an additional factor of $1/p_T^2$. There is no such suppression at low p_T, and the differential cross section for $(\bar{c}q)$ production at the q-quark-production angle $\theta = 0$ involves a large numerical coefficient in relation to conventional photon–gluon production [8]:

$$\frac{d\hat{\sigma}(\gamma + q \to (\bar{c}q) + c)}{d\hat{\sigma}(\gamma + g \to \bar{c}c)} \simeq \frac{256\pi}{81}\alpha_s. \qquad (5)$$

Thus, the large numerical factor compensates for the smallness of α_s. At the same time, the cross section at the production angle of $\theta = \pi$ is suppressed by an additional factor inversely proportional to energy. It is also important that the contribution under consideration depends only weakly on the light-quark mass and does not vanish for $m_q \to 0$.

The contribution from production on valence quarks in the primary proton was used [6] to evaluate the possible asymmetry in the photoproduction of D^+/D^- and $D^0/\bar{D}^0$. In both the ZEUS and the H1 kinematical domain, the experimental value of the asymmetry was about 2 to 3%, which is on the order of the experimental errors. However, the asymmetry increases as the rapidity interval over which the measurements are performed is extended. The contribution under consideration becomes significant at low energies of γp collisions, yielding an asymmetry in the production rates that is commensurate with the experimental asymmetries both for particles involving valence quarks of initial-state hadrons and for particles involving no such quarks [8]. If one assumes that the production asymmetry is due to perturbative recombination, which involves an extra factor of $1/p_T^2$

in relation to the leading contributions, the asymmetry must therefore decrease with increasing p_T. If, on the other hand, this asymmetry is associated with the interaction of c quarks with the valence-quark remnant of the initial-state hadron, then there must be a contribution from the respective interaction with sea quarks. Such a contribution does indeed exist; surprisingly, it is similar to the octet contribution in the present model both in form and in absolute value. In contrast to the octet contribution, however, this quark contribution does not contain an additional normalization factor. The two contributions in question to deep-inelastic D^*-meson production are compared in Fig. 8 over the H1 kinematical domain. It can be seen that, apart from a coefficient close to unity, the $\log x$ and p_T distributions of these two contributions coincide over the entire region under consideration. The Q^2 distributions also behave almost identically up to $Q^2 = 10\,\mathrm{GeV}^2$. The distinctions between the W, $\eta(D^*)$, and $z(D^*)$ distributions are greater, but these distributions for the different contributions are qualitatively similar. The sum of the contributions from the γg and $\gamma\bar{d}$ production mechanisms to the $c\bar{d}$ production in a singlet state throughout the H1 kinematical domain is shown in Fig. 9. It is seen that the description of the data is not poorer, at least at moderate Q^2, than in the case where the octet contribution is taken into account.

Thus, the singlet contribution to the production of $c\bar{d}$ pairs will suffice for an adequate description of data on charm photo- and electroproduction at the HERA energies. Significant contributions to the production of singlet states at these energies come from both photon–gluon and photon–quark scattering subprocesses as classified in Section 1, the contribution of the latter subprocess becoming less important with decreasing energy. Serious arguments in favor of the importance of the sea-quark contribution to charm production were adduced by Braaten *et al.* [8], who were able to describe the asymmetry of charmed-meson production in the E687 and E691 experiments successfully.

6. CONCLUSION

The proposed model of charm production is based both on perturbation theory, which adequately describes heavy-quark production, and on a nonperturbative approach to the formation of a hadron from quarks. This model provides a good fit to existing data on the photo- and electroproduction of charmed particles throughout the entire range of kinematical variables.

The results of the present study can be summarized as follows:

(i) At high transverse momenta of the $c\bar{d}$ system, the results coincide with the prediction of the model based on the factorization theorem (2). To put it differently, the momentum distribution of the pair $c\bar{d}$ can be represented as a convolution of the heavy-quark spectrum with the fragmentation function evaluated to the same order of perturbation theory.

(ii) The main contribution to the inclusive spectrum at low transverse momenta and low values of Q^2 comes from diagrams that decrease in proportion to $1/p_T^6$ with p_T (rather than from those that decrease in proportion to $1/p_T^4$, which is what occurs in the fragmentation region). Here, $g\gamma$ and $q\gamma$ collisions make commensurate contributions to the production processes under consideration.

(iii) The inclusion of the second term in expansion (1) ($C_c \otimes f_c$) is not yet needed in describing the main contributions to the structure function F_2^c. According the results presented in [1], its role is expected to be significant at high Q^2; in terms of the present model under study, this term takes into account higher corrections to the Born terms discussed above.

Thus, our main conclusion is as follows: in D^*-meson production, the spectator mechanism, which is independent of the flavors of the quarks in the remnant of the initial-state hadron, is dominant for $p_T > 10$ GeV. At lower transverse momenta, the main contribution comes from the interaction with the hadron remnant. Its valence part determines the observed flavor dependence of the asymmetry in the charm yield.

ACKNOWLEDGMENTS

This work was supported in part by the Russian Foundation for Basic Research (project nos. 01-02-99315, 01-02-16585, and 00-15-96645), the Ministry for Higher Education of the Russian Federation (grant no. 00-3.3-62), and the CRDF (grant no. CRDF-M0-011-0).

APPENDIX 1

Hard Production of Four Quarks in the Gluon–Photon Subprocess

In the present model, it is assumed that, in the case of a hard process, a heavy and a light valence quark are produced simultaneously.

In the tree approximation, the subprocess $g(p_g) + \gamma(p_\gamma) \to c(q_c) + \bar{c}(q_{\bar{c}}) + d(q_d) + \bar{d}(q_{\bar{d}})$ can be described by 24 Feynman diagrams in Fig. 1, where it is necessary to remove the vertices corresponding to $(c\bar{d})$-quarkonium production. (In this figure, thick

and thin fermion lines denote c and d quarks, respectively.) In this study, the amplitudes are computed by means of a straightforward numerical evaluation of the products of γ matrices, spinors, and polarization vectors.

Let us introduce the notation

$$q_c^2 = q_{\bar{c}}^2 = m_c^2, \qquad q_d^2 = q_{\bar{d}}^2 = m_d^2, \tag{A.1}$$
$$q_{c\bar{c}} = -q_c - q_{\bar{c}}, \quad q_{d\bar{d}} = -q_d - q_{\bar{d}}, \quad p_{g\gamma} = p_g + p_\gamma,$$
$$k_{g,c\bar{c}} = p_g + q_{c\bar{c}}, \quad k_{g,d\bar{d}} = p_g + q_{d\bar{d}}.$$

The three-gluon vertex can be represented in the form

$$\Gamma^\mu(p_a, p_b, \epsilon_a, \epsilon_b) = -((2p_a + p_b)\epsilon_b)\epsilon_a^\mu \tag{A.2}$$
$$+ (p_a - p_b)^\mu(\epsilon_a\epsilon_b) + ((2p_b + p_a)\epsilon_a)\epsilon_b^\mu,$$
$$\Gamma'^\mu(p_a, p_b, \epsilon_a, \epsilon_b) = \Gamma^\mu(p_a, p_b, \epsilon_a, \epsilon_b)/(p_a + p_b)^2.$$

The two-quark currents are defined as

$$J^\mu_{c\bar{c}} = \frac{\bar{u}(q_c)\gamma^\mu v(q_{\bar{c}})}{q^2_{c\bar{c}}}, \quad J^\mu_{d\bar{d}} = \frac{\bar{u}(q_d)\gamma^\mu v(q_{\bar{d}})}{q^2_{d\bar{d}}}. \tag{A.3}$$

For the case of photoproduction, we also introduce the auxiliary spinors

$$\bar{u}_{c(d)g(\gamma)} = \bar{u}(q_{c(d)})\hat{\epsilon}_{g(\gamma)}\frac{(\hat{q}_{c(d)} - \hat{p}_{g(\gamma)} + m_{c(d)})}{(q_{c(d)} - p_{g(\gamma)})^2 - m^2_{c(d)}}, \tag{A.4}$$

$$v_{\bar{c}(\bar{d})g(\gamma)} = \frac{(\hat{p}_{g(\gamma)} - \hat{q}_{\bar{c}(\bar{d})} + m_{\bar{c}(\bar{d})})}{(p_{g(\gamma)} - q_{\bar{c}(\bar{d})})^2 - m^2_{\bar{c}(\bar{d})}}\hat{\epsilon}_{g(\gamma)},$$

$$\bar{u}_{c,d\bar{d}} = \frac{\bar{u}(q_c)\hat{J}_{d\bar{d}}(\hat{q}_c - \hat{q}_{d\bar{d}} + m_c)}{(q_c - q_{d\bar{d}})^2 - m_c^2},$$

$$\bar{u}_{d,c\bar{c}} = \frac{\bar{u}(q_d)\hat{J}_{c\bar{c}}(\hat{q}_d - \hat{q}_{c\bar{c}} + m_d)}{(q_d - q_{c\bar{c}})^2 - m_d^2},$$

$$v_{\bar{c},d\bar{d}} = \frac{(\hat{q}_{d\bar{d}} - \hat{q}_{\bar{c}} + m_c)\hat{J}_{d\bar{d}}v(q_{\bar{c}})}{(q_{d\bar{d}} - q_{\bar{c}})^2 - m_c^2},$$

$$v_{\bar{d},c\bar{c}} = \frac{(\hat{q}_{c\bar{c}} - \hat{q}_{\bar{d}} + m_d)\hat{J}_{c\bar{c}}v(q_{\bar{d}})}{(q_{c\bar{c}} - q_{\bar{d}})^2 - m_d^2}.$$

The gluon and photon polarization vectors are denoted by ϵ_g and ϵ_γ, respectively.

The summation of the matrix element squared is performed over the orthonormalized gluon polarization states

$$\epsilon' = (0, 1, 0, 0), \qquad \epsilon'' = (0, 0, 1, 0).$$

It should be noted that $\epsilon'^2 = \epsilon''^2 = -1$ and that $p \cdot \epsilon = 0$, where p is the gluon 4-momentum.

In the case of deep-inelastic production, the photon is off the mass shell; therefore, the matrix $\hat{\epsilon}_\gamma$ in (A.4) must be replaced by γ^i. Hence, the resulting matrix element has one free Lorentz index; the product of the matrix element and the photon density must be contracted over this index by formula (3).

The notation for the color indices is as follows: the superscripts j_g denote the color states of the gluon, while the subscripts i_c, $i_{\bar{c}}$, i_d, and $i_{\bar{d}}$ denote the color states of the $c, \bar{c}, d$, and $\bar{d}$ quarks.

By e_c and e_q, we denote the charges of the c and q quarks, respectively.

In the Feynman gauge, the contributions of the respective diagrams to the amplitude are given by (the coefficients in braces are color factors)

$$T_1 = e_c \cdot \bar{u}(q_d)\hat{\Gamma}'(p_g, q_{c\bar{c}}, \epsilon_g, J_{c\bar{c}})v_{\bar{d}\gamma} \tag{A.5}$$
$$\times \{if^{n_1n_2j_g}t^{n_1}_{i_ci_{\bar{c}}}t^{n_2}_{i_di_{\bar{d}}}\},$$

$$T_2 = e_c \cdot \bar{u}_{d\gamma}\hat{\Gamma}'(p_g, q_{c\bar{c}}, \epsilon_g, J_{c\bar{c}})v(q_{\bar{d}}) \tag{A.6}$$
$$\times \{if^{n_1n_2j_g}t^{n_1}_{i_ci_{\bar{c}}}t^{n_2}_{i_di_{\bar{d}}}\},$$

$$T_3 = e_q \cdot \bar{u}(q_c)\hat{\Gamma}'(p_g, q_{d\bar{d}}, \epsilon_g, J_{d\bar{d}})v_{\bar{c}\gamma} \tag{A.7}$$
$$\times \{if^{n_1n_2j_g}t^{n_1}_{i_di_{\bar{d}}}t^{n_2}_{i_ci_{\bar{c}}}\},$$

$$T_4 = e_q \cdot \bar{u}_{c\gamma}\hat{\Gamma}'(p_g, q_{d\bar{d}}, \epsilon_g, J_{d\bar{d}})v(q_{\bar{c}}) \tag{A.8}$$
$$\times \{if^{n_1n_2j_g}t^{n_1}_{i_di_{\bar{d}}}t^{n_2}_{i_ci_{\bar{c}}}\},$$

$$T_5 = e_c \cdot \bar{u}_{cg}\gamma^\alpha v(q_{\bar{c}})\bar{u}(q_d)\gamma_\alpha v_{\bar{d}\gamma}/k^2_{g,c\bar{c}} \tag{A.9}$$
$$\times \{t^{j_g}_{i_cl}t^n_{li_{\bar{c}}}t^n_{i_di_{\bar{d}}}\},$$

$$T_6 = e_c \cdot \bar{u}(q_c)\gamma^\alpha v_{\bar{c}g}\bar{u}(q_d)\gamma_\alpha v_{\bar{d}\gamma}/k^2_{g,c\bar{c}} \tag{A.10}$$
$$\times \{t^n_{i_cl}t^{j_g}_{li_{\bar{c}}}t^n_{i_di_{\bar{d}}}\},$$

$$T_7 = e_c \cdot \bar{u}_{cg}\gamma^\alpha v(q_{\bar{c}})\bar{u}_{d\gamma}\gamma_\alpha v(q_{\bar{d}})/k^2_{g,c\bar{c}} \tag{A.11}$$
$$\times \{t^{j_g}_{i_cl}t^n_{li_{\bar{c}}}t^n_{i_di_{\bar{d}}}\},$$

$$T_8 = e_c \cdot \bar{u}(q_c)\gamma^\alpha v_{\bar{c}g}\bar{u}_{d\gamma}\gamma_\alpha v(q_{\bar{d}})/k^2_{g,c\bar{c}} \tag{A.12}$$
$$\times \{t^n_{i_cl}t^{j_g}_{li_{\bar{c}}}t^n_{i_di_{\bar{d}}}\},$$

$$T_9 = e_q \cdot \bar{u}_{dg}\gamma^\alpha v(q_{\bar{d}})\bar{u}(q_c)\gamma_\alpha v_{\bar{c}\gamma}/k^2_{g,d\bar{d}} \tag{A.13}$$
$$\times \{t^n_{i_ci_{\bar{c}}}t^{j_g}_{i_dl}t^n_{li_{\bar{d}}}\},$$

$$T_{10} = e_q \cdot \bar{u}(q_d)\gamma^\alpha v_{\bar{d}g}\bar{u}(q_c)\gamma_\alpha v_{\bar{c}\gamma}/k^2_{g,d\bar{d}} \tag{A.14}$$
$$\times \{t^n_{i_ci_{\bar{c}}}t^n_{i_dl}t^{j_g}_{li_{\bar{d}}}\},$$

$$T_{11} = e_q \cdot \bar{u}_{dg}\gamma^\alpha v(q_{\bar{d}})\bar{u}_{c\gamma}\gamma_\alpha v(q_{\bar{c}})/k^2_{g,d\bar{d}} \tag{A.15}$$
$$\times \{t^n_{i_ci_{\bar{c}}}t^{j_g}_{i_dl}t^n_{li_{\bar{d}}}\},$$

$$T_{12} = e_q \cdot \bar{u}(q_d)\gamma^\alpha v_{\bar{d}g}\bar{u}_{c\gamma}\gamma_\alpha v(q_{\bar{c}})/k^2_{g,d\bar{d}} \tag{A.16}$$
$$\times \{t^n_{i_ci_{\bar{c}}}t^n_{i_dl}t^{j_g}_{li_{\bar{d}}}\},$$

$$T_{13} = e_q \cdot \bar{u}_{c,d\bar{d}}\hat{\epsilon}_g v_{\bar{c}\gamma} \cdot \{t^n_{i_cl}t^{j_g}_{li_{\bar{c}}}t^n_{i_di_{\bar{d}}}\}, \tag{A.17}$$

$$T_{14} = e_q \cdot \bar{u}_{cg}\hat{J}_{d\bar{d}}v_{\bar{c}\gamma} \cdot \{t^{j_g}_{i_cl}t^n_{li_{\bar{c}}}t^n_{i_di_{\bar{d}}}\}, \tag{A.18}$$

$$T_{15} = e_q \cdot \bar{u}_{cg}\hat{\epsilon}_\gamma v_{\bar{c},d\bar{d}} \cdot \{t^{j_g}_{i_c l} t^n_{l i_{\bar{c}}} t^n_{i_d i_{\bar{d}}}\}, \quad (A.19)$$

$$T_{16} = e_c \cdot \bar{u}_{c,d\bar{d}}\hat{\epsilon}_\gamma v_{\bar{c}g} \cdot \{t^n_{i_c l} t^{j_g}_{l i_{\bar{c}}} t^n_{i_d i_{\bar{d}}}\}, \quad (A.20)$$

$$T_{17} = e_q \cdot \bar{u}_{c\gamma}\hat{J}_{d\bar{d}} v_{\bar{c}g} \cdot \{t^n_{i_c l} t^{j_g}_{l i_{\bar{c}}} t^n_{i_d i_{\bar{d}}}\}, \quad (A.21)$$

$$T_{18} = e_q \cdot \bar{u}_{c\gamma}\hat{\epsilon}_g v_{\bar{c},d\bar{d}} \cdot \{t^{j_g}_{i_c l} t^n_{l i_{\bar{c}}} t^n_{i_d i_{\bar{d}}}\}, \quad (A.22)$$

$$T_{19} = e_c \cdot \bar{u}_{d,c\bar{c}}\hat{\epsilon}_g v_{\bar{d}\gamma} \cdot \{t^n_{i_d l} t^{j_g}_{l i_{\bar{d}}} t^n_{i_c i_{\bar{c}}}\}, \quad (A.23)$$

$$T_{20} = e_c \cdot \bar{u}_{dg}\hat{J}_{c\bar{c}} v_{\bar{d}\gamma} \cdot \{t^{j_g}_{i_d l} t^n_{l i_{\bar{d}}} t^n_{i_c i_{\bar{c}}}\}, \quad (A.24)$$

$$T_{21} = e_c \cdot \bar{u}_{dg}\hat{\epsilon}_\gamma v_{\bar{d},c\bar{c}} \cdot \{t^{j_g}_{i_d l} t^n_{l i_{\bar{d}}} t^n_{i_c i_{\bar{c}}}\}, \quad (A.25)$$

$$T_{22} = e_q \cdot \bar{u}_{d,c\bar{c}}\hat{\epsilon}_\gamma v_{\bar{d}g} \cdot \{t^n_{i_d l} t^{j_g}_{l i_{\bar{d}}} t^n_{i_c i_{\bar{c}}}\}, \quad (A.26)$$

$$T_{23} = e_c \cdot \bar{u}_{d\gamma}\hat{J}_{c\bar{c}} v_{\bar{d}g} \cdot \{t^n_{i_d l} t^{j_g}_{l i_{\bar{d}}} t^n_{i_c i_{\bar{c}}}\}, \quad (A.27)$$

$$T_{24} = e_c \cdot \bar{u}_{d\gamma}\hat{\epsilon}_g v_{\bar{d},c\bar{c}} \cdot \{t^{j_g}_{i_d l} t^n_{l i_{\bar{d}}} t^n_{i_c i_{\bar{c}}}\}. \quad (A.28)$$

The spinor basis is chosen to be formed by two independent states characterized by specific spin projections onto the z axis in the quark rest frame. In the computations, we have used the Dirac representation of the γ matrices and taken the spinors involved in the explicit form

$$u(p,+) = \frac{1}{\sqrt{E+m}} \begin{pmatrix} E+m \\ 0 \\ p_z \\ p_x + ip_y \end{pmatrix}, \quad (A.29)$$

$$u(p,-) = \frac{1}{\sqrt{E+m}} \begin{pmatrix} 0 \\ E+m \\ p_x - ip_y \\ -p_z \end{pmatrix},$$

$$v(p,+) = -\frac{1}{\sqrt{E+m}} \begin{pmatrix} p_z \\ p_x + ip_y \\ 0 \\ E+m \end{pmatrix},$$

$$v(p,-) = \frac{1}{\sqrt{E+m}} \begin{pmatrix} p_x - ip_y \\ p_z \\ 0 \\ E+m \end{pmatrix}.$$

The γ matrices in the Dirac representation have the form

$$\gamma^0 = \begin{pmatrix} 1 & 0 \\ 0 & -1 \end{pmatrix}, \qquad \boldsymbol{\gamma} = \begin{pmatrix} 0 & \boldsymbol{\sigma} \\ -\boldsymbol{\sigma} & 0 \end{pmatrix},$$

$$\boldsymbol{\sigma} = \{\sigma_x, \sigma_y, \sigma_z\}$$

$$= \left\{ \begin{pmatrix} 0 & 1 \\ 1 & 0 \end{pmatrix}, \quad \begin{pmatrix} 0 & -i \\ i & 0 \end{pmatrix}, \quad \begin{pmatrix} 1 & 0 \\ 0 & -1 \end{pmatrix} \right\}.$$

The Gell-Mann matrices are given by

$$\lambda^1 = \begin{pmatrix} 0 & 1 & 0 \\ 1 & 0 & 0 \\ 0 & 0 & 0 \end{pmatrix}, \qquad \lambda^2 = \begin{pmatrix} 0 & -i & 0 \\ i & 0 & 0 \\ 0 & 0 & 0 \end{pmatrix},$$

$$\lambda^3 = \begin{pmatrix} 1 & 0 & 0 \\ 0 & -1 & 0 \\ 0 & 0 & 0 \end{pmatrix}, \qquad \lambda^4 = \begin{pmatrix} 0 & 0 & 1 \\ 0 & 0 & 0 \\ 1 & 0 & 0 \end{pmatrix},$$

$$\lambda^5 = \begin{pmatrix} 0 & 0 & -i \\ 0 & 0 & 0 \\ i & 0 & 0 \end{pmatrix}, \qquad \lambda^6 = \begin{pmatrix} 0 & 0 & 0 \\ 0 & 0 & 1 \\ 0 & 1 & 0 \end{pmatrix},$$

$$\lambda^7 = \begin{pmatrix} 0 & 0 & 0 \\ 0 & 0 & -i \\ 0 & i & 0 \end{pmatrix}, \qquad \lambda^8 = \frac{1}{\sqrt{3}} \begin{pmatrix} 1 & 0 & 0 \\ 0 & 1 & 0 \\ 0 & 0 & -2 \end{pmatrix}.$$

The t matrices are defined by the equation $t^i = \lambda^i/2$.

The values of the antisymmetric structure constants f_{abc} used in the computations are

$$f_{123} = 1,$$
$$f_{147} = -f_{156} = f_{246} = f_{257} = f_{345} = -f_{367} = 1/2,$$
$$f_{458} = f_{678} = \sqrt{3}/2.$$

APPENDIX 2

Soft Process of $(c\bar{d})$-Quarkonium Formation through the Fusion of c and $\bar{d}$ Quarks

In describing $(c\bar{d})$-quarkonium formation from c and $\bar{d}$ quarks, we assume that the parton distributions in the D^* meson involve terms associated with valence quarks and that the c and $\bar{d}$ quarks produced in a hard process go over to valence quarks in the meson. In the infinite-momentum frame, the distributions of valence quarks can be represented as

$$f^v_c(x, p_\perp) = f_c(x, p_\perp) - f_{\bar{c}}(x, p_\perp),$$

$$f^v_{\bar{d}}(x,p_\perp) = f_{\bar{d}}(x,p_\perp) - f_d(x,p_\perp).$$

The momentum fractions carried away by valence quarks have the form

$$\langle x^v_c\rangle = \int d^2p_\perp dx x\cdot f^v_c(x,p_\perp) \approx \frac{m_c}{m_{D^*}}, \quad \text{(A.30)}$$

$$\langle x^v_{\bar{d}}\rangle = \int d^2p_\perp dx x\cdot f^v_{\bar{d}}(x,p_\perp) \approx \frac{\bar{\Lambda}}{m_{D^*}}, \quad \text{(A.31)}$$

where $\bar{\Lambda}$ is the quark-binding energy in the meson, and satisfy the approximate relation

$$\langle x^v_c\rangle + \langle x^v_{\bar{d}}\rangle \approx 1. \quad \text{(A.32)}$$

In our calculations, we disregard the spread of the momentum fraction carried away by quarks; that is, we assume that Eqs. (A.30)–(A.32) are exact. We also assume that the effective light-quark mass is about $\bar{\Lambda}$.

In the doubly heavy quarkonium, the singlet component of the state of the valence-quark pair is dominant, because the octet component is suppressed in proportion to the third power of the relative velocity of the quarks [9]. This is not so for the $(c\bar{d})$ quarkonium; therefore, both components must be taken into account in that case.

The quantities $\langle O_{(1)}\rangle$ and $\langle O_{(8)}\rangle$, which, in our model, describe the hadronization of the singlet and the octet quark-pair state, cannot be evaluated within perturbation theory since they involve interactions at the scale $\Lambda_{\rm QCD}$. In the nonrelativistic potential model, they would correspond to the square of the wave function at the origin: $\langle O_{(1,8)}\rangle|_{\rm NR} = |\Psi(0)|^2$. In the model under study, we have

$$\langle O_{(1)}\rangle = \frac{1}{12M_{D^*}}\left(-g^{\mu\nu} + \frac{p^\mu p^\nu}{M^2_{D^*}}\right) \quad \text{(A.33)}$$
$$\times \langle D^*(p)|(\bar{c}\gamma_\mu d)(\bar{d}\gamma_\nu c)|D^*(p)\rangle,$$

$$\langle O_{(8)}\rangle = \frac{1}{8M_{D^*}}\left(-g^{\mu\nu} + \frac{p^\mu p^\nu}{M^2_{D^*}}\right) \quad \text{(A.34)}$$
$$\times \langle D^*(p)|(\bar{c}\gamma_\mu \lambda^a d)(\bar{d}\gamma_\nu \lambda^b c)|D^*(p)\rangle\frac{\delta^{ab}}{8}.$$

Within the proposed model, the probability that the D^* meson is produced through the fragmentation of a c quark in e^+e^- annihilation, $W(c\to D^*)$, is expressed in terms of the parameters $\langle O_{(1)}\rangle$ and $\langle O_{(8)}\rangle$ as

$$W(c\to D^*) = \int_0^1 D_{c\to D^*}(z)dz \quad \text{(A.35)}$$
$$= \frac{\alpha_s^2(\mu_R)\langle O^{\rm eff}(\mu_R)\rangle}{m_d^3} I\left(\frac{m_d}{m_d+m_c}\right),$$

where $\langle O^{\rm eff}(\mu_R)\rangle = \langle O_{(1)}\rangle + \langle O_{(8)}\rangle/8$ and

$$I(r) = \frac{8}{27}\left[\frac{24+109r-126r^2-174r^3-89r^4}{15(1-r)^5}\right. \quad \text{(A.36)}$$
$$\left. + \frac{r(7-4r-3r^2+10r^3+2r^4)}{(1-r)^6}\ln r\right].$$

REFERENCES

1. J. C. Collins, A. D. Martin, and M. G. Ryskin, in *Proceedings of the Low-x Physics Conference, Madrid, 1997*, p. 134; hep-ph/9709440; Eur. Phys. J. C **2**, 287 (1998).
2. J. Amundson *et al.*, hep-ph/0005221; J. High Energy Phys. **0010**, 031 (2000); J. C. Collins and W. Tung, Nucl. Phys. B **278**, 934 (1986); F. I. Olness and W. Tung, Nucl. Phys. B **308**, 813 (1988); M. A. Aivazis, F. I. Olness, and W. Tung, Phys. Rev. D **50**, 3085 (1994); M. A. Aivazis *et al.*, Phys. Rev. D **50**, 3102 (1994); J. C. Collins, Phys. Rev. D **58**, 094002 (1998); W. K. Tung, in *Proceedings of the 5th International Workshop on Deep-Inelastric Scattering, Chicago, 1997*; R. S. Thorne and R. G. Roberts, Phys. Rev. D **57**, 6871 (1998); M. Buza *et al.*, Eur. Phys. J. C **1**, 301 (1998); M. Cacciari, M. Greco, and P. Nason, J. High Energy Phys. **9805**, 007 (1998); A. Chuvakin, J. Smith, and W. L. van Neerven, Phys. Rev. D **61**, 096004 (2000); A. V. Kisselev, V. A. Petrov, and R. A. Ryutin, hep-ph/0109271.
3. ZEUS Collab. (J. Breitweg *et al.*), Eur. Phys. J. C **12**, 35 (2000); H1 Collab. (C. Adloff *et al.*), hep-ex/0108039; submitted to Phys. Lett. B.
4. C. Peterson *et al.*, Phys. Rev. D **27**, 105 (1983); V. G. Kartvelishvili, A. K. Likhoded, and V. A. Petrov, Phys. Lett. B **78B**, 615 (1978).
5. OPAL Collab. (K. Akerstaff *et al.*), Eur. Phys. J. C **1**, 439 (1998); L. Gladilin, hep-ph/9912064; ALEPH Collab. (R. Barate *et al.*), Eur. Phys. J. C **16**, 597 (2000).
6. A. V. Berezhnoy, V. V. Kiselev, and A. K. Likhoded, Phys. Rev. D **62**, 074013 (2000).
7. ZEUS Collab. (J. Breitweg *et al.*), Eur. Phys. J. C **6**, 67 (1999).
8. E. Braaten, Y. Jia, and T. Mehen, hep-ph/0108201.
9. G. T. Bodwin, E. Braaten, and G. P. Lepage, Phys. Rev. D **51**, 1125 (1995); T. Mannel and G. A. Shuller, Z. Phys. C **67**, 159 (1995); E. Braaten, S. Fleming, and T. C. Yuan, Annu. Rev. Nucl. Part. Sci. **46**, 197 (1996).

Translated by R. Rogalyov